

Mechanisms and Machine Science

Doina Pisla
Burkhard Corves
Calin Vaida *Editors*

New Trends in Mechanism and Machine Science

EuCoMeS



 Springer

The Springer logo features a white chess knight piece on a pedestal, positioned to the left of the word "Springer" in a white serif font.

Mechanisms and Machine Science

Volume 89

Series Editor

Marco Ceccarelli, Department of Industrial Engineering, University of Rome Tor Vergata, Roma, Italy

Editorial Boards

Alfonso Hernandez, Mechanical Engineering, University of the Basque Country, Bilbao, Vizcaya, Spain

Tian Huang, Department of Mechatronical Engineering, Tianjin University, Tianjin, China

Yukio Takeda, Mechanical Engineering, Tokyo Institute of Technology, Tokyo, Japan

Burkhard Corves, Institute of Mechanism Theory, Machine Dynamics and Robotics, RWTH Aachen University, Aachen, Nordrhein-Westfalen, Germany

Sunil Agrawal, Department of Mechanical Engineering, Columbia University, New York, NY, USA

This book series establishes a well-defined forum for monographs, edited Books, and proceedings on mechanical engineering with particular emphasis on MMS (Mechanism and Machine Science). The final goal is the publication of research that shows the development of mechanical engineering and particularly MMS in all technical aspects, even in very recent assessments. Published works share an approach by which technical details and formulation are discussed, and discuss modern formalisms with the aim to circulate research and technical achievements for use in professional, research, academic, and teaching activities.

This technical approach is an essential characteristic of the series. By discussing technical details and formulations in terms of modern formalisms, the possibility is created not only to show technical developments but also to explain achievements for technical teaching and research activity today and for the future.

The book series is intended to collect technical views on developments of the broad field of MMS in a unique frame that can be seen in its totality as an Encyclopaedia of MMS but with the additional purpose of archiving and teaching MMS achievements. Therefore, the book series will be of use not only for researchers and teachers in Mechanical Engineering but also for professionals and students for their formation and future work.

The series is promoted under the auspices of International Federation for the Promotion of Mechanism and Machine Science (IFTToMM).

Prospective authors and editors can contact Mr. Pierpaolo Riva (publishing editor, Springer) at: pierpaolo.riva@springer.com

Indexed by SCOPUS and Google Scholar.

More information about this series at <http://www.springer.com/series/8779>

Doina Pisla · Burkhard Corves ·
Calin Vaida
Editors

New Trends in Mechanism and Machine Science

EuCoMeS

 Springer

Editors

Doina Pislă
Technical University of Cluj-Napoca
Cluj-Napoca, Romania

Burkhard Corves
IGMR
RWTH Aachen University
Aachen, Germany

Calin Vaida
Technical University of Cluj-Napoca
Cluj-Napoca, Romania

ISSN 2211-0984 ISSN 2211-0992 (electronic)
Mechanisms and Machine Science
ISBN 978-3-030-55060-8 ISBN 978-3-030-55061-5 (eBook)
<https://doi.org/10.1007/978-3-030-55061-5>

© The Editor(s) (if applicable) and The Author(s), under exclusive license
to Springer Nature Switzerland AG 2020

This work is subject to copyright. All rights are solely and exclusively licensed by the Publisher, whether the whole or part of the material is concerned, specifically the rights of translation, reprinting, reuse of illustrations, recitation, broadcasting, reproduction on microfilms or in any other physical way, and transmission or information storage and retrieval, electronic adaptation, computer software, or by similar or dissimilar methodology now known or hereafter developed.

The use of general descriptive names, registered names, trademarks, service marks, etc. in this publication does not imply, even in the absence of a specific statement, that such names are exempt from the relevant protective laws and regulations and therefore free for general use.

The publisher, the authors and the editors are safe to assume that the advice and information in this book are believed to be true and accurate at the date of publication. Neither the publisher nor the authors or the editors give a warranty, expressed or implied, with respect to the material contained herein or for any errors or omissions that may have been made. The publisher remains neutral with regard to jurisdictional claims in published maps and institutional affiliations.

This Springer imprint is published by the registered company Springer Nature Switzerland AG
The registered company address is: Gewerbestrasse 11, 6330 Cham, Switzerland

Preface

This book presents the most recent research results in the area of mechanism science, intended to improve a variety of applications in daily life and industry. The book is published under the Machine and Mechanism Science Series in Springer. The issues addressed are: computational kinematics, control issues in mechanical systems, mechanisms for medical rehabilitation, mechanisms for minimally invasive techniques, gears, dynamics of multi-body systems, industrial applications, cable robots, design issues for mechanisms and robots, teaching and history of mechanisms.

This book was initially the subject of the European Conference on Mechanism Science (EUCOMES 2020 Conference) which was supposed to be held in Cluj-Napoca, Romania between 7–10 September, 2020. Due to the Worldwide COVID–19 pandemic, we decided to change the schedule of the conference in two years from now, in 2022. This decision was taken with the approval of the EUCOMES International Scientific Committee.

The European Conference on Mechanism Science (EUCOMES 2020 Conference) was supposed to be the 8th event of a series that has been started in 2006 under the patronage of IFToMM, the International Federation for the Promotion of Mechanism and Machine Science. The previous EUCOMES conferences were successfully held in Innsbruck, Austria (2006); Cassino, Italy (2008); Cluj-Napoca, Romania (2010); Santander, Spain (2012); Guimarães, Portugal (2014); Nantes, France (2016); Aachen, Germany (2018).

The aim of the conference is to bring together researchers, industry professionals and students from the broad ranges of disciplines referring to machine and mechanism science, in order to stimulate exchange of new and innovative ideas both on the academic and industrial levels.

In total, we received a number of 65 papers which were carefully reviewed by two reviewers per paper. Finally, 59 papers were accepted for publication in this book.

We would like to thank the authors who have contributed excellent papers on different subjects, covering many fields of machine and mechanism science.

We want to express our gratitude to the reviewers who contributed to this process with their experience and scientific background.

We would like to express our gratitude to IFToMM, the members of the International Scientific Committee for the EUCOMES Conference for their cooperation: Marco Ceccarelli (Univ. of Rome Tor Vergata, Italy), Burkhard Corves (RWTH Aachen Univ., Germany), Manfred Husty (Univ. Innsbruck, Austria), Philippe Wenger (CNRS, France), Doina Pisla (Tech. Univ. Cluj-Napoca, Romania), Fernando Viadero (Univ. Cantabria, Spain) and Teresa Zielinska (Warsaw Tech. Univ., Poland).

We hope that this book contributes to the scientific progress and opens up discussions in this challenging field of mechanism science.

We also thank the staff of Springer for their excellent editorial support.

June 2020

Doina Pisla
Burkhard Corves
Calin Vaida

Contents

Computational Kinematics

A New 3T Parallel Mechanism: Topological Design, Analysis and Symbolic Position Solutions	3
Huiping Shen, Hao Ji, Jiaming Deng, and Guanglei Wu	
Damping Mechanisms of a Vibration-Reduction System Using Granules	11
Tomoko Koga, Taichi Sato, and Shunta Koyanagi	
Design Parameter Space of Spherical Four-Bar Linkages	19
M. John D. Hayes, Mirja Rotzoll, Colin Ingalls, and Martin Pfurner	
Ball's Point Construction Revisited	28
Stefan Gössner	
The Effect of Selection of Virtual Variable on the Direct Kinematics of Parallel Mechanisms	35
Huiping Shen, Qing Xu, Ju Li, Guanglei Wu, and Ting-li Yang	
Function Generation Synthesis of Planar Slider-Crank Linkages for Given 3 Positions and a Dead-Center Position	41
Gökhan Kiper, İbrahimcan Görgülü, and Sefa Furkan Küçüköğlü	
Multidual Algebra and Higher-Order Kinematics	48
Daniel Condurache	
On Homotopy Continuation Based Singularity Distance Computations for 3-RPR Manipulators	56
Aditya Kapilavai and Georg Nawratil	

Control Issues in Mechanical Systems

Assistive Handwriting Haptic Mechanism Using Deep Learning Speech Recognition	67
Erdi Sayar	

Design and Development of a Mobile Robot Equipped with Perception Systems for Autonomous Navigation	78
Razvan Patcas, Bogdan Mocan, Mircea Fulea, Mircea Murar, and Mihai Steopan	

Validation of Flatness-Based Feedforward Control for a Four-Chain Crane Manipulator	86
Erik Hildebrandt, Tobias Handreg, Pascal Froitzheim, Wilko Flügge, and Christoph Woernle	

The Model of a Controlled Mechanical System of an Air-Jet Loom Shedding Mechanism	95
Jiří Ondrášek and Petr Karel	

Dynamics and Motion Control of a Three Degree of Freedom 3-PRRR Parallel Manipulator	103
Parvathi Sunilkumar, Rutupurna Choudhury, Santhakumar Mohan, and Larisa Rybak	

Mechanisms for Medical Rehabilitation

Numerical and Experimental Validation of ExoFing, a Finger Exoskeleton	115
Cuahtémoc Morales-Cruz, Cristian Enrico Capalbo, Giammarco Caroleo, Marco Ceccarelli, and Giuseppe Carbone	

Serious Gaming Approach to Rehabilitation Using a 1 DOF Upper Limb Exerciser	123
Alexandru Ianoși-Andreeva-Dimitrova, Dan Silviu Mândru, and Lorin Bîrle	

Rehabilitation System with Integrated Visual Stimulation	131
Florin Covaciu, Bogdan Gherman, Adrian Pîsla, Giuseppe Carbone, and Doina Pîsla	

A Numerical Method for Determining the Workspace of a Passive Orthosis Based on the RRRR Mechanism in the Lower Limb Rehabilitation System	138
Dmitry Malyshev, Anna Nozdracheva, Grigory Dubrovin, Larisa Rybak, and Santhakumar Mohan	

Static and Dynamic Analysis of a Prosthetic Human Knee	146
Daniela Tarnita, Marius Georgescu, Nicolae Dumitru, and Danut-Nicolae Tarnita	

Dimensional and Workspace Analysis of RAISE Rehabilitation Robot 155
 Doina Pisla, Calin Vaida, Nicoleta Pop, Ionut Ulinici, Alexandru Banica, Iosif Birlescu, Paul Tucan, Giuseppe Carbone, and Adrian Pisla

Mechanisms for Minimally Invasive Techniques

On the Collision Free-Trajectories of a Multiple-needle Robot Based on the Fibonacci Sequence 169
 Ciprian Dragne, Veturia Chiroiu, Ligia Munteanu, Cornel Brişan, Cristian Rugină, Rodica Ioan, Nicolae-Doru Stănescu, and A. Florentin Stan

Joint Space and Workspace Analysis of a 2-DOF Spherical Parallel Mechanism 181
 Damien Chablat, Guillaume Michel, Philippe Bordure, Ranjan Jha, and Swaminath Venkateswaran

Kinematic Analysis of Two Innovative Medical Instruments for the Robotic Assisted Treatment of Non-resectable Liver Tumors ... 189
 Bogdan Gherman, Iosif Birlescu, Alin Burz, Ionut Ulinici, Paul Tucan, and Doina Pisla

Modeling a Cannula Insertion into a Phantom of Biological Tissue Using a Piezoelectric Actuator 198
 Marat Dosaev, Irina Goryacheva, Ming-Shaung Ju, Cheng-Hao Hsiao, Chih-Yuan Huang, Yury Selyutskiy, Anastasia Yakovenko, and Chien-Hsien Yeh

Robot-Assisted Ablation of Liver Hepatocellular Carcinoma and Colorectal Metastases: A Systematic Review 206
 Andra Ciocan, Radu Elisei, Florin Graur, Emil I. Mois, Sorana D. Bolboaca, Corina Radu, Calin Vaida, and Nadim Al Hajjar

Towards Building a Computerized System for Modelling Advanced HCC Tumors, in Order to Assist Their Minimum Invasive Surgical Treatment 219
 Delia Mitrea, Tiberiu Marita, Flaviu Vancea, Sergiu Nedevschi, Paulina Mitrea, Gabriel Mihai Neamt, Sanda Timoftei, Vlad Florian, Corina Radu, Mihai Socaciu, Horia Stefanescu, and Nadim Al Hajjar

Gears

Load Sharing and Quasi-Static Transmission Error of Non-Standard Tooth Height Spur Gears 231
 José I. Pedrero, Míryam B. Sánchez, and Miguel Pleguezuelos

A Transmission Error Analysis of a Herringbone Gear Set Considering Manufacturing Error	239
Huimin Dong, Xuefei Zhao, Chu Zhang, and Delun Wang	
Meshing Limit Line of Conical Worm Pair	247
Yaping Zhao and Xiao Zhang	
Acoustic Emission Monitoring of Teeth Surface Damage Process in a Planetary Gearbox	256
Enrique Caso, Alfonso Fernandez-del-Rincon, Pablo Garcia, Alberto Diez-Ibarbia, and Javier Sanchez-Espiga	
Impact of Position and Tooth Thickness Errors on Planetary Transmission Under Different Meshing Phase	265
Javier Sanchez-Espiga, Alfonso Fernandez-del-Rincon, Miguel Iglesias, Ana de-Juan, and Fernando Viadero	
Profile Shifting Coefficients of Spur Gears with Balanced Specific Sliding Coefficients at the Points Where the Meshing Stars and Ends	272
Tiberiu Alexandru Antal	
Dynamics of Multi-body Systems	
Simplified Method to Predict Clearance Evolution Effects Due to Wear Through MBD Simulation	281
Manuel Ordiz, Javier Cuadrado, Mario Cabello, Daniel Dopico, Iban Retolaza, and Aitor Cenitagoya	
A Modular Geometric Approach to Dynamics Modeling of Fully-Parallel PKM by Example of a Planar 3RPR Mechanism	289
Andreas Müller	
Chaos Illustrations in Dynamics of Mechanisms	297
Stelian Alaci, Catalin Alexandru, Florina-Carmen Ciornei, Ioan Doroftei, and Luminita Irimescu	
Cartesian Elastodynamics Model of a Full-Mobility PKM with Flexible Links	305
Qi Sun, Jorge Angeles, and James Richard Forbes	
Synthesis of Function Generator Four-Bar Linkages: Minimization of the Joint-Forces Constraining Structural-Related Quantities	314
Claudio Villegas, Mathias Hüsing, and Burkhard Corves	
Parametrization of a Real-Time Vehicle Model from Driving Tests for HiL Testing of Hydraulic Steering Systems	322
Ingomar Schröder, Thomas Schmidt, Jørgen Krusborg, and Christoph Woernle	

Graphic Analysis of the Linear and Angular Momentum of a Dynamically Balanced 1-DoF Pantographic Linkage 331
 Volkert van der Wijk

Inverse Dynamics and Simulation of a Parallel Robot Used in Shoulder Rehabilitation 339
 Paul Tucan, Nicolae Plitea, Calin Vaida, Bogdan Gherman, Giuseppe Carbone, Iosif Luchian, and Doina Pisla

Periodic Walking Motion of a Humanoid Robot Based on Human Data 349
 Anne Kalouguine, Christine Chevallereau, Sébastien Dalibard, and Yannick Aoustin

Industrial Applications

Sailing/Coasting Enabled by Mechatronic Starting Devices 363
 Madhusudan Raghavan

Embedded Installation of Robot Operating System on Elbrus-Based Control Platform—High-Reliable Industrial Application 370
 Alexander Tachkov and Andrei Vukolov

Calibration Study of a Continuously Variable Transmission System Designed for pHRI 381
 Emir Mobedi and Mehmet İsmet Can Dede

Maneuvers Possibility for the Spacecraft Equipped with Liquid-Fuelled Engines Operating with Different Kinds of Fuel 389
 Alexander Titov, Andrei Vukolov, Margarita Lapteva, and Gleb Prokurat

HiL Test Bench as a Development Environment for Hydraulic Steering Systems 397
 Michael Bruns, Ludger Schütz, Poul Ennemark, Thomas Schmidt, Jørgen Krusborg, and Jens Falkenstein

Contact Detection Approach Between Wheel and Rail Surfaces 405
 Filip Marques, Hugo Magalhães, Joao Pombo, Jorge Ambrósio, and Paulo Flores

Counter-Rotating Savonius Wind Turbine 413
 Marat Dosaev, Liubov Klimina, Anna Masterova, Vitaly Samsonov, and Yury Selyutskiy

Cable Robots

An Inverse Kinematic Code for Cable-Driven Parallel Robots Considering Cable Sagging and Pulleys 423
 Marc Fabritius and Andreas Pott

Motion Generation for a Cable Based Rehabilitation Robot	432
Nicoleta Pop, Ionut Ulinici, Doina Pislă, and Giuseppe Carbone	
Failure Analysis of a Collaborative 4-1 Cable-Driven Parallel Robot . . .	440
Stéphane Caro and Jean-Pierre Merlet	
Design Issues for Mechanisms and Robots	
Software Optimization Problem Solver for Automated Linkage Design	451
Kirill Kuprianoff, Christina Shutova, and Andrei Vukolov	
Static Analysis and Design Strategy of Two Antagonistically Actuated Joints	459
Vimalesh Muralidharan, Philippe Wenger, and Matthieu Furet	
An Approach to Robotic End Effectors Based on Multistable Tensegrity Structures	470
V. Böhm, P. Schorr, T. Feldmeier, J.-H. Chavez-Vega, S. Henning, K. Zimmermann, and L. Zentner	
Experimental Analysis of an MBS System with Two Degrees of Freedom Used in an Eolian Water Pump	479
Eliza Chircan, Maria Luminita Scutaru, Ioan Calin Roșca, Sorin Vlase, and Marius Păun	
Design and Characterization of a 3D Printed Soft Pneumatic Actuator	488
Ditzia Susana Garcia Morales, Serhat Ibrahim, Benjamin-Hieu Cao, and Annika Raatz	
Novel Planar Parallel Manipulator Using Geared Slider-Crank with Linear Actuation as Connection Kinematic Chain	496
Sanda Margareta Grigorescu, Antonio-Marius-Flavius Lupuți, Inocentiu Maniu, and Erwin-Christian Lovasz	
Teaching and History of Mechanisms	
Including the United Nations Sustainable Development Goals in Teaching in Engineering: A Practical Approach	509
Mikel Diez, Javier Corral, Asier Zubizarreta, and Charles Pinto	
Computer-Assisted Learning Used to Overconstrained Mechanism's Mobility	519
Simona Mariana Cretu and Ionut Daniel Geonea	
Petrovaradin Fortress: Clock Tower Mechanism	528
Dijana Čavić, Maja Čavić, Marko Penčić, and Milan Rackov	
Author Index	537

Computational Kinematics



A New 3T Parallel Mechanism: Topological Design, Analysis and Symbolic Position Solutions

Huiping Shen¹(✉), Hao Ji¹, Jiaming Deng¹, and Guanglei Wu²

¹ Research Center for Advanced Mechanism Theory,
Changzhou University, Changzhou 213016, People's Republic of China
shp65@126.com

² School of Mechanical Engineering,
Dalian University of Technology, Dalian 116024, People's Republic of China
gwu@dlut.edu.cn

Abstract. According to the topology design method of parallel mechanism based on position and orientation characteristic equations, a new type of three-translation parallel mechanism with symbolic forward position solution and partial motion decoupling is designed. Firstly, its topological characteristics such as position and orientation characteristic, degree of freedom and coupling degree, are analyzed and obtained. Secondly, using the kinematics modeling principle based on topological characteristics proposed by the author, the symbolic forward position solutions of the parallel mechanism are derived.

Keywords: Parallel mechanism · Three-translation · Symbolic forward position solutions

1 Introduction

In 1988, Clavel [2] designed the famous Delta mechanism. After that, many scholars carried out the optimization on the Delta mechanism [1] and proposed some meaningful three-translation (3T) parallel mechanisms (PM) [3–8] respectively.

However most of these 3T PMs mentioned above do not have symbolic forward position solutions (FPS), which makes the error analysis, dynamic analysis and dimension synthesis of the PM more complex. While for a PM that has symbolic FPS, these problems can be carried out easily.

In this paper, a new 3T PM with symbolic FPS is designed according to the topological design method of PMs based on the position and orientation characteristics (POC) equations. Based on the topological characteristics of the PM obtained [6], such as POC, degree of freedom (DOF) and coupling degree (κ), a kinematic modeling of the PM is built to obtain the symbolic forward and inverse solutions in this paper.

2 Topological Design and Analysis

A new 3T PM with symbolic FPS is designed, shown in Fig. 1. The fixed platform 0 is connected with the moving platform 1 through two hybrid branches I and II.

© The Editor(s) (if applicable) and The Author(s), under exclusive license to Springer Nature Switzerland AG 2020

D. Pisla et al. (Eds.): EuCoMeS 2020, MMS 89, pp. 3–10, 2020.

https://doi.org/10.1007/978-3-030-55061-5_1

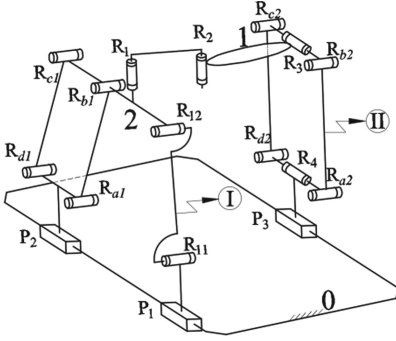


Fig. 1. Diagram of a new 3T PM

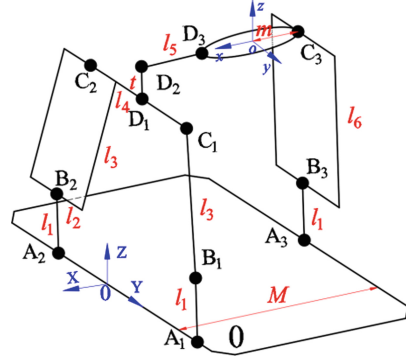


Fig. 2. The kinematic modeling and parameters

The hybrid branch I is composed of prismatic joints P_1 and P_2 , parallelogram joint P_{a1} , rotating joints R_{11} , R_{12} , R_1 and R_2 . The prismatic joint P_1 is connected with the guide rail on one side of the fixed platform 0, then it is connected with rotating joints R_{11} and R_{12} in parallel axes in series to form the first simple-open-chain (SOC₁). The prismatic joint P_2 , on the same guide rail with the prismatic joint P_1 , is connected with parallelogram joint P_{a1} in series to form the second simple-open-chain (SOC₂). Then the SOC₁ and SOC₂ are connected to form a sub-PM by the coplanarity of joint R_{12} , R_{b1} and R_{c1} that these three axes are parallel and that they have a common normal parallel to the prismatic joints P_1 and P_2 . The axes of all rotating joints in the sub-PM are parallel to the plane of the fixed platform 0. Finally, the rotating joints R_1 and R_2 whose axes are parallel to each other are perpendicular to the fixed platform 0. The moving platform 1 is connected by rotating joint R_2 of the hybrid branch I.

The hybrid branch II consists of prismatic joint P_3 , parallelogram joint P_{a2} , rotating joints R_4 and R_3 . Among them, the prismatic joint P_3 is connected with the guide rail on the other side of the fixed platform 0 and then connected with the parallelogram joint P_{a2} in series. The rotating joints R_4 and R_3 are located at the midpoint of two sides of the parallelogram joint P_{a2} respectively. The hybrid branch II is connected with the moving platform 1 through the rotating joint R_3 .

2.1 Topology Analysis of the PM

Calculation of POC

① The POC equations of the serial and parallel mechanism are as follows, respectively [7, 8].

$$M_{bi} = \bigcup_{j=1}^m M_{ji} \tag{1}$$

$$M_{Pa} = \bigcap_{i=1}^n M_{bi} \tag{2}$$

Here, M_{J_i} represents the POC of the i -th joint. The M_{b_i} represents the POC of the end of the i -th branch chain; The M_{P_a} represents POC of the moving platform of the PM.

② Calculation of POC of the PM

The first hybrid branch (HB_1) consists of a sub-PM composed of $SOC_1\{P_1//R_{11}//R_{12}\}$ and $SOC_2\{P_2//P_{a1}\}$, and then connected with sub-chain $\{R_1//R_2\}$ in series.

The second hybrid branch (HB_2) is composed of equivalent branched chain $\{P_3-P_{a2}\}$ and sub-chain $\{R_3//R_4\}$.

Firstly, from Eq. (2), the POC of the sub-PM is derived as follows:

$$M_{Sub-PM} = \bigcap_{i=1}^2 M_{soc_i} = M_{soc_1} \cap M_{soc_2} = \begin{bmatrix} t^2 \\ r^0 \end{bmatrix} \cap \begin{bmatrix} t^2 \\ r^1(//R_{11}) \end{bmatrix} = \begin{bmatrix} t^2 \\ r^0 \end{bmatrix} \quad (3)$$

From Eq. (3), we can see that the link 2 has output motions of two-translation and zero rotation, denoted as t^2 and r^0 , respectively. The same denotations are below.

According to Eq. (1), the POC of the HB_1 and HB_2 are obtained respectively.

$$M_{HB_1} = M_{Sub-PM} \cup M_{R_1//R_2} = \begin{bmatrix} t^2 \\ r^0 \end{bmatrix} \cup \begin{bmatrix} t^1(\perp R_1) \\ r^1(//R_1) \end{bmatrix} \cup \begin{bmatrix} t^1(\perp R_2) \\ r^1(//R_2) \end{bmatrix} = \begin{bmatrix} t^3 \\ r^1(//R_2) \end{bmatrix}$$

$$M_{HB_2} = \begin{bmatrix} t^1(//P_3) \\ r^0 \end{bmatrix} \cup \begin{bmatrix} t^1(//\diamond P_{a2}) \\ r^0 \end{bmatrix} \cup \begin{bmatrix} t^1(\perp R_3) \\ r^1(//R_3) \end{bmatrix} \cup \begin{bmatrix} t^1(\perp R_4) \\ r^1(//R_4) \end{bmatrix} = \begin{bmatrix} t_3 \\ r^1(//R_3) \end{bmatrix}$$

Therefore, from Eq. (2), the POC of the PM is calculated as follows.

$$M_{P_a} = M_{HB_1} \cap M_{HB_2} = \begin{bmatrix} t^3 \\ r^1(//R_2) \end{bmatrix} \cap \begin{bmatrix} t^3 \\ r^1(//R_3) \end{bmatrix} = \begin{bmatrix} t^3 \\ r^0 \end{bmatrix} \quad (4)$$

Equation (4) shows the moving platform 1 of the PM produces a three-translation motion in space.

Calculation of DOF

① The full-cycle degree of freedom of a PM is shown below [7, 8].

$$\xi_{L_j} = \dim \left\{ \left(\bigcap_{i=1}^j M_{b_i} \right) \cup M_{b_{(j+1)}} \right\} \quad (5)$$

$$F = \sum_{i=1}^m f_i - \sum_{j=1}^v \xi_{L_j} \quad (6)$$

Here, F denotes the degree of freedom (DOF) of the PM; f_i denotes the DOF of the i -th joint; m denotes the number of the joint; v denotes the number of independent loops, and $v = m - n + 1$, n denotes the number of links; ξ_{L_j} denotes the independent displacement equation number of the j -th independent loops, i.e., the rank of the velocity equations; M_{b_i} and $M_{b_{(j+1)}}$ denotes the POC of the i -th and the $(j+1)$ -th chain respectively.

② Calculating the DOF of the PM

The sub-PM in HB_1 are selected as the first loop, which is recorded as

$$\text{Loop}\{P_1//R_{11}//R_{12} - P_{a_1}//P_2\}$$

According to the Eq. (5), the number of independent displacement equation of the first loop is obtained as follows:

$$\xi_{L_1} = \dim\left\{\left[\begin{array}{c} t^2 \\ r^0 \end{array}\right] \cup \left[\begin{array}{c} t^2 \\ r^1(//R_{11}) \end{array}\right]\right\} = \dim\left\{\left[\begin{array}{c} t^2 \\ r^1(//R_{11}) \end{array}\right]\right\} = 3$$

According to the Eq. (6), the DOF of the sub-PM is obtained as follows:

$$F_1 = \sum_{i=1}^m f_i - \sum_{j=1}^1 \xi_{L_j} = 5 - 3 = 2$$

The remaining sub-chain $\{R_1//R_2\}$ of HB_1 and HB_2 constitute the second loop, i.e.,

$$\text{Loop}\{R_1//R_2 - R_3//R_4 - P_{a_2}//P_3\}$$

According to Eq. (5), its number of independent displacement equation is gotten:

$$\xi_{L_2} = \dim\left\{\left[\begin{array}{c} t^2 \\ r^0 \end{array}\right] \cup \left[\begin{array}{c} t^3 \\ r^2(//\diamond(R_1, R_3)) \end{array}\right]\right\} = 5$$

According to Eq. (6), the DOF of the PM is obtained as follows:

$$F_{(1-2)} = \sum_{i=1}^m f_i - \sum_{j=1}^2 \xi_{L_j} = (5 + 6) - (3 + 5) = 3$$

Therefore, the DOF of the PM is 3. When three inputs on the fixed platform 0 are provided, the moving platform of the PM has three-translation motion output.

Calculation of Coupling Degree

① Constraint degree of SOC and coupling degree of sub-kinematic chain

According to the mechanism composition principle based on SOC units [7, 8], any PM can be decomposed into three kinds of SOCs whose constraint degree are positive, zero and negative, respectively. The constraint degree of the j -th SOC are defined by

$$\Delta_j = \sum_{i=1}^{m_j} f_i - I_j - \xi_{L_j} = \begin{cases} \Delta_j^- = -5, -4, -3, -2, -1 \\ \Delta_j^0 = 0 \\ \Delta_j^+ = +1, +2, +3, +4, +5 \end{cases} \quad (7)$$

In Eq. (7), m_j denotes the number of the joint in the j -th SOC. I_j is the actuated joint of the j -th SOC. The meaning of f_i , ξ_{L_j} are the same as the mentioned in Eq. (6).

Furthermore, the ν ordered SOCs can form a sub-kinematic chain (SKC) with ν independent loops. It contains only one Assur Kinematic Chain whose DOF is 0.

Therefore, the coupling degree of a SKC is defined by [8]:

$$\kappa = \Delta_j^+ = |\Delta_j^-| = \frac{1}{2} \min \left\{ \sum_{j=1}^v |\Delta_j| \right\} \quad (8)$$

Equation (8) means that there are many allocation schemes that can decompose the SKC into v SOC. The smallest value of the $(\sum |\Delta_j|)$ should be taken into consideration when calculating the coupling degree of the SKC.

The coupling degree k means the degree of correlation and dependence among the motion variables of the loops of the PM. When the coupling degree k of the PM is higher, and the kinematics and dynamics analysis is more complex.

② Calculating the coupling degree of the PM

Firstly, the constraint degree of the first and second loop are respectively given by:

$$\Delta_1 = \sum_{i=1}^m f_i - I_1 - \xi_{L_1} = 5 - 2 - 3 = 0$$

$$\Delta_2 = \sum_{i=1}^m f_i - I_2 - \xi_{L_2} = 6 - 1 - 5 = 0$$

Therefore, the PM is composed of two SKCs, i.e., SKC₁ and SKC₂. According to Eq. (8), the coupling degree of each SKC is calculated respectively by

$$k_1 = k_2 = \frac{1}{2} \sum_{j=1}^v |\Delta_j| = \frac{1}{2} (0) = 0$$

$k = 0$ means that the FPS of the SKC₁ and SKC₂ can be solved independently without needing to assign virtual variable.

3 Forward and Inverse Position Solutions

As shown in Fig. 2, the O-XYZ coordinate system is established on the fixed platform 0. O is a point on the guideway. The direction of X-axis is perpendicular to the guide rail, and the direction of Y-axis coincides with the guide rail.

The $o-xyz$ coordinate system is established on the moving platform 1. o is the midpoint of the line D₃C₃. The direction of x -axis coincides with the line D₃C₃, The direction of y -axis is perpendicular to the line D₃C₃.

The interval between the two guide ways on the fixed platform 0 is M , while the length of D₃C₃ on the moving platform is m . The length of the link connecting the three actuated joints is equal, that is A₁B₁ = A₂B₂ = A₃B₃ = l_1 . The length of long-side and short-side of parallelogram joint P_{a1} is l_3 and $2l_2$. The length of the link B₁C₁ is l_3 . The length of C₁D₁ and C₂D₁ are the same and equal to $(l_2 + l_4)$. The length of the link D₁D₂ and D₂D₃ is t and l_5 respectively, and the length of the long side of the parallelogram joint P_{a2} is l_6 .

Let the distance between the actuated joint P₁ (point A₁) and the point O be S_1 , the actuated joint P₂ (point A₂) and the point O be S_2 , and the Y-direction distance between the actuated joint P₃ (A₃) and the point O be S_3 .

3.1 Solving Symbolic Forward Position

According to the kinematic modeling principle and method based on topological characteristics [6], [9] proposed by the author, the symbolic FPS of this PM can be performed below.

The forward solution of the PM is that the length of travel between the actuated joint P_1, P_2, P_3 and the point O is known as S_1, S_2, S_3 respectively, the coordinates (x, y, z) of the moving platform o needs to be solved.

In the fixed coordinate system, the coordinates of A_1, A_2, A_3, B_1, B_2 and B_3 are easily obtained as follows:

$$A_1 = (0, S_1, 0), B_1 = (0, S_1, l_1); A_2 = (0, S_2, 0), B_2 = (0, S_2, l_1); A_3 = (-M, S_3, 0), B_3 = (-M, S_3, l_1).$$

Solution for the Forward Position of SKC₁

In the first loop $\{P_1//R_{11}//R_{12}-P_{a1}/P_2\}$, that is, the loop $\{A_1-B_1-C_1-D_1-C_2-B_2-A_2\}$ in Fig. 2, it is already proved that the motion of the link C_1C_2 is a two-translation in the YOZ-plane. So the coordinates of D_1 point can be set as $D_1 = (0, y_{D1}, z_{D1})$, then it can be deduced that the coordinates of C_1 and C_2 are $C_1 = (0, y_{D1} - (l_2 + l_4), z_{D1})$ and $C_2 = (0, y_{D1} + (l_2 + l_4), z_{D1})$ respectively. Two equations are obtained from geometry constraints $B_1C_1 = B_2C_2 = l_3$, and their solutions can be obtained under condition $S_1 - S_2 \neq 2(l_2 + l_4)$

$$\begin{cases} y_{D1} = \frac{S_1 + S_2}{2} \\ z_{D1} = l_1 + \sqrt{l_3^2 - \left[\frac{S_1 - S_2 - 2(l_2 + l_4)}{2} \right]^2} \end{cases}$$

The other value of Z_{D1} that causes configuration interference is discarded.

Solution for the Forward Position of SKC₂

In the second loop $\{R_1//R_2-R_3//R_4.P_{a2}/P_3\}$, that is, the loop $\{D_2-D_3-C_3-B_3-A_3\}$ in Fig. 2, it is already proved that the motion of the moving platform 1 is a three-translation. Let the coordinates of o point at the center of the moving platform be (x, y, z) . Then it can be seen that the coordinates of D_3 and C_3 are $C_3 = (x - m, y, z)$ and $D_3 = (x + m, y, z)$ respectively. The coordinates of D_1 points have been obtained above, hence the coordinates of point D_2 are $D_2 = (0, y_{D1}, z_{D1} + t)$. Then constraint equations are established from constraints $D_2D_3 = l_5$ and $B_3C_3 = l_6$, and the coordinates of o point can be obtained easily as

$$\begin{cases} x = F_4 - \frac{F_5 H_2 \pm F_5 \sqrt{H_2^2 - 4H_1 H_3}}{2H_1} \\ y = \frac{H_2 \pm \sqrt{H_2^2 - 4H_1 H_3}}{2H_1} \\ z = l_1 + t + \sqrt{l_3^2 - \left[\frac{S_1 - S_2 - 2(l_2 + l_4)}{2} \right]^2} \end{cases} \quad (9)$$

Here,

$$H_1 = (F_5^2 + 1); H_2 = 2F_4 F_5 + 2m F_5 + 2y_{D1}; H_3 = F_4^2 + m^2 + 2m F_4 + y_{D1}^2 - l_5^2; F_1 = 4m - 2M;$$

$$F_2 = 2(S_3 - y_{D1}); F_4 = F_3 / F_1; F_3 = l_3^2 - E + (M - m)^2 - m^2 - y_{D1}^2 + S_3^2; F_5 = F_2 / F_1;$$

$$E = l_6^2 - (Z_{D1} + t - l_1)^2,$$

From Eq. (9), it is readily known that z is determined by only S_1 and S_2 . Therefore, the input-output motion of the PM is partially decoupled, which is beneficial to the trajectory planning and motion control of the PM.

3.2 Solving Inverse Positions

The inverse solution of the PM is that when the moving platform $\mathbf{o}(x, y, z)$ is known, the travel S_1, S_2 and S_3 of the actuated joints P_1, P_2 and P_3 needs to be solved.

Due to the limitation of the space, we directly derive the inverse position solutions.

In SKC₁, based on the constraint $B_1C_1 = B_2C_2 = l_3$, the solutions are as follows:

$$\begin{cases} S_1 = \pm \sqrt{l_3^2 - (z - t - l_1)^2} + (l_2 + l_4) + y_{D1} \\ S_2 = \mp \sqrt{l_3^2 - (z - t - l_1)^2} - (l_2 + l_4) + y_{D1} \end{cases} \quad (10)$$

In SKC₂, based on the constraint $B_3C_3 = l_6$, the travel S_3 is obtained as follows:

$$S_3 = y \pm \sqrt{l_6^2 - (z - l_1)^2 - (x - m + M)^2} \quad (11)$$

From the above analysis, it is known that there are two sets of solutions for input S_3 of the PM, and two sets solutions also for input S_1 and S_2 of the PM. Therefore the PM has four configurations.

3.3 Numerical Validation

Lengths of each link of the PM are set as follows: $l_1 = 55, l_2 = 40, l_3 = 160, l_4 = 35, l_5 = 80, l_6 = 200, m = 30, M = 200, t = 20$. The inputs of the three actuated joints are set as $S_1 = 120, S_2 = 100, S_3 = 0$ (Unit: *mm*). By substituting the three inputs into Eq. (9), the forward solution of the PM is obtained, as shown in Table 1, which has been proved by the inverse solutions in Eqs. (10) and (11).

Table 1. The value of forward solutions of the PM

No	x	y	z
1	-94.5212	57.2971	231.1249
2	-87.1437	-45.9874	231.1249

4 Conclusions

A new 3T PM with symbolic FPS and partially decoupled input-output motion is proposed. Based on the topological characteristics of the PM such as POC, DOF and coupling degree κ , the symbolic forward and inverse solutions are obtained. This work is the foundation for the velocity/acceleration, workspace, singularity, error, dynamic analysis and dimension synthesis of this PM.

Acknowledgement. The support by the National Natural Science Foundation of China (Grant Nos. 51975062, 51475050, 51375062) is greatly appreciated.

References

1. Bouri, M., Clavel, R.: The linear delta: developments and applications. In: Robotics. VDE, pp. 1–8 (2010)
2. Clavel, R.: A fast robot with parallel geometry. In: Proceeding of the 18th International Symposium on Industrial Robots, pp. 91–100 (1988)
3. Kong, X., Gosselin, C.M.: Type synthesis of 3-DOF translational parallel manipulators based on screw theory. *J. Mech. Des.* **126**, 83–92 (2008)
4. Mazare, M., Taghizadeh, M., Rasool Najafi, M.: Kinematic analysis and design of a 3-DOF translational parallel robot. *Int. J. Autom. Comput.* **14**(4), 432–441 (2017)
5. Zeng, Q., Ehmann, K., Cao, J.: Tri-pyramid robot: design and kinematic analysis of a 3-DOF translational parallel manipulator. *Rob. Comput.-Integr. Manuf.* **30**(6), 648–657 (2014)
6. Shen, H., Yang, T., Li, J., Zhang, D., Deng, J., Liu, A.: Evaluation of topological properties of parallel manipulators based on the topological characteristic indexes. *Robotica* **38**(8), 1–19 (2019)
7. Yang, T., et al.: *Theory and Application of Robot Mechanism Topology*. Science Press, Beijing (2012)
8. Yang, T., Liu, A., Shen, H., et al.: *Topology Design of Robot Mechanisms*. Springer, Singapore (2018)
9. Shen, H., Chablat, D., Zen, B., Li, J., Wu, G., Yang, T.A.: Translational three-degrees-of-freedom parallel mechanism with partial motion decoupling and analytic direct kinematics. *Journal of Mechanisms and Robotics* **12**(2), 021112-1–021112-7 (2019)



Damping Mechanisms of a Vibration-Reduction System Using Granules

Tomoko Koga^(✉), Taichi Sato, and Shunta Koyanagi

Tokyo Denki University, Tokyo, Japan

tomoko.koga.bf@hitachi.com, taichi@mail.dendai.ac.jp,

koya222@satolab.n.dendai.ac.jp

Abstract. The damping mechanism of damping system using granules—applied to reduce vibration in structures with high natural frequency and small vibration displacement—was investigated. A computational model of a single-degree-of-freedom vibration system with a granular-material damper was constructed and used to study the mechanism of the granular-material damping system. On the basis of the fundamental idea that the damping effect of the granular-material damper is governed by the motion of the granules, the granules were classified as the following mass components: “relative-motion mass” and “equivalent added mass” in the translational motion and “rotational-motion mass” and “non-rotational-motion mass” in the rotational motion. The relationships of these mass components with the damping characteristics of the damper were then considered. Moreover, as for structures with high natural frequency and small vibration displacement, the relationships between the motion of the granules, “relative-motion mass” and “rotational-motion mass”, and damping ratio were investigated by experiments and calculations.

Keywords: Damper · Granular-materials · Single-degree-of-freedom system · Damping ratio

1 Introduction

A granular-material damper is a damping element that consists of a container filled with granules placed on the mass part of the primary vibration system, and it uses the motion of the granules to produce a damping effect. The damping characteristics of a granular-material damper are thus governed by the motion of the granules, so they can be understood by analyzing the motion of the granules.

In previous related studies, a powder-impact damper was applied to vibration systems with a single degree of freedom and multiple degrees of freedom, and the damping effect due to the powder (which was considered as a single mass with coefficient of restitution of zero) was considered [7]. Moreover, the discrete-element method was used to calculate the motion of individual granules and study the damping characteristics of granules [5]. In these studies, granules are treated differently, such as a single mass or individual

mass, but the movement of the granules is both greater than the movement of the primary system. Accordingly, the impact force of the granules on the primary system can be taken as the basis of the damping mechanism. In addition to the studies cited above, the effects of size, quantity of granules, and shape and number of granular-material containers on the damping characteristics have also been studied [3, 4, 6].

In general, previous researches like those described above have mostly assumed a large movement of granules. Considerable knowledge concerning damping characteristics thus already exists in the case that granular-material dampers are applied to structures with large displacement amplitude. On the other hand, it is not sufficiently clear what factors need to be focused on to attain a high degree of damping from a granular-material damper in a structure with relatively high natural frequency and small displacement amplitude.

In this study, the damping mechanism of a granular damper (when a structure with small vibration displacement is used as a damping object) is investigated. In our previous report [2] concerning a granular damper, on the basis on the most-basic idea that the motion of a granules can provide a damping effect, the total mass of the granules enclosed in a container was classified as “moving mass” and “stationary mass”, and the relationship between these masses and damping characteristics was considered. In this report, to deepen this consideration, a one-degree-of-freedom vibration model including the granular container was constructed, and experiments and calculations were performed by changing the total mass of the granules.

2 Experimental Apparatus and Methods

The experimental apparatus composing the granular-material damper is shown in Fig. 1. The mass, which also serves as the granular container, is placed at the center, and two plates (i.e., “beams” acting as spring elements) are attached to the left and right ends of the container to form the vibration system. The mass of the main system (“granular container” hereafter) is 16.58 kg, the spring constant is 1845 kN/m, and the natural frequency of the system is 53.1 Hz. The system is mounted on a hydraulic shaker to give a horizontal forced displacement to the base.

Multiple granules were placed in the container as shown in the figure. The granules used in the experiment were cylindrical carbon tool steel with diameter of 25 mm and length of 17 mm. The mass per granule was about 65.6 g. In the experiment, first, the natural frequency with the enclosed granules was measured, and then the steady excitation was applied at that frequency. During the steady excitation, two accelerometers (one attached to the granular container and one attached to the base) measured the horizontal acceleration at both places simultaneously. From the measurements by these accelerations, the damping ratio was calculated by using the relative-motion mass proposed in our previous report [2].

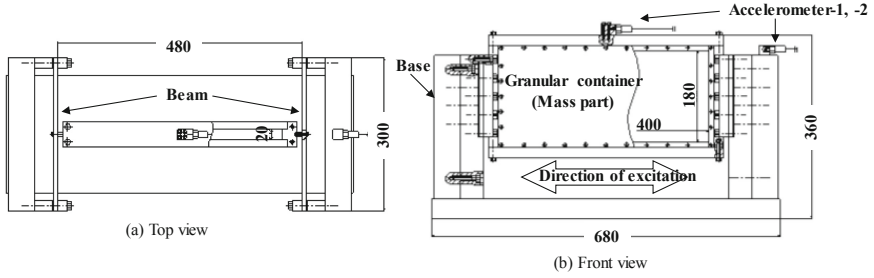


Fig. 1. Experimental apparatus

3 Calculation Model of Granular-Material Damper

3.1 Calculation Model

The calculation model is shown in Fig. 2. The calculation model is a one-degree-of-freedom vibration system with mass M , spring constant K , and damping coefficient C . The granules are arranged horizontally and vertically in a container that also serves as a mass. Forced displacement x_b is applied to the base of the vibration system, and horizontal displacement x_m of the container, as well as horizontal displacement $z_h(i, j)$, vertical displacement $z_v(i, j)$, and rotation angle $z_\theta(i, j)$ of the granules at that time are obtained.

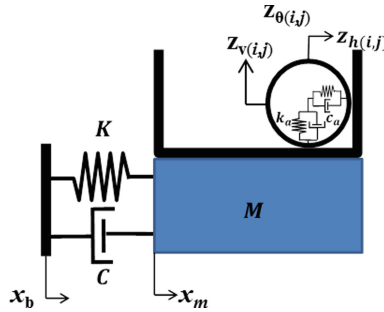


Fig. 2. Granule-damper model used for the numerical simulation

Here, i and j indicate the position of each granule, and i and j are row number and column number of the granule, respectively. It is assumed that all the granules are cylindrical with the same size, mass m_p , and radius r . Contact between the granules and contact between the granules and the inner wall of the container are replaced by springs and dampers on the basis of Hertzian contact [1, 5]. In other words, in the calculation model shown in Fig. 2, the base and container move only in the horizontal direction, while the granules move in three directions: horizontal, vertical, and rotational about their length direction.

3.2 Equations of Motion for Main System

In this study, a vibration system with natural frequency of about 50 Hz is targeted for vibration suppression. The displacement of the main system at resonance is several tens of microns; therefore, as for the granules in the container in the case of both the experiment and the calculation, it is assumed that the arrangement of left and right granules and top and bottom granules does not change (i.e., granules do not jump over each other or change places). According to the models shown in Fig. 2, the equations of motion of the main system are given below.

$$\begin{aligned}
 M\ddot{x}_m = & -K(x_m - x_b) - C(\dot{x}_m - \dot{x}_b) \\
 & - \sum_{i=1}^p N_{L(i,1)} \left\{ k_a (-z_{h(i,1)} + x_m)^{1.08} \right. \\
 & \quad \left. + c_{aa} (-z_{h(i,1)} + x_m)^{0.04} (-\dot{z}_{h(i,1)} + \dot{x}_m) \right\} \\
 & + \sum_{i=1}^p N_{R(i,q)} \left\{ k_a (z_{h(i,q)} + (x_m + cle))^{1.08} \right. \\
 & \quad \left. + c_{aa} (z_{h(i,q)} - (x_m + cle))^{0.04} (\dot{z}_{h(i,q)} - \dot{x}_m) \right\} \\
 & + \sum_{j=1}^q N_{B(1,j)} \operatorname{sgn}(\dot{z}_{v(1,j)} - \dot{x}_m - r\dot{z}_{\theta(1,j)}) \mu_a \left\{ k_a (-z_{v(1,j)})^{1.08} \right. \\
 & \quad \left. + c_{aa} (-z_{v(1,j)})^{0.04} (-\dot{z}_{v(1,j)}) \right\}
 \end{aligned} \tag{1}$$

Here, $N_{L(i,1)}$ is a constant for judging contact between the left container wall and the leftmost granule ($i,1$), and it is 1 in the case of contact; otherwise, it is 0. $N_{R(i,q)}$ is a constant for determining contact between the right container wall and the rightmost granule (i,q). $N_{B(1,j)}$ is a constant that determines contact between granule (1, j) in the bottom row and the bottom of the container. sgn is a function that determines the direction of frictional force, and it is taken as 1 if the value in the parentheses is positive, -1 if the value is negative, and zero if it is zero. And μ_a is the coefficient of friction between a granule and the bottom of the container.

4 Results of Experiment and Calculation

4.1 Damping Ratio and Relative-Motion Mass

The total mass of the granules enclosed in the container was varied from 1 to 8 kg, and the acceleration of the base and the main system were measured by experiments and calculated under the same conditions. Damping ratio and relative-motion mass were calculated by the method described in a previous report [2] on the basis of base acceleration and acceleration of the main system.

Damping ratio and relative-motion mass for variable total mass of granules are shown in Fig. 3. The solid lines show calculated values, and the crosses show values obtained by

experiment. Although the calculation results and experimental results are not completely consistent, they show similar tendencies in terms of the following two points (results):

- (1) In the range in which total mass of granules is small, relative-motion mass increases and damping ratio increase with increasing total mass.
- (2) When total mass of the granules increases, relative-motion mass changes from an increasing trend to a decreasing one. Even if relative-motion mass decreases, damping ratio stays almost constant or increases.

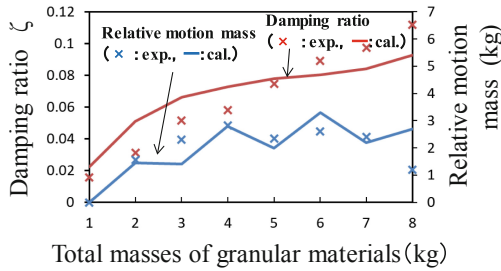


Fig. 3. Behavior of damping ratio (ζ) and relative-motion mass

As described above, relative-motion mass represents the mass of granules that move in the translation direction independently of the main system. In consideration that damping force is generated by collision of the granules with the container wall, result (1) listed above (namely, damping ratio increases as relative-motion mass increases) is considered to be valid.

On the contrary, another explanation must be considered in regard to result (2) listed above, namely, damping ratio does not decrease even if relative-motion mass decreases. Motion of the granules includes not only a translational component but also a rotational component. Therefore, the behavior indicated by result (2) is considered below with a focus on rotational motion of the granules.

4.2 Consideration of Rotational Motion and Damping Mechanism of Granular Material

When the time history of the vibration of a system with a granular-material damper is calculated, it became clear that all the granules rotate, although in the magnitude of rotation of each granule differs. Some granules have a very small rotation angle, so they can be regarded as not rotating, while others have a considerable rotation angle.

Translational motion of the granules has been roughly classified as two components: relative-motion mass and equivalent added mass, and the relationship between the size and damping characteristics of these components has been studied.

As for rotational movement, a similar idea is introduced as follows. A certain threshold value is set for the rotation angle. The total mass of granules with a larger rotation

angle than the threshold is called “rotational-motion mass”; conversely, the total mass of granules with rotation angle smaller than the threshold is defined as “non-rotational motion mass.”

Note that there is no particular way to determine the rotational-angle threshold. If the calculation results are considered, it was determined that if rotation angle was about 0.03 radians per second, it can be considered that the granule is not rotating. Accordingly, a rotation angle of 0.03 rad during the calculation time of 10.0 to 11.0 s was determined as the threshold.

The results of the calculation are shown in Fig. 4. In this figure, rotation angles of the granules are divided into values above (black circles) and below (white circles) the threshold. In addition, the figure shows several results when the total mass of the granules is changed from 1 to 8 kg. The numbers in the figure indicate the number of granules that are above the threshold (black circles).

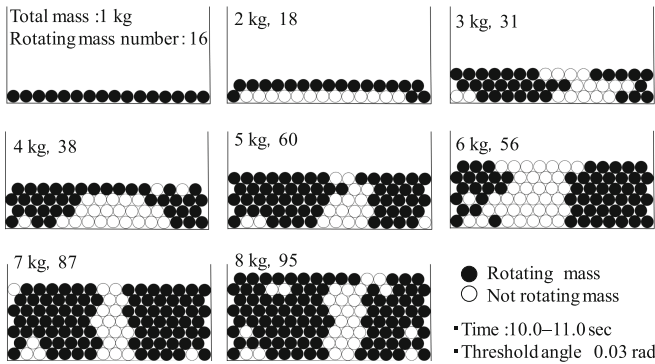


Fig. 4. Distribution of rotational-motion masses at each total mass of granules

For example, when the total mass of granules is 1 kg, the rotation angles of all 16 granules are more than the threshold value (shown by black circles); as a result, the rotational-motion mass becomes 1 kg, and the non-rotational-motion mass becomes 0 kg. From this viewpoint, when the characteristic of the phenomenon by which total mass of the granules increases is examined, it can be seen that (i) rotational-motion mass increases and (ii) the granules near the wall of the container rotate significantly.

Rotational-motion mass plotted over the results for damping ratio and relative-motion mass shown in Fig. 3 is shown in Fig. 5. Up to a total mass of granules of 6 kg, although relative-motion mass slightly increases or decreases, it generally tends to increase. In that region, rotational-motion mass also increases monotonically. On the contrary, when total mass of granules exceeds 6 kg, relative-motion mass tends to decrease. However, to compensate for that decrease, rotational-motion mass has a larger increasing tendency than before.

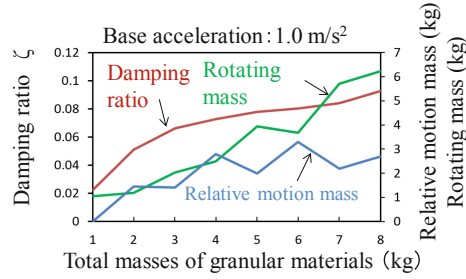


Fig. 5. Tendency of damping ratio (ζ), relative-motion mass, and rotational-motion mass.

Relative-motion mass is the total mass of granules that move differently from the main system. In other words, it can be interpreted as corresponding to the amount of granules that collide with the container wall. On the contrary, rotational-motion mass is considered to correspond to the amount of granules involved in frictional damping due to rotational motion of the granules.

If the above-described interpretation is supposed, it can be considered that in the region in which total mass of granules is up to 6 kg, both collision between granules and the wall and friction due to rotational movement of granules dominate the damping characteristics of the granular-material damper. Furthermore, it can be interpreted that when the total mass of granules exceeds 6 kg, the damping effect is produced mainly by the friction due to rotational motion of the granules, and the damping ratio tends to increase even if the relative-motion mass decreases.

In summary, when the total mass of the granules increases, the lower granules are affected by the weight of the upper granules, making it difficult for them to move in the translation direction; that is, relative-motion mass decreases. However, this effect does not lead to a decrease in damping ratio because the rotational-motion mass increases.

The force exerted on the mass of the main system (container) is limited to that due to the granules that contact the container wall and the bottom surface of the container. Strictly speaking, the damping characteristic of the granular-material damper is determined by the flow of vibrational energy between those granules and the main system. However, it can be considered that under the current proposal that the movement of the granules is the basic principle of the granular-material damper, it is possible to evaluate the damping mechanism of the granular-material damper on the basis of relative-motion mass as well as rotational-motion mass.

5 Conclusions

On the basis of the basic idea that the damping effect of a granular-material damper is governed by the motion of the granules, “relative-motion mass” and “rotational-motion mass” are respectively proposed for translational motion and rotational motion of the granules. Experiments and calculations were performed by changing the total mass of the granules, and the obtained results were compared with the proposed masses and damping ratio. The damping mechanism was considered, and the following findings were obtained.

- (1) Damping ratio tends to increase with increasing total mass of granules.
- (2) Increasing damping ratio with increasing total mass of granules can be explained by the fact that relative-motion mass increases in the region in which total mass of granules is relatively small.
- (3) As total mass of granules increases, the trend of relative-motion mass changes from an increasing one to a decreasing one. However, even if relative-motion mass decreases, damping ratio tends to stay nearly constant or increase. This result can be explained by the increase of rotational-motion mass due to the increase of total mass of granules.

References

1. Hongo, T., Sato, H., Iwata, Y., Komatsuzaki, T., Hongo, Y.: Modeling and analysis of impact system composed of ball and plane. *Trans. Jpn. Soc. Mech. Eng. Ser. C* **65**(634), 2287–2293 (1999)
2. Koga, T., Sato, T., Weller, A., Ono, K.: Numerical simulation of a granular material damper. *New Trends Mech. Mach. Sci.* **24**, 515–522 (2015)
3. Makino, T., Nakahara, K., Nakao, S., Sato, T.: Vibration control characteristics of structures that use granular material impact phenomena. *JSME Dyn. Des. Conf. Proc.* **685**, 1929–1934 (2003)
4. Park, J., Palumbo, D.L.: Damping of structural vibration using lightweight granular materials. *Exp. Mech.* **49**(5), 697–705 (2009)
5. Saeki, M.: Impact damping with granular materials in a horizontally vibrating system. *J. Sound Vib.* **251**(1), 153–161 (2002)
6. Tanaka, Y., Makino, T., Sato, N.: Study of particle size characteristics using a granular material damper. *JSME Kyushu Conf. Proc.* **61**, 193–194 (2008)
7. Yokomichi, I., Araki, Y., et al.: Impact damper with granular materials for multibody system. *J. Press. Vessel Technol.* **118**(1), 95–103 (1996)



Design Parameter Space of Spherical Four-Bar Linkages

M. John D. Hayes¹(✉), Mirja Rotzoll¹(✉), Colin Ingalls², and Martin Pfurner³

¹ Mechanical and Aerospace Engineering, Carleton University, Ottawa, Canada
{john.hayes,mirja.rotzoll}@carleton.ca

² School of Mathematics and Statistics, Carleton University, Ottawa, Canada
colin.ingalls@carleton.ca

³ Unit Geometry and Surveying, University of Innsbruck, Innsbruck, Austria
martin.pfurner@uibk.ac.at

Abstract. Four link twist angles are the design parameters for spherical 4R linkages: changing the magnitudes of the twist angles changes the motion characteristics of the linkage. A new quartic algebraic input-output equation for spherical four-bar linkages, obtained in another paper, contains four terms which each factor into pairs of distinct cubics in the link twist parameters. These eight cubic factors possess a symmetry that suggest they combine to form a shape that, at least locally, bears a remarkable resemblance to a pair of dual tetrahedra in the design parameter space of the link twists. In this paper we show that the location of points relative to the eight distinct cubic surfaces implies a complete classification scheme for all possible spherical 4R linkages. Moreover, we show that the design parameter spaces of both the spherical and planar 4R linkages, with suitable scaling, intersect in 12 lines which form the 12 edges of a pair of dual tetrahedra.

Keywords: Spherical four-bar linkages · Design parameter space · Uniform polyhedral compound

1 Introduction

Over the millennia four-bar linkages have become ubiquitous, with applications ranging from aircraft landing gear deployment systems to beer bottle cap clamps. One might, however naïvely, be led to the conclusion that all is known. Nonetheless, commencing with the ground breaking work of Ferdinand Freudenstein in the 1950s [5], new discoveries and new insight continue to be obtained, often with surprising results. See [10] for a comprehensive collection of detailed examples and results offered by a vast array of investigators over the last 175 years.

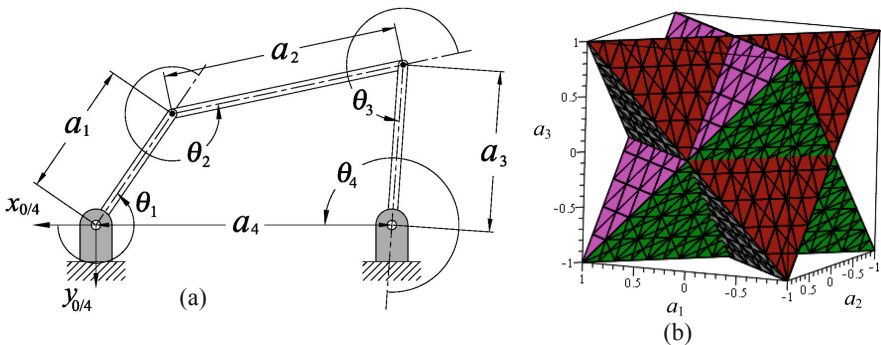
The algebraic input-output (IO) equation for any planar four-bar linkage is a polynomial equation in the variable input link (driver) and output link (follower) angle parameters expressed in terms of the link lengths. Because the link lengths

Table 1. Denavit-Hartenberg parameters for a planar 4R chain.

joint axis i	link length a_i	link angle θ_i	link offset d_i	link twist τ_i
1	a_1	θ_1	0	0
2	a_2	θ_2	0	0
3	a_3	θ_3	0	0
4	a_4	θ_4	0	0

impose mobility constraints on the input and output links, they are considered design parameters. Since the coupler motion is embedded in the polynomial, the IO equation is well suited to function generation synthesis. Moreover, it is an algebraic equation so the theory of algebraic geometry [2] can be applied to reveal characteristics of the IO relationship that may otherwise be occluded by trigonometry.

Individual link coordinate systems are assigned according to the original Denavit-Hartenberg (DH) convention [4]. Link parameters of length, a_i , joint angle, θ_i , link offset, d_i , and link twist angle, τ_i , are all defined relative to these coordinate systems. For a planar 4R linkage the design parameters are the four link lengths, a_1 , a_2 , a_3 , and a_4 , see Fig. 1(a), because the relative lengths determine the mobility capability of the linkage. The relative angles between the links θ_1 , θ_2 , θ_3 , and θ_4 , are variables in the IO equation. The link offsets and twist angles are all identically zero, see Table 1. Note that the base coordinate system illustrated in Fig. 1(a) is an artifact of the method used to derive the algebraic IO equation, see [13] for the details. Regardless, only the coincident origins and directions of the $z_{0/4}$ -axes are fixed by the DH convention while the direction of the coincident $x_{0/4}$ -axes are rotated by π radians compared to the usual representation, and the $y_{0/4}$ -axes complete the two coincident right-handed coordinate systems.

**Fig. 1.** Planar 4R chain and associated design parameter tetrahedra.

The algebraic IO equation for a planar 4R linkage is a planar quartic curve in the IO angle parameters $v_1 = \tan \theta_1/2$ and $v_4 = \tan \theta_4/2$ [6]. The design parameters are embedded in four quadratic terms that are each comprised of two factors that are linear sums and differences of link lengths. The algebraic IO equation, as derived in [13], is

$$Av_1^2v_4^2 + Bv_1^2 + Cv_4^2 - 8a_1a_3v_1v_4 + D = 0, \quad (1)$$

where

$$\begin{aligned} A &= (a_1 - a_2 + a_3 - a_4)(a_1 + a_2 + a_3 - a_4) = A_1A_2, \\ B &= (a_1 + a_2 - a_3 - a_4)(a_1 - a_2 - a_3 - a_4) = B_1B_2, \\ C &= (a_1 - a_2 - a_3 + a_4)(a_1 + a_2 - a_3 + a_4) = C_1C_2, \\ D &= (a_1 + a_2 + a_3 + a_4)(a_1 - a_2 + a_3 + a_4) = D_1D_2. \end{aligned}$$

The overall scale of the linkage is irrelevant since we are dealing with function generators. Without loss in generality, we can normalise the four link lengths by a_4 , the distance between the centres of the two ground fixed R-pairs, thereby setting $a_4 = 1$. Projected into this hyperplane, the remaining three lengths can be used to establish three mutually orthogonal basis vectors. The eight symmetric linear factors, having the form $(a_1 \pm a_2 \pm a_3 \pm 1)$, can be considered as eight planes in the a_i for the eight permutations in sign. These eight planes intersect in the 12 edges of a pair of dual regular tetrahedra [7] while the plane segments bounded by the 12 edges are the tetrahedra faces, see Fig. 1(b).

These two tetrahedra belong to the only uniform polyhedral compound, called the stellated octahedron, which has order 48 octahedral symmetry [3]. This double tetrahedron has a regular octahedron at its core and shares its eight vertices with the cube [3]. Distinct points in this design parameter space represent distinct function generators and the locations of the points relative to the eight planes containing the faces of the double tetrahedron completely determine the mobility of the input and output links. There are 27 types of mobility conditions, determined using the techniques found in [7, 11], which depend on the signs of the sums of lengths in the three terms A_1 , B_1 , and C_1 from Eq. (1).

The focus of this paper is the design parameter space corresponding to spherical 4R linkages. Thus, the quartic algebraic IO equation for spherical 4R mechanisms, as derived in [13], is manipulated to examine the design parameter space implied by the magnitudes of the link twist angle parameters defined as $\alpha_i = \tan(\tau_i/2)$, where τ_i specifies the twist angles according to the original Denavit-Hartenberg convention [4]. For a spherical 4R the design parameters are therefore the four link twist angle parameters, α_i , while the relative link angles are the four variable θ_i . The link lengths and offsets are identically zero, see Table 2. In comparison with the design parameter space of planar 4R mechanisms [7] we see some startling similarities. But first, the spherical 4R algebraic IO equation requires some discussion.

Table 2. DH parameters a spherical 4R chain.

joint axis i	link length a_i	link angle θ_i	link offset d_i	link twist τ_i
1	0	θ_1	0	τ_1
2	0	θ_2	0	τ_2
3	0	θ_3	0	τ_3
4	0	θ_4	0	τ_4

2 The Spherical 4R Algebraic IO Equation

The R-pair axes of a spherical 4R mechanism all intersect at the centre of the sphere. Those of a planar 4R mechanism are all parallel; they can be thought of as intersecting in a common point at infinity of the projective extension of the Euclidean plane of the planar 4R. As shown in [9, 13], this means that the planar 4R mechanism is a special case of the spherical 4R. In the limit, as the radius of the sphere tends towards infinity, the algebraic IO equations of the spherical and planar 4R mechanisms are projectively equivalent. This suggests that there should be some similarities between the respective design parameter spaces.

A new and general method for deriving an algebraic form of the spherical 4R mechanism IO equation is presented in [13]. This method, using Study's kinematic mapping [1, 15], can also be used to derive the algebraic IO equation for planar 4R mechanisms, and we are working towards applying it to spatial linkages. Regardless, the algebraic IO equation for spherical 4R's has the form

$$Av_1^2v_4^2 + Bv_1^2 + Cv_4^2 + 8\alpha_1\alpha_3(\alpha_4^2 + 1)(\alpha_2^2 + 1)v_1v_4 + D = 0, \quad (2)$$

where

$$\begin{aligned} A &= (\alpha_1\alpha_2\alpha_3 - \alpha_1\alpha_2\alpha_4 + \alpha_1\alpha_3\alpha_4 - \alpha_2\alpha_3\alpha_4 + \alpha_1 - \alpha_2 + \alpha_3 - \alpha_4) \\ &\quad (\alpha_1\alpha_2\alpha_3 - \alpha_1\alpha_2\alpha_4 - \alpha_1\alpha_3\alpha_4 - \alpha_2\alpha_3\alpha_4 - \alpha_1 - \alpha_2 - \alpha_3 + \alpha_4), \\ B &= (\alpha_1\alpha_2\alpha_3 + \alpha_1\alpha_2\alpha_4 - \alpha_1\alpha_3\alpha_4 - \alpha_2\alpha_3\alpha_4 + \alpha_1 + \alpha_2 - \alpha_3 - \alpha_4) \\ &\quad (\alpha_1\alpha_2\alpha_3 + \alpha_1\alpha_2\alpha_4 + \alpha_1\alpha_3\alpha_4 - \alpha_2\alpha_3\alpha_4 - \alpha_1 + \alpha_2 + \alpha_3 + \alpha_4), \\ C &= (\alpha_1\alpha_2\alpha_3 - \alpha_1\alpha_2\alpha_4 - \alpha_1\alpha_3\alpha_4 + \alpha_2\alpha_3\alpha_4 - \alpha_1 + \alpha_2 + \alpha_3 - \alpha_4) \\ &\quad (\alpha_1\alpha_2\alpha_3 - \alpha_1\alpha_2\alpha_4 + \alpha_1\alpha_3\alpha_4 + \alpha_2\alpha_3\alpha_4 + \alpha_1 + \alpha_2 - \alpha_3 + \alpha_4), \\ D &= (\alpha_1\alpha_2\alpha_3 + \alpha_1\alpha_2\alpha_4 + \alpha_1\alpha_3\alpha_4 + \alpha_2\alpha_3\alpha_4 - \alpha_1 - \alpha_2 - \alpha_3 - \alpha_4) \\ &\quad (\alpha_1\alpha_2\alpha_3 + \alpha_1\alpha_2\alpha_4 - \alpha_1\alpha_3\alpha_4 + \alpha_2\alpha_3\alpha_4 + \alpha_1 - \alpha_2 + \alpha_3 + \alpha_4). \end{aligned}$$

In this equation the joint angle parameters are $v_i = \tan \theta_i/2$, where the IO angle parameter pair are v_1 and v_4 , while the four link twist angle parameters are $\alpha_i = \tan \tau_i/2$. The link twist angles, τ_i , are defined using the original Denavit-Hartenberg assignment convention [4]. It can be shown that Eq. (2) is identical to the corresponding trigonometric IO equation for spherical four-bar linkages found in [11].

2.1 Interpreting the Spherical 4R Algebraic IO Equation

Analysing Eq. (2) using the theory of planar algebraic curves [12] one can see that it has characteristics which are independent of the constant design parameters α_i . Clearly, Eq. (2) is of degree $n = 4$ in variables v_1 and v_4 . It is also of interest to determine the planar curve's double, or singular, points: locations where the curve self-intersects. To identify the double points of Eq. (2) it must first be homogenised. We arbitrarily select w to be the homogenising coordinate, which gives

$$k_h : Av_1^2v_4^2 + Bv_1^2w^2 + Cv_4^2w^2 + 8\alpha_1\alpha_3(\alpha_4^2 + 1)(\alpha_2^2 + 1)v_1v_4w^2 + Dw^4 = 0. \quad (3)$$

The double points are revealed by the locations where the Jacobian ideal vanishes [12]. This ideal is generated by

$$\left\langle \frac{\partial k_h}{\partial v_1}, \frac{\partial k_h}{\partial v_4}, \frac{\partial k_h}{\partial w} \right\rangle. \quad (4)$$

Solving the system of four equations implied by Eqs. (3, 4) for v_1 , v_4 , and w reveals two double points located at infinity along the v_1 - and v_4 -axes, which exactly mirrors the results reported in [8] for planar 4R mechanisms:

$$(v_1 : v_4 : w) = (1 : 0 : 0); (0 : 1 : 0). \quad (5)$$

These two double points are common to all algebraic IO curves for every spherical 4R four-bar mechanism. Each of these double points can have real or complex tangents depending on the values of the four constant link twist parameters, α_i , which in turn determines the nature of the mobility of the input and output links.

The discriminant of Eq. (3), evaluated at a double point, reveals whether that double point has a pair of real or complex conjugate tangents [2] in turn yielding information about the topology of the mechanism [8]. The discriminant and the meaning of its value are [2]

$$\Delta = \left(\frac{\partial^2 k_h}{\partial v_i \partial w} \right)^2 - \frac{\partial^2 k_h}{\partial v_i^2} \frac{\partial^2 k_h}{\partial w^2} \begin{cases} > 0 \Rightarrow \text{two real distinct tangents (crunode),} \\ = 0 \Rightarrow \text{two real coincident tangents (cusp),} \\ < 0 \Rightarrow \text{two complex conjugate tangents (acnode).} \end{cases}$$

For the homogeneous IO equation of an arbitrary spherical 4R linkage, Eq. (3), the discriminant of the point at infinity $(v_1 : v_4 : w) = (1 : 0 : 0)$ on the v_1 -axis is obtained by setting $i = 4$ in the discriminant equation, i.e. ∂v_4 , while the discriminant of the other point at infinity on the v_4 -axis is obtained by setting $i = 1$ in the discriminant equation, i.e. ∂v_1 , giving

$$\Delta_{v_1} = -4AB, \quad \Delta_{v_4} = -4AC. \quad (6)$$

Since the signed numerical values of Eq. (6) depend on the products and sums of link twist angle parameters their values may be either greater than, less than,

or identically equal to zero. Certainly, the classification of the mobility of the input and output links is determined by these values.

Finally, because an equation of degree $n = 4$ can have a maximum of three double points, the algebraic IO equation possesses genus 1 since it has only two. Because of this, it cannot be parameterised by rational functions, and is defined to be an *elliptic* curve [12]. Moreover, since the curve has genus 1 for every spherical 4R linkage, there are, at most, two assembly modes roughly corresponding to the “elbow-up” and “elbow-down” configurations [8].

3 Spherical 4R Design Parameter Space

The eight factors in the four coefficients A , B , C , and D in Eq. (2) are cubics in the α_i design constant twist angle parameters and have an intoxicating symmetric structure. When α_1 , α_2 , and α_3 are projected into the hyperplane $\alpha_4 = 1$ for a spherical 4R function generator, we can treat the three twist angle parameters α_1 , α_2 , and α_3 as mutually orthogonal basis vector directions. Figures 2(a) and (b) illustrate the eight factors in each of the planar and spherical 4R algebraic IO equations where the surfaces are plotted in the ranges $a_i = \pm 1$ and $\alpha_i = \pm 1$ in the respective projections $a_4 = \alpha_4 = 1$. The planar 4R surface is a regular double tetrahedron with the special property of being the only uniform polyhedral compound [3]. The eight spherical 4R cubic surfaces have the appearance of being a double tetrahedron in the range of $\alpha_i = \pm 1$, but they are not planar and therefore are not tetrahedron faces.

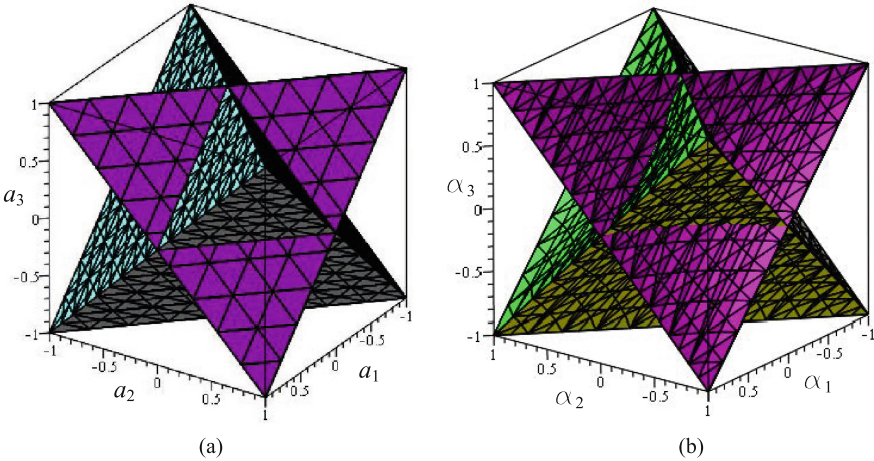


Fig. 2. Design parameter space surfaces: (a) planar 4R; (b) spherical 4R.

Cubic surfaces have fascinated mathematicians for several centuries. Clearly, the eight cubic factors in Eq. (2) possess some special properties. The first cubic factor in coefficient A from Eq. (2), which we will name A_1 , after normalising with α_4 , can be homogenised with coordinate w to reveal

$$A_{1,h} : \alpha_1\alpha_2\alpha_3 - \alpha_1\alpha_2w + \alpha_1\alpha_3w - \alpha_2\alpha_3w + \alpha_1w^2 - \alpha_2w^2 + \alpha_3w^2 - w^3. \quad (7)$$

The double points for this cubic are revealed by the locations of where the Jacobian ideal generated by

$$\left\langle \frac{\partial A_{1,h}}{\partial \alpha_1}, \frac{\partial A_{1,h}}{\partial \alpha_2}, \frac{\partial A_{1,h}}{\partial \alpha_3}, \frac{\partial A_{1,h}}{\partial w} \right\rangle \quad (8)$$

vanishes. It turns out that all eight cubics share the same three double points, namely

$$(\alpha_1 : \alpha_2 : \alpha_3 : w) = (1 : 0 : 0 : 0); (0 : 1 : 0 : 0); (0 : 0 : 1 : 0). \quad (9)$$

The discriminant evaluated at each of the three double points, common to all eight cubics, is $\Delta = 4$ for each double point. Since this discriminant is always greater than zero, the double points are all ordinary, or crunodes [2], because there are two distinct, real tangents at each double point. Alternately, we observe that each cubic surface meets the plane at infinity in the three lines $\alpha_1 = \alpha_2 = \alpha_3 = 0$. The double points are the vertices of this triangle. It can be shown that the two lines through each vertex are in the tangent singular cone at the vertex, and because the Hessian of $A_{1,h}$ is non-zero at each vertex then each one is an ordinary double point.

It is well known that cubic surfaces can contain as many as 27 lines [14]. It is also shown in [14] that a cubic surface possessing three ordinary double points can have, at most, 12 lines. The procedure for determining the lines is not particularly germane to this paper, nonetheless it can be shown that of these 12 lines six are complex and six are real. Of the six real lines three are at infinity. The remaining three lines on each surface intersect each other in an equilateral triangle. Moreover, different pairs of the cubics share a line, meaning that there are only 12 distinct finite lines among the eight cubics. The set of 12 distinct lines on each of the eight surfaces intersect to form the 12 edges of a double tetrahedron! This double tetrahedron can be regarded as the intersection of the planar and spherical 4R design parameter spaces. Treating the α_i as directed distances, each distinct point in this space determines a unique function generator, as well as the mobility of it's input, and output links (Fig. 3).

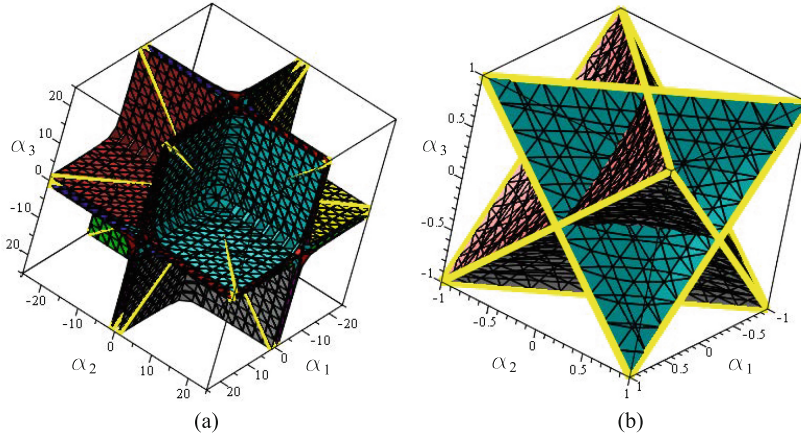


Fig. 3. 12 distinct lines, three on each of eight cubics: (a) zoomed out; (b) zoomed in.

4 Conclusions

In this paper we have shown that there is a profound relationship between the design parameter spaces of planar and spherical 4R linkages. Indeed, if we ignore the difference between units of length for the a_i and measures of angle for the α_i and simply consider the magnitudes, we see that the design parameter spaces of planar and spherical 4R linkages intersect in the edges of the only uniform polyhedral compound. It is called the stellated octahedron, which has order 48 octahedral symmetry: a regular double tetrahedron that intersects itself in a regular octahedron. We believe that there is something of remarkable beauty in this new and elegant result: the design parameter spaces of these two classes of mechanism intersect along the edges of the only uniform polyhedral compound in the universe of polyhedra!

References

1. Bottema, O., Roth, B.: *Theoretical Kinematics*. Dover Publications Inc., New York (1990)
2. Cipolla, R., Giblin, P.: *Visual Motion of Curves and Surfaces*. Cambridge University Press, Cambridge (2000)
3. Coxeter, H.S.M.: *Regular Polytopes*, 3rd edn. Dover Publications Inc., New York (1973)
4. Denavit, J., Hartenberg, R.S.: A kinematic notation for lower-pair mechanisms based on matrices. *Trans ASME J. Appl. Mech.* **23**, 215–221 (1955)
5. Freudenstein, F.: An analytical approach to the design of fourlink mechanisms. *Trans. ASME* **77**, 483–492 (1954)
6. Hayes, M.J.D., Husty, M.L., Pfüner, M.: Input-output equation for planar four-bar linkages. In: Lenarčič, J., Parenti-Castelli, V. (eds.) *Advances in Robotic Kinematics*, 16th edn., pp. 12–19. Springer, New York (2018)

7. Hayes, M.J.D., Rotzoll, M., Husty, M.L., Pfulner, M.: Design parameter space of planar four-bar linkages. In: Proceedings of the 15th IFToMM World Congress, 30 June – 4 July 2019 (2019)
8. Husty, M.L., Pfulner, M.: An algebraic version of the input-output equation of planar four-bar mechanisms. In: International Conference on Geometry and Graphics, Milan, Italy, pp. 746–757 (2018)
9. McCarthy, J.M.: Planar and spatial rigid motion as special cases of spherical and 3-spherical motion. *J. Mech. Transm. Autom. Des.* **105**(3), 569–575 (1983)
10. McCarthy, J.M., Soh, G.S.: Geometric Design of Linkages. Interdisciplinary Applied Mathematics, 2nd edn. Springer, New York (2011)
11. Murray, A.P., Larochelle, P.M.: A classification scheme for planar $4R$, spherical $4R$, and spatial $RCCR$ linkages to facilitate computer animation. In: Proceedings of 1998 ASME Design Engineering Technical Conferences (DETC'1998), 13-16 September 1998, Atlanta, Georgia, U.S.A. (1998)
12. Primrose, E.: Plane Algebraic Curves. MacMillan, New York (1955)
13. Rotzoll, M., Hayes, M.J.D., Husty, M.L., Pfulner, M.: A general method for determining algebraic input-output equations for planar and spherical $4R$ linkages. In: Accepted for publication in the 17th International Symposium: Advances in Robotic Kinematics, June 28-July 2, 2020, Ljubljana, Slovenia (2020)
14. Segre, B.: The Non-singular Cubic Surfaces; A New Method of Investigation with Special Reference to Questions of Reality. The Clarendon Press, Oxford (1942)
15. Study, E.: Geometrie der Dynamen. Teubner Verlag, Leipzig, Germany (1903)



Ball's Point Construction Revisited

Stefan Gössner^(✉)

Dortmund University of Applied Sciences and Arts, Dortmund, Germany
stefan.goessner@fh-dortmund.de

Abstract. Two well known graphical methods based on *Bobillier's* construction of the inflection pole and *Bereis's* construction of *Ball's* point on the inflection circle are used for many decades. In this paper a new general-purpose method of *step-by-step* vectorization of constructions like these is introduced. It is based on *symplectic geometry* in its simplest possible 2D case and is making use of loop closure equations exclusively. The vectorization process is coordinate and trigonometry free. The formulas found by this method are new and their correctness is easily verified by comparison with results of the corresponding graphical methods.

Keywords: Vectorization · Bobillier construction · Inflection circle · Bereis' construction · Ball's point

1 Introduction

In the sense “*kinematics is the geometry of motion*” some important methods to determine kinematic points of interest are based on pure geometric constructions. In this paper two famous constructions are revisited: *Bobillier's* construction for finding the inflection point and circle as well as *Bereis's* Ball's point or *undulation point* construction, which is based upon the former, as that point is located on the inflection circle. *Bobillier's* construction is well described by Uicker et al. [1] and an illustrative description of *Bereis's* undulation point construction is given by Modler [2].

In this paper a new method of creating planar vector equations directly from these constructions by a vectorization of each single construction process step is introduced the first time. Formally loop closure equations are used and treated according to the rules of *symplectic geometry* [3]. The symplectic vector space \mathbb{R}^2 is equipped with a *compatible complex structure*, which in this case is an *orthogonal operator* [4]. Orthogonal vectors are indicated here by an overwritten ‘ \sim ’-symbol as in \vec{a} .

The paper is structured as follows. At first *Bobillier's* construction, then Ball's point construction is vectorized. A short example shows, how to apply the found vector equations.

2 Bobillier's Construction of the Inflection Pole

Two points A and B on the moving plane as well as their center points of curvature A_0 and B_0 are given. Then Bobillier's construction process for determining the inflection pole goes like this [1] (Fig. 1).

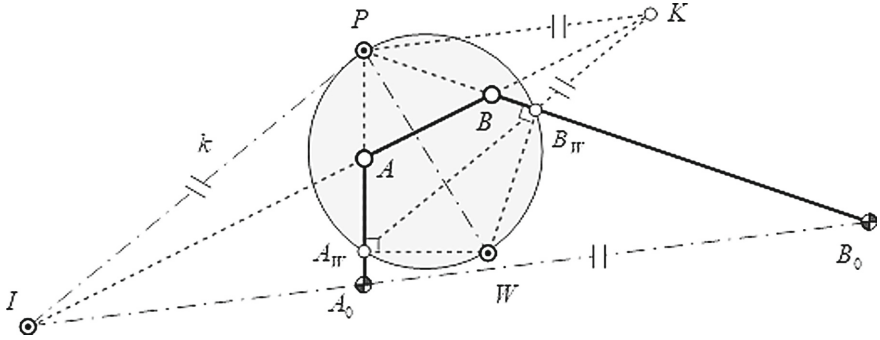


Fig. 1. Bobillier's construction of inflection pole and circle

1. Get velocity pole P as intersection point of lines A_0A and B_0B .
2. Get relative pole I as intersection point of lines AB and A_0B_0 .
3. Define collineation axis through points P and I .
4. Get K as intersection point of line AB and parallel line to A_0B_0 through P .
5. Draw parallel line to PI through K , which intersects A_0A in point A_W and B_0B in point B_W .
6. Perpendicular lines to A_0A in A_W and to B_0B in B_W intersect in inflection pole W .

Poles P and W together build the diameter of the inflection circle.

3 Vectorization of Bobillier's Construction

In order to vectorize Bobillier's construction we will go through it step-by-step while formulating loop closure equations – mostly of triangles. We introduce vectors a, b, c, d such that they conform to loop closure equation (Fig. 2).

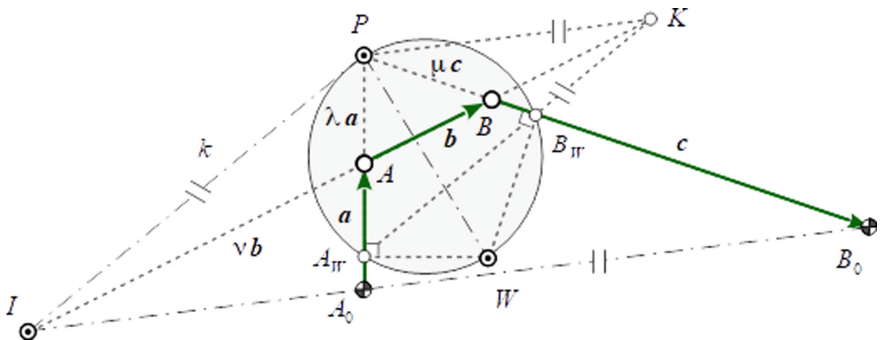


Fig. 2. Vectorization of Bobillier's construction

$$\mathbf{a} + \mathbf{b} + \mathbf{c} - \mathbf{d} = 0. \tag{1}$$

Please note that variable τ is used as a temporary variable in different contexts below. Let's start with Bobillier's first step.

1. Get velocity pole P as intersection point of lines A_0A and B_0B .

Taking triangle ABP we write down its closure equation

$$\mathbf{b} - \mu\mathbf{c} - \lambda\mathbf{a} = 0. \quad (2)$$

Resolving this equation for dimensionless parameters λ and μ via multiplying it by $\tilde{\mathbf{c}}$ and $\tilde{\mathbf{a}}$ respectively, we get

$$\lambda = -\frac{\tilde{\mathbf{b}}\mathbf{c}}{\tilde{\mathbf{c}}\mathbf{a}} \text{ and } \mu = -\frac{\tilde{\mathbf{a}}\mathbf{b}}{\tilde{\mathbf{c}}\mathbf{a}}. \quad (3)$$

2. Get relative pole I as intersection point of lines AB and A_0B_0 .

Now taking triangle A_0AI and its closure equation $\mathbf{a} - \nu\mathbf{b} + \tau\mathbf{d} = 0$ we are able to resolve it for ν , while substituting $\mathbf{d} = \mathbf{a} + \mathbf{b} + \mathbf{c}$ and using expressions (3).

$$\nu = \frac{\tilde{\mathbf{a}}\mathbf{d}}{\tilde{\mathbf{b}}\mathbf{d}} = \frac{\tilde{\mathbf{a}}\mathbf{b} - \tilde{\mathbf{c}}\mathbf{a}}{\tilde{\mathbf{b}}\mathbf{c} - \tilde{\mathbf{a}}\mathbf{b}} = \frac{1 + \mu}{\lambda - \mu}. \quad (4)$$

3. Define collineation axis through points P and I .

Assuming the collineation axis vector \mathbf{k} being directed from P to I , the closure equation of triangle API reads $\lambda\mathbf{a} + \mathbf{k} + \nu\mathbf{b} = 0$. Resolving it for \mathbf{k} , while substituting \mathbf{b} via (2) and reusing (3) and (4), delivers the *collineation axis formula*.

$$\mathbf{k} = -\frac{(\lambda^2 + \lambda)\mathbf{a} + (\mu^2 + \mu)\mathbf{c}}{\lambda - \mu}. \quad (5)$$

4. Get K as intersection point of line AB and parallel line to A_0B_0 through P .

Focusing on triangle PBK in Fig. 2 and its closure equation $\mu\mathbf{c} + \beta\mathbf{b} - \tau\mathbf{d} = 0$ allows to resolve for β after multiplication by \mathbf{d} .

The substitution $\mathbf{d} = \mathbf{a} + \mathbf{b} + \mathbf{c}$ is used again and yields.

$$\beta = \frac{\mu(1 + \lambda)}{\lambda - \mu}. \quad (6)$$

5. Draw parallel line to PI through K , which intersects A_0A in point A_W and B_0B in point B_W .

Using triangle AKA_W and its closure equation $(1 + \beta)\mathbf{b} - \tau\mathbf{k} + \alpha\mathbf{a} = 0$ as well as triangle BKB_W with $\beta\mathbf{b} + \tau\mathbf{k} - \gamma\mathbf{c} = 0$ results in two nice simple expressions already known from Eq. (5).

$$\alpha = \lambda^2 \text{ and } \gamma = \mu^2. \quad (7)$$

6. Perpendicular lines to \tilde{A}_0A in A_W and to B_0B in B_W intersect in inflection pole W .

For this last step we are focusing on quadrilateral PB_WWA_W with its loop closure equation $(\mu + \gamma)\mathbf{c} + \tau\tilde{\mathbf{c}} + \eta\tilde{\mathbf{a}} + (\alpha + \lambda)\mathbf{a} = 0$. Multiplication by \mathbf{c} and reusing expressions (7) results in

$$\eta = \frac{(\lambda^2 + \lambda)(\mathbf{a} \mathbf{c}) + (\mu^2 + \mu)\mathbf{c}^2}{\tilde{\mathbf{c}} \mathbf{a}}.$$

Now the vector from pole P to inflection pole W can be written as $\mathbf{w} = -(\lambda^2 + \lambda)\mathbf{a} - \eta\tilde{\mathbf{a}}$. Inserting expression for η yields

$$\mathbf{w} = \frac{(\lambda^2 + \lambda)[\mathbf{a}(\tilde{\mathbf{c}} \mathbf{a}) + \tilde{\mathbf{a}}(\mathbf{c} \mathbf{a})] + (\mu^2 + \mu)\mathbf{c}^2\tilde{\mathbf{a}}}{\tilde{\mathbf{c}} \mathbf{a}}.$$

Yet applying Grassmann identity $\mathbf{a}(\tilde{\mathbf{c}} \mathbf{a}) + \tilde{\mathbf{a}}(\mathbf{c} \mathbf{a}) - \mathbf{a}^2\tilde{\mathbf{c}} = 0$ [3] we finally get the vector $\mathbf{w} = PW$ of the inflection circle's diameter.

$$\mathbf{w} = -\frac{(\mu^2 + \mu)\mathbf{c}^2\tilde{\mathbf{a}} + (\lambda^2 + \lambda)\mathbf{a}^2\tilde{\mathbf{c}}}{\tilde{\mathbf{c}} \mathbf{a}}. \quad (8)$$

Vector Eq. (8) of the inflection pole is identical to that one in [5], where it was derived by a pure kinematic approach. Please note the symmetry and similarity of inflection pole Eq. (8) and collineation axis Eq. (5). Also note both variants of vectorial Euler-Savary formula, which are easily derived from (8).

$$-\mathbf{w} \mathbf{a} = (\lambda^2 + \lambda)\mathbf{a}^2 \text{ and } \mathbf{w} \mathbf{c} = (\mu^2 + \mu)\mathbf{c}^2.$$

4 Ball's Point Construction

A particular point of interest on the inflection circle is the so called *undulation point* or *Ball's point* U [6]. It is a point of intersection of the cubic of stationary curvature and with the inflection circle. So its path has stationary curvature and as a coupler point it describes a straight line of higher order. There is also a construction given by Bereis [2]. It requires having determined the inflection point W beforehand and works like this (Fig. 3).

1. Get helper point A_H as intersection point of perpendicular line to A_0A through A_0 and parallel line to A_0A through W .
2. Get helper point B_H as intersection point of perpendicular line to B_0B through B_0 and parallel line to B_0B through W .
3. Get A_U as intersection of AA_H and perpendicular line to A_0A through P .
4. Get B_U as intersection of BB_H and perpendicular line to B_0B through P .
5. Helper point U_H is the intersection of parallel line to A_0A through A_U and parallel line to B_0B through B_U .
6. Undulation point U is the intersection of line U_HP with the inflection circle.

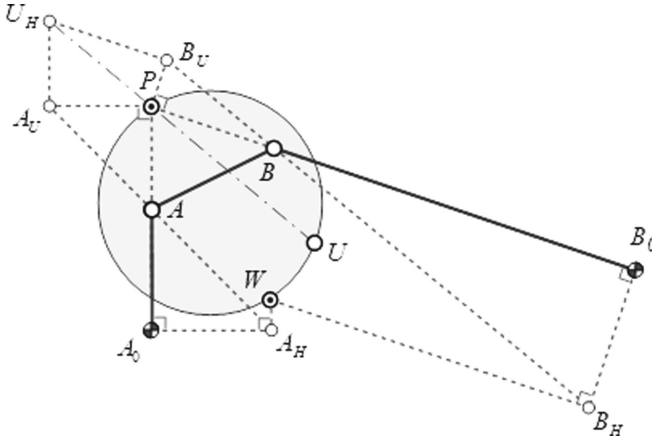


Fig. 3. Ball's point construction according to Bereis

5 Vectorization of Ball's Point Construction

In order to vectorize Ball's point construction we go through it step by step. And again τ is used as a temporary variable in different contexts below.

1. Get helper point A_H as intersection point of perpendicular line to A_0A through A_0 and parallel line to A_0A through W .
2. Get helper point B_H as intersection point of perpendicular line to B_0B through B_0 and parallel line to B_0B through W .

Consider the quadrilateral A_0PWA_H in Fig. 4 with its closure equation $(1 + \lambda)\mathbf{a} + \mathbf{w} - \tau\mathbf{a} + \alpha\tilde{\mathbf{a}} = 0$, as well as quadrilateral B_0PWB_H in Fig. 4 with its closure equation $-(1 + \mu)\mathbf{c} + \mathbf{w} + \tau\mathbf{c} + \gamma\tilde{\mathbf{c}} = 0$, Multiplying them by $\tilde{\mathbf{a}}$ and $\tilde{\mathbf{c}}$ respectively we get the parameters of interest.

$$\alpha = \frac{\tilde{\mathbf{w}}\mathbf{a}}{\mathbf{a}^2} \text{ and } \gamma = \frac{\tilde{\mathbf{w}}\mathbf{c}}{\mathbf{c}^2}. \quad (9)$$

3. Get A_U as intersection of AA_H and perpendicular line to A_0A through P .
4. Get B_U as intersection of BB_H and perpendicular line to B_0B through P .

A closer look at the similar triangles AA_0A_H and APA_U as well as BB_0B_H and BPB_U in Fig. 4 leads us to the parameter relations

$$\kappa = \lambda\alpha \text{ and } \delta = \mu\gamma. \quad (10)$$

5. Helper point U_H is the intersection of parallel line to A_0A through A_U and parallel line to B_0B through B_U .

6 Example

The four-bar used in all figures in this paper is based on the vectors $\mathbf{a} = \begin{pmatrix} 0 \\ 2e \end{pmatrix}$, $\mathbf{b} = \begin{pmatrix} 2e \\ e \end{pmatrix}$, $\mathbf{c} = \begin{pmatrix} 6e \\ -2e \end{pmatrix}$... with some length unit e .

Expressions (3) give us $\lambda = \frac{5}{6}$ and $\mu = \frac{1}{3}$. Equations (8), (11) and (12) then yield the inflection pole $\mathbf{w} = \begin{pmatrix} 1.944e \\ -3.056e \end{pmatrix}$ and Ball's point $\mathbf{u} = \begin{pmatrix} 2.654e \\ -2.200e \end{pmatrix}$ seen from the pole P .

7 Conclusions

Two well known graphical methods based on *Bobillier's* construction of the inflection pole and *Bereis's* construction of *Ball's* point on the inflection circle are used for many decades. Analytical formulas for determining these points of interest are available and mostly make use of famous *Euler-Savary* formula and the knowledge of the *circling-point curve*.

In this paper a new general-purpose method of *step-by-step* vectorization of constructions like these is introduced. It is based on *symplectic geometry* – equipped with a *compatible complex structure* – in its simplest possible 2D case [3] and is making use of loop closure equations exclusively. The vectorization process is coordinate and trigonometry free. The formulas found by this method are new and characterized through their areal terms. The correctness of them is easily verified by comparison with results of the corresponding graphical methods.

References

1. Uicker, J.J., et al.: Theory of Machines and Mechanisms. Oxford Press, Oxford (2011). ISBN 978-0-19-977781-5
2. Modler, K.-H.: Getriebetechnik. Springer, Heidelberg (1995). ISBN 3-540-57001-2
3. Gössner, S.: Symplectic Geometry for Engineers - Fundamentals (2019). https://www.researchgate.net/publication/338124384_Symplectic_Geometry_for_Engineers_-_Fundamentals
4. Gössner, S.: Mechanismtechnik Vektorielle Analyse ebener Mechanismen. Logos Verlag, 2017, ISBN 978-3-8325-4362-4
5. Gössner, S.: The Planar Euler-Savary Equation in Vectorial Notation (2017). https://www.researchgate.net/publication/318661368_The_Planar_Euler-Savary_Equation_in_Vectorial_Notation
6. Dijkman, E.A.: Motion Geometry of Mechanisms. Cambridge University Press, Cambridge (1976). ISBN 0-521-20841-6



The Effect of Selection of Virtual Variable on the Direct Kinematics of Parallel Mechanisms

Huiping Shen¹(✉), Qing Xu¹, Ju Li¹, Guanglei Wu², and Ting-li Yang¹

¹ Research Center for Advanced Mechanism Theory,
Changzhou University, Changzhou 213164, People's Republic of China
shp65@126.com

² School of Mechanical Engineering,
Dalian University of Technology, Dalian 116024, People's Republic of China
gwu@dlut.edu.cn

Abstract. This paper has an interesting observation, i.e., the selection of the loop virtual variable position has an important effect on the direct kinematics analysis of PMs. The correct selection of the virtual variable position will directly affect the effectiveness of solving the direct kinematics of a PM and even affect the form of the direct kinematics. If the virtual variable position is properly selected, the symbolic solutions can be obtained. Otherwise, only closed-form solutions or numerical solutions can be obtained. A one-translation and one-rotation PM as an example is used to derive its symbolic direct kinematics for verification.

Keywords: Parallel mechanisms · Virtual variable · Direct kinematics · Coupling degree

1 Introduction

Solving the direct kinematics is one of the most important and basic problems in the investigation of a parallel mechanism (PM). The direct kinematics of the PMs generally includes two items, i.e., 1) the establishment of input-output position equations, and 2) the numerical or algebraic solutions of the position equations. At present, there is a fewer investigation on how to establish input-output position equations with fewer variables although there are many case studies on the applications of mathematical methods (numerical method [1], algebra method [2, 3]) to the solution of the position equations.

While establishing the input-output position equation of the PM involves the kinematics modeling principle, which mainly includes the link-joint-based method and the loop-based method [1–4].

The authors pay attention to the kinematics modeling and solution method based on the topological characteristics of the PM [5], by which authors recently find that: 1) the correct selection of the virtual variable position will directly affect the efficiency and even the form of the direct solutions, and 2) the symbolic solutions can be obtained if the virtual variable position is properly selected. Otherwise, only the closed-form or numerical solutions can be obtained.

2 Two Selection Methods for Virtual Variable

Based on the extensive experience on direct kinematics analysis of spatial PMs, the authors found that the selection of the loop virtual variable position (for PM with coupling degree $k \geq 1$) has an important impact on the direct kinematics and that the selection method of the virtual position variable is related to the topology of the loop to be solved and the pose property of the moving platform. Therefore, the authors propose two selection methods of the virtual variable.

1) When the loop to be solved contains or passes through the moving platform, it is preferred to select one of (if $k = 1$) or κ of the output elements (if $k > 1$) of the moving platform as the virtual variable(s). Then, calculations start from the moving platform to the different input joints at the same time. Since such calculations work simultaneously in a parallel way, it is called as parallel-way- computing. Its characteristics are: (1) the calculation path is short, and there are more ways to establish position constraint equations; (2) the computing way can avoid to take angle(s) as variable(s) but cartesian coordinate(s) as virtual variable(s), which can reduce the multi-value properties and more calculation errors caused by trigonometric functions.

2) When the loop to be solved does not contain or pass through the moving platform, it is generally preferred to select the angle(s) of the joint(s) that is adjacent to the actuated joint as the virtual variable(s). Then, calculations start from one side of the loop (e.g., left side) to the other side of the loop (e.g., right side) in a serial way. Therefore it is called as serial-way-computing. Its characteristics are: (1) calculation path is relatively long. For each loop, only one position constraint equation is established. (2) angle virtual variable(s) will bring multiple values and more calculation errors caused by trigonometric functions.

In the following, a one-translation and one-rotation (1T1R) PM is taken as an example to illustrate the application of these two computing methods and how they affect on the solution efficiency and the form of the direct kinematics (i.e., numerical one or symbolic one).

3 An Example-Position Analysis of 1T1R PM

3.1 Mechanism Design

The 1T1R PM designed by the authors is shown in Fig. 1. The PM consists of the fixed platform 0, the moving platform 1 and three chains.

Among them, the first and second chains are denoted as $R_{i1}-U_{i2}-S_{i3}$ ($i = 1, 2$), which are connected to the fixed platform 0 through the revolute joints R_{11} and R_{21} , respectively, and to the moving platform 1 through the spherical joints S_{13} and S_{23} , respectively. Here the joint U_{i2} can be replaced by spherical joints S_{i2} . The chain III is only one cylindrical joint C_{14} that is equivalent to one prismatic joint P_{14} serially connected with one revolute joints R_{14} . A chain is also called a single-open-chain(SOC) [6, 7], that is, the serial connection of links and joints.

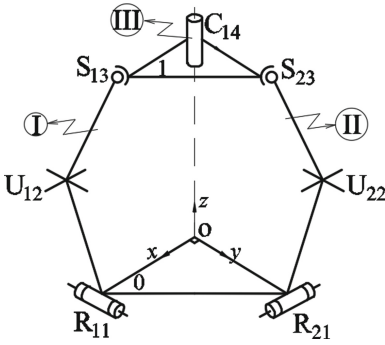


Fig. 1. One-translation and one-rotation PM

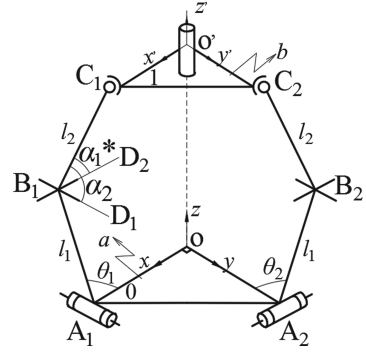


Fig. 2. Kinematic modeling

3.2 Analysis of Topological Characteristics

Due to the limitation of the space, this section directly gives the analysis results of topological characteristics of the PM [8] below.

- 1) The position and orientation characteristics (POC) [6, 7, 9] of the moving platform 1 of the PM is one-translation along the P_{14} direction and one-rotation around the axis of the revolute joint R_{14} that is also the normal direction of the moving platform.
- 2) The full-cycle DOF of the PMs is two. Therefore, R_{11} and R_{21} on the fixed platform 0 are taken as the actuated joints.
- 3) The PM contains two loops, i.e., $Loop_1\{-R_{11}-U_{12}-S_{13}-C_{14}-\}$ and $Loop_2\{-R_{21}-U_{22}-S_{23}-\}$. The coupling degree [6, 7, 9, 10] of the PM is one, therefore only one virtual variable needs to be assigned when the direct kinematics of the PM is performed.

3.3 Direct Kinematics

The kinematic modeling of the PM is shown in Fig. 2. Let the fixed platform 0 be an isosceles right triangle with a right-angle side length a . The point O is selected as the origin of the frame coordinate system, with the x -axis along the OA_1 direction and the y -axis along the OA_2 direction. Let moving platform 1 be an isosceles right-angled triangle with a right-angled side length b . The point O' is selected as the origin of the moving coordinate system; the x' axis is along the $O'C_1$ direction; the y' axis is along the $O'C_2$ direction. Let the two actuated input angles of the revolute joints R_{11} , R_{21} be θ_1 and θ_2 , respectively, and $A_iB_i = l_1$, $B_iC_i = l_2$ ($i = 1, 2$). The rotation angle of the moving platform is γ that is around the z axis, and the coordinate of the origin O' is $O' = (0, 0, z)$.

To solve the direct kinematics, i.e., to compute the position $O'(0, 0, z)$ and attitude angle γ of the moving platform 1 when assigning the angle θ_1 and θ_2 .

It is easy to know that the coordinates of points A_1, A_2, B_1 and B_2 are: $A_1 = (a, 0, 0)$, $A_2 = (0, a, 0)$, $B_1 = (a-l_1\cos\theta_1, 0, l_1\sin\theta_1)$, $B_2 = (0, a-l_1\cos\theta_2, l_1\sin\theta_2)$, respectively.

Serial-way-computing

Due to the coupling degree $\kappa = 1$, let the angle α_1^* be a virtual variable. α_1^* is defined a angle between B_1C_1 and the line B_1D_2 that is parallel to the line OA_1 . At the same time, assign another angle between B_1C_1 and the line B_1D_1 that are parallel to the line OA_2 be α_2 .

- (1) Solve the position of the first loop ($Loop_1: A_1-B_1-C_1-O'$) with a positive constraint degree [7, 9].

It is easy to know that the coordinate of point C_1 is given by geometry as,

$$C_1 = (x_{B_1} - l_2 \cos \alpha_1^*, l_2 \sin \alpha_1^* \cos \alpha_2, z_{B_1} + l_2 \sin \alpha_1^* \sin \alpha_2)^T \quad (1)$$

The coordinates of points C_1 and C_2 are also obtained by D-H method below.

$$C_1 = (b \cos \gamma, b \sin \gamma, z)^T \quad (2)$$

$$C_2 = (-b \sin \gamma, b \cos \gamma, z)^T \quad (3)$$

Known from Eqs. (1) and (2),

$$\begin{cases} b \cos \gamma = x_{B_1} - l_2 \cos \alpha_1^* \\ b \sin \gamma = l_2 \sin \alpha_1^* \cos \alpha_2 \\ z = z_{B_1} + l_2 \sin \alpha_1^* \sin \alpha_2 \end{cases} \quad (4)$$

From Eq. (4), we can get,

$$\alpha_2 = \arccos \frac{\sqrt{2x_{B_1} l_2 \cos \alpha_1^* - x_{B_1}^2 + b^2 - (l_2 \cos \alpha_1^*)^2}}{l_2 \sin \alpha_1^*} \quad (5)$$

- (2) Solve the position of the second loop ($Loop_2: A_2-B_2-C_2$) with a negative constraint degree [7, 9].

From Eqs. (2) and (3), we can get

$$x_{C_2} = -y_{C_1}, y_{C_2} = x_{C_1}, z_{C_2} = z_{C_1}$$

$$C_2(-l_2 \sin \alpha_1^* \cos \alpha_2, x_{B_1} - l_2 \cos \alpha_1^*, z_{B_1} + l_2 \sin \alpha_1^* \sin \alpha_2)^T.$$

According to the geometric constraint of link length $B_2C_2 = l_2$, we can get,

$$\begin{aligned} f(\alpha_1^*) = & (-l_2 \sin \alpha_1^* \cos \alpha_2)^2 + (x_{B_1} - y_{B_2} - l_2 \cos \alpha_1^*)^2 \\ & + (z_{B_1} - z_{B_2} + l_2 \sin \alpha_1^* \sin \alpha_2)^2 - l_2^2 \end{aligned}$$

It can be seen that this is a closed-form non-linear equation with independent variable α_1^* , and then the numerical solutions can be obtained by using the one-dimensional

search method. That is, changing the assignment of α_1^* from 0 to 360° until $f(\alpha_1^*) = 0$ is satisfied, and then substituting real α_1^* obtained into Eq. (5), we can obtain real α_2 . And then substituting real α_1 and α_2 into Eq. (4), the numerical values of z and γ can be easily obtained.

Parallel -way-computing

Since the first loop of the PM passes through the moving platform 1 and the coupling degree is $k = 1$, the translation amount z (or rotation angle γ) of the moving platform is assumed to be the virtual variable.

(1) Solve the position of the first loop (*Loop*₁: A₁-B₁-C₁-O')

The coordinates of the points C₁ and C₂ can be obtained from the Eqs. (2) and (3). According to the geometric constraint of link length B₁C₁ = l_2 , we can get,

$$(x_{B_1} - b\cos\gamma)^2 + (-b\sin\gamma)^2 + (z_{B_1} - z)^2 = l_2^2 \tag{6}$$

(2) Solving the position of the second loop (*Loop*₂: A₂-B₂-C₂)

According to the geometric constraint of link length B₂C₂ = l_2 , we also have,

$$(b\sin\gamma)^2 + (y_{B_2} - b\cos\gamma)^2 + (z_{C_2} - z)^2 = l_2^2 \tag{7}$$

From Eqs. (6) and (7), we can directly get the symbolic solutions below.

$$\begin{cases} z = \frac{-B_0 \pm \sqrt{B_0^2 - 4C_0}}{2} \\ \gamma = \arccos(A_0z + D_0) \end{cases} \tag{8}$$

Where, $A_0 = \frac{z_{B_2} - z_{B_1}}{b(x_{B_1} - y_{B_2})}$, $D_0 = \frac{x_{B_1}^2 + z_{B_1}^2 - y_{B_2}^2 - z_{B_2}^2}{2b(x_{B_1} - y_{B_2})}$, $B_0 = -2(z_{B_1} + bx_{B_1}A_0)$, $C_0 = x_{B_1}^2 + z_{B_1}^2 + b^2 - l_2^2 - 2bx_{B_1}D_0$.

By comparing the two computing methods, it is easily found that 1) the parallel-way-computing method is simpler and more efficient than the serial-way-computing method does, and 2) the selection of the different virtual variable position not only affects the efficiency of solving the direct kinematics, but also the form of the direct kinematics, i.e., the former is closed-form but the later is symbolic. In short, the virtual variable position has a greater impact on direct kinematics.

Inverse kinematics of the PM is simpler, which is omitted here due to the limitation of the space.

Let the structural parameters of the PM be: $a = 40$, $b = 30$, $l_1 = 30$, $l_2 = 35$ (unit: mm), and input angles be $\theta_1 = 60^\circ$, $\theta_2 = 60^\circ$. From Eqs. (1) to (5), or from Eq. (8), the two direct solutions of the PM are calculated by MATLAB respectively, as shown in Table 1, which have been verified by the inverse kinematics of the PM.

Table 1. The values of direct kinematics of the PM

	$\alpha_1^*/^\circ$	$\gamma/^\circ$	z/mm
1	-93.9651	23.9350	-6.7455
2	77.9223	53.8982	50.1434

4 Conclusions

The symbolic direct kinematics for the one-translation and one-rotation PM are obtained by the selection of the virtual variable z rather than α_1^* , which shows that reasonable selection of the virtual variable position will directly affect the easiness of solving the direct kinematics of the PM, and even the forms of the solutions (closed-form one or symbolic one).

Acknowledgment. The support by the National Natural Science Foundation of China (Grant Nos. 51975062, 51475050, 51375062) is greatly appreciated.

References

1. Luo, Y., Li, D.: Finding all solutions to forward displacement analysis problem of 6-SPS parallel robot mechanism with chaos-iteration method. *J. Eng. Des.* **10**(2), 70–74 (2003)
2. Pennock, G.R., Hasan, A.: A polynomial equation for a coupler curve of the double butterfly linkage. *J. Mech. Des.* **124**(1), 39–46 (2002)
3. Husty, M.L.: Algorithm for solving the direct kinematic of Stewart-Gough-type platforms. *Mech. Mach. Theory* **31**(4), 365–380 (1996)
4. Rooney, G.T.: Constraint approach to displacement analysis of planer linkages. *Mechanism* (9), 60–63 (1972)
5. Shen, H., Yin, H., Wang, Z., et al.: Research on direct kinematics for 6-SPS parallel mechanisms based on topology structure analysis. *J. Mech. Eng.* **49**(21), 70–80 (2013)
6. Yang, T., Liu, A., Luo, Y., et al.: *Theory and Application of Robot Mechanism Topology*. Science Press, Beijing (2012)
7. Yang, T., Liu, A., Shen, H., et al.: *Topology design of robot Mechanisms*. Springer, Heidelberg (2018)
8. Shen, H., Xu, Q.: *Kinematics Modeling and Solving for Direct Kinematics of Parallel Mechanisms Based on Topological Characteristics*. Changzhou University, Changzhou (2019)
9. Shen, H., Yang, T., Li, J., et al.: Evaluation of topological properties of parallel manipulators based on the topological characteristic indexes. *Robotica* **38**(8), 1381–1399 (2019)
10. Shen, H., Chablat, D., Zen, B., et al.: A translational three-degrees-of-freedom parallel mechanism with partial motion decoupling and analytic direct kinematics. *J. Mech. Rob.* **12**(2), 021112-1–7 (2020)



Function Generation Synthesis of Planar Slider-Crank Linkages for Given 3 Positions and a Dead-Center Position

Gökhan Kiper^(✉), İbrahimcan Görgülü, and Sefa Furkan Küçükkoğlu

İzmir Institute of Technology, Urla, Turkey

{gokhankiper, ibrahimcangorgulu, sefakucukoglu}@iyte.edu.tr

Abstract. Function generation for finitely many positions and dead-center design problems are generally separately handled in the literature. This paper presents a mixed formulation for planar slider-crank linkages where three precision points and a folded or extended dead-center position are to be satisfied. The formulation results in an 8th degree univariate. Examples show that generally there are four real solutions, only two of which result in distinct solutions.

Keywords: Function generation synthesis · Slider-crank linkage · Finitely many positions · Dead-center design

1 Introduction

Designing linkages for given input/output requirements is formulated as a function generation synthesis problem. In most applications, finitely many desired values for the input/output joint variables of a linkage are given and link length dimensions are to be determined accordingly. Many textbooks issue only this type of function generation problem [1–3]. We shall call this problem as the function generation for finitely many positions. Another common problem in applications, which can be considered as a special case of function generation problem, is the dead-center design, where a desired limited range of output joint variable is specified for corresponding variation of the input joint variable. The linkage is designed to be at the dead-center position (DCP) at the limits of the output joint variable, where the output speed is instantaneously zero, hence it is dead. Hall [4] and Norton [5] treat the function generation for finitely many positions and the dead-center design problems as separate problems. The dead-center problem is even treated as a fourth type of synthesis problem in addition to motion, path and function generation problems by Mallik et al. [6].

The planar four-bar and the planar slider-crank linkages are the two most commonly used linkages in applications used as function generators. There are several graphical and analytical methods for function generation synthesis of the four-bar and the slider-crank linkage in the literature. The analytical function generation synthesis methods for the four-bar and the slider-crank linkages for two and three prescribed positions and also

the dead-center design problems were summarized by Pennestrì and Valentini [7]. The four-bar and slider-crank function generators can be designed for up to five precision points [3].

In some applications, it is required to design linkages for some specific values of the input/output joint variables and also one or more DCPs. Until recently such function generation synthesis problems formulated as a mixture of function generation for finitely many positions and dead-center design have not been noted in the literature. Although these problems can rapidly and easily be solved using CAD software, analytical formulations are necessary when these problems are merely a small part of a large design problem involving linkages with many loops and many link length parameters. Recently Kiper and Erez [8] formulated the analytical design equations for a planar four-bar function generator for two specified general positions and a DCP as the third position, where coupler link is folded upon one of the cranks whereas the other crank angle at this position is irrelevant. Similar problem for three positions can be addressed for a planar slider-crank linkage as well. In this paper, we extend our formulation for three general positions and a (folded or extended) DCP as fourth position for a slider-crank linkage.

2 Design Equations

Figure 1 illustrates a general position and extended/folded DCPs of a planar slider-crank linkage. Crank length is a , coupler length is b , distance between linear path of joint B and fixed joint A_0 is d and the orientation angle of a fixed reference from which the crank angle is measured is α . This angular link parameter, α , may correspond to an angular link parameter connected to the crank or the fixed link, which needs to be designed as well. These four design parameters, a , b , d and α , are to be determined for 3 given general positions expressed in terms of pairs (θ_1, q_1) , (θ_2, q_2) and (θ_3, q_3) , and an extended or folded DCP, where only the output slider displacement, q_e or q_f is specified.

For a general position of the slider-crank linkage

$$|\overrightarrow{AB}| = |\overrightarrow{A_0B} - \overrightarrow{A_0A}| \Rightarrow b^2 = [q_i - a\cos(\alpha + \theta_i)]^2 + [d - a\sin(\alpha + \theta_i)]^2 \quad (1)$$

Let $c_i = \cos(\alpha + \theta_i)$ and $s_i = \sin(\alpha + \theta_i)$. Expanding and rearranging Eq. (1):

$$b^2 - a^2 - d^2 + 2aq_i c_i + 2ad s_i = q_i^2 \quad (2)$$

Let $P_1 = b^2 - a^2 - d^2$, $P_2 = 2a$ and $P_3 = 2ad$. Equation (2) is linear in P_1 , P_2 and P_3 . For given (θ_1, q_1) , (θ_2, q_2) and (θ_3, q_3) , P_1 , P_2 and P_3 can be linearly solved from Eq. (2) as function of α :

$$\begin{aligned} P_1 + q_1 c_1 P_2 + s_1 P_3 &= q_1^2 \\ P_1 + q_2 c_2 P_2 + s_2 P_3 &= q_2^2 \\ P_1 + q_3 c_3 P_2 + s_3 P_3 &= q_3^2 \end{aligned} \Rightarrow \begin{bmatrix} P_1 \\ P_2 \\ P_3 \end{bmatrix} = \begin{bmatrix} 1 & q_1 c_1 & s_1 \\ 1 & q_2 c_2 & s_2 \\ 1 & q_3 c_3 & s_3 \end{bmatrix}^{-1} \begin{bmatrix} q_1^2 \\ q_2^2 \\ q_3^2 \end{bmatrix} \quad (3)$$

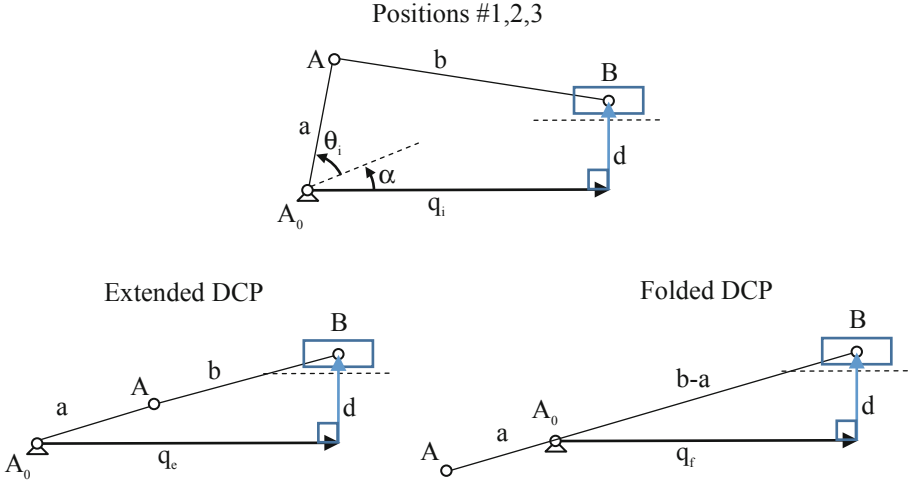


Fig. 1. A general position, extended and folded DCP of a slider-crank linkage

Using Cramer's rule:

$$\begin{aligned}
 P_1 &= \frac{q_1^2(q_2c_2s_3 - q_3c_3s_2) - q_2^2(q_1c_1s_3 - q_3c_3s_1) + q_3^2(q_1c_1s_2 - q_2c_2s_1)}{q_2c_2s_3 - q_3c_3s_2 - q_1c_1s_3 + q_3c_3s_1 + q_1c_1s_2 - q_2c_2s_1} \\
 P_2 &= \frac{(q_3^2 - q_2^2)s_1 + (q_1^2 - q_3^2)s_2 + (q_2^2 - q_1^2)s_3}{q_2c_2s_3 - q_3c_3s_2 - q_1c_1s_3 + q_3c_3s_1 + q_1c_1s_2 - q_2c_2s_1} \\
 P_3 &= \frac{(q_2^2 - q_3^2)q_1c_1 + (q_3^2 - q_1^2)q_2c_2 + (q_1^2 - q_2^2)q_3c_3}{q_2c_2s_3 - q_3c_3s_2 - q_1c_1s_3 + q_3c_3s_1 + q_1c_1s_2 - q_2c_2s_1} \quad (4)
 \end{aligned}$$

Solving for a , d , b^2 (expressed as a function of α):

$$a = P_2/2, \quad d = P_3/P_2, \quad b^2 = P_1 + a^2 + d^2 \text{ or } b = \sqrt{P_1 + a^2 + d^2} \quad (5)$$

For the extended/folded DCPs

$$\begin{aligned}
 (a + b)^2 &= q_e^2 + d^2 \Rightarrow a^2 + b^2 - d^2 - q_e^2 = -2ab \\
 (b - a)^2 &= q_f^2 + d^2 \Rightarrow a^2 + b^2 - d^2 - q_f^2 = 2ab \quad (6)
 \end{aligned}$$

In order not to have a square root expression (b^2 is given in Eq. (5)), taking square of Eq. (6):

$$(a^2 + b^2 - d^2 - q_{dc}^2)^2 = 4a^2b^2 \quad (7)$$

where q_{dc} is either q_e or q_f . By taking square of Eq. (6), the solution formulation for the extended DCP and folded DCP problems becomes identical. Writing Eq. (7) terms of P_1 , P_2 , P_3 and rearranging:

$$(P_1 - q_{dc}^2)^2 - P_3^2 - q_{dc}^2P_2^2 = 0 \quad (8)$$

Equation (8) is an equation in terms of α and can be numerically solved using a root finding algorithm. Then the corresponding a, b and d values can be determined using Eq. (5). In order to find an upper bound for the number of roots let $t = \tan \frac{\alpha}{2}$ so that

$$c_i = \frac{1 - t^2}{1 + t^2} \cos \theta_i - \frac{2t}{1 + t^2} \sin \theta_i \quad \text{and} \quad s_i = \frac{1 - t^2}{1 + t^2} \sin \theta_i + \frac{2t}{1 + t^2} \cos \theta_i \quad (9)$$

Substituting Eq. (9) into Eq. (4) and substituting Eq. (4) into Eq. (8) results in an 8th degree polynomial in t. So there are at most 8 real solutions.

3 Computer Implementation

The formulations in Sect. 2 were implemented in Excel (Fig. 2). The design inputs $\theta_1, \theta_2, \theta_3, q_1, q_2, q_3, q_{dc}$ can be altered with the associated spin buttons. The matrix inversion in Eq. (3) for evaluating P_1, P_2, P_3 is performed in cells A6:F8 for an assumed α value in cell H1. Equation (8) is in cell F5. All spin buttons for the design inputs are associated with a single line code, which runs a Newton-Raphson method based goal-seek algorithm which seeks a suitable α value in cell H1 in order to make the cell F5 value equal to zero. That is, the equation is instantaneously solved when the design inputs are altered. In order to fasten the numerical solution, the slider displacement values are normalized to be around 1. The analysis of the resulting mechanism is performed and the mechanism can be animated.

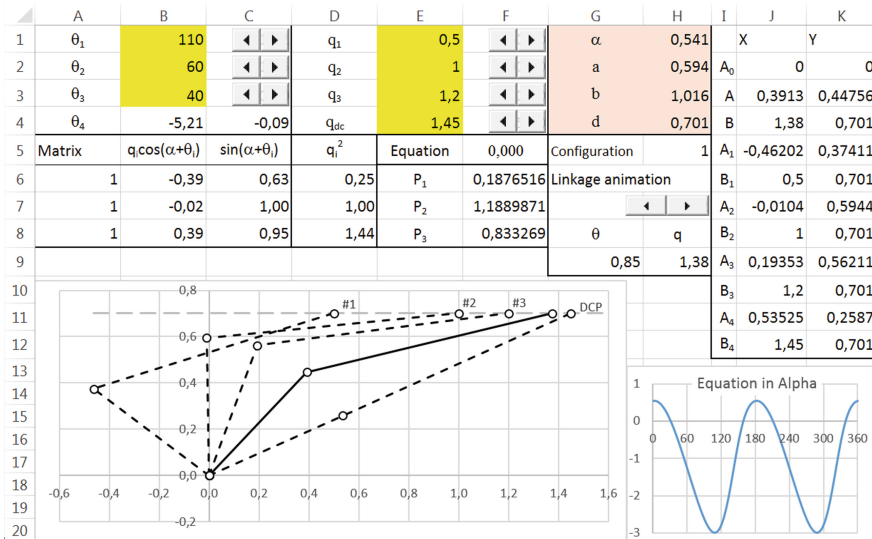


Fig. 2. Excel model

In order to see the number of roots of Eq. (8), the left hand side of the equation is plotted for $0^\circ \leq \alpha < 360^\circ$. For several examples that were worked out, it is seen that generically there are 4 real roots. We observed that two of the solutions result in positive

values of crank length a and the other two result in a negative a . Indeed the α solutions can be listed as $\alpha_1, \alpha_2, \alpha_1 + 180^\circ$ and $\alpha_2 + 180^\circ$. The 180° angle difference results in positive or negative value of a . Also it can be noticed that the curve in Fig. 2 is 180° -periodic. Therefore, actually there are two solutions. Note that Eq. (8) holds for both folded and extended dead-center position problems. For the specific numerical example in Fig. 2, two solutions are found as $\alpha = 31^\circ$ and $\alpha = 338.8^\circ$ (or equivalently -21.2°) result in feasible solutions. The linkage for $\alpha = 31^\circ$ can be seen in Fig. 2, whereas the linkage for $\alpha = 338.8^\circ$ is given in Fig. 3. The corresponding link lengths are listed in Table 1.

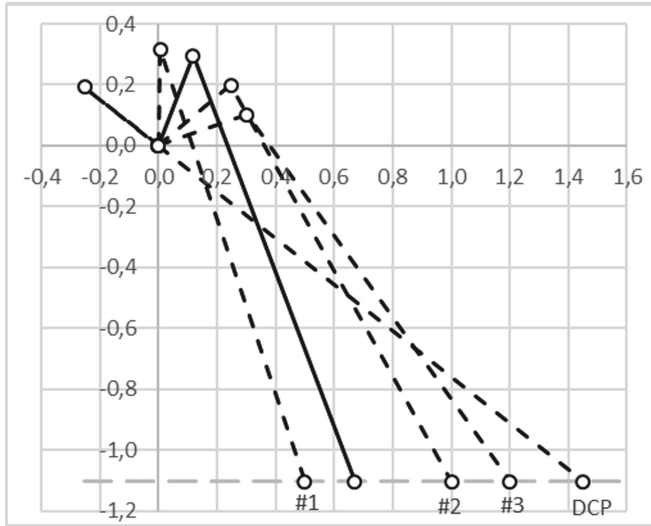


Fig. 3. Second solution for example 1

Table 1. Computed link length values for two examples

Example 1	θ_1	θ_2	θ_3	q_1	q_2	q_3	q_{dc}
		110°	60°	40°	0.5	1	1.2
	α		a		b		d
Solution 1	-21.2°		0.318		1.504		-1.103
Solution 2	31°		0.594		1.016		0.701
Example 2	θ_1	θ_2	θ_3	q_1	q_2	q_3	q_{dc}
	110°	60°	40°	0.5	1	1.2	0.25
	α		a		b		d
Solution 1	-2.55°		0.551		0.809		0.065
Solution 2	117.4°		0.323		2.667		2.330

Several examples for 3 general positions and a folded DCP (q_{cd} should be less than q_1, q_2, q_3) are also worked out. In order to have a comparable example with the one in Fig. 2, consider the case where $\theta_1 = 110^\circ, \theta_2 = 60^\circ, \theta_3 = 40^\circ, q_1 = 0.5, q_2 = 1, q_3 = 1.2$

as in Fig. 2, but $q_{cd} = 0.2$. Again two solutions for α are obtained as $\alpha = 179.36^\circ$ and $\alpha = 294.15^\circ$. Corresponding link lengths are listed in Table 1. The resulting linkages are depicted in Fig. 4.

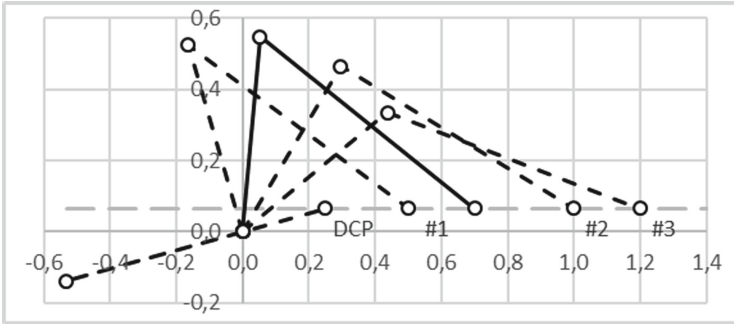


Fig. 4. First solution for example 2

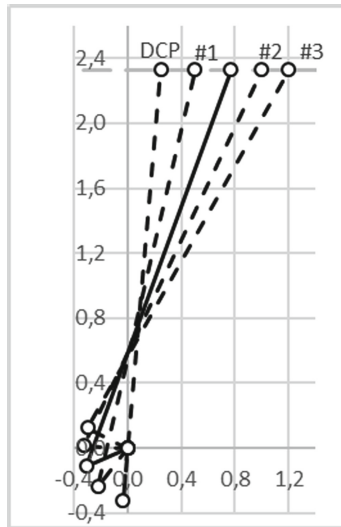


Fig. 5. Second solution for example 2

4 Conclusions and Discussions

In this paper, function generation problem for three precision points and a DCP is formulated for a slider-crank linkage. Similar formulations may be derived for other single loop linkages such as the four-bar and the inverted slider-crank. Also two precision points and two (folded and extended) DCPs can be considered. Such mixed function generation problems can also be handled for optimum transmission angle as well.

References

1. Hartenberg, R.S., Denavit, J.: Kinematic Synthesis of Linkages. McGraw-Hill, New York (1964)
2. Sandor, G.N., Erdman, A.G.: Advanced Mechanism Design: Analysis and Synthesis, vol. II. Prentice Hall, New Jersey (1984)
3. McCarthy, J.M., Soh, G.S.: Geometric Design of Linkages, 2nd edn. Springer, New York (2011)
4. Hall, A.S.: Kinematics and Linkage Design. Prentice-Hall, Englewood Cliffs (1961)
5. Norton, R.L.: Design of Machinery, 6th edn. McGraw-Hill, Boston (2019)
6. Mallik, A.K., Ghosh, A., Dittrich, G.: Kinematic Analysis and Synthesis of Mechanisms. CRC Press, Boca Raton (1994)
7. Pennestrì, E., Valentini, P.P.: A review of simple analytical methods for the kinematic synthesis of four-bar and slider-crank function generators for two and three prescribed finite positions. *Buletin Stiintific Seria Mecanica Aplicata* **25**, 128–143 (2009)
8. Kiper, G., Erez, M.: Function generation synthesis with planar 4-Bar linkage as a mixed problem of correlation of crank angles and dead-center design. In: Wang, D., Petuya, V., Chen, Y., Yu, S. (eds.) MeTrApp 2019. MMS, vol. 79, pp. 42–47. Springer, Singapore (2020). https://doi.org/10.1007/978-981-15-0142-5_5



Multidual Algebra and Higher-Order Kinematics

Daniel Condurache^(✉)

Technical University of Iasi, D. Mangeron Street no. 59, 700050 Iasi, Romania
daniel.condurache@tuiasi.ro

Abstract. In this paper, using the vector and tensor calculus and the multidual algebra, a new computing method for studying the higher-order acceleration field properties in the case of the general rigid body motion is proposed. The results are coordinate-free and in a closed-form. Higher-order kinematics analysis of lower-pair serial chains with multidual algebra will be done. In particular cases, the properties for velocity, acceleration, jerk and jounce fields are given. This approach uses the morphism between the Lie group of the rigid displacements and the Lie group of the orthogonal multidual tensors.

Keywords: Multidual algebra · Higher-order kinematics · Lie group SE_3

1 Introduction

Let be \mathbb{R} the set of real numbers and $n \in \mathbb{N}$ a natural number. We will introduce the set of multidual number [4] by $\hat{\mathbb{R}} = \mathbb{R} + \varepsilon\mathbb{R} + \dots + \varepsilon^n\mathbb{R}; \varepsilon \neq 0, \varepsilon^{n+1} = 0$.

Two generic elements $\hat{x}, \hat{y} \in \hat{\mathbb{R}}$ will be written as following:

$$\hat{x} = x + x_1\varepsilon + \dots + x_n\varepsilon^n; x, x_k \in \mathbb{R}, k = \overline{1, n} \quad (1)$$

$$\hat{y} = y + y_1\varepsilon + \dots + y_n\varepsilon^n; y, y_k \in \mathbb{R}, k = \overline{1, n} \quad (2)$$

We will denote by $x = Re\hat{x}$ and $Mu\hat{x} = \sum_{k=1}^n x_k\varepsilon^k$ the real parts and respectively, multidual parts of the multidual number \hat{x} . Also, we will denote by $x_k = \frac{d\hat{x}}{d\varepsilon^k}; k = \overline{1, n}$, the k order multidual component of the multidual number \hat{x} (1).

We will define the operations of additions and, respectively, multiplication of two multidual number by

$$\hat{x} + \hat{y} = \sum_{k=0}^n (x_k + y_k) \varepsilon^k \quad (3)$$

$$\hat{x}\hat{y} = \sum_{k=0}^n \left(\sum_{p=0}^k x_p y_{k-p} \right) \varepsilon^k \quad (4)$$

In order to simplify the writing, in Eqs. (3) and (4), we will denote by $\varepsilon^0 = 1$, $x_0 = x$, $y_0 = y$.

It can be easily proved that the set $\hat{\mathbb{R}}$ with the addition operation (3) and multiplication operation (4) is a commutative ring with unit. An element $\hat{x} \in \hat{\mathbb{R}}$ is invertible if and only if $Re\hat{x} \neq 0$. The zero divisor in the ring $\hat{\mathbb{R}}$ is characterized by $Re\hat{x} = 0$. An element from $\hat{\mathbb{R}}$ is either invertible or zero divisor.

Let be $f : \mathbb{I} \subseteq \mathbb{R} \rightarrow \mathbb{R}$, $f = f(x)$ a n -times differentiable real function. We will define the multidual function \hat{f} of multidual variable \hat{x} by equation:

$$f(\hat{x}) = f(x) + \sum_{k=1}^n \frac{\Delta^k}{k!} f^{(k)}(x) \quad (5)$$

where we denoted by Δ : $\Delta = \hat{x} - x = \sum_{k=1}^n x_k \varepsilon^k$.

Due to multinomial formula:

$$\Delta^k = \sum_{k_1+k_2+\dots+k_n=k} \frac{k!}{k_1!k_2!\dots k_n!} x_1^{k_1} x_2^{k_2} \dots x_n^{k_n} \varepsilon^{k_1+2k_2+\dots+nk_n} \quad (6)$$

and $\Delta^p = 0$, $p \geq n + 1$, the Eq. (5) becomes:

$$f(\hat{x}) = f(x) + \sum_{k=1}^n \varphi_k(x, x_1, \dots, x_k) \varepsilon^k \quad (7)$$

where the functions with real variables φ_k have the following form:

$$\varphi_k = g_1 f'(x) + g_2 f''(x) + \dots + g_k f^{(k)}(x) \quad (8)$$

where $g_k, k = \overline{1, n}$ are the k -th degree homogeneous functions with x_1, x_2, \dots, x_k .

Regarding the Eq. (7), we will denote $\varphi_k = \frac{df(\hat{x})}{d\varepsilon^k}$, $k = \overline{1, n}$.

Using the Eq. (5), we will define the following multidual functions:

$$\sin \hat{x} = \sin x + \sum_{k=1}^n \frac{\Delta^k}{k!} \sin \left(x + k \frac{\pi}{2} \right) \quad (9)$$

$$\cos \hat{x} = \cos x + \sum_{k=1}^n \frac{\Delta^k}{k!} \cos \left(x + k \frac{\pi}{2} \right) \quad (10)$$

$$\hat{x}^{-1} = \frac{1}{x} + \sum_{k=1}^n (-1)^k \Delta^k \frac{1}{x^{k+1}}; Re\hat{x} \neq 0 \quad (11)$$

1.1 Multidual Vectors

Let be \mathbb{V}_3 the set of free vectors from three-dimensional Euclidean space. We will introduce the set of multidual vectors by: $\hat{\mathbb{V}}_3 = \mathbb{V}_3 + \varepsilon \mathbb{V}_3 + \dots + \varepsilon^n \mathbb{V}_n; \varepsilon \neq 0$, $\varepsilon^{n+1} = 0$.

Two generic vectors from $\hat{\mathbf{V}}_3$ will be written as below:

$$\begin{aligned}\hat{\mathbf{a}} &= \mathbf{a} + \mathbf{a}_1\varepsilon + \dots + \mathbf{a}_n\varepsilon^n; \mathbf{a}, \mathbf{a}_k \in \mathbf{V}_3 \\ \hat{\mathbf{b}} &= \mathbf{b} + \mathbf{b}_1\varepsilon + \dots + \mathbf{b}_n\varepsilon^n; \mathbf{b}, \mathbf{b}_k \in \mathbf{V}_3\end{aligned}\quad (12)$$

The addition of two multidual vectors is defined by

$$\hat{\mathbf{a}} + \hat{\mathbf{b}} = \mathbf{a} + \mathbf{b} + (\mathbf{a}_1 + \mathbf{b}_1)\varepsilon + \dots + (\mathbf{a}_n + \mathbf{b}_n)\varepsilon^n \quad (13)$$

The multiplication of a multidual vector by a scalar $\hat{x} \in \hat{\mathbb{R}}$ is defined by:

$$\hat{x}\hat{\mathbf{a}} = \sum_{k=0}^n \sum_{p=0}^k (x_p \mathbf{a}_{k-p}) \varepsilon^k \quad (14)$$

It can be easily proven that the set of vectors $\hat{\mathbf{V}}_3$ is a free module of rank 3 over the multidual number ring $\hat{\mathbb{R}}$.

We will define the scalar product respectively the vector product of two vectors from $\hat{\mathbf{V}}_3$ by:

$$\hat{\mathbf{a}} \cdot \hat{\mathbf{b}} = \sum_{k=0}^n \sum_{p=0}^k (\mathbf{a}_p \cdot \mathbf{b}_{k-p}) \varepsilon^k \quad (15)$$

$$\hat{\mathbf{a}} \times \hat{\mathbf{b}} = \sum_{k=0}^n \sum_{p=0}^k (\mathbf{a}_p \times \mathbf{b}_{k-p}) \varepsilon^k \quad (16)$$

The triple vector product of three multidual vectors $\hat{\mathbf{a}}, \hat{\mathbf{b}}, \hat{\mathbf{c}}$ is defined by:

$$\langle \hat{\mathbf{a}}, \hat{\mathbf{b}}, \hat{\mathbf{c}} \rangle = \hat{\mathbf{a}} \cdot (\hat{\mathbf{b}} \times \hat{\mathbf{c}}).$$

All three multidual vectors $\hat{\mathbf{e}}_1, \hat{\mathbf{e}}_2, \hat{\mathbf{e}}_3$ represent a basis in the free module $\hat{\mathbf{V}}_3$ if and only if $Re(\hat{\mathbf{e}}_1, \hat{\mathbf{e}}_2, \hat{\mathbf{e}}_3) \neq 0$.

1.2 Multidual Tensors

An $\hat{\mathbb{R}}$ -linear application of $\hat{\mathbf{V}}_3$ into $\hat{\mathbf{V}}_3$ is called a Euclidean multidual tensor:

$$\mathbf{T}(\hat{\lambda}_1 \hat{\mathbf{v}}_1 + \hat{\lambda}_2 \hat{\mathbf{v}}_2) = \hat{\lambda}_1 \mathbf{T}(\hat{\mathbf{v}}_1) + \hat{\lambda}_2 \mathbf{T}(\hat{\mathbf{v}}_2); \hat{\lambda}_1, \hat{\lambda}_2 \in \hat{\mathbb{R}}; \forall \hat{\mathbf{v}}_1, \hat{\mathbf{v}}_2 \in \hat{\mathbf{V}}_3. \quad (17)$$

Let $\mathbf{L}(\hat{\mathbf{V}}_3, \hat{\mathbf{V}}_3)$ be the set of tensors, then any $\hat{\mathbf{T}} \in \mathbf{L}(\hat{\mathbf{V}}_3, \hat{\mathbf{V}}_3)$, the multidual transposed tensor denoted by $\hat{\mathbf{T}}^T$ is defined by $\hat{\mathbf{v}}_1 \cdot (\hat{\mathbf{T}}\hat{\mathbf{v}}_2) = \hat{\mathbf{v}}_2 \cdot (\hat{\mathbf{T}}^T \hat{\mathbf{v}}_1)$; $\forall \hat{\mathbf{v}}_1, \hat{\mathbf{v}}_2 \in \hat{\mathbf{V}}_3$.

While $\forall \hat{\mathbf{v}}_1, \hat{\mathbf{v}}_2, \hat{\mathbf{v}}_3 \in \hat{\mathbf{V}}_3, Re(\langle \hat{\mathbf{v}}_1, \hat{\mathbf{v}}_2, \hat{\mathbf{v}}_3 \rangle) \neq 0$, the determinant is:

$$\langle \hat{\mathbf{T}}\hat{\mathbf{v}}_1, \hat{\mathbf{T}}\hat{\mathbf{v}}_2, \hat{\mathbf{T}}\hat{\mathbf{v}}_3 \rangle = \det \hat{\mathbf{T}} \langle \hat{\mathbf{v}}_1, \hat{\mathbf{v}}_2, \hat{\mathbf{v}}_3 \rangle. \quad (18)$$

For any dual vector $\hat{\mathbf{a}} \in \hat{\mathbf{V}}_3$, the associated skew-symmetric dual tensor will be denoted by $\hat{\mathbf{a}} \times$ and will be defined $(\hat{\mathbf{a}} \times) \hat{\mathbf{b}} = \hat{\mathbf{a}} \times \hat{\mathbf{b}}, \forall \hat{\mathbf{b}} \in \hat{\mathbf{V}}_3$.

The previous definition can be directly transposed into the following result: for any skew-symmetric multidual tensor $\hat{\mathbf{A}} \in \mathbf{L}(\hat{\mathbf{V}}_3, \hat{\mathbf{V}}_3)$, $\hat{\mathbf{A}} = -\hat{\mathbf{A}}^T$, a uniquely defined multidual vector $\hat{\mathbf{a}} = \text{vect}(\hat{\mathbf{A}})$, $\hat{\mathbf{a}} \in \hat{\mathbf{V}}_3$ exists in order to have $\hat{\mathbf{A}}\hat{\mathbf{b}} = \hat{\mathbf{a}} \times \hat{\mathbf{b}}, \forall \hat{\mathbf{b}} \in \hat{\mathbf{V}}_3$. The set of skew-symmetric multidual tensors is structured as a free $\hat{\mathbb{R}}$ - module of rank 3 and is isomorphic with $\hat{\mathbf{V}}_3$.

1.3 Multidual Differential Transform

In this section will introduce a transformation that associates a hypercomplex function of a real variable to a real function of a real variable. This transformation permits a simultaneous determination of vector fields of the higher - order acceleration for a given rigid body motion.

So, being $f : I \subseteq \mathbb{R} \rightarrow \mathbb{R}, f = f(t)$, a real function of real variable, n -th differentiable, $n \in \mathbb{N}$. To this function, it will be associated the multidual function of real variable \widehat{f} given by the following equation:

$$\widehat{f} = f + \varepsilon \dot{f} + \dots + \frac{\varepsilon^n}{n!} f^{(n)} \quad (19)$$

The properties of this transformation are given by the following theorem.

Theorem 1. *Being f and g two real function of class $C^n(I)$. The following properties take place:*

$$\widehat{f + g} = \widehat{f} + \widehat{g} \quad (20)$$

$$\widehat{fg} = \widehat{f} \widehat{g} \quad (21)$$

$$\widehat{\lambda f} = \lambda \widehat{f}, \forall \lambda \in \mathbb{R} \quad (22)$$

$$\widehat{f(\alpha)} = \widehat{f}(\widehat{\alpha}), \alpha \in C^n(I) \quad (23)$$

$$\dot{\widehat{f}} = \widehat{\dot{f}} \quad (24)$$

Proof: The properties of the multidual algebra and the below relation are used:

$$\widehat{f} = e^{\varepsilon \mathbf{D}} f \quad (25)$$

where $e^{\varepsilon \mathbf{D}} = 1 + \varepsilon \mathbf{D} + \dots + \frac{\varepsilon^n}{n!} \mathbf{D}^n$ with $\mathbf{D} = \frac{d}{dt}$ the derivative operator with respect to time.

2 Higher-Order Kinematics with Multidual Transform

Let be a rigid motion given by a curve in Lie group of the rigid displacements SE_3 given by the homogeneous matrix $\mathbf{g} = \begin{bmatrix} \mathbf{R} & \boldsymbol{\rho} \\ \mathbf{0} & 1 \end{bmatrix}$ where $\mathbf{R} \in S\mathbb{O}_3$ is a proper orthogonal tensor [2,3,5], $\mathbf{R} = \mathbf{R}(t)$, and $\boldsymbol{\rho} = \boldsymbol{\rho}(t)$ a vector function of a time variable. As shown in [1–3], the vector field of the higher-order accelerations is given by the below matrix:

$$\boldsymbol{\Psi}_n = \begin{bmatrix} \boldsymbol{\Phi}_n & \mathbf{a}_n \\ \mathbf{0} & 0 \end{bmatrix} \quad (26)$$

where the tensor $\boldsymbol{\Phi}_n$ and the vector \mathbf{a}_n are given by the below equations:

$$\boldsymbol{\Phi}_n = \mathbf{R}^{(n)} \mathbf{R}^T \quad (27)$$

$$\mathbf{a}_n = \boldsymbol{\rho}^{(n)} - \boldsymbol{\Phi}_n \boldsymbol{\rho}. \quad (28)$$

The n -th order acceleration of a point of the rigid body given by the position vector \mathbf{r} can be computed with the following relation:

$$\mathbf{a}_r^{[n]} = \mathbf{a}_n + \boldsymbol{\Phi}_n \mathbf{r}; n \in \mathbb{N} \quad (29)$$

In [1–3], is described an iterative procedure used to determine the instantaneous tensor $\boldsymbol{\Phi}_n$ using the time derivative of the spatial twist of rigid body motion. Next, a new non-iterative procedure that permits the determination of the higher-order acceleration field using the multidual differential transformation will be presented.

So, for $\mathbf{R} = \mathbf{R}(t) \in S\mathbb{O}_3$ and $\boldsymbol{\rho} = \boldsymbol{\rho}(t) \in \mathbf{V}_3; \forall t \in I \subseteq \mathbb{R}$, can be defined:

$$\widehat{\mathbf{R}} = \mathbf{R} + \dot{\mathbf{R}}\varepsilon + \dots + \frac{\mathbf{R}^{(n)}}{n!} \varepsilon^n \quad (30)$$

$$\widehat{\boldsymbol{\rho}} = \boldsymbol{\rho} + \dot{\boldsymbol{\rho}}\varepsilon + \dots + \frac{\boldsymbol{\rho}^{(n)}}{n!} \varepsilon^n \quad (31)$$

Theorem 2. For any $\mathbf{R} = \mathbf{R}(t) \in S\mathbb{O}_3$, a n -th order differentiable function, the below relation takes place:

$$\widehat{\mathbf{R}} \widehat{\mathbf{R}}^T = \widehat{\mathbf{R}}^T \widehat{\mathbf{R}} = \widehat{\mathbf{I}} \quad (32)$$

$$\det \widehat{\mathbf{R}} = 1 \quad (33)$$

If $\mathbf{R} = \mathbf{R}(\alpha, \mathbf{u})$ where the angle α and the unit vector \mathbf{u} are the natural invariants of the orthogonal tensor \mathbf{R} , takes place a Rodrigues-like formula:

$$\widehat{\mathbf{R}} = \mathbf{I} + \sin \widehat{\alpha} \widehat{\mathbf{u}} \times + \left(1 - \cos \widehat{\alpha}\right) \left(\widehat{\mathbf{u}} \times\right)^2 \quad (34)$$

where

$$\widehat{\alpha} = \alpha + \dot{\alpha}\varepsilon + \dots + \frac{\alpha^{(n)}}{n!}\varepsilon^n \quad (35)$$

$$\widehat{\mathbf{u}} = \mathbf{u} + \dot{\mathbf{u}}\varepsilon + \dots + \frac{\mathbf{u}^{(n)}}{n!}\varepsilon^n \quad (36)$$

Proof. The proof of this theorem uses Rodrigues' formula for the tensors in $S\mathbb{O}_3$ and the results of Theorem 1.

Let be the following multidual matrix:

$$\widehat{\mathbf{g}} = \begin{bmatrix} \widehat{\mathbf{R}} & \widehat{\boldsymbol{\rho}} \\ \mathbf{0} & 1 \end{bmatrix} \quad (37)$$

and

$$\widehat{\boldsymbol{\Psi}} = \begin{bmatrix} \widehat{\mathbf{R}} & \widehat{\boldsymbol{\rho}} \\ \mathbf{0} & 1 \end{bmatrix} \begin{bmatrix} \mathbf{R}^T & -\mathbf{R}^T \boldsymbol{\rho} \\ \mathbf{0} & 1 \end{bmatrix}. \quad (38)$$

After some algebra in Eq. (38), results:

$$\widehat{\boldsymbol{\Psi}} = \begin{bmatrix} \widehat{\boldsymbol{\Phi}} & \widehat{\mathbf{a}} \\ \mathbf{0} & 1 \end{bmatrix} \quad (39)$$

with

$$\widehat{\boldsymbol{\Phi}} = \widehat{\mathbf{R}} \mathbf{R}^T \quad (40)$$

$$\widehat{\mathbf{a}} = \widehat{\boldsymbol{\rho}} - \widehat{\mathbf{R}} \mathbf{R}^T \boldsymbol{\rho}. \quad (41)$$

From (27), (28), (30), (31), results:

$$\widehat{\boldsymbol{\Phi}} = \mathbf{I} + \boldsymbol{\Phi}_1\varepsilon + \dots + \frac{\boldsymbol{\Phi}_n}{n!}\varepsilon^n \quad (42)$$

$$\widehat{\mathbf{a}} = \mathbf{a}_1\varepsilon + \frac{\mathbf{a}_2}{2}\varepsilon^2 + \dots + \frac{\mathbf{a}_n}{n!}\varepsilon^n \quad (43)$$

If $\mathbf{R} \in S\mathbb{O}_3$ models a spherical motion around a fixed axis, than $\widehat{\mathbf{u}} = \mathbf{u}$ and the relation (34) become:

$$\widehat{\mathbf{R}} = \mathbf{I} + \sin \widehat{\alpha} \mathbf{u} \times + \left(1 - \cos \widehat{\alpha}\right) (\mathbf{u} \times)^2 \quad (44)$$

with $\sin \widehat{\alpha}$ and $\cos \widehat{\alpha}$ given in Eqs. (9) and (10).

In the case of helical rigid body motion ($\mathbf{u} = \text{const.}$), from Eqs. (40), (41) and (44) and Theorem 2, after some algebra, results that:

$$\begin{cases} \widehat{\boldsymbol{\Phi}} = \mathbf{I} + \sin \Delta \widehat{\alpha} \mathbf{u} \times + \left(1 - \cos \Delta \widehat{\alpha}\right) (\mathbf{u} \times)^2 \\ \widehat{\mathbf{a}} = \Delta \widehat{\boldsymbol{\rho}} - \sin \Delta \widehat{\alpha} \mathbf{u} \times \boldsymbol{\rho} - \left(1 - \cos \Delta \widehat{\alpha}\right) \mathbf{u} \times (\mathbf{u} \times \boldsymbol{\rho}) \end{cases} \quad (45)$$

where with $\Delta \widehat{x}$ was denoted the multidual part of the number \widehat{x} .

Thus, it results the possibility of the derivative of the matrices Ψ_k , with $k = \overline{1, n}$ from the equation $\Psi_k = k! \frac{d\widehat{\Psi}}{d\varepsilon^k}$.

The multidual vector $\widehat{\mathbf{a}}_{\mathbf{r}} = \widehat{\Psi} \begin{bmatrix} \mathbf{r} \\ 1 \end{bmatrix}$ contains all information regarding the position and the high-order acceleration: $\widehat{\mathbf{a}}_{\mathbf{r}} = \mathbf{r} + \mathbf{v}_{\mathbf{r}}\varepsilon + \mathbf{a}_{\mathbf{r}}\frac{\varepsilon^2}{2} + \dots + \frac{\mathbf{a}_{\mathbf{r}}^{[n]}}{n!}\varepsilon^n$.

Thus, $\mathbf{a}_{\mathbf{r}}^{[k]} = k! \frac{d\widehat{\mathbf{a}}_{\mathbf{r}}}{d\varepsilon^k}$, $k = \overline{1, n}$. For $n = 4$ ($\varepsilon^5 = 0$), the velocity, acceleration, jerk and jounce vector fields of rigid body motion will be simultaneously described.

3 Higher-Order Kinematics of Lower-Pair Chains with Multidual Algebra

Let be a lower-pair chain described by kinematic mapping [5]:

$$\mathbf{g} = f_i(\mathbf{q}) = \exp(\mathbf{Y}_1\mathbf{q}_1) \exp(\mathbf{Y}_2\mathbf{q}_2) \dots \exp(\mathbf{Y}_i\mathbf{q}_i), \quad i \in \mathbb{N} \quad (46)$$

known also as Brockett formula.

In Eq. (46), $\mathbf{Y}_j, j = \overline{1, i}$ denotes the screw coordinate vectors and $\mathbf{q}_j, j = \overline{1, i}$ denotes the joint variable [5].

The results proven in Sect. 2 allow us to determine simultaneously the vector fields of higher – order acceleration for terminal body of kinematic chain given by the kinematic equation (46).

The result is given by:

Theorem 3. *The vector field of higher-order acceleration on terminal body of kinematic chain given by the kinematic mapping (1) it results from multidual matrix:*

$$\widehat{\Psi} = \exp(\mathbf{S}_1\Delta\widehat{\mathbf{q}}_1) \exp(\mathbf{S}_2\Delta\widehat{\mathbf{q}}_2) \dots \exp(\mathbf{S}_i\Delta\widehat{\mathbf{q}}_i) \quad (47)$$

where

$$\mathbf{S}_j = \mathbf{Ad}_{f_{j-1}} \mathbf{Y}_j, j = \overline{1, i} \quad (48)$$

is instantaneous joint screw coordinate of joint j and $\Delta\widehat{\mathbf{q}}_j$ denote the multidual part of multidual variable $\widehat{\mathbf{q}}_j, j = \overline{1, i}$.

Proof. Applying to the Eq. (46) the multidual differential transform presented in Sect. 2 and the properties from Theorem 1 and Theorem 2, we will obtain:

$$\widehat{\mathbf{g}} = \exp(\mathbf{Y}_1\widehat{\mathbf{q}}_1) \exp(\mathbf{Y}_2\widehat{\mathbf{q}}_2) \dots \exp(\mathbf{Y}_i\widehat{\mathbf{q}}_i) \quad (49)$$

Also, from (46) it follows:

$$\mathbf{g}^{-1} = \exp(-\mathbf{Y}_i\mathbf{q}_i) \dots \exp(-\mathbf{Y}_2\mathbf{q}_2) \exp(-\mathbf{Y}_1\mathbf{q}_1) \quad (50)$$

Taking into account that the multidual matrix $\widehat{\Psi}$ is defined by equation:

$$\widehat{\Psi} = \widehat{\mathbf{g}} \mathbf{g}^{-1} \quad (51)$$

with Eqs. (49) and (50), the Eqs. (47) and (48) are obtained.

4 Conclusions

Using the morphism between the Lie group of the rigid displacements SE_3 and the Lie group of the orthogonal multidual tensors, a general method for the study of the vector field of arbitrary higher-order accelerations is described. It is proved that all information regarding the properties of the distribution of high-order accelerations are contained in the specified multidual tensor. In particular cases the properties for velocity, acceleration, jerk, hyper-jerk (jounce) fields are given. Higher-order kinematics properties of lower-pair serial chains with multidual algebra is proposed. The results interest the theoretical kinematics, higher-order kinematics analysis in the case of serial manipulator, control theory and multibody kinematics.

References

1. Condurache, D.: Higher-order acceleration centers and kinematic invariants of rigid body. In: The 5th Joint International Conference on Multibody System Dynamics (2018)
2. Condurache, D.: Higher-order kinematics of rigid bodies: a tensors algebra approach. In: Interdisciplinary Applications of Kinematics. Mechanisms and Machine Science, vol. 71. Springer, Cham (2019)
3. Condurache, D.: Higher-order relative kinematics of rigid body motions: a dual lie algebra approach. In: Advances in Robot Kinematics 2018, ARK 2018, vol. 8. Springer, Cham (2019)
4. Messelmi, F.: Multidual numbers and their multidual functions. Electron. J. Math. Anal. Appl. **3**(2), 154–172 (2015)
5. Müller, A.: An overview of formulae for the higher-order kinematics of lower-pair chains with applications in robotics and mechanism theory. Mech. Mach. Theory **142**, 103594 (2019)



On Homotopy Continuation Based Singularity Distance Computations for 3-RPR Manipulators

Aditya Kapilavai^(✉) and Georg Nawratil

Institute of Discrete Mathematics and Geometry, TU Wien, Vienna, Austria
{[akapilavai](mailto:akapilavai@geometrie.tuwien.ac.at),[nawratil](mailto:nawratil@geometrie.tuwien.ac.at)}@geometrie.tuwien.ac.at

Abstract. It is known that parallel manipulators suffer from singular configurations. Evaluating the distance between a given configuration to the closest singular one is of interest for industrial applications (e.g. singularity-free path planning). For parallel manipulators of Stewart-Gough type, geometric meaningful distance measures are known, which are used for the computation of the singularity distance as the global minimizer of an optimization problem. In the case of hexapods and linear pentapods the critical points of the corresponding polynomial Lagrange function cannot be found by the Gröbner basis method due to the degree and number of unknowns. But this polynomial system of equations can be solved by software tools of numerical algebraic geometry relying on homotopy continuation. To gain experiences for the treatment of the mentioned spatial manipulators, this paper attempts to find minimal multi-homogeneous Bézout numbers for the homotopy continuation based singularity distance computation with respect to various algebraic motion representations of planar Euclidean/equiform kinematics. The homogenous and non-homogenous representations under study are compared and discussed based on the 3-RPR manipulator.

Keywords: 3-RPR manipulator · Singularity distance · Homotopy continuation · Bézout number

1 Introduction

A 3-RPR manipulator (cf. Fig. 1) is a three degree-of-freedom (dof) planar parallel manipulator (two translational and one rotational dof) where each leg is composed of a revolute joint (R)¹, a prismatic joint (P) and a further R-joint. The manipulator is actuated by changing the three lengths of the prismatic joints.

According to [11], the distance between two poses of the moving platform can be computed as:

¹ We consider R-joints as points and refer them as base/platform anchor points.

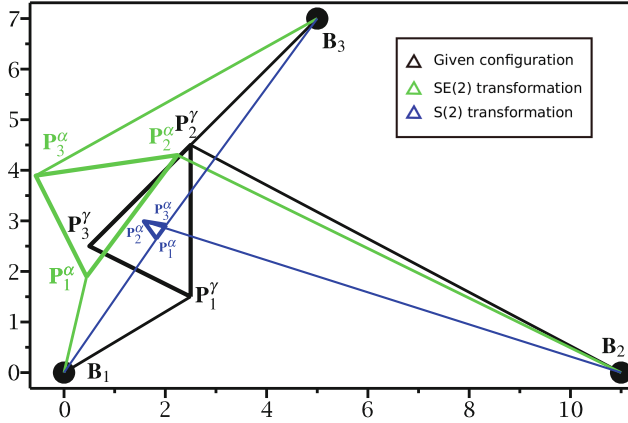


Fig. 1. 3-RPR manipulator: The results obtained in this paper are based on the illustrated example taken from [11, Section 3] for $\phi = \frac{\pi}{2}$. The given configuration is illustrated in black and the closest singular one under Euclidean/equiform transformations of the platform is displayed in green/blue.

$$d_3 := \sqrt{\frac{1}{3} \sum_{i=1}^3 \langle \mathbf{P}_i^\alpha - \mathbf{P}_i^\gamma, \mathbf{P}_i^\alpha - \mathbf{P}_i^\gamma \rangle} \quad (1)$$

where $\mathbf{P}_i^\gamma = (x_i^\gamma, y_i^\gamma)^T$ (resp. $\mathbf{P}_i^\alpha = (x_i^\alpha, y_i^\alpha)^T$) denotes the i th platform anchor point in the given (resp. α -transformed) manipulator configuration for $i = 1, 2, 3$. Both coordinate vectors \mathbf{P}_i^γ and \mathbf{P}_i^α are computed with respect to the fixed frame and $\langle \cdot, \cdot \rangle$ denotes the standard scalar product. The coordinate vectors of the platform anchor points with respect to the moving frame are given by $\mathbf{P}_i = (x_i, y_i)^T$. Moreover it was mentioned in [11] that α has not to be restricted to the planar Euclidean motion group SE(2), but it can also be an element of the planar equiform motion group S(2) or an affine motion.

It is well known that the α -transformed configuration is singular if and only if the carrier lines of three legs intersect in a common point or are parallel. This line-geometric characterization is equivalent to the algebraic condition $V_3 = 0$ with

$$V_3 = \det \begin{pmatrix} \mathbf{P}_1^\alpha - \mathbf{B}_1 & \mathbf{P}_2^\alpha - \mathbf{B}_2 & \mathbf{P}_3^\alpha - \mathbf{B}_3 \\ \det(\mathbf{B}_1, \mathbf{P}_1^\alpha - \mathbf{B}_1) & \det(\mathbf{B}_2, \mathbf{P}_2^\alpha - \mathbf{B}_2) & \det(\mathbf{B}_3, \mathbf{P}_3^\alpha - \mathbf{B}_3) \end{pmatrix} \quad (2)$$

where \mathbf{B}_i denotes the coordinate vector of the i th base anchor point with respect to the fixed system. For determining the singularity distance one has to find the transformation α that minimizes Eq. (1) under the side condition that $V_3 = 0$ holds. For $\alpha \in \text{SE}(2)$ we denote the singularity distance by s_3 and for $\alpha \in \text{S}(2)$ by e_3 , respectively. For the determination of s_3 and e_3 we compute the critical points of the corresponding polynomial Lagrange function L , i.e. the zero set of the polynomial system of equations arising from the partial derivatives of L . Finally, one only has to pick out the solution which yields the global minimum.

Commonly, Newton’s method is simple and quick to solve a polynomial system. However, in general it only converges when a good initial guess is used, and even then this only yields one solution. In contrast, the homotopy continuation method allows an efficient and reliable computation of all solutions to polynomial systems. The newest open-source numerical continuation software packages are HomotopyContinuation.jl [3] and Bertini 1.6v [1]. These packages and other available software and their performances are compared in [3]. We have chosen Bertini 1.6v for computing the singularity distance of parallel manipulators due to (a) its exceptional features mentioned in [13, p. 156] which will be useful for our future research and (b) the longevity of the Bertini software.

Under the default settings, declaration of all unknown variables n of the polynomial system into a single *variable group* causes Bertini to form a *total-degree homotopy*, which in general does not result in a minimal Bézout number. The partition of the variables into multiple groups lead to a *multi-homogeneous homotopy*. The grouping of the n unknown variables affects the resulting minimal multi-homogeneous Bézout number² (B_{min}). As Bertini does not group the variables automatically, the user is responsible for choosing the variable groups in a way that a minimal multi-homogeneous Bézout number (B_{min}) is obtained, which improves the computational costs/time. For this purpose, attempts have been made on search algorithms (e.g. [7, 12]) to find the optimal partition of variables groups, but in [2, p. 72] it is stated that “*there does not yet exist a truly efficient algorithm for finding optimal groupings, and the combinatorics are such that an exhaustive examination of all possible groupings becomes impractical as the number of variables grows much larger than 10*”. Investigating the optimal variable group search algorithms is out of the scope of the paper, but as mentioned in [2, p. 73], “*with a little practice, a user can identify and check the most promising candidates*” resulting in B_{min} .

According to [2, p. 96] the “*use of isotropic coordinates is advantageous when applying multi-homogeneous homotopy, since it converts many of the quadratic expressions that appear in planar kinematics into bilinear expressions*” but no attempts have been made so far to compare this approach with other algebraic motion representations. Hence, we determine B_{min} for the singularity distance computation of 3-RPR manipulators based on homotopy continuation with respect to various algebraic motion representations of SE(2) and S(2). In addition this study is useful to gain experience for the spatial case.

The rest of the paper is organized as follows: We divide the investigated algebraic motion representations into two classes, namely the non-homogenous ones (Sect. 2) and the homogenous ones (Sect. 3). In both of these two sections we give a brief introduction of the representations followed by the discussion of the results. Finally, Sect. 4 concludes the paper.

² The Bézout number of a system of multi-homogeneous polynomial equations is the largest Bézout number of non-singular solutions such a system can have, and it is also the number of solution paths used to compute all geometrically isolated solutions of the system using multi-homogeneous polynomial continuation [12].

2 Non-homogeneous Representations

In this section, we present three non-homogeneous algebraic representations for each of the motion groups $SE(2)$ and $S(2)$, respectively.

Point Based Representation (PBR): We call the approach given in [11] *point based representation* as the transformation is formulated in terms of the first and second platform anchor points. For the third platform point the transformation reads as

$$\mathbf{P}_3^\alpha = \frac{1}{\sqrt{(x_2-x_1)^2+(y_2-y_1)^2}} \begin{pmatrix} x_2^\alpha - x_1^\alpha & y_1^\alpha - y_2^\alpha \\ y_2^\alpha - y_1^\alpha & x_2^\alpha - x_1^\alpha \end{pmatrix} \begin{pmatrix} x_3 - x_1 \\ y_3 - y_1 \end{pmatrix} + \mathbf{P}_1^\alpha. \quad (3)$$

Then the Lagrange function L for the computation of e_3 can be written as

$$L : d_3^2 - \lambda V_3 = 0. \quad (4)$$

The additional constraint $M = 0$ with $M := \overline{\mathbf{P}_1^\alpha \mathbf{P}_2^{\alpha 2}} - \overline{\mathbf{P}_1 \mathbf{P}_2^2}$ results in the computation of s_3 from the Lagrange function

$$L : d_3^2 - \lambda V_3 - \mu M = 0. \quad (5)$$

Planar Euler-Rodrigues Representation (PERR): Using this representation the transformation $\alpha : \mathbb{R}^2 \rightarrow \mathbb{R}^2$ can be written as

$$\alpha : \mathbf{P}_i \mapsto \mathbf{P}_i^\alpha := \begin{pmatrix} a_1^2 - a_2^2 & -2a_1a_2 \\ 2a_1a_2 & a_1^2 - a_2^2 \end{pmatrix} \mathbf{P}_i + \begin{pmatrix} a_3 \\ a_4 \end{pmatrix} \quad \text{with } a_1, \dots, a_4 \in \mathbb{R}. \quad (6)$$

The computation of e_3 and s_3 is based on the same Lagrange function as for the PBR with the sole difference that M is given by $M := a_1^2 + a_2^2 - 1$.

Isotropic Coordinates Representation (ICR): Using this approach the point \mathbf{P}_i is represented by the pair (z_i, \bar{z}_i) of conjugate complex numbers with $z_i = x_i + iy_i$. This isotropic coordinates are transformed by $\alpha : \mathbb{C}^2 \rightarrow \mathbb{C}^2$ as follows (e.g. [10]):

$$\alpha : (z_i, \bar{z}_i) \mapsto (z_i^\alpha, \bar{z}_i^\alpha) := (\kappa z_i + \tau, \tilde{\kappa} \bar{z}_i + \tilde{\tau}) \quad \text{with } \kappa, \tau, \tilde{\kappa}, \tilde{\tau} \in \mathbb{C}. \quad (7)$$

Note that $(z_i^\alpha, \bar{z}_i^\alpha)$ is a real point if and only if $\tilde{z}_i^\alpha = \bar{z}_i^\alpha$ holds; i.e. $\tilde{\kappa} = \bar{\kappa}$ and $\tilde{\tau} = \bar{\tau}$. Again the computation of e_3 and s_3 is based on the same Lagrange function as for the PBR with the sole difference that M is given by $M := \kappa \tilde{\kappa} - 1$.

In summary the transformation α is given by the non-homogenous 4-tuple $(x_1^\alpha, y_1^\alpha, x_2^\alpha, y_2^\alpha)$ in PBR, (a_1, a_2, a_3, a_4) in PERR and $(\kappa, \tau, \tilde{\kappa}, \tilde{\tau})$ in ICR, respectively.

2.1 Results

The results are based on the example illustrated in Fig. 1. The system of n partial derivatives L_j ($j = 1, \dots, n$) of L results in all cases in a non-homogenous system of equations. The number n of unknown variables in this polynomial system is 5 for $\alpha \in S(2)$ and 6 for $\alpha \in SE(2)$. The total number of all possible groupings of the n variables is given by the so-called *Bell number*³ $B(n)$ with $B(5) = 52$

³ In case if $n > 6$ the Bell number $B(n)$ increases very quickly (see [2, p. 72, Table 5.1]).

Table 1. Comparison of Bézout numbers for all studied representations of SE(2)

Method	Best groupings	B_{min}	T_{avg}	Worst groupings	B_{max}	DOL
PBR	$\{(x_1^\alpha, y_1^\alpha, x_2^\alpha, y_2^\alpha), (\lambda, \mu)\}$	144	1 800	$\{(x_1^\alpha), (x_2^\alpha, \mu), (y_1^\alpha, \lambda), (y_2^\alpha)\}$	8 448	4
				$\{(x_1^\alpha, \mu), (y_2^\alpha, \lambda), (x_2^\alpha), (y_1^\alpha)\}$	8 448	
PERR	$\{(a_1, a_2), (a_3, a_4), (\lambda, \mu)\}$	360	45 920	$\{(a_1, \lambda, a_3), (a_2, \mu, a_4)\}$	50 992	6
	$\{(a_1, a_2, a_4), (a_3), (\lambda, \mu)\}$	360	35 640	$\{(a_1, \mu, a_4), (a_2, \lambda, a_3)\}$	50 992	
ICR	$\{(\kappa), (\tilde{\kappa}), (\lambda), (\mu), (\tau, \tilde{\tau})\}$	136	249 880	$\{(\kappa, \tilde{\tau}), (\tilde{\kappa}, \mu, \tau, \lambda)\}$	2 187	4
				$\{(\kappa, \mu, \lambda, \tilde{\tau}), (\tilde{\kappa}, \tau)\}$	2 187	
BGR	$\{(e_0, e_3, t_1, t_2)_h, (\lambda)\}$	300	122 180	–	–	$\frac{5}{4}$
DCKR	$\{(\theta, \tilde{\theta}, \sigma, \tilde{\sigma})_h, (\lambda)\}$	300	115 283	–	–	$\frac{5}{4}$

Table 2. Comparison of Bézout numbers for all studied representations of S(2)

Method	Best groupings	B_{min}	T_{avg}	Worst groupings	B_{max}	DOL
PBR	$\{(x_1^\alpha, y_1^\alpha, x_2^\alpha, y_2^\alpha), (\lambda)\}$	96	970	$\{(x_1^\alpha, y_1^\alpha), (x_2^\alpha, y_2^\alpha, \lambda)\}$	1 296	4
				$\{(x_1^\alpha, y_2^\alpha), (y_1^\alpha, x_2^\alpha, \lambda)\}$	1 296	
PERR	$\{(a_1, a_2), (a_3, a_4), (\lambda)\}$	828	73 000	$\{(a_1, a_2), (a_3, a_4, \lambda)\}$	14 025	6
				$\{(a_2, a_3), (a_1, a_3, \lambda)\}$	14 025	
ICR	$\{(\kappa, \tilde{\kappa}, \tau, \tilde{\tau}), (\lambda)\}$	96	61 870	$\{(\tilde{\kappa}, \tau), (\kappa, \tilde{\tau}, \lambda)\}$	1 296	4
				$\{(\kappa, \tilde{\tau}), (\tau, \tilde{\kappa}, \lambda)\}$	1 296	
DHR	$\{(e_0, \dots, t_3)_h, (\lambda, \mu)\}$	165 240	–	$\{(e_0, \dots, t_3)_h, (\lambda), (\mu)\}$	194 400	$\frac{11}{10}$
QBR	$\{(e_0, \dots, t_2)_h, (\lambda, \mu)\}$	41 160	–	$\{(e_0, \dots, t_2)_h, (\lambda), (\mu)\}$	82 320	$\frac{7}{6}$

and $B(6) = 203$. For every representation all the possible groupings are tested by using default settings in Bertini 1.6v with a multi-homogeneous homotopy continuation method. We used Linux OS (Ubuntu 18.04) with a 1.80 GHz Intel i5-6260U CPU. Comparison of Bézout numbers and degree of the Lagrange function (DOL) for all the presented representations are summarized in the Tables 1 and 2, where B_{min} and B_{max} indicates the Bézout number for best and worst groupings of unknown variables. We are also interested in average total tracking time T_{avg} in Milliseconds for B_{min} . We took T_{avg} because there will be variations in total tracking time for each run, depending upon the random seed chosen by Bertini.

To verify the solutions obtained by Bertini, we solved the polynomial system also in Maple 2018 using Gröbner basis method. In all cases the Maple solutions matched with those received from Bertini. The total number of solutions for all three representations are summarized in Table 3. For $\alpha \in SE(2)$ we get for PERR double the solutions of PBR and ICR as $\pm(a_1, a_2)$ describe the same rotation. For $\alpha \in S(2)$ we obtain for PERR 86 solutions, where 76 correspond to the 19 solutions of PBR and ICR as $\pm(a_1, a_2)$ and $\pm(-a_2i, a_1i)$ result in the same rotation matrix. The remaining 10 solutions (given in [6, App. A]) lie on the quadric $a_1^2 + a_2^2 = 0$ rendering this matrix singular.

Table 3. Total number of solutions (counted including multiplicity) for studied representations

Motion group	PBR and ICR	PERR	BGR and DCKR (Bertini)	BGR and DCKR (Maple)
SE(2)	32	64	162	32 & 1-dim set & 2-dim set
S(2)	19	86		

3 Homogeneous Representations

In this section, we present two homogeneous algebraic representations for each of the motion groups SE(2) and S(2), respectively. Two of them are based on Study’s kinematic mapping (e.g. [5, p. 86]), where each element of SE(3) is represented by a point $(e_0 : e_1 : e_2 : e_3 : t_0 : t_1 : t_2 : t_3)$ in the projective 7-dimensional space P^7 located on the so-called Study quadric given by

$$e_0t_0 + e_1t_1 + e_2t_2 + e_3t_3 = 0 \tag{8}$$

sliced along the 3-dimensional generator space $e_0 = e_1 = e_2 = e_3 = 0$.

Blaschke-Grünwald Representation (BGR): This representation is obtained by restricting Study’s parametrization to the planar case i.e. $e_1 = e_2 = t_0 = t_3 = 0$. According to [5, p. 91] the transformation $\alpha : \mathbb{R}^2 \rightarrow \mathbb{R}^2$ can be written as:

$$\alpha : \mathbf{P}_i \mapsto \mathbf{P}_i^\alpha := \frac{1}{\Delta} \left[\begin{pmatrix} e_0^2 - e_3^2 & -2e_0e_3 \\ 2e_0e_3 & e_0^2 - e_3^2 \end{pmatrix} \mathbf{P}_i + \mathbf{t} \right] \tag{9}$$

with $\mathbf{t} := [-2(e_0t_1 - e_3t_2), -2(e_0t_2 + e_3t_1)]^T$, $\Delta := e_0^2 + e_3^2$ and $e_0, e_3, t_1, t_2 \in \mathbb{R}$. The computation of e_3 is based on the Lagrange function L given in Eq. (4).

Davidson-Hunt Representation (DHR): Based on the analogy of the Study parameters to homogenous screw coordinates (for details see e.g. [9, Section 1.1]) Davidson and Hunt [4, p. 409] suggested to interpret the points in the ambient space P^7 of the Study quadric as spatial similarity transformations. Following this idea and restricting it to S(2) we end up with the following representation of $\alpha : \mathbb{R}^2 \rightarrow \mathbb{R}^2$:

$$\alpha : \mathbf{P}_i \mapsto \mathbf{P}_i^\alpha := \frac{1}{\Delta^2} \left[(\Delta + e_0t_0 + e_3t_3) \begin{pmatrix} e_0^2 - e_3^2 & -2e_0e_3 \\ 2e_0e_3 & e_0^2 - e_3^2 \end{pmatrix} \mathbf{P}_i + \Delta \mathbf{t} \right] \tag{10}$$

with $e_0, e_3, t_0, t_1, t_2, t_3 \in \mathbb{R}$. The computation of s_3 is based on the Lagrange function (5) with the constraint $M := e_0t_3 - e_3t_0$.

Quaternion Based Representation (QBR): In [8, Section 2] a quaternionic formulation of S(4) and S(3) is given, which can also be restricted to S(2). Within

this approach the transformation $\alpha : \mathbb{R}^2 \rightarrow \mathbb{R}^2$ reads as:

$$\alpha : \mathbf{P}_i \mapsto \mathbf{P}_i^\alpha := \frac{1}{\Delta} \left[\begin{array}{cc} (e_0 f_0 - e_3 f_3 & -e_0 f_3 - e_3 f_0) \\ (e_0 f_3 + e_3 f_0 & e_0 f_0 - e_3 f_3) \end{array} \mathbf{P}_i + \mathbf{t} \right] \quad (11)$$

with $e_0, e_3, f_0, f_3, t_1, t_2 \in \mathbb{R}$. The computation of s_3 is based on the Lagrange function (5) where the constraint M is given by $M := e_0 f_3 - e_3 f_0$.

Dual Cayley-Klein Representation (DCKR): By using the dual Cayley-Klein parameters of $\text{SE}(2)$, which are introduced in [10], the isotropic point coordinates (z_i, \bar{z}_i) are transformed by $\alpha : \mathbb{C}^2 \rightarrow \mathbb{C}^2$ as follows:

$$\alpha : (z_i, \bar{z}_i) \mapsto (z_i^\alpha, \bar{z}_i^\alpha) := \frac{1}{\theta\bar{\theta}} \left(\theta(\theta z_i + 2\sigma), \bar{\theta}(\bar{\theta} \bar{z}_i + 2\bar{\sigma}) \right) \quad (12)$$

with $\theta, \sigma, \bar{\theta}, \bar{\sigma} \in \mathbb{C}$. The homogenous 4-tuple $(\theta : \sigma : \bar{\theta} : \bar{\sigma})$ corresponds to a real displacement α if and only if there exists a value $c \in \mathbb{C} \setminus \{0\}$ such that $\bar{\theta}c = \bar{\theta}c$ and $\bar{\sigma}c = \bar{\sigma}c$ hold, which is equivalent to the condition $\theta\bar{\sigma} = \bar{\theta}\sigma$. The computation of e_3 is based on the Lagrange function L given in Eq. (4).

Remark 1. Note that according to [10], BGR and DCKR are linked by the relation: $e_0 = (\theta + \bar{\theta})/2$, $e_3 = -i(\theta - \bar{\theta})/2$, $t_1 = (\sigma + \bar{\sigma})/2$ and $t_2 = -i(\sigma - \bar{\sigma})/2$. \diamond

In summary, $\alpha \in \text{SE}(2)$ is given by homogenous 4-tuples $(e_0 : e_3 : t_1 : t_2)$ in BGR and $(\theta : \sigma : \bar{\theta} : \bar{\sigma})$ in DCKR. In contrast, $\alpha \in \text{S}(2)$ is determined by homogenous 6-tuple $(e_0 : e_3 : t_0 : t_1 : t_2 : t_3)$ in DHR and $(e_0 : e_3 : f_0 : f_3 : t_1 : t_2)$ in QBR.

3.1 Results

The following results are again based on the example illustrated in Fig. 1. In all cases the Lagrange function is rational⁴ where the polynomials in the numerator and denominator are homogenous and of the same degree with respect to the motion parameters m_1, \dots, m_k , where $k = 4$ holds for BGR and DCKR and $k = 6$ holds for DHR and QBR. Therefore the system of n partial derivatives L_j ($j = 1, \dots, n$) of L results in a homogenous system of equations with respect to m_1, \dots, m_k . Due to the homogeneity this polynomial system is overdetermined but it can easily be checked that the relation $\sum_{j=1}^k m_j \frac{\partial L}{\partial m_j} = 0$ holds. Bertini cannot handle overdetermined systems⁵ without the following user interaction: One has to square up the system [2, p. 14] by replacing the k equations $\frac{\partial L}{\partial m_j} = 0$ for $j = 1, \dots, k$ by $k - 1$ linear combinations of the form $\sum_{j=1}^k \square \frac{\partial L}{\partial m_j}$ where each \square indicates a randomly chosen complex number. The resulting system can then be passed on to Bertini by using the command `hom_variable_group` for

⁴ The degrees of the polynomials in the numerator and denominator with respect to all n unknowns are given as fraction (deg numerator)/(deg denominator) in the column DOL of Tables 1 and 2.

⁵ In contrast to the software package HomotopyContinuation.jl [3].

grouping the homogenous variables m_1, \dots, m_k into one group, which is indicated in Tables 1 and 2 by the notation $(m_1, \dots, m_k)_h$. Therefore there is only one possible grouping for BGR and DCKR and two possible groupings for DHR and QBR. For both of these groupings the resulting Bézout numbers are too large (cf. Table 2) to expect reasonable computation times thus we abstained from tracking the paths.

All additional 130 solutions received by Bertini based on BGR and DCKR (cf. Table 3) fulfill $\Delta = 0$ resp. $\theta\tilde{\theta} = 0$ implying a division by zero in Eq. (9) resp. (12). But it turns out that 128 of these solutions either result from squaring up the system [2, p. 15] (cf. [6, Apps. B & C]) or belong to the 2-dimensional solution set⁶ $e_0 = e_3 = 0$ resp. $\theta = \tilde{\theta} = 0$. There also exists a 1-dimensional solution set (see footnote 6) (cf. [6, Apps. B & C]), which corresponds to two conics on the hyperquadric $\Delta = 0$ resp. $\theta\tilde{\theta} = 0$. The remaining two solutions represent a point on each of these two curves.

4 Conclusions

It can be observed (cf. Table 1) that the B_{min} value obtained for ICR is the best one of all SE(2) representations as suggested in [2, p. 96]. For S(2) the lowest number of tracked paths is obtained by ICR and PBR (cf. Table 2). Surprisingly the PBR has in both motion groups by far the best computational performance with respect to T_{avg} . It can also be seen by B_{max} that the grouping has huge effects on the number of tracked paths and therefore on the computation time. Moreover, due to the large Bézout numbers of DHR and QBR the question arises whether a computationally more efficient homogenous representation of S(2) exists.

All in all, this study suggests the usage of PBR for the future research on the spatial case (i.e. hexapods and linear pentapods) due to the good B_{min} values and the best results for T_{avg} .

Acknowledgements. This research is supported by the Grant No.P 30855-N32 of the Austrian Science Fund FWF. The first author would like to thank Arvin Rasoulzadeh for his valuable suggestions and technical discussions.

References

1. Bates, D.J., Hauenstein, J.D., Sommese, A.J., Wampler, C.W.: Bertini: Software for numerical algebraic geometry. Available at bertini.nd.edu with permanent. <https://doi.org/10.7274/R0H41PB5>
2. Bates, D.J., Sommese, A.J., Hauenstein, J.D., Wampler, C.W.: Numerically Solving Polynomial Systems with Bertini. SIAM, Philadelphia (2013)
3. Breiding, P., Timme, S.: HomotopyContinuation.jl: a package for homotopy continuation in Julia. In: Davenport, J.H., Kauers, M., Labahn, G., Urban, J. (eds.) Mathematical Software – ICMS 2018, pp. 458–465. Springer (2018)

⁶ Positive-dimensional solution sets cannot be detected by Bertini using default settings.

4. Davidson, J.K., Hunt, K.H.: *Robots and Screw Theory: Applications of Kinematics and Statics to Robotics*. Oxford University Press, Oxford (2004)
5. Husty, M.L., Schröcker, H.P.: Kinematics and algebraic geometry. In: McCarthy, J.M. (ed.) *21st Century Kinematics*, pp. 85–123. Springer (2013)
6. Kapilavai, A., Nawratil, G.: On homotopy continuation based singularity distance computations for 3-RPR manipulators. [arXiv:2004.08359](https://arxiv.org/abs/2004.08359) (2020)
7. Li, T., Bai, F.: Minimizing multi-homogeneous Bézout numbers by a local search method. *Math. Comput.* **70**(234), 767–787 (2001)
8. Nawratil, G.: Quaternionic approach to equiform kinematics and line-elements of Euclidean 4-space and 3-space. *Comput. Aided Geom. Des.* **47**, 150–162 (2016)
9. Nawratil, G.: Kinematic interpretation of the Study quadric’s ambient space. In: Lenarcic, J., Parenti-Castelli, V. (eds.) *Advances in Robot Kinematics*, pp. 3–11. Springer (2018)
10. Nawratil, G.: Parallel manipulators in terms of dual Cayley-Klein parameters. In: Zegloul, S., Romdhane, L., Laribi, M. (eds.) *Computational Kinematics*, pp. 265–273. Springer (2018)
11. Nawratil, G.: Singularity distance for parallel manipulators of Stewart Gough type. In: Uhl, T. (ed.) *Advances in Mechanism and Machine Science*, pp. 259–268. Springer (2019)
12. Wampler, C.W.: Bezout number calculations for multi-homogeneous polynomial systems. *Appl. Math. Comput.* **51**(2–3), 143–157 (1992)
13. Wampler, C.W., Sommese, A.J.: Applying numerical algebraic geometry to kinematics. In: McCarthy, J.M. (ed.) *21st Century Kinematics*, pp. 125–159. Springer (2013)

Control Issues in Mechanical Systems



Assistive Handwriting Haptic Mechanism Using Deep Learning Speech Recognition

Erdi Sayar^(✉)

RWTH Aachen University, Aachen, Germany
erdi.sayar@rwth-aachen.de

Abstract. Haptic devices become widespread in education and training. Learning to handwrite for visually impaired people is a difficult task. Using assistive haptic device during handwriting learning for people having a visual impairment is the objective of this work. They don't need anyone to help them in this process. By giving speech command, they can make the mechanism draw the number between any 0–9. Convolutional Neural Network (CNN) is used for speech recognition. Speech recognition for this study is limited only in numbers (0–9) and “unknown” which may occur due to network's inability or given speech command except for a trained number. This paper focuses on dynamic analysis and control of 5R mechanism by using deep learning for speech recognition.

Keywords: Planer 5R mechanism · Convolutional Neural Network · Haptic assistive device · Speech recognition · Learning handwriting

1 Introduction

The word haptic stems from Ancient Greek (haptikós, “able to come in contact with”) and (háptō, “to touch”). In other words, haptics is anything involving touch¹. Haptics technology emerges as different applications such as alleviation problem for blind people [8], education [5], training [1], medical field [4], computer-aided design [7]. This study deals with the application of assistive handwriting for visually impaired people. Since many years, visually impaired people cannot reach educational opportunities as much as normal people. This study enables them to learn how to write on their own by using a speech recognition command. An example prototype of handwriting assistive haptic 5R device is taken from the work (Dede & Kiper) and illustrated in Fig. 1. In dynamic analysis and control part for the sake of simplicity, the gripper is not taken into consideration in the calculations. Calculations are based on the model shown in Fig. 2.

For the speech recognition part, Convolutional Neural Network (CNN) is used and trained in Matlab and connected to Simulink to provide 5R with the desired trajectory based on speech command.

¹ <https://en.wiktionary.org/wiki/haptic>.

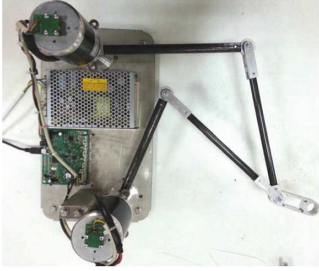


Fig. 1. Handwriting assistive haptic device

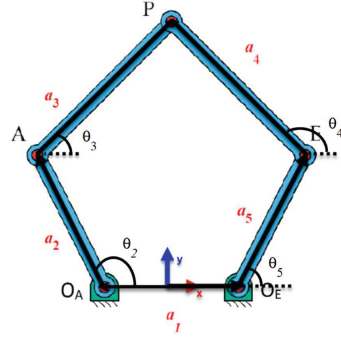


Fig. 2. 5R model

2 Kinematic Analysis

Each link of 5R can be defined by a fixed vector as shown in Fig. 2. Let us define vector $\overrightarrow{O_A A}$ for link2, $\overrightarrow{A P}$ for link3, $\overrightarrow{E P}$ for link4, $\overrightarrow{O_E E}$ for link5 and $\overrightarrow{O_A O_E}$ for link1. Except $\overrightarrow{O_A O_E}$, the other vectors will be the function of time since the mechanism contains only revolute joints.

2.1 Position Analysis

For position analysis, loop closure equations of vectors on Fig. 2 can be written by using Euler equations as below.

$$\frac{-a_1}{2} + a_2 \cdot e^{i\theta_2} + a_3 \cdot e^{i\theta_3} = \frac{a_1}{2} + a_5 \cdot e^{i\theta_5} + a_4 \cdot e^{i\theta_4} \tag{1}$$

Reel part $\Re\{Eq.(1)\}$ and imaginary part $\Im\{Eq.(1)\}$

$$\begin{aligned} \frac{-a_1}{2} + a_2 \cdot \cos(\theta_2) + a_3 \cdot \cos(\theta_3) &= \frac{a_1}{2} + a_5 \cdot \cos(\theta_5) + a_4 \cdot \cos(\theta_4) \\ a_2 \cdot \sin(\theta_2) + a_3 \cdot \sin(\theta_3) &= a_5 \cdot \sin(\theta_5) + a_4 \cdot \sin(\theta_4) \end{aligned} \tag{2}$$

Equation 2 is arranged as below and taking square of both side gives us the form shown in Eq. 3.

$$\begin{aligned} (a_4 \cdot \cos(\theta_4))^2 &= (a_2 \cdot \cos(\theta_2) + a_3 \cdot \cos(\theta_3) - a_5 \cdot \cos(\theta_5) - a_1)^2 \\ (a_4 \cdot \sin(\theta_4))^2 &= (a_2 \cdot \sin(\theta_2) + a_3 \cdot \sin(\theta_3) - a_5 \cdot \sin(\theta_5))^2 \end{aligned}$$

$$A \cdot \cos(\theta) + B \cdot \sin(\theta) = C \tag{3}$$

$$\begin{aligned}
A &= 2a_2a_3 \cos(\theta_2) - 2a_3a_5 \cos(\theta_5) - 2a_3a_1 \\
B &= 2a_2a_3 \sin(\theta_2) - 2a_3a_5 \sin(\theta_5) \\
C &= -a_1^2 - a_2^2 - a_3^2 - a_5^2 + a_4^2 + 2a_2a_5 \cos(\theta_5) \cos(\theta_2) + 2a_1a_2 \cos(\theta_2) \\
&\quad + 2a_2a_5 \sin(\theta_2) \sin(\theta_5) - 2a_1a_5 \cos(\theta_5)
\end{aligned}$$

Solution of Eq.(3) is given in Eq.(4).

$$\begin{aligned}
t_{1,2} &= \frac{B \pm \sqrt{A^2 + B^2 - C^2}}{A + C} \\
\theta_3 &= 2\text{atan}(t_1) \quad \text{or} \quad \theta_3 = 2\text{atan}(t_2) \\
\theta_4 &= \text{atan2}(a_2 \sin(\theta_2) + a_2 \sin(\theta_3) - a_5 \sin(\theta_5), -a_1 + a_2 \cos(\theta_2) + a_3 \cos(\theta_3) - a_5 \cos(\theta_5))
\end{aligned} \tag{4}$$

End Effector position can be expressed 2 different ways shown in Eq. (5).

$$\begin{aligned}
x &= \frac{-a_1}{2} + a_2 \cos(\theta_2) + a_3 \cos(\theta_3) \quad \text{or} \quad x = \frac{a_1}{2} + a_5 \cos(\theta_5) + a_4 \cos(\theta_4) \\
y &= a_2 \sin(\theta_2) + a_3 \cos(\theta_3) \quad \text{or} \quad y = a_5 \sin(\theta_5) + a_4 \sin(\theta_4)
\end{aligned} \tag{5}$$

2.2 Velocity Analysis

As an initial value, $\dot{\theta}_2$ and $\dot{\theta}_5$ are given.

Taking derivative both Eq. (2) with respect to time, we can obtain Eq. (6).

$$\begin{aligned}
-a_2 \sin(\theta_2) \dot{\theta}_2 + a_5 \sin(\theta_5) \dot{\theta}_5 - a_3 \sin(\theta_3) \dot{\theta}_3 + a_4 \sin(\theta_4) \dot{\theta}_4 &= 0 \\
a_2 \cos(\theta_2) \dot{\theta}_2 - a_5 \cos(\theta_5) \dot{\theta}_5 + a_3 \cos(\theta_3) \dot{\theta}_3 - a_4 \cos(\theta_4) \dot{\theta}_4 &= 0
\end{aligned} \tag{6}$$

The matrix form is given in Eq. 7.

$$\begin{bmatrix} -a_3 \sin(\theta_3) & a_4 \sin(\theta_4) \\ a_3 \cos(\theta_3) & -a_4 \cos(\theta_4) \end{bmatrix} \cdot \begin{bmatrix} \dot{\theta}_3 \\ \dot{\theta}_4 \end{bmatrix} = \begin{bmatrix} a_2 \sin(\theta_2) \dot{\theta}_2 - a_5 \sin(\theta_5) \dot{\theta}_5 \\ -a_2 \cos(\theta_2) \dot{\theta}_2 + a_5 \cos(\theta_5) \dot{\theta}_5 \end{bmatrix} \tag{7}$$

2.3 Acceleration Analysis

As an initial value, $\ddot{\theta}_2$ and $\ddot{\theta}_5$ are given.

Taking derivative both Eq. (6) with respect to time, we can obtain Eq. (8).

$$\begin{aligned}
-a_2 \sin(\theta_2) \ddot{\theta}_2 + a_2 \cos(\theta_2) \dot{\theta}_2^2 + a_5 \sin(\theta_5) \ddot{\theta}_5 + a_5 \cos(\theta_5) \dot{\theta}_5^2 - a_3 \sin(\theta_3) \ddot{\theta}_3 \\
-a_3 \cos(\theta_3) \dot{\theta}_3^2 + a_4 \sin(\theta_4) \ddot{\theta}_4 + a_4 \cos(\theta_4) \dot{\theta}_4^2 &= 0 \\
a_2 \cos(\theta_2) \ddot{\theta}_2 - a_2 \sin(\theta_2) \dot{\theta}_2^2 - a_5 \cos(\theta_5) \ddot{\theta}_5 + a_5 \sin(\theta_5) \dot{\theta}_5^2 + a_3 \cos(\theta_3) \ddot{\theta}_3 \\
-a_3 \sin(\theta_3) \dot{\theta}_3^2 - a_4 \cos(\theta_4) \ddot{\theta}_4 + a_4 \sin(\theta_4) \dot{\theta}_4^2 &= 0
\end{aligned} \tag{8}$$

The matrix form is given in Eq. 9.

$$\begin{bmatrix} -a_3 \sin(\theta_3) & a_4 \sin(\theta_4) \\ a_3 \cos(\theta_3) & -a_4 \cos(\theta_4) \end{bmatrix} \cdot \begin{bmatrix} \ddot{\theta}_3 \\ \ddot{\theta}_4 \end{bmatrix} = \begin{bmatrix} A_1 \\ A_2 \end{bmatrix} \tag{9}$$

where

$$\begin{aligned}
 A_1 &= a_2 \sin(\theta_2) \ddot{\theta}_2 - a_2 \cos(\theta_2) \dot{\theta}_2^2 - a_5 \sin(\theta_5) \ddot{\theta}_5 - a_5 \cos(\theta_5) \dot{\theta}_5^2 + a_3 \cos(\theta_3) \dot{\theta}_3^2 - \\
 & a_4 \cos(\theta_4) \dot{\theta}_4^2 \\
 A_2 &= -a_2 \cos(\theta_2) \ddot{\theta}_2 + a_2 \sin(\theta_2) \dot{\theta}_2^2 + a_5 \cos(\theta_5) \ddot{\theta}_5 - a_5 \sin(\theta_5) \dot{\theta}_5^2 + a_3 \sin(\theta_3) \dot{\theta}_3^2 - \\
 & a_4 \sin(\theta_4) \dot{\theta}_4^2
 \end{aligned}$$

3 Dynamic Analysis

For Dynamic Analysis, Lagrange method is used [6]. In total there are 4 angles $\theta_1, \theta_2, \theta_3, \theta_4$ and θ_3, θ_4 are the functions of θ_2, θ_5 as shown in Eq. (10).

$$\begin{aligned}
 \theta_3 &= f(\theta_2, \theta_5) \\
 \theta_4 &= g(\theta_2, \theta_3, \theta_5) = g(\theta_2, f(\theta_2, \theta_5), \theta_5)
 \end{aligned} \tag{10}$$

Position vectors of tip points of each link are given in Eq. (11).

$$\begin{aligned}
 r_2 &= \begin{bmatrix} \frac{-a_1}{2} + \frac{a_2 \cos(\theta_2)}{2} \\ \frac{a_2 \sin(\theta_2)}{2} \\ 0 \end{bmatrix} & r_3 &= \begin{bmatrix} \frac{-a_1}{2} + a_2 \cos(\theta_2) + \frac{a_3 \sin(\theta_3)}{2} \\ a_2 \sin(\theta_2) + \frac{a_3 \sin(\theta_3)}{2} \\ 0 \end{bmatrix} \\
 r_5 &= \begin{bmatrix} \frac{a_1}{2} + \frac{a_5 \cos(\theta_5)}{2} \\ \frac{a_5 \sin(\theta_5)}{2} \\ 0 \end{bmatrix} & r_4 &= \begin{bmatrix} \frac{a_1}{2} + a_5 \cos(\theta_5) + \frac{a_4 \cos(\theta_4)}{2} \\ a_5 \cos(\theta_5) + \frac{a_4 \sin(\theta_4)}{2} \\ 0 \end{bmatrix}
 \end{aligned} \tag{11}$$

We can substitute θ_3 and θ_4 from Eq. (10) as a function of θ_2 and θ_5 for θ_3 and θ_4 in Eq. (11).

Thus, Eq. (12) is obtained as showned below. All position vectors of links depend on the variable θ_2 and θ_5 .

$$\begin{aligned}
 r_2 &= \begin{bmatrix} \frac{-a_1}{2} + \frac{a_2 \cos(\theta_2)}{2} \\ \frac{a_2 \sin(\theta_2)}{2} \\ 0 \end{bmatrix} & r_3 &= \begin{bmatrix} \frac{-a_1}{2} + a_2 \cos(\theta_2) + \frac{a_3 \sin(f(\theta_2, \theta_5))}{2} \\ a_2 \sin(\theta_2) + \frac{a_3 \sin(f(\theta_2, \theta_5))}{2} \\ 0 \end{bmatrix} \\
 r_5 &= \begin{bmatrix} \frac{a_1}{2} + \frac{a_5 \cos(\theta_5)}{2} \\ \frac{a_5 \sin(\theta_5)}{2} \\ 0 \end{bmatrix} & r_4 &= \begin{bmatrix} \frac{a_1}{2} + a_5 \cos(\theta_5) + \frac{a_4 \cos(g(\theta_2, f(\theta_2, \theta_5), \theta_5))}{2} \\ a_5 \cos(\theta_5) + \frac{a_4 \sin(g(\theta_2, f(\theta_2, \theta_5), \theta_5))}{2} \\ 0 \end{bmatrix}
 \end{aligned} \tag{12}$$

As a next step, Positional jacobian matrices are calculated.

$$J_{p_{link_i}} = \begin{bmatrix} \frac{\partial r_i}{\partial \theta_2} & \frac{\partial r_i}{\partial \theta_5} \end{bmatrix} \tag{13}$$

$$J_{p_{link_2}} = \begin{bmatrix} \frac{-a_2 \sin(\theta_2)}{2} & 0 \\ \frac{a_2 \cos(\theta_2)}{2} & 0 \\ 0 & 0 \end{bmatrix} \tag{14}$$

$$J_{p_{link_3}} = \begin{bmatrix} -a_2 \sin(\theta_2) - \frac{a_3}{2} \sin(f(\theta_2, \theta_5)) \frac{\partial f(\theta_2, \theta_5)}{\partial \theta_2} & -\frac{a_3}{2} \sin(f(\theta_2, \theta_5)) \frac{\partial f(\theta_2, \theta_5)}{\partial \theta_5} \\ a_2 \cos(\theta_2) + \frac{a_3}{2} \cos(f(\theta_2, \theta_5)) \frac{\partial f(\theta_2, \theta_5)}{\partial \theta_2} & \frac{a_3}{2} \cos(f(\theta_2, \theta_5)) \frac{\partial f(\theta_2, \theta_5)}{\partial \theta_5} \\ 0 & 0 \end{bmatrix} \quad (15)$$

$$J_{p_{link_4}} = \begin{bmatrix} -\frac{a_4}{2} \sin(\sigma) \frac{\partial \sigma}{\partial \theta_2} & -a_5 \sin(\theta_5) + \frac{a_4}{2} \sin(\sigma) \frac{\partial \sigma}{\partial \theta_5} \\ \frac{a_4}{2} \cos(\sigma) \frac{\partial \sigma}{\partial \theta_2} & a_5 \cos(\theta_5) + \frac{a_4}{2} \cos(\sigma) \frac{\partial \sigma}{\partial \theta_5} \\ 0 & 0 \end{bmatrix} \quad (16)$$

where $\sigma = g(\theta_2, f(\theta_2, \theta_5), \theta_5)$

$$J_{p_{link_5}} = \begin{bmatrix} 0 & -\frac{a_5}{2} \sin(\theta_5) \\ 0 & \frac{a_5}{2} \cos(\theta_5) \\ 0 & 0 \end{bmatrix} \quad (17)$$

Calculation of rotation matrices for each link is given in Eq. (19). All links rotate about its own z axis. Equation (18) demonstrates the rotation matrix about z axis by θ .

$$R_z(\theta) = \begin{bmatrix} \cos(\theta) & -\sin(\theta) & 0 \\ \sin(\theta) & \cos(\theta) & 0 \\ 0 & 0 & 1 \end{bmatrix} \quad (18)$$

$$\begin{aligned} R_{link_2,z}(\theta) &= \begin{bmatrix} \cos(\theta_2) & -\sin(\theta_2) & 0 \\ \sin(\theta_2) & \cos(\theta_2) & 0 \\ 0 & 0 & 1 \end{bmatrix} & R_{link_3,z}(\theta) &= \begin{bmatrix} \cos(f(\theta_2, \theta_5)) & -\sin(f(\theta_2, \theta_5)) & 0 \\ \sin(f(\theta_2, \theta_5)) & \cos(f(\theta_2, \theta_5)) & 0 \\ 0 & 0 & 1 \end{bmatrix} \\ R_{link_4,z}(\theta) &= \begin{bmatrix} \cos(\theta_4) & -\sin(\theta_4) & 0 \\ \sin(\theta_4) & \cos(\theta_4) & 0 \\ 0 & 0 & 1 \end{bmatrix} & R_{link_5,z}(\theta) &= \begin{bmatrix} \cos(\sigma) & -\sin(\sigma) & 0 \\ \sin(\sigma) & \cos(\sigma) & 0 \\ 0 & 0 & 1 \end{bmatrix} \end{aligned} \quad (19)$$

where $\sigma = g(\theta_2, f(\theta_2, \theta_5), \theta_5)$

Orientalional Jacobian matrix for each link is calculated using Eq. (20).

$$J_{O_{link_i}} = \left[col \left[\frac{\partial R_{link_i,z}(\theta_i)}{\partial \theta_2} \cdot R_{link_i,z}^T(\theta_i) \right] col \left[\frac{\partial R_{link_i,z}(\theta_i)}{\partial \theta_5} \cdot R_{link_i,z}^T(\theta_i) \right] \right] \quad (20)$$

where $col^2 \left[\begin{bmatrix} 0 & -w_z & w_y \\ w_z & 0 & -w_x \\ -w_y & w_x & 0 \end{bmatrix} \right] = \begin{bmatrix} w_x \\ w_y \\ w_z \end{bmatrix}$

$$\begin{aligned} J_{O_{link_2}} &= \begin{bmatrix} 0 & 0 \\ 0 & 0 \\ 1 & 0 \end{bmatrix} & J_{O_{link_3}} &= \begin{bmatrix} 0 & 0 \\ 0 & 0 \\ \frac{\partial f(\theta_2, \theta_5)}{\partial \theta_2} & \frac{\partial f(\theta_2, \theta_5)}{\partial \theta_5} \end{bmatrix} \\ J_{O_{link_4}} &= \begin{bmatrix} 0 & 0 \\ 0 & 0 \\ \frac{\partial g(\theta_2, f(\theta_2, \theta_5), \theta_5)}{\partial \theta_2} & \frac{\partial g(\theta_2, f(\theta_2, \theta_5), \theta_5)}{\partial \theta_5} \end{bmatrix} & J_{O_{link_5}} &= \begin{bmatrix} 0 & 0 \\ 0 & 0 \\ 0 & 1 \end{bmatrix} \end{aligned} \quad (21)$$

² Column operator.

Dynamic Equation of Motion

$$M(q)\ddot{q} + G(q, \dot{q}) = \tau \quad (22)$$

where Inertia I_{link_i} , Mass $M(q)$, Gyroscope $G(q, \dot{q})$

$$I_{link_i} = \begin{bmatrix} I_{xx_{link_i}} & -I_{xy_{link_i}} & -I_{xz_{link_i}} \\ -I_{xy_{link_i}} & I_{yy_{link_i}} & -I_{yz_{link_i}} \\ -I_{xz_{link_i}} & -I_{yz_{link_i}} & I_{zz_{link_i}} \end{bmatrix} \quad (23)$$

$$M(q) = \sum_{n=1}^N m_{link_i} J_{p_{link_i}}^T J_{p_{link_i}} + J_{O_{link_i}}^T R_{link_i} I_{link_i} R_{link_i}^T J_{O_{link_i}} \quad (24)$$

$$G = \begin{bmatrix} g_{11} & g_{12} \\ g_{21} & g_{22} \end{bmatrix} \quad \text{where} \quad g_{ij} = \sum_{k=1}^N g_{ijk} \dot{q}_k \quad g_{ijk} = \frac{1}{2} \left(\frac{\partial m_{ij}}{\partial q_k} + \frac{\partial m_{ik}}{\partial q_j} + \frac{\partial m_{jk}}{\partial q_i} \right) \quad (25)$$

4 Dynamic Control

$x = f(q)$ $x \in \mathbb{R}^n$ and $f: \mathbb{R}^n \rightarrow \mathbb{R}^n$

Differentiation Forward Kinematic yields $\dot{x} = J\dot{q}$ where $J(q) \in \mathbb{R}^{n \times n}$ is the Jacobian matrix. $x(t)$, $\dot{x}(t)$, $q(t)$, $\dot{q}(t)$ are available for control design and $M(q)$, $G(q, \dot{q})$, $J(q)$ are known. Let's define $e(t) \in \mathbb{R}^n$ task space tracking error $e = x_d - x$ where $x_d \in \mathbb{R}^n$ is the desired end effector trajectory.

Differentiation velocity kinematic yields $\ddot{x} = \dot{J}\dot{q} + J\ddot{q}$ so $\ddot{q} = J^{-1}(\ddot{x} - \dot{J}\dot{q})$

Design Controller [3]

$$\tau = M(q)J(q)^{-1} \left(\ddot{x}_d + K_v \dot{e} + K_p e - \dot{J}\dot{q} \right) + G(q, \dot{q}) \quad (26)$$

where K_p , $K_n \in \mathbb{R}^{n \times n}$ are diagonal, positive definite control gain matrices.

4.1 Speech Command Recognition Using Deep Learning

This part shows how to create a simple deep learning model and recognize the speech command. Labelled dataset is downloaded from TensorFlow³. The dataset includes recorded wav files which is recorded from various people. Recorded speeches are labelled as ["zero", "one", "two", "three", "four", "five", "six", "seven", "eight", "nine", "background_noise"]. So the neural network is trained to recognize only these speech commands. Speeches except for specified given as a speech command will be recognized as "unknown" command by the trained network. Before speech signals are given to the neural work, they

³ http://download.tensorflow.org/data/speech_commands_v0.01.tar.gz.

are converted into log-mel spectrogram. Since records are one-channel audio and their duration and magnitude do not exceed 40 and 98, the input size for the neural network is chosen as $40 \times 98 \times 1$. Output size of the neural network is chosen as 12 because it classifies input as numbers from zero to nine, background noise and unknown.

Fully simplified used architecture are listed below.

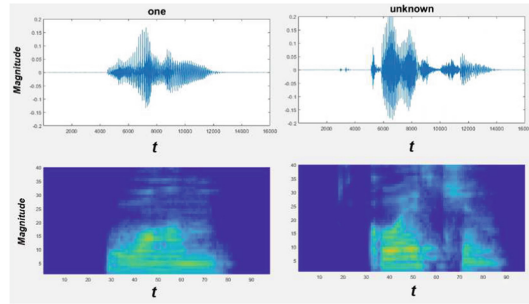


Fig. 3. Wave-forms and spectrogram of my own voices for in recognition process. The word “one” is given as a speech and network recognized successfully. Any word except for trained word is given as a speech. Since the network was not trained by this labeled word, It gives a message as “unknown” to indicate that the given speech could not be recognized.

[40x98x1] INPUT	[5x13x48] MAXPOOL3: 12 3x3
[40x98x12] CONV1: 12 3x3 filters	filters at stride 2, pad 0
at stride 1, pad 0	[5x13x48] CONV4: 48 3x3 filters at
[40x98x12] NORM1	stride 1, pad 0
[40x98x12] RELU1	[5x13x48] NORM4
[20x49x12] MAXPOOL1: 3x3 filters	[5x13x48] RELU4
at stride 2, pad 0	[5x13x48] CONV5: 48 3x3 filters at
[20x49x24] CONV2: 24 3x3 filters	stride 1, pad 0
at stride 1, pad 0	[5x13x48] NORM5
[20x49x24] NORM2	[5x13x48] RELU5
[20x49x24] RELU2	[5x1x48] MAXPOOL4: 1x13 filters
[10x25x24] MAXPOOL2: 12 3x3	at stride 1, pad 0
filters at stride 2, pad 0	[5x1x48] DROPOUT: 20 %
[10x25x48] CONV3: 48 3x3 filters	[1x1x12] FC: 12 fully connected
at stride 1, pad 0	layer
[10x25x48] NORM3	[1x1x12] SOFTMAX
[10x25x48] RELU3	[1x12] OUTPUT

Results of trained network

About 32000 data is used. 80% (25000) of it is used for training, 10% of it is used for validation and the rest is used for test.

Training error: 1.3632% and Validation error: 3.885%

zero	256	1						1	1	1		98.5%	1.5%
one		217		1					3	9		94.3%	5.7%
two	1	1	225						2	7		95.3%	4.7%
three			4	233			1			3	7	94.0%	6.0%
four		2		1	268	2		2		3	1	95.7%	4.3%
five	1	2				231			3	5		95.5%	4.5%
six	3						254		3	2		96.9%	3.1%
seven		2	1		2	1		255		1	1	97.0%	3.0%
eight	1		3						237		2	97.5%	2.5%
nine										227	3	98.7%	1.3%
unknown	3	13	5	5	3	7	2	3	3	9	89	93.6%	6.4%
background											400	100.0%	
	96.0%	91.2%	94.5%	97.1%	98.2%	95.9%	98.8%	96.1%	97.5%	89.4%	95.7%	99.0%	
	3.4%	8.8%	5.5%	2.9%	1.8%	4.1%	1.2%	1.9%	2.5%	10.6%	4.3%	1.0%	
	zero	one	two	three	four	five	six	seven	eight	nine	unknown	background	

Fig. 4. Confusion Matrix

Confusion Matrix is shown in Fig. 4, which is also known as error matrix.

5 Simulation

Simulation is run in Matlab/Simulink environment. Controller gain matrices K_p and K_d are selected $\begin{bmatrix} 7 & 0 \\ 0 & 7 \end{bmatrix}$, $\begin{bmatrix} 7 & 0 \\ 0 & 7 \end{bmatrix}$ respectively.

Link lengths are taken from the paper (Dede & Kiper) [2] and are shown in the Table 1. For links, hollow carbon fiber links are taken into account. Determined mass and inertia tensors are illustrated in Table 1.

Table 1. Designed link lengths

a_1	a_2	a_3	a_4	a_5
250 mm	250 mm	250 mm	250 mm	200 mm
m_1	m_2	m_3	m_4	m_5
0.85 kg	0.85 kg	0.85 kg	0.85 kg	0.75 kg

$$I_{link2} = I_{link3} = I_{link4} = \begin{bmatrix} 2 & 0 & 0 \\ 0 & 2 & 0 \\ 0 & 0 & 2 \end{bmatrix} \text{ kgm}^2, I_{link5} = \begin{bmatrix} 1.3 & 0 & 0 \\ 0 & 1.3 & 0 \\ 0 & 0 & 1.3 \end{bmatrix} \text{ kgm}^2$$

The desired trajectory followed by the mechanism is given as input and depends on the recognized speech command. For example, desired input in the case for recognized number 2 is demonstrated in Fig. 7.

5.1 Results

After the simulation is executed, the acquired results are given below. Because actuators cannot provide unlimited torque, torque is limited between $+3\text{ Nm}$ and -3 Nm . Torque with saturation block and without saturation block are shown in the Fig. 5 and Fig. 6. Since results aren't much different between Torque with saturation and without saturation, results shown below are calculated with regard to Torque without saturation.

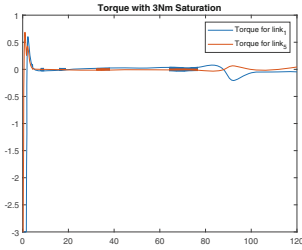


Fig. 5. Torque with saturation $\pm 3\text{ Nm}$

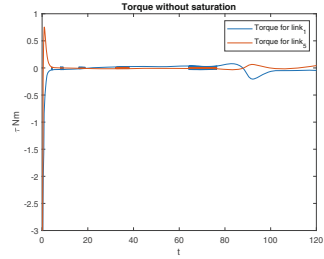


Fig. 6. Torque without saturation

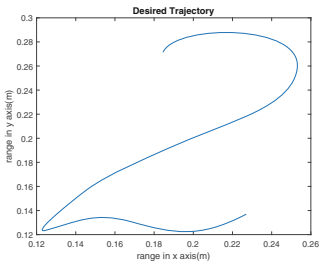


Fig. 7. Desired trajectory for #2

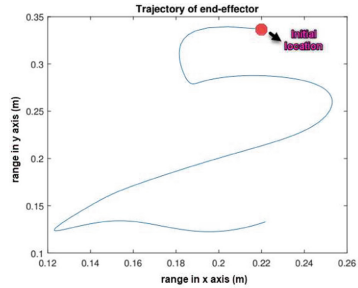


Fig. 8. Trajectory of end-effector

The curve over number 2 in Fig. 8 is due to initial conditions of the mechanism.

It can be seen from Fig. 9 that the error value fluctuates between -0.01 and 0.01 . In other words, given the desired trajectory in Fig. 7 is followed by the end effector of 5R mechanism deviating given trajectory with the amount of error shown in Fig. 9.

Figure 10 shows that changing angles of each links while the 5R mechanism follows the given trajectory. Figure 11 supports that the mechanism does not step in singularity configuration while following the desired trajectory because the determinant of the Jacobian Matrix does not equal to the zero.

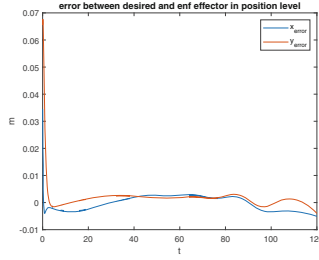


Fig. 9. Task space tracking error $e = x_d - x$. As the mechanism operates in 2D plane, x_{error} and y_{error} mean the error in x axis and y axis.

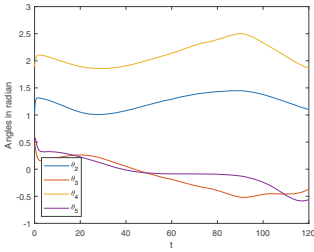


Fig. 10. Changing angles of each links

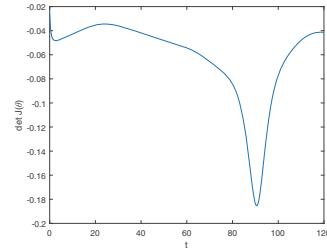


Fig. 11. Determinant of Jacobian Matrix

6 Conclusions

The idea of using handwriting haptic device with deep learning proposed successfully. The proposed model with deep learning has been performed within simulation environment in Matlab/Simulink. Obtained results have been indicated. Based on the results, the idea can be actualized in real life application and it will give great benefit to the people and make their life easier.

Acknowledgements. I acknowledge and extend my thanks to Prof. Dr.-Ing. Corves and IGMR Institute at the RWTH Aachen University.

References

1. Coles, T.R., Meglan, D., John, N.W.: The role of haptics in medical training simulators: a survey of the state of the art. *IEEE Trans. Haptics* **4**(1), 51–66 (2011). <https://doi.org/10.1109/TOH.2010.19>
2. Dede, M.İ.C., Kiper, G.: Mechanism design for haptic handwriting assistance device. In: *Mechanisms, Transmissions and Applications*, pp. 271–278. Springer, Heidelberg (2015)
3. Hsu, P., Mauser, J., Sastry, S.: Dynamic control of redundant manipulators. *J. Robot. Syst.* **6**(2), 133–148 (1989)

4. Liu, X., Dodds, G., McCartney, J., Hinds, B.: Virtual designworks-designing 3d cad models via haptic interaction. *Comput.-Aided Des.* **36**(12), 1129–1140 (2004). <https://doi.org/10.1016/j.cad.2003.10.003>
5. Minogue, J., Jones, M.G.: Haptics in education: exploring an untapped sensory modality. *Rev. Educ. Res.* **76**(3), 317–348 (2006). <https://doi.org/10.3102/00346543076003317>
6. Siciliano, B., Sciavicco, L., Villani, L., Oriolo, G.: *Robotics: Modelling, Planning and Control*. Springer, Heidelberg (2010)
7. Tarwala, R., Dorr, L.D.: Robotic assisted total hip arthroplasty using the MAKO platform. *Curr. Rev. Musculoskelet. Med.* **4**(3), 151 (2011)
8. Yu, W., Ramloll, R., Brewster, S.: Haptic graphs for blind computer users. In: Brewster, S., Murray-Smith, R. (eds.) *Haptic Human-Computer Interaction*, pp. 41–51. Springer, Heidelberg (2001)



Design and Development of a Mobile Robot Equipped with Perception Systems for Autonomous Navigation

Razvan Patcas^(✉), Bogdan Mocan, Mircea Fulea, Mircea Murar, and Mihai Steopan

UTCN Technical University of Cluj-Napoca, Cluj-Napoca, Romania
razvan.patcas@student.utcluj.ro, {bogdan.mocan,mircea.murar,
mihai.steopan}@muri.utcluj.ro, mircea.fulea@staff.utcluj.ro

Abstract. This paper presents a complete mechatronic approach in design and development of a mobile robot equipped with perception systems for autonomous navigation. The mechanical design, system and control architecture are presented in detail, followed by a description of the locomotion mechanism and the sensory system of the mobile robot. The developed robot has two degrees of freedom (DOF), eight revolute joints (8R) with parallel leg structure using 3D printed parts, commercially available embedded microcontrollers and sensors. The autonomous robotic system was controlled and managed by ROS packages. The experimental results are presented to validate robot functionalities.

Keywords: Mobile robot · ROS control architecture · 3D printed structure · Kinect sensorial system

1 Introduction

Nowadays, mobile robots are used in many applications, from domestic activities to military surveillance [1], from industry actions to security missions [2]. Mobile robots usually can carry out their tasks without the continuous guidance and supervising by human beings [5]. Developing a mobile robot equipped with perception systems for autonomous navigation is a very complex approach involving integration of different technologies and equipment and entail challenges which require significant research and development process.

The research conducted on mobile robots can be separated into three categories: kinematic control, the dynamic control and the navigation of mobile robots. Mobile robot's navigation has been investigated in many researches, but reference [5] is using an inference system based on fuzzy logic adaptive network. The applied approach requires a lot of training and, thus, needs rich training data. Another drawback of the presented approach is the large number of fuzzy rules required. Most of the developed controllers in the scientific literature have been designed based on the kinematic model only [3]. The model-based prediction control [8] and kinematic control using the Lyapunov [4]

are presented for various mobile robots. In reference [6] a PID controller is used for path tracking. Regarding the dynamic control researches we can point several: double Q-PID algorithm [12], disturbance observer based [16], robust NN-based tracking [7], nonlinear control based on optimization in [15], feedforward NNs [17], a non-linear adaptive controller for NNs [13] and adaptive control [14], to name just a few.

In this paper, by using a complete mechatronic [10] approach we deal with designing and developing a mobile robot equipped with perception systems for autonomous navigation. The structure of this paper is as follows: Sect. 1 makes the introduction and highlights several researches in developing mobile robots, then Sect. 2 presents the problem statement, preliminaries, and the design concept of the proposed mobile robot with a novel shape. Section 3 describes the experimental results: the developed prototype, functional simulation, test results and limitations. Section 4 highlights the conclusions and discussions.

2 Overall Design

The objective of this paper is to highlight the development of a mobile robot capable of autonomous navigation integrating visual and functional characteristics that will lead humans to find similarities with a dog. Some researches, [11, 12], highlighted that the humans can attribute a sort of individuality and personality to their dogs what determines them to love them and accept their faults. But, at the same time a dog tends to misbehave and not always respond promptly or correctly to the commands coming from the owner. This fact goes to strengthen the need for an autonomous behaviour in the case of a robot. The ability to handle unknown environments and the high level of complexity needed by a robot can raise the interest of the users and instil a sense of curiosity by the fact that they cannot fully predict the behaviour of the robot. All these factors are contributing to the robot “personality”. Having these in mind, the design of the robot was concentrated on the following assumptions: a) Providing a familiar shape of the robot – four legs attached by a torso; b) Using ROS (Robot Operating System) nodes for complete control and full flexibility of the robot; c) Use of 3D printing technology for most of the robot parts; d) Provide the ability to transport various objects of max. 5 kg; e) Reliability, time durability, and energy efficiency are not considered; f) The robot will not interact directly with the individuals.

2.1 Mechanical Design of the Main Parts of the Robot

The designed robot consists of four tracks, four legs, a torso and a Kinect sensor.

The main components of the robot are made by 3D printed using Polylactic Acid (PLA) and Acrylonitrile Butadiene Styrene (ABS). The four tracks are powered by DC motors in order to provide good mobility over a great variety of surfaces and to ease the steering process. The torso contains all the controllers, battery and power circuits while the perception system is placed on top of the torso, resembling the head of the robot, and providing a clear field of view for the vision system.

The robot measures 520×570 [mm] in length \times width and a height of 550 [mm]. The tracks integrate three wheels with a diameter of 60 [mm].

2.2 Locomotive Mechanism

The locomotion mechanism of the robot consists of four levers, parallels two by two, compounded by a set of tubes and fittings. The track assembly components (1 ÷ 6) are highlighted in Fig. 1. The tubes are hollow inside and the cables from the motors are led through the tubes and connected to the controller board in the torso of the robot.

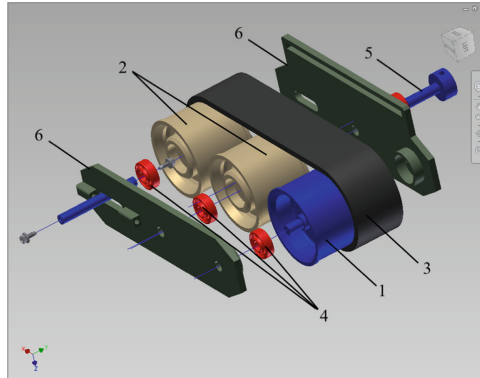


Fig. 1. Exploded view of the track assembly

The four tracks are comprised (Fig. 1) of one driving wheel (1) and two driven wheels (2) coupled to a rubber track (3). The wheels are mounted on the shafts with ZZ809 bearings (4) in order to reduce the load on the motors and to maximize battery life. The track can rotate around the shaft of the middle wheel (5) in order to allow the robot to overcome obstacles. The back driven wheel can slide inside the small channel of the side plates (6), in order to ease the process of fitting the rubber track properly. The other end of each leg is mounted on the torso using two radial ZZ809 ball bearings which allow the legs to work as a passive cylindrical joint that is useful while maneuvering over rough terrain, acting like a suspension.

2.3 Sensors, Interfaces and Micro-controllers Used for Control and Navigation

In order to provide full-autonomous navigation, it is crucial to have information regarding the objects that are in the surrounding environment and their position relative to the robot [9].

Regarding the developed robot, there were some limitations concerning the size and cost of the sensors as well as the availability of support and guidelines from the robotics community that led to the decision of using a Kinect sensor from Microsoft which consists of a RGB and infrared cameras, an infrared dot projector for depth measurement and four microphones [16].

The data from camera and the depth sensor were used to identify objects and retrieve their relative position to the sensor, which made the Kinect sensor suitable for this application [16]. In tandem with the Kinect system, an ultrasonic sensor mounted on

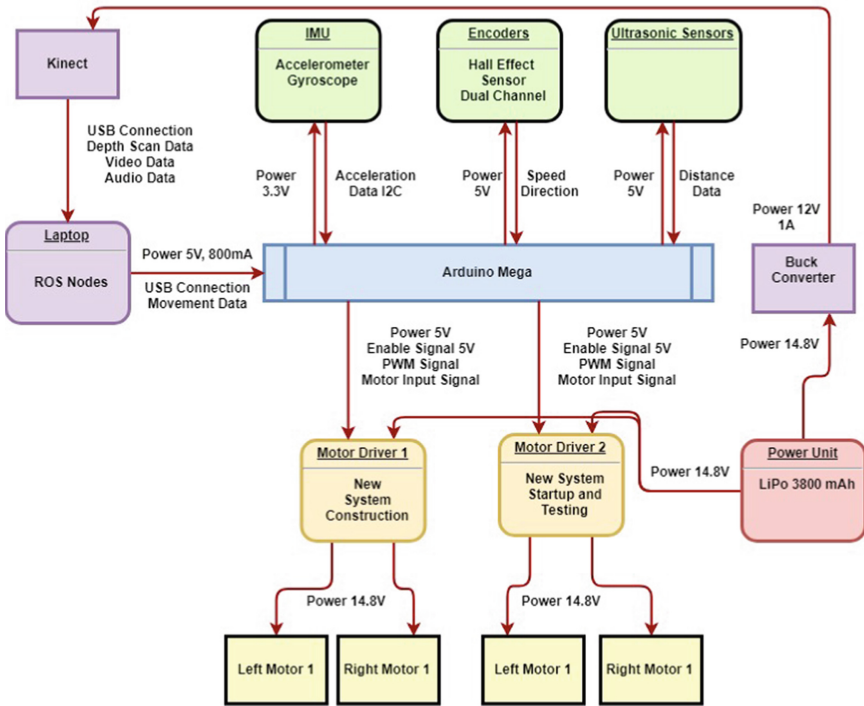


Fig. 2. Robot hardware connections diagram

the front side of the robot's torso was used to detect any obstacle that could be in the direction of the robot movement. For localization and tracking, additional sensors were used, such as Hall Effect speed encoders mounted on the back shaft of each of the four DC motors and an IMU (Inertial Measurement Unit) on six axes.

An overview diagram (Fig. 2) of all the hardware connections between the sensors, boards, motors and controllers. Figure 2 turns out that four 12 V brushed DC motors were used to operate the robot. The data acquisition process was done on the Arduino board for the motor speed encoders, IMU and the ultrasonic sensor, and then sent to the laptop via serial USB communication, while the data coming from the Kinect sensor was sent directly to the laptop. In order to get the data on the Arduino board, a source code was developed. The code for the ultrasonic sensor data acquisition have used the function `Update_Ultra_Sonic()` that programs the board to send small triggers to the sensor and the function `microsecondsToCentimeters(duration)` that converts the time of the echo into distance up to the obstacle. The speed encoders were determined a rise and fall in the output current when the motor rotates. The functions `do_Left_Encoder` and `do_Right_Encoder` read a digital signal on the B channels of the encoders and increment or decrement the value of the `Encoder_Ticks` variables according to the speed and sense of rotation. In order to get the data from the Kinect we had to install the OpenNI packages and drivers. The packages containing ROS nodes that acquired the data from the Kinect and publish them onto dedicated topics for depth, RGB data, Laser data, etc. was also

developed. Regarding the differential control of the four motors an algorithm has been developed based on ROS nodes, using guidance from reference [17].

3 Experimental Results

3.1 Prototype and Functional Simulation

The distinctive shape of the robot required that many components had to be fabricated (Fig. 3). In order to be able to transpose into practice the design recommendation, most of the robot parts had been fabricated from PLA and ABS plastic through a Fused Deposition Modelling process executed on the Anet A8 3D printer, one of the most popular 3D printers available on the market [13, 18].



Fig. 3. The prototype of the robot.

To realize this robot, we printed 57 individual parts (Fig. 3), ranging from 10 g to 150 g with a total printing time of 273.5 h. As for the robot hardware control a microcontroller board Arduino Mega 2560 has been used to control four 12 V Brushed DC motors which powered the tracks of the robot.

Behavioral simulations are a crucial element in the development of a robotic system. Since the robot hardware is often expensive and not available due to the long time needed for development, assembly and implementation, a simulation provides a convenient and fast way to test and develop robot software for a specific hardware without the need to build it. For the simulation of the developed robot we used the Gazebo simulator based on two ROS packages containing the 3D model of the developed robot, the 3D models for the simulation environments and the files defining the kinematic joints of the robot, the sensors and their parameters.

The simulation environment allowed driving the robot manually from the keyboard, using the *keyboard_teleoperation* package and with the help of the Kinect sensor the simulated environment could be scanned/mapped and a topological map was generated using SLAM (Simultaneous Localization and Mapping) infrastructure. The rotating joints were connected to robot model and for differential control the Kobuki controller was used.

3.2 Tests and Results

In the testing phase, the focus was not concentrated on the quality of the topological map developed from the data points scanned by the Kinect sensor but rather on the performance of the SLAM algorithm in reaching the desired pose. For this, we used a variety of locations in order to establish the test benchmark: outside scenario on a surface covered in grass and stone pavement, inside scenario in a laboratory with a laminated floor, inside scenario in an office space with chairs and tables and floor covered with carpet.

Test environment surface	Test speed average [km/h]	Average rotational deviation [degrees]	Average longitudinal deviation [mm]	Track length [mm]
Indoors laminated	2.1	12.3	853	17000
Indoors laminated	1.3	6.4	164	5000
Indoors carpet	1.8	7.9	549	18000
Indoors carpet	1.2	5.2	128	6200



Fig. 4. Deviation from the poses estimated by the SLAM algorithm

In the process of scanning the map for the SLAM algorithm, we eliminated the outside scenario test because the scanned points presented an excessive noise level. The errors were caused by the vibrations and movement transmitted to the Kinect sensor due to the roughness of the terrain and lack of rigidity and cushioning of the robot structure. For the inside scenarios, the performance assessment was done by comparing the deviation from the poses estimated by the SLAM algorithm a_x to the final poses reached by the robot $a_x + \Delta$ as presented in Fig. 4.

The results show greater deviation from the estimated pose on slippery surfaces due to wheel slip and overall poor performance of the robot structure and locomotive system. On longer paths, the error induced a deviation from the clear path towards an obstacle. This caused the robot to stop due to the obstacle being detected by the ultrasonic sensors and interrupted the navigation task.

3.3 Discussion and Limitations

The designed and developed mobile robot had some drawbacks that are highlighted hereinafter. The 3D printed robot's mechanical structure had reduced rigidity and certain printed parts did not comply with the prescribed geometrical tolerances which led to a

decrease in robot performance. The reduced rigidity of the robot structure induces in the Kinectic sensor a lot of noise, due to the frequent vibrations during the robot movements, which makes the navigation very difficult and sometimes impossible if the surface is not perfectly smooth.

In terms of maneuverability the robot can make turns easily and all the motion commands could be submitted successfully from the laptop keyboard. The selected motors provided enough torque and speed, robot being able to move with the max. speed of 3 km/h while it has been driving with a mass of 5 kg on its torso.

4 Conclusions

Our experimental result shows that through the proposed approach we have managed to design and control a mobile robot that is capable of autonomous navigation, while using ROS packages, a set of sensors and Kinect system.

By developing this mobile robot and testing it, the technical feasibility of integrating the highlighted sensors and Kinect system together with the ROS packages was demonstrated. Generally, the robot has performed as expected on a very smooth surfaces, but on the other types of surfaces failed. There were two types of problems: the rigidity of the legs and torso which induces a lot of noise in the sensory system and the tracks that suffered modifications from the initial design, due to the poor dimensional and geometrical precision of the 3D printed wheels that guide the track belt which caused the belt to slip off over the wheels in rotation. Improvements will have to be made in the future in order to improve the dynamic performance of the robot, some parts will be machined from aluminum for the next robot iteration.

References

1. Bhat, S., Meenakshi, M.: Military robot path control using RF communication. In: Proceedings of the First International Conference on Intelligent Computing and Communication, pp. 697–704. Springer, Singapore (2017)
2. Gu, W., Cai, S., Hu, Y., Zhang, H., Chen, H.: Trajectory planning and tracking control of a ground mobile robot: a reconstruction approach towards space vehicle. *ISA Trans.* **87**, 116–128 (2019)
3. Huang, D., Zhai, J., Ai, W., Fei, S.: Disturbance observer-based robust control for trajectory tracking of wheeled mobile robots. *Neurocomputing* **198**, 74–79 (2016)
4. Huang, H., Zhou, J., Di, Q., Zhou, J., Li, J.: Robust neural network-based tracking control and stabilization of a wheeled mobile robot with input saturation. *Internat J. Robust Nonlinear Control* **29**, 375–392 (2019)
5. Klancar, G., Zdesar, A., Blazic, S., Skrjanc, I.: *Wheeled Mobile Robotics: From Fundamentals Towards Autonomous Systems*. Butterworth-Heinemann, Elsevier Science, Oxford, Amsterdam (2017)
6. Lee, M.-F.R., Hung, N.T., Chiu, F.-H.S.: An autonomous mobile robot for indoor security patrol. In: *International Conference on Fuzzy Theory and its Applications*, pp. 189–194 (2013)
7. Matraji, I., Al-Durra, A., Haryono, A., Al-Wahedi, K., Abou-Khousa, M.: Trajectory tracking control of skid-steered mobile robot based on adaptive second order sliding mode control. *Control Eng. Pract.* **72**, 167–176 (2018)

8. Mihelj, M., Bajd, T., Ude, A., Lenarčič, J., Stanovnik, A., Munih, M., et al.: Mobile robots. In: *Robotics*, pp. 189–208. Springer, Cham (2018)
9. Mocan, B., Fulea, M., Brad, E., Brad, S.: State-of-the-art and proposals on reducing energy consumption in the case of industrial robotic systems. In: *Proceedings of the 2014 International Conference on Production Research – Regional Conference Africa, Europe and the Middle East; 3rd International Conference on Quality and Innovation in Engineering and Management, Cluj-Napoca, Romania, 1–5 July*, pp. 328–334 (2014)
10. Mocan, B., Fulea, M., Brad, S.: Designing a multimodal human-robot interaction interface for an industrial robot. In: *Proceedings of 24th International Conference on Robotics in Alpe-Adria-Danube Region (RAAD), Advances in Robot Design and Intelligent Control*, vol. 371, pp. 255–263. Springer, Berlin, Heidelberg (2016). Platz 3, D-14197 Berlin, Germany
11. Mocan, B., Fulea, M., Olaru, M., Buchmüller, M.: From intuitive programming of robotic systems to business sustainability of manufacturing SMEs. *Amfiteatru Econ.* **18**(41), 215–231 (2016)
12. Mohanty, P.K., Parhi, D.R.: Navigation of autonomous mobile robot using adaptive network based fuzzy. *J. Mech. Sci. Technol.* **28**, 2861–2868 (2014)
13. Pourboghra, F., Karlsson, M.P.: Adaptive control of dynamic mobile robots with nonholonomic constraints. *Comput. Electr. Eng.* **28**, 241–253 (2002)
14. Refoufi, S., Benmahammed, K.: Control of a manipulator robot by neuro-fuzzy subsets form approach control optimized by the genetic algorithms. *ISA Trans.* **77**, 133–145 (2018)
15. Reyes-Acosta, A.V., Lopez-Juarez, I., Osorio-Comparan, R., Lefranc, G.: 3D pipe reconstruction employing video information from mobile robots. *Appl. Soft Comput.* **75**, 562–574 (2019)
16. Shirzadeh, M., Amirkhani, A., Jalali, A., Mosavi, M.R.: An indirect adaptive neural control of a visual-based quadrotor robot for pursuing a moving target. *ISA Trans.* **59**, 290–302 (2015)
17. Shirzadeh, M., Shojaeefard, M.H., Amirkhani, A., Behroozi, H.: Adaptive fuzzy nonlinear sliding-mode controller for a car-like robot. In: *5th Conference on Knowledge-Based Engineering and Innovation*, pp. 686–691 (2019)
18. Wang, X., Jiang, M., Zhou, Z., Gou, J., Hui, D.: 3D printing of polymer matrix composites: a review and prospective. *Compos. B Eng.* **110**, 442–458 (2017)



Validation of Flatness-Based Feedforward Control for a Four-Chain Crane Manipulator

Erik Hildebrandt¹(✉), Tobias Handreg², Pascal Froitzheim², Wilko Flügge²,
and Christoph Woernle¹

¹ Chair of Technical Mechanics/Dynamics, University of Rostock, Rostock, Germany
{erik.hildebrandt,woernle}@uni-rostock.de

² Fraunhofer Institute for Large Structures in Production Engineering IGP,
Rostock, Germany
{tobias.handreg,pascal.froitzheim,wilko.fluegge}@igp.fraunhofer.de

Abstract. Flatness-based feedforward trajectory control is experimentally validated for a crane manipulator that suspends a flexible metal sheet by four chain hoists each positioned by an overhead crane gear. For a desired spatial trajectory of the sheet the control inputs of the individual drives are calculated by an inverse dynamics model that takes the load sway dynamics, an approximated dynamic transfer behaviour of the controlled drive axes and the stiffness of the payload into account. A forward kinematics measurement model enables an estimation of the actual pose of the platform from measured drive positions and chain inclinations. Experimental results show the effect of the control concept.

Keywords: Crane manipulator · Parallel kinematics · Flatness-based feedforward control · Trajectory tracking · Flexible crane payload

1 Introduction

Metal sheets can be formed by a three-point bending process with a sword and a pair of dies as forming tool [2]. The metal sheet is suspended by four chain hoists that are mounted on trolleys of an overhead crane with two bridges each with two trolleys as shown in Fig. 1. Due to the heavy payloads two-strand chain hoists are provided. The lower pulley blocks include springs in order to isolate the crane gear from excessive process forces especially in off-nominal situations. To estimate the actual position of the sheet, the fixed chain strands bear two-axis inertial inclination sensors (Sick TMM88B-ACC090).

A desired sheet motion is achieved by coordinated control of bridges, trolleys and chain hoists, whereby the flexibility of the workpiece is also to be taken into account. By this, the system represents an underconstrained 4-4 cable-driven parallel manipulator (CDPM) with movable winch mounts [4]. After a forming

tool engagement the sheet is moved by the crane system from the actual into the desired subsequent equilibrium position without residual sway. There, the next tool engagement takes place. In each step a desired spatial trajectory between the rest positions is planned by the process scheduler [3]. For tracking these trajectories flatness-based feedforward control based on nonlinear and linearised control design models of the crane system has been described in [6] and [5], respectively. The present contribution extends these results by a description of experimental validations on the actual crane system shown in Fig. 1. This includes (1) the enhancement of the control design model by a simplified dynamic transfer behaviour of the individual drive axis controllers, (2) a forward kinematics measurement model to estimate the actual platform position from measured bridge and trolley positions, chain lengths and load chain inclinations and (3) presentation of some experimental results showing the effect of the control.

The paper is organised as follows. In Sects. 2 and 3 the control design model of the crane system and flatness-based feedforward control from [6] are briefly summarised. The forward kinematics measurement model is described in Sect. 4 followed by experimental results shown in Sect. 5.

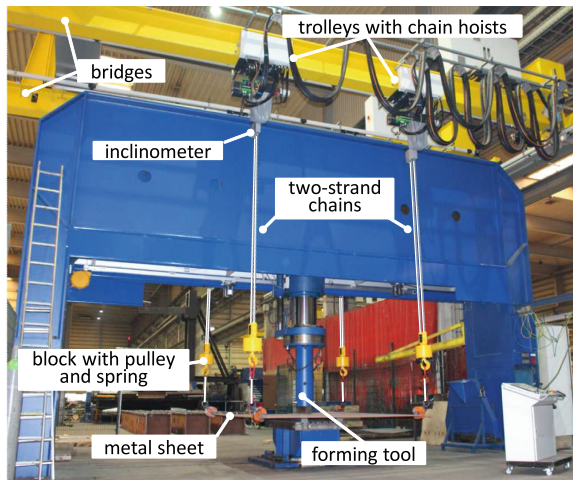


Fig. 1. Four-chain crane manipulator for positioning metal sheets under a forming tool.

2 Nonlinear Dynamics of the Crane Manipulator

As described in more detail in [6] the control design model of the crane manipulator is formulated in the absolute position coordinates of the flexible plate. The masses of the chains are neglected. The displacements of the bridges, trolleys and chain lengths are treated as kinematic inputs for the individual axis drive controllers.

Coordinates. According to Fig. 2 the independently controllable actuator coordinates $\mathbf{p} \in \mathbb{R}^{10}$ include the two bridge positions $\mathbf{p}_b = [p_{b1} \ p_{b2}]^T$, the four trolley positions $\mathbf{p}_t = [p_{t11} \ p_{t12} \ p_{t21} \ p_{t22}]^T$ and the four chain lengths $\mathbf{p}_l = [p_{l11} \ p_{l12} \ p_{l21} \ p_{l22}]^T$,

$$\mathbf{p} = [\mathbf{p}_b^T \ \mathbf{p}_t^T \ \mathbf{p}_l^T]^T. \tag{1}$$

The spatial pose of the flexible sheet with respect to the fixed coordinate system C_0 is described by the platform coordinates $\mathbf{y} \in \mathbb{R}^7$. They comprise the three Cartesian coordinates $\mathbf{r} = [r_x \ r_y \ r_z]^T$ of O_1 , the three Cardan angles $\boldsymbol{\vartheta} = [\vartheta_1 \ \vartheta_2 \ \vartheta_3]^T$ of a payload-fixed coordinate system C_1 and a coordinate to describe the elastic deformation of the plate η ,

$$\mathbf{y} = [\mathbf{r}^T \ \boldsymbol{\vartheta}^T \ \eta]^T. \tag{2}$$

The spatial velocity $\mathbf{z} \in \mathbb{R}^7$ of the sheet is described by the coordinates of the velocity \mathbf{v} of the origin O_1 , the platform-fixed coordinates of the angular velocity $\boldsymbol{\omega}$ of C_1 relative to C_0 and the time derivative of the deformation $\dot{\eta}$. The relation between $\dot{\mathbf{y}}$ and \mathbf{z} is given by a kinematic differential equations of the form [8]

$$\dot{\mathbf{y}} = \mathbf{H}(\mathbf{y}) \mathbf{z}. \tag{3}$$

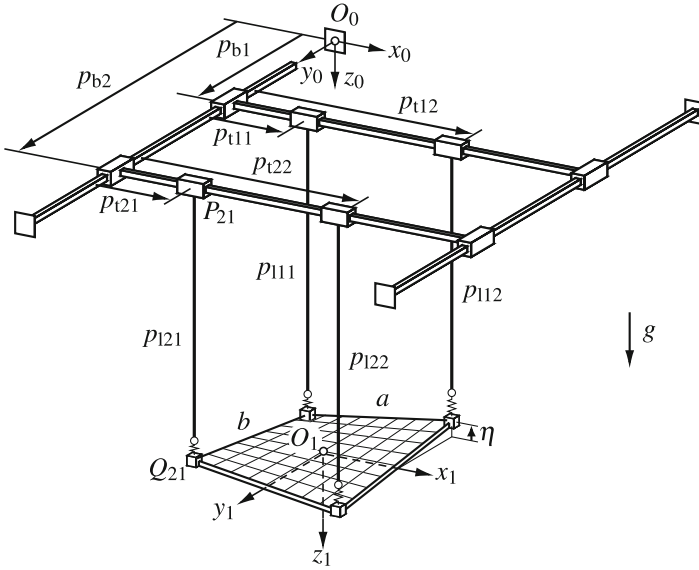


Fig. 2. Coordinates of the chain-suspended manipulator with a flexible payload.

Flexible Platform Dynamics. The sheet is modelled by a rectangular Kirchhoff plate (mass m , edge length a, b , torsional stiffness c_f) suspended at its corner

points. Compared to the other flexible modes of the sheet, the torsion dominates the distribution of forces over the four load chains and is therefore considered only. The displacement of the plate in z_1 -direction is modelled by the shape function $\phi(x, y)$ and the elastic coordinate $\eta(t)$ which describes the torsion [1],

$$W(x, y, t) = \phi(x, y) \eta(t) \quad \text{with} \quad \phi(x, y) = 4 \frac{x y}{a b}. \quad (4)$$

The vectors from O_1 to the suspension points Q_{ij} then are

$$\mathbf{d}_{ij} = \mathbf{T}(\boldsymbol{\vartheta}) \mathbf{d}_{ij,0} + \phi_{ij} \mathbf{e}_{z_1} \eta \quad (5)$$

with the rotation matrix $\mathbf{T}(\boldsymbol{\vartheta})$ from O_1 to O_0 , the constant coordinates $\mathbf{d}_{ij,0}$ of the flat plate in O_1 as well as $\phi_{ij} = 1$ for $i = j$ and $\phi_{ij} = -1$ for $i \neq j$.

The dynamic equations for the flexible payload in the coordinates \mathbf{y} comprise the kinematic differential Eq. (3) and the kinetic differential Eq. [6]

$$\begin{aligned} \begin{bmatrix} m\mathbf{I} & \mathbf{0} & \mathbf{0} \\ \mathbf{0} & \boldsymbol{\Theta} & \mathbf{0} \\ \mathbf{0} & \mathbf{0} & \frac{1}{9}m \end{bmatrix} \begin{bmatrix} \dot{\mathbf{v}} \\ \dot{\boldsymbol{\omega}} \\ \dot{\eta} \end{bmatrix} + \begin{bmatrix} \mathbf{0} \\ \tilde{\boldsymbol{\omega}} \boldsymbol{\Theta} \boldsymbol{\omega} \\ 0 \end{bmatrix} + \begin{bmatrix} \mathbf{0} \\ \mathbf{0} \\ c_f \eta \end{bmatrix} = \begin{bmatrix} \mathbf{f}_g + \mathbf{f}_{11} + \mathbf{f}_{12} + \mathbf{f}_{21} + \mathbf{f}_{22} \\ \tilde{\mathbf{d}}_{11} \mathbf{f}_{11} + \tilde{\mathbf{d}}_{12} \mathbf{f}_{12} + \tilde{\mathbf{d}}_{21} \mathbf{f}_{21} + \tilde{\mathbf{d}}_{22} \mathbf{f}_{22} \\ \mathbf{e}_{z_1}^T (\mathbf{f}_{11} - \mathbf{f}_{12} - \mathbf{f}_{21} + \mathbf{f}_{22}) \end{bmatrix} \\ \mathbf{M} \quad \quad \quad \ddot{\mathbf{z}} + \mathbf{k}^c(\dot{\mathbf{z}}) + \mathbf{k}^{\text{el}}(\mathbf{y}) = \quad \quad \quad \mathbf{k}^e(\mathbf{y}, \mathbf{p}) \end{aligned} \quad (6)$$

with the constant mass matrix $\mathbf{M} \in \mathbb{R}^{7 \times 7}$ (inertia tensor of the platform relative to its center of mass $\boldsymbol{\Theta} = \text{diag}\{\frac{1}{12}mb^2, \frac{1}{12}ma^2, \frac{1}{12}m(a^2 + b^2)\}$), the generalised centrifugal and Coriolis forces $\mathbf{k}^c \in \mathbb{R}^7$, the generalised elastic force $\mathbf{k}^{\text{el}} \in \mathbb{R}^7$ and the applied generalised forces $\mathbf{k}^e \in \mathbb{R}^7$. Applied forces are the gravity force $\mathbf{f}_g = mg \mathbf{e}_{z_0}$ and, considering linear attachment springs (stiffness c), the chain forces

$$\mathbf{f}_{ij} = c(l_{ij} - p_{ij}) \quad \text{with} \quad \mathbf{e}_{ij} = \frac{\mathbf{l}_{ij}}{l_{ij}}, \quad \mathbf{l}_i = \mathbf{r}_{P_{ij}} - \mathbf{r}_{Q_{ij}}, \quad l_{ij} = |\mathbf{l}_{ij}| \quad (7)$$

with the position vector $\mathbf{r}_{P_{ij}} = \mathbf{e}_{x_0} p_{t_{ij}} + \mathbf{e}_{y_0} p_{b_{ij}}$ of P_{ij} and $\mathbf{r}_{Q_{ij}} = \mathbf{r} + \mathbf{d}_{ij}$ of Q_{ij} .

Dynamics of the Independent Axis Controllers. The independent drives of the bridges, trolleys and hoists of the prototype system are controlled by underlying speed controllers. Therefore, a reactionless dynamic behaviour of the drives is assumed as a simple first-order transfer function. The equations of motion of the controlled drives then have the form

$$\mathbf{T} \ddot{\mathbf{p}} + \dot{\mathbf{p}} = \mathbf{K} \mathbf{u} \quad (8)$$

with time constants $\mathbf{T} = \text{diag}\{T_1, \dots, T_{10}\}$ and gains $\mathbf{K} = \text{diag}\{K_1, \dots, K_{10}\}$. The control inputs $\mathbf{u} \in \mathbb{R}^{10}$ of the system then are the desired speeds of the bridge, trolley and hoist actuators. The parameters in \mathbf{T}, \mathbf{K} were identified from recorded measurement data by least-squares optimisation.

3 Flatness-Based Feedforward Control

The objective of the feedforward control is to move the payload along desired spatial trajectories $\check{\mathbf{y}}(t)$. By exploiting the flatness property of the system, the required control inputs \mathbf{u} can be calculated in two consecutive steps, the so-called generalised inverse kinematics and the inverse dynamics, refer also to [7].

Generalised Inverse Kinematics. In the first step the actuator coordinates $\check{\mathbf{p}}$ are calculated in terms of the desired outputs $\check{\mathbf{y}}$ following the outline of [6]. According to (6) there are seven nonlinear equations for the ten actuator coordinates. Thus, the problem is kinematically triple redundant which means that a certain platform position can be realised by a wide variety of actuator coordinates. Technically appropriate solutions can be found by optimisation. A useful criterion proved to be minimisation of the chain lengths l_{ij} , coming along with small inclination angles of the load chains. The constrained optimisation problem then is

$$\underset{\check{\mathbf{p}}}{\text{minimise}} \quad Z(\check{\mathbf{p}}, \check{\mathbf{y}}) = \sum_{i=1}^2 \sum_{j=1}^2 l_{ij}^2 \quad (9)$$

$$\text{subject to} \quad \mathbf{\Gamma}(\check{\mathbf{p}}, \check{\mathbf{y}}, \dot{\check{\mathbf{y}}}, \ddot{\check{\mathbf{y}}}) \equiv \mathbf{M}\ddot{\check{\mathbf{z}}} + \mathbf{k}^c + \mathbf{k}^{\text{el}} - \mathbf{k}^e = \mathbf{0},$$

whereby the nonlinear equation constraint $\mathbf{\Gamma} = \mathbf{0}$ from (6) ensures that for a desired motion the payload platform is continuously in dynamic equilibrium in terms of d'Alembert's principle.

Inverse Dynamics. The second step is the calculation of the control inputs \mathbf{u} in terms of $\check{\mathbf{p}}$. They are obtained directly by solving (8) with respect to \mathbf{u} , leading to

$$\mathbf{u} = \mathbf{K}^{-1} (\mathbf{T}\ddot{\check{\mathbf{p}}} + \dot{\check{\mathbf{p}}}). \quad (10)$$

Thus, in addition to the actuator coordinates $\check{\mathbf{p}}$, their speeds $\dot{\check{\mathbf{p}}}$ and accelerations $\ddot{\check{\mathbf{p}}}$ are needed. The total time derivatives can be obtained numerically by forward difference quotients or analytically by using the linearised equations of motion derived in [5]. Altogether a feedforward control law is received that calculates the control inputs \mathbf{u} for the desired coordinates $\check{\mathbf{y}}$ specified up to fourth-order time derivatives,

$$\mathbf{u} = \mathbf{\Psi}(\check{\mathbf{y}}, \dot{\check{\mathbf{y}}}, \ddot{\check{\mathbf{y}}}, \check{\mathbf{y}}^{(3)}, \check{\mathbf{y}}^{(4)}). \quad (11)$$

The inverse system model (11) moves the flexible sheet along desired spatial trajectories $\check{\mathbf{y}}$ under ideal conditions, thus sufficient accuracy of the feedforward control model, no unmodelled disturbances and consistent initial conditions.

4 Kinematic Measurement Model

To evaluate accuracies achievable with the flatness-based feedforward control during a controlled motion, the actual position of the payload has to be estimated. Assuming the chains between the suspension and attachment points

P_{ij}, Q_{ij} to be rigid links, the position of the payload can be calculated by means of a forward kinematic transformation from the ten measured actuator coordinates \mathbf{p} and the eight measured chain inclination angles (two inclination angles per chain)

$$\boldsymbol{\varphi} = [\varphi_{11} \bar{\varphi}_{11} \varphi_{12} \bar{\varphi}_{12} \varphi_{21} \bar{\varphi}_{21} \varphi_{22} \bar{\varphi}_{22}]^T, \quad \boldsymbol{\varphi} \in \mathbb{R}^8, \quad (12)$$

similar to the procedure described in [7]. In the kinematic measurement model shown in Fig. 3 the measurement axes of the chain inclinometers are modelled by revolute joints. The four kinematic loops are cut at the spherical joints at the sheet attachment points leading to four nonlinear loop closure conditions with three equations each,

$$\begin{aligned} \mathbf{h}_{ij} &\equiv \mathbf{r}_{Q_{ij}}(p_{bi}, p_{vij}, p_{lij}, \varphi_{ij}, \bar{\varphi}_{ij}) - \mathbf{r}_{Q'_{ij}}(\mathbf{y}) = \mathbf{0}, \quad i = 1, 2, \quad j = 1, 2, \\ &\Rightarrow \mathbf{h}(\mathbf{p}, \boldsymbol{\varphi}, \mathbf{y}) = \mathbf{0}. \end{aligned} \quad (13)$$

The Eqs. (13) ensure the kinematic compatibility in the four kinematic loops and are fulfilled when the distance between the cut points Q_{ij}, Q'_{ij} disappears. They are a set of twelve non-linear equations to calculate the seven unknown platform coordinates \mathbf{y} from the eighteen measured quantities $\mathbf{p}, \boldsymbol{\varphi}$. The overdetermined set of Eqs. (13) is solved numerically with the Levenberg-Marquardt algorithm.

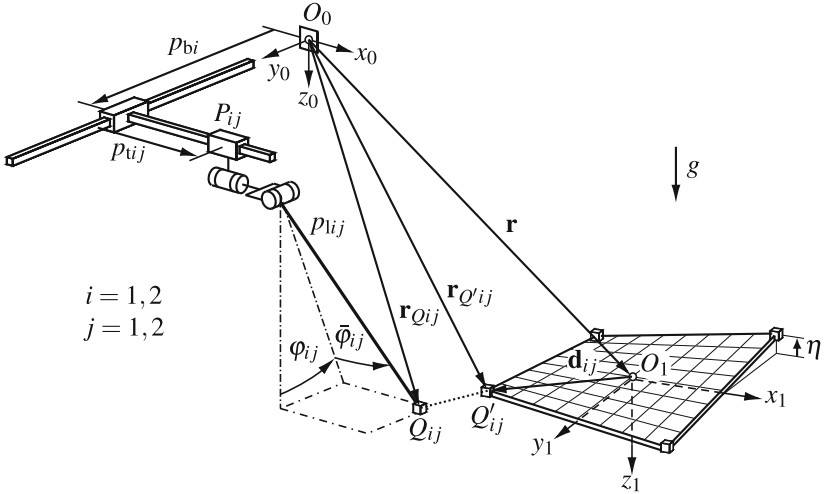


Fig. 3. Kinematic measurement model to calculate the platform coordinates \mathbf{y} .

5 Simulation and Experimental Results

The effect of the feedforward control on the prototype system is exemplarily illustrated in Fig. 4 by a translational movement of the sheet between given rest

positions in the time interval between $t_0 = 0$ s and $t_1 = 18$ s with a sufficiently steady reference trajectory. Subfigures 4a–c show the time histories of the bridge displacements $\Delta \mathbf{p}_b(t) = \mathbf{p}_b(t) - \mathbf{p}_b(t_0)$, the trolley displacements $\Delta \mathbf{p}_t(t) = \mathbf{p}_t(t) - \mathbf{p}_t(t_0)$ and the chain lengths $\Delta \mathbf{p}_l(t) = \mathbf{p}_l(t) - \mathbf{p}_l(t_0)$ from the generalised inverse kinematics calculation and from measurements. Subfigure 4d represents the time histories of the trajectories of the platform center $\Delta \mathbf{r}(t) = \mathbf{r}(t) - \mathbf{r}(t_0)$. The corresponding tracking errors e_{r_x} , e_{r_y} and e_{r_z} in Subfigures 4e–g show how the flatness-based feedforward control moves the platform to a desired end position with small residual oscillation at the time $t \approx 15$ s.

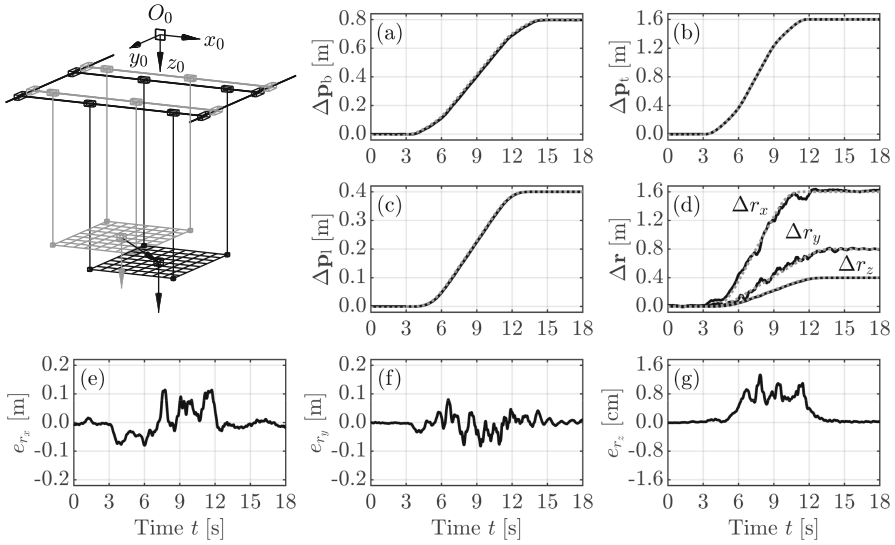


Fig. 4. Translational movement of the payload in space (— measurement, ··· reference).

As another example, Fig. 5 illustrates the results for the rotation of the payload around a fixed vertical axis over a rotation angle $\Delta \vartheta_3 = 30^\circ$. The movement is primarily achieved by moving the bridges and trolleys in opposite directions, whereby the chain lengths are adjusted accordingly as shown in Subfigures 5a–c. The comparison of the Cardan angles in Subfigure 5d demonstrate how the desired end position is reached without load sway at the time $t \approx 15$ s.

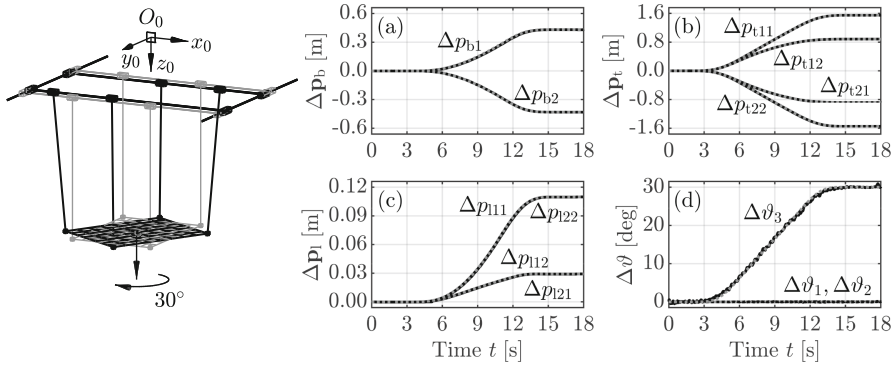


Fig. 5. Rotation of the payload around a fixed vertical axis (— measurement, ··· reference).

6 Conclusions

For the four-chain suspension manipulator with kinematically indeterminate payload position, a non-linear feedforward control was presented, utilising the flatness property of the system model. The feedforward control considers the kinematic nonlinear parallel structure of the four-chain suspension as well as an approximated dynamics of the underlying velocity controllers of the drives. For estimation of the platform pose a kinematical measurement model is presented. Experimental results confirm the effectiveness of the chosen approach.

Under ideal conditions the presented feedforward control moves the flexible payload platform along desired trajectories. If the idealised conditions are not given, tracking errors occur. Therefore, ongoing research is devoted to the design of a suitable feedback controller that reduces tracking errors and actively dampens load swings.

Acknowledgements. This research and development project was supported by the European Regional Development Fund (EFRE). Support was also provided by the lead partner Technologie-Beratungsinstitut (TBI) according to the directive for support, development and innovation of the Ministry of Economics, Construction and Tourism of Mecklenburg-Vorpommern.

References

1. Bhaskar, K., Varadan, T.: *Plates: Theories and Applications*. Wiley (2014)
2. Froitzheim, P., Stoltmann, M., Fuchs, N., Woernle, C., Flüge, W.: Prediction of metal sheet forming based on a geometrical model approach. *Int. J. Mater. Form.* (2019). <https://doi.org/10.1007/s12289-019-01529-9>
3. Handreg, T., Froitzheim, P., Fuchs, N., Flüge, W., Stoltmann, M., Woernle, C.: Concept of an Automated Framework for Sheet Metal Cold Forming. In: *Tagungsband des 4. Kongresses Montage Handhabung Industrieroboter*, pp. 117–127. Springer, Heidelberg (2019)

4. Pott, A.: Cable-Driven Parallel Robots. Springer, Heidelberg (2018)
5. Stoltmann, M., Froitzheim, P., Fuchs, N., Flügge, W., Woernle, C.: Linearised feedforward control of a four-chain crane manipulator. In: Pott, A., Bruckmann, T. (eds.) Cable-Driven Parallel Robots, pp. 233–244. Springer, Cham (2019)
6. Stoltmann, M., Froitzheim, P., Fuchs, N., Woernle, C.: Flatness-based feedforward control of a crane manipulator with four load chains. In: Corves, B., Wenger, P., Hüsing, M. (eds.) EuCoMeS 2018, pp. 61–68. Springer, Cham (2018)
7. Woernle, C.: Trajectory tracking for a three-cable suspension manipulator by non-linear feedforward and linear feedback control. In: Bruckmann, T., Pott, A. (eds.) Cable-Driven Parallel Robots, pp. 371–386. Springer, Berlin (2013)
8. Woernle, C.: Mehrkörpersysteme. Springer, Heidelberg (2016)



The Model of a Controlled Mechanical System of an Air-Jet Loom Shedding Mechanism

Jiří Ondrášek^(✉) and Petr Karel

VÚTS, a.s., Liberec, Czech Republic
{jiri.ondrasek, petr.karel}@vuts.cz

Abstract. The aim of the paper is to provide information about a simulated model creation of the shedding mechanism of an air-jet weaving machine. The loom is meant for production of leno weave fabrics. The loom is characterized with the system of the adaptive change of beating-up and shed mechanisms function with picking angle maximization, direct drive of mechanisms and energy recuperation. The possibilities of modern commercial software systems are used to create a computational model of the mentioned mechanism. The main subject of the computations is the estimation of the dynamic properties and behavior of the shedding mechanism, including its drive and control structure.

Keywords: Computational model · Weaving machine · Shedding mechanism · Energy recuperation

1 Introduction

With the increasing pressure on the size and quality of weaving machine production, the demand for its increased performance, reliability and service life is growing. This fact is closely related to the detailed knowledge of the dynamic properties and behavior of this machinery during its operation. In this context, the importance to its quality design is attached which is supported by computational simulations and experiments. For the objective description of the mentioned system, it is necessary that it is mathematically modeled and solved as a whole, including its individual subsystems, i.e. a so-called controlled mechanical system is created. This requirement results from the fact that, in practical implementation, all subsystems work together and interact with each other. In the case of the shedding mechanism, we will consider as the individual systems the respective mechanical system of the shedding mechanism, its drive and control structure. With the development of numerical mathematics, informatics and computer technology there has been a rapid growth of various expert-computing systems to solve a wide range of technical problems that could not be solved beforehand or very difficult without their contribution.

2 Controlled Mechanical System

The computation model of a controlled mechanical system consists mainly of abstract systems, which describe a multibody mechanical system, its drive and control by mathematical equations. One possible method of creating the computation model of the mentioned system is the process of composing abstract dynamic systems with causal input-output orientation. Individual abstract dynamic systems are most often described either by state or transmission descriptions. This combination is simple because the outputs of one model are inputs of the other model, as is shown in Fig. 1. In this figure, the *Control* block represents the mathematical description of the control structure, the *Electric Motor* block represents the mathematical model of the electric motor and the *Mechanical Subsystem* block represents the mathematical model of a multibody mechanical system. Electric current I , voltage U , electromagnetic torque M_{EIMg} and mechanical variable s and its time derivative \dot{s} are input and output signals. The main objective of creating the model is to determine the time course of the dynamic behavior of the system, which consists in the numerical solution of the resulting system of differential equations or system of algebraic-differential equations. We can find detailed knowledge of this issue for example in [1, 2] and [3].

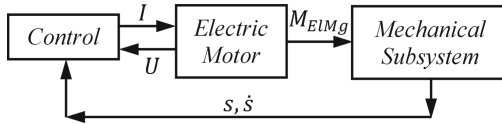


Fig. 1. Block diagram of a controlled mechanical system

Provided that a multibody mechanical system with flexible members is described by redundant physical coordinates $s(t)$ in the number of m , they are constrained by a set of implicit functions (constraints) in the number of r

$$\mathbf{f}^V(s(t), t) = \mathbf{0} \tag{1}$$

The vector $s_i(t)$ of the physical coordinates of i th-flexible body may be expressed by the form $s_i(t) = [\mathbf{r}_i(t), \mathbf{p}_i(t), \mathbf{q}_{ei}(t)]^T$ where the vector of the coordinates $\mathbf{r}_i(t)$ determines the position of the given member in the basic space. The body orientation in the basic space is given by Euler parameters $\mathbf{p}_i(t)$. The elastic deformations of the flexible member are expressed by the vector $\mathbf{q}_{ei}(t)$ of the elastic coordinates. The motion equations of such a mechanical system are derived based on the Langrangian equations of a mixed type – LEMT [1] in the form

$$\mathbf{M}\ddot{\mathbf{s}} + \dot{\mathbf{M}}\dot{\mathbf{s}} - \frac{1}{2} \left[\frac{\partial \mathbf{M}}{\partial \mathbf{s}} \dot{\mathbf{s}} \right]^T \dot{\mathbf{s}} + \mathbf{D}\dot{\mathbf{s}} + \mathbf{K}\mathbf{s} + \mathbf{f}^g = \mathbf{Q} + \mathbf{J}^T \boldsymbol{\lambda} \tag{2}$$

In Eq. (2), the time-varying mass matrix \mathbf{M} and time-varying the center of gravity position are taken into consideration in the case of flexible bodies. Matrices \mathbf{K} and \mathbf{D} represent the stiffness and damping matrix of the mechanical system as a whole.

The vector \mathbf{Q} expresses the vector of generalized forces, whose components associate with relevant coordinates s_j and vector \mathbf{f}^g is the gravity forces vector. The vector of Lagrange multipliers $\boldsymbol{\lambda}$ relates to the forces and moments required to maintain the constraints. The matrix $\mathbf{J} = \partial \mathbf{f}^V / \partial \mathbf{s}^T$ expresses the Jacobi matrix of constraint equations set. In the case of Eq. (2), it is a set of $(m + r)$ differential/algebraic equations for the $(m + r)$ unknown variables – the generally dependent physical coordinates \mathbf{s} in the number of m and the Lagrange multipliers $\boldsymbol{\lambda}$ in the number of r . The constrained multibody mechanical system is characterized by $(i = m - r)$ degrees of freedom. We can currently use commercially available expert systems to set and numerically solve the motion equations of the described mechanical system, for example MSC.ADAMS.

In the case of the shedding mechanism, its drive is implemented by a three-phase permanent magnet synchronous electric motor – PMSM. For simulations, the common description of this motor type is the so-called idealized DQ-model, which consists in converting a three-phase machine to an equivalent two-phase machine using complex space phasors [2]. Using a 2-phase motor model reduces the number of equations and simplifies the control design. Essentially, variables (current, voltage, or flux linkage) associated with the stator windings of a synchronous machine are transformed to a synchronously rotating reference frame (d, q) fixed in the rotor at speed ω_0 . The voltage equations of the synchronous servomotor expressed in the component shape in rotor reference frame (d, q) [4] are given in Laplace transform by equations

$$U_d = R_s I_d + s L_d I_d - \omega_0 \psi_q, \quad U_q = R_s I_q + s L_q I_q + \omega_0 \psi_d \quad (3)$$

where s is a complex number. The equation of electromagnetic torque on the rotor is expressed as

$$M_{EIMg} = \frac{3}{2} p_p [\psi_d I_q - \psi_q I_d], \quad \psi_d = L_d I_d + \psi_m, \quad \psi_q = L_q I_q \quad (4)$$

where the relation of current to flux linkage is expressed through inductances. In Eq. (3) and Eq. (4), quantities I_d and I_q are current components expressed in the rotor reference frame (d, q) and R_s denotes electrical resistance of a stator coil. L_d and L_q are stator winding inductances in the direct (d) and quadrature (q) axis, $\psi_m = const$ represents the flux linkage due to a permanent magnet and p_p is the number of pole pairs.

The vector control of the three-phase permanent magnet synchronous electric motor described using idealized DQ-model is given by the condition $I_d = 0$ A. In this case, the stator current vector \mathbf{i} is perpendicular to the flux linkage vector $\boldsymbol{\psi}$ and the stator electromagnetic torque M_{EIMg} reaches maximum [4]. During the vector control of this electric motor type, its control structure is almost exclusively made up of a cascade control loop with three hierarchically arranged feedbacks: current, speed, and position, as it is shown in Fig. 3. Compliance the desired values of position φ^* , speed ω^* and the components of the electric current vector \mathbf{i}^* is ensured by PID linear controllers. The control action is thus the sum of the three terms: proportional feedback, the integral term and derivative action. The relation between the output value – the control value $u(t)$ and the input value – the tracking error $e(t)$ is given by equation [3]

$$u(t) = K \left(e(t) + \frac{1}{T_i} \int_0^t e(\tau) d\tau + T_d \frac{de(t)}{dt} \right) + u_f(t), \quad e(t) = w(t) - y(t) \quad (5)$$

The controller parameters are the proportional gain $r_0 = K$, the integral gain $r_{.1} = K/T_i$ and the derivative gain $r_1 = K \cdot T_d$. The time constants T_i and T_d are called integral time constant and derivative time constant. The tracking error $e(t)$ expresses the difference between the desired input value ($w(t) = \{\varphi_{21}^*, \omega_{21}^*, I_d^*, I_q^*\}$) and the actual output ($y(t) = \{\varphi_{21}, \omega_{21}, I_d, I_q\}$) of the controlled system according to Fig. 2. In Eq. (5), $u_f(t)$ expresses a feedforward term that is adjusted to give the desired value. Figure 3 shows the block diagram of the cascade control loop with ideal P and PI controllers and speed $\omega_{21,f}^*$ and current $I_{q,f}^*$ feedforward which is formed on the basis of Laplace transform of Eq. (5).

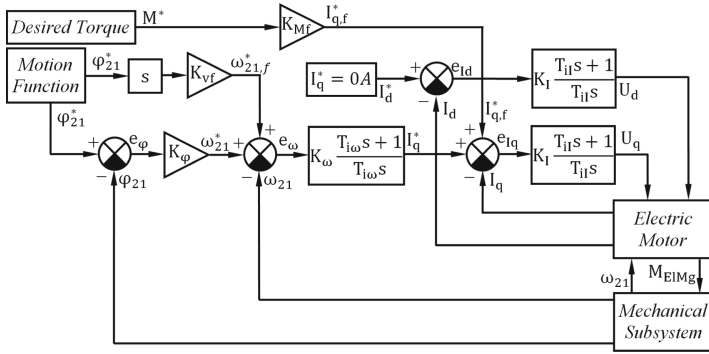


Fig. 2. Block diagram of the cascade control loop with P and PI controllers and feedforwards

3 Shedding Mechanism Model

The working cycle of a weaving machine consists of 4 phases: shed opening, weft insertion, shed closing, and weft beat-up. The shed opening and the shed closing are ensured by a shedding mechanism. As part of the development of a new weaving machine, its novelty shedding mechanism was also developed. The shedding mechanism is a crank mechanism, which is primarily composed of 2-Crank, 3-Connecting Rod and 4-Shedding Beam according to Fig. 3. It is characterized by the individual drive with the centrally placed servomotor with a continuous rotor shaft and recuperation of kinetic energy of the given mechanism and deformation energy of four pairs of leaf springs, which are made of C/E composite material.

The shedding mechanism drive has to satisfy such a movement function to reach the maximum picking angle during non-uniform rotation of the servomotor stator depending on the operating frequency Ω of the weaving machine with optimal utilization of the dynamic properties of the devised mechanism. The movement function is in this form

$$\varphi_{21}^*(t) = \Omega t + A \sin(\Omega t) + A \sin[\Omega t + A \sin(\Omega t)], \quad \Omega = \frac{2\pi}{60} \cdot n \quad (6)$$

where A is a parameter which expresses the irregularity level of the shedding mechanism running and n denotes the working revolutions of the machine. This function is also the

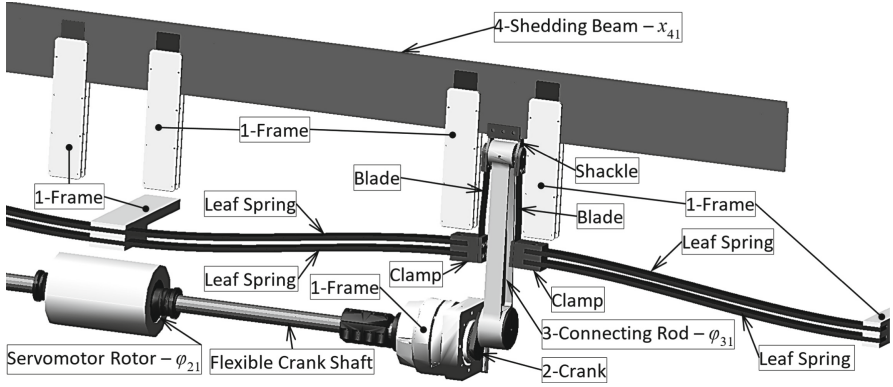


Fig. 3. Shedding mechanism model

desired movement function of the control system, which is shown in Fig. 4 for $n = 600$ rpm and $A = 0.47$.

In the case of the mathematical model of the shedding mechanism, this is a dynamic analysis of a spatial multi-body system with flexible elements – the crank shafts are made of steel, the leaf springs are made of C/E composite material, the blades are made of steel and the shedding beam is made of C/E composite material. C/E composite material is the orthogonal anisotropic material and its material properties differ at each point of the body in three orthogonal directions [5]. The compliance matrix \mathbf{S} is determined by nine independent elastic constants expressed by engineering constants such as a tensile elasticity modulus, shear modulus and Poisson's ratios and is in this form

$$\mathbf{S} = \begin{bmatrix} \mathbf{E} & \mathbf{0} \\ \mathbf{0} & \mathbf{G} \end{bmatrix}, \quad \mathbf{E} = \begin{bmatrix} \frac{1}{E_x} & -\frac{\nu_{yx}}{E_y} & -\frac{\nu_{zx}}{E_z} \\ -\frac{\nu_{xy}}{E_x} & \frac{1}{E_y} & -\frac{\nu_{zy}}{E_z} \\ -\frac{\nu_{xz}}{E_x} & -\frac{\nu_{yz}}{E_y} & \frac{1}{E_z} \end{bmatrix}, \quad \mathbf{G} = \begin{bmatrix} \frac{1}{G_{yz}} & 0 & 0 \\ 0 & \frac{1}{G_{zx}} & 0 \\ 0 & 0 & \frac{1}{G_{yx}} \end{bmatrix}, \quad \mathbf{0} = \begin{bmatrix} 0 & 0 & 0 \\ 0 & 0 & 0 \\ 0 & 0 & 0 \end{bmatrix} \quad (7)$$

The elastic constants were determined based on an appropriate method and they are given in Table 1. The elastic properties of the flexible bodies were determined using the finite element method, which is part of the Siemens NX CAD system.

Table 1. The elastic constants of C/E composite material

E_x [GPa]	E_y [GPa]	E_z [GPa]	G_{yz} [GPa]	G_{zx} [GPa]	G_{yx} [GPa]	ν_{yz} [-]	ν_{zx} [-]	ν_{yx} [-]
108	18	18	6	13	13	0.5	0.1	0.62

The desired driving torque used in the control structure is determined based on the quasi-dynamic solution. It is given by the equation

$$M^* = -I_2 \ddot{\varphi}_{21} - I_2 (k_p x_{41} + m_4 \ddot{x}_{41}) \cdot (\sin \varphi_{21} - \cos \varphi_{21} \tan \varphi_{31}) \quad (8)$$

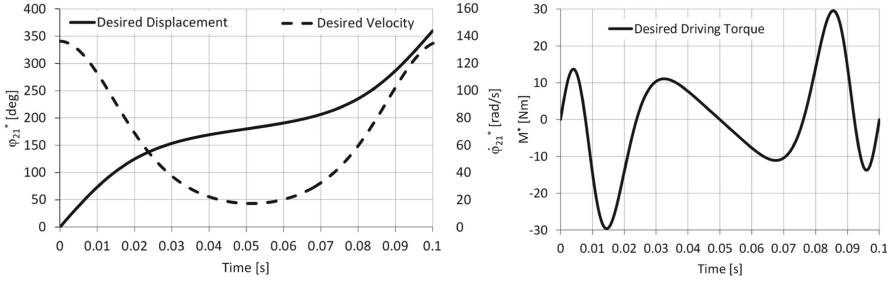


Fig. 4. Desired control signals

where φ_{21} is rotor angular displacement, φ_{31} is connecting rod angular displacement and x_{41} is shedding beam displacement, $l_2 = 0.029$ m is crank length, $I_2 = 0.01057$ kgm² is the moment of inertia of rotating masses, $m_4 = 6.43$ kg is the mass of moving masses and $k_p = 51000$ Nm⁻¹ is the total stiffness of the four pairs of leaf springs. The time course of torque M^* is shown in Fig. 4 for working revolutions $n = 600$ rpm and $A = 0.47$, when the RMS value of the torque time course is minimal in the steady state of the weaving machine running. The value of the current feedforward constant k_{Mf} of the control structure is determined based on the electromagnetic moment M_{EIMg} of the 3-phase permanent magnet synchronous electric motor. For rotor pole with saliency ratio $L_d/L_q \approx 1$, the electromagnetic moment is [2]

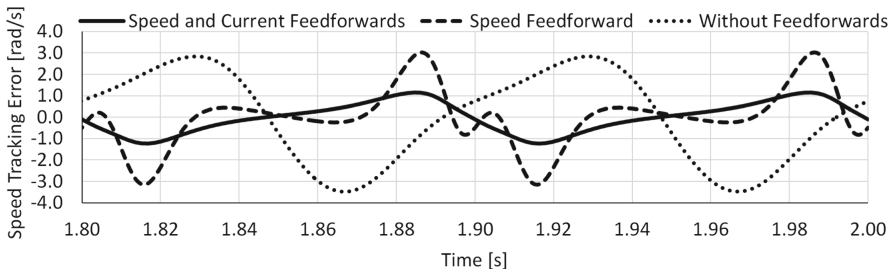
$$M_{EIMg} = \frac{3}{2} p_p \psi_m I_q = \frac{1}{k_{Mf}} I_q, \quad k_{Mf} = \frac{2}{3 p_p \psi_m}, \quad \psi_m = k_E \frac{60}{2\pi 1000 \sqrt{3}} \quad (10)$$

where $k_E = 183$ V1000⁻¹rpm expresses electromotor voltage constant, which is from the data sheet provided by the manufacturer.

With the use of knowledge included in paragraph 2, the mathematical models of the drive and its control system were created. The appropriate parameters of PID controllers were tuned on the basis of the Ziegler–Nichols tuning rules [3], see Table 2. The motion equations of the controlled mechanical system of the shedding mechanism were set and numerically computed by MSC.ADAMS. The main aim of the calculations was to determine the control accuracy and the dynamic behavior and properties of the whole system dependent on the operating frequency and the irregularity level of the shedding mechanism running. Figure 5 shows the time course of the speed tracking error of the shedding mechanism control system as an example of one of the possible simulation results.

Table 2. Drive and control system parameters

Description	Symbol	Servomotor TGN5-2400-15-560
Number of pole pairs	p_p [–]	5
Rated speed	n_n [rpm]	1500
Rated torque	M_n [Nm]	21.0
Peak torque	M_{Max} [Nm]	63.0
Stator coil electrical resistance	R_s [Ω]	0.85
D-axis stator inductance	L_d [mH]	5.1
Q-axis stator inductance	L_q [mH]	5.1
Rotor permanent magnetic flux linkage	ψ_m [NmA ⁻¹]	1.008932
Current controller proportional component	K_I [VA ⁻¹]	5
Current controller time integration constant	T_I [s]	0.0005
Speed controller proportional component	K_ω [As/rad]	2
Speed controller time integration constant	T_ω [s]	0.08
Position controller proportional component	K_ϕ [s ⁻¹]	5
Speed feedforward constant	K_{vf} [–]	1
Current feedforward constant	K_{Mf} [A/Nm]	0.132

**Fig. 5.** Speed tracking error of the control system

4 Conclusions

The novelty machine is equipped with the system of an adaptive change of beating-up and shedding mechanisms functions with picking angle maximization. Traditional shedding and slay mechanisms mounting on the machine frame by means of bearings has been substituted by an originality system of leaf springs. This solution leads to

the recuperation of kinetic energy of mechanisms and deformation energy of springs, which are made from C/E composite material. The results of the innovation process are a significant increasing of machine performance, lower energy consumption and reduced noise level and vibrations of the machine. Patent applications have been filed for some innovative solutions of parts of the air-jet weaving machine, which also includes a shedding mechanism.

Acknowledgments. This paper was created within the work on the TRIO-FV10215 project – Project supported by the Ministry of Industry and Trade of the Czech Republic.

References

1. Stejskal, V., Valášek, M.: Kinematics and Dynamics of Machinery. Marcel Dekker Inc., New York (1996). ISBN 0-8247-9731-0
2. Bose, B.K.: Modern Power Electronics and AC Drives. Prentice-Hall Inc., Upper Saddle River (2001). ISBN 0-13-016743-6
3. Åström, J.K., Murray, M.R.: Feedback Systems: An Introduction for Scientists and Engineers. <http://www.cds.caltech.edu/~murray/FBSwiki>
4. Ondrášek, J.: The mathematical model of a weaving machine, mechanisms, transmissions and applications. In: Proceedings of the Third MeTrApp Conference 2015. Mechanism and Machine Science, vol. 31, pp. 323–331. Springer (2015). ISBN 978-3-319-17066-4
5. Zbončák, R.: Elastic properties prediction models of continuous fibers composites. VÚTS, a.s. (2018). ISBN 978-80-87184-81-3



Dynamics and Motion Control of a Three Degree of Freedom 3-PRRR Parallel Manipulator

Parvathi Sunilkumar¹, Rutupurna Choudhury², Santhakumar Mohan^{1(✉)},
and Larisa Rybak³

¹ IIT Palakkad, Palakkad, India

131913002@smail.iitpkd.ac.in, santhakumar@iitpkd.ac.in

² NIT Silchar, Silchar, India

rutupurna.choudhury10@gmail.com

³ Belgorod State Technological University (BSTU) named after V.G. Shukhov,
Belgorod, Russia
rlbgtu@gmail.com

Abstract. This work focuses on the dynamic modelling and motion control scheme of a parallel manipulator which has three legs of prismatic-revolute-revolute-revolute joint setup. In each of the legs, the prismatic (P)-joint is active and the rotary (R)-joints are passive. The three legs further join into an end-effector in a right-angled triangle shape. The Euler-Lagrangian approach is followed to achieve the dynamics of the manipulator. The formulations are detailed and simulated. This paper also presents an augmented proportional-derivative (PD) controller along with gravity compensation for the motion control. This control method transforms the closed-loop dynamics of the manipulator into decoupled, and thus it becomes easier to quantify the motion performance. The trajectory tracking performance and its accompanying errors are also discussed.

Keywords: Parallel manipulator · Motion control · Inverse dynamics · Cartesian manipulator · Proportional derivative control

1 Introduction

Parallel manipulators are mechanisms forming closed loops which connect the fixed base to the moving platform with the help of independent serial chains. They have a robust construction as they consist of revolute and prismatic actuators. They are capable to move large bodies at high velocities and accelerations. One such example is the motion platforms which are based on parallel manipulators. They can perform tasks at high velocities with very less effort and they have varying applications. Parallel manipulators are studied vastly in the recent decades [1, 2]. Parallel manipulators attained prominence amongst researchers

© The Editor(s) (if applicable) and The Author(s), under exclusive license

to Springer Nature Switzerland AG 2020

D. Pisla et al. (Eds.): EuCoMeS 2020, MMS 89, pp. 103–111, 2020.

https://doi.org/10.1007/978-3-030-55061-5_13

and industries worldwide due to their grade of accuracy and precision in performing tasks [2,6,8,9]. When compared to serial manipulators, they exhibit increased payload capacity, greater stiffness and improved precision [3]. Theoretically, this is said so because there is no error accumulation in case of parallel manipulators [2]. In contrast to their serial counterparts, parallel manipulators possess lower inertia of moving parts, more speed and more accuracy [2]. Parallel manipulators exhibit confined workspace and complex singularities [2,3,5,6,8,9]. From the literature study, it can be seen that there is a need of a sturdy control scheme for motion mechanisms to smoothly execute tasks. Various challenges have to be faced while developing such controllers, which are not usually coming across for serial manipulators [7,9]. Major hindrance is the nonlinear dynamics and the coupled system parameters that determines the dynamics of the manipulator [6,8,9]. The parallel manipulator dynamic analysis becomes a challenging task due to the domination of gravitational, inertial and frictional factors. The behaviour of these mechanisms are governed by nonlinear dynamic models and these mechanisms may not follow the desired trajectory due to uncertainties in their link lengths, masses and inertia, and other undesired effects like friction, backlash, etc. Hence the feedback control is necessary leading to achieve closed-loop tracking.

The objective of this paper is to study the dynamics of the 3-PRRR manipulator (commonly known as “Tripteron”) [8] and to develop a simple motion control for the lower limb rehabilitation mechanisms. The lower limb rehabilitation therapies involved motion of hip, knee and ankle joints [4,10], however, for providing better motion of the hip and knee in three dimensional space as per the clinical studies [4], one of the Cartesian manipulators is required, therefore, in this paper, the 3-PRRR spatial parallel manipulator is considered. In order to execute this manipulator as a lower limb rehabilitation robot, the behaviour of the manipulator in both open and closed loops should be known [10]. Hence, the dynamic analysis is carried out by Euler-Lagrange method and an augmented proportional derivative controller is used for the motion control.

The following portion of the paper is systemized as: Sect. 2, 3 and 4 discuss the conceptual design, kinematic model and dynamic model of the system proposed. The control scheme designs are described in Sect. 5. The performance analysis along with how the model tracks a complex trajectory is depicted in Sect. 6. Lastly, Sect. 7 sums up the concluding remarks of the paper.

2 Conceptual Design

The suggested 3-PRRR spatial parallel manipulator’s conceptual design is shown in Fig. 1. It includes three kinematic legs. Each leg consists of a single active prismatic joint (P) and three revolute joints (R). The active linear (prismatic) joints are connected with linear actuators driven by a direct current (DC) motor. The linear actuator is placed on a guide rail which tends to constitute the active prismatic joint. To this a passive RRR-chain is attached and the ends are connected to the vertex of the right-angled triangle (mobile platform) which act as

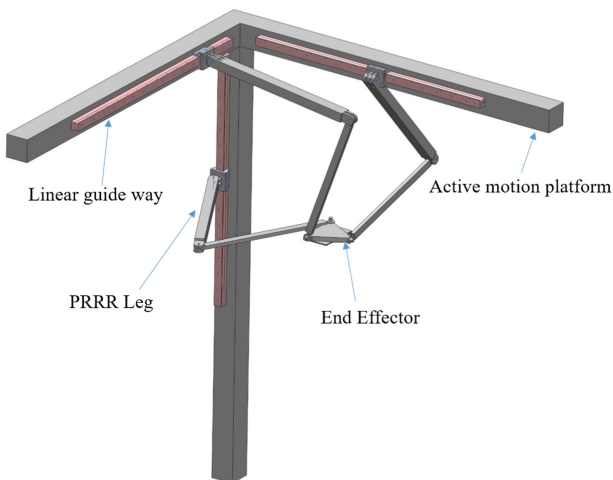


Fig. 1. Conceptual design of a 3-PRRR manipulator

the end-effector. In total, the manipulator consists of ten links (including the end-effector), three prismatic joints and nine revolute joints. Based on this, the movement of the parallel manipulator is three, that is, the suggested mechanism has three DOF. The beauty of the 3-PRRR manipulator or *Tripteron* is that it provides the Cartesian motion in space and it is completely decoupled, which results in simple kinematic relationships and eventually the Jacobian of the mechanism forms an identity matrix.

3 Kinematic Model

The kinematic configuration with the joints and links of the proposed driving mechanism is depicted in Fig. 2. This 3-PRRR motion mechanism consists

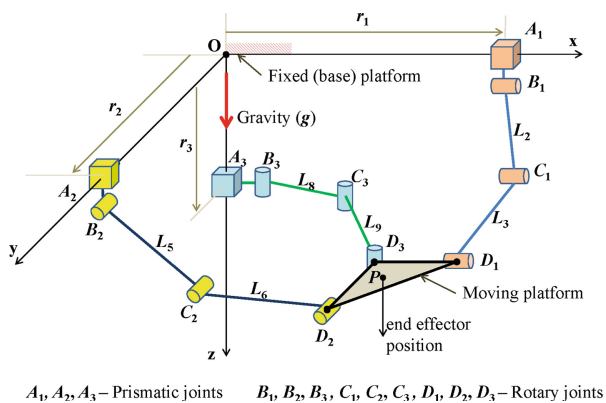


Fig. 2. Kinematic configuration of the 3-PRRR manipulator

of three active prismatic joints and the corresponding joint displacements are denoted as r_1 , r_2 and r_3 , respectively. The three active prismatic joints are placed along the three mutually perpendicular axes as given in Fig. 2. The proposed driving mechanism has three PRRR (prismatic-revolute-revolute-revolute) legs namely $A_1B_1C_1$, $A_2B_2C_2$ and $A_3B_3C_3$ which connect the end-effector (mobile stage) $D_1D_2D_3$ with the fixed base as given in Fig. 2.

The inverse (indirect) kinematics of the parallel mechanism gives the linear displacements which are the inputs as given in equation 1. ζ gives the linear displacement of the active prismatic joint. P_x, P_y and P_z are the task space coordinates of the end-effector point from the origin (base frame) in the Cartesian coordinate system. The kinematic arrangement of each leg along with their locations of center of masses are given in Fig. 3.

$$\zeta = \begin{bmatrix} r_1 \\ r_2 \\ r_3 \end{bmatrix} = \begin{bmatrix} P_x - a_x + c_x \\ P_y - a_y + c_y \\ P_z \end{bmatrix} \quad (1)$$

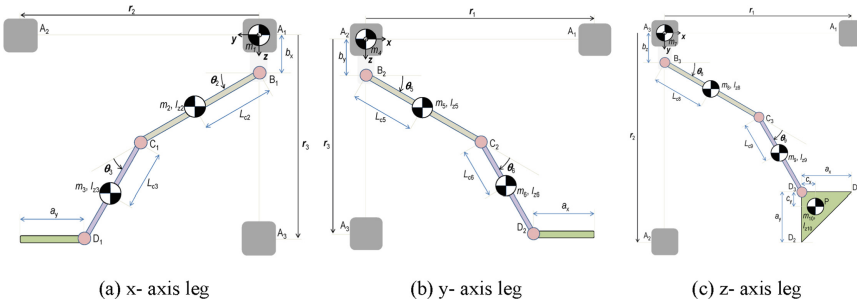


Fig. 3. Locations of center of masses of the manipulator

$$\theta_2 = \tan^{-1} \left(\frac{D_{1z} - B_{1z}}{D_{1y} - B_{1y}} \right) - \tan^{-1} \left(\frac{L_3 S_3}{L_2 + L_3 C_3} \right) \quad (2)$$

$$\theta_3 = \tan^{-1} \left(\frac{S_3}{C_3} \right)$$

$$\theta_5 = \tan^{-1} \left(\frac{D_{2z} - B_{2z}}{D_{2x} - B_{2x}} \right) - \tan^{-1} \left(\frac{L_6 S_6}{L_5 + L_6 C_6} \right) \quad (3)$$

$$\theta_6 = \tan^{-1} \left(\frac{S_6}{C_6} \right)$$

$$\theta_8 = \tan^{-1} \left(\frac{D_{3y} - B_{3y}}{D_{3x} - B_{3x}} \right) - \tan^{-1} \left(\frac{L_9 S_9}{L_8 + L_9 C_9} \right) \quad (4)$$

$$\theta_9 = \tan^{-1} \left(\frac{S_9}{C_9} \right)$$

$$\begin{aligned}
 \text{where } C_3 &= \frac{(D_{1y}-B_{1y})^2+(D_{1z}-B_{1z})^2-L_2^2-L_3^2}{2L_2L_3}, S_3 = \sqrt{1-C_3^2}, C_6 = \\
 &= \frac{(D_{2x}-B_{2x})^2+(D_{2z}-B_{2z})^2-L_5^2-L_6^2}{2L_5L_6}, \\
 S_6 &= \sqrt{1-C_6^2}, C_9 = \frac{(D_{3x}-B_{3x})^2+(D_{3y}-B_{3y})^2-L_8^2-L_9^2}{2L_8L_9}, S_9 = \sqrt{1-C_9^2}, B_{1y} = \\
 &0, B_{1z} = b_x, \\
 D_{1y} &= r_2 - a_y, D_{1z} = r_3, B_{2x} = 0, B_{2z} = b_y, D_{2x} = r_1 - a_x, D_{2z} = r_3, B_{3x} = 0, \\
 B_{3y} &= b_z, D_{3x} = r_1 - a_x, D_{3y} = r_2 - a_y.
 \end{aligned}$$

4 Dynamic Formulation

This section describes the Euler-Lagrangian based dynamic formulation of the suggested 3-PRRR parallel mechanism. The Euler-Lagrange has been used because of its simplicity, iterative structure and accuracy in predicting the relationship between joint forces and mechanism motion. This method gives the formulation depending on the energy difference of the system. It means, Lagrangian (L) is the difference between the total kinetic (KE) and potential (PE) energies of the system. Total kinetic and potential energies of the mechanism is the summation of the kinetic energy along with potential energy of each component of the mechanism. The suggested manipulator has 3-legs, each having one slider i.e. prismatic (P) joint and two links are connected through 3-rotary (R) joints. It is assumed that the mass of the link is concentrated at the centre of each link. So there are totally ten bodies including the end-effector (mobile platform). Equation 5 present the total kinetic energy as well as total potential energy and the Lagrangian of the proposed parallel manipulator.

$$\begin{aligned}
 KE &= \frac{1}{2} \sum_{i=1}^{10} (m_i [\dot{u}_i^2 + \dot{v}_i^2 + \dot{w}_i^2] + I_{zzi} \omega_i^2) \\
 PE &= \sum_{i=1}^{10} m_i g w_i \\
 L &= KE - PE
 \end{aligned} \tag{5}$$

where m_i is the mass of the i^{th} link respectively. I_{zzi} is the rotational inertia of the i^{th} link. u_i, v_i and w_i are the positions of the center of masses of the individual link. \dot{u}_i, \dot{v}_i and \dot{w}_i are the translational velocities and ω_i is the angular velocity of the center of mass of each link. L is the Lagrangian of the proposed manipulator and g is the acceleration due to gravity.

The joint forces are evaluated and expressed in Eq. 6.

$$f_i = \frac{d}{dt} \frac{\partial L}{\partial \dot{r}_i} - \frac{\partial L}{\partial r_i} \tag{6}$$

On the basis of Euler-Lagrange dynamic formulation, the dynamic motion equation of the parallel mechanism is expressed in state-space form as given in Eq. 7.

$$\mathbf{D}(\zeta) \ddot{\zeta} + \mathbf{C}(\zeta, \dot{\zeta}) \dot{\zeta} + \mathbf{h}(\zeta) + \mathbf{q}(\dot{\zeta}) = \mathbf{f} \tag{7}$$

where $\mathbf{D}(\zeta)$ represents the inertial matrix of the manipulator, $\ddot{\zeta}$ represents the linear acceleration of the translational joint or the vector task space acceleration, $\mathbf{C}(\zeta, \dot{\zeta})$ gives the centripetal and Coriolis matrix of the parallel mechanism, $\mathbf{h}(\zeta)$ is the gravitational force vector and $\mathbf{q}(\dot{\zeta})$ is the friction vector. In this paper, the viscous frictional effects only considered, however, the model is not restricted to only this kind of effect.

5 Motion Control Scheme

The proposed close loop tracking of the driving mechanism is controlled with the aid of augmented proportional-derivative (PD) controller. The PD controller is used because it can calculate the joint space positions and velocities using inverse kinematic relations along with positions and velocities of end-effector. The known inertia matrix $\mathbf{D}(\zeta)$, is multiplied to the error vector to obtain better tuning and accuracy. The known gravity vector $\mathbf{h}(\zeta)$, should be added to the input vector \mathbf{f} to have better control of the manipulator. The suggested PD with gravity compensation control strategy to capture the targeted profile positions is shown in Eq. 8.

$$\mathbf{f} = \mathbf{D}(\zeta) \left[\Gamma_p \tilde{\zeta} + \Gamma_d \dot{\tilde{\zeta}} \right] + \mathbf{h}(\zeta) \quad (8)$$

where \mathbf{f} is the vector giving input to the manipulator through the control scheme, Γ_d and Γ_p are the derivative control gain and proportional gain values respectively. $\tilde{\zeta} = \zeta_d - \zeta$ gives the position error vector, ζ_d represents the vector of the desired position of the joints in work space and ζ gives the position of the joints in work space achieved by the dynamic model. $\dot{\tilde{\zeta}}$ represents the error derivatives vector.

6 Results and Discussion

The performance analysis of the proposed model is done by executing the simulation of the dynamic analysis using MATLAB under standard parameters. The link length and mass of first link are taken as 0.6 m and 10.5 kg respectively and those of the second link are taken as 0.55 m and 2.1 kg respectively, in each leg. The mass at each of the prismatic joint is taken to be 1 kg. The end-effector has a mass of 2.8 kg. The value of controller gains Γ_d and Γ_p are 2δ and δ^2 , respectively chosen to provide an approximate critical damping (ideal) performance, where $\delta = 2$ is the required or designed output frequency. By increasing the value of δ , the rise time and the tracking errors can be reduced, however, the required control activity (rate of control activity) would be increased. The overall performance and the choice of the control parameters would be affected based on the actuator characteristics. In this paper, the actuator dynamics is considered as a first order system with a time constant of unity. The input is given at the three active joints, say r_1, r_2, r_3 . For the profile shown in Fig. 4, sinusoidal input is

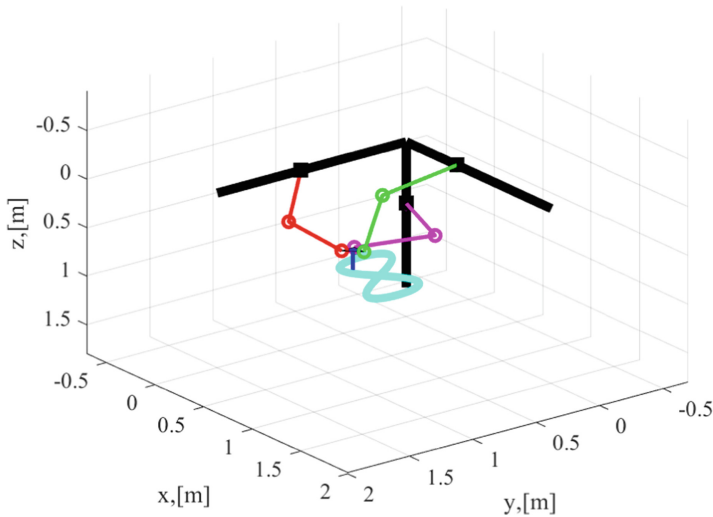


Fig. 4. Desired end-effector profile used for the simulation along with manipulator configuration

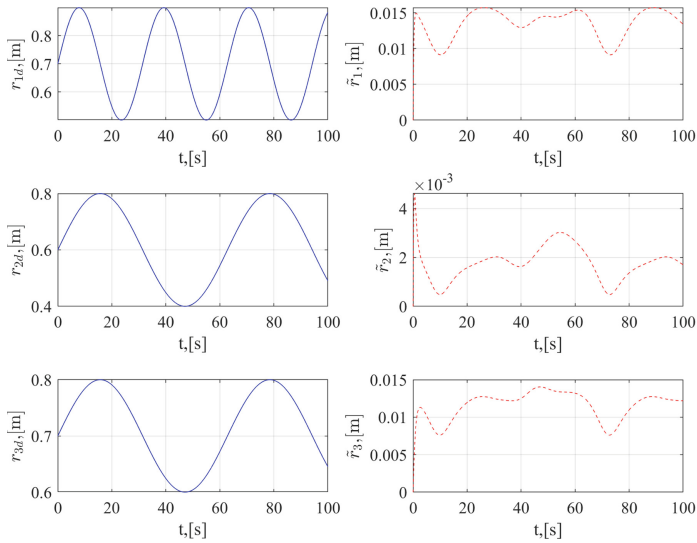


Fig. 5. Time histories of the desired positions and tracking position errors of the linear joints

given at the three P joints. The given (desired) required profile is achieved with the help of the proposed motion control scheme as shown in the Fig. 4. The time histories of the required profile and the tracking results are shown in Fig. 5.

The proposed dynamic model follows the desired trajectory. It can be seen that r_1, r_2, r_3 comfortably following their corresponding desired values through the help of the proposed motion control scheme. It was also observed that the dynamic model and the performance of controller is sound in tracking and the errors of tracking are within the limits of the design. The closed-loop system's stability can be proved easily with the help of Lyapunov's direct method [7] and the control parameters can be optimized by considering actual actuator and sensor characteristics through the help of one of the optimization methods. However, these are left for future work.

7 Conclusions

The dynamic analysis and the motion control scheme of a 3-PRRR parallel mechanism is discussed in this research paper. The prime motive of this configuration is to propose a manipulator for the lower limb rehabilitation robot wherein different forms of strategies for lower limb therapy can be imposed in three dimensional space or in real-time. The numerical simulations show that the augmented proportional derivative controller enables to obtain a reliable control strategy. Although, if an advanced controller is used, the error would have been further decreased, the proposed controller gives advantage of being simple to use with the help of low-cost micro-controllers. There is future scope in performing complex operations in the real-time along with advanced controllers for providing finite time stability and better results.

Acknowledgements. This research is partly assisted by the Russian Science Foundation (RSF), Russia, the agreement number 19-19-00692 and partly assisted by the Council of Scientific and Industrial Research (CSIR), India, the project number 22(0829)/19/EMR-II.

References

1. Bonev, I.A., Chablat, D., Wenger, P.: Working and assembly modes of the Agile Eye. In: Proceedings of International Conference on Robotics & Automation, pp. 2317–2322 (2006)
2. Briot, S., Bonev, I.A.: Are parallel robots more accurate than serial robots. *Trans. Canadian Soc. Mech. Eng.* **31**(4), 445–455 (2007)
3. Briot, S., Arakelian, V., Guégan, S.: PAMINSA: a new family of partially decoupled parallel manipulators. *Mech. Mach. Theory* **44**(2), 425–444 (2009)
4. Diaz, I., Gil, J.J., Sanchez, E.: Lower-limb robotic rehabilitation: literature review and challenges. *J. Robot.* **2011**, 1–11 (2011)
5. Elkady, A., Elkobros, G., Sobh, T.: Cartesian parallel manipulator modelling, control and simulation. In: *Parallel manipulators, Towards New Applications*, pp. 506–532 (2008)
6. Gogu, G.: *Structural Synthesis of Parallel Robots*. Springer, Dordrecht (2008)
7. Kelly, R., Davila, V.S., Perez, J.A.: *Control of Robot Manipulators in Joint Space*. Springer, London (2006)

8. Kong, X., Gosselin, C.M.: Type Synthesis of Parallel Mechanisms. Springer, Heidelberg (2007)
9. Merlet, J.P.: Parallel Robots. Springer, Dordrecht (2006)
10. Mohan, S., Mohanta, J.K., Kurtenbach, S., Paris, J., Corves, B., Huesing, M.: Design, development and control of a 2 PRP-2 PPR planar parallel manipulator for lower limb rehabilitation therapies. *Mech. Mach. Theory* **112**, 272–294 (2017)

Mechanisms for Medical Rehabilitation



Numerical and Experimental Validation of ExoFing, a Finger Exoskeleton

Cuahtémoc Morales-Cruz^{1,3} , Cristian Enrico Capalbo² ,
Giammarco Caroleo² , Marco Ceccarelli³ , and Giuseppe Carbone² 

¹ Instituto Politécnico Nacional, GIIM: Group of Research and Innovation in Mechatronics,
07700 Mexico City, Mexico

cmoralesc0600@alumno.ipn.mx

² DIMEG, University of Calabria, Rende, Italy

{cristian.capalbo, giuseppe.carbone}@unical.it,

giammarcocaroleo@gmail.com

³ LARM2: Laboratory of Robot Mechatronics, University of Roma Tor Vergata,
Via del Politecnico 1, 00133 Rome, Italy

marco.ceccarelli@uniroma2.it

Abstract. This paper addresses the numerical and experimental validation of a finger exoskeleton exercising device. The exoskeleton device is analyzed from a kinematic and dynamic viewpoint. Experimental tests are carried out with different users to demonstrate the adaptability and effectiveness of the proposed device in finger exercising and motor rehabilitation tasks.

Keywords: Finger exoskeleton · Motion assistance · Performance evaluation · Experimental robotics

1 Introduction

Nowadays the design of exoskeletons focuses on solving the principal challenges of the following three applications: rehabilitation, exercising, and assistance. The main problem with existing exoskeletons is that they often are not usable for the fingers of different subjects as in [1], bulky such as in [2], with overall equipment not easily transportable such as in [3] or heavy such as in [4]. A specific research line has been addressing the development of exoskeletons for motion assistance, as reported, for example, in [5, 6]. Moreover, [7, 8] focus on fundamental grasping mechanics as well as at the design and validation of anthropomorphic robotic hands. The LARM robotic hands are based on a driving mechanism with linkages that remains within the finger body during its operation, as reported in [9]. The design of such a driving mechanism is the conceptual reference for the exoskeleton solution that is reported in [6] and preliminary exoskeleton designs, as reported in [10–12]. This paper aims to report experiences and results for validating the primary operating characteristics from different users and operation conditions of the exoskeleton device, named as ExoFing.

© The Editor(s) (if applicable) and The Author(s), under exclusive license
to Springer Nature Switzerland AG 2020

D. Pisla et al. (Eds.): EuCoMeS 2020, MMS 89, pp. 115–122, 2020.

https://doi.org/10.1007/978-3-030-55061-5_14

2 The ExoFing Finger Exoskeleton

The ExoFing device is designed and prototyped by LARM2 in Rome. The parameters and the configuration of the proposed eight-bar mechanism for mimicking the human finger motion are part of an Italian patent [12]. The system consists of two interconnected four-bar mechanisms of 2 Degrees-Of-Freedom (DOF) that are driven using two servomotors. The performance acquisition of the system is carried out using four different types of sensors as in Fig. 1. A temperature sensor (1) is located on the metacarpus phalange to identify the change of temperature during the moving process. A bio-electrical activity sensor (2) is installed to determine the electrical response of the finger. A current sensor (3) is used to estimate the energy consumption of the device. Two IMU sensors (4) are set up on the metacarpus and distal phalanges to identify the angle displacements and angular velocities of the finger joints. Figure 1 shows a conceptual design of ExoFing, where the inputs, sensors, and outputs are described in detail according to a human finger.

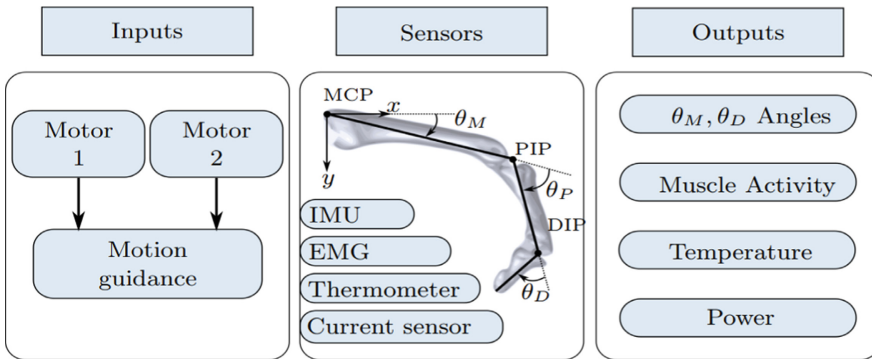


Fig. 1. A conceptual and kinematic scheme of ExoFing exoskeleton device

ExoFing is designed with features of portability and adaptability for a wide range of users. In fact, the design considers possible attachment regions where the attachment points could fix the device to the finger for different subjects. Figure 2 shows a kinematic design with motors to drive each DOF in a general position to be installed on the human hand and finger. The input angle for the first four-bar mechanism is labeled as δ , and the input angle for the second mechanism is marked as β . The device uses four attachment points namely, one for the palm and the back of the hand (A_1), two for the metacarpus phalange (A_2 , A_3), and the last one for distal phalange (A_4). These four points give the device the possibility to be fixed for different anthropomorphic sizes. Therefore the behavior of the system could differ from one to another user since the distances between the MCP, PIP, and DIP joints can be different.

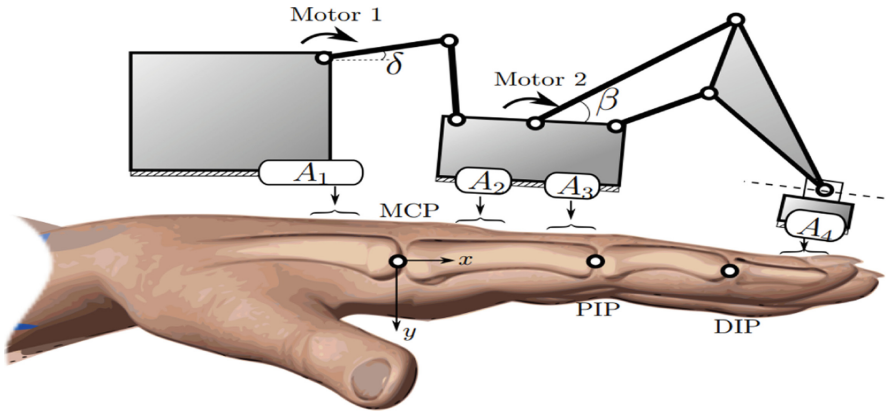


Fig. 2. A kinematic design of ExoFing

3 Numerical Evaluation of Operation Performance

The behavior of the prototyped device is compared with a numerical solution using the kinematic configuration in a numerical simulator. Figure 3 shows the CAD of ExoFing where Fig. 3a is the frontal view indicating the position of the inputs δ and β . In Fig. 2, the point A_4 stands for the attachment point of the exoskeleton with the fingertip while A_1 is the attachment point between second servo housing and finger. The kinematic analysis aims to obtain the angular position of the DIP joint to be compared with the angular displacement measured with the prototype in laboratory tests. The spatial position of the fingertip vary according to the finger size of each patient. However, the change of behavior in each joint should not be important and is verified by comparing the behavior of multiple subjects.

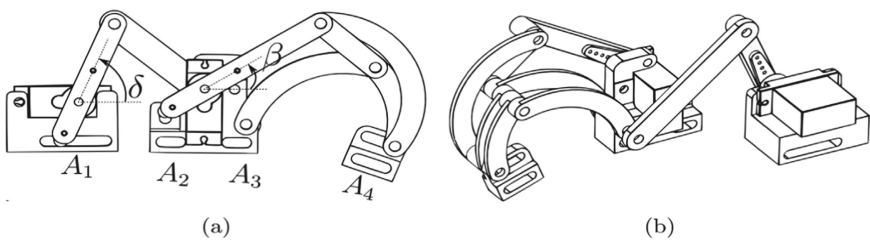


Fig. 3. CAD of ExoFing: a) Frontal view, b) Isometric view

A simulation using Working Model estimates fingertip position, velocity, acceleration, and input torques for a specific size of a finger whose numerical results are reported in Sect. 5. Especially a simulation of the second four-bar linkage is computed by modeling links attached to the second servo housing. The simulation time is 2 s for a complete flexion of the finger and other 2 s for its extension, considering a task of finger motion assistance. For the purpose of the simulation and experimental comparison, the simulation uses an input velocity of $\beta = 3$ deg/sec. Figure 4 shows a scheme of the configuration

used in a simulation in Working Model. In Fig. 4a for the extended position and Fig. 4b for the complete flexion position.

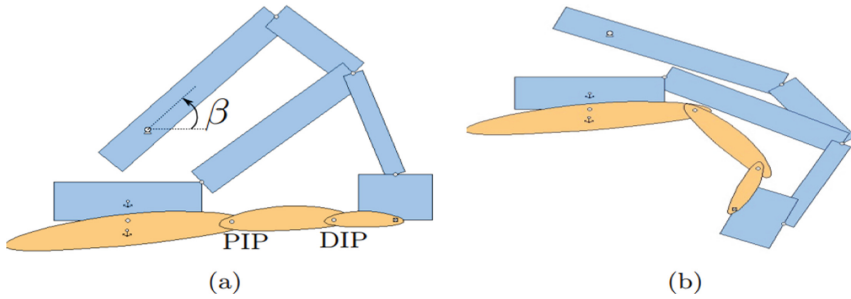


Fig. 4. Configuration of the second four-bar mechanism in the physics engine: a) Complete extension, b) Complete flexion

4 Experimental Setup and Tests

A prototype solution is implemented for laboratory testing with the four mentioned types of sensors, the motors, and one Arduino control board. Figure 5 shows the architecture of the electronic hardware and its implementation in ExoFing when it is attached to a human finger. Figure 5a shows the details of the connections for each element. The location of the motors and the sensors in the prototype can be seen in Fig. 5b. with: 1) thermometer attached to the metacarpus phalanx; 2) electrodes for the EMG sensor. 4); one IMU on the metacarpus phalanx to measure the angular displacement a velocity of θ_M and the second IMU attached to the distal phalanx for θ_D ; 5) one servo motor drives the first four-bar mechanism with input mentioned before as δ , and the other servo motor drives the second linkage with input labeled as β .

The experiments are carried out using two testing modes. For the first mode, the complete motion is considered by driving the two motors. The second test mode considers only the activation of the second motor to drive the second linkage and consequently, only the motions of the proximal (PIP) and distal (DIP) phalanx are activated.

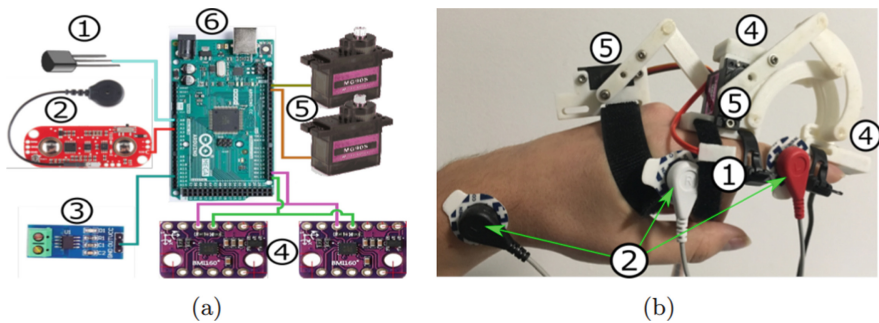


Fig. 5. Design of experimental setup: a) A scheme, b) A laboratory setup. (1: Thermometer, 2: EMG, 3: Current sensor, 4: IMU's, 5: Motors, and 6: Arduino)

5 Experimental Results

The laboratory prototype has been tested experimentally to drive the motion of the finger and the information collected with the four types of sensors is used to determine the effectiveness of the device when used by different subjects. The resulting motion produced by the prototype attached to the finger is shown in Fig. 6 with a complete extension in Fig. 6a, partial flexion in Fig. 6b and c, and a complete flexion in Fig. 6d.

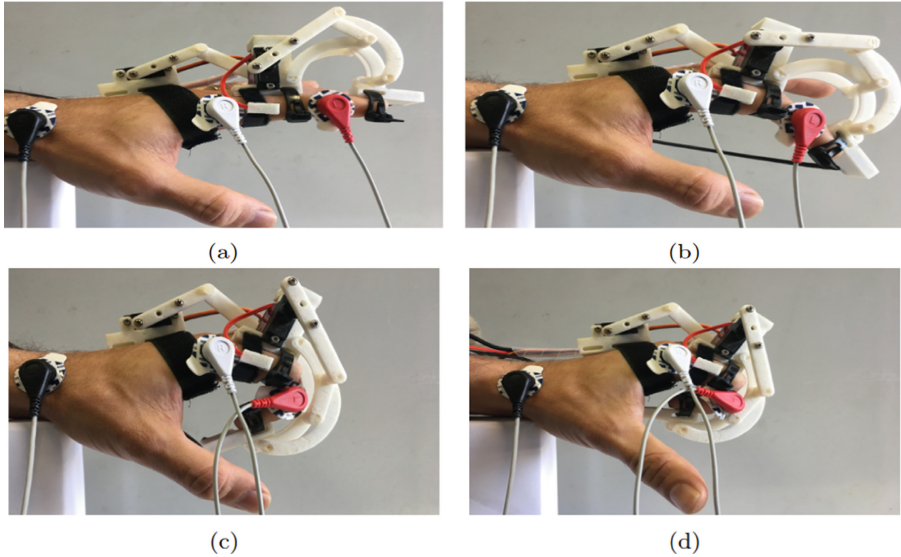


Fig. 6. Snapshots of the exoskeleton motion during a test with sensors

The results are reported in Fig. 7, and Fig. 8. The Figs. 7a and 8a show the angular displacement and angular velocity of the metacarpus joint for the complete motion test, and Figs. 7b and 8b show the angle and velocity of the distal joint. From the plots, it can be verified that the device motion occurs according to the modeling of the system. Despite the different sizes of fingers among different subjects, the motion remains within a margin similar to the desired motion.

On the other hand, the behavior of the input angles driven by the motors is reported in Fig. 9a. The power consumption of the device considering the motors and sensors is given in Fig. 9b. The electrical activity in the finger of the subject is reported in Fig. 10a and the temperature measured in in the metacarpus phalanx is showed in Fig. 10b.

From Fig. 9b the maximum power consumption when doing the flexion motion is around 3.5 W, and the maximum value for the extension motion is around 1 W.

The electrical activity of the finger is not significant but had to be verified by measuring the finger and the change of the temperature describes that the finger is incrementing the activity and the use of energy when exercising. Temperature suggests that tissue on the finger is actually working and receiving assistance.

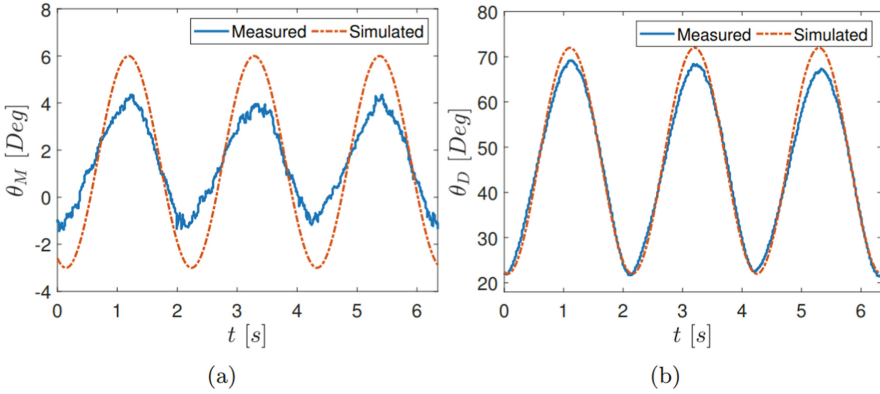


Fig. 7. Results for the simulated and measured motion in terms of orientation of: a) MCP angle; b) DIP angle

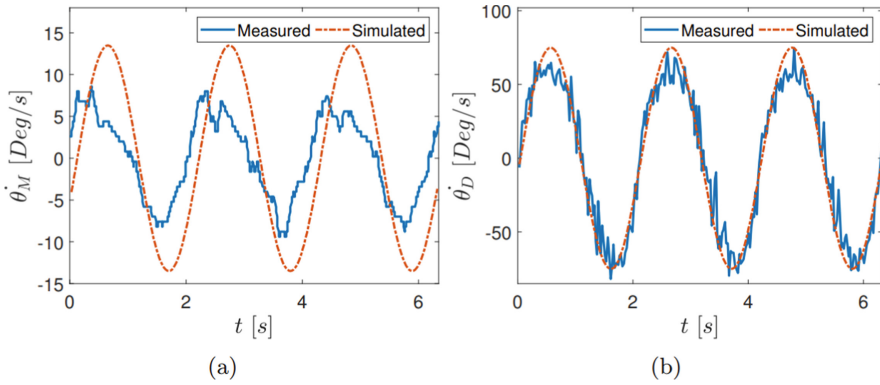


Fig. 8. Results for the simulated and measured motion in terms of angular velocity of: a) MCP; b) DIP

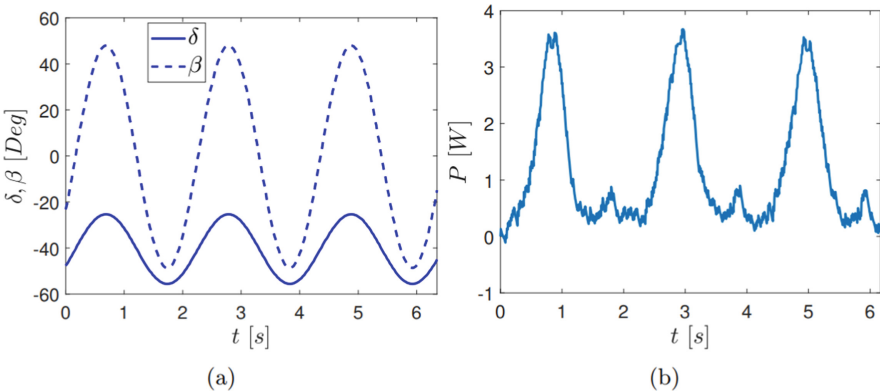


Fig. 9. Test results in terms of: a) Angular inputs for motors and b) Power consumption

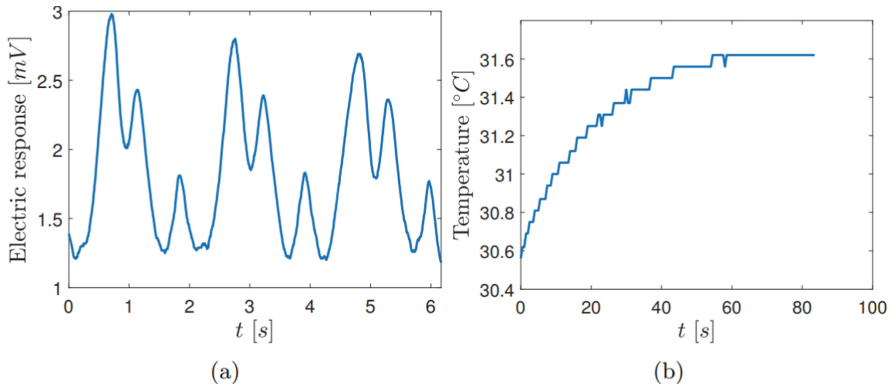


Fig. 10. Test results in terms of: a) Finger electrical activity and b) Temperature

6 Conclusions

This paper introduces the validation of ExoFing exoskeleton finger device using different types of sensors to measure its behavior and to compare it with design simulations results. The results show that the system moves according to expected motions. The exercising task for the finger is performed properly by ExoFing and the results show that it stands as a good alternative for developing this task instead of the medical staff. The prototype design fulfil the requirements of adaptability to different subjects, portability to use the device in a convenient place for the final user, and affordability to increase the accessibility for hospitals and patients.

Acknowledgments. The first author acknowledge Consejo Nacional de Ciencia y Tecnología and Instituto Politécnico Nacional for supporting his period of study at LARM2 of Rome Tor Vergata University in the A.Y. 2019–20 within a double Ph.D. degree program.

References

1. Bataller, A., Cabrera, J., Clavijo, M., Castillo, J.: Evolutionary synthesis of mechanisms applied to the design of an exoskeleton for finger rehabilitation. *Mech. Mach. Theory* **105**, 31–43 (2016)
2. Agarwal, P., Fox, J., Yun, Y., O'Malley, M.K., Deshpande, A.D.: An index finger exoskeleton with series elastic actuation for rehabilitation: design, control and performance characterization. *Int. J. Robot. Res.* **34**(14), 1747–1772 (2015)
3. Stein, J., Bishop, L., Gillen, G., Helbok, R.: Robot-assisted exercise for hand weakness after stroke: a pilot study. *Am. J. Phys. Med. Rehabil.* **90**(11), 887–894 (2011)
4. Cempini, M., Cortese, M., Vitiello, N.: A powered finger-thumb wearable hand exoskeleton with self-aligning joint axes. *IEEE/ASME Trans. Mechatron.* **20**(2), 705–716 (2015)
5. Copilusi, C., Ceccarelli, M., Carbone, G.: Design and numerical characterization of a new leg exoskeleton for motion assistance. *Robotica* **33**(5), 1147–1162 (2015)
6. Cafolla, D., Carbone, G.: A study of feasibility of a human finger exoskeleton. In: Borangiu, T., Trentesaux, D., Thomas, A. (eds.) *Service Orientation in Holonic and Multi-Agent Manufacturing and Robotics*, vol. 544, pp. 355–364. Springer, Cham (2014)

7. Ceccarelli, M.: *Fundamentals of Mechanics of Robotic Manipulation*, 1st edn. Springer, Cham (2004)
8. Carbone, G.: *Grasping in Robotics*, 1st edn. Springer Cham (2012)
9. Carbone, G., Iannone, S., Ceccarelli, M.: Regulation and control of LARM hand III. *Robot. Comput.-Integr. Manuf.* **26**(2), 202–211 (2010)
10. Carbone, G., Gerding, E.C., Corves, B., Cafolla, D., Russo, M., Ceccarelli, M.: Design of a Two-DOFs driving mechanism for a motion-assisted finger exoskeleton. *Appl. Sci.* **10**(7), 1–23 (2020)
11. Gerding, E.C., Carbone, G., Cafolla, D., Russo, M., Ceccarelli, M., Rink, S., Corves, B.: Design and testing of a finger exoskeleton prototype. In: Carbone, G., Gasparetto, A. (eds.) *Advances in Italian Mechanism Science*, pp. 342–349. Springer, Cham (2019)
12. Gerding, E.C., Ceccarelli, M., Carbone, G., Cafolla, D., Russo, M.: Mechanism for a finger exoskeleton. Italian Patent application No. 102018000003847 (2018)



Serious Gaming Approach to Rehabilitation Using a 1 DOF Upper Limb Exerciser

Alexandru Ianoși-Andreeva-Dimitrova^(✉), Dan Silviu Mândru, and Lorin Bîrle

Technical University of Cluj-Napoca, Cluj-Napoca, Romania
{Alexandru.Ianosî, Dan.Mandru}@mdm.utcluj.ro

Abstract. This paper presents a system developed by the authors that makes use of a new trend in rehabilitation, serious gaming. Short introduction and state of the art is presented in the first part of the paper, after which the main design steps are given and explained. Finally, the testing of the prototype as well as the lesson learnt from building it are discussed in the last part of the paper. The aim of the research was to create an equipment that might be further developed into a fully-fledged rehabilitation device that uses the serious gaming paradigm.

Keywords: Serious gaming · Upper-limb exerciser · Rehabilitation equipment · Rehabilitation robot

1 Introduction

It is well known that the human mind is geared toward games, engaging in such activities activates the reward pathways and pleasure centers of the brain; computer games, due to their capacity of generating captivating scenarios, are especially prone to stimulate said centers of the brain, a fact proven by the \$119.6 billion in revenue generated by the video game industry in the year 2018 alone [1].

There are many working definitions for serious games, but every actor involved agrees to the core concept that a serious game must serve a purpose of more than mere entertainment [2]. This concept is used in many fields, but important to the present paper is the fact that gaming provides a motivational tool for better patient engagement in the rehabilitation session, as these are usually long and the progress is more often than not tedious and hard to ascertain by the untrained eye of the subject, which leads to a sharp decline in interest after a few number of sessions. It is presumed that the nature of a gaming environment has the potential of making the rehabilitation exercises more appealing and the concept of in-game scoring might provide to the patient a quick self-assessment tool for his/her progress.

Current paper focuses on the design and prototyping of a 1 degree-of-freedom (DOF) upper-limb active and passive rehabilitation device that is connected to a computer on which runs a custom-made serious game build in Unity3D; the upper-limb rehabilitation device is used as an input computer peripheral when in active mode, respectively as an output peripheral when in passive mode. Before further description of the system, a summary for the current state of the art is made in the following chapter.

2 State of the Art

Serious games used in health care sciences is a fairly new concept, as revealed by the relatively low number of articles (a number of 1005 indexed by PubMed) that deal with this subject, as well as the fact that more than half of them were published after the year 2016. The same trend is true also for other popular indexing services (e.g. SpringerLink: as of today, out of 257 of English sources related to serious gaming in medicine and public health, 70% of them were submitted starting with the year 2016). Figure 1 is illustrative to the general trend of the interest generated by this particular field of study; in this chapter of the paper, several research articles considered relevant to the current state of the art were selected and shortly discussed.

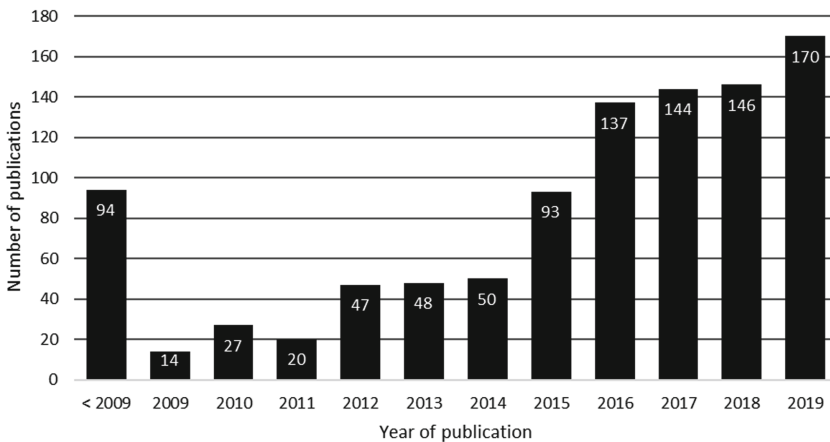


Fig. 1. Yearly number of publications related to serious gaming

Drumond et al. [3] distinguishes between three main categories of learners: a motivated, extrinsically motivated and intrinsically motivated. While the first category is interested only in the sensory delight provided by the game, the second and third category has a motivation to actually involve themselves in the learning process dictated by the serious game; the cited paper asserts that for amotivated users, this method yields no better results than traditional tools, therefore, one might not expect that designing a serious game represents an all-encompassing solution, and make recommendation to developers to consider the convergence of extrinsically and intrinsically motivations. Horne Moyer et al. [4] argues that while therapies based on computer (serious) games are not superior to traditional ones in terms of results, they are definitely more enjoyable; the mechanism of action mentioned are: attention, distraction, problem-solving, feedback, emotional expression, socialization and exposure.

An obvious choice for serious gaming is the management of various psychological or psychiatric disorders. Serret et al. [5] studied how usable is a game platform dedicated to patients with Autism Spectrum Conditions (ASC) to teach them emotions independently of their age, intellectual, verbal and academic level. ASC is characterized by a very low capacity for social interaction, therefore, teaching these persons the basics of emotions

via a gamified environment is hypothesized to improve these skills. The cited paper claims that the tested serious game is a promising tool by helping ASC patients to compensate for their difficulties with intuitive social processing by teaching them to use a logical model of processing social information and cues. Another similar study is presented by Derks et al. [6] that investigates how a serious game might change mentalizing abilities and stress regulation in the case of adults that suffer from mild to borderline intellectual disabilities. Even at low levels of effectiveness, due to the very low entry barrier (only a computer with an internet connection is needed) such a method might prove to be cost effective if deployed on a large scale. By the time of publication, the cited study claimed that the study is still a work in progress, but the researchers were very positive about the results. Wijnhoven et al. [7] proposes a study to investigate how a specifically designed computer game might decrease anxiety in children that suffer from ASC and expects that those included in the clinical trial will show a lower level of anxiety compared to the control group. Podina et al. [8] proposes a smartphone app designed for cognitive behavioral therapy (CBT) in the case of maladaptive eating habits; it gamifies the process of weight and calorie intake monitoring as well as physical activities with a scoring system and targets food cravings, binge eating and emotional eating.

The widespread use of mobile personal miniature computers (colloquially referred as smartphones) has led to a previously unimaginable number of applications dedicated to health; some of them gamify the process, with the hope of increasing user interaction and involvement. Schoeppe et al. [9] examines the efficacy of such apps by systematic review of multiple studies published between 2006–2016, and concludes that overall there is modest evidence that app-based intervention significantly improve diet, physical activity and sedentary behaviors, but the large demographics provided by the huge smartphone market makes even minute improvements to have a significant impact regarding public health. Also, the cited study states that usage of apps in conjunction with other methods (coaching, motivational e-mails, etc.) improves the overall effect. Hochsmann et al. [10] investigates whether a smartphone-based game-like app can increase the level of physical activity in sedentary individuals and hypothesizes that post interventional physical activity in selected individuals will be greater than in the control group.

Even though computer gaming is an activity rarely associated with elderly, there are some research initiatives that try to reach this population segment. Wiemeyer et al. [11] identifies that reasons for insufficient engagement of elderly people in regular exercises is lack of access to necessary equipment, fear of injury and lack of positive reinforcement; it identifies the need for appropriate interface design and game demands, but warns that the positive results of successful implementation of serious games might be transitory, given by the novelty character and that there are but few studies that address long term involvement. Money et al. [12] proposes a falls education tool in the form of a 3D exploration game, in order to raise the awareness of fall hazards in one's home environment, and reports that the results support the idea that a serious game is a more engaging tool (compared to leaflets, booklets, etc.) for educating older adults about fall risk factors and the need for adapting the home to mitigate these factors.

Combining serious gaming with robot assisted rehabilitation therapies are motivated by the fact that often patients tend to become bored during the session, especially after the novelty of the procedure wears out, which is detrimental to the rehabilitation process.

Serious gaming becomes in this case a tool for maintaining a high level of motivation. Dehem et al. [13] proposes a system designed for children with cerebral palsy composed of a rehabilitation robot and a serious game that allow continuous adaptation of the therapy based on measured performances in terms of passive range of motion, isometric and isokinetic strength and upper limb kinematics. Another research study by the same first author [14] investigates a similar system dedicated for motor and cognitive post-stroke rehabilitation; the game provides several targets on a graphical interface and the patient, assisted by the robot, tries to meet them. The system is also suitable for different levels of impairment, as the robot is configurable to fully assist or to oppose the movement in order to train the strength of the subject. The cited study claims that the patients found the game enjoyable and expressed the desire to play it again. Proenca et al. [15] synthesizes 38 studies regarding upper limb rehabilitation by means of serious games and concludes that this is a new paradigm in rehabilitation with apparent beneficial results, but notes that more in-depth clinical evidence is needed in order to fully understand the limits of this approach.

3 Design and Testing of the System

From the study of the literature it was concluded that a rehabilitation device using a serious gaming approach must consider the convergence of extrinsically and intrinsically motivations, has to provide an enjoyable experience without sacrificing the goals and guidelines set by the rehabilitation procedures, must captivate the attention of the subject, motivate him/her through problem-solving scenarios, has to provide constant, easy to understand feedback and, if possible, provide an outlet for social expression and social interaction. These aspects were taken into consideration for our design.

Our proposed system consist of a stationary 1-DOF upper-limb exerciser (Fig. 2(a)); this is built around a linear rail system (R) on which a carriage (C) slides between the limits set by the frame (F); on the carriage various shaped (depending on the subject pathology) handgrips (H) may be attached. A resistance-based encoder permanently tracks the linear position of the carriage with a theoretical maximum precision of 0.5 mm, which is used as input into the serious game for the active exercises. For the passive exercises, an electrical servomotor (M) moves the carriage with a maximum speed of 0.1 m/s, which is a value in accordance to the general practice as found in the literature; the motor has an included gearbox (gear ratio 100:1), which transfer a high enough torque for a seamless operation. Transition between active and passive mode is done by manually coupling the carriage to the driving cable (not pictured). Amplitude of motion is 440 mm, which was set in accordance with the mean travel distance for the hand; there is no need for a larger amplitude as this will make the device cumbersome. It is important that the device remains easy to set-up and reconfigurable, for the 1-DOF makes the equipment quite versatile: it can be repositioned at various vertical and horizontal angles relative to the patient (Fig. 2(b)).

The control architecture of the device (Fig. 2(d)) consist of a power driver for the electrical servomotor and an embedded control system build around the well-known ATmega328P microcontroller; on this, a simple program logic runs indefinitely checking the position of the carriage: in active mode, this position is reported to the computer via

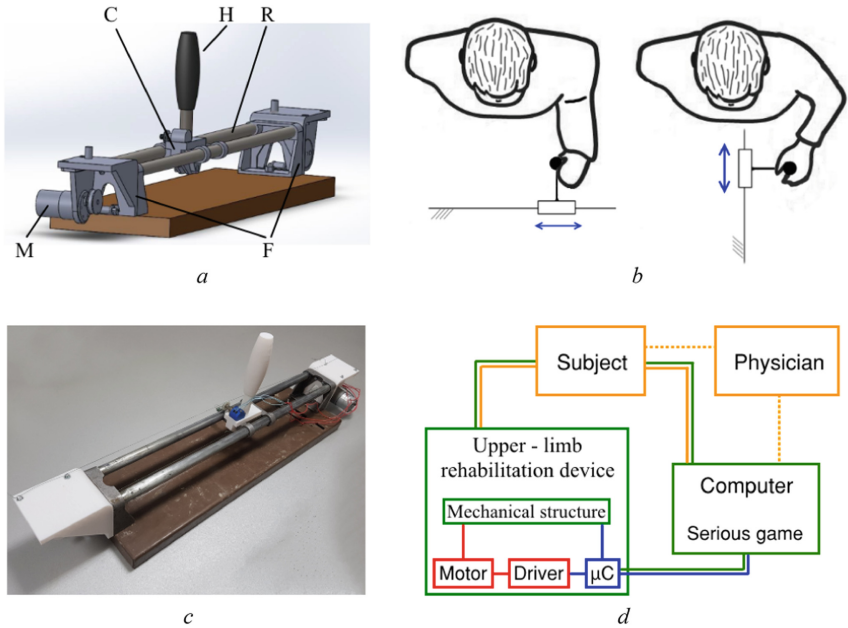


Fig. 2. Upper-limb rehabilitation device: (a) 3D model, (b) examples of use cases, (c) prototype and (d) system architecture

USB (CH340 interface) and is used as input to control the serious game. In passive mode, the position is used as reference in order to prevent overrunning of the carriage. The subject interacts both with the equipment as well as with the computer, on which the serious game is running. Optionally, a physician might monitor the exercise, but as a general rule the system is designed to run without supervision (however, a physician is needed for the initial setup of the game variables that dictates the difficulty of the exercise and for the final assessment of the procedure). The assembled device is pictured in Fig. 2(c).

In this stage, the serious game was designed only for movements in the sagittal plane; it used the software package Unity, a very popular game engine for designing electronic 2D and 3D games, virtual reality environments, augmented reality, etc. The game was devised as a flight simulator, in which the subject controls the pitch axis (nose up, nose down) of a virtual airship as he/she navigates through a series of circles (Fig. 3). The plane model was imported from the Unity Store library, and the terrain was generated using the build-in option, where the width and length dimensions are coded, the topographical relief manually defined and various textures (grass, stone, etc.) and vegetal elements (e.g. trees) are added. The sky model was also imported from the library. The scene is viewed through a third-person view camera, fixed at a certain distance behind the airship.

The main parameters for difficulty setting are (Fig. 3): speed of the airship (v), relative height difference between consecutive checkpoint circles (h_r), horizontal distance between consecutive circles (d), length of track (l) and height of the circle above the terrain (h). The speed of the airship correlates to the reaction speed of the patient and

is the main variable that sets the difficulty of the game. The amplitude of upper-limb motion correlates with the relative height difference between consecutive circles and together with the horizontal distance between consecutive circles gives the slope (s) of the trajectory which is also an important variable that defines the difficulty of the game. Of secondary importance to the difficulty settings is the height of the circle above the terrain, as close proximity to it can lead to the airship crash – from a game design perspective, it is recommended that only a few of them and evenly spaced out to be near the terrain, to act as “progress checkpoint”, but this is at the physician’s discretion. The length of the track defines the length of the exercise and must be chosen in accordance to the physical capabilities of the subject.

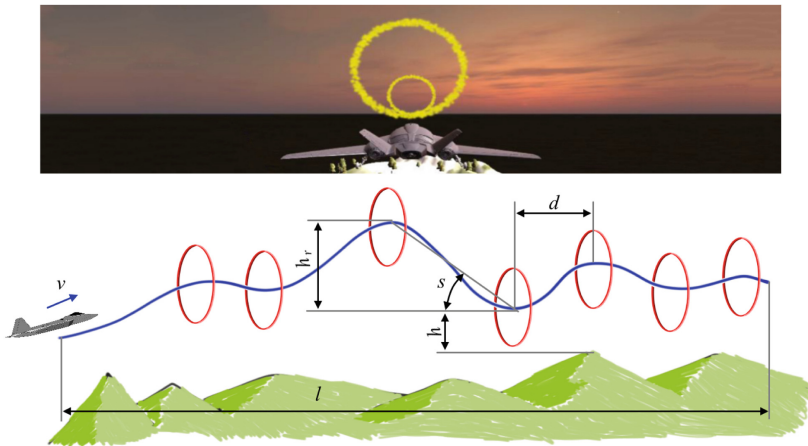


Fig. 3. Serious game: (above) user view, (below) game design parameters

The prototype was preliminary tested by a number of three able-bodied male subjects, with an average age of 25; the aim of this testing was to validate the mechanical structure, device communication with the computer and interaction with the designed game. The test protocol consisted of loading of the application, verifying for the correct communication exerciser/computer and navigating the airship through the circles for a predetermined speed and track length. The subjects were asked to describe their experience, general impression and to give suggestions, if they had any. Apart from a slight communication glitch between the device and the software, the system performed as expected and the subjects reported a positive experience. They suggested more scenarios, better and more realistically 3D models and redesign of the handgrip. No clinical testing was yet performed.

4 Conclusions

Serious gaming in rehabilitation is an emerging field of study with great future potential. As shown, current state of the art propose multiple solutions, most of them strictly

software-based; as such, the current proposal fills a need for integration between hardware and software based rehabilitation.

The main advantage of the presented system is the integration with a gaming platform, which opens many possibilities for developing interesting and more engaging rehabilitation exercises. Its simplicity and robustness make this system easy to use and understand even by the less technically minded persons, its similar appearance to a traditional game controller contributing to the self-explanatory character of the device.

There remain several challenges to address before commencing clinical trials: on the software side, a procedurally generated terrain algorithm is necessary in order to increase replayability (otherwise, boredom is a real risk, which would defeat the purpose of integrating a serious game in the first place); in the same idea of replayability is the procedurally generating of flight trajectory based on difficulty settings defined by the physician. Another planned improvement is a hybrid mode of operation which would consist of simultaneous active and passive exercises (as mentioned, the system requires manual switching between active and passive mode). Also important is establishing a relationship between a certain set of parameters and the currently used scales for measuring degree of disability (e.g. Modified Rankin Scale, Barthel Scale, etc.).

References

1. Webb, K.: The \$120 billion gaming industry is going through more change than it ever has before, and everyone is trying to cash in. In: Business Insider (2019). <https://www.businessinsider.com/video-game-industry-120-billion-future-innovation-2019-9>
2. Susi, T., et al.: Serious games - an overview, Technical report, HS-IKI-TR-07-001, University of Skövde (2007). <https://www.diva-portal.org/smash/get/diva2:2416/.pdf>
3. Drumond, D., et al.: Serious games for health—three steps forward. *Adv. Simul.* **2**, 3 (2017). <https://doi.org/10.1186/s41077-017-0036-3>
4. Horne-Moyer, L.H., Moyer, B.H., Messer, D.C., Messer, E.S.: The use of electronic games in therapy: a review with clinical implications. *Curr. Psychiatry Rep.* **16**(12), 1–9 (2014). <https://doi.org/10.1007/s11920-014-0520-6>
5. Serret, S., et al.: Facing the challenge of teaching emotions to individuals with low- and high-functioning autism using a new serious game: a pilot study. *Molecular Autism* **5**, 37 (2014). <https://doi.org/10.1186/2040-2392-5-37>. <http://www.molecularautism.com/content/5/1/37>
6. Derks, S., et al.: Effectiveness of the serious game ‘You & I’ in changing mentalizing abilities of adults with mild to borderline intellectual disabilities: a parallel superiority randomized controlled trial. *Trials* **20**(500), 1–10 (2019). <https://doi.org/10.1186/s13063-019-3608-9>
7. Wijnhoven, L.A.M.W., et al.: The effect of the video game Mindlight on anxiety symptoms in children with an Autism Spectrum Disorder. *BMC Psychiatry* **15**, 1–9 (2015). <https://doi.org/10.1186/015-0522-x>
8. Podina, I.R., et al.: An evidence-based gamified mHealth intervention for overweight young adults with maladaptive eating habits: study protocol for a randomized controlled trial. *Trials* **18**, 592 (2017). <https://doi.org/10.1186/s13063-017-2340-6>
9. Schoeppe, S., et al.: Efficacy of interventions that use apps to improve diet, physical activity and sedentary behaviour: a systematic review. *Int. J. Behav. Nutr. Phys. Act.* **13**, 127 (2016). <https://doi.org/10.1186/s12966-016-0454-y>
10. Hochsmann, C., et al.: Mobile Exergaming for Health—Effects of a serious game application for smartphones on physical activity and exercise adherence in type 2 diabetes mellitus—study protocol for a randomized controlled trial. *Trials* **18**, 103 (2017). <https://doi.org/10.1186/017-1853-3>

11. Wiemeyer, J., Kliem, A.: Serious games in prevention and rehabilitation—a new panacea for elderly people? *Eur. Rev. Aging Phys. Act.* **9**(1), 41–50 (2011). <https://doi.org/10.1007/s11556-011-0093-x>
12. Money, A.G., et al.: Falls Sensei: a serious 3D exploration game to enable the detection of extrinsic home fall hazards for older adults. *BMC Med. Inf. Decis. Mak.* **19**, 85 (2019). <https://doi.org/10.1186/s12911-019-0808-x>
13. Dehem, S., et al.: Assessment of upper limb motor impairments in children with cerebral palsy using a rehabilitation robot and serious game exercise. In: Poster at the 5th IEEE Conference on Serious Games and Applications for Health, Perth, Australia (2017). <http://www.segah.org/2017/docs/Papers/Poster%20Session/P-PS-03-12.pdf>
14. Dehem, S., et al.: Robotic-assisted serious game for motor and cognitive post-stroke rehabilitation. In: Paper at the 5th IEEE Conference on Serious Games and Applications for Health, Perth, Australia (2017). <https://doi.org/10.1109/segah.2017.7939262>
15. Proenca, J.P., et al.: Serious games for upper limb rehabilitation: a systematic review. *Disabil. Rehabil. Assistive Technol.* **13**(1), 95–100 (2017). <https://doi.org/10.1080/2017.1290702>



Rehabilitation System with Integrated Visual Stimulation

Florin Covaciu¹(✉), Bogdan Gherman¹(✉), Adrian Pisla^{1,3}, Giuseppe Carbone^{1,2},
and Doina Pisla¹

¹ CESTER – Research Center for Industrial Robots Simulation and Testing,
Technical University of Cluj-Napoca, Cluj-Napoca, Romania
{florin.covaciu, adrian.pisla}@muri.utcluj.ro,
{bogdan.gherman, doina.pisla}@mep.utcluj.ro

² DIMEG, University of Calabria, Rende, Italy
Giuseppe.Carbone@unical.it

³ DSSL – Dynamic Systems Simulation Laboratory, Technical University of Cluj-Napoca,
Cluj-Napoca, Romania

Abstract. The paper presents a Virtual Reality application (VR) related to a robotic assisted lower limb rehabilitation system. The considered robotic system is dedicated to the patient by performing rehabilitation exercises, that vary in terms of amplitude and duration. The patient performance is measured and the progress registered. The patient received instructions are via a VR headset. The robotic system assists a set of pre-defined exercises in parallel with a real-time control of the motion parameters. The VR exercises are reproduced within in Unity environment. The robotic structure is also represented in the VR together with the patient avatar, in order to suggest the type of exercises that must be practiced.

Keywords: Lower limb rehabilitation · Rehabilitation robotic system · Virtual reality · User interface

1 Introduction

Stroke is the leading cause of disability among adults. After a stroke, disorders such as loss of motion range, muscular weakness, is affecting the survivor's ability to have an independent life-course and may require assistance from other people. To promote functional recovery within rehabilitation process, many traditional therapeutic interventions have been used and mostly results have been obtained through studies [1]. It has been shown by evidence that in order to modify the patient neural organization, an intense practice with different kind of exercises are necessary to recover the functional motor skills [2, 3]. Virtual reality adds advantages to the traditional therapeutic approaches, as it can offer people the opportunity to practice daily activities with a virtual assistant [4]. Modeling and simulation of a new orthotic device has been addressed in [5]. For example, RehabMaster [6] and YouGrabber [7] are systems based on VR, being used

for the rehabilitation of the upper limbs within stroke patients. For describing the developed solution, the paper is organized as follows: after Introduction the second section presents the kinematics of the robotic structure, continuing with its control system and the user interface in Sect. 3. Section 4 presents development of virtual reality application followed in Sect. 5 by conclusions, acknowledgments and references.

2 Kinematics of the Robotic Structure

In the following it is presented the kinematic modelling for a new 4-DOF parallel robot named RECOVER used for lower limb rehabilitation for bedridden patients. The application of the inverse kinematics model starts by considering as input the coordinates of points E and E', Fig. 1, with the task to determine the active coordinates q_1, q_2, q_3, q_4 . The use of these two points coordinates is difficult during programming rehabilitation exercises, and the natural body angles (hip and knee flexion, as well as plantar flexion-dorsiflexion and eversion/inversion) are more natural and easy to understand. The kinematic model, presented in [8], supposes that the following angles are given: the θ_4 (the angle between the thigh and the horizontal plane or the patient's body, actually the hip flexion), θ_5 (the angle between the thigh and leg, the knee flexion), θ'_3 (the angle between the plantar and the leg, the flexion flexion-dorsiflexion) and θ'_4 (rotasstion the angle the plantar around the OY^* , the plantar eversion-inversion) (Fig. 2).

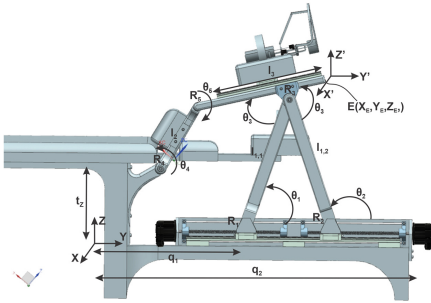


Fig. 1. Kinematics of the hip/knee rehabilitation module

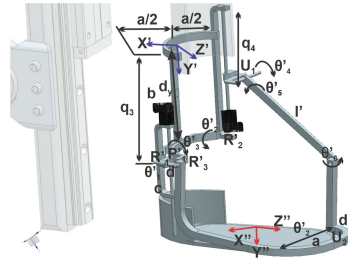


Fig. 2. Kinematics of the ankle rehabilitation module

Starting with the relations:

$$\begin{aligned} y_1 &= l_2 \cdot \cos(\theta_4); & z_1 &= l_2 \cdot \sin(\theta_4) \\ y_2 &= l_3 \cdot \cos(\theta_5/2); & z_2 &= l_3 \cdot \sin(\theta_5/2) \end{aligned} \tag{1}$$

the coordinates of points E and E' are computed by:

$$\begin{aligned} Y_E &= y_1 + z_1; & Z_E &= y_2 + z_2 + t_z \\ X_{E'} &= x_1 + y_1; & Y_{E'} &= x_2 + y_2 + t_z; \end{aligned} \tag{2}$$

Mechanical construction imposes that $q_1 < q_2$, yielding:

$$q_1 = 1/2 \cdot (Y_E + y_1/2 - R_t); \quad q_2 = q_1 + 2 \cdot \sqrt{l_1^2 - (y_1 + t_z + y_2/2)^2}$$

$$q_3 = a/2 \cdot \tan(\theta'_2); \quad q_4 = \sqrt{l^2 - (c + d \cos(\theta'_4))^2} - q_{40} + d \sin(\theta'_4) \quad (3)$$

where:

$$R_i = \sqrt{-(X_E - x_1)^2 - 2Y_E^2 + 4l_1^2 + l_3^2 - 2(t_z + y_1)^2} \quad (4)$$

The direct kinematics supposes that active coordinates are known (q_1, q_2, q_3, q_4) and the natural body angles, $\theta_4, \theta_5, \theta'_3$ and θ'_4 will be determined. Thus:

$$Y_E = Y_{R3} + y_2/2; \quad Z_E = Z_{R3} - z_2/2 \quad (5)$$

where:

$$\begin{aligned} Y_{R3} &= (q_2 - q_1)/2; \quad Z_{R3} = \sqrt{l_1^2 - ((q_2 - q_1)/2)^2} \\ y_2 &= l_3 \sin\left(\delta + a \tan 2\left((q_2 - q_1)/2, \sqrt{l_1^2 - ((q_2 - q_1)/2)^2}\right)\right); \quad z_2 = \sqrt{l_3^2 - y_2^2} \\ \delta &= \pi - \gamma_1 - \gamma_2 - 2a \tan 2\left((q_2 - q_1)/2, \sqrt{l_1^2 - ((q_2 - q_1)/2)^2}\right) \end{aligned} \quad (6)$$

where γ_1 and γ_2 can be obtained from:

$$\begin{aligned} t_z^2 + q_1^2 &= A^2 + l_1^2 - 2A \cdot l_1 \cdot \cos(\gamma_1); \quad l_1^2 = A^2 + l_3^2/4 - 2A \cdot l_3/2 \cdot \cos(\gamma_2) \\ A &= q_1^2 + t_z^2 + l_1^2 - 2l_1 \sqrt{q_1^2 + t_z^2} \cos(\pi - \alpha - \beta) \\ \alpha &= \text{atan2}(t_z, q_1); \quad \beta = \text{atan2}(Y_{R3}, q_2 - q_1/2) \end{aligned} \quad (7)$$

And finally:

$$\begin{aligned} \theta_4 &= \text{atan2}(Z_{R3} - t_z, Y_{R3}) + \text{acos}\left(\left(l_3^2/4 - l_2^2 - A^2\right) / (2l_2A)\right) \\ \theta_5 &= 2 \cdot \text{atan2}(Z_{R3} - Z_E, Y_E - Y_{R3}) \end{aligned} \quad (8)$$

In the case of the ankle module, θ'_3 and θ'_4 can be obtained from:

$$\begin{aligned} \theta'_2 &= \text{atan2}(2q_3, a) \\ (c + d \cos(\theta'_4))^2 + (q_4 + q_{40} - d \cos(\theta'_4))^2 &= l^2 \end{aligned} \quad (9)$$

3 The Control System and User Interface

For the ‘‘RECOVER’’ rehabilitation system [9], in parallel with the mechanical structure development was also developed the control system and the user interface using the kinematic model presented in Sect. 2. Figure 3 illustrates the block diagram of the rehabilitation control system. The components of the rehabilitation robotic system can be divided on three levels: User level; Command and Control level; Physical level.

A. The User level consists of a computer, the Unity programming environment and Visual Studio integrated development environment. The Unity development program was used to develop the VR components and the control interface (Fig. 4) for the robotic rehabilitation structure manipulation, consisting in the following components:

- **Video cameras:** with position selection and changing capacity of the video cameras viewing angle;
- Keys for the lower limb predefined exercises selection (i.e. **Exercise 1**, **Exercise 2**, **Exercise 3**). **Exercises** defined by the clinical doctors;
- Robotic structure manual control, through sliders, as the 3 ones depicted in Fig. 4.
- User graphical interface, with the patient monitoring and patient progress display (Fig. 4a., group 2).

Using the Visual Studio development environment, in the user interface (Fig. 4b.) data collected in real time from sensors are connected to the ESP32 microcontroller. The following functions were developed:

- **ConnectESP32:** when this button is pressed, the Wi-Fi connection is made between the computer with the user interface and the ESP32 microcontroller and the implicit connected sensors.
- **Start:** is the key that starts displaying the values received from the muscle activity sensor, the accelerometer and the gyroscope.
- **ConnectUnity:** with this button pressed, the connection from the Visual Studio interface and the Unity environment is made for sending data from the sensors, using the TCP/IP protocol.
- **Exit:** key is closing the user interface.

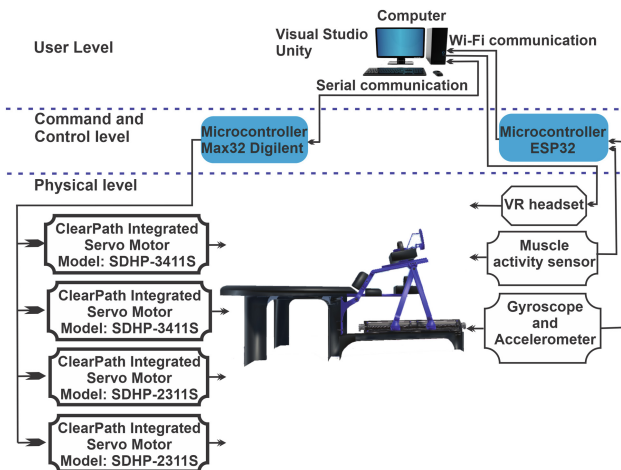


Fig. 3. Block diagram of the rehabilitation robot control system

- **B. The Command and Control level** integrates two types of microcontrollers, ESP32 and Max33.
- **C. The Physical level** - contains the following components: Mechanical structure of the parallel kinematics rehabilitation robot, two servomotors, the HTC Vive Pro VR headset, the MyoWare Muscle Sensor, an accelerometer and a gyroscope MPU6050. The latest two displaying the acceleration and position on three axes.

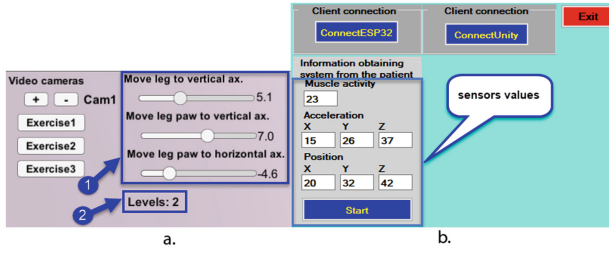


Fig. 4. User interface: a. VR application; b. Client application

Using the UML (Unified Modeling Language) [10], the computer system analysis the data within used cases diagram and the activity diagrams generating the corresponding diagrams [11]. Each case describes the user-software interactions. Use case diagram is presented in Fig. 5, containing an actor, five use cases describing the system functionalities, the relations between the user and the use cases (five association relations), as well as relations between the use cases (four dependency relationships).

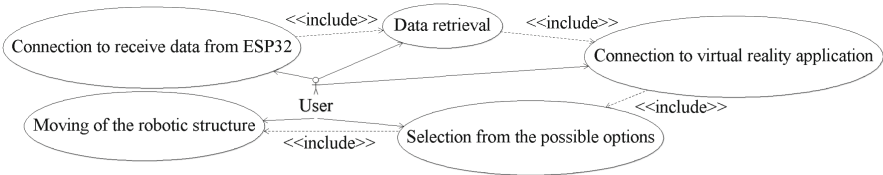


Fig. 5. Use case diagram

4 Development of the Virtual Reality Application

Virtual reality is one of the state-of-the-art technologies, which has experienced incredible development and increasing popularity. In a developed virtual reality application, the RECOVER robotic rehabilitation system is also integrated. A virtual human male avatar (Fig. 6) was created using the 3D avatar creation program called Make Human. This program is providing a complete tool that allows managing the components required to create realistic virtual people. The last step is to put the texture on the avatar through settings that have been made for this stage. Once that the avatar and the robotic structures 3D models are imported in the Unity environment, a logical connection is made in order to “connect” the two 3D models by attaching the avatar to the robotic structure.

Within the virtual reality application, the inserted and coupled 3D models must interact with the user interface, offering a controlled motion of the robotic rehabilitation system, a customized task programmed with C# language.

The patient receives the sets of rehabilitation exercises for the lower limb via a VR headset, “obliged” to perform these exercises, while on the user interface the progress achieved by the patient is displayed. The robotic structure together with the avatar is

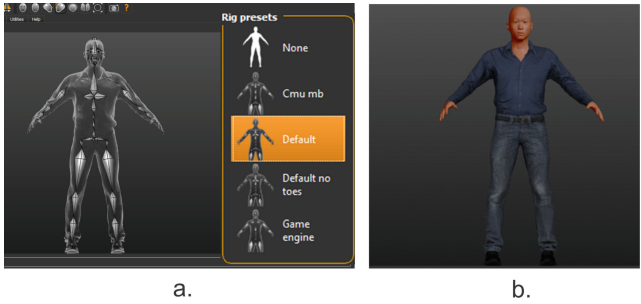


Fig. 6. Creating the human male avatar: a. setting the number of bones; b. setting the texture

introduced in the VR environment and the patient is suggested to exercise by generating the avatar motion in the virtual reality, the robotic structure together with the avatar. The implemented sensors (muscle sensors, gyroscope and accelerometer) are placed on the patient’s foot and on the robotic structure, offers to the control system a feedback signal regarding the patient lower limb motion. During exercises, medical therapist can control manually the robotic rehabilitation structure, or place the structure in an automatic mode (Fig. 7).



Fig. 7. The virtual reality application

5 Conclusions

The paper presents a robotic rehabilitation system “RECOVER” with integrated visual stimulation, designed for the lower limb medical rehabilitation. Via the VR headsets the patient is required to perform different rehabilitation exercises and the level of accomplishment (progress) is measured and displayed on the user interface. Future work targets the implementation of the developed application into a physical robot control system and the achievement of clinical trials in order to validate the developed solution.

Acknowledgments. The paper presents results from the research activities of the project: “Entrepreneurial competences and excellence research in doctoral and postdoctoral studies programs – ANTREDOC”, code: POCU/380/6/13/123927, co-financed by the European Social Fund through the Human Capital Operational Program 2014–2020, Priority Axis 6: Education and skills, “Support for post-doctoral students and researchers”. Beneficiary: Technical University of Cluj-Napoca/Partner: ROBERT BOSCH SRL, and the project ID 37_215, MySMIS code 103415 “Innovative approaches regarding the rehabilitation and assistive robotics for healthy ageing” co-financed by the European Regional Development Fund through the Competitiveness Operational Programme 2014–2020, Priority Axis 1, Action 1.1.4, through the financing contract 20/01.09.2016, between the Technical University of Cluj-Napoca and ANCSI as Intermediary Organism in the name and for the Ministry of European Funds.

References

1. Duncan, P.: Synthesis of intervention trials to improve motor recovery following stroke. *Stroke Rehab.* **3**(4), 1–20 (1997)
2. Jenkins, W., Merzenich, M.: Reorganization of neocortical representations after brain injury: a neurophysiological model of the bases of recovery from stroke. *Prog. Brain Res.* **71**, 249–266 (1987)
3. Kopp, B., Kunkel, A., Mühlnickel, W., Villringer, K., Taub, E., Flor, H.: Plasticity in the motor system related to therapy-induced improvement of movement after stroke. *NeuroReport* **10**(4), 807–810 (1999)
4. Laver, K.E., Lange, B., George, S., Deutsch, J.E., Saposnik, G., Crotty, M.: Virtual reality for stroke rehabilitation. *Cochrane Database Syst. Rev.* **11**(11), CD008349 (2017). <https://doi.org/10.1002/14651858.cd008349.pub4>
5. Tarnita, D., Catana, M., Tarnita, D.N.: Design and simulation of an orthotic device for patients with osteoarthritis. In: *New Trends in Medical and Service Robots*, pp. 61–77. Springer Publishing House (2016). ISBN 978-3-319-23832-6
6. Joon, S., Hokyong, R., Seong, H.: A task-specific interactive game-based virtual reality rehabilitation system for patients with stroke: a usability test and two clinical experiments. *J. Neuroeng. Rehabil.* **11**, 32 (2014). <https://doi.org/10.1186/1743-0003-11-32>
7. Brunner, I., Skouen, J., Hofstad, H., Strand, L., Becker, F., Sanders, A., Pallesen, H., Kristensen, T., Michielsen, M., Verheyden, G.: Virtual reality training for upper extremity in subacute stroke (VIRTUES): study protocol for a randomized controlled multicenter trial. *BMC Neurol.* **14**, 186 (2014). <https://doi.org/10.1186/s12883-014-0186-z>
8. Gherman, B., Birlescu, I., Tucan, P., Vaida, C., Pisla, A., Pisla, D.: Modelling and simulation of a robotic system for lower limb rehabilitation. In: *ASME 2018*, 26–29 August 2018, Quebec City, Quebec, Canada (2018). ISBN 978-0-7918-5181-4
9. Pisla, D., Gherman, B., Nadas, I., Pop, N., Craciun, F., Tucan, P., Vaida, C., Carbone, G.: Innovative parallel robot for the rehabilitation of the lower limb, Patent pending no. A00391/27.06.2019 (2019)
10. Iordan, A.E.: Design with UML of an interactive software for the study of the two surfaces of revolution. *Ann. Fac. Eng. Hunedoara* **12**, 275–280 (2014)
11. Iordan, A.E., Panoiu, M., Muscalagiu, I., Rob, R.: Using UML diagrams for object oriented implementation of an interactive software for studying the circle. *Int. J. Comput.* **5**(3), 431–439 (2011). ISSN 1998-4308



A Numerical Method for Determining the Workspace of a Passive Orthosis Based on the RRRR Mechanism in the Lower Limb Rehabilitation System

Dmitry Malyshev¹(✉), Anna Nozdracheva², Grigory Dubrovin³, Larisa Rybak¹, and Santhakumar Mohan⁴

¹ Belgorod State Technological University named after V.G. Shukhov, Belgorod, Russia
rlbgtu@gmail.com

² Gamaleya National Research Center for Epidemiology & Microbiology, Moscow, Russia
nozdracheva0506@gmail.com

³ Kursk State Medical University, Kursk, Russia
grig-d31@yandex.ru

⁴ Indian Institute of Technology Palakkad, Palakkad, India
santharadha@gmail.com

Abstract. The article describes the structure of the lower limb rehabilitation system based on serial RRRR mechanism as a passive orthosis and an active parallel 3-PRRR mechanism. A mathematical model of the kinematics of the RRRR mechanism is presented. A description of a numerical method for determining the workspace of the RRRR mechanism based on the approximation of solutions of nonlinear inequalities systems to provide the required rotation angles in joints for rehabilitation is considered. A calculation algorithm, a software, and a visualization system for export the three-dimensional workspaces in STL format are synthesized. The results of mathematical modeling and analysis of the results are presented.

Keywords: Workspace · Rehabilitation system · Orthosis · Non-uniform covering

1 Introduction

Robotic mechanotherapy is a new direction in the rehabilitation of patients with lesions of the musculoskeletal system (MS). Its basis is the use of specialized robotic systems to restore the functions of the upper and lower limbs through passive and active movements with feedback. Robotic mechanotherapy has significant advantages in restoring the skills of individual limb movements and generally walking patients with severe lesions of neurohumoral regulation and MS [1–3]. Recently, in the early rehabilitation, after injuries and surgical interventions on the musculoskeletal system, CPM therapy

(Continuous Passive Motion) has become widespread. The basis of this technique is the implementation of long-repeating movements in the joints with the use of a specialized robot simulator without the participation of the patient’s muscle strength. The advantage of robot therapy is a higher quality training compared to classical rehabilitation due to longer duration, the accuracy of repetitive cyclic movements, a constant training program, the availability of tools to evaluate progress with the possibility of demonstration to the patient [4]. The article proposes a new structure of a robotic system for lower limb rehabilitation.

2 Formulation of the Problem

The conceptual design of the lower limb rehabilitation system is shown in Fig. 1 a, b. The structure of the rehabilitation system (Fig. 1b) used an active 3-PRRR parallel robot proposed by Kong and Gosselin [5] and a passive orthosis.

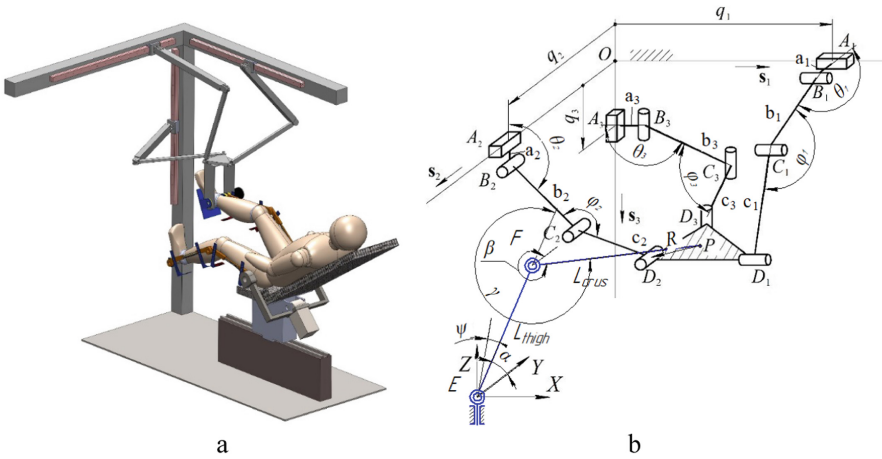


Fig. 1. Lower limb rehabilitation system: a-3D-model of the system; b-design scheme

The platform for fixing the patient’s foot is an equilateral triangle $D_1D_2D_3$ centered in the joint P for flexion and extension in the ankle joint. Joints of serial RRRR mechanism correspond to the patient joints. In the joint E, two movements of the hip joint are provided: rotation in the sagittal plane with angle α and abduction of the leg with angle ψ - between the projection of the EF link on the XOY plane and the OY axis. In the knee joint F, the link FP is rotated relative to EF by an angle θ . During rehabilitation [6], it is required to provide walking angles of joints: $\alpha \in [-20^\circ, 10^\circ]$, $\theta \in [120^\circ, 180^\circ]$, $\psi \in [0^\circ, 25^\circ]$. We set the task of determining the workspace of the RRRR mechanism under the walking clinical data.

3 A Mathematical Model of a Passive RRRR Mechanism

The passive orthosis would benefit the overall rehabilitation system in two ways.

It acts as a support system or exoskeleton to enhance the limb movements and make sure the proper joints only actuated, and the second one, that it acts as a feedback system through the help of the joint sensors (encoders) presented in the orthosis system. Further, the gravity would affect the overall performance of the physiotherapist due to too much manual effort required during the initial therapies set. To reduce and enhance the physiotherapist efforts, in this proposal, the static balanced passive orthosis is proposed. This proposed system reduces the therapist effort and the overall power requirement of the rehabilitation system. The conceptual passive orthosis design based on a serial RRRR chain is shown in Fig. 2.

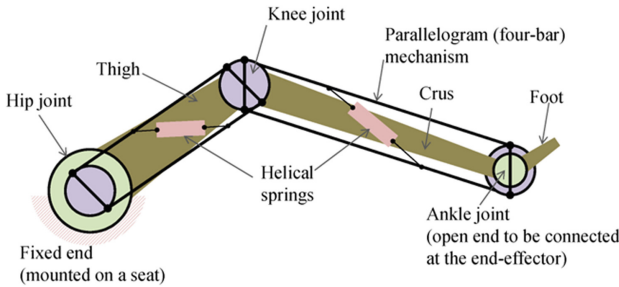


Fig. 2. Conceptual design of the proposed passive orthosis system

We compose a system of equations for the connection of the passive mechanism that describes the position of the point P - the center of the rotational joint of the ankle joint, depending on the rotation angles ψ and α in the hip joint and the rotation angle $\gamma = 180 - \theta$ in the knee joint. The coordinates of the center of the P joint:

$$\begin{cases} x_P = \sin \psi (L_{thigh} \cos \alpha + L_{cruis} \cos \beta) \\ y_P = -\cos \psi (L_{thigh} \cos \alpha + L_{cruis} \cos \beta) \\ z_P = -L_{thigh} \sin \alpha - L_{cruis} \sin \beta \end{cases} \quad (1)$$

where $\beta = \alpha + \gamma$, L_{thigh} is the link EF length, L_{cruis} is the link FP length.

Let $L_{PE} = L_{thigh} \cos \alpha + L_{cruis} \cos \beta$ is the EP link projection onto the XOY plane.

4 Method for Determining the Workspace of the RRRR Mechanism

Consider the task of determining the boundaries of the workspace of the RRRR mechanism when changing the parameters of the mechanism: rotation angles in the hip joint in the sagittal plane α , in the knee joint γ , and the angle of leg abduction in the hip joint ψ . For this purpose, we will use the method of non-uniform coverings, which is described in detail in [7, 8] for other types of parallel robots. Workspace covering is a set of n-dimensional boxes bounded by intervals of variable values. In the process of performing calculations involving these intervals, we will use the interval analysis methods described in detail in [9].

We define a set of coordinate values x_P, y_P, z_P when the angles ψ, α, γ change. System (1) includes six variables, which is a problem of dimension 26. To reduce the dimension of the problem, we bring it to dimension 24. We set intervals of values that are guaranteed to include ranges of permissible values $\mathbf{Z}_P := \{\underline{Z}_P \leq z_P \leq \overline{Z}_P\}$, $\mathbf{X}_P := \{\underline{X}_P \leq x_P \leq \overline{X}_P\}$, $\mathbf{Y}_P := \{\underline{Y}_P \leq y_P \leq \overline{Y}_P\}$ and the interval \mathbf{B} according to clinical data. For them, the joint intervals $\mathbf{A}', \mathbf{\Gamma}', \mathbf{\Psi}'$ are determined and compared with the clinical data - the intervals $\mathbf{A}, \mathbf{\Gamma}, \mathbf{\Psi}$. The interval \mathbf{L}'_{PE} is calculated for the intervals \mathbf{X}_P and \mathbf{Y}_P and the interval \mathbf{L}''_{PE} is calculated for the intervals \mathbf{Z}_P and \mathbf{B} and are compared with each other. In the case of the intersection of the intervals \mathbf{L}'_{PE} and \mathbf{L}''_{PE} , as well as the intervals of the calculated and clinically given angles of rotation of the joints, there is a solution to system (1). The lower boundary of the intervals corresponds to the minimum angles necessary for rehabilitation, and the upper maximum, that is: for the angle α : $\mathbf{A} := \{\underline{\mathbf{A}} \leq \alpha \leq \overline{\mathbf{A}}\}$; for the angle γ : $\mathbf{\Gamma} := [\underline{\mathbf{\Gamma}}, \overline{\mathbf{\Gamma}}] = \{\underline{\mathbf{\Gamma}} \leq \gamma \leq \overline{\mathbf{\Gamma}}\}$; for the angle ψ : $\mathbf{\Psi} := \{\underline{\mathbf{\Psi}} \leq \psi \leq \overline{\mathbf{\Psi}}\}$; for the angle β : $\beta = \alpha + \gamma$, that is, $\mathbf{B} := [\underline{\mathbf{B}}, \overline{\mathbf{B}}] = \{\underline{\mathbf{A}} + \underline{\mathbf{\Gamma}} \leq \beta \leq \overline{\mathbf{A}} + \overline{\mathbf{\Gamma}}\}$. For intervals \mathbf{X}_P and \mathbf{Y}_P , we define the interval $\mathbf{\Psi}'$ of the values of the angle ψ and the interval \mathbf{L}'_{PE} , which is equal to the length of the projection of the segment EP onto the XY plane:

$$\mathbf{\Psi}' := [\underline{\mathbf{\Psi}'}, \overline{\mathbf{\Psi}'}] \tag{2}$$

$$\underline{\mathbf{\Psi}'} = \min_{x_P \in \mathbf{X}_P, y_P \in \mathbf{Y}_P} \left(\tan^{-1} \frac{x_P}{y_P} \right), \overline{\mathbf{\Psi}'} = \max_{x_P \in \mathbf{X}_P, y_P \in \mathbf{Y}_P} \left(\tan^{-1} \frac{x_P}{y_P} \right)$$

$$\mathbf{L}'_{PE} := [\underline{\mathbf{L}'_{PE}}, \overline{\mathbf{L}'_{PE}}], \text{ where} \tag{3}$$

$$\underline{\mathbf{L}'_{PE}} = \min_{x_P \in \mathbf{X}_P, y_P \in \mathbf{Y}_P} \left(\sqrt{x_P^2 + y_P^2} \right), \overline{\mathbf{L}'_{PE}} = \max_{x_P \in \mathbf{X}_P, y_P \in \mathbf{Y}_P} \left(\sqrt{x_P^2 + y_P^2} \right)$$

We express the angle α taking into account (1): $\alpha = \sin^{-1} \frac{L_{crus} \sin \beta}{L_{thigh}}$. For the interval \mathbf{Z}_P and the interval \mathbf{B} we define the interval \mathbf{A}' of the values of the angle α :

$$\mathbf{A}' := [\underline{\mathbf{A}'}, \overline{\mathbf{A}'}], \text{ where} \tag{4}$$

$$\underline{\mathbf{A}'} = \min_{z_P \in \mathbf{Z}_P, \beta \in \mathbf{B}} \left(\sin^{-1} \frac{L_{crus} \sin \beta}{L_{thigh}} \right), \overline{\mathbf{A}'} = \max_{z_P \in \mathbf{Z}_P, \beta \in \mathbf{B}} \left(\sin^{-1} \frac{L_{crus} \sin \beta}{L_{thigh}} \right)$$

For the interval \mathbf{A}' and the interval \mathbf{B} we define $\mathbf{\Gamma}'$:

$$\mathbf{\Gamma}' = \mathbf{B} - \mathbf{A}' \tag{5}$$

Then, for the intervals \mathbf{A}' and \mathbf{B} , we calculate the interval \mathbf{L}''_{PE} :

$$\mathbf{L}''_{PE} := [\underline{\mathbf{L}''_{PE}}, \overline{\mathbf{L}''_{PE}}], \text{ where} \tag{6}$$

$$\underline{\mathbf{L}''_{PE}} = \min_{a \in \mathbf{A}', \beta \in \mathbf{B}} (L_{thigh} \cos \alpha + L_{crus} \cos \beta), \overline{\mathbf{L}''_{PE}} = \max_{a \in \mathbf{A}', \beta \in \mathbf{B}} (L_{thigh} \cos \alpha + L_{crus} \cos \beta)$$

Using Eqs. (2)–(6), we compose a system of inequalities that takes into account the intersection of intervals in the form

$$\begin{cases} \Psi \cap \Psi' \neq \emptyset \\ \mathbf{A} \cap \mathbf{A}' \neq \emptyset \\ \Gamma \cap \Gamma' \neq \emptyset \\ L'_{PE} \cap L''_{PE} \neq \emptyset \end{cases} \quad (7)$$

If the system (7) is satisfied, then for intervals X_P , Y_P , Z_P and \mathbf{B} there is at least one point entering the workspace. Thus, the volume of the workspace is calculated.

Further, to determine the boundary of the workspace, we introduce an additional condition in the system (7), which takes into account that at the boundary of the workspace, the intervals of angles \mathbf{A} , Γ , Ψ cannot simultaneously completely include the intervals \mathbf{A}' , Γ' , Ψ' , respectively.

$$\begin{cases} (\underline{\Psi} \in \Psi') \vee (\overline{\Psi} \in \Psi') \vee (\underline{\mathbf{A}} \in \mathbf{A}') \vee (\overline{\mathbf{A}} \in \mathbf{A}') \vee (\Gamma \in \Gamma') \vee (\overline{\Gamma} \in \Gamma') \\ (\Psi \cap \Psi' \neq \emptyset) \wedge (\mathbf{A} \cap \mathbf{A}' \neq \emptyset) \\ (\Gamma \cap \Gamma' \neq \emptyset) \wedge (L'_{PE} \cap L''_{PE} \neq \emptyset) \end{cases} \quad (8)$$

The interval constraints of the variables is n -dimensional box, where n is the number of variables, i.e., $n = 4$. To determine the workspace boundary, the initial and subsequent boxes, for which (8) holds, are divided into smaller boxes. For each box B obtained as a result of the partition, the verification is performed similarly. The workspace boundary is described by the set \mathbb{P}_I of boxes B , for which $d(P_i) \leq \delta$, where δ is a given positive value that determines the accuracy of the approximation. For the subsequent use of the set of boxes for visualization, the resulting four-dimensional workspace \mathbb{P}_I is projected onto the 3D space XYZ . The projection is to exclude all boxes, except for one, having the same values of the intervals Z_P , X_P and Y_P for different values of the interval B . The resulting set \mathbb{P}_J of boxes describes the workspace boundary.

5 Algorithm Synthesis

Synthesizing an algorithm for determining the workspace boundary based on the approximation of the solutions set of the resulting systems of nonlinear inequalities. The algorithm works with two lists of 4-dimensional boxes \mathbb{P} , \mathbb{P}_I and a list of 3-dimensional boxes \mathbb{P}_J . Each of the box dimensions in the list \mathbb{P}_J corresponds to the intervals X_P , Y_P and Z_P , the 4th dimension of the lists \mathbb{P} and \mathbb{P}_I corresponds to the interval B . Initially the lists of internal approximations \mathbb{P}_I and \mathbb{P}_J are empty, the list \mathbb{P} consists of box Q , including the intervals X_P , Y_P , Z_P and \mathbf{B} : $X_P = Y_P = Z_P = [-(L_{high} + L_{crus}), L_{high} + L_{crus}]$. The algorithm works as follows:

1. Set the geometric parameters of the mechanisms, the accuracy of the approximation δ , and the initial value of the intervals Q_i .
2. Extract box B from list \mathbb{P} .
3. If $d(B) < \delta$, then add B to the list \mathbb{P}_I and go to step 6.
4. Calculate Ψ' , \mathbf{A}' , Γ' , L'_{PE} and L''_{PE} using formulas (2)–(6).

5. If the system (8) does not hold, then exclude B and go to step 8. Otherwise, divide B by two equal boxes and add to list \mathbb{P} .
6. If $\mathbb{P} \neq \emptyset$, then go to step 2. Otherwise project \mathbb{P}_I in \mathbb{P}_J .

The algorithm is implemented in the C++ programming language using the Snow-goose interval analysis library [10]. Visualization of the results of modeling the workspace is done by converting a list of three-dimensional boxes that describe the workspace into a universal format for 3D models - an STL file.

6 Simulation Results

Geometric parameters of the computational experiment: $\mathbf{A} = [-20^\circ, 10^\circ]$, $\mathbf{\Gamma} = [-60^\circ, 0^\circ]$, $\mathbf{\Psi} = [0^\circ, 25^\circ]$, $L_{thigh} = L_{crus} = 450$ mm. In Fig. 3 shows the projections of the boundary of the workspace on the plane: a - on the XOY plane, b - XOZ, c - YOZ. Maximum dimensions along the X axis - 383 mm, along Y - 450 mm, along Z - 759 mm. The visualization of the constructed boundary of the three-dimensional workspace is shown in two projections in Fig. 4. Calculation time for approximation accuracy $\delta = 8$ mm 19 s.

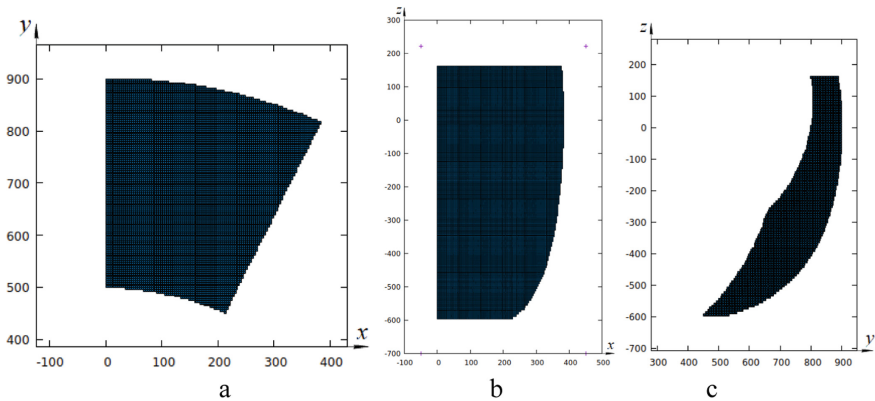


Fig. 3. Projections of the boundary of the workspace on the plane.

Let us analyze the effect of the size of the patient’s legs on the overall dimensions of the workspace. The graph (Fig. 5) shows the dependency between the length of a patient’s legs and the overall dimensions of the workspace.

It can be seen that for the case when $L_{thigh} = L_{crus}$ there is a linear relationship between the length of a person’s legs and the overall dimensions Δx , Δy , and Δz of the workspace along each axis. It allows us to quickly determine the overall dimensions of the passive orthosis workspace, depending on the size of the patient’s legs.

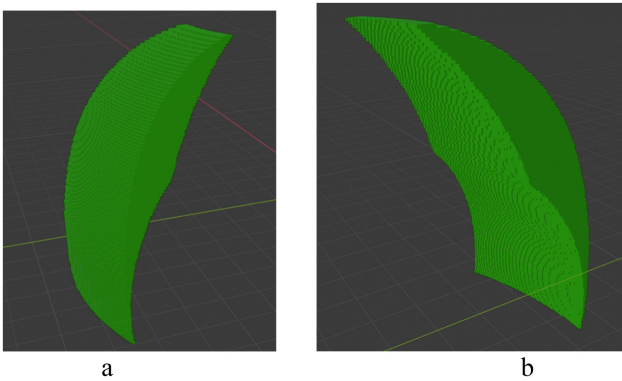


Fig. 4. Three-dimensional workspace in two projections.

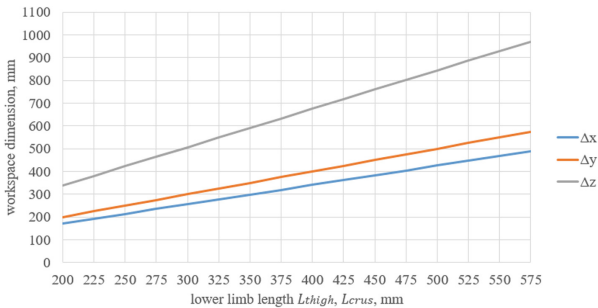


Fig. 5. The effect of the patient's foot size on the overall dimensions of the workspace.

7 Conclusions

In conclusion, it can be noted that for a passive orthosis in the system of lower limb rehabilitation, effective numerical methods and algorithms were developed and tested that made it possible to determine the boundary of the workspace of the RRRR mechanism. The calculation time for the approximation accuracy $\delta = 8$ mm on a personal computer was 19 s. Developed methods and algorithms can be used to determine the workspace of other mechanisms. The RRRR mechanism workspace boundary will be used for rehabilitation system design. An active 3-PRRR robot must ensure the movement of a passive orthosis within the workspace defined in this work. The obtained dependences of the workspace on the size of the patient's legs allow for accounting depending on the requirements for the designed system.

Acknowledgments. This work was supported by the Russian Science Foundation, the agreement number 19-19-00692.

References

1. Ada, L., Dean, C.M., Vargas, J., Ennis, S.: Mechanically assisted walking with body weight support results in more independent walking than assisted over-ground walking in non-ambulatory patients early after stroke: a systematic review. *J. Physiother.* **56**(3), 153–161 (2010)
2. Hachisuka, K.: Robot-aided training in rehabilitation. *J. Brain Nerve* **2**, 133–140 (2010)
3. Hidler, J., Nichols, D., Pelliccio, M., Brady, K.: Multicentre randomized clinical trial evaluating the effectiveness of the Lokomat in subacute stroke. *J. Neurorehabil. NeuralRepair* **1**, 5–13 (2009)
4. Baranova, E.A., Bredikhina, Yu.P., Kabachkova, A.V., Kalinnikova, Yu.G., Pashkov, V.K.: Modern approaches to robotic mechanotherapy with elements of biocontrol and telemedicine to restore lost motor functions. *Bull. Tomsk State Univ.* **433**, 127–134 (2018)
5. Kong, X., Gosselin, C.M.: Kinematics and singularity analysis of a novel type of 3-CRR 3 DOF translational parallel manipulator. *Int. J. Robot. Res.* **21**(9), 791–798 (2002)
6. Loeb, G.E.: Neural control of locomotion. *BioSciences* **39**, 800–804 (1989)
7. Malyshev, D., Posypkin, M., Rybak, L., Usov, A.: Approaches to the determination of the working area of parallel robots and the analysis of their geometric characteristics. *Eng. Trans.* **67**(3), 333–345 (2019)
8. Evtushenko, Y., Posypkin, M., Rybak, L., Turkin, A.: Approximating a solution set of non-linear inequalities. *J. Global Optim.* **71**(1), 129–145 (2017). <https://doi.org/10.1007/s10898-017-0576-z>
9. Jaulin, L.: *Applied interval analysis: with examples in parameter and state estimation, robust control and robotics*. Springer, New York (2001)
10. Posypkin, M., Usov, A.: Implementation and verification of global optimization benchmark problems. *Open Eng.* **7**(1), 470–478 (2017)



Static and Dynamic Analysis of a Prosthetic Human Knee

Daniela Tarnita¹ (✉), Marius Georgescu¹, Nicolae Dumitru¹,
and Danut-Nicolae Tarnita²

¹ University of Craiova, Craiova, Romania
tarnita.daniela@gmail.com

² University of Medicine and Pharmacy, Craiova, Craiova, Romania

Abstract. The first objective of this paper is to study the influence of a prosthesis on the maximum values of contact stresses developed in the components of the virtual model of a prosthetic knee assembly, using Finite element analysis (FEA). The second objective is to estimate Lyapunov exponents (LEs) in order to quantify the local dynamic stability of the human knee joint during walking overground for healthy subjects and for patients suffering of osteoarthritic knee (OAK), before and after total knee replacement (TKR), using tools of dynamics stability analysis. The values of the LEs are obtained based on the experimental time series of the flexion-extension movements in sagittal plane and the rotational movements in frontal plane for both knees, collected from a sample of healthy subjects and a sample of patients suffering by OAK before and after TKR. The influence of prosthesis mounted in OAK is positive, the values of LEs obtained for OAK four month after TKR are associated with increased stability, being smaller than those computed for OAK before TKR, and closer than those obtained for healthy knees.

Keywords: Virtual knee prosthesis · Virtual prosthetic knee · Finite element analysis · Von mises stress · Lyapunov exponent · Phase planes · State space reconstruction

1 Introduction

The knee joint is a very important and complex human joint, considering the number of its components, their spatial geometry and their mechanical properties, the complex contacts between elements as well as the pressures acting on them. Virtual modeling and finite element analysis (FEA) of human knee joint has been addressed in several articles [1–13], becoming very important tools in orthopaedic biomechanics. They are used more and more in order to analyse the tibio–femoral contact geometry, the influence of the contact force model and contact material properties on the dynamic response of a human knee joint model, the stresses and displacements developed in the human knee joint' components under different solicitations. In [2, 5, 8, 11, 12] different studies regarding the osteoarthritic knee (OAK), a frequent disease associated with pain and destroyed cartilages, disease that, finally, leads to TKR, are presented. FEA allows

researchers to, virtually, test human bones, joint, orthopaedic implants or endoprostheses and has been used in several biomechanical studies [6–10]. FE method is used to evaluate biomechanical behavior of the knee and of its components, to evaluate the tibio-femoral contact stress [11, 17]. In these papers the FEA is used in order to simulate the loading conditions applied to the prosthesis and the contact stress in its components. Many studies investigate the normal and pathological human movements [12, 18–20] or the movements of bioinspired robotic structures used especially in the field of rehabilitation, or minimally invasive surgery [14–20].

The first objective of this paper is to study the influence of a prosthesis mounted on an OAK on the maximum values of contact stresses, applying FEA on a virtual assembly prosthesis - OAK joint. The second objective is to estimate LEs in order to quantify the local dynamic stability of the human knee joint during walking overground for healthy subjects and for OAK patients, before TKR and 4 month after TKR, by using tools of dynamics stability analysis.

2 Virtual Modeling of the Prosthetic Knee Joint

We used, as model, Scorpio Stryker type knee prosthesis, a common prosthesis used by orthopaedic surgeons in the Emergency Hospital of Craiova. It is composed of three components: the femoral prosthesis (FP), the tibial prosthesis (TP) and the polyethylene insert (POLI). The real models of the three prosthesis components are presented in Fig. 1 a). To achieve the virtual knee prosthesis model (Fig. 1 b), the DesignModeler application, a preprocessor of the ANSYS Workbench 15.07 program, was used. The developed model is presented in [8].

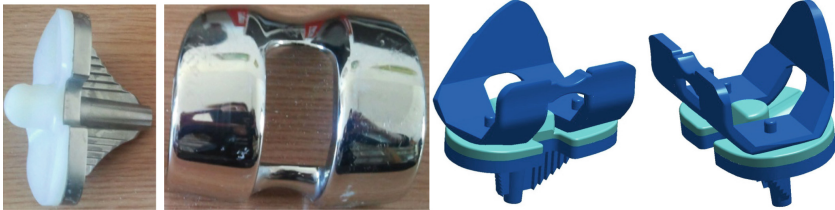


Fig. 1. a) Physical prosthesis for human knee joint; a) femoral component; b) tibial component and polyethylene insert; b) Two isometric views of the virtual model of knee prosthesis.

Three virtual 3D models of the prosthetic knee joint assemblies including femur, tibia, and the three prosthesis components have been developed, based on the 3D virtual model of human knee joint elaborated by our team [2, 5].

The mesh geometry was realised using Solid186 hexahedral elements and Solid187 tetrahedral elements (Fig. 2). For each of studied cases: OAK and three OAK-prosthesis assemblies obtained for three FTA angles, each virtual model is discretized individually, the contact areas are readjusted and the analysis is run. The material properties are assigned to the different components of the assembly based on previously published data and they are found in [2, 5, 8].

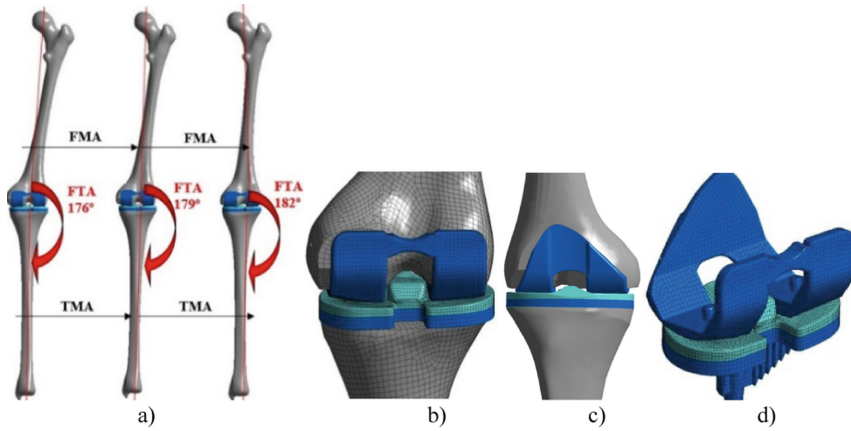


Fig. 2. a) Virtual knee-prosthesis assemblies (tibia mechanical axis (TMA)); femur mechanical axis (FMA); femur-tibia angle (FTA); b) Mesh network of prosthetic knee joint-frontal image; c) Prosthetic knee joint-back image; d) Prosthesis mesh network-isometric view

3 Results

By using ANSYS Workbench15.07 software, and applying a loading force of 800 N on the femoral head, the numerical simulations and FEA analyses were processed. For all studied cases, the maximum von Mises stress maps are obtained, as we can see in Fig. 3 a). In Fig. 3b), the stress map for the OAK with 5° in varus is shown. By comparing the results obtained in Fig. 3 a) and b) we can see that in the OAK case, the maximum values of stress are almost double than in the prosthetic knee. In Fig. 3 c) the stress maps obtained in POLI, FP and TP for 5° in varus are shown.

Von Mises stress maps (top and bottom views) developed in POLI, polyethylene insert, TP and FP for a FTA angle equal to 182° are shown in Fig. 4, while the maximum values of von Mises stress for each component of the three studied virtual models of prosthesis-OAK joint (176°, 179°, 182°) are presented in Table 1.

By analysing the results obtained by numerical simulations presented in Table 1, it is noticed that, as the angle of inclination in varus (FTA) increases, the values of von Mises stresses increase in bones and in all prosthesis components. In all cases, the stress values on components are similar, but we can conclude that the bigger values are developed on POLI, followed by the values developed on FP and on TP. Increased varus frontal plane tibio-femoral alignment leads to an increase of the mechanical loading on the medial compartment of the knee. In all three cases of varus inclinations, the stress values developed on OAK prosthetic joint assembly are smaller than those developed in the OAK joint assembly. The prosthetic joint is more stable and the pain decreases and, finally, disappears.

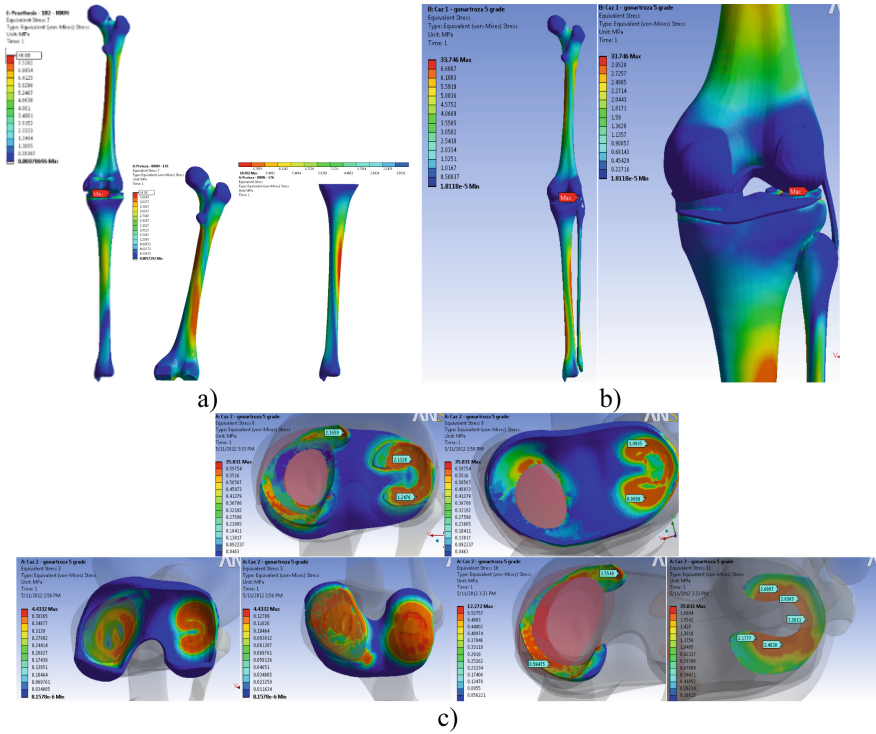


Fig. 3. Von Mises stress maps for: a) prosthetic knee joint assembly- 182°; b) OAK with FTA - 181°; c) tibial cartilage (top and bottom views); femoral cartilage (top and bottom views); menisci.

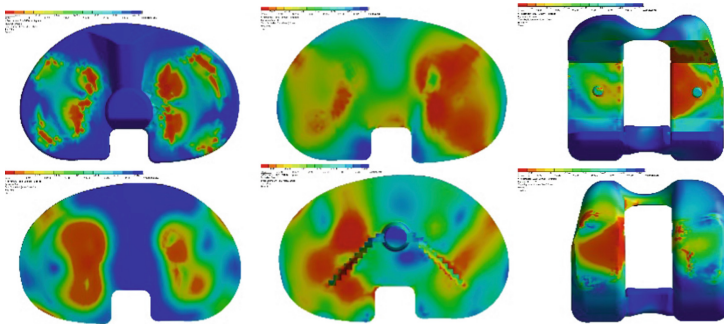


Fig. 4. Von Mises stress maps (top view-first row and bottom view-second row) obtained for a loading force equal to 800 N in POLI, TP and FP for 182°.

4 Experimental Measurements

For normal walking experimental study, a Biometrics data acquisition system based on electrogoniometers and Datalog devices mounted on the human subjects (Fig. 5 a) are used [18–20]. The tests were performed by a sample of 8 healthy subjects (average data:

Table 1. Maximum values of von Mises stress developed in the prosthesis components

Cases	No. nodes	No. elements	POLI. stress [MPa]	TP stress [MPa]	FP stress [MPa]	Femur stress [MPa]	Tibia stress [MPa]
176°	351.324	107.128	18.14	16.82	17.28	10.45	14.08
179°	352.123	106.143	18.65	17.13	17.53	10.89	14.49
182°	347.939	106.853	19.03	17.41	17.92	11.13	14.78

age: 34.6 years, weight: 72.4 kg; height: 174.6 cm) with any musculoskeletal disorders, and a sample of 3 patients with left OAK (average data: age: 66.7 years, weight: 76.8 kg; height: 165.3 cm), two days before TKR and 3 month after TKR. The subjects and patients gave their written consent for performing the tests. Ethics Committee of the University of Craiova approved the research. The data series collected from both knees of the subjects and patients (fl-ext in sagittal plane and var-valg in frontal plane) (Fig. 5b) are used to quantify the dynamic stability of these joints' movements.

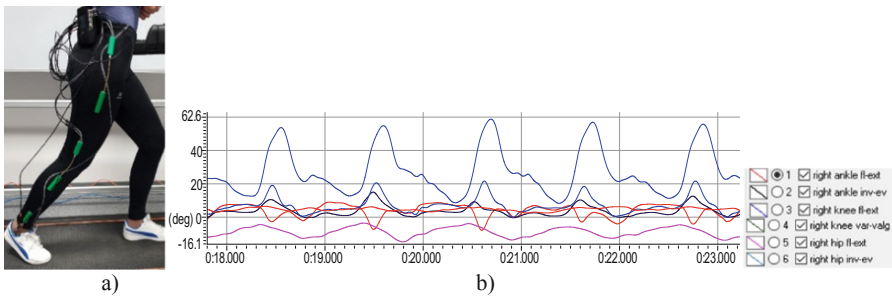


Fig. 5. a) Subject with electrogoniometers and DataLog mounted; b) angular joints diagrams plotted in Biometrics software

5 Dynamic Analysis

In this paper, a nonlinear analysis approach is applied in order to quantify local dynamic stability of human OAK and prosthetic knee joints during walking with normal speed, using LE, which are computed, based on the experimental time series collected for both knee joints movements: flexion-extension (fl-ext) in sagittal plane and varus-valgus rotation (var-valg) in frontal plane. In this study, the human knee is considered as a nonlinear system. The schema of the algorithm used for determining of the LEs and for estimating the system stability is shown in Fig. 6.

Phase plane portraits are used, in order to characterize the kinematics of the system, by correlating the knee angular rotations with the knee angular velocities [11, 19, 20]. For all patients, the right knee is the osteoarthritic one. An important step to quantify

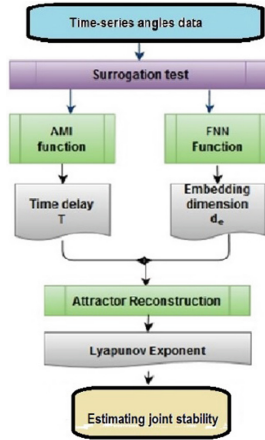


Fig. 6. Algorithm for study the joint stability

the knee stability consists into the state space reconstruction S , by using the method that consists in to generate the delay coordinates vectors [21]:

$$x_n = [s(t_0 + nT_s); s(t_0 + nT_s + T), \dots s(t_0 + nT_s + (d_E - 1)T)] \quad (1)$$

where the integer d_E is the embedding dimension, the notation $s(\cdot)$ is a measured scalar function, T_s is the sampling time, $n = 1, 2, \dots, d_E$, while $T = kT_s$ is an appropriately time delay. In [22] is demonstrated that the dynamics in the reconstructed state space and the original dynamics are equivalent, the two spaces have the same invariants, such as LE. In Fig. 7 and Fig. 8, state-space reconstruction and phase-plane portraits corresponding to both movements of Subject 5 and Patient 2 are shown. Similar plots are obtained for the other subjects and patients. It can be seen that for healthy knee the cycle’s curves show less divergence in their trajectories, are more compact, the amplitudes tend to be constant, while the curves traced for OAKs show more divergence and increased spread in their trajectories.

By using TISEAN software, an appropriate time lag, T , is computed for each time series, by using the average mutual information (AMI) function [23], which sets the time lag equal to the value of delay corresponding to the first minimum of the AMI function (Fig. 9a). A suitable embedding dimension, which is the minimum value that trajectories of the reconstructed state vector may not cross over each other in state space, was chosen by using the false nearest neighbour method (FNN) [24].

The LEs are computed using ‘lyap_r’ routine, based on the Rosenstein algorithm [25] and available in TISEAN package. If LEs increase, then the local dynamic stability decreases. The LEs calculated for all time series were positive, that means the human knee joint is a deterministic chaotic system, in accordance with [24]. In Table 2 the average values of the computed LEs for both knee movements of healthy subjects and of patients are presented and in Fig. 7 these values are plotted.

The values of LEs obtained for the OAK before TKR are associated with more divergence and less stability, being generally, larger than those obtained for OAK after

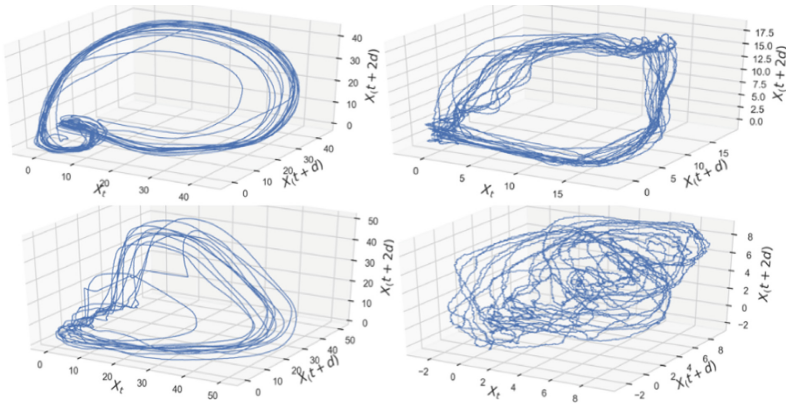


Fig. 7. State space reconstruction of a Subject’s joints (first row) and a Patient’s joints before surgery (second row) for normal walking on ground

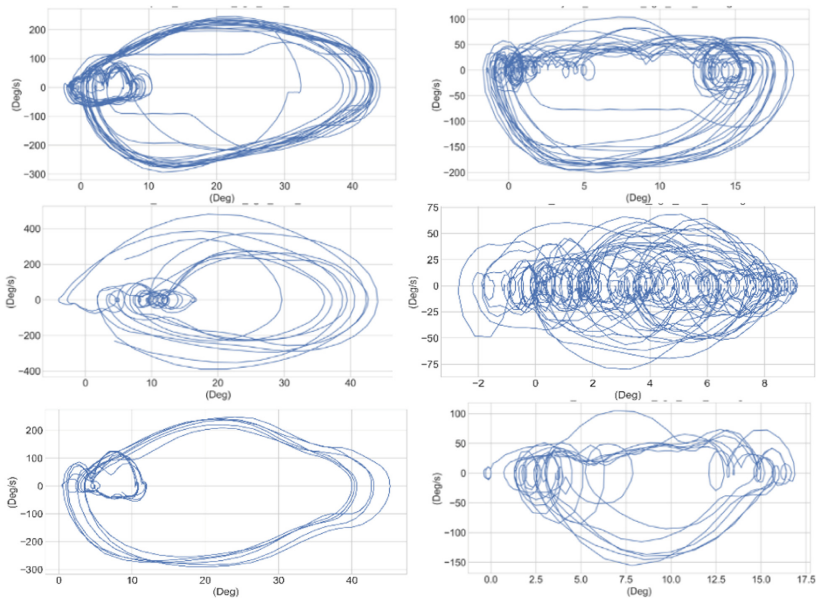


Fig. 8. Phase planes for right knee movements (fl-ext on left column and var-valg on right column) of Subject5 (first row) and of Patient2 before TKR (middle row) and after TKR (third row)

TKR, and larger than LEs computed for healthy knees. Larger values of LEs obtained for OAKs are explained by the influence of the pain and are associated with more divergence, more instability and variability, while smaller values obtained for healthy subjects reflect a stability, less divergence and less variability.

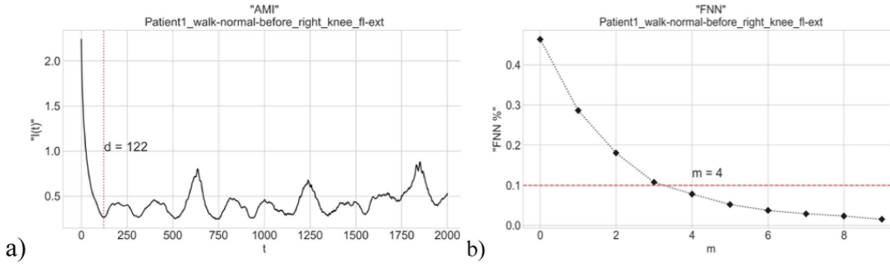


Fig. 9. a) AMI function diagram for patient 1; b) FNN diagram for patient 1

Table 2. Average values of Lyapunov exponents

Joint movement	Patients before TKR	Patients after TKR	Healthy subjects
Left knee fl-ext	2.109233408	1.686468872	1.774056786
Right knee fl-ext	1.626800786	1.292752718	1.577676677
Left knee var-valg	1.512875858	1.316156738	1.244535068
Right knee var-valg	1.667655977	1.272491764	1.002864274

6 Conclusions

In this paper, starting from the virtual model of the human knee joint and of an existent knee prosthesis, three virtual models of OAK–prosthesis assemblies are analysed and the stress maps are obtained. FEA is used to investigate the contact stresses in the components of total knee prosthesis. The parameterized virtual models of the knee prosthesis allow different changes in shape or dimensions, which means an advantage that can lead to the implant optimization and to the knee biomechanics improvement. The influence of prosthesis on the OAK stability and on the gait stability is positive, the LEs obtained for prosthetic OAK being smaller than those computed for OAK before TKR surgery.

References

1. Penrose, J.M.T.: Development of an accurate three dimensional finite element knee model. *Comp. Meth. Biomech. Biomed. Eng.* **5**, 291–300 (2002)
2. Tarnita, D., Catana, M., Tarnita, D.N.: Modeling and finite element analysis of the human knee joint affected by osteoarthritis. *Key Eng. Mater.* **601**, 147–150 (2014)
3. Donahu, T.L.H., et al.: A finite element model of the Human knee joint for the study of tibio-femoral contact. *J. Biomech. Eng.* **124**, 279–280 (2002)
4. Cafolla, D., Ceccarelli, M.: Design and simulation of humanoid Spine. *Mech. Mach. Sci.* **24**, 585–593 (2015)
5. Tarnita, D., et al.: Contributions on the modeling and simulation of the human knee joint with applications to the robotic structures. In: “New Trends on Medical and Service Robotics”, *Mechanisms and Machine Science* 20, pp. 283–297. Springer (2014)

6. Zach, L., Ruzicka, P., et al.: Stress analysis of knee joint endoprosthesis. *J. Biomech.* 40(S2) XXI ISB Congress, Poster Sessions, July 2007
7. Villa, T., et al.: Contact stresses and fatigue life in a knee prosthesis: comparison between in vitro measurement and computational simulations. *J. Biomech.* **37**, 45–53 (2004)
8. Tarnita, D., et al.: Effects of malalignment angle on the contact stress of knee prosthesis components, using finite element method. *Rom. J. Morphol. Embryol.* **58**(3), 831–836 (2017)
9. Liao, J.J., et al.: The effect of malalignment on stresses in polyethylene component of total knee prostheses—a finite element analysis. *Clin. Biomech. (Bristol)* **17**(2), 140–146 (2002)
10. Yang, R.S., Lin, H.J.: Contact stress on polyethylene components of a new rotating hinge with a spherical contact surface. *Clin. Biomech. (Bristol, Avon)* **16**(6), 540–546 (2001)
11. Tarnita, D., Pislă, D., et al.: Static and dynamic analysis of osteoarthritic and orthotic human knee. *J. Bionic Eng.* **16**, 514–525 (2019)
12. Tarnita, D., Catana, M., Dumitru, N., Tarnita, D.N.: Design and simulation of an orthotic device for patients with osteoarthritis. In: Bleuler, H., Bouri, M., Mondada, F., Pislă, D., Rodić, A., Helmer, P. (eds.) *New Trends in Medical and Service Robots. MMS*, vol. 38, pp. 61–77. Springer, Cham (2016)
13. Alexandru, C.: Optimal design of the mechanical systems using parametric technique & MBS (multi-body systems) software. *Adv. Mater. Res.* **463–464**, 1129–1132 (2012)
14. Pislă, D., et al.: Kinematics and design of a 5-DOF parallel robot used in minimally invasive surgery. *Adv. Robot Kinematics: Motion Man Mach. Part 2*, 99–106 (2010)
15. Carbone, G., Ceccarelli, M.: A serial-parallel robotic architecture for surgical tasks. *Robotica* **23**(3), 345–354 (2005)
16. Pislă, D., Plitea, N., et al.: Kinematical analysis and design of a new surgical parallel robot. In: 5th International Workshop on Comput. Kinematics 6–8 May, 2009, Duisburg, Germany (2009)
17. Cafolla, D., Chen, I.-M., Ceccarelli, M.: An experimental characterization of human torso motion. *Front. Mech. Eng.* **10**(4), 311–325 (2015). <https://doi.org/10.1007/s11465-015-0352-z>
18. Tarnita, D.: Wearable sensors used for human gait analysis. *Rom. J. Morphol. Embryol.* **57**(2), 373–382 (2016)
19. Tarnita, D., et al.: Applications of nonlinear dynamics to human knee movement on plane & inclined treadmill. *New Trends Med. Serv. Robots* **39**, 59–73 (2016)
20. Tarnita, D., Marghitu, D.: Nonlinear dynamics of normal and osteoarthritic human knee. *Proc. Romanian Acad.* **18**, 353–360 (2017)
21. Packard, N.H., Crutchfield, J.P., Farmer, J.D., Shaw, R.S.: Geometry from a time series. *Phys. Rev. Lett.* **45**, 712–716 (1980)
22. Nayfeh, A.H.: *Introduction to Perturbation Techniques*. Wiley-Interscience, NY (1981)
23. Fraser, A.M., Swinney, H.L.: Independent coordinates for strange attractors from mutual information. *Phys. Rev. vol. A* **33**, 1134–1140 (1986)
24. Kennel, M.B., Brown, R., Abarbanel, H.D.I.: Determining minimum embedding dimension using a geometrical construction. *Phys. Rev. vol. A* **45**, 3403–3411 (1992)
25. Rosenstein, M.T., Collins, I.J., Deluca, C.J.: A practical method for calculating largest Lyapunov exponents from small data sets. *Physics D* **65**, 117–134 (1993)



Dimensional and Workspace Analysis of RAISE Rehabilitation Robot

Doina Pislă¹(✉), Calin Vaida¹, Nicoleta Pop¹(✉), Ionut Ulinici¹, Alexandru Banica¹, Iosif Birlescu¹, Paul Tucan¹, Giuseppe Carbone^{1,2}, and Adrian Pislă¹

¹ CESTER, Technical University of Cluj-Napoca, Cluj-Napoca, Romania
{Doina.Pislă, Calin.Vaida, Nicoleta.Pop, Iosif.Birlescu, Paul.Tucan}@mep.utcluj.ro,
{Ionut.Ulinici, Alexandru.Banica}@omt.utcluj.ro,
Adrian.Pislă@muri.utcluj.ro

² DIMEG, University of Calabria, Rende, Italy
Giuseppe.Carbone@unical.it

Abstract. Stroke is a serious disabling affecting care problem worldwide. Unfortunately, the incidence of stroke is increasing which causes a growing demand for alternatives, mainly robotic assisted solutions. The major benefit of using robotic technologies in post stroke rehabilitation process is the ability to deliver high intensity customized training which improves motor and locomotor function. This paper focuses on lower limb rehabilitation and presents a parallel kinematic robot used for the hip, knee and ankle joints rehabilitation. For the developed robotic system, a dimensional analysis and synthesis of the robotic key components with the increase adaptability to different anthropometric characteristics as well as the mirroring of the system's workspace with the lower limb operational space is presented.

Keywords: Lower limb rehabilitation · Robotic assisted rehabilitation · Workspace · Modeling · Simulation

1 Introduction

According to [1], stroke is one of the main causes of death worldwide and is the leading cause of disability in the US. Conforming to MAR (Multi Annual Roadmap) the ageing population will increase from a 17.1% in 2008 to approximate 30% by the year of 2060 in people aged over 65 and similar from 4.4% to 12.1% in people aged over 80 [2].

In Romania, was stated in EHLEIS [3] that healthy ageing around age of 65 has decreased between 2007 – 2010 for the male gender from 7.7 to 5.9 years and for the female gender from 7.8 to 5 years.

Moreover, in Romania, the number of stroke patients treated in stroke units is only 1%, positioning the country on the last place among European countries, the first place being held by Sweden with 88%. In addition, it has been estimated that the number of

stroke events in Romania will increase from 60000 in 2015 to 80000 in 2035, placing it on the top 5 EU countries with the largest increase in the number of stroke cases [4].

All the above statistical data reveal several critical conclusions:

- in the next decades the medical system will be unable to treat the increased number of stroke patients,
- there is a clear need of a change in paradigm, to enable physician to treat more patients in the same time,
- the need for development of specialized robotic devices.

Many robotic devices that target lower limb rehabilitation are already available such as cable driven devices [5, 6], orthotic devices [7], exoskeleton based solutions [8], treadmill based [9] etc. According to [10], in the acute stage of post stroke, patients may not participate actively in the training therapy and this brings the necessity for the development of a system capable to rehabilitate the patient at its bed [17]. In the after stroke acute stage, so far, the development of the used robotic systems has received limited attention [11].

Based on these factors, there is a strong need for development of systems capable of performing rehabilitation exercises in the acute phase, offering intense training and for a large variety of patients. The paper [12] presents RAISE, a stationary training system used for lower limb rehabilitation for patients in the acute phase.

The paper presents the optimized dimensioning for the key components of the RAISE [12] system in order to become adaptable for treatment and dedicated to a large anthropomorphic variety of patients. The workspace of the system is also displayed so that the mirroring of the lower limb segments can be reflected into the robotic structure of the device.

The paper is structured as follows: Sect. 1 introduces the necessity of development for devices capable of robotic assisted acute post stroke assisted rehabilitation. Section 2 briefly describes the model of an innovative parallel kinematic robotic system, RAISE, respectively the Sect. 3 presents the anthropometric data of the lower leg and ankle. Section 4 continues with the dimensional analysis of the relevant robotic elements. Section 5 illustrates the system workspace of the system. Section 6 describes the validation of the RAISE system and Sect. 7 contains the preliminary conclusions.

2 RAISE Robotic Model for Lower Limb Rehabilitation

RAISE [16] is an innovative parallel kinematic robotic structure designed for lower limb robotic assisted rehabilitation, dedicated for patients in an acute post stroke state which cannot be lifted from bed within the rehabilitation process. The robotic system kinematic model and singularity analysis have been previously presented in [12]. This robotic architecture is dedicated to hip and knee flexion extension exercises designed for rehabilitation purposes, as well as ankle plantar flexion/dorsiflexion and the eversion/inversion, a brief understanding of the mechanism is presented in this section.

The robotic system is composed of two modules: one dedicated for the hip-knee motions (Fig. 1), and the second one dedicated for the ankle rehabilitation (Fig. 2).

From the kinematic point of view, the first module (Fig. 1 a), is structured into multiple kinematic chains [12]. The first two kinematic chains are presented with blue outline and the third is marked with orange.

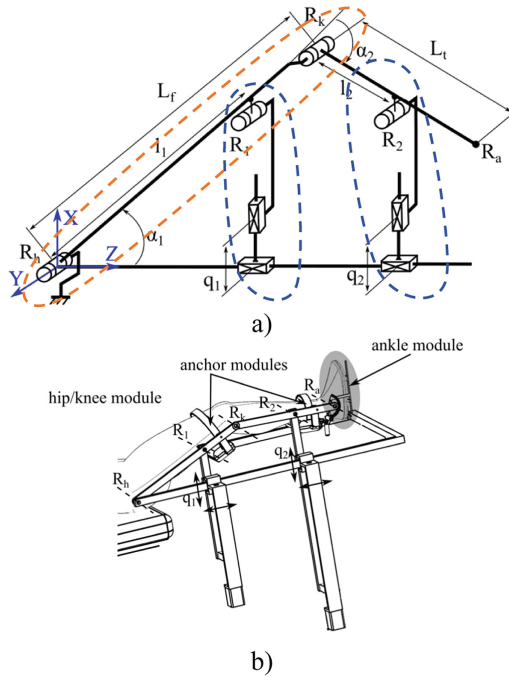


Fig. 1. Kinematic scheme of the system and CAD model [11]

1. The PPR type, one DoF linear chain, parallel to OX represented by q_1 and one passive rotation around OY of the R_1 joint – determining the flexion/extension motion of the hip.
2. The PPR type, also one DoF linear active chain, parallel to OX represented by q_2 and one passive rotation around OY of the R_2 joint – determining the flexion/extension motion of the knee.
3. The RR type with two passive revolutions around OY of the R_h and R_k joints – that represent the joints of the lower limb mirrored in the robotic structure.

Figure 1 b) represents the robotic system CAD model. The entire structure is supported by the frame positioned at the end of the therapeutical bed.

The patient’s leg is placed alongside the robotic system. The q_1 and q_2 joints which represent the active DoF for the first module, execute a vertical linear motion generation of resulting the passive rotation of the R_1 and R_2 joints. This motion is followed up by the next two passive rotations of the R_h and R_k , that are mirrored with the lower leg joints (respectively the hip and knee) and therefore the flexion and extension of the leg from the hip and the knee joints is achieved.

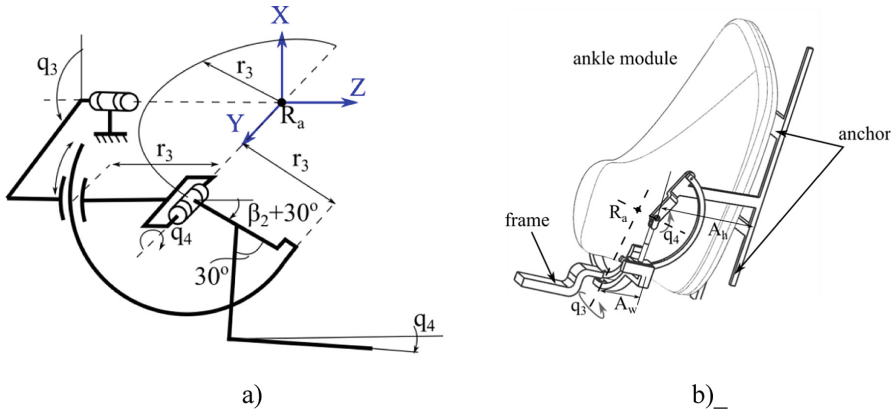


Fig. 2 Kinematic scheme and CAD of the ankle module [11]

The second module (Fig. 2) is responsible for the ankle rehabilitation. The kinematic scheme (Fig. 2 a) [12] has attached the coordinate system R_aXYZ attached at the ankle's center of rotation. In this case, the kinematic chain is of RR type with the active rotations DoF q_3 (around the R_aZ axis) and q_4 (around the R_aY axis) resulting in the plantar flexion – dorsiflexion and the eversion – inversion rehabilitation motions. The CAD model is represented in Fig. 2 b). The patient's feet are attached to the module frame in an ergonomic position. This module has 2 active DoF composed by the q_3 and q_4 joints. The rotational motion of those joints performs the plantar flexion/dorsiflexion and the eversion/inversion of the ankle.

When leg rehabilitation motions are performed, the ankle module is in a standstill position, attached to the leg module. While the ankle module coordinate system will rotate around the R_aY axis with the α angle result in a change of direction for the R_aZ axis. The inverse kinematic model uses the medical data motion amplitudes, as computational input values.

Using the inverse kinematic model [12], the values for the $\alpha_1, \alpha_2, \beta_1, \beta_2$ angles represent the input data of the problem, with the $q_1 - q_4$ as actuated DoF, and l_f, l_t, l_1, l_2 as geometric parameters. Considering the q_1, q_2 presented in [12], the final Eqs. (1), (2) of the system model are:

Equations for the hip joint

$$X_{Rh} = 0, \quad Y_{Rh} = 0, \quad Z_{Rh} = 0 \tag{1}$$

Equations for the knee joint

$$X_{Rk} = L_f \cdot \frac{q_1}{l_1}, \quad Y_{Rk} = 0, \quad Z_{rk} = L_f \cdot \left(1 - \frac{q_1}{l_1}\right) \tag{2}$$

Equations for the ankle joint:

$$X_{Ra} = L_f \cdot \frac{q_1}{l_1} + l_2 \cdot \sin(\alpha_1 - \alpha_2) \tag{3}$$

$$\begin{aligned}
 Y_{Ra} &= 0, & Z_{Ra} &= q_2 - \cos(\alpha_1 - \alpha_2)(l_1 - l_2) \\
 q_3 &= \beta_1, & q_4 &= \beta_2
 \end{aligned} \tag{4}$$

3 Anthropometric Data for the Lower Limb and Motion Amplitudes

Considering the kinematic model, the geometrical parameters, l_f and l_t , which represent the length of the femur and the length of tibia, can be modified in a way that the system adapts to the different anthropometric characteristics.

Table 1 and Table 2 show the calculated lengths for body segments, such as: upper leg, lower leg and ankle, using the Contini Model. The limb segment values are based on patient heights, ranging from 140 cm to 190 cm [13].

Table 1. The length of lower limb segments [13]

Patient's height [cm]	Upper leg [cm]		Lower leg [cm]	
	Female	Male	Female	Male
140	33.32	34.3	39.48	39.9
150	35.7	36.75	42.3	42.75
160	38.08	39.2	45.12	45.6
170	40.46	41.65	47.94	48.45
180	42.84	44.1	50.76	51.3
190	45.22	46.55	53.58	54.15

Table 2. Ankle dimensions [11]

Patient's height [cm]	Ankle height [cm]		Ankle width [cm]	
	Female	Male	Female	Male
140	6.72	6.02	7.98	7.7
150	7.2	6.45	8.55	8.25
160	7.68	6.88	9.12	8.8
170	8.16	7.31	9.69	9.35
180	8.64	7.74	10.26	9.9
190	9.12	8.17	10.83	10.45

The motion amplitudes of the lower limb joints representing the maximum angular ranges that can be achieved, without causing any unwanted muscular strain for the patient,

are presented in Table 3. The registered values are pivotal for the development of a robotic rehabilitation device, as these influence the mechanical structures, the actuation solutions and the safety margins within which the device operates.

Table 3. The motion amplitudes of the lower limb for rehabilitation exercises [12].

Joint	Rehabilitation motions	Angular ranges	Corresponding rotation with the robotic element
Hip	Flexion	0°–80°	Joint R _h along the OY axis
	Extension	0°–5°	
Knee	Flexion	0°–80°	Joint R _k along the OY axis
Ankle	Dorsiflexion	0°–20°	Joint R _a q ₄ along the R _a Y axis
	Plantar flexion	0°–35°	
	Inversion	0°–20°	
	Eversion	0°–20°	Joint R _a q ₃ along the R _a Z axis

4 Dimensioning of the Key Components of the RAISE System Using the Anthropomorphic Data

In order to possess the ability to work with various patients, the system must have the key components dimensioned so that they fit various anthropometric lower limb data of the patients. The dimensioning procedure will take place for the first module’s elements, and for the ankle module. Accordingly to the kinematic model, the constructive elements L_f and L_t have to be determined for a variety of upper leg patient data whereas ankle_h and ankle_w are the key components for the ankle module.

The human limb segments have been dimensioned using the standard deviation.

Considering a variable vector A made of N scalar observation, the standard deviation, σ, may be defined as:

$$\sigma = \sqrt{\frac{1}{N - 1} \sum_{i=1}^N |A_i - \mu|^2} \tag{5}$$

Whereas μ represents the mean value:

$$\mu = \frac{1}{N} \sum_{i=1}^N A_i \tag{6}$$

The upper leg values from (Table 1) have been used to determine the interval of the element length of L_f. The numerical values were σ_{femur}, μ_{femur} (dimensions in cm). For the upper segment of the lower limb (femoral part) the extreme values (min/max) of the considered patient data (Table 1) lie within 2 X σ_{femur} from the mean value (μ_{femur}).

To ensure a broader group of patients it was decided that the parameters interval was extended to three standard deviations yielding the interval that can be seen in Table 3, which also represents the dimensioning interval for L_f .

Considering the lower segment of the lower limb the values from (Table 1) have been used to determine the interval of the robotic system constructive element L_t . The resulting numerical values were σ_{tibia} , μ_{tibia} (cm). In the lower segment case, the extremity values (min/max) of the used group are also within the range of $2 \times \sigma_{tibia}$ from the mean value μ_{tibia} . The same procedure has been used for the case of the lower segment of the limb and of the upper segment.

For robotic system ankle module, two variable dimensions are used. The respective segment of the patient is kept fixed and as ergonomic as possible to ensure correct rehabilitation exercises without damage in any way the patient’s joints. In this case, the width and the height of the patient’s ankle are considered and the constructive elements of the robot should be designed in such a manner that the ankle module will be adaptable to the patient’s ankle dimensions. For these reasons, using the data from Table 2, the values have been grouped for both female and male subjects for the ankle heights and separately for ankle widths. The standard deviation of each group has been calculated σ_{ankle_h} , σ_{ankle_w} together with the corresponding mean values. The extremities (min/max) values were found within $2 \times \sigma_{ankle_h}/\sigma_{ankle_w}$ and therefore the intervals were calculated using $3 \times \sigma_{ankle_h}/\sigma_{ankle_w}$ for each of the two individual provided dimensions.

The following table (Table 4) presents a summary of the calculated values and the resulted intervals for the robot’s constructive elements of interest.

Table 4. Summary of dimensional values for the robotic system.

Lower limb segments	Standard deviation	Mean Value	Adjustable robot dimensions [cm]	Key components
Upper leg	4.35	39.84	25–52	L_f
Lower leg	5.06	46.77	31–61	L_t
Ankle height	0.92	7.50	4–10	Ankle_h
Ankle width	1.01	9.24	6–12	Ankle_w

Besides the above mentioned components, the system elements l_1 and l_2 of the system must be considered for dimensioning as well, and for this reason we can take into account the following cases:

- Case 1: $R_1-R_k = \text{constant}$, then $l_1 < [25-52] \text{ cm} + \zeta(\text{interval of the } l_f \text{ element determined by the above calculations})$ where, ζ represents a dimensional tolerance for the mechanical components
- Case 2: $l_1 = \text{constant}$, meaning that $R_k-R_1 = l_f - l_1$ where $l_f = [25-52] \text{ cm}$
- Case 3: $R_2-R_a = \text{constant}$, then $l_2 < l_t = [31-61] \text{ cm} + \zeta$
- Case 4: $l_2 = \text{constant}$, meaning that $R_2-R_k = l_t - l_1$ where $l_f = [31-61] \text{ cm}$
- Case 5: ankle_h (Fig. 2) = $[4-10] \text{ cm}$ – this defines the element for the ankle height values interval

- Case 6: ankle_w (Fig. 2) = [6–12] cm – this defines the element for the ankle width values interval

5 Workspace Modeling of RAISE Robot

The RAISE system [16] can mirror the lower limb motions, and therefore the workspace is important in motion zones and interference zones identification, as long as is defined as a no singularities space for safety reasons, as it was demonstrated in [12]. The data flow to generate the robotic workspace has been obtained using the inverse kinematic model of the system. The rehabilitation device is capable of moving the limbs beyond their natural operating ranges leading to unwanted damage [14]. For this reason the motion amplitudes have been defined with lower values than those of healthy subjects, the flexibility of a post stroke patient cannot be achieved equally. With the above considerations, the workspace of the system for the leg module can be seen in Fig. 3, respectively the ankle module in Fig. 4.

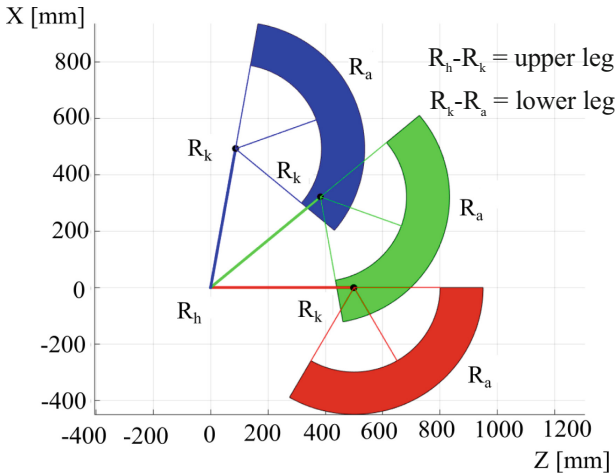


Fig. 3 Workspace for the leg module

The workspace of the leg module has been defined considering 3 cases for the upper leg (R_h-R_k) position in the following angles: red color (intermediate gray) = horizontal position of the upper leg, green color (light gray) = 40° angle of the upper leg, and in blue color (dark grey) = 80° of the upper leg whereas R_k-R_a is the lower leg segment represented by the flexion extension of the lower leg from the knee joint. The workspace of the ankle module is represented as 3D plot due to the existence of two rotational motions from the system active joints q_3 and q_4 in two different geometrical planes. The revolute motions are around the R_aZ and R_aY axis. The red hatch represents the plantarflexion-dorsiflexion motion and the blue hatch represents the eversion-inversion one.

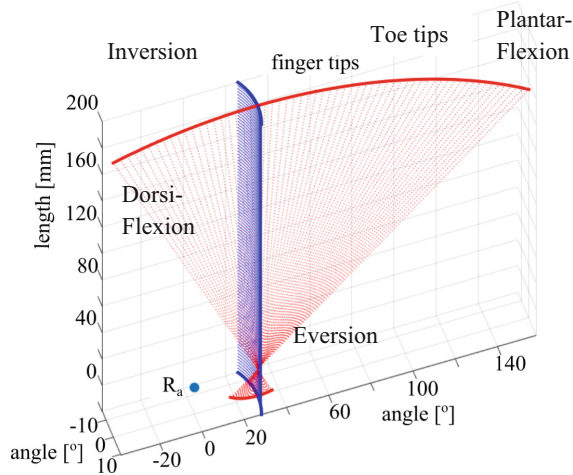


Fig. 4. Workspace for the ankle module

6 Validation of the RAISE Structure

The experimental model of the RAISE robotic device is presented in the figure below. Figure 5 a) illustrates the experimental model of the hip-knee rehabilitation module, while Fig. 5 b) presents the experimental model of the ankle rehabilitation module.



a) experimental model of the hip-knee rehabilitation module



b) experimental model of the ankle rehabilitation module

Fig. 5. Experimental model of RAISE robotic system

The proof that validates the RAISE [15] model shows that:

- The limb and the robotic system should be capable of motions below the level of the therapeutical bed;

- All the actuation systems are going to be placed towards the exterior of the limb to allow the development of a solution for both lower limbs;
- The structure will be used for other trauma that lead to the loss of mobility in one or both limbs.

7 Conclusions

The paper provides a dimensional analysis of the key elements of RAISE an innovative parallel-kinematic lower limb rehabilitation robot. With the combination of the anthropometric data gathered from the Contini models and the calculated standard deviation and mean values, the dimensional analysis for the key components of the system has been achieved. Moreover, the consideration of the workspace of the robotic system illustrates the capability of the system to select and apply desired rehabilitation motions and mirroring the robotic structure with the lower limb segments. Future research work will include the study of the complex and combined therapeutic exercises and constructive design.

Acknowledgments. The paper presents results from the research activities of the project ID 37_215, MySMIS code I03415 “Innovative approaches regarding the rehabilitation and assistive robotics for healthy ageing” co-financed by the European Regional Development Fund through the Competitiveness Operational Programme 2014-2020, Priority Axis 1, Action 1.1.4, through the financing contract 20/01.09.2016, between the Technical University of Cluj-Napoca and ANCSI as Intermediary Organism in the name and for the Ministry of European Funds.

References

1. Lopez-Meyer, P., et al.: Automatic detection of temporal gait parameters in post stroke individuals. *IEEE Trans. Inf. Tech. Biomed.* **15**, 594–601 (2011)
2. Robotics Multi-Annual Roadmap 2014–2020
3. Steven, E., et al.: The burden of stroke in Europe Report King’s College London for the Stroke Alliance for Europe (2017)
4. Robine, J.: European Health and Life Expectancy Information System, Issue 6. Health expectancy in Romania, EHLEIS Country Reports France (2013)
5. Cafolla, D., et al.: CUBE, a Cable-driven Device for Limb Rehabilitation. *J. Bionic Eng.* **16**(3), 492–502 (2019)
6. Cafolla, D., et al.: 3D printing for feasibility check of mechanism design. *Int. J. Mech. Control* **17**(1), 3–12 (2016)
7. Tarnita, D., Catana, M., Dumitru, N., Tarnita, D.N.: Design and simulation of an orthotic device for patients with osteoarthritis. In: Bleuler, H., Bouri, M., Mondada, F., Pisla, D., Rodić, A., Helmer, P. (eds.) *New Trends in Medical and Service Robots. MMS*, vol. 38, pp. 61–77. Springer, Cham (2016)
8. Geonea, I., Tarnita, D.: Design and evaluation of a new exoskeleton for gait rehabilitation. *Mech. Sci.* **8**(2), 307–322 (2017)
9. Díaz, I., et al.: Lower-limb robotic rehabilitation: literature review and challenges. *J. Robot.* **2011**, 1–11 (2011)

10. Brandstater, M., Shutter, L.: Rehabilitation interventions during acute care of stroke patients. *Top. Stroke Rehabil.* **9**, 48–56 (2002)
11. Poli, P., et al.: Robotic technologies and rehabilitation: new tools for stroke patients' therapy. *Biomed. Res. Int.* **2013**, 1–8 (2013)
12. Vaida, C., et al.: Raise – an innovative parallel robotic system for lower limb rehabilitation. *New Trends Med. Serv. Robot., MMS* **65**, 293–302 (2019)
13. Drillis, R., Contini, R.: Body segment parameters, New York, USA, (1996)
14. Carbone, G., et al.: Design Issues for an Inherently Safe Robotic Rehabilitation Device, *MMS*, 49. Springer, Cham (2018)
15. Pisla, D., et al.: Parallel robot for lower limb rehabilitation, A/00334/04.06.2019 (2019)
16. Vaida, C., Birlescu, I., Pisla, A., Ulinic, I., Tarnita, D., Carbone, G., Pisla, D.: Systematic design of a parallel robotic system for lower limb rehabilitation. *IEEE Access* **8**, 34522–34537 (2020)
17. Gherman, B., Birlescu, I., Plitea, N., Carbone, G., Tarnita, D., Pisla, D.: On the singularity-free workspace of a parallel robot for lower-limb rehabilitation. *Proc. Rom. Acad.* **20**(4), 383–391 (2019)

Mechanisms for Minimally Invasive Techniques



On the Collision Free-Trajectories of a Multiple-needle Robot Based on the Fibonacci Sequence

Ciprian Dragne¹ (✉), Veturia Chiroiu¹, Ligia Munteanu¹, Cornel Brişan², Cristian Rugină¹, Rodica Ioan¹, Nicolae-Doru Stănescu³, and A. Florentin Stan³

¹ Institute of Solid Mechanics, Romanian Academy, Bucharest, Romania
ciprian_dragne@yahoo.com, veturiachiroiu@yahoo.com,
ligia_munteanu@hotmail.com, rugina.cristian@gmail.com,
rodicaioan08@yahoo.com

² Technical University of Cluj-Napoca, Cluj-Napoca, Romania
cornel.brisan@yahoo.com

³ University of Piteşti, Piteşti, Romania
s_doru@yahoo.com, stanalin91@gmail.com

Abstract. We study a model for a multiple-needle robot based on the Fibonacci sequence scaling. The paper determines the collision-free trajectories of the robot who is carrying drugs into a tumoral target. The purpose of the paper is to predict the insertion trajectories for all needles so as the trajectories should avoid the collisions to ribs, blood vessels and tissues in the abdominal area, the interference between trajectories and finally, to reach the target. Comparison with genetic algorithm and the particle swarm optimization algorithm are performed.

Keywords: Fibonacci sequence · Collision-free trajectories · Surgery

1 Introduction

This paper presents a model for a multiple-needle robot whose collision-free trajectories scale according to the Fibonacci sequence. This robot is designed to carry out drugs into the tumoral liver target. The trajectories are determined by using the restrictions of avoiding the collisions with blood vessels, ribs and surrounding tissues, and also the interference of needles with each other.

The trajectory of each needle $j = 1, \dots, n$, is defined as a set of segments connecting the insertion point with the tumor. Two binary control parameters are introduced on each needle. The first parameter is the length of the k^{th} segment of the j^{th} needle's trajectory, $l_{kj} = f_k / r_{kj}$, where f_k is the k^{th} Fibonacci number and r_{kj} a scaling number. The second control parameter is the angle ω between the current needle and the previous one, $\omega \in (0, \pi)$ [1, 2].

Fibonacci introduced in 1202 the sequence who received his name, as the following hypothetical situation: "A man put a pair of rabbits in a place surrounded by a wall. How

many pairs of rabbits can be produced from that pair in a year, if each month each pair gives birth to a new pair that becomes productive from the second month?" [3, 4]. When Fibonacci examines this issue, he discovered a sequence of numbers which involves the number of pairs of rabbits. The sequence terms in the Fibonacci problem are 1, 1, 2, 3, 5, 8, 13, 21, 34, 55, 89, 144. Based on the Fibonacci's findings, it is clear that each term is a sum of two preceding sequence term [4]. In fact, the sequence can be recursively defined in the form $f_n = f_{n-1} + f_{n-2}$, $f_0 = 0$, $f_1 = 1$. The limit of the ratio of two consecutive terms in the Fibonacci string tends to the gold ratio $\varphi = (1 + \sqrt{5})/2$.

The Fibonacci sequence was highlighted in nature for example in the arrangement of the flower petals, in seeds and in the spiral arrangement of pine cones and pineapple. The keys on a piano are divided into Fibonacci numbers, and numerous classical compositions implement the golden section. Such an example is found in the Alleluia Choir in Handel's Messiah and in many of Chopin's preludes [5].

2 Model

The using of not only a single needle but also of several needles in surgery is analyzed by many researchers especially for large liver tumor treatment [6, 7]. The needles are inserted one by one and must avoid the collision with the tissues, blood vessels, ribs and previously inserted needles.

Development of a target drug delivery technique usually consisted of three steps. In step 1, a 2D ultrasound image of the tumor is obtained. The size and position of the tumor are analyzed by the surgeon who decides the number of required needles. In step 2, the insertion points on the skin of the needles and the positions of the targets in the tumor are established. In step 3, once the needles are placed at the target points on the skin, they are guided according to a precise surgical planning based on the optimization of the collision-free trajectories to avoid the ribs, blood vessels and tissues in the abdominal area.

Figure 1 shows three needles and the environment containing the organs, ribs, blood vessels and the target point. The base coordinate frame is established on the first needle with the vertical axis Oz and the origin in the insertion point (Fig. 2). The workspace boundary is a 1D curve in each xy -plane, i.e. the z_h -plane for $z = h$, $h \in [0, h_{\max}]$ with a clinical value $h = 200$ mm. The S is the plan of the first needle-insertion trajectory, (θ_k, φ_k) are the rotation angles with respect to y and z axes $\theta_{\min} \leq \theta_k \leq \theta_{\max}$, $\varphi_{\min} \leq \varphi_k \leq \varphi_{\max}$ [8]. Related issues can also be found in [9, 10].

The first control parameter is the length of the k^{th} segment of the j^{th} needle, $l_{kj} = f_k/r^{kj}$, $k = 1, \dots, m_{lk}$, $j = 1, \dots, n$ where f_k is the k^{th} Fibonacci number

$$f_0 = f_1 = 1, f_{k+2} = f_{k+1} + f_k, k \geq 0. \quad (1)$$

and r_{kj} a scaling number. The second control parameter is the angle φ between the current needle and the previous one, $\varphi \in (0, \pi)$ [6].

The kinematic constraint of the j^{th} needle, $j = 1, \dots, n$, is given by

$$\phi = \begin{bmatrix} x_j - x_{0j} - \delta_{xj} - (h - z_{0j} - \delta_{zj}) \tan \theta_j \cos \varphi_j \\ y_j - y_{0j} - \delta_{yj} - (h - z_{0j} - \delta_{zj}) \tan \theta_j \cos \varphi_j \end{bmatrix} = 0, \quad (2)$$

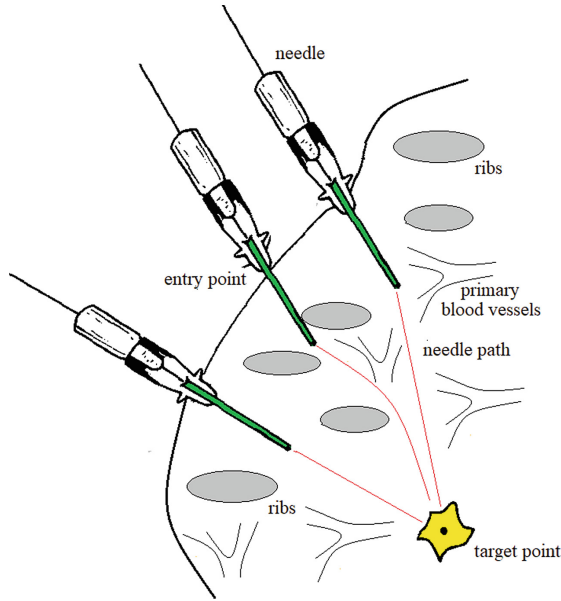


Fig. 1. Diagram of the surgery 3D environment

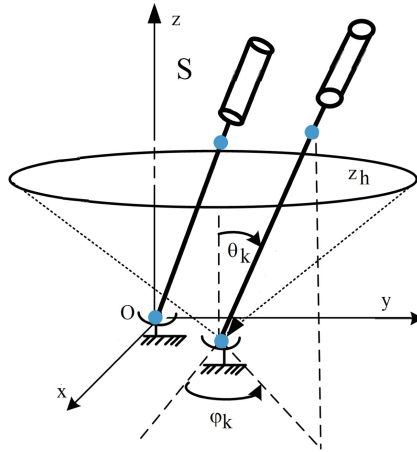


Fig. 2. The base coordinate frame

where $[x_{0j} + \delta_{xj}, y_{0j} + \delta_{yj}, z_{0j} + \delta_{zj}]^T$ is the actual target of the tip of needle $(j - 1)$, (θ_j, φ_j) are the rotation angles with respect to y and z axes $\theta_{\min} \leq \theta_j \leq \theta_{\max}$, $\varphi_{\min} \leq \varphi_j \leq \varphi_{\max}$ and $(\delta_{xj}, \delta_{yj}, \delta_{zj})$ denote the deformation of the liver.

The choice of the scaling number r_{kj} is done by a binary control

$$l_{kj} = \|x_k - x_{k-1}\| = \frac{u_{ki} f_k}{r^{kj}}. \tag{3}$$

By introducing the binary control

$$\omega_m = v_m \omega, \tag{4}$$

the angle between the $(m - 1)^{\text{th}}$ and the m^{th} needles is $\pi - \omega_k$.

The geometric relation between the coordinate system of the $(m - 1)^{\text{th}}$ and the m^{th} needles, $m = 1, \dots, n$, is

$$A_m = \begin{pmatrix} \cos \omega_m & -\sin \omega_m & 0 & \frac{u_m f_m}{r^m} \cos \omega_m \\ \sin \omega_m & \cos \omega_m & 0 & -\frac{u_m f_m}{r^m} \cos \omega_m \\ 0 & 0 & 1 & 0 \\ 0 & 0 & 0 & 1 \end{pmatrix}. \tag{5}$$

The relation between the base coordinate frame $Oxyz$ associated to the first needle and the other coordinate frames associated to the rest of the needles, is

$$T_m = \prod_{j=0}^m A_j. \tag{6}$$

The possible collision point between the needle and the tissue is analyzed by an identifier to check the minimum distance between needle and the surrounding tissue [12, 13]. The minimum distance is expressed as

$$\min \left(\frac{1}{2} (r_1 - r_2)^T (r_1 - r_2) \right), \tag{7}$$

With $g_1(r_1) \leq 0$, $g_2(r_2) \leq 0$, r_1, r_2 , the position vectors of two points belonging to the needle and the tissue, respectively, and g_1, g_2 , the surfaces to the needle and the tissue, respectively. The interference distance or penetration is defined as

$$\min(-d), \quad g_1(r_1) \leq -\frac{d}{2}, \quad g_2(r_2) \leq -\frac{d}{2}, \tag{8}$$

where d is the penetration. The configuration of the collision-free trajectories of each needle is defined as a sequence of trajectories corresponding to a particular choice for the control (u, v) . The set of all collision-free trajectories are computed based on the kinematic constraint (2) as

$$R = \left\{ \sum_{k=0}^n \frac{u_k f_k}{r^k} \exp(-i\omega \sum_{j=0}^k v_j |v_j \in \{0, 1\}) \right\}. \tag{9}$$

A collision-free needle trajectory for a certain needle given by (9) can be associated to a navigation system. In the simulation, three needle-insertion trajectories were obtained.

The optimisation techniques often faces difficulties briefly suggested in Fig. 3. The small bubbles represent possible solutions, arrows mean new solutions found by applying one search operation to the first one. Figure 3a is the best case for optimization. Figure 3b shows a low total variation, while Fig. 3c and Fig. 3d show a multimodal case with

multiples local minima and the rugged case, respectively, where there are no useful gradient information. Figure 3e presents in the middle of the graph surrounded by a green circle, a region with misleading gradient information, and Fig. 3f shows in the middle of the graph surrounded by a green circle, a neutral area. Figure 3g shows an isolated minimum at the green point and a neural area without much information inside the green circle, the last image being a disaster and a nightmare for optimization [12].

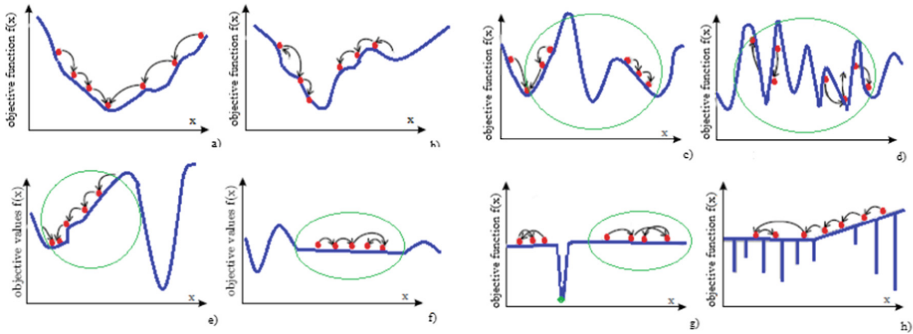


Fig. 3. Different properties of optimization problem

The brute force optimization, the controlled random search optimization, the Culling algorithm and the differential dynamic logic optimization are the most popular optimization techniques [12]. The techniques classified as intelligent such as the genetic algorithms, the particle swarm optimization and the neural networks, significantly reduce the difficulty of solving the optimization problems.

The genetic algorithms are inspired by the genetics of the mechanisms from the natural systems. They keep the information regarding the populations in individual encoded information that evolves in time. The particle swarm optimization is a stochastic optimization technique which simulates the behavior of birds flocking and fish schooling, while neural networks mimics the computational model of the brain.

In this article, we test the genetic algorithm and the particle swarm optimization, and beyond these algorithms, another one based on the Fibonacci sequence scaling. The reason of the choice it consists in the small number of iterations in comparison to the above-mentioned algorithms.

3 Results

As application, the case of a tumor with a difficult location in the vicinity of the portal tree of the vascular territory in the liver, is considered (Fig. 4a). The tumor image seen on the microscope is shown in Fig. 4b. White and grey denote forbidden areas while the shade of purple are safe regions. The tumor is drawn in red. The genetic algorithm, the particle swarm optimization and the Fibonacci algorithm are applied to a three-needles robot with restrictions to avoid the collision with the tissues, blood vessels, ribs and previously inserted needles.

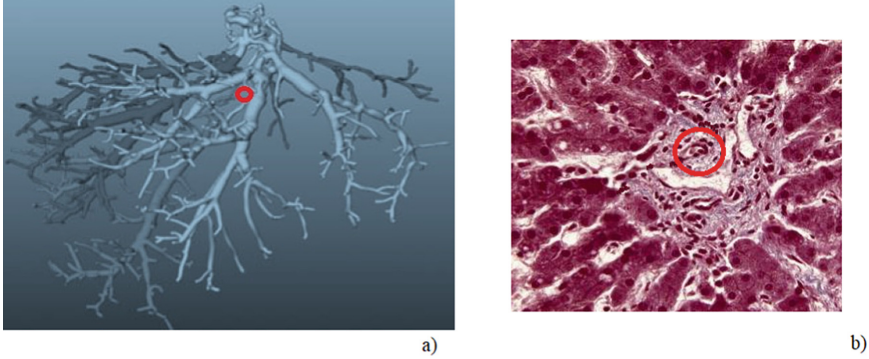


Fig. 4. a) Location of the tumor; b) Tumor image seen on the microscope

The task of our simulation is to determine the boundaries of each needle as a *collision-free surface* which represents the feasible insertion area based on given constraints. Then, the optimal trajectory of each needle can be chosen in this surface automatically.

Two simultaneously distinct system of coordinates are introduced for each needle, i.e. a fixed system with origin O and axes Ox_1, Ox_2, Ox_3 . In this system a point belonging to the collision-free surface is $(x_1, x_2, x_3) \equiv (x, y, z)$. The second system of coordinates is a current system with origin in an arbitrary centre O' of coordinates x_G, y_G, z_G of the needle. In this system a point belonging to the needle is $(x'_1, x'_2, x'_3) \equiv (x', y', z')$. The orientation of the axes x'_1, x'_2 (usually randomly oriented) is determined by the angle ψ . The needle rotates about the vertical x'_3 -axis. The transformation from (x', y', z') to (x, y, z) is given by

$$x_i = u_i + R_{ik}x'_k, \quad (10)$$

where R_{ij} is the rotation matrix

$$R = R(z, \varphi)R(x, \theta)R(z, \psi),$$

with

$$R(z, \psi) = \begin{bmatrix} \cos \psi & -\sin \psi & 0 \\ \sin \psi & \cos \psi & 0 \\ 0 & 0 & 1 \end{bmatrix}, \quad R(x, \theta) = \begin{bmatrix} 1 & 0 & 0 \\ 0 & \cos \theta & -\sin \theta \\ 0 & \sin \theta & \cos \theta \end{bmatrix},$$

$$R(z, \varphi) = \begin{bmatrix} \cos \varphi & -\sin \varphi & 0 \\ \sin \varphi & \cos \varphi & 0 \\ 0 & 0 & 1 \end{bmatrix}, \quad (11)$$

and u the translation vector. The unknown *collision-free surface* Γ is defined as a n -ellipsoid [14–16]. The goal of the optimization problem is to find Γ such that (8) and (9) to be fulfilled.

An n -ellipsoid has 10 shape parameters $d_i, i = 1, 2, \dots, 10$ defined as: arbitrary center coordinates x_G, y_G, z_G , principal axes a, b, c , the principal directions defined by Euler

angles ξ , ψ , ζ and the exponent n . The Γ is the image of the unit n -sphere S of equation

$$x^n + y^n + z^n = 1, \quad (12)$$

through the affined transformation

$$y = (Y_1, Y_2, Y_3) \in S \rightarrow y = (y_1, y_2, y_3) \in \Gamma, \quad (13)$$

$$\begin{aligned} y_1 &= x_G + r_{11}aY_1 + r_{12}bY_2 + r_{13}cY_3, \\ y_2 &= y_G + r_{21}aY_1 + r_{22}bY_2 + r_{23}cY_3, \\ y_3 &= z_G + r_{31}aY_1 + r_{32}bY_2 + r_{33}cY_3, \end{aligned} \quad (14)$$

where $r_{ij} = r_{ij}(\xi, \psi, \zeta)$ are the rotation components which transforms the coordinate axes into the principal axes of the ellipsoid. These components are given by (11) by replacing θ with ξ , and φ with ζ .

The principle of the optimization problem is: the *collision-free surface* Γ is embedded in a 3D box. Inside this box, a volumetric grid of points is defined, which links the box to the needle. A function named *the deformation function* will describe the deformation of the box during the needle movement in compliance with all restrictions, and consequently the modification of Γ during iterations. In other words, the box is *deformed* during the needle motion, and so, the optimum solutions will give the position of each point of Γ .

This is modeled as $X = BP$, where B is *the deformation matrix* $ND \times NP$ (ND is the number of points on the discretised n -ellipsoid and NP is the number of control points of the grid), P is a matrix $NP \times 3$ which contains coordinates of the control points and X is a matrix $ND \times 3$ with coordinates of the model points.

The optimization problem is defined as: first compute a displacement field δX between the n - ellipsoid and $3M$ point data, and then, after having put the n -ellipsoid in a 3D box, search for the *deformation* δP of this box which will best minimize the displacement field δX [17]

$$J(\Gamma) = \min_{\delta P} \|B \delta P - \delta X\|^2. \quad (15)$$

Once all needles are placed at the predetermined epidermis and the ordering of entry is chosen to be 1, 2 and 3, following the first needle's insertion, the operation is repeated for the needles 2 and 3.

Firstly, (15) is solved by using a genetic algorithm. The numerical experiments show that the solution is obtained after 117 iterations (Fig. 5). Three sets of solutions are obtained after 51 iterations and two set of solutions after 100 iterations.

Next, the particle swarm optimization algorithm is applied. The Θ point represents the solution obtained after 93 iterations (Fig. 6).

The last applied algorithm is the Fibonacci. The insertion scheme is determined by using the Fibonacci spirals. A set of free-collision trajectories (red) in the immediate vicinity of the epidermis, is suggested. From these possible collision-free trajectories (red) the green paths corresponding to the Fibonacci spirals (black) are chosen. These trajectories avoid the blood vessels (purple) and the coasts (brown) in all directions until the tumor (Fig. 7).

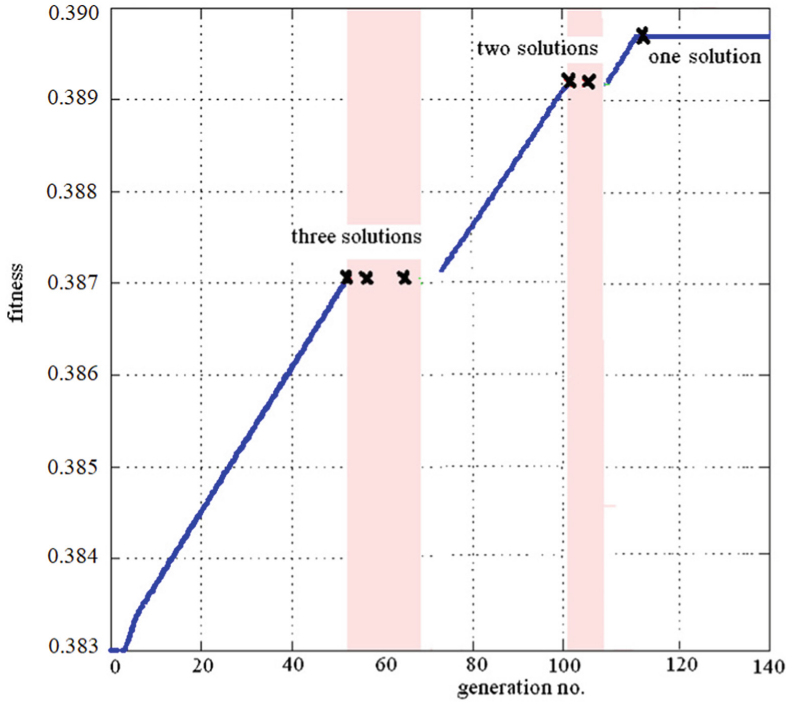


Fig. 5. Number of solutions of the genetic algorithm.

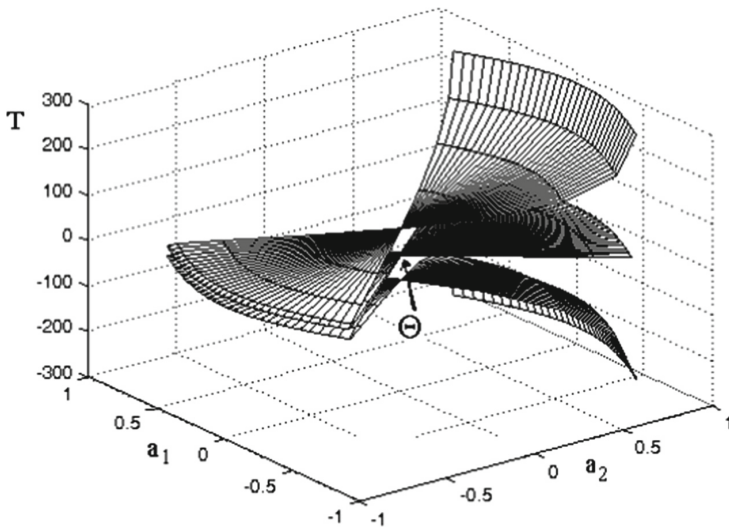


Fig. 6. The point Θ corresponding to the minimum value of the problem

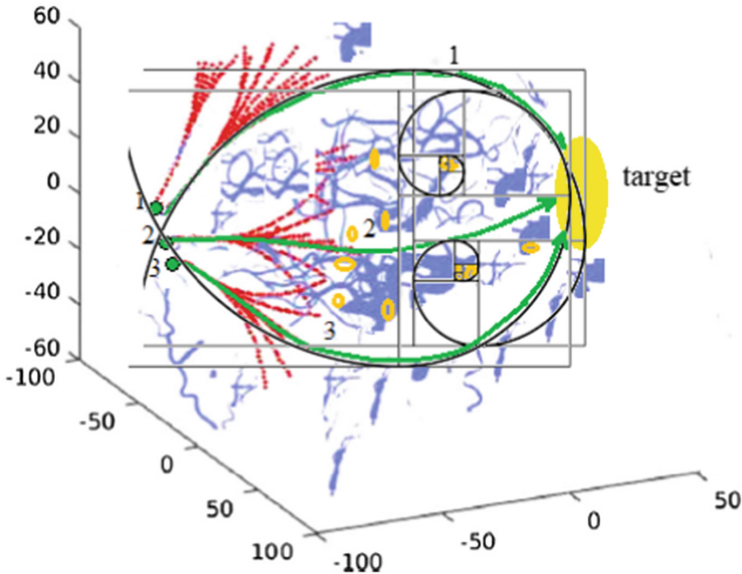


Fig. 7. Simulation of the collision-free trajectories for a three-needle robot.

The Fibonacci spirals with the centers in ribs (brown) are displayed for needles 1 and 3. For the needle 2, the Fibonacci diagram comes out of the graph and for the sake of simplicity, it has not been shown. The Fibonacci algorithm reaches the optimum after 50 iterations.

It follows now the comparisons between the results obtained by applied methods. All the algorithms have led to the same optimal solution with 3 collision-free trajectories to the target, presented in Fig. 8, as yellow circles. The convergence is very good for all three methods. The number of iterations for each method is presented in Fig. 9. We observe that Fibonacci algorithm reaches the optimum after the smallest number of iterations.

We end with a possible conflict situation in which the trajectories of the needles can intersect but not at the same time. We simulate this situation with the Fibonacci algorithm. The algorithm carefully simulates this conflict situation that may occur in the way of the needle. For example, the sporadic crossing of a needle path may be accepted only if the surgery conditions are met, but permanent the placement of a needle at same location may not be accepted. Figure 10 presents this critical case when the trajectories of the B and C needles intersect, but without causing the surgical program. If the purpose of a needle is to reach a certain space, the other needles cannot reach this space. In the presence of obstacles, the needle sometimes has to move away from goal to finally achieve it.

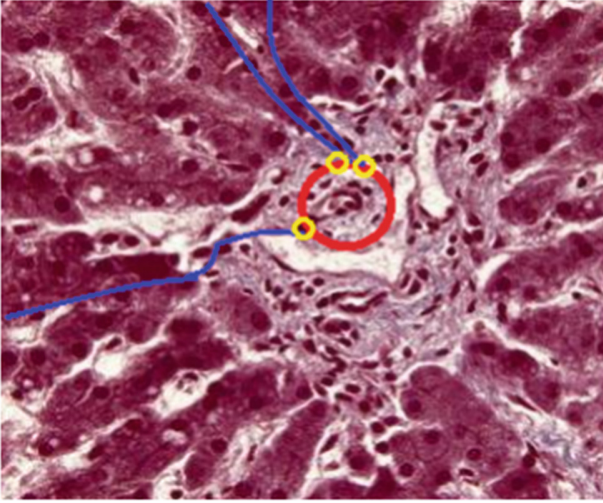


Fig. 8. Optimal solution with 3 collision-free trajectories to the target

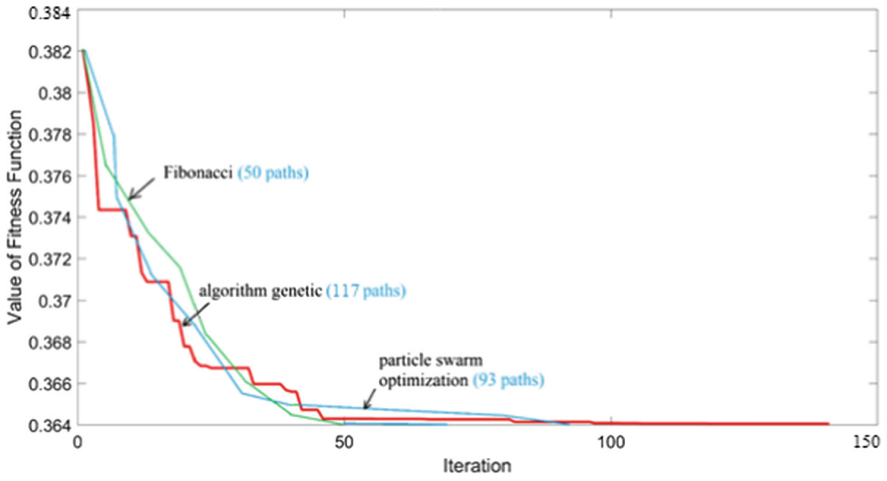


Fig. 9. Number of iterations for each method

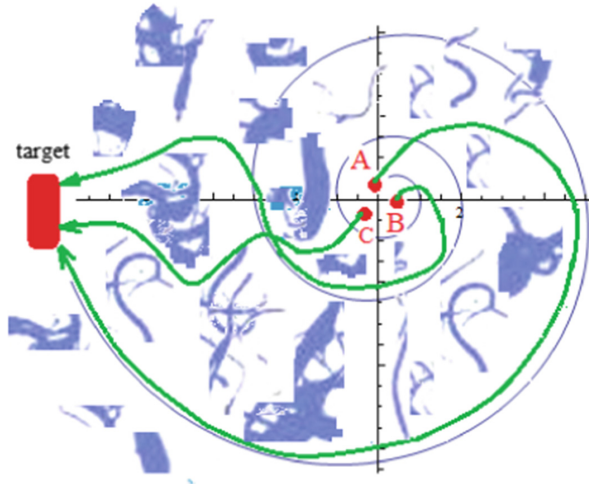


Fig. 10. The case when the trajectories intersect

4 Conclusions

To sum up, the paper applied the Fibonacci sequence to predict a model for a multiple-needle robot whose collision-free trajectories are determined by using the restrictions of avoiding the collisions with blood vessels, ribs and surrounding tissues, and also the interference of needles with each other.

We highlighted the results for a three-needles robot whose free-collision trajectories are induced by the Fibonacci sequence and avoid the difficulties of optimization algorithms that are frequently used in such problems.

Comparison with genetic algorithm and the particle swarm optimization algorithm highlighted that the Fibonacci algorithm requires the smallest number of iterations until the optimal solution is reached.

Acknowledgments. This work was supported by a grant of the Romanian ministry of Research and Innovation, CCCDI – UEFISCDI, project number PN-III-P1-1.2-PCCDI-2017-0221/59PCCDI/2018 (IMPROVE), within PNCDI III.

References

1. Lai, A.C., Loreti, P., Velluci, P.: A model for robotic hand based on fibonacci sequence. In: Proceedings of the 11th International Conference on Informatics in Control, Automation and Robotics (ICINCO-2014), pp. 577–584 (2014)
2. Aghili, F., Parsa, K.: Design of a reconfigurable space robot with lockable telescopic joints. In: Conference IEEE/RSJ, International Conference on Intelligent Robots and Systems (2006)
3. Burton, D.M.: Elementary Number Theory, 5th edn. McGraw-Hill, New York (2002)
4. Fox, W.P.: Fibonacci Search in Optimization of Unimodal Functions. Department of Mathematic Francis Marion University, Florence, SC 29501 (2002)

5. Silverman, J.H.: A friendly introduction to number theory, 3rd edn. Pearson Education, Upper Saddle River (2006)
6. Liu, S., Xia, Z., Liu, J., Xu, J., Ren, H., Lu, T., Yang, X.: Automatic Multiple-Needle Surgical Planning of Robotic-Assisted Microwave Coagulation in Large Liver Tumor Therapy, PLOS ONE, pp. 1–34 (2016)
7. Cristina, S.M., Gorka, G.C., Purificación, G.S., Tomás, G.C., Carlos, P.C.: Personalized surgical planning to support interventions and training of surgeons. In: Drechsler, K., Erdt, M., Linguraru, M., Oyarzun, L.C., Sharma, K., Shekhar, R., et al., editors. *Clinical Image-Based Procedures From Planning to Intervention*. Lecture Notes in Computer Science, vol. 7761, pp. 83–90 Springer, Heidelberg (2013)
8. Butnariu, S., Gîrbacia, F.: Methodology for the identification of needles trajectories in robotic brachytherapy procedure using VR technology. *Appl. Mech. Mater.* **332**, 503–508 (2013)
9. Munteanu, I., Rugină, C., Dragne, C., Chiroiu, V.: On the Robotic Control Based on Interactive Activities of Subjects. *Proceedings of the Romanian Academy, series A: Mathematics, Physics, Technical Science Information Science* (in press)
10. Chiroiu, V., Munteanu, L., Ioan, R., Dragne, C., Majercsik, L.: Using the Sonification for Hardly Detectable Details in Medical Images. *Scientific Reports*, 9, article number 17711 (2019)
11. Pislă, D., Bîrlescu, I., Vaida, C., Tucan, P., Pislă, A., Gherman, B., Crișan, N., Plitea, N.: Algebraic modeling of kinematics and singularities for a prostate biopsy parallel robot. *Proc. Romanian Acad. Ser. A Math. Phys. Tech. Sci. Inf. Sci.* **19**(3), 489–498 (2018)
12. Brișan, C., Boantă, C., Chiroiu, V.: Introduction in optimization of industrial robots. Theory and applications, Editura Academiei (2019)
13. Zhang, D., Wei, B., IEEE Int. Conf., Kinematic Analysis and Optimization for 4PUS-RPU Parallel Mechanism. *Advanced Intelligent Mechatronics (AIM)*, pp. 330–335 (2015)
14. Popa, D., Munteanu, L., Chiroiu, V.: On the shape reconstruction of 3D Stokes flows. *Proc. Romanian Acad. Ser. A Math. Phys. Tech. Sci. Inf. Sci.* **10**(3), 254–260 (2009)
15. Chiroiu, V., Munteanu, L., Nicolescu, C.M.: A shape description model by using sensor data from touch. In: Fourth Symposium on Multibody Dynamics and Vibration at the Nineteenth Biennial Conference on Mechanical Vibration and Noise ASME International Design Engineering Technical Conference Chicago, 2–6 September., paper nr. DETC2003/VIB-48337 (2003)
16. Chiroiu, V., Munteanu, L., Nicolescu, C.M.: Shape description of general 3D object using tactile sensing information. *AMSE: Advances in Modelling, Series B: Signal Processing and Pattern Recognition* (2003)
17. Bonnet, M.: Shape identification problems using boundary elements and shape differentiation. In: *Proceedings of the 2nd National Conference on Boundary and Finite Element, ELFIN2, Sibiu*, pp. 35–48 (1993)



Joint Space and Workspace Analysis of a 2-DOF Spherical Parallel Mechanism

Damien Chablat¹(✉), Guillaume Michel^{1,2}, Philippe Bordure², Ranjan Jha³,
and Swaminath Venkateswaran¹

¹ Laboratoire des Sciences du Numérique de Nantes (LS2N), UMR CNRS 6004,
Nantes, France

Damien.Chablat@cnrs.fr, Guillaume.Michel@chu-nantes.fr,
Swaminath.Venkateswaran@ls2n.fr

² CHU de Nantes, 44093 Nantes, France

Philippe.Bordure@chu-nantes.fr

³ CSIR-Central Scientific Instruments Organisation, Chandigarh, India
Ranjan.Jha@csio.res.in

Abstract. This paper deals with the joint space and workspace analysis of a two degree of freedom spherical parallel mechanism designed to be used to handle an endoscope. This mechanism is composed of the three legs (2USP-U) to connect the base to a moving platform. As the manipulator can get up to six solutions to the direct kinematic problem (DKP) in four aspects, non-singular assembly modes changing trajectories may exist. The aim of the paper is to check whether a regular workspace centred on home pose can be defined in such a way that no such trajectory exists in this workspace.

Keywords: Spherical parallel robot · Singularity · Cusp point · Aspect

1 Introduction

In the context of designing a robot to assist the surgeon in otologic surgery, a spherical robot with a parallel structure associated with a double parallelogram was studied [1]. This robot can handle an endoscope to increase the efficiency of the surgeon with compare to classical binocular. The parallel structure should increase the rigidity compared to the existing solution [2]. Many spherical mechanisms exist in the literature and can be divided into two main families (i) those with a virtual center of rotation and (ii) those constrained by a spherical joint or a universal joint (three or two DOF) [3–8]. To form an remote center of motion (RCM), one solution is to use to an universal joint associated with two parallelograms where the motion can be done with prismatic or revolute actuators. The advantage of prismatic actuators is that there is only one solution to the inverse geometric model or a single “working mode” [9, 10]. In order to give the surgeon more mobility, it is necessary to have the largest working space without

singularity. By adding an offset in the classical design, we are able to increase this workspace but the properties of the robot change [11] ie the number of aspects and the number of solutions to the DKP increases. In this paper we will present the robot properties for a given offset that allow non-singular assembly mode changing trajectories [13]. The SIROPA library written in Maple will be used to compute the singularity equations using Groebner bases, the cylindrical algebraic decompositions (CAD) as well as the trajectory planning [14, 15]. The outline of this paper will be the following. We will first introduce the kinematic equations, then the singularities in the joint space and the workspace to insert a prescribed regular workspace.

2 Mechanism Under Study

Figure 1 shows an RCM mechanism carrying an endoscope for operations in the ears made by coupling two DOF spherical mechanism with double parallelograms. This mechanism is coupled to a translation mechanism for positioning in the middle ear centre. Another mechanism allows translation of the endoscope for insertion, cleaning and ejection in case the patient wakes up, not addressed in this article. The spherical parallel mechanism is composed of three limbs and one moving platform. The two first legs, UPS, are composed of a universal joint, a prismatic joint and a spherical joint and the last one is made by a single universal joint and constrains its mobility. The two prismatic joints are actuated. The double parallelogram is attached to the two axes of this joint. Usually, the end points of the UPS legs are in the same plane as the axes of rotation of the universal joint. To increase the orientation range, an offset is added.

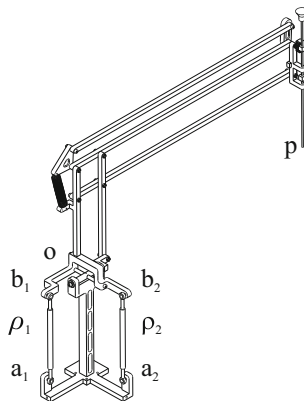


Fig. 1. RCM Mechanism with spherical parallel mechanism in its home pose where o and p are the centers of motions

Let \mathbf{a}_1 and \mathbf{a}_2 be attached to the base, O the center of the universal joint and \mathbf{b}_1 and \mathbf{b}_2 be attached to the mobile platform in the moving reference frame.

The coordinates are given by $\mathbf{a}_1 = [1, 0, -1]^T$, $\mathbf{a}_2 = [0, 1, -1]^T$, $\mathbf{b}_1 = [1, 0, h]^T$, $\mathbf{b}_2 = [0, 1, h]^T$. The orientation space of the moving platform is fully represented with the variables (α, β) . The rotation matrix \mathbf{R} from the base frame to the moving frame is expressed as follows:

$$\mathbf{R} = \mathbf{R}_\alpha \mathbf{R}_\beta = \begin{bmatrix} \cos(\beta) & 0 & \sin(\beta) \\ \sin(\alpha) \sin(\beta) & \cos(\alpha) - \sin(\alpha) \cos(\beta) & \\ -\cos(\alpha) \sin(\beta) \sin(\alpha) & \cos(\alpha) \cos(\beta) & \end{bmatrix} \quad (1)$$

The orientation angles are defined in such a way that $\alpha = \beta = 0$, which represents the “home” pose as depicted in Fig. 1. The coordinates of \mathbf{b}_1 and \mathbf{b}_2 can be written in the base frame as

$$\mathbf{c}_1 = \mathbf{R}\mathbf{b}_1 \quad \mathbf{c}_2 = \mathbf{R}\mathbf{b}_2 \quad (2)$$

The distance constraints from the two prismatic joints are

$$\|\mathbf{a}_i \mathbf{c}_i\| = \rho_i \quad \text{with } i = 1, 2 \quad (3)$$

This leads to the two constraint equations:

$$-2(\cos(\alpha) + h) \sin(\beta) + 2(\cos(\alpha)h - 1) \cos(\beta) + h^2 + 3 = \rho_1^2 \quad (4)$$

$$2(\cos(\beta)h - 1) \cos(\alpha) + 2(\cos(\beta)h + 1) \sin(\alpha) + h^2 + 3 = \rho_2^2 \quad (5)$$

3 Singularity and Workspace Analysis

The singularity analysis is done by differentiating the two constraint equation with respect to time that leads the velocity model:

$$\mathbf{A}\mathbf{t} + \mathbf{B}\dot{\boldsymbol{\rho}} = 0 \quad (6)$$

where \mathbf{A} and \mathbf{B} are the parallel and serial Jacobian matrices, respectively, \mathbf{t} is the angular velocity and $\dot{\boldsymbol{\rho}} = [\dot{\rho}_1 \ \dot{\rho}_2]^T$ joint velocities [9]. Let set $h = 0$, then the singularity locus C_W in the workspace and C_Q in the joint space can be written as follow:

$$C_W : (\sin(\alpha) + \cos(\alpha))(-\cos(\alpha) \cos(\beta) + \sin(\beta)) = 0 \quad (7)$$

$$C_Q : (\rho_2^4 - 6\rho_2^2 + 1)$$

$$(4\rho_1^8 + \rho_2^8 - 48\rho_1^6 - 12\rho_2^6 + 168\rho_1^4 + 46\rho_2^4 - 144\rho_1^2 - 60\rho_2^2 + 45) = 0 \quad (8)$$

Upon factorization of both the equations, there exists four solutions to the DKP out of which only four aspects, ie the maximum singularity free regions, can be found which are represented in Fig. 2(a) [9]. In the joint space, Fig. 2(b), there are regions depicted in green where the DKP admits two real solutions and in red where there are four real solutions.

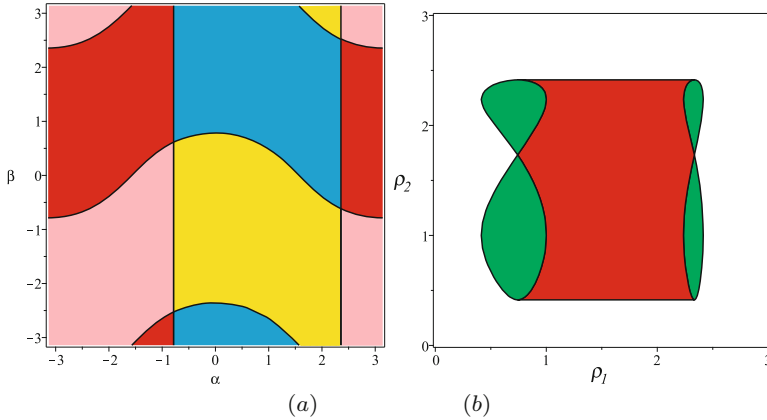


Fig. 2. Singularity locus in the workspace (a) and the joint space (b) with $h = 0$

The objective of our study is to use the robot for the largest possible range of motion, depending on the size of the ear and the placement of the patient in relation to the robot. The expressed need is a workspace close to ± 60 degrees which we will keep as ± 1 radians. Several design parameters can be varied to increase the workspace without singularity. We have chosen to study variations in h to keep the mechanism as compact as possible. Unfortunately, the properties of the robot are not stable when h is different from 0 and the locus of the singularities changes and the equations cannot be factorized. The singularity as a function of parameter h can be depicted in Fig. 3. A regular range of $[-1 \ 1]$ can be observed for α and β . Several values can be considered for h but this optimization could not be done in this article due to lack of space. Thus, a value of $h = 1$ will be considered. This value allows to have well separated curves in the joint space and workspace as shown in Fig. 4 and also include the regular workspace $\alpha = \beta = [-1 \ 1]$.

For $h = 1$, the singularity locus in the workspace is defined as

$$2(C_\beta + S_\beta + 1)C_\alpha^2 + (2C_\beta^2 + (-2S_\beta + 2S_\alpha + 2)C_\beta + (-2S_\alpha + 2)C_\beta^2 + (2S_\beta - 2)S_\alpha - 2S_\beta)C_\alpha + ((2S_\beta + 2)S_\alpha + 2S_\beta)C_\beta - 2S_\alpha S_\beta = 2 \quad (9)$$

The first analysis that can be done in the joint space will be to evaluate the number of real solutions to the DKP. In Fig. 4 in the joint space, the green regions admit two real solutions to the DKP, the red regions admit four solutions and the yellow regions admit six solutions. Eight cusps exist, (i) C_1 is on the border of the joint space, (ii) C_2 and C_3 are between the two- and four-solution regions solutions to the DKP, and (iii) C_4, C_5, C_6, C_7 and C_8 are between the four- and six-solution regions. The workspace consists of four colour aspects in orange, pink, blue and yellow.

To know if the mechanism changes assembly mode in the workspace defined by $\alpha = \beta \in [-1 \ 1]$, a trajectory is defined along this boundary, through the S_1 ,

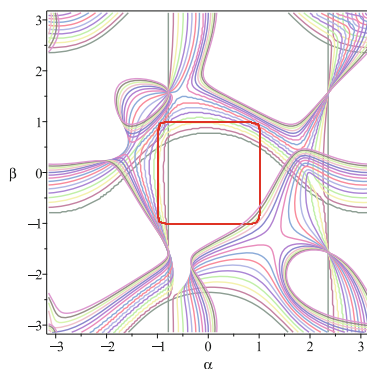


Fig. 3. Singularity locus in the workspace of the spherical joint for $h \in [0..1.5]$

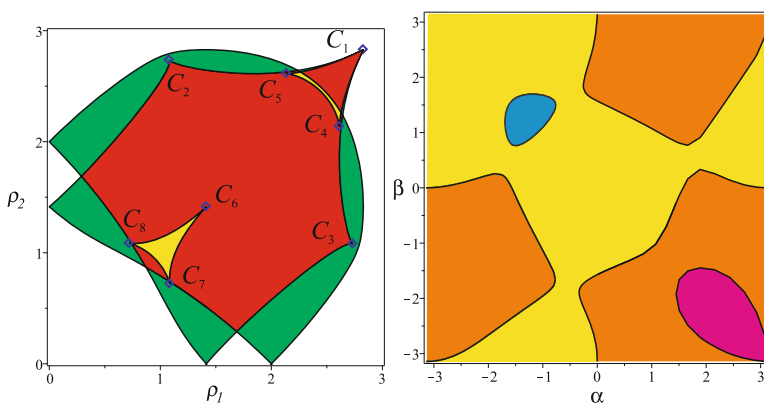


Fig. 4. Joint space with height cusps points, C_i and workspace with four aspects with $h = 1$

S_2, S_3, S_4 points, as well as its image in the joint space (Fig. 5). We can notice that the trajectory surrounds 3 cusp points C_4, C_5 and C_6 . Indeed, knowing that the trajectory is inscribed in an aspect, it does not allow to know if it is in the same uniqueness domain i.e. there is no change in the assembly mode.

To investigate the properties of the workspace, the characteristic surface must be studied. This notion was introduced in [16] to define the uniqueness domains for serial robots and was extended to parallel robots with one inverse kinematic solution in [13], several inverse kinematic solutions in [12] and several operation modes [17]. These characteristic surfaces (or curve in 2D) are the images in the workspace of the singularity surfaces. By using the singularity and characteristic surfaces, we can compute the *basic regions* as defined in [13]. The joint space is divided by the singularity surfaces in regions where the number of solutions for the DKP is a constant. These regions can also be named as the *basic components* as in [13]. The existence of cusp points could be noticed in Fig. 5. Thus, it is

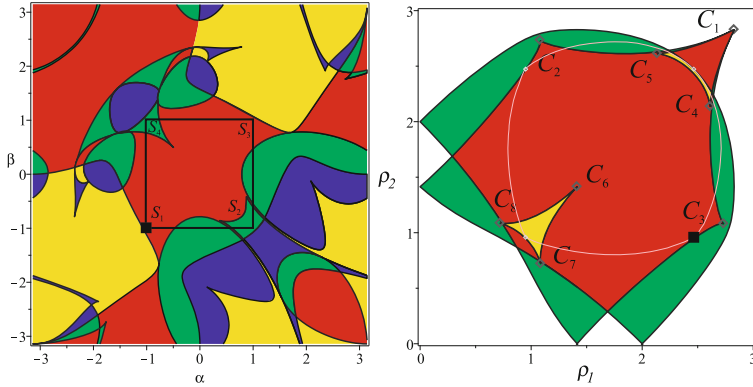


Fig. 5. Regular trajectory in the workspace and its image in the joint space

very easy to recognize images of cusp points in the workspace, either it is a point on a tangent between a singularity curve and characteristic curve or it is a cusp point and it has no influence on the trajectories [18]. In the joint space, this trajectory encircles three cusp points. A similar behaviour as described in [19] can be obtained. The image in the workspace of a loop in the joint space can be (i) the loop in the same aspect with the same starting and target point, (ii) a trajectory where the starting point and target point are in two aspects (a singular trajectory), or (iii) a trajectory where the starting point and target point are in the same aspect (a non-singular mode assembly trajectory).

In Fig. 6, a joint trajectory is defined to encircle a cusp point. The starting point, Q , is located in the yellow region where the DKP admits six real solutions P_i , depicted in the workspace. The images of this trajectory in the workspace are located in basic regions depicted in yellow and blue regions where $\det(\mathbf{A}) > 0$ and in basic region depicted in red and green where $\det(\mathbf{A}) < 0$. In Fig. 7, we can observe from any starting point P_i (i) two singular trajectories between two aspects ($P_4 - P_6$ and $P_5 - P_6$) and meet singular positions in S_1 and S_2 , respectively, (ii) one non-singular changing trajectory in the same aspect ($P_4 - P_5$), and (iii) three loops in the workspace located in the same aspect ($P_1 - P_1$, $P_2 - P_2$, $P_3 - P_3$). Only the trajectory ($P_1 - P_1$) is located in the regular workspace. So we can conclude that even if this trajectory surrounds a cup point in the joint space, it is not a non-singular changing assembly mode trajectory.

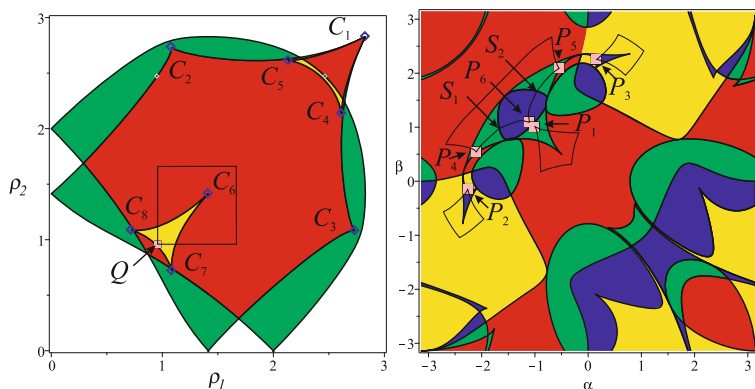


Fig. 6. Trajectory that encircles a cusp point in the joint space and its image in the workspace

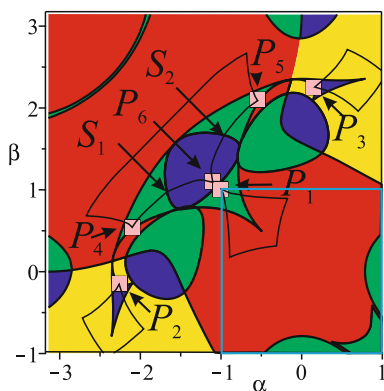


Fig. 7. Zoom on the trajectories in the workspace

4 Conclusions

The properties of a 2-DOF spherical parallel mechanism were studied in this article. The increasing size of the workspace yields to several changes as the increasing number of solutions to the direct kinematics problem. Four aspects were described by using cylindrical algebraic decomposition. A regular workspace is inscribed around the home pose. Joint limits on the passive joint α and β guarantees that non-singular assembly mode trajectory may appear. Additional research shall be conducted to verify the collision between the legs and the limits of the passive joints and to investigate variations in other design parameters.

References

1. Schena, B.: Robotic manipulator with remote center of motion and compact drive, Patent WO 2008/157225 (2007)

2. Rosen, J., Brown, J.D., Chang, L., Barreca, M., Sinanan, M., Hannaford, B.: The Blue-DRAGON - a system for measuring the kinematics and dynamics of minimally invasive surgical tools in-vivo. In: Proceedings IEEE International Conference on Robotics and Automation (2002)
3. Gosselin, C., Hamel, J.-F., The agile eye: a high-performance three-degree-of-freedom camera-orienting device. In: Proceedings IEEE International Conference on Robotics and Automation, pp. 781–786 (1994)
4. Cheng, H.H.: Real-time manipulation of a hybrid serial-and-parallel driven redundant industrial manipulator. *ASME J. Dyn. Syst. Meas. Control* **116**(4), 687–701 (1994)
5. Agrawal, S.K., Desmier, G., Li, S.: Fabrication and analysis of a novel 3 DoF parallel wrist mechanism. *ASME J. Mech. Des.* **117**(2), 343–345 (1995)
6. Caron, F.: Analyse et développement d'un manipulateur parallèle sphérique à deux degrés de liberté pour l'orientation d'une caméra. M. Sc., Université Laval, Québec, August 1997
7. Karouia, M., Hervé, J.M.: A three-DoF tripod for generating spherical motion. In: ARK, Piran, pp. 395–402, 25–29 June 2000
8. Li, J., Zhang, G., Müller, A., Wang, S.: A family of remote center of motion mechanisms based on intersecting motion planes. *J. Mech. Des.* **135**(9), 091009 (2013)
9. Chablat, D., Wenger, P.: Working modes and aspects in fully parallel manipulators. In: Proceedings, 1998 IEEE International Conference on Robotics and Automation, vol. 3 (1998)
10. Bonev, I.A., Chablat, D., Wenger, P.: Working and assembly modes of the Agile Eye. In: Proceedings 2006 IEEE International Conference on Robotics and Automation (2006)
11. Kumar, S., Nayak, A., Peters, H., Schulz, C., Müller, A.: Kinematic analysis of a novel parallel 2SPRR+ 1U ankle mechanism in humanoid robot. In: International Symposium on Advances in Robot Kinematics. Springer, Cham (2018)
12. Chablat, D., Wenger, P.: Séparation des solutions aux modèles géométriques direct et inverse pour les manipulateurs pleinement parallèles. *Mech. Mach. Theor.* **36**(6), 763–783 (2001)
13. Wenger, P.H., Chablat, D.: Definition sets for the direct kinematics of parallel manipulators. In: 8th International Conference in Advanced Robotics, pp. 859–864 (1997)
14. Jha, R., Chablat, D., Baron, L., Rouillier, F., Moroz, G.: Workspace, joint space and singularities of a family of delta-like robot. *Mech. Mach. Theor.* **127**, 73–95 (2018)
15. Chablat, D., Moroz, G., Rouillier, F., Wenger, P.: Using Maple to analyse parallel robots. In: Maple Conference 2019, October 2019
16. Wenger, P.: A new general formalism for the kinematic analysis of all nonredundant manipulators. In: IEEE Robotics and Automation, pp. 442–447 (1992)
17. Chablat, D., Jha, R., Rouillier, F., Moroz, G.: Non-singular assembly mode changing trajectories in the workspace for the 3-RPS parallel robot. In: Advances in Robot Kinematics, pp. 149–159. Springer, Cham (2014)
18. Chablat, D., Moroz, G., Wenger, P.: Uniqueness domains and non singular assembly mode changing trajectories. In: 2011 IEEE International Conference on Robotics and Automation (2011)
19. Mazen, Z., Wenger, P., Chablat, D.: Non-singular assembly-mode changing motions for 3-RPR parallel manipulators. *Mech. Mach. Theor.* **43**(4), 480–490 (2008)



Kinematic Analysis of Two Innovative Medical Instruments for the Robotic Assisted Treatment of Non-resectable Liver Tumors

Bogdan Gherman, Iosif Birlescu, Alin Burz, Ionut Ulinici, Paul Tucan,
and Doina Pisla^(✉)

Technical University of Cluj-Napoca, Cluj-Napoca, Romania
{Bogdan.Gherman, Iosif.Birlescu, Alin.Burz, Paul.Tucan,
Doina.Pisla}@mep.utcluj.ro, Ionut.Ulinici@omt.utcluj.ro

Abstract. The paper presents the kinematic analysis of two medical instruments to be used in a robotic system designed for the minimally invasive treatment of non-resectable liver tumors. The instruments will be attached to a parallel robotic system having two modules, one for guiding each instrument. The first one targets the multiple needle insertion for brachytherapy procedures, while the other one is used for guiding a intra-operatory ultrasound probe used for the visual control of the trajectory of the brachytherapy needles. The paper analyses the constraint equations of the two robotic instruments and their integration into the robotic system, using an algebraic method based on the Study parameters of the special Euclidean transformation Lie group $SE(3)$.

Keywords: Medical robotics · Kinematics · Robotic instruments · Minimally invasive treatment of non-resectable liver tumors

1 Introduction

Liver cancer is the fifth common type of cancer, with the vast majority (75–90%) being hepatocellular carcinomas (HCCs), while intrahepatic cholangiocarcinoma (ICC) accounting for most of the other cancer subtypes [1]. Some of the most used treatment methods are: radiofrequency ablation and high-dose rate brachytherapy (HDRBT). Robotic assisted HDRBT has been subject of research in many research centers, with mixed results [2]. Systems like MrBot [3] or Euclidean [4] are considered as very good for prostate cancer treatment using brachytherapy, used in conjunction with the MRI. The MIRAB [5] is another robotic system developed for prostate cancer, but as the other systems, these are used in safer conditions and in areas of the body where the risk of hitting unwanted organs or large blood vessels is practically missing. Pro-Hep-LCT [6–8] is a parallel robotic system designed for the percutaneous treatment of non-resectable liver tumors (using HDRBT or targeted chemotherapy) guided by intra-operatory ultrasonography. To achieve the medical task the robotic system consists of two identical parallel modules: one for guiding the ultrasound probe (USP) and the other the brachytherapy

needles (BTN). In [6] the mechanism analysis for the Pro-Hep-LCT was achieved using the Study parameters of SE(3) showing the constraints, singularities and the operational workspace of the robotic system. However, the authors considered only one DOF for the medical instrument attached to the mobile platform, namely the linear insertion (for USP or BTN). The medical procedure however, requires more complex automated instruments, with the following distinct characteristics: the needle insertion instrument [9] must insert multiple needles on parallel trajectories; the USP guiding instrument [10], must manipulate an USP (such as [11]) by inserting and changing the orientation of the probe transducer to accurately determine the needle position in the target tissue.

In this paper the constraints of the two medical instruments [9, 10] (designed as the Pro-Hep-LCT end effectors) are derived using the Study parameters of SE(3). The resulted constraints can be used together with the Pro-Hep-LCT constraints (derived in [6]) to enable the kinematic description of the hybrid system (composed of Pro-Hep-LCT and the instruments). Sections 2 and 3 present the multiple needles brachytherapy medical instrument and the ultra sound guiding instrument respectively and derives their constraints using the Study parameters. Section 4 presents numerical examples for the inverse kinematics where the targeted points for the needles are given. Finally the conclusions are presented in Sect. 5.

2 The Multiple Needles Insertion Brachytherapy Robotic Instrument

During the procedure treatment, the brachytherapy seeds are inserted (after a pre-planning in which the precise location of the tumor(s) inside the liver are determined) using the catheters of specific brachytherapy needles, which are inserted using the robotic instrument presented in this paper and attached to one of the Pro-Hep-LCT parallel robotic modules.

Figure 1 presents the kinematic scheme of the brachytherapy needle insertion robotic instrument [9]. It has 3 degrees of freedom (DoF) and uses Gantry architecture to position the brachytherapy needle in the XOY plane, using the q_{6n} and q_{7n} actuators. The coordinate system attached to the instrument (OXYZ) matches the one attached to the mobile platform of Pro-Hep-LCT. Usually, the treatment procedure requires up to 6 brachytherapy needles which are percutaneously inserted (from the outside of the patient's body) in a matrix form (which is a positive aspect from the mechanical point of view, since the needles collision is automatically avoided), using the actuator q_{8n} at a distance of 10 mm from each other (both on OX and OY axes). The number of needles is limited since the dimensions of the tumors that can be treated this way are also limited. The needles are taken from the needles rack, which is attached to the robotic instrument, one by one using the needle gripper, which is designed specifically for this application. The first needle is placed in the middle of the tumor (approximately), followed by the others, using the pre-planned trajectories. Thus, the needle insertion BT instrument has a very simple structure, having a serial kinematic chain of type PPP and a specially designed BT needles gripper.

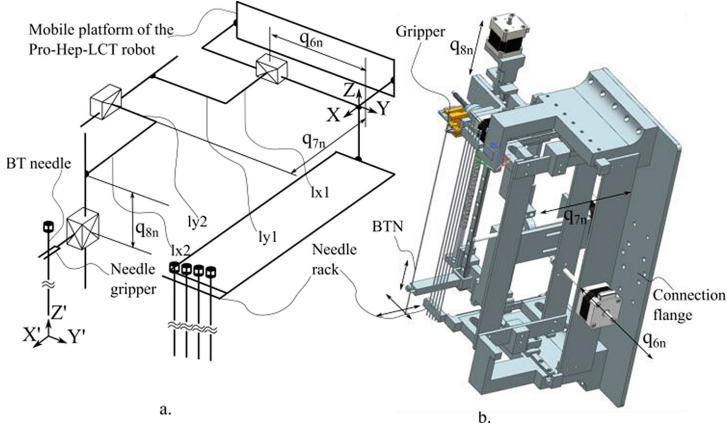


Fig. 1. The multiple needles insertion BT robotic instrument: a. kinematic scheme; b. CAD model

The instrument kinematics is achieved using the Study parameters of SE(3) (Eq. (1)) and it offers the mathematical connection between the Pro-Hep-LCT mobile platform and the target points (i.e. Eq. (1) represent the inputs for both inverse and forward kinematics).

$$\begin{aligned}
 M_{BTN} &= M_{TinsP} \cdot M_{Rx1} \cdot M_{Ry1} \cdot M_{Tinstr} \\
 M_{BTN}(x_i, y_i) &\rightarrow [x_0 : x_1 : x_2 : x_3 : y_0 : y_1 : y_2 : y_3], \\
 x_0 &= 1, \quad x_1 = t_1, \quad x_2 = t_2, \quad x_3 = -t_1 t_2, \\
 y_0 &= 1/2(t_1((q_{8n} - z_T)t_2 - q_{7n} + x_T - l_{x1} - l_{x2}) + t_2(q_{6n} - y_T + l_{y1} + l_{y2})), \\
 y_1 &= 1/2(t_2((q_{6n} + y_T + l_{y1} + l_{y2})t_1 - q_{8n} - z_T) + q_{7n} - x_T + l_{x1} + l_{x2}), \\
 y_2 &= 1/2(t_1((-q_{7n} - x_T - l_{x1} - l_{x2})t_2 - q_{8n} - z_T) + q_{6n} - y_T + l_{y1} + l_{y2}), \\
 y_3 &= 1/2((q_{6n} + y_T + l_{y1} + l_{y2})t_1 + (-q_{7n} + x_T + l_{x1} + l_{x2})t_2 + q_{8n} - z_T),
 \end{aligned} \quad (1)$$

where t_1 and t_2 are the half tangent angles of rotations representing the orientation of the instrument given by the Pro-Hep-LCT robotic module. The dual quaternions used in obtaining the M_{BTN} are detailed in Table 1, where the orientation (R_{x1} and R_{y1}) is achieved by Pro-Hep-LCT.

Table 1. The dual quaternions used in defining the multiple BTNs insertion instrument

Symbol	Dual quaternion	Description
M_{TinsP}	$[1:0:0:0:0:-x_T/2: -y_T/2: -z_T/2]$	Translation at the target point (inside the tumor)
M_{Rx1}	$[1:t_1:0:0:0:0:0:0]$	Rotation around the OX axis
M_{Ry1}	$[1:0:t_2:0:0:0:0:0]$	Rotation around the OY axis
M_{TInstr}	$[1:0:0:0:0:1/2(q_{7n} + l_{x1} + l_{x2}): 1/2(q_{6n} + l_{y1} + l_{y2}): q_{8n}/2]$	Conjugate dual quaternion for active positioning along the OZ, OY and OX axes (in reverse order than in Eq. (1)) using the q_{6n}, q_{7n}, q_{8n}

3 The Ultrasound Probe Manipulation Robotic Instrument (USP)

The USP manipulation robotic instrument (Fig. 2) [10] is attached to the other robotic module of the Pro-Hep-LCT parallel robot [6], having the task to position and orient the distal head of the USP (namely the transducer).

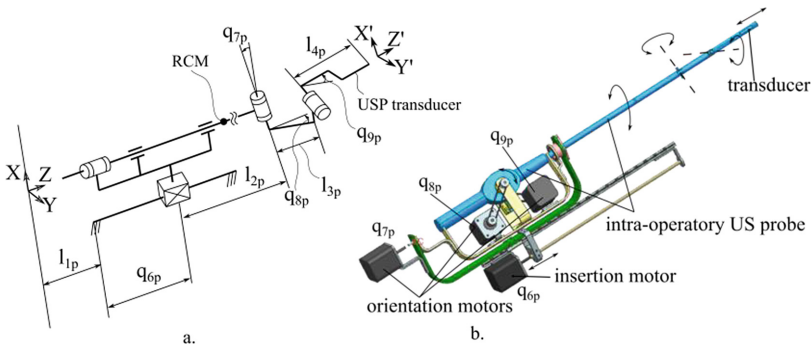


Fig. 2. The USP robotic instrument: a. kinematic scheme; b. CAD model

In order to see the needle on the USP screen, the transducer and the BTNs have to be located in the same plane. The instrument has 4 DoF (being of type PRRR): one translation along the instrument’s OZ axis (q_{6p}) and three rotations: one around the OZ axis (q_{7p}), one around the OX axis (q_{8p}) and one around the OY axis (q_{9p}). As opposed to the needle insertion brachytherapy robotic instrument, which inserts the needles percutaneously, the USP instrument is constrained by the insertion point into the patient’s body, namely the Remote Center of Motion (RCM).

Regarding the kinematics of the USP instrument, the algorithm is similar, leading to the following dual quaternion that describes the instrument:

$$\begin{aligned}
 M_{USP} &= M_{Tz1} \cdot M_{Rz} \cdot M_{Rx} \cdot M_{Tz2} \cdot M_{Ry} \cdot M_{Tz3} \\
 M_{USP}(x_i, y_i) &\rightarrow [x_0 : x_1 : x_2 : x_3 : y_0 : y_1 : y_2 : y_3], \\
 x_0 &= 1 - t_7 t_8 t_9, \quad x_1 = t_8 - t_7 t_9, \quad x_2 = t_9 + t_7 t_8, \quad x_3 = t_7 + t_8 t_9, \\
 y_0 &= 1/2(t_7(q_{6p} + l_{1p} + l_{2p} + l_{3p}) + t_8 t_9(q_{6p} + l_{1p} - l_{2p} + l_{3p})), \\
 y_1 &= 1/2(t_7 t_8(q_{6p} + l_{1p} - l_{2p} - l_{3p}) + t_9(q_{6p} + l_{1p} + l_{2p} - l_{3p})), \\
 y_2 &= 1/2(t_7 t_9(q_{6p} + l_{1p} + l_{2p} - l_{3p}) + t_8(q_{6p} + l_{1p} - l_{2p} - l_{3p})), \\
 y_3 &= 1/2(t_8 t_9(q_{6p} + l_{1p} - l_{2p} + l_{3p}) + (q_{6p} - l_{1p} - l_{2p} - l_{3p})),
 \end{aligned} \tag{2}$$

where t_7, t_8, t_9 represent the half tangent of the respective active rotation joint. The dual quaternions used in obtaining the M_{USP} are detailed in Table 2.

Table 2. The dual quaternions used in defining the USP instrument

Symbol	Dual quaternion	Description
M_{Tz1}	$[1:0:0:0:0:0:-1/2(q_{6p} + l_{1p})]$	Translation along the OZ axis of the instrument. l_{1p} - inserted by the robot, q_{6p} instrument active joint
M_{Rz}	$[1:0:0:t_7:0:0:0:0]$	Active rotation around the OZ axis (actuated by q_{7p})
M_{Rx}	$[1:t_8:0:0:0:0:0:0]$	Active rotation around the OX axis (actuated by q_{8p})
M_{Tz2}	$[1:0:0:0:0:0:-l_{2p}/2]$	Passive translation along the OZ axis
M_{Ry}	$[1:0:t_9:0:0:0:0:0]$	Active rotation around the OY axis (actuated by q_{9p})
M_{Tz3}	$[1:0:0:0:0:0:-l_{3p}/2]$	Passive translation along the OZ axis

The obtained dual quaternion shown in Eq. (2) will be used in the kinematic model developed in [6] in conjunction with the orientation of the instrument, and the coordinates of the RCM point (as in [6]) and the active coordinates of the Pro-Hep-LCT robotic module will be determined.

4 Numerical Examples

This section illustrates a scenario where the two medical instruments are mounted on the Pro-Hep-LCT parallel robotic system to achieve the medical task (percutaneous needle insertion guided by real time intra-operatory US). Since the tumor position and the target points inside it are difficult to define in the robot coordinate system before the intervention, their exact position is determined using the UPS module and visual confirmation using the US screen and laparoscopic imaging. That is why for the UPS

module, only direct kinematics is used. The inverse kinematics would yield multiple solutions and it would be difficult to apply in practice. Three target points are assumed to be located within a tumor of size 4 cm, with the distance between each pair of points being of about 10 mm (constraint imposed by the brachytherapy protocol as pointed out by oncologists), 3 needles being appropriate for the tumor volume. Furthermore, the needle insertion linear trajectory should be included in the transducer imaging plane (to confirm the position of the needle and make adjustments if necessary). Figure 3 presents a working scenario and Table 3 details the quaternions associated with the target points (the insertion trajectories must be parallel due to the brachytherapy protocol and the instrument design), obtained using the inverse kinematics of the BTNs insertion instrument.

Table 3. Defined target points for the needle insertion

BTN	Dual quaternion (target point)	Target point description	Active joints (instrument)
BT_0	$[1:1/10:0:0:7:-70:-485/11:97/22]$	$T_0[x_T = 200 \text{ mm}, y_T = 200 \text{ mm}, z_T = -200 \text{ mm}]^T$ Cartesian coord.; orientation -11.42° (about X axis), 0° (about Y axis)	$q_{6n} = 30 \text{ mm},$ $q_{7n} = 30 \text{ mm},$ $q_{8n} = -218.18 \text{ mm}$
BT_1	$[1:1/10:0:0:15/2:-75:-1068989/22000:-2411/2200]$	$T_1[x_T = 210 \text{ mm}, y_T = 209.8 \text{ mm}, z_T = -198.01 \text{ mm}]^T$ Cartesian coord.; orientation -11.42° (about X axis), 0° (about Y axis)	$q_{6n} = 40 \text{ mm},$ $q_{7n} = 40 \text{ mm},$ $q_{8n} = -228.18 \text{ mm}$
BT_2	$[1:1/10:0:0:13/2:-65:-54432/1375:217989/2200]$	$T_2[x_T = 190 \text{ mm}, y_T = 190.19 \text{ mm}, z_T = -201.98 \text{ mm}]^T$ Cartesian coord.; orientation $-Nr^\circ$ (about Z axis), 0° (about X axis)	$q_{6n} = 20 \text{ mm},$ $q_{7n} = 20 \text{ mm},$ $q_{8n} = -208.18 \text{ mm}$

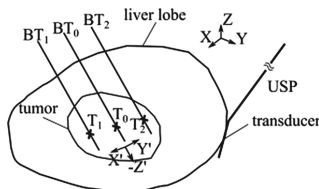


Fig. 3. A possible working scenario: tumor with defined initial target point trajectory

The active joints q_{6n} and q_{7n} are given for each needle (to determine the needle path through the instrument matrix) whereas the value for q_{8n} is determined using the constraints of Pro-Hep-LCT in order to not over-constrain the mechanism. Multiplying each dual quaternion representing the target point from Table 3 with the dual quaternion describing the BTN instrument (Eq. 1 yields the numerical solutions for the Study parameters describing the mobile platform of Pro-Hep-LCT. Using the inverse kinematic model presented in [6], the solutions for the active joints of the robot are: $q_4 = 117.5201609$ mm, $q_5 = 47.77$ mm, $t_3 = -0.063$ (as the half tangent of the q_3 active joint), $w_1 = -0.82$ (as the half tangent of the q_4 active joint), $q_1 = 200$ mm. The solutions for the active joints of Pro-Hep-LCT are the same for all target points since the simulation was designed such that the needles are inserted at the target points while the position of the insertion instrument is not changing (the robot is stiff). The numerical results describe the medical procedure in the correct way (as it was defined by engineers and medical experts) [12, 13].

The relative displacement between the US probe tip (the mobile) platform and the robot base, while maintaining a given RCM point, was described in [6] and it is not considered in the numerical simulation presented in this paper. However, the US probe instrument presented in this paper has 4 DOF (in contrast to the 1 DOF instrument assumed in [6]), therefore the numerical simulation will account for the constraints of the US probe guiding instrument (Eq. 2). Moreover, since Pro-Hep-LCT consists of twin modules which operate in opposite sides of the patient (Fig. 4), a dual quaternion pre-multiplication is required for the forward kinematic models derived in [6] with $[0:0:0:1:0:-300:250:0]$ (to account for the displacement between the bases of the two robotic modules, displaced with 500 mm on OX, 600 mm on OY and rotated around OZ by π). The imaging plane of the transducer is considered to be X'Z' and one simulated pose (since there are infinitely many) of the US probe that has the needle path (e.g. BT₀) entirely in the imaging plane is given by the numerical values: $l_{1p} = 30$ mm, $l_{2p} = 100$ mm, $l_{3p} = 10$ mm, $l_{4p} = 20$ mm for the geometric parameters of the US probe and $q_{6p} = 104.53$ mm, $q_{7p} = 0$, $q_{8p} \equiv t_1 = 0.44$ and $q_{9p} \equiv t_2 = 0$ for the active joints of the US probe guiding instrument.

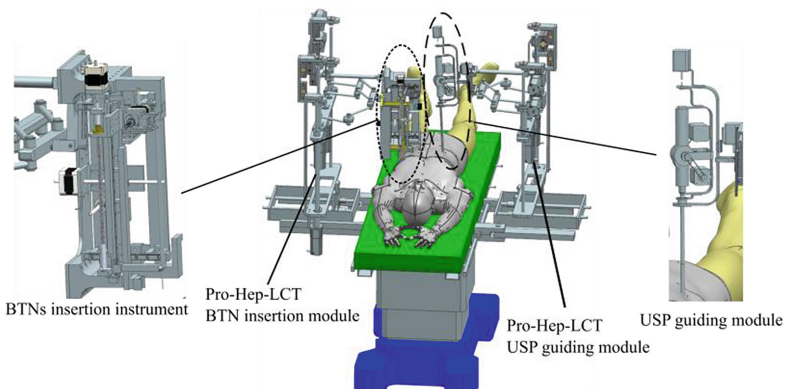


Fig. 4. The Pro-Hep-LCT robotic system with the two medical instruments attached

5 Conclusions

The paper presents the constraint analysis and describes the proper ways of connecting the two developed innovative instruments to the Pro-Hep-LCT robotic system. The geometry of the BTN insertion instrument shows that the system has the ability to achieve its task, once the main BTN is defined (in the middle of the tumor). The redundancies of the USP instrument become helpful, since the control system has to be adaptive and once the RCM point is defined, finding the right planes to get a clear image of the needles is difficult. The achievement of the control system for both instruments and their integration into the robotic system is a matter of future work.

Acknowledgments. The results presented in this paper have been financed by the grant of the Romanian Ministry of Research and Innovation, PCCCDI – UEFISCDI, project number PN-III-P1-1.2-PCCDI-2017-0221/59 PCCDI/2018 (IMPROVE) within PNCDDI III, within the framework of the GNaC 2018 ARUT grant “Innovative robotized instruments for treatment in surgical abdominal procedures”, research Contract no. 3216/06.02.2019, with the financial support of the Technical University of Cluj-Napoca and project no. 10338/27.04.2020 “Innovative robotic system for cancer treatment – HEAL4LIV”.

References

1. Wong, M., et al.: International incidence and mortality trends of liver cancer: a global profile. *Sci. Rep.* **7**, 45846 (2017). <https://doi.org/10.1038/srep45846>
2. Schnapauff, D., et al.: Interstitial brachytherapy in combination with previous transarterial embolization in patients with unresectable hepatocellular carcinoma. *Int. Inst. Anticancer Res.* **39**(3), 1329–1336 (2019)
3. Stoianovici, D., et al.: MR safe robot, FDA clearance, safety and feasibility prostate biopsy clinical trial. *IEEE ASME Trans. Mechatron.* **22**(1), 115–126 (2017)
4. Podder, T.K., et al.: Reliability of EUCLIDIAN: an autonomous robotic system for image-guided prostate brachytherapy. *Med. Phys.* **38**(1), 96–106 (2011)
5. Podder, T., Buzurovici, I., Huang, K., Yu, Y.: MIRAB: an image-guided multichannel robot for prostate brachytherapy. *Int. J. Rad. Onc. Biol. Phys.* **78**(3), S810 (2010)
6. Birlescu, I., Husty, M., Vaida, C., Plitea, N., Nayak, A., Pisla, D.: Complete geometric analysis using the study SE(3) parameters for a novel, minimally invasive robot used in liver cancer treatment. *Symmetry* **11**, 1491 (2019). <https://doi.org/10.3390/sym11121491>
7. Plitea, N., Pisla, D., Vaida, C., Gherman, B., Tucan, P.: PRoHep-LCT- Parallel robot for the minimally invasive treatment of hepatic carcinoma. Patent pending A1017/03.12.2018
8. Vaida, C., Tucan, P., Plitea, N., Lazar, V., Hajjar, A.N., Pisla, D.: Kinematic analysis of a new parallel robotic system for minimally invasive therapy of non-resectable hepatic tumors. In: Uhl T. (eds) *Advances in Mechanism and Machine Science*. IFToMM WC 2019. *Mechanisms and Machine Science*, vol. 73, pp. 719–728 (2019). https://doi.org/10.1007/978-3-030-20131-9_72
9. Gherman, B., Birlescu, I., Burz, A., Pisla, D.: Automated medical instrument for the insertion of brachytherapy needles on parallel trajectories, Patent pending A00806/28.11.2019
10. Birlescu, I., et al.: Automated medical instrument for ultrasound laparoscopic probe guiding, Patent pending A00752/15.11.2019
11. Arietta 70 for surgical oncology (2010). <http://www.hitachi-aloka.com/products/arietta-70/surgery/surgical-oncology>. Accessed 27 Jan 2020

12. Berceanu, C., Tarnita, D.: Aspects regarding the fabrication process of a new fully sensorized artificial hand. In: MODTECH 2010: New face of TMCR, pp. 123–126 (2010)
13. Berceanu, C., Tarnita, D., Filip, D.: About an experimental approach used to determine the kinematics of the human finger. *J. Sol. St. Phen. Rob. Aut. Syst.* **166**, 45–50 (2010)



Modeling a Cannula Insertion into a Phantom of Biological Tissue Using a Piezoelectric Actuator

Marat Dosayev¹ (✉), Irina Goryacheva², Ming-Shaung Ju³, Cheng-Hao Hsiao³, Chih-Yuan Huang³, Yury Selyutskiy¹, Anastasia Yakovenko², and Chien-Hsien Yeh³

¹ Institute of Mechanics, Lomonosov Moscow State University, Moscow, Russia
dosayev@imec.msu.ru

² Ishlinsky Institute for Problems in Mechanics RAS, Moscow, Russia
goryache@ipmnet.ru

³ National Cheng Kung University, Tainan, Taiwan
msju@mail.ncku.edu.tw

Abstract. Using different imaging techniques (primarily, magnetic resonance imaging or MRI) as guidance in robotic-assisted brain surgery becomes more and more wide-spread. One of important issues in this area is using these imaging technologies in online mode. For that, robotic devices that are compatible with MRI systems are required. In particular, conventional electric drives are not suitable; some alternatives should be used, such as piezoelectric drives (PED). In this paper, a robotic system is described intended to deliver a needle (cannula) to a given point by means of a PED. Dependence of the driving force generated by PED upon the needle speed is studied. In order to describe the contact interaction between the cannula and the soft tissue, a mathematical model of their interaction is developed based on modified Kelvin-Voigt approach. A phantom of porcine brain is manufactured. Experiments are carried out where the cannula was indented into the phantom. Based on the obtained experimental data, parameters of the mathematical model are identified. Numerical simulation of the insertion of the cannula into the soft tissue is performed, and the effect of parameters of the feedback control loop upon the cannula dynamics is analysed.

Keywords: Piezoelectric actuator · Mathematical model · Contact characteristics · Control algorithm

1 Introduction

One of the modern areas of minimally invasive medicine is stereotactic surgery, in which a flexible needle is inserted into the internal organs for medical procedures (for example, deep brain stimulation in the treatment of diseases such as Parkinson's disease). Special robotic systems designed for such operations are being created and improved. The main objective of such a system is to ensure accurate positioning of the needle tip at the target point. Many modern works (for example [1, 2]) in biomechanics and biomedicine have

been devoted to solving this problem. The most promising way to visualize a position of a needle relative to a target point in the human body is magnetic resonance imaging (MRI) [3], giving an error of up to 1 mm. One type of motors that are compatible with MRI is piezoelectric drive (PED) [4]. Due to its advantages, such as quick response, sufficiency of effort, safety of friction transmission, in recent years, PED have been increasingly offered as engines for various biomedical devices [5, 6]. Simultaneously, methods for modeling piezoelectric motors are being developed. Wurpts and Twifel [7] proposed simulating PED actuator using an oscillator with two degrees of freedom. A similar approach was developed in [8].

When controlling the needle, many factors must be taken into account: the rigidity of the needle, the mechanical properties of biological tissues, various medical aspects, such as, for example, the permissible speed of insertion of the needle, at which unacceptable damage will not occur in the tissue, etc. The introduction of new devices into clinical practice requires lengthy preliminary tests. One of the recognized methods for testing innovative methods and mechanisms is an experimental study of the use of such tools on phantoms of biological tissues [9].

In a number of works (in particular, [10]), the process of introducing a needle into soft tissues is modeled using the finite element method. However, this method does not allow you to effectively build an algorithm for controlling the movement of the needle. It is advisable to develop a phenomenological model in which the interaction of tissue with a needle would be described by a dynamic system (if possible, of a low order). To create a model for the interaction of a needle with a phantom of biological tissue, a contact problem should be solved that describes two processes: a penetration of a rigid indenter into the base and its detention at a certain depth. In this case, it is necessary to take into account the relaxation properties of the phantom. In [11], a simplified model of the mechanical behavior of the viscoelastic base was used for analysis of the hysteretic loop area at different values of the material relaxation time, and the applicability of the offered analytical model was discussed.

In this study, we developed a simplified one-dimensional model of the mechanical behavior of the phantom, which makes it possible to analyze the experimentally investigated process of introducing a needle into a phantom of biological tissue. We propose a novel finite-dimensional mathematical model of a robotic system that moves a cannula along a given straight line and uses PED as a drive. A porcine brain phantom was made. Experiments with indentation of the cannula into the phantom body were carried out. Based on the experiments, the procedure for identifying the parameters of the contact model is performed. An algorithm is proposed for controlling the frequency of the PED, which ensures an insertion of the cannula into the phantom at a given depth. A numerical simulation of the cannula insertion into a soft tissue using the algorithm was carried out aimed to evaluate influence of feedback coefficients.

2 Description of the Model

The mechanical system under consideration consists of a thin indenter (cannula), which is installed in the guides and can perform translational motion along the longitudinal axis (see Fig. 1). The cannula motion is provided by piezoelectric actuator that pressed against the cannula with some force N (Fig. 1b).

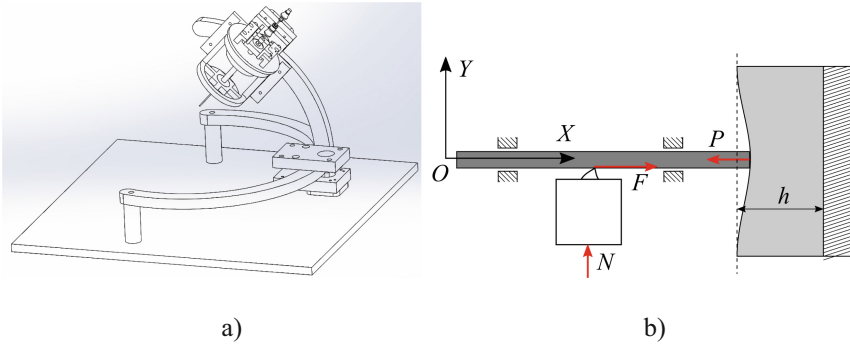


Fig. 1. Mechanical system. a. setup side view; b. indentation scheme.

We introduce a fixed coordinate system Oxy , the abscissa of which is directed along the direction of indenter motion. Friction in the indenter guides is neglected. The equation of dynamics of the indenter in the projection onto the Ox axis looks like following:

$$m\ddot{x} = F - P \tag{1}$$

Here m is the mass of the indenter, P is the force acting on the indenter from the side of a tissue, F is the force acting on the indenter from the side of the actuator head.

We model the dynamics of PED using the empirical approach described, in particular, in [8]. Under the action of an alternating electric voltage with a frequency applied to the actuator, the drive head oscillates at which the trajectories of its points are close to ellipses. We assume that the coordinates, the middle of the base of the head depend on time as follows:

$$x_b = A_x \sin 2\pi\omega t, y_b = A_{y0} + A_y \sin(2\pi\omega t + \Phi).$$

Within the framework of the phenomenological approach used, the dynamics of the drive head is described using an oscillator with two degrees of freedom (see Fig. 2).

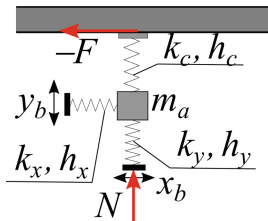


Fig. 2. Piezoelectric drive model

Denote the corresponding generalized coordinates by x_a, y_a . We compose the equations of motion of this oscillator:

$$m_a\ddot{x}_a = -k_x(x_a - x_b) - h_x(\dot{x}_a - \dot{x}_b) - F$$

$$m_a \ddot{y}_a = -k_y(y_a - y_b) - h_y(\dot{y}_a - \dot{y}_b) - k_c y_a - h_c \dot{y}_a \quad (2)$$

Here m_a is the mass of the oscillator, k_x , k_y , k_c are the stiffness coefficients of the oscillator springs, h_x , h_y , h_c are the damping coefficients. The force F developed by PED, is determined by the following ratio:

$$F = \mu \operatorname{sgn}(\dot{x}_a - V)(k_c x_a + h_c \dot{x}_a)$$

Here V is the speed of the surface point with which the drive head is in contact (in this case $V = \dot{x}$).

We find the average displacement A_{y0} from the equilibrium conditions:

$$0 = -k_y(y_{a0} - A_{y0}) - k_c y_{a0}; \quad k_y(y_{a0} - A_{y0}) = N.$$

Here y_{a0} is the position of the oscillator in equilibrium. So, $y_{a0} = -N/k_c$, $A_{y0} = -N(1/k_y + 1/k_c)$.

Since the frequency ω that is needed to be applied to the PED is high enough, the numerical integration of system (2) takes a relatively long time. On the other hand, the characteristic time of the indenter movement is significantly longer than the characteristic period of oscillation of the oscillator. Therefore, when analyzing the dynamics of the PED head, we can assume that the indenter speed V does not change during the period. Accordingly, when modeling the dynamics of indenter penetration into the control loop, it is advisable to use the results of preliminary calculation of the average value of the force developed by the drive at various values of the excitation frequency.

When indented into a sufficiently "soft" and/or sensitive tissue, the force developed by the drive should be small (otherwise the indenter will be too fast, which can lead to tissue damage). In this situation, it becomes significant that this force depends not only on the excitation frequency, but also on the magnitude of the indenter speed V .

We carry out a numerical simulation of the dynamics of system (2) at different values V and ω , using the following values of the model parameters:

$$m_a = 0.4 \cdot 10^{-3} \text{ kg}, \quad k_x = k_y = 10^7 \text{ N/m}, \quad h_x = h_y = 0.6 \text{ Ns/m}, \quad k_c = 10^6 \text{ N/m}, \\ h_c = 2 \text{ Ns/m}, \quad \mu = 0.28, \quad N = 4 \text{ N}, \quad A_x = 0.41 \text{ } \mu\text{m}, \quad A_y = 0.76 \text{ } \mu\text{m}, \quad \Phi = 0.$$

Figure 3 shows the dependences of the period average value of the force F (solid grey lines). It can be seen that at low speeds, the force F (at a fixed frequency) decreases almost linearly with growing V . This effect is described, in particular, in [12]. Note that the rate of this decrease increases (in absolute value) with increasing frequency ω .

The maximum force F_{\max} developed by PED for these parameter values is approximately equal 0.56 N (achieved at $\omega = \omega_* \approx 26400$ Hz and $V = 0$).

The following approximation can be used to describe the dependence of the force F upon the frequency and the speed:

$$F_a = \begin{cases} \frac{1}{1.77 + 2.7 \cdot 10^{-6} |\omega - \omega_*|} - \frac{0.48 + 0.8(\omega - \omega_*)^2}{|\omega - \omega_*| + 500} V, & \omega \leq 27.2 \text{ kHz} \\ \frac{1}{1.2 + 2.9 \cdot 10^{-3} (\omega - \omega_*)^2} - \frac{0.48 + 0.8(\omega - \omega_*)^2}{|\omega - \omega_*| + 500} V, & \omega > 27.2 \text{ kHz} \end{cases}$$

These dependences are shown in Fig. 3 with dotted lines. One can readily see that the quality of the approximation is good enough in the considered range ω of and V .

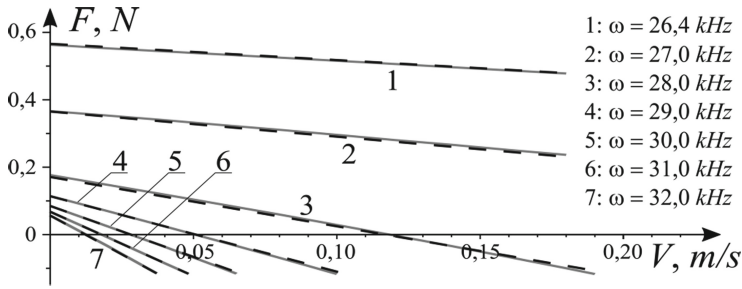


Fig. 3. Dependence of the force developed by PED on the excitation frequency and the indenter speed.

In what follows, we will use these simulation results in order to determine the excitation frequency necessary to realize the required value of the force developed by PED.

Now we need to study, how the process of introducing an indenter into a viscoelastic tissue at a fixed frequency of external voltage applied to the PED will occur. To do this, it is necessary to build a model describing an interaction of tissue with the indenter.

3 Verification of Contact Model

The axisymmetric contact problem of the interaction of a rigid indenter is considered, the contact surface of which is described by a function $f(r)$ with a viscoelastic layer of thickness h lying on a rigid base. The layer material is assumed to be homogeneous isotropic linearly viscoelastic. The speed V_1 of loading is constant. When introducing a spherical or cylindrical indenter, the contact area will be a circle of radius a . To describe the behavior of the viscoelastic layer, we choose the generalized Kelvin – Voigt model. For the force acting from the tissue side on the indenter during loading, we obtain the following expression:

$$T_{\sigma}^{(i)} \dot{p}_i = -p_i + E_i \left(x + T_{\varepsilon}^{(i)} \dot{x} \right) / h(1 - \nu^2), i = 1, 2; P = \pi R^2 (p_1 + p_2) \quad (3)$$

Here, E_i are the elastic moduli, ν is Poisson ratio, $T_{\sigma}^{(i)}$ and $T_{\varepsilon}^{(i)}$ are the relaxation and creep times.

To identify the parameters of the contact model, a phantom of porcine brain was made at the National Chen Kung University, The phantom has shape of a hemisphere with a radius of $h = 0.065$ m. It is made from agar-agar of a certain concentration. During the experiment, a cannula with a radius of $R = 0.9$ mm was indented into the phantom lying on a rigid surface along its axis of symmetry with a given constant speed. After reaching a predetermined penetration depth, the cannula position was fixed. During the experiment, the axial force of tissue resistance was recorded using a force sensor. An example of experimental time dependences of the axial force is presented in Fig. 4 by blue and green curves.

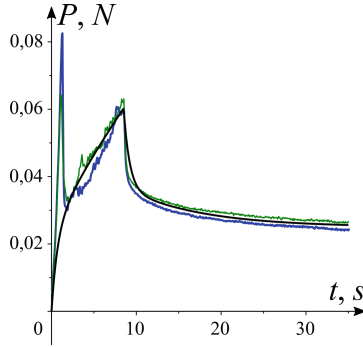


Fig. 4. Identification of the parameters of the contact interaction model.

The following parameters of the proposed contact interaction model ($N = 2$) were selected using the expert assessment method (similar to [13]):

$$E_1 = 5000 \text{ Pa}, E_2 = 23000 \text{ Pa}, T_\sigma^{(1)} = 9 \text{ s}, T_\sigma^{(2)} = 0.7 \text{ s}, T_\varepsilon^{(2)} = 5T_\sigma^{(1)}, T_\varepsilon^{(2)} = 15T_\sigma^{(2)}$$

The black line in Fig. 4 shows the result of the axial load calculation for the selected set of parameters. It can be seen that, at the selected parameter values, the calculation results are in fairly good agreement with the experimental data.

4 Numerical Simulation

We carry out a numerical simulation of the indentation process into a soft tissue. The goal of indentation is the achievement of a certain given depth x_* of insertion of the indenter to the tissue.

We choose the frequency ω providing the necessary value of the control force F created by PED. We set it in the form of feedback on the current immersion depth and speed of the indenter, given that the force developed by PED cannot exceed the maximum value F_{\max} indicated earlier:

$$F = \begin{cases} -F_{\max}, & F_* - K(x - x_*) - H\dot{x} < -F_{\max} \\ F_* - K(x - x_*) - H\dot{x}, & -F_{\max} < F_* - K(x - x_*) - H\dot{x} < F_{\max} \\ F_{\max}, & F_* - K(x - x_*) - H\dot{x} > F_{\max} \end{cases} \quad (4)$$

Here $F_* = \pi R^2(E_1 + E_2)x_*/h(1 - \nu^2)$ is the force value corresponding to the target depth penetration.

The dynamics of the “indenter + viscoelastic tissue” system is described by Eqs. (1, 3) and the relation (4). We study the influence of feedback coefficients K and H on the process of reaching the target immersion depth.

The examples of the time dependences of the penetration depth are shown in Figs. 5, 6 for different values of the target depth and different values of feedback coefficients K and H .

It can be seen that increasing K leads to an acceleration of the process of reaching the target value x_* . However, fluctuations occur in this case, so that even the opposite

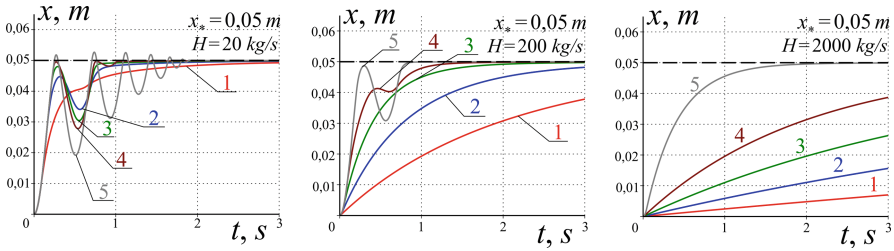


Fig. 5. Time dependences of penetration depth for different values of K (1: $K = 100$ N/m; 2: $K = 250$ N/m; 3: $K = 500$ N/m; 4: $K = 1000$ N/m; 5: $K = 5000$ N/m).

direction of the indenter movement can be observed in certain sections of the trajectory. The amplitude of these oscillations grows with increasing x_* . In addition, overshoot may occur when the indenter penetrates to a depth exceeding the target. In actual use, this is undesirable.

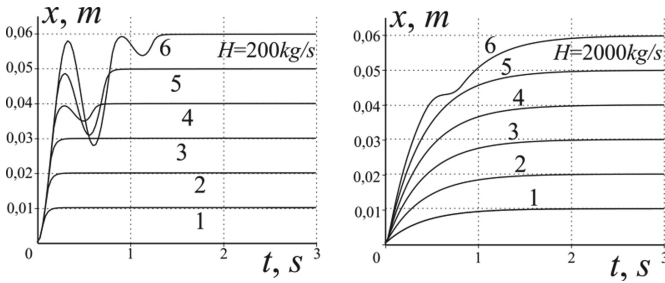


Fig. 6. Time dependences of penetration depth for different values of the target depth (1: $x_* = 0.01$ m; 2: $x_* = 0.02$ m; 3: $x_* = 0.03$ m; 4: $x_* = 0.04$ m; 5: $x_* = 0.05$ m; 6: $x_* = 0.06$ m).

Increasing H allows to reduce the amplitude of such oscillations or to avoid their occurrence altogether, but at the same time, the time to reach the target depth increases slightly.

5 Conclusions

The robotic system using PED actuator for performing the indentation of the needle (cannula) into soft biological tissue is considered. A finite-dimensional mathematical model of the mechanism was constructed. The porcine brain phantom was manufactured. To describe the cannula interaction with the soft tissue phantom, a mathematical model of their contact was used. Experiments with indentation of the cannula into the phantom body were carried out. Based on the experiments, parameters of the contact model were identified. A PED control algorithm is proposed that ensures the insertion of a cannula into soft biological tissue at a given depth. A numerical simulation of the insertion of a cannula into a soft tissue using the algorithm was carried out.

Results of this study can be applied in the development of a new biomedical device that allows for indentation of a cannula with the necessary accuracy inside the MRI device.

Acknowledgments. This work was partially supported by the Russian Foundation for Basic Research (project # 19-58-52004) and Taiwan Ministry of Science and Technology (project # 108-2923-E-006-003-MY3).

References

1. Li, P., et al.: Modeling of path planning and needle steering with path tracking in anatomical soft tissues for minimally invasive surgery. *Med. Eng. Phys.* **41**(C), 35–45 (2017). <https://doi.org/10.1016/j.medengphys.2017.01.006>
2. Gao, D., Lei, Y., Lian, B., Yao, B.: Modeling and simulation of flexible needle insertion into soft tissue using modified local constraints. *J. Manuf. Sci. Eng.* **138**(12), 121012 (2016)
3. Park, Y.L., et al.: Real-time estimation of 3-D needle shape and deflection for MRI-guided interventions. *IEEE ASME Trans. Mechatron.* **15**(6), 906–915 (2010)
4. McPherson, T., Ueda, J.: A force and displacement self-sensing piezoelectric MRI-compatible tweezer end effector with an on-site calibration procedure. *IEEE/ASME Trans. Mechatron.* **19**(2), 755–764 (2014)
5. Cappelleri, D.J., Frecker, M.I., Simpson, T.W., Snyder, A.: Design of a PED bimorph actuator using a metamodel-based approach. *J. Mech. Des.* **124**(2), 354–357 (2002)
6. Yeh, C.-H., et al.: Application of piezoelectric actuator to simplified haptic feedback system. *Sens. Actuators A Phys.* **303**, 111820 (2020). <https://doi.org/10.1016/j.sna.2019.111820>
7. Wurpts, W., Twiefel, J.: An ultrasonic motor with intermittent contact modeled as a two degree of freedom oscillator in time domain. *PAMM* **9**, 287–288 (2009). <https://doi.org/10.1002/pamm.200910117>
8. Dosaev, M.Z., Selyutskiy, Yu.D., Yeh, C.-H., Su, F.-C.: Modeling tactile feedback realized by piezoelectrical actuator. *Mekhatronika Avtomatizatsiya Upravlenie* **19**(7), 480–485 (2018). <https://doi.org/10.17587/mau.19.480-485>. (in Russian)
9. Aranda-Lara, L., Torres-García, E., Oros-Pantoja, R.: Biological tissue modeling with agar gel phantom for radiation dosimetry of ^{99m}Tc. *Open J. Radiol.* **4**, 44–52 (2014). <https://doi.org/10.4236/ojrad.2014.41006>
10. Oldfield, M., Dini, D., Giordano, G., Rodriguez y Baena, F.: Detailed finite element modelling of deep needle insertions into a soft tissue phantom using a cohesive approach. *Comput. Methods Biomech. Biomed. Eng.* **16**(5), 530–543 (2013). <https://doi.org/10.1080/10255842.2011.628448>
11. Lyubicheva, A.: Closed-form solution of axisymmetric contact problem for a viscoelastic base within cycle of increasing and decreasing of load on the indenter. *J. Friction Wear* **38**(2), 138–143 (2017)
12. Liu, Z., Yao, Z., Li, X., Fu, Q.: Design and experiments of a linear piezoelectric motor driven by a single mode. *Rev. Sci. Instrum.* **87**, 115001 (2016). <https://doi.org/10.1063/1.4966251>
13. Klimina, L., Shalimova, E., Dosaev, M., Garziera, R.: Closed dynamical model of a double propeller HAWT. *Procedia Eng.* **199**, 577–582 (2017). <https://doi.org/10.1016/j.proeng.2017.09.179>



Robot-Assisted Ablation of Liver Hepatocellular Carcinoma and Colorectal Metastases: A Systematic Review

Andra Ciocan^{1,3}, Radu Elisei², Florin Graur^{2,3}(✉), Emil I. Mois^{2,3}, Sorana D. Bolboaca¹, Corina Radu³, Calin Vaida⁴, and Nadim Al Hajar^{2,3}

¹ Department of Medical Informatics and Biostatistics, “Iuliu Hațieganu” University of Medicine and Pharmacy, Cluj-Napoca, Romania

² Department of Surgery, “Iuliu Hațieganu” University of Medicine and Pharmacy, Cluj-Napoca, Romania
graurf@yahoo.com

³ Regional Institute of Gastroenterology and Hepatology “Prof. Dr. Octavian Fodor”, Cluj-Napoca, Romania

⁴ CESTER, Technical University of Cluj-Napoca, Cluj-Napoca, Romania

Abstract. Introduction: Robot-assisted liver tumor ablation has emerged as a new minimally invasive therapeutic strategy for hepatocellular carcinoma, as well as colorectal metastases with higher accuracy, in a smaller time span and with a lower radiation dose than in the manual approach. Several ablation methods count, mostly used are radiofrequency ablation, microwave ablation and cryoablation. **Materials and methods:** The specialty literature was surveyed in order to retrieve manuscripts reporting “robot-assisted”, “liver tumor”, “ablation”. The search strategy was applied in three different databases, Scopus, Web of Science and Embase. Fifteen original articles were selected and seven were excluded from the study, in order to compare results of robotic ablation for liver tumors both on patient series or on experimental models. **Results:** Out of a total of fifteen articles included in the study, six articles focused on the clinical aspect of robotic liver tumor aspect, providing patients description and characteristics on a total of 172 subjects. There were nine studies, which focused on the technical assessment of the robot during ablation on experimental model. The indications for percutaneous ablation usually include malignant tumors, hepatocellular carcinoma (55 tumors) or colorectal liver metastases (92 tumors) for lesions smaller than 3 cm in diameter, which cannot benefit from liver resection. The most commonly reported type of ablation was microwave technique (43%), followed by radiofrequency (40%). Only one article evaluated laser ablation effects and another one reported irreversible electroporation. The number of needles used for ablation according to the tumor volume varied from 1 in 50% of cases to 5 and the number of needle readjustments reached 1 to 14. The type of robot used was different in the fifteen studies. **Conclusions:** Development of more versatile robots and intuitive software that will reduce the total time of the procedures is highly expected, thus transforming imaging guided robotic ablation into the golden standard procedure for inoperable primary hepatic tumors or liver metastases.

Keywords: Robot-assisted · Radiofrequency ablation · Hepatocellular carcinoma · Colorectal metastases

1 Introduction

Hepatocellular carcinoma is a malignant tumor, derived from the hepatocyte that, if not treated, leads to death in about two years. Of the primary hepatic malignancies, the most frequent are hepatocellular carcinomas, which occur in most cases on the cirrhotic liver. On the other hand, liver is the most common organ in which metastases from cancers with other location occur [1].

Surgical resection and liver transplant are currently the only curative therapeutic methods for hepatocellular carcinomas. Unfortunately, less than 30% of patients are eligible for resection due to advanced tumor invasion or associated cirrhosis. Morbidity and mortality related to hepatectomy in these patients are increased (10–30%). In addition, postoperative recurrence frequently occurs (at least 75%), due to its multicentric character, which requires repeated treatment. Five-year survival for patients, who benefitted from liver resection is approximately 25–50% [2].

Surgical resection remains the standard treatment in liver metastases, being the only one shown with curative potential. The most common liver metastases are those of colorectal cancers, which occur mostly on normal liver. At the time of diagnosis, 25% of colorectal cancer patients have liver metastases and another 25% will develop them later. Survival at 5 years after the resection of liver metastases from colorectal cancer is 20–40%. Unfortunately, only 20% of colorectal cancer metastases are surgically resectable and resection is associated with morbidity and mortality of 2–10%. In addition, hepatic recurrences occur in 53–68% of patients and from these, iterative resection is only in few cases feasible [1].

The limiting factors for the surgical treatment are the large number of tumors, high volume tumors, location in proximity of large vessels, tumors with major vascular invasion, insufficient hepatic reserve in the case of cirrhosis, previous liver resections, comorbidities which contraindicate surgery [2].

Over time, new therapeutic modalities have emerged and developed as alternatives to liver resection. Currently these methods include systemic and regional chemotherapy, intra-arterial irradiation with yttrium-90 and local ablation techniques. Techniques for local destruction of liver tumors are: 1) chemical ablation by percutaneous intratumoral injection of ethanol, acetic acid, sodium hydroxide or hot saline; 2) thermal ablation; 3) intraarterial chemo-embolization – TACE (lipiodolized); 4) percutaneous injection of cytostatics and 5) electrolysis.

Thermal ablation can be performed at low temperatures (cryoablation) or at high temperatures (hyperthermia ablation). The destruction of liver tumors by hyperthermia is achieved by the use of microwaves, radiofrequency, laser or high intensity ultrasound [3].

The ablation works best for tumors smaller than 3 cm. For larger tumors (between 3 and 5 cm), it can be used in conjunction with embolization. Because ablation usually destroys healthy tissue around the tumor, it is not the best option for treating tumors near major blood vessels or biliary ducts, subdiaphragmatic or subcapsular location [3].

This type of treatment does not usually require long hospitalization. In most cases, the ablation can be done without surgery, by inserting, percutaneously, a needle or a probe, directly into the tumor. The needle or probe is guided to the right place by ultrasound or tomography. However, in some cases, for greater accuracy, it may be done within a surgical procedure.

Radiofrequency Ablation (RFA). This procedure uses high intensity electromagnetic waves. A thin, needle-like probe is inserted into the tumor. A high-frequency current passes through the tip of the probe, which heats the tumor and destroys cancer cells. This is a common treatment for small tumors [4].

Microwave Thermotherapy. In this procedure, microwaves produce overheating and destroy abnormal tissue by protein denaturation, which leads to apoptosis. Microwaves are transmitted using a probe or needle [5].

Cryotherapy. In this procedure, the tumor is destroyed by freezing it, using a thin metal probe. The probe is guided into the tumor and then, with this instrument, cold gases are transmitted that freeze the tumor, destroying the cancer cells. This method can be used to treat larger tumors than other types of ablation, but sometimes it is necessary to be performed under general anesthesia [6, 7].

Side effects of ablative therapy

Possible side effects of ablative therapy include abdominal pain, liver abscess and haemorrhage. Severe complications are not common, but possible.

As of late robots were embraced to build the precision of needle through imaging direction. Abdullah et al. detailed their initial understanding of performing RFA on the liver utilizing the ROBIO EX workstation [7]. Koethe et al. played out a ghost investigation of percutaneous biopsy and removal utilizing mechanical help under CT direction for RFA with the automated interventional radiologist help stage MAXIO [8]. These investigations show the upsides of mechanical stages to help RFA treatment. What is more, Yang et al. proposed a mechanical removal framework for huge tumor treatment, which joined a robot and a voxel able to develop calculation in order to accomplish removal circles that encases the entire tumor [9]. In any case, the creators neither considered staying away from key anatomical structures nor performed quantitative assessment in the arranging [10, 11, 23].

2 Materials and Methods

A specialty literature survey was performed guided by the phrases “robot-assisted ablation”, “robotic liver tumors ablation”, “colorectal metastases ablation” using three databases Scopus, Web of Science and Embase. All titles referred in English, published in a determined time span from 2010 to 2019, were checked for eligibility by title and abstract, by two different researchers in order to remove double counting. There were 27,277 results provided in Pubmed. The full-texts of the eligible original articles were reviewed entirely. Series approaching robot-assisted liver surgery, liver resections, ALPPS or renal tumors ablation were excluded from the current study. We divided the

total of fifteen eligible studies into two categories, 6 focusing on patients and clinical outcome and 9 using experimental model, porcine or rabbit liver (Fig. 1). We analyzed the method used for ablation, radiofrequency versus microwave or cryoablation, patient demographics (age, sex, male to female ratio), tumors number and diameter, primary tumors versus metastases, intervention characteristics (mean time necessary for the procedure, number of needles used, type of robot), oncological outcomes and complications during and after procedure. Consequently, the studies were compared between each other.

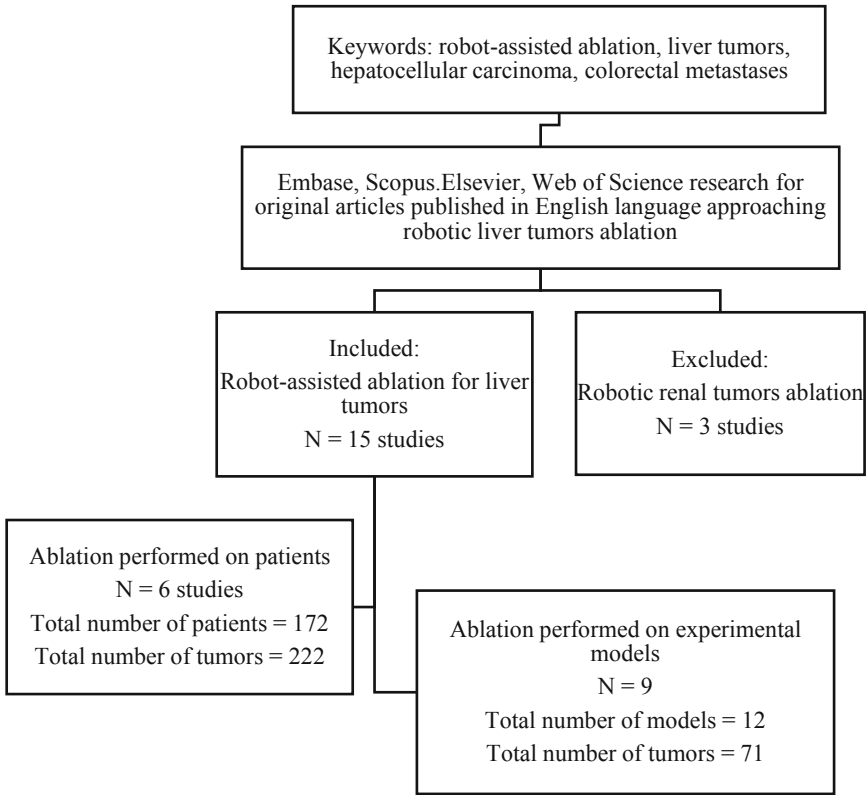


Fig. 1. Systematic review flow diagram

3 Results

A total of 22 publications were considered relevant for robot-assisted tumors ablation. Fifteen of these approached liver tumors ablation and were eligible for inclusion in the study. Six articles focused on the clinical aspect of robotic liver tumor aspect, providing patients description and characteristics on a total of 172 subjects (Table 2). There were nine studies, which focused on the technical assessment of the robot during ablation on experimental model, such as phantom tumor, porcine or rabbit livers with artificially

embedded tumors, made of molden agar (Table 3). Each of the clinical studies included more than 10 patients and varied from 11 to 46, information thoroughly depicted in Table 1.

Table 1. Publications according to number of patients or experimental models

Authors	Year of publication	Journal	Number of patients	Number of experimental models	HCC/CRLM/Experimental model
Abdullah et al.	2014	Eur Radiol	11	0	6 HCC 5 CRLM
Stintzing et al.	2013	Acta Oncol.	30	0	30 CRLM
Yang et al.	2010	IEEE/ASME Trans Mechatron	0	1	Phantom tumor
Liu et al.	2016	PLoS ONE	0	1	Porcine liver
Abdullah et al.	2015	Eur Radiol	20	0	10 HCC 10 CRLM
Mbalisike et al.	2015	Eur Radiol	30	0	11 NCC 5 CRLM
Franco et al.	2015	IEEE/ASME Trans Mechatron	0	1	Phantom tumor
Wen et al.	2014	Compute Meth Prog Bio	0	2	Phantom tumor
Chang et al.	2011	Ann Acad Med Singap	0	1	Porcine liver
Beyer et al.	2016	Int J Cars	46	0	10 HCC 24 CRLM
Won et al.	2017	Diagn Interv Radiol	0	1	Phantom tumor
Beyer et al.	2017	Int J Cars	35	0	18 HCC 18 CRLM
Li et al.	2018	Int J Hyperther	0	2	Porcine liver + Rabbit liver
Liu et al.	2018	Int J Med Robot Comp	0	2	Phantom tumor + Swine
An et al.	2019	J Med Biol Eng	0	1	Phantom tumor

Traditional indications for percutaneous ablation usually include malignant tumors, hepatocellular carcinoma (55 tumors) or colorectal liver metastases (92 tumors) for lesions smaller than 3 cm in long axis, which cannot benefit from liver resection. Although a new method emerged, overlapping radiofrequency ablation, that with the help of robotic systems multiple electrodes can be concomitantly inserted in order to produce necrosis on large volume tumors, showed by Liu et al. [1]. This require special kinematic systems calculated by mathematical algorithms (Table 3).

The mean tumor size approached in the surveyed series is 2.6 cm in diameter, within the range of 1.91 cm (Beyer et al.) [13] and 4 cm (An et al.) [14].

The most commonly reported type of ablation was microwave technique (43%), followed by radiofrequency (40%). Only one article evaluated laser ablation effects and another one reported irreversible electroporation (Table 6).

Table 2. Patient demographics

Authors	Number of patients	Number of controls	Age range (years)	Gender M:F
Abdullah et al.	11	0	42–80	9:2
Stinzing et al.	30	30	39–80	17:13
Abdullah et al.	20	30	32–80	12:8
Mbalisike et al.	30	40	33–83	10:11
Beyer et al.	46	30	54–85	36:10
Beyer et al.	35	19	46–78	29:6

Table 3. Experimental models details

Authors	Precision TPI	Accuracy (mm)	Overlapping ablation plan
Yang et al.	1.20	± 0.05	Voxel Growing Algorithm
Liu et al.	1×10^{-4}	2.1 ± 0.6	MathLab Algorithm
Franco et al.	0.05	1.5 ± 1.1	Voxel Growing Algorithm
Wen et al.	1.34–2.07	1.85–1.92	Baum–Welch Algorithm
Chang et al.	1.65	1.5	
Won et al.	0.2–0.5	2	iSYS1
Li et al.	0.9–1.5	1.3	NASA-TRX
Liu et al.	3–5	2	SIP-BASED Overlap Ablation
An et al.	1.7 ± 1.2	3 ± 1.24	

Out of the fifteen studies included, a number of 9 studies were experimental. In terms of technique precision, Liu’s study had the best precision (0.0001) [15], at the opposite pole is Wen’s study (1.34–2.07) [16]. Also, the studies carried out by Franco and Won had a good precision of the technique [17, 18]. In terms of accuracy, Yang’s study ranks first (0.05) and at the opposite pole is An’s study [9, 14]. Regarding the overlapping ablation plan every experimental study used a different plan (Table 4).

Table 4. Procedure details

Authors	Mean time (min)	Number of needles	Number of readjustments
Abdullah et al.		1	4
Stinzing et al.		1	
Yang et al.		>2	
Liu et al.		2–4	10
Abdullah et al.		1–5	12
Mbalisike et al.	25.2	2	3
Franco et al.	30	1	10
Wen et al.		2	
Chang et al.		2	
Beyer et al.	18.3	1	14
Won et al.		1	4
Beyer et al.	19.3	1–3	7
Li et al.	5	1	1
Liu et al.		1	3
An et al.		1	2

Analyzing the fifteen studies from the point of view of the procedure, only in five studies the time for a procedure was scored. Of these studies, three were clinical trials and two were experimental studies.

Needle positioning, number of needles used and methods used for the minimization of liver excursions between inspiration and expiration and liver banding at entrance of liver capsule were assessed. The number of needles used for ablation according to the tumor volume varied from 1 in 50% of cases to 5. The highest number of adjustments was noted in clinical trials with a maximum number of adjustments of 14 in Beyer's [19]. At the opposite end are the experimental studies, most with only one adjustment.

The robotic arm brings accuracy and precision in the multiple needle insertion, while minimising the burden brought by inspiratory excursions on the procedure. Immobilisation devices, ablation in apnea or vacuum mattresses were used as error minimization methods.

In order to achieve target displacement compensation following characteristics were taken into account: no-collision constraint, safety margin around tumor, tangency constraint, distance to critical structures, trajectory length and soft tissue deformation, depicted in Stinzing's, Li's and Chang's studies [20–22] (Table 5).

Table 5. Liver tumors characteristics

Authors	Number of tumors	Diameter of tumor (cm)	Mean diameter (cm)	Distance from skin surface (cm)	HCC/CRLM/EM
Abdullah et al.	17	1.1–3.0	2.2	6.2–13.7	6 HCC/5 CRLM
Stinzing et al.	35	0.8–5.3	3.3		35 CRLM
Yang et al.	1	>3			Phantom tumor
Liu et al.	9	3–6	3		Swine liver
Abdullah et al.	40	0.6–4.9	2.3	1.6–4	10 HCC/10 CRLM
Mbalisike et al.	30	1.1–4.6	2.3	0.61–1.66	11 HCC/5 CRLM
Franco et al.	4	1–5		2.8–4.7	Phantom tumor
Wen et al.	22	0.5			Phantom tumor
Chang et al.		<3			Swine liver
Beyer et al.	64	1–2.8	1.91	6.48 ± 2.35	10 HCC/24 CRLM
Won et al.	2	1–2			
Beyer et al.	36	1.53–3.36	2.49	4.43–10.51	18 HCC/18 CRLM
Li et al.					Porcine liver/Rabbit liver
Liu et al.	8	3.2–8.7			Phantom tumor/swine
An et al.	25		4		Phantom tumor

The type of robot used was different in the fifteen studies. Yang, Wen, Liu and An used prototypes of robotic systems in their studies [9, 14–16] and Abdullah, Mbalisike, Beyer and Won used the Maxio robotic model in their studies [7, 19, 20, 23]. From the point of view of the system used, most researchers used StarBurst microwave and radiofrequency ablation. Franco was the only one to perform laser ablation and An was the only one to use ultrasound to perform ablation [14, 17]. Most pre-procedural investigations were performed by CT, Liu and An, used the ultrasound to perform this evaluation. Post procedurally, the authors used most of the same technique used preoperatively.

Complications rated in the evaluated studies were infected bilioma (1 case), incomplete ablation (1 case), bleeding around puncture region, thermal collateral damage with bile ducts stenosis and laceration of vessels with haemorrhage. In most cases no complication appeared on the robot-assisted ablation cases.

Table 6. Technical characteristics

Authors	Type of robot	Ablation system	Method of procedure planning	Method of assessment	Total radiation dose/lesion (mGyxcm)
Abdullah et al.	ROBIO EX	Radiofrequency	CT Imaging	Contrast-enhanced CT	956.09 ± 400.33
Stinzing et al.	Cyber Knife™	Radiofrequency	CT fluoroscopy	CT fluoroscopy/MRI scans	240–360
Yang et al.	Novel overlapping RFA robotic system	Radiofrequency	CT	CT	
Liu et al.	5-DOF-needle driven robot	Microwave	2D US + EM tracker	2D US	
Abdullah et al.	Maxio/ROBIO Ex	Radiofrequency/Microwave	CT fluoroscopy	Contrast Enhanced CT	352 ± 228
Mbalisike et al.	Maxio	Microwave	CT fluoroscopy	MRI	193.8 ± 93
Franco et al.	4-DOF needle guiding robot	Laser	MRI	MRI	
Wen et al.	Novel Robot/Kinect Device/Procam	Radiofrequency	CT	CT	
Chang et al.	TRAINS	Radiofrequency	MRI/CT	MRI/CT	
Beyer et al.	Maxio	Microwave	CT	MRI	221.6 ± 105.7
Won et al.	Maxio	Radiofrequency	CT	CT	
Beyer et al.	Maxio	IRE	CT	CT	213
Li et al.	6-DOF UR5/CP3	Microwave	MRI/CT	MRI/CT	
Liu et al.	Novel robotic system	Radiofrequency	US	US	
An et al.	Novel robotic system	Ultrasound	US	US	

Beyer et al. states that a combination of CT and MRI is the favoured way of outcome assessment after liver tumor ablation in short-term follow-up, 6 weeks after procedure. Complete ablation was observed in 94.1% of robot-assisted cases versus 96.7% in manually ablated ones.

4 Discussion

The imaging, CT, US or MRI guided robotic ablation procedure (radiofrequency, microwave, laser, ultrasound or irreversible electroporation) involves a pre-procedural CT scan, the planning of the procedure and the programming of the robotic arm, the ablation performed by the robot under CT guidance and finally a control CT scan after completion, in order to have a reference point for follow-ups [16, 18].

The guided imaging robotic ablations has similar results to those performed manually without a significant difference in patient outcome [7, 23].

The number of repositions of the RFA needle is much more reduced in the case of the robotic procedure, which leads to the decrease of the duration of the procedure itself, but is prolonged by the longer planning time needed in advance [21]. The reason why the total time is higher in the case of the robotic procedure is especially due to the pre-procedural preparation and programming of the robotic arm, which are time-consuming stages.

Also, a small number of the RFA needle repositioning can be translated by an increased accuracy, thus reducing the total dose of ionizing radiation that the patient receives [23].

The robotic procedure is more expensive than the manual procedure in terms of costs, due to the still high prices of acquisition of the surgical robots.

Another problem of this procedure that should be carefully taken into account is the cranio-caudal movement of the liver during the respiratory movements. The robotic ablation procedure can only be performed in close collaboration with the anesthetic team. This is because the patient needs to be very well fixed on the CT table under total anesthesia with orotracheal intubation or several other mechanisms of displacement compensation should be used during ablation [14, 21]. One is mechanical ventilation with total muscle relaxation for minimizing the cranio-caudal respiratory movements of the liver triggered by the otherwise patient's spontaneous breathing. Also, to minimize the cranio-caudal respiratory movements of the liver it is useful to use low tidal volumes with high O₂ and high respiratory rate. Moreover, the pre-procedural CT scans, the placement of the needles and the CT performed during the procedure, as well as the post-procedural scans to verify the efficiency of the procedure were performed at the end of the expiration with the airways disconnected from the ventilator, so that the liver to be in exactly the same position as calculated.

We consider that a surgical robot in order to be used for the minimally invasive ablation is necessary to fulfill certain characteristics. It should be small size robot easily mounted on the CT table [12, 22]. The components of the robotic arm that come into contact with the patient and those which support the ablation needle should be made out of materials that withstand sterilization methods.

The robotic arm is necessary to have at least four degrees of freedom and easy to assemble and disassemble, especially the components that need sterilization [9, 16, 17].

Ideally, the robot should have low costs and high versatility, so it can be used for performing other invasive procedures, where there is a need for accuracy and precision in the execution of the procedure.

On the other side, is mandatory to have a safety system that allows the device to be stopped and withdrawn at the “0” pre-procedural set point at any time, when the robotic arm makes a wrong movement or does not work according to the plan, also at any time when the operator wants it for other reasons, especially when patients’ safety could be jeopardized [7, 19, 20].

The complications of this procedure do not differ from those of the manual procedure: haemorrhage, bilioma, hematoma, abscesses or even lesions of the structures adjacent to the liver [7, 13]. All of this can be avoided through proper pre-intervention planning.

Analyzing the data, we can highlight a number of aspects favorable to the application of this technique and some that require further attention. Pros for robotic surgery are: small incision, quicker patient recovery, small risk of infection, shorter hospital stay, better view for surgeons, easier access for hard to reach places, more precision in surgery, due to the software, that reduces the surgeon’s tremor. Cons for this technique are highlighted by higher costs, the robot itself is very expensive and the cost of disposable supplies are even higher [24].

The choice of the ablation system is solely influenced by the type of robot used, the preparation of the medical team and the financial capacity of the hospital to purchase a certain robot.

5 Conclusions

Imaging guided robotic ablation for liver tumors, primary or metastases is feasible and even if the total cost and duration of the procedure is higher than the manual procedure, it offers a number of advantages over the first one, such as a high accuracy with a minimum number of needle position readjustments and a lower total radiation, consecutively a much lower risk of complications. In the future, greater competition will be needed in the medical device market for a reduction of the costs of acquisition and use of these surgical robots. Development of more versatile robots and intuitive software that will reduce the total time of the procedures is highly expected, thus transforming robotic ablation guided by CT into the golden standard procedure for inoperable tumors or liver metastases.

Acknowledgments. This work was supported by a grant of the Romanian Ministry of Research and Innovation, PCCCDI – UEFISCDI, project number PN-III-P1-1.2-PCCDI-2017-0221/59PCCDI/2018 (IMPROVE), within PNCDI III.

Abbreviations

HCC	= hepatocellular carcinoma
CRLM	= colorectal liver metastases
M:F	= male to female ratio
EM	= experimental model

RFA	= radiofrequency ablation
CT	= computed tomography scan
MRI	= magnetic resonance imaging
US	= ultrasound
RITA	= radiofrequency interstitial tissue ablation
IRE	= irreversible electroporation
DLP	= dose length product
TRAINS	= transcutaneous robot-assisted ablation with 3D navigation
ALPPS	= associating liver partition and portal vein ligation for staged hepatectomy

References

1. Fan, S.T., Mau, L.C., Poon, R.T., et al.: Continuous improvement of survival outcomes of resection of hepatocellular carcinoma: a 20-year experience. *Ann. Surg.* **253**, 745–758 (2011)
2. Tranchart, H., Di Giuro, G., Lainas, P., Roudie, J., Agostini, H., Franco, D., et al.: Laparoscopic resection for hepatocellular carcinoma: a matched-pair comparative study. *Surg. Endosc.* **24**, 1170–1176 (2010)
3. Garcea, G., Lloyd, T.D., Aylott, C., Maddern, G., Berry, D.P.: The emergent role of focal liver ablation techniques in the treatment of primary and secondary liver tumours. *Eur. J. Cancer* **39**, 2150 (2003)
4. Krishnamurthy, V., Casillas, V., Latorre, L.: Radiofrequency ablation of hepatic lesions: a review. *Appl. Radiol.* **32**, 11 (2003)
5. Seki, T., Kubota, Y., Wakabayashi, M., Kuneida, K., Nakatani, S., Shiro, T., et al.: Percutaneous trans-hepatic microwave coagulation therapy for hepatocellular carcinoma proliferating in the bile duct. *Dig. Dis. Sci.* **39**, 663 (1994)
6. Morikawa, S., Inubushi, T., Kurumi, Y., Naka, S., Sato, K., Tani, T.: New assistive devices for MR-guided microwave thermocoagulation of liver tumors. *Acad. Radiol.* **10**, 180 (2003)
7. Abdullah, B.J.J., et al.: Robotic-assisted thermal ablation of liver tumours. *Eur. Radiol.* **25**, 246–257 (2015)
8. Koethe, Y., Xu, S., Velusamy, G., Wood, B.J., Venkatesan, A.M.: Accuracy and efficacy of percutaneous biopsy and ablation using robotic assistance under computed tomography guidance: a phantom study. *Eur. Radiol.* **24**, 723–730 (2014)
9. Yang, L., Wen, R., Qin, J., et al.: A robotic system for overlapping radiofrequency ablation in large tumor treatment. *IEEE/ASME Trans. Mechatron.* **15**, 887–897 (2010)
10. Schumann, C., Bieberstein, J., Braunewell, S., Niethammer, M., Peitgen H-O: visualization support for the planning of hepatic needle placement. *Int. J. CARS* **7**, 191–197 (2012)
11. Kloeckner, R., Dos Santos, D.P., Schneider, J., Kara, L., Dueber, C., Pitton, M.B.: Radiation exposure in CT-guided interventions. *Eur. J. Radiol.* **82**, 2253–2257 (2013)
12. Liu, P., Qin, J., Duan, B., et al.: Overlapping radiofrequency ablation planning and robot-assisted needle insertion for large liver tumors. *Int. J. Med. Robot. Comput. Assist. Surg.* **15**, 1952 (2019)
13. Beyer, L.P., Pregler, B., Niessen, C., Dollinger, M., Graf, B.M., Müller, M., Schlitt, H.J., Stroszczyński, C., Wiggermann, P.: Robot-assisted microwave thermoablation of liver tumors: a single-center experience. *Int. J. CARS* **11**, 253–259 (2016)
14. An, Chih Yu., Hsu, Y.L., Tseng, C.S.: An ultrasound-guided robotic HIFU ablation system with respiration induced displacement and time delay compensation. *J. Med. Biol. Eng.* **39**, 796–805 (2019)

15. Liu, S., Xia, Z., Liu, J., et al.: Automatic multiple-needle surgical planning of robotic-assisted microwave coagulation in large liver tumor therapy. *PLoS ONE* **11**, 149482 (2016)
16. Wen, R., Tay, W., Nguyen, B.P., Chng, C.-B., Chui, C.-K.: Hand gesture guided robot-assisted surgery based on a direct augmented reality interface. *Comput. Methods Programs Biomed.* **116**, 68–80 (2014)
17. Franco, E., Brujic, D., et al.: Needle-guiding robot for laser ablation of liver tumors under MRI guidance. *IEEE/ASME Trans. Mechatron.* **21**, 931–944 (2016)
18. Won, H.J., Kim, N., Kim, G.B., Seo, J.B., Kim, H.: Validation of a CT-guided intervention robot for biopsy and radiofrequency ablation: experimental study with an abdominal phantom. *Diagn. Interv. Radiol.* **23**, 233–237 (2017)
19. Beyer, L.P., Pregler, B., Michalik, K., et al.: Evaluation of a robotic system for irreversible electroporation (IRE) of malignant liver tumors: initial results. *Int. J. CARS* **12**, 803 (2017)
20. Stintzing, S., Grothe, A., Hendrich, S., Hoffmann, R.-T., Heinemann, V., Rentsch, M., et al.: Percutaneous radiofrequency ablation or robotic radiosurgery for salvage treatment of colorectal liver metastases. *Acta Oncol.* **52**, 971–977 (2013)
21. Li, D., Cheng, Z., Chen, G., Liu, F., Wu, W., Yu, J., et al.: A multimodality imaging-compatible insertion robot with a respiratory motion calibration module designed for ablation of liver tumors: a preclinical study. *Int. J. Hyperth.* **34**, 1194–1201 (2018)
22. Chang, S., Yang, L.: Current technology in navigation and robotics for liver tumours ablation. *Ann. Acad. Med. Singap.* **40**, 231–236 (2011)
23. Mbalisike, E.C., Vogl, T.J., Zangos, S., Eichler, K., Balakrishnan, P., Paul, J.: Image-guided microwave thermoablation of hepatic tumours using novel robotic guidance: an early experience. *Eur. Radiol.* **25**, 454–462 (2015)
24. Gerboni, G., Greer, J.D., Laeseke, P.F., Hwang, G.L., Okamura, A.M.: Highly articulated robotic needle achieves distributed ablation of liver tissue. *IEEE Robot. Autom. Lett.* **2**(3), 1367–1374 (2017)



Towards Building a Computerized System for Modelling Advanced HCC Tumors, in Order to Assist Their Minimum Invasive Surgical Treatment

Delia Mitrea¹(✉), Tiberiu Marita¹, Flaviu Vancea¹, Sergiu Nedeveschi¹, Paulina Mitrea¹, Gabriel Mihai Neamt¹, Sanda Timoftei¹, Vlad Florian¹, Corina Radu², Mihai Socaciu³, Horia Stefanescu², and Nadim Al Hajjar³

¹ Technical University of Cluj-Napoca, Cluj-Napoca, Romania
delia.mitrea@cs.utcluj.ro

² O. Fodor Regional Institute of Gastroenterology-Hepatology,
Cluj-Napoca, Romania
drcorinaradu@gmail.com

³ I. Hatieganu University of Medicine and Pharmacy, Cluj-Napoca, Romania
na_hajjar@yahoo.com

Abstract. Hepatocellular Carcinoma (HCC) is the most frequent form of liver cancer, being the fourth leading cause of cancer-related death worldwide. The curative treatment in most cases is the tumor removal from the body (surgery), but more than 70% of HCC patients have advanced tumors and cannot be treated with such procedures. Alternative laparoscopic surgical treatments, such as high dosage radiation-brachytherapy (HDR-BT) or inside-tumor drug release (IDR), are currently researching for tumor size reduction. Our target is to develop computerized methods for assisting the medical robot used in such treatments, to make them safer and more efficient. We build an accurate 3D model of the HCC anatomical context, based on Computed Tomography (CT) images acquired before surgery, putting into evidence the HCC tumor, its position within the liver and the most important blood vessels connected to it. We also highlight, in real time, during surgery, the 2D slice corresponding to the transducer position. In this article, we describe the corresponding software system, focusing on the segmentation and 3D reconstruction techniques, assessed through specific experiments.

Keywords: Hepatocellular Carcinoma (HCC) · Minimum -invasive surgery · Image processing and analysis · 3D computerized model · Contrast enhanced CT images

1 Introduction

HCC is the most often met malignant liver tumor, identified in 70% of the liver cancer cases. In adult men, HCC is the fifth most frequently diagnosed cancer, and in adult women, it is the ninth most commonly diagnosed cancer worldwide. HCC is the fourth leading cause of cancer-related death in the world [5]. One of the curative treatments for HCC tumors is the surgical resection, but in the case of advanced HCC, extensive resection presents important risks, such as the liver dysfunction [5]. Alternative laparoscopic surgical treatments, based on local intervention techniques (HDR-BT or IDR) are preferred in order to reduce the tumour size [5]. Computerized methods can be very helpful in order to assist these surgical treatments, making them safer and more efficient. Relevant methods that approach this subject are described in [5,13]. We develop a complex computerized system, involving artificial vision techniques, which interacts with a medical robot. This robot is built in order to assist a minimum invasive surgical treatment which assumes to treat HCC tumor through Radio-Frequency Ablation (RFA), HDR-BT or IDR during laparoscopic surgery. The robot will interactively control, during surgery, the position of an ultrasound machine transducer and will apply the treatment at the right moment. In this work, we describe the structure of our computerized system, focusing on the specific segmentation and 3D reconstruction techniques. For segmentation, we compare Convolutional Neural Network (CNN) based techniques [2], with an improved version of Fuzzy C-means Clustering [12], within contrast enhanced CT images. For 3D reconstruction, we present the adopted methods and relevant experiments. The rest of this paper is organized as follows: after the introduction, the state of the art is described, then the computerized system and the experimental results are presented. At the end, conclusions and further development possibilities are formulated.

2 State of the Art

2.1 Computerized Systems for Surgical Treatment Assistance

A computerized system that generates, before surgery, a 3D model of the liver and tumor anatomical model is described in [5]. In this context, the Myrian-XP-Live application was employed in order to automatically extract information concerning the liver or tumor parenchyma, respectively the important arteries and veins, finally generating 3D reconstructed images of the liver, estimating the liver volume in the same time, together with the location and size of the tumor. In this case, the final purpose was the destruction of the HCC tumor through RFA. In [13], another computerized procedure, based on CEUS-CT or CEUS-MRI images was described, aiming for evaluating the ablation margins of the HCC tumor. The existing systems either perform the generation of a 3D anatomical model before surgery, or they apply image fusion techniques during surgery, while computerized, image analysis methods are not extensively employed. Thus, there does not exist a computerized system, performing both the generation of a 3D

model before surgery and specific processing operations during surgery, so we aim to do this in our research.

2.2 Tumor Segmentation and 3D Reconstruction

Concerning *the traditional approach for tumor segmentation*, classical methods were widely implemented for tumor segmentation within multiple types of medical images, involving Gabor filters, Support Vector Machines (SVM), 3D deformable models [21] and complex clustering techniques [20]. Lately, *the deep learning techniques*, based on complex neural network architectures, were successfully employed for both recognition and segmentation within medical images. Stacked Denoising Autoencoders (SAE) [6] and CNNs [3,9] were mostly implemented in this context. In [3], liver and tumor segmentation within MRI and CT images was performed, using Cascaded Fully Convolutional Neural Networks (CFCNs). Two CNNs were trained and cascaded, for performing the segmentation of both liver and suspect lesions. The resulting accuracy, measured through the Dice score, was above 94%. In [9], an Attention Hybrid Connection Network (AHCNet) was proposed to process CT volumes, integrating high-level semantic information with low-level location information. The authors cascaded three AHCNets, the first being used to detect 3D bounding boxes for the liver, the second being able to segment the liver, while the third to segment the tumor. As we can notice, there are many approaches addressing the problem of segmenting CT images using both traditional and CNN techniques. However, no systematic comparison between CNN architectures, respectively conventional techniques, was performed, in order to segment the HCC tumor within contrast enhanced CT images, so we do this in the present article. Concerning the field of *medical image based 3D reconstruction*, many approaches exist, aiming to visualize the bone structure, to estimate the volume of organs and tumors, such as [1,4]. Thus, the 3D reconstruction techniques were widely implemented in various situations in medical imaging. We also adopt appropriate 3D reconstruction methods in order to develop our computerized system, as further described.

3 Description of the Computerized System

The computerized system for 3D HCC modeling will communicate with a medical robot that interactively manipulates the ultrasound transducer during a minimum invasive, laparoscopic surgical intervention and injects, at the right moment, a harmful agent in the HCC tumor. The medical robot used in this intervention is a parallel robotic system, specially designed for the treatment of HCC. The robotic system consists of two arms, one for holding the ultrasound transducer, while the other one will handle the needle injection in the given/computed pose (position and orientation). The computerized system will perform the following tasks: **before surgery**, the generation of the 3D model of HCC, referring to the position and extension of the tumor, as well as to the relation with the most important blood vessels, based on CT images acquired

before surgery; **during surgery**, on user demand, the computerized system will acquire the ultrasound image corresponding to the current transducer position, will get from the robot the parameters corresponding to the current pose and will blend the US image (slice) within the 3D CT model, obtaining thus an enhanced view of the analysed section of the 3D model; the user (surgeon) will analyze this blended slice and will establish if this is the right moment for treatment application (if the position is close to the tumor center and if there are no important blood vessels nearby). The computerized system for the generation of the HCC 3D model consists of the following modules, illustrated in Fig. 1: **the segmentation module**, which performs 2D and 3D segmentation of the liver, HCC tumor, and blood vessels using methods like clustering [12], region growing or active contour models (*snakes*) [15], respectively CNN [9], within CT images acquired before surgery; **the 3D reconstruction module**, which performs 3D reconstruction from segmented 2D CT images, generating the 3D anatomical model; **the fusion module**, which receives the ultrasound image, as well as the current transducer pose and blends it in the segmented 3D volume by fusing the US image with the virtual (co-planar) section of the CT; **the communication module**, assuring the communication of the computerized system with the ultrasound machine, respectively with the robot. Having the complete parameters of the US transducer integrated in the kinematic model of the robot, the correlation of the US images with the current transducer pose is computed by the robot controller and then fed to the communication module.

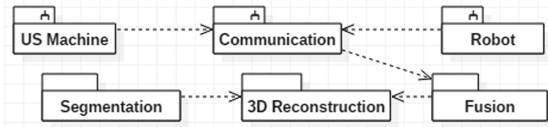


Fig. 1. The main components of the computerized system

3.1 Methods

3.1.1 Segmentation of the HCC Tumors

In order to perform HCC segmentation *through conventional methods*, the Fast and Robust Fuzzy-C-means Clustering (FRFCM) technique [12] was adopted. After employing FRFCM, we performed image thresholding, morphological closing, the labelling of the resulted objects, then we selected the object having the maximum area. This segmentation algorithm was applied on the liver surface, within contrast enhanced CT images. The images that resulted after the application of the FRFCM technique were also provided as input for the CNN classifiers. Regarding *the deep learning approach*, we took advantage of recent advances in *CNN based solutions* for semantic segmentation for the task of pixel-wise HCC segmentation. Due to the low number of training images available, we employed

transfer learning using a DeepLab-v3 [2] model with a ResNet-101 [7] backbone pretrained on the COCO dataset [14]. The neural network input was composed of three channels, the first being the grayscale image, the second being the morphological reconstruction and the third being the FRFCM result. We studied the effect of how much the number of clusters used in FRFCM affected the detection results by training two different models. The first model used FRFCM with 50 clusters and the second one used FRFCM with 100 clusters in order to produce the third channel of the network input. We used the IoU loss function [17] in order to update the weights in the model. The IoU loss function is shown in Eq. (1):

$$L_{IoU} = -\log \left(\frac{\sum_{i=1}^N p_i g_i}{\sum_{i=1}^N p_i + g_i - p_i g_i} \right) \quad (1)$$

where N is the number of pixels in the batch, p is the predicted probability of a pixel to be a HCC pixel and g is the ground truth.

3.1.2 3D Reconstruction and Anatomical Model Elaboration

The 3D space reconstruction of the anatomical structures of interest (HCC, blood vessels) from the CT image sequence are implemented using functions from dedicated libraries in the field: Visualization Toolkit (VTK) [19] for rendering and visualization and Insight segmentation and registration ToolKit (ITK) [8], respectively Elastix [10] for segmentation and fusion (registration). Elastix is an open source toolkit that relies on ITK and provides a broad range of rigid and non-rigid registration algorithms. The fusion/registration between the 3D model obtained from the pre-operator CT image sequence and the US images will be a 2 fold process: *for preparatory planning*, the 2D virtual CT sections obtained by fusing Contrast Enhanced Ultrasound (CEUS) images with the CT volume through the RVS (Real-time Virtual Sonography) module attached to the Arietta V70 (Hitachi) ultrasound platform will be aligned with the 3D model by a rigid transformation obtained by a systematic search; *for the intra-operative procedure*, a non-rigid transformation will be applied to the intra-operative US image aligned with the 3D model based on the pose of the robotic arm that holds the US probe. The VTK-based spatial reconstruction uses a specific visualization pipeline [16] that is responsible for constructing the geometric representation which is then rendered using the graphical pipeline. The elements of the pipeline are: “Reader”; “Filters”, which can be optionally added in order to modify the data in a user specific way; “Mappers”, providing the transition between the processing and the visualization segments of the pipeline; “Actors”, representing a component used to control and modify the visual appearance of the displayed data, being associated to a “Renderer Window”; “Interactors”, which allow users to interact with the graphical data.

4 Experimental Results

We have collected a dataset of 152 contrast enhanced CT images from 24 patients. These patients were affected by HCC and underwent biopsy for diag-

nostic confirmation. The images were acquired during the arterial phase, using a Siemens Somatom Perspective machine (2015), with 64 detectors, after the injection of the contrast agent. All the images were 512×512 pixels in size. Within these images, the HCC structures were manually annotated by medical professionals.

4.1 HCC Segmentation

The dataset was randomly split into a training set consisting of 92 images, a validation set consisting of 30 images and a test set consisting of 30 images. While training, we augmented the images using random rotation with an angle in the range $[-5, 5]$, random translation with offsets sampled from the range $[-26, 26]$, random scaling between $[0.95, 1.05]$ of the original image size and random horizontal flipping with a probability of 50%. We trained the CNN for 150 epochs using the AdamW [11] optimizer with β_1 and β_2 set to 0.9 and 0.99 respectively, a weight decay of 0.001 and a batch size of 4. Every epoch, we adjusted the learning rate using a one cycle scheduler [18] that increased the learning rate from an initial value up to a maximum value after which we decreased it. In our experiments, we increased the learning rate from $2e-4$ up to $2e-3$ for the first 40% iterations and decreased it to $2e-9$ in the remaining iterations. For the model trained with just the original image, we found that the increase of the learning rate from $1.8e-4$ to $1.8e-3$ and back to $1.8e-9$ led to better results. We evaluated the performance of the models using the Intersection over Union (IoU) metric like in [2]. Figure 2 and Table 1 illustrate prediction results on images from the test set. It can be observed that the model using just the original image as input performs better. This demonstrates that the network can come up with good features on its own and that heavy pre-processing of the data is not needed. We also employed the **improved FRFCM technique** [12]. The experiments were performed in Matlab 2016, on the dataset described above. The best performance was achieved for 10 clusters, the highest IoU being 40%.

Table 1. IoU on the test set

	50 clusters	100 clusters	Original image
IoU	57.35%	70.63%	73.20%

4.2 3D Reconstruction of the Anatomical Context

A 3D reconstruction tool based on the VTK library [19] is under development by our team. In the current phase the tool provides functions for native CT series visualization along with the other two orthogonal sections (sagittal and coronal - generated from the native series). A volume can be also rendered from the native series and basic segmentation filters can be applied. In Fig. 3a, a native axial CT section is presented along with the generated sagittal (Fig. 3b) and coronal

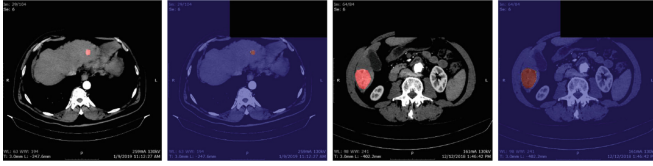


Fig. 2. DeepLab-v3 results for input with 100 clusters segmentation as third channel. The first and third column shows the ground truth, while the second and fourth column shows the prediction result. The results are colored such that blue represents low probabilities and red represents high probabilities. Parts of the image containing confidential information have been covered.

(Fig. 3c) views. The rendering of the 3D volume after applying a VTK filter that segments the bright pixels (bones) is shown in Fig. 3d. Zoom-in, zoom-out, respectively custom rotation (as shown in Fig. 3b–d) are also available. Other filters for the 3D segmentation and visualization of the anatomical structures of interest (liver, HCC, blood vessels, etc.) will be implemented together with the integration of the 2D segmentation methods.

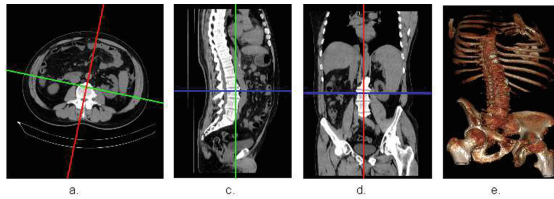


Fig. 3. Illustration of the 3D reconstruction process from an axial CT series

5 Conclusions

The computerized system described in this paper will assist the minimum invasive, laparoscopic procedure of reducing the size of the advanced HCC tumors. The preliminary experiments presented above show promising results, considering both the segmentation and 3D reconstruction tasks. Concerning the segmentation, due to the complexity of the HCC tumor structure, as well as to the variation of the aspect of this tumor, from case to case, the CNN based method overpassed in accuracy the traditional method, finally leading to an increased value of IoU, over 70%. In our future work, we aim to enhance our experimental dataset and to further improve the performances of our methods, by also experimenting other CNN architectures.

Acknowledgements. This work was funded by the Romanian National Authority for Scientific Research and Innovation under Grant number PN-III-P1-1.2-PCCDI2017-0221 Nr. 59/1st March 2018.

References

1. Al-Zu'bi, S., Al-Ayyoub, M., et al.: Enhanced 3D segmentation techniques for reconstructed 3D medical volumes: robust and accurate intelligent system. *Procedia Comput. Sci.* **113**, 531–538 (2017)
2. Chen, L., Papandreou, G., Schroff, F., Adam, H.: Rethinking Atrous Convolution for Semantic Image Segmentation. *CoRR*, vol. abs/1809.06323 (2018)
3. Christ, P.F., Ettliger, F., et al.: Automatic liver and tumor segmentation of CT and MRI volumes using cascaded fully convolutional neural networks. *CoRR*, vol. abs/1702.05970, (2017)
4. Chiorean, L., Szasz, T., Vaida, M., Voina, A.: 3D Reconstruction and volume computing in medical imaging. *Acta Technica Napocensis. Electron. Telecommun.* **58**(3), 18–24 (2011)
5. Gong, Y., Tang, Y., Geng, Y., et al.: Comparative safety and effectiveness of ultrasound-guided radiofrequency ablation combined with preoperative three-dimensional reconstruction versus surgical resection for solitary hepatocellular carcinoma of 3–5 cm. *J. Cancer* **10**(22), 5568–5574 (2019)
6. Hassan, T.M., Elmogy, M., Sallam, E.S.: Diagnosis of focal liver diseases based on deep learning technique for ultrasound images. *Arab. J. Sci. Eng.* **42**(8), 3127–3140 (2017)
7. He, K., Zhang, X., Ren, S., Sun, J.: Deep residual learning for image recognition. In: 2016 IEEE Conference on Computer Vision and Pattern Recognition (CVPR), pp. 770–778, June 2016
8. Insight segmentation and registration ToolKit (ITK). <https://itk.org/>
9. Jiang, H., Shi, T., et al.: An application of attention mechanism and hybrid connection for liver tumor segmentation in CT volumes. *IEEE Access* **7**, 24898–24909 (2019)
10. Klein, et al.: elastix: a toolbox for intensity-based medical image registration. *IEEE Trans. Med. Imaging* **29**(1) (2010). <http://elastix.isi.uu.nl/index.php>
11. Loshchilov, I., Hutter, F.: Fixing weight decay regularization in adam. *CoRR*, vol. abs/1711.05101 (2017)
12. Lei, T., Jia, X.Y., Zhang, L., He, H., et al.: Significantly fast and robust fuzzy c-means clustering algorithm based on morphological reconstruction and membership filtering. *IEEE Trans. Fuzzy Syst.* **26**(5), 3027–3041 (2018)
13. Li, K., Su, Z., Xu, E., Huang, Q., et al.: Evaluation of the ablation margin of hepatocellular carcinoma using CEUS-CT/MR image fusion in a phantom model and in patients. *BMC Cancer* **17**, 61 (2017)
14. Lin, T., Marie, M., Belongie, S.J., Bourdev, L.D., Girshick, R.B., Hays, J., Perona, P., Ramanan, D., Dollar, P., Zitnick, C.L.: Microsoft COCO: common objects in context. *CoRR*, vol. abs/1405.0312 (2014)
15. Masood, S., et al.: A survey on medical image segmentation. *Curr. Med. Imaging Rev.* **11**, 3–14 (2015)
16. Nysjo, J.: Introduction to Python and VTK. In: Scientific Visualization, HT 2014: lecture 2. Upsala University, Centre for Image Analysis (2014)
17. Rahman, M.A., Wang, Y.: Optimizing intersection-over-union in deep neural networks for image segmentation. In: International Symposium on Visual Computing (ISVC), vol. 10072, pp. 234–244. Springer (2016)
18. Smith, L.N., Topin, N.: Super-convergence: very fast training of residual networks using large learning rates. *CoRR* vol. abs/1708.07120 (2017)
19. The Visualization Toolkit (VTK). <https://vtk.org/>

20. Zhang, D., Xu, M., Quan, L., Yang, Y., Qin, Q., Zhu, W.: Segmentation of tumor ultrasound image in hifu therapy based on texture and boundary encoding. *Phys. Med. Biol.* **60**(5), 1807–1830 (2015)
21. Zhan, Y., Shen, D.: Deformable segmentation of 3-D ultrasound prostate images using statistical texture matching method. *IEEE Trans. Med. Images* **25**(3), 256–272 (2006)

Gears



Load Sharing and Quasi-Static Transmission Error of Non-Standard Tooth Height Spur Gears

José I. Pedrero^(✉), Miryam B. Sánchez, and Miguel Pleguezuelos

UNED, Madrid, Spain

{jpedrero, msanchez, mpleguezuelos}@ind.uned.es

Abstract. A simple, analytical model for load sharing and quasi-static transmission error of spur gears with non-standard tooth height is presented. It is based on the minimum elastic potential energy principle and considers the influence of profile modifications and tooth deflections. In addition, it is suitable for different tooth height on pinion and wheel, as well as for standard and high-contact-ratio spur pairs.

Keywords: Spur gears · Load sharing · Quasi-static transmission error · Meshing stiffness

1 Introduction

Many studies on the calculation of the meshing stiffness (MS) of a spur gear pair can be found in literature [1–3, 9, 10]. All of them obtain a symmetric -or almost symmetric- curve of MS respect to the midpoint of the path of contact. But these studies always consider equal tooth height on pinion and wheel. For non-equal tooth height, the MS curve loses its symmetry, which alters the curve of load sharing ratio (LSR) and therefore influences the critical load points, the critical load conditions and the final load carrying capacity.

Non equal tooth height is not unusual in internal gears, in which small tooth number difference is frequently required, resulting in secondary interference problems, which should be avoided by reducing the wheel tooth height. But the same problem can arise in external tooth gears with undercut pinion teeth if the amount of undercut reduces the effective length of contact (which is called ‘vacuum gearing’).

The authors developed a model for the MS and the LSR for standard (SCR) [4] and high contact ratio (HCR) [6, 7] gears. This model was improved later to describe the quasi-static transmission error (QSTE) and the influence of profile modifications for symmetric MS curves [5, 8], and consequently for standard tooth height. In this work, this model of QSTE and profile modification is extended to non-standard tooth height spur gears, including different tooth height on both gears, keeping the simple, analytic formulation of previous models.

2 Meshing Stiffness and Load Sharing Ratio

Different models of MS have been developed, both from analytical approaches and finite element (FE) analyses. For standard tooth height, i.e. tooth addendum equal to the module m , all of them result in a K_M curve as one in Fig. 1 (left). From this curve, the LSR can be computed with the equation:

$$R(\xi) = \frac{K_M(\xi)}{\sum_j K_M(\xi + j)} \tag{1}$$

where ξ is the contact point parameter [4–8] and the sum is extended to all the tooth pairs in simultaneous contact.

Three different zones can be distinguished in the contact interval: premature contact ($\xi_{min} \leq \xi \leq \xi_{inn}$), theoretical contact ($\xi_{inn} \leq \xi \leq \xi_o$), and delayed contact ($\xi_o \leq \xi \leq \xi_{max}$). Premature and delayed contact intervals are induced by the tooth deflections under load, which causes a non-conjugate contact outside the pressure line between the root of one tooth and the tip of the other [5, 8]. As seen in Fig. 1 (left), the MS along these additional contact intervals is quite uniform, and very close to the value at the limits of the theoretical contact interval. From the same figure, the loading and unloading processes along the additional contact intervals can be described by a parabolic function [5, 8]. Though the lengths of both additional intervals are not identical, they are very similar because, due to the symmetry of the MS function, the tooth pair deflections at theoretical inner and outer points of contact are equal.

Figure 1 (right) presents the MS curve for a tooth pair with reduced addendum on wheel. This case corresponds to undercut pinion teeth inducing vacuum gearing. Along the theoretical contact interval, the curve is identical to one in Fig. 1 (left) but truncated at the point corresponding to the actual inner point of contact (described by the reduced wheel addendum or the limit of undercut pinion profile) [6]. The loading and unloading processes are described by similar parabolic functions, but in this case the lengths of the additional contact intervals are different, because the tooth deflections at inner and outer points of contact are not equal.

All these diagrams have been obtained from a simple model based on the hypothesis of equal approach between driving and driven teeth for all the tooth pairs in simultaneous

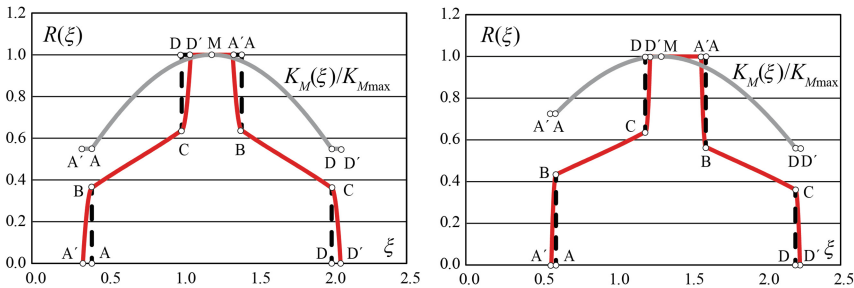


Fig. 1. MS and LSR for standard tooth height (left) and reduced addendum on wheel (right)

contact, which is congruent with the hypothesis of minimum elastic potential energy [5, 8]. Accordingly, the load transmitted by the tooth pair j is described by:

$$F_j(\xi) = K_M(\xi + j)(\delta(\xi) - \delta_G(\xi + j)) \tag{2}$$

where $\delta(\xi)$ is the approached distance between teeth on the pressure line at contact point ξ and $\delta_G(\xi)$ is the distance the mating teeth should approach each other to start the contact inside the additional contact intervals. This distance can be computed from [8]:

$$\begin{aligned} \delta_G(\xi) &= \left(\frac{2\pi}{z_1}\right)C_p r_{b1}(\xi_{im} - \xi) \text{ for } \xi_{\min} \leq \xi \leq \xi_{im} \\ \delta_G(\xi) &= \left(\frac{2\pi}{z_1}\right)C'_p r_{b1}(\xi - \xi_o) \text{ for } \xi_o \leq \xi \leq \xi_{\max} \end{aligned} \tag{3}$$

where coefficients C_p and C'_p can be computed as described in [5, 8]. Applying Eq. (2) to all the pairs in contact, after some calculations, the following expression is obtained for the approach distance:

$$\delta(\xi) = \frac{F_T + \sum_j K_M(\xi + j)\delta_G(\xi + j)}{\sum_j K_M(\xi + j)} \tag{4}$$

From Eq. (4), the load at tooth pair j and the LSR curves in diagrams of Fig. 1 are obtained by replacing Eq. (4) in Eq. (2). But the approach distance given by Eq. (4) also describes the QSTE, since the transmission error is the difference between the actual and theoretical output angle, thus the QSTE is given by:

$$\varphi_2(\xi) = \frac{\delta(\xi)}{r_{b2}} \tag{5}$$

Figure 2 presents the QSTE curves for standard (left) and non-standard (right) tooth height spur gears.

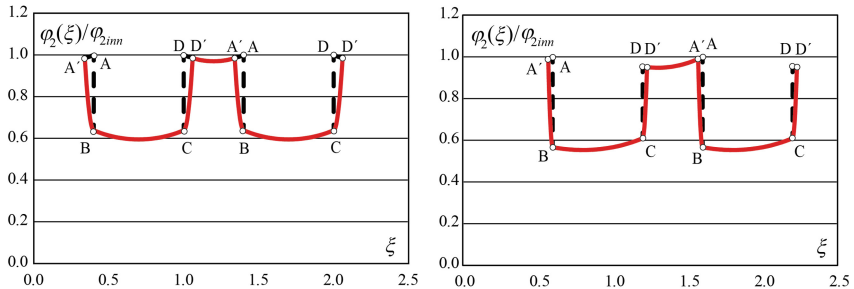


Fig. 2. QSTE for standard tooth height (left) and reduced addendum on wheel (right)

3 Profile Modification

To avoid the shock induced by the earlier start of contact between loaded teeth, profile modifications are often used. To optimize the modification (shock completely avoided, and contact ratio not reduced) the amount of relief at the driven tooth tip should be equal to the approach distance between teeth at the theoretical inner point of contact. Similarly, the amount of relief at the driving tooth tip should be equal to the approach distance at the theoretical outer point of contact. However, the length and shape of modification at both teeth will influence the LSR and QSTE. In fact, along the interval of modification, the load transmitted by the tooth pair is given as follows:

$$F_j(\xi) = K_M(\xi + j)(\delta(\xi) - \delta_G(\xi + j) - \delta_R(\xi + j)) \tag{6}$$

where $\delta_R(\xi)$ is the amount of modification at contact point described by ξ . Figure 3 shows the geometry of a profile modification with tip relief at both pinion and wheel teeth.

For linear tip relief and lengths of modification $\Delta\xi_{r-inn}$ and $\Delta\xi_{r-o}$, $\delta_R(\xi)$ is given by:

$$\begin{aligned} \delta_R(\xi) &= \delta_{Rmax-inn} \cdot \left(\frac{\xi_{inn} + \Delta\xi_{r-inn} - \xi}{\Delta\xi_{r-inn}} \right) \text{ for } \xi_{inn} \leq \xi \leq \xi_{inn} + \Delta\xi_{r-inn} \\ \delta_R(\xi) &= \delta_{Rmax-o} \cdot \left(\frac{\xi_o - \Delta\xi_{r-o} + \xi}{\Delta\xi_{r-o}} \right) \text{ for } \xi_o - \Delta\xi_{r-o} \leq \xi \leq \xi_o \end{aligned} \tag{7}$$

where $\delta_{Rmax-inn}$ and δ_{Rmax-o} are equal to $\delta(\xi_{inn})$ and $\delta(\xi_o)$, respectively. From Eq. (6), the LSR and QSTE can be computed by following the same procedure as described above. The approach distance is obtained as follows:

$$\delta(\xi) = \frac{F_T + \sum_j K_M(\xi + j)(\delta_G(\xi + j) + \delta_R(\xi + j))}{\sum_j K_M(\xi + j)} \tag{8}$$

Note that $\delta_G(\xi) = 0$ along the complete theoretical contact interval, and consequently along the interval of modification. However, for spur gears with no profile modification at the outer limit of the path of contact, $\delta_G(\xi)$ will be equal to 0 along the modification

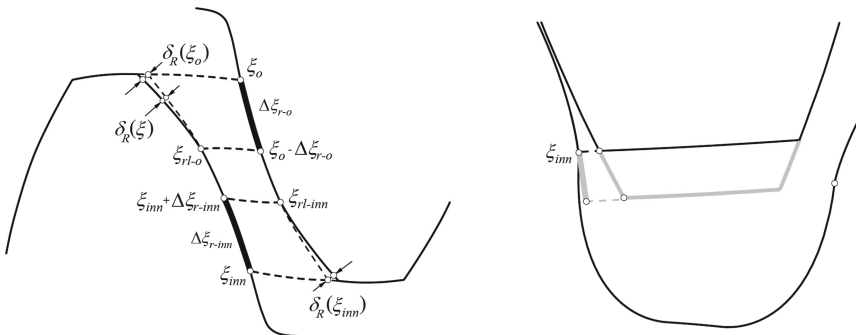


Fig. 3. Geometry of profile modification (left); addendum reduction by vacuum gearing (right)

interval $\xi_{inn} \leq \xi \leq \xi_{inn} + \Delta\xi_{r-inn}$, but may be different from 0 for previous tooth pair j if $\xi_o \leq \xi + j \leq \xi_{max}$. Figure 4 presents the LSR and QSTE for standard tooth height and profile modification at both limits of the interval (left), and for reduced addendum on pinion and profile modifications at wheel tooth tip (right).

4 High Contact Ratio Spur Gears

To ensure that contact occurs inside the pressure line, at least one tooth pair should be in contact at points of the involute profile, at any contact position. This means that the length of the interval of modification is limited by:

$$\Delta\xi_r = \Delta\xi_{r-inn} + \Delta\xi_{r-o} \leq \varepsilon_\alpha - 1 \tag{9}$$

where ε_α is the theoretical contact ratio. For standard contact ratio spur gears ($1 < \varepsilon_\alpha < 2$), Eq. (9) means that the length of modification $\Delta\xi_r$ should be smaller than the fractional part of ε_α (denoted by d_α), and according to Fig. 4 the QSTE curve of the modified profile will contain at least one point of the interval BC of minimum QSTE of the unmodified profile curve. Since both curves must contain point A to shift the actual start of contact to its theoretical location, the peak-to-peak amplitude of the QSTE cannot be reduced. This is not a good result as the peak-to-peak amplitude of the QSTE increases the dynamic response of the gear pair.

However, Eq. (9) is less restrictive for HCR spur gears ($2 \leq \varepsilon_\alpha < 3$), in which the length of modification may be greater than d_α , even greater than 1. In these cases, there

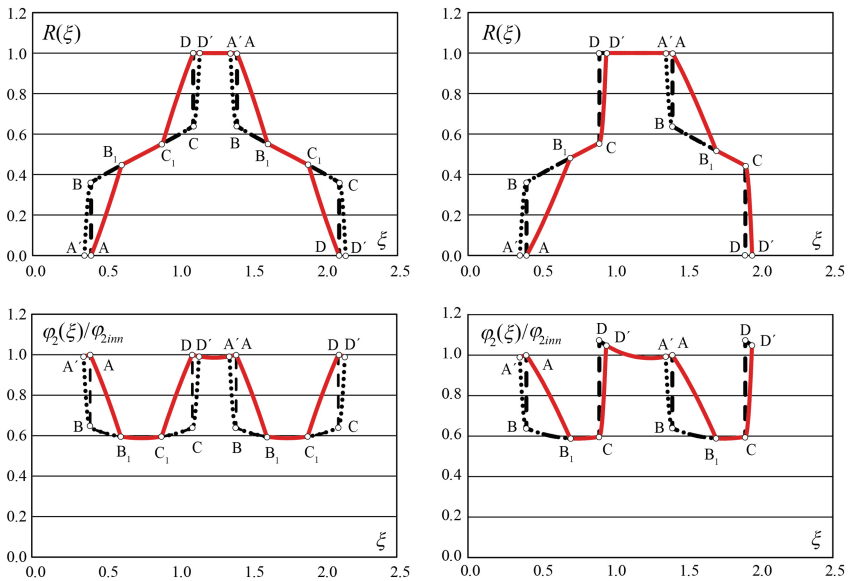


Fig. 4. LSR and QSTE for standard tooth height, symmetric tip relief (left) and reduced addendum on pinion and asymmetric tip relief (right)

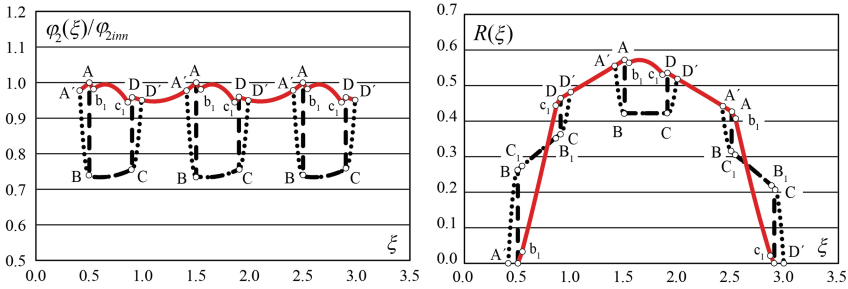


Fig. 5. QSTE (left) and LSR (right) for minimum peak-to-peak QSTE tip relief

will be contact positions with two tooth pairs in contact at relieved profile points. This is called long profile modification and provides interesting optimization opportunities.

For example, long profile modifications at both limits of the path of contact (at the tip of both gears) may reduce the peak-to-peak amplitude of QSTE. Figure 5 (left) shows the QSTE of a HCR spur gear with $\varepsilon_\alpha = 2.4$ and $\Delta\xi_{r-inn} = \Delta\xi_{r-o} = 0.91 \cdot d_\alpha = 0.364$, with a total length of modification $\Delta\xi_r = 0.728$. The pinion tooth height has been reduced, resulting in a reduction of the contact ratio of $\Delta\varepsilon_\alpha = -0.1$, and the wheel tooth height has been increased, resulting in an increase of the contact ratio of $\Delta\varepsilon_\alpha = 0.1$. Point b_1 corresponds to the tooth pair $j = 2$ in contact at the inner point of the outer interval of modification, i.e., $\xi + 2 = \xi_o - \Delta\xi_{r-o}$. Point c_1 corresponds to the tooth pair $j = 0$ in contact at the outer point of the inner interval of modification, $\xi = \xi_{inn} + \Delta\xi_{r-inn}$. The peak-to-peak amplitude of QSTE for unmodified teeth is determined by points A and B, while for relieved teeth it is determined by points A and c_1 . It can be observed that the peak-to-peak amplitude of QSTE is drastically reduced (77,7% reduction, in this example). Figure 5 (right) shows the corresponding LSR curve.

Figure 6 shows another interesting result. Since the transmission error represents the angle deviation of the output gear respect to its conjugate, ideal position, for uniform input velocity the QSTE also represents the fluctuation of the output velocity. In consequence, the slope of the curve of transmission error will be proportional to the instantaneous acceleration of the output gear and therefore to the instantaneous induced dynamic load. Although the dynamic load depends on some other factors, minimizing the maximum slope of the QSTE curve will result in minimum induced dynamic load.

From Fig. 5, the maximum slope of the QSTE curve occurs at the intervals A– b_1 and c_1 –D. The length of these intervals decreases with the length of modification, and it is eliminated for a length of relief at each gear equal to the fractional part of ε_α . The HCR spur gear transmission represented in Fig. 6 corresponds to $\varepsilon_\alpha = 2.3$, with reduced wheel tooth height (in an amount resulting in $\Delta\varepsilon_\alpha = -0.2$) and enlarged pinion tooth height (resulting in $\Delta\varepsilon_\alpha = 0.1$). The length of profile modification at both gears is $\Delta\xi_{r-inn} = \Delta\xi_{r-o} = d_\alpha = 0.30$, and a total length of modification $\Delta\xi_r = 0.60$. Points A and b_1 are coincident in QSTE diagram; points c_1 and D are coincident as well. This results in a smooth QSTE curve, with small slopes. In this example, the maximum slope, and therefore the induced dynamic load, is reduced by 88,5%, respect to the unmodified teeth.

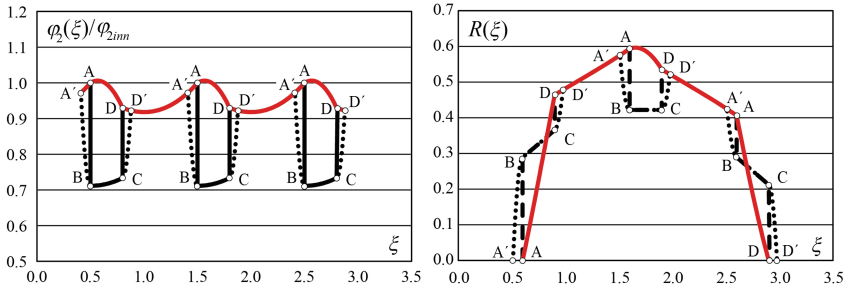


Fig. 6. QSTE (left) and LSR (right) for minimum dynamic load tip relief

5 Conclusions

A simple, analytical model for load sharing and quasi-static transmission error of spur gears based on the minimum elastic potential energy principle, has been applied to non-standard tooth height, including standard and high contact ratio gear pairs. Gear pairs with different tooth height on pinion and wheel, describing specific cases, as ‘vacuum gearing’ due to undercut or reduced addendum to avoid interferences, are involved in the study. Profile modifications have been also considered.

From this model, high contact ratio spur gears with long profile modifications have been studied. It has been obtained that suitable long profile modification at the tooth tip of both gears may reduce significantly the peak-to-peak amplitude of the quasi-static transmission error -which influences the dynamic response of the gear pair- or minimize the slope of the quasi static transmission error curve -minimizing the induced dynamic load-.

Acknowledgements. The authors express their gratitude to the Spanish Council for Scientific and Technological Research for the support of the project PID2019-110996RB-I00 “Simulation and Control of transmission error of cylindrical Gears”, as well as the School of Engineering of UNED for the support of the action 2020-MEC25, “Simulation of the transmission error of spur gears with profile modification”.

References

1. Chen, Z., Shao, Y.: Mesh stiffness calculation of a spur gear pair with tooth profile modification and tooth root crack. *Mech. Mach. Theory* **62**, 63–74 (2013)
2. del Rincón, A.F., et al.: A model for the study of meshing stiffness in spur gear transmissions. *Mech. Mach. Theory* **61**, 30–58 (2013)
3. Ma, H., et al.: An improved analytical method for mesh stiffness calculation of spur gears with tip relief. *Mech. Mach. Theory* **98**, 64–80 (2016)
4. Pedrero, J.I., et al.: Load distribution model along the line of contact for involute external gears. *Mech. Mach. Theory* **45**, 780–794 (2010)
5. Pedrero, J.I., Pleguezuelos, M., Sánchez, M.B.: Control del error de transmisión cuasi-estático mediante rebaje de punta en engranajes rectos de perfil de evolvente. *Revista Iberoamericana de Ingeniería Mecánica* **22**(2), 71–90 (2018)

6. Sánchez, M.B., Pleguezuelos, M., Pedrero, J.I.: Enhanced model of load distribution along the line of contact for non-standard involute external gears. *Meccanica* **48**, 527–543 (2013)
7. Sánchez, M.B., Pleguezuelos, M., Pedrero, J.I.: Approximate equations for the meshing stiffness and the load sharing ratio of spur gears including Hertzian effects. *Mech. Mach. Theory* **109**, 231–249 (2017)
8. Sánchez, M.B., Pleguezuelos, M., Pedrero, J.I.: Influence of profile modifications on meshing stiffness, load sharing, and transmission error of involute spur gears. *Mech. Mach. Theory* **139**, 506–525 (2019)
9. Sun, Y., et al.: A revised time-varying mesh stiffness model of spur gear pairs with tooth modifications. *Mech. Mach. Theory* **129**, 261–278 (2018)
10. Xie, C., et al.: Improved analytical models for mesh stiffness and load sharing ratio of spur gears considering structure coupling effect. *Mech. Syst. Signal Process.* **111**, 331–347 (2018)



A Transmission Error Analysis of a Herringbone Gear Set Considering Manufacturing Error

Huimin Dong^(✉), Xuefei Zhao, Chu Zhang, and Delun Wang

School of Mechanical Engineering, Dalian University of Technology, Dalian 116024, China
donghm@dlut.edu.cn

Abstract. This paper proposes a quasi-static model with 12 degree-of-freedom (DOF) for the transmission error (TE) analysis of a single-pair of herringbone gear drive. In this model, the manufacturing errors of the gear set are considered, such as the asymmetric error of the double helical line in the pitch cylinder, tooth profile error and circular pitch accumulated error at the transverse plane, which is converted to the common normal direction of the gear pair. To calculate the clearance between the gear pair, the piecewise discrete method is adopted, the meshing of the herringbone gear set, then, can be regarded as that of a series of slice-units. The kinematic relationship between each of the slices and the gear pair is established by equilibrium equations and complimentary equations. Thus, the TE of a herringbone gear drive can be simulated. The influences of various errors on the TE of a herringbone gear set are analysed, to show the proposed method feasible and effective.

Keywords: Herringbone gear · Transmission error · Discrete model · Manufacturing error

1 Introduction

TE of a gearing reflects the transmission accuracy of the gear system. In fact, TE between the pinion (drive wheel) and the gear (driven wheel) is the main source of noise and vibration [1, 2]. Many researchers had studied the TE of spur or helical gear drives. Li set up a modified TE model, and compared it with the error free model, which was shown that the tooth profile modification has a significant effect on TE [3]. Hu established a load distribution model and predicted TEs of a planetary helical gear set with different phase conditions [4]. Leque D proposed a three-dimensional load sharing model of planetary gear sets, the model is used to show combined influence of the manufacturing errors on planet load sharing to consider manufacturing tolerances in gear design for a planetary gear set [5]. Bonori G and Pellicano F analyzed the nonlinear dynamics of spur gears with manufacturing by means of a one-degree-of-freedom system. The presence of manufacturing errors magnifies the amplitude of vibration when the external torque is small [6]. Guo and Fang proposed a dynamic model of a helical gear pair with tooth surface modification and machining errors. The dynamic response of the gear system

was analyzed in time and frequency domains [7]. However, the TE of a herringbone gear set effects of manufacturing errors, especially the asymmetric error of the double helical line at the pitch cylinder, are rarely studied.

In this paper, a quasi-static model and solution method of TE for a herringbone gear set are established at first. Based on the model, the influence of manufacturing errors on TE is further studied. Finally, the conclusion is given in Sect. 5.

2 Manufacturing Error Description

In this section, the errors of the asymmetric error of the double helical line, tooth profile and circular pitch are expressed on the line of action of the gear pair transverse planes, deviated from the ideal position equivalent to the clearance, in which the asymmetric error and the tooth profile error exists only in the gear.

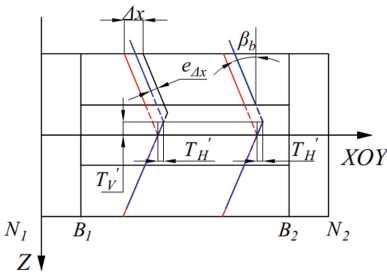


Fig. 1. The asymmetric error at transmission plane

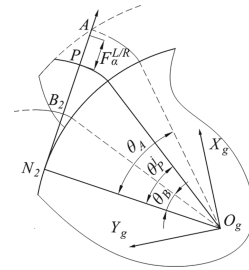


Fig. 2. Tooth profile error diagram

The asymmetric error of the double helical line Δx is measured at the transmission plane, the common tangent plane of the two base cylinders, shown in Fig. 1.

When the pinion rotating, the asymmetric error will generate an axial movement and small rotation to make the tooth pair contact. The clearance $e_{\Delta x}$ caused by the asymmetric error can be expressed as Eq. (1).

$$e_{\Delta x} = (\Delta x - T'_V \tan \beta_b - T'_H) \cos \beta_b \tag{1}$$

Where T'_H and T'_V are the minimum values of the axial and tangential error among all the gear teeth meshing at the same time; β_b is the base cylinder helix angle.

The tooth profile error is measured on the transverse plane at the normal direction of the involute tooth profile deviates from the ideal one, as Fig. 2, point A is the intersection of the addendum circle and the line of action, point B₂ is the limit contact point, and point P is a contact point on the working tooth profile. A simple harmonic function is used to describe the clearance $e_{\alpha}^{L/R}$ caused by tooth profile error [7], which is written by Eq. (2), for the i -th tooth on the left and right sides.

$$e_{\alpha}^{L/R} = F_{\alpha}^{L/R} \cdot \sin \left(\frac{2\pi}{z_g \theta_{AB}} \left((i - 1)\theta_{AB} + \theta_{PB}^j \right) + \varphi_0 \right) \cos \beta_b \tag{2}$$

Where $F_{\alpha}^{L/R}$ is the maximum value of the total tooth profile error; $\theta_{AB} = \theta_A - \theta_B$, $\theta_{PB}^j = \theta_P^j - \theta_B$. θ_{PB}^j is the angle of the j -th discrete slice which will be explained in Sect. 3; φ_0 is the initial phase of the tooth profile error.

The circular pitch accumulated error F_{pkJ}^i is a large periodic error, set as a harmonic function, which is on the standard pitch circle, expressed by Eq. (3). Then project it on the line of action at the normal plane, the clearance e_P^i caused by the relative base-pitch deviation of the herringbone gear set is written by Eq. (4).

$$F_{pkJ}^i = F_{pJ} / 2 \cdot \sin(\omega_J t_J^i + \varphi_{fpJ}); \quad J = p, g \tag{3}$$

$$e_P^i = (F_{pkp}^i - F_{pkg}^i) \cos \beta_b \cos \alpha_t \tag{4}$$

Where F_{pJ} is the total cumulative error of the gear circular pitch; ω_J is the angular velocity of the gear; t_J^i is the taken time of the gear rotated i teeth; φ_{fpJ} is the initial phase, set $\varphi_{fpp} = 3\pi/2$, $\varphi_{fpg} = \pi/2$; α_t is the transverse pressure angle.

3 Transmission Error Analysis Model

To investigate TE of a herringbone gear set, the piecewise discrete method is adopted, and based on the equilibrium equations and compatibility conditions, a quasi-static model of the TE analysis with 12-DOF is established in this section.

3.1 Discrete Model of a Herringbone Gear Set

A herringbone tooth profile is a double helicoid, and the tooth pair contact is very complicated under manufacturing errors condition. The instantaneous clearance is difficult to determine, therefore, the discrete method is adopted to deal with. The coordinate systems and some parameters are defined in Fig. 3. Establish the global coordinate system $S\{O; X, Y, Z\}$ at the center of the drive gear and the driven wheel fixed coordinate system $S_g\{O_g; X_g, Y_g, Z_g\}$. The gear moving frame s_J ($J = p, g$) at each gear center are defined and the y -axis of s_J goes through the symmetric line of the first gear tooth.

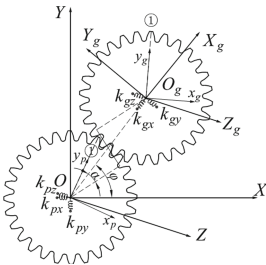


Fig. 3. Some parameters definitions

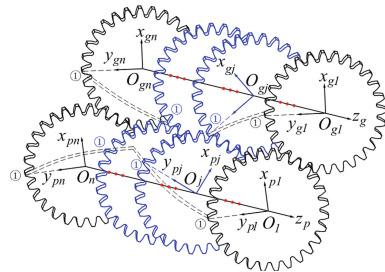


Fig. 4. Slices of discretized herringbone gear

The herringbone gear is discretized into a series of slice units along the tooth width, $j = 1, 2 \dots n$ counted from the front end face of each gear as, in which $s_{Jj} (J = p, g)$ is the j -th slice-unit coordinate system at its front end face, as Fig. 4. According to the principle of involute helicoid surface generation, the relative angle about z -axis between s_J and s_{Jj} is expressed as Eq. (5), where l is the tooth width.

$$\Delta\beta_{j}^{L/R} = [l/2 - \Delta l(j - 1)]\tan \beta_J / r_J; J = p, g; \Delta l = l/n \quad (5)$$

The meshing of each sliced gear pair can be approximated by a spring connection, then that of the gear pair is actually a series of springs in parallel. The model is shown in Fig. 5, where $e_{pg}^{L/R}$ is the each slice-unit clearance on the left/right of the gear pair due to the manufacturing errors; $k_{pg}^{L/R}$ is the meshing stiffness of each slice on the left/right side of the gear pair composed of bending, shear, axial compressive, gear foundational and contact stiffness. Using the principle of potential energy, the meshing stiffness of the gear can be calculated [8, 9]. The time varying meshing stiffness for the j -th slice unit can be obtained by Eq. (6).

$$\frac{1}{k_{pg,j}^{L/R}} = \frac{1}{kb_{p,j}} + \frac{1}{ks_{p,j}} + \frac{1}{ka_{p,j}} + \frac{1}{kf_{p,j}} + \frac{1}{kb_{g,j}} + \frac{1}{ks_{g,j}} + \frac{1}{ka_{g,j}} + \frac{1}{kf_{g,j}} + \frac{1}{kh_j} \quad (6)$$

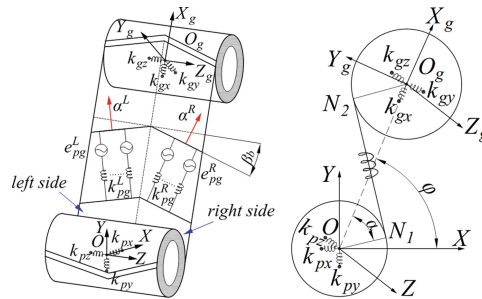


Fig. 5. The equivalent model of a pair of herringbone gear set system

By definition of TE, it can be expressed by the actual angular displacement of the output φ_{out} and the theoretical angular displacement of the input φ_{in} .

$$TE = \varphi_{out} - \varphi_{in}z_p / z_g \quad (7)$$

Where z_p and z_g are the number of teeth of the pinion and the gear.

The φ_{out} needs to be solved through the generalized displacement of the gear pair. The generalized displacement can be obtained by the static equilibrium equation and compatibility condition.

3.2 Equilibrium and Compatibility Equations

Each gear has six-DOF in space, thus, the generalized displacement of the gear pair can be written as Eq. (8).

$$\mathbf{X} = (x_p, y_p, z_p, u_{px}, u_{py}, u_{pz}, x_g, y_g, z_g, u_{gx}, u_{gy}, u_{gz})^T \quad (8)$$

When the meshing deformation of the j -th slice-unit gear pair $\delta_{pg,j}^{L/R} > 0$, the slice unit is in the meshing state, and the meshing stiffness of the slice-unit gear pair is $k_p^{L/R}$. Compatibility conditions of the left/right slice-unit gear pairs along the normal direction of the meshing pair satisfy Eq. (9a). Otherwise, the slice-unit gear pair is not in meshing state, so its stiffness satisfies Eq. (9b).

$$\delta_{pg,j}^L = \boldsymbol{\alpha}^L \cdot \mathbf{X} - e_{pg,j}^L; \delta_{pg,j}^R = \boldsymbol{\alpha}^R \cdot \mathbf{X} - e_{pg,j}^R \quad (9a)$$

$$k_{pg}^{L/R} = \begin{cases} k_{pg}^{L/R}, \delta_{pg,j}^{L/R} > 0 \\ 0, \delta_{pg,j}^{L/R} \leq 0 \end{cases} \quad (9b)$$

Where $\boldsymbol{\alpha}^{L/R}$ is a projection vector of a pair of gears 12-DOF motion displacement along the direction of contact normal [8, 10], its direction is shown in Fig. 5 and can be expressed as Eq. (10).

$$\begin{aligned} \boldsymbol{\alpha}^{L/R} = & [-\sin \phi \cos \beta_b, \cos \phi \cos \beta_b, -\sin(\pm\beta_b), -r_{b1} \sin \phi \sin(\pm\beta_b) \\ & -L_1 \cos \phi \sin(\pm\beta_b) - \lambda \cos \phi, r_{b1} \cos \phi \sin(\pm\beta_b) - L_1 \sin \phi \sin(\pm\beta_b) \\ & -\lambda \sin \phi, r_{b1} \cos \beta_b, -\sin \alpha \cos \beta_b; -\cos \alpha \cos \beta_b, \sin(\pm\beta_b), r_{b2} \sin \alpha \sin(\pm\beta_b) \\ & -L_2 \cos \alpha \sin(\pm\beta_b) + \lambda \cos \alpha, r_{b2} \cos \alpha \sin(\pm\beta_b) + L_2 \sin \alpha \sin(\pm\beta_b) \\ & -\lambda \sin \alpha, r_{b2} \cos \beta_b] \end{aligned} \quad (10)$$

where $\Phi = \varphi - \alpha$; L_1 and L_2 are the distances from a certain contact point in the middle of the tooth width to the two theoretical contact point N_1 and N_2 , N_1 and N_2 are show in Fig. 5; λ is the distance from a contact point on the tooth to the middle of the tooth width.

The meshing stiffness matrix $\mathbf{K}_m = \mathbf{K}_m^L + \mathbf{K}_m^R$, specifically as shown in Eq. (11).

$$\mathbf{K}_m^R = \left(\sum_{i=1}^N \sum_{j=1}^{n/2} k_{pg}^R \cdot (\boldsymbol{\alpha}^R)^T \cdot \boldsymbol{\alpha}^R \right); \mathbf{K}_m^L = \left(\sum_{i=1}^N \sum_{j=n/2+1}^n k_{pg}^L \cdot (\boldsymbol{\alpha}^L)^T \cdot \boldsymbol{\alpha}^L \right) \quad (11)$$

The additional meshing force caused by the error can be expressed as Eq. (12).

$$\mathbf{f} = \sum_{i=1}^N \left(\sum_{j=1}^{n/2} k_{pg}^R \cdot e_{pg}^R \cdot (\boldsymbol{\alpha}^R)^T + \sum_{j=n/2+1}^n k_{pg}^L \cdot e_{pg}^L \cdot (\boldsymbol{\alpha}^L)^T \right) \quad (12)$$

Where N is the gear tooth number, and n is the number of the discrete slice.

The support stiffness matrix \mathbf{K}_h can be expressed as Eq. (13).

$$\mathbf{K}_h = \text{diag}(k_{px}, k_{py}, k_{pz}, k_{pbx}, k_{pby}, k_{pu}, k_{gx}, k_{gy}, k_{gz}, k_{gbx}, k_{gby}, 0) \quad (13)$$

Among them, let the axial stiffness k_{pz} of the pinion be zero, due to the gear needs to freely move in the z -axis direction with the asymmetric error.

Establishing herringbone teeth static equations by Eqs. (8)–(13). Where $\mathbf{T} = [0, 0, 0, 0, 0, 0, T_p, 0, 0, 0, 0, T_g]^T$, it is the generalized force on the gear system.

$$(\mathbf{K}_h + \mathbf{K}_m) \cdot \mathbf{X} - \mathbf{f} = \mathbf{T} \quad (14)$$

By combining the static equations of herringbone teeth, the generalized displacement vector \mathbf{X} can be solved, and the TE can be solved. In this model, because the torsional stiffness k_{pu} added to the input direction of rotation is infinite, $\varphi_{in} = 0$, so the TE is the output wheel output angle, that is $TE = \varphi_{out} = u_{gz}$.

4 Case Study

The related parameters of herringbone gear are shown in Table 1. The influence of each manufacturing error on TE when acting alone is simulated as shown in Fig. 6.

Table 1. Herringbone gear parameters

	Number of teeth z_j	Modulus $m(\text{mm})$	Pressure angle $\alpha(\text{deg})$
Pinion	21	5	20
Gear	49	5	20
	Tooth width $l(\text{mm})$	Helix angle $\beta(\text{deg})$	Center distance $a(\text{mm})$
Pinion	16	15	175
Gear	16	15	

Figure 6(a) is the results of the TE with equal asymmetry error of teeth $6.95 \mu\text{m}$; Fig. 6(b) is that with variation asymmetry error range is $0\text{--}15 \mu\text{m}$ according to the requirement of symmetry, the error value of each tooth is not equal. During the meshing process, the pinion moved axially to eliminate part of the clearance, and errors still existed, the curve shows a step change and with the variation of the asymmetry error less, the TE decreases. The Variation of the TE depends on the difference between the asymmetric errors of the all teeth on the meshing surface.

Figure 6(c) shows the TE variation with only the tooth profile error. As shown in the figure, the larger the tooth profile error, the larger the TE. Observing a single curve, due to the value of tooth profile error is different along the involute tooth profile, which cause small fluctuations in the large cyclical TE. Figure 6(d) shows a TE variation with only the circular pitch accumulated error. The TE changes when the gear tooth enters and exits. It can be seen from the comparison of different data curves that the TE increases with the increase of the pitch error. When the difference between the total cumulative pitch error of the pinion and the gear increases, the amplitude of the TE decreases at the first peak and trough.

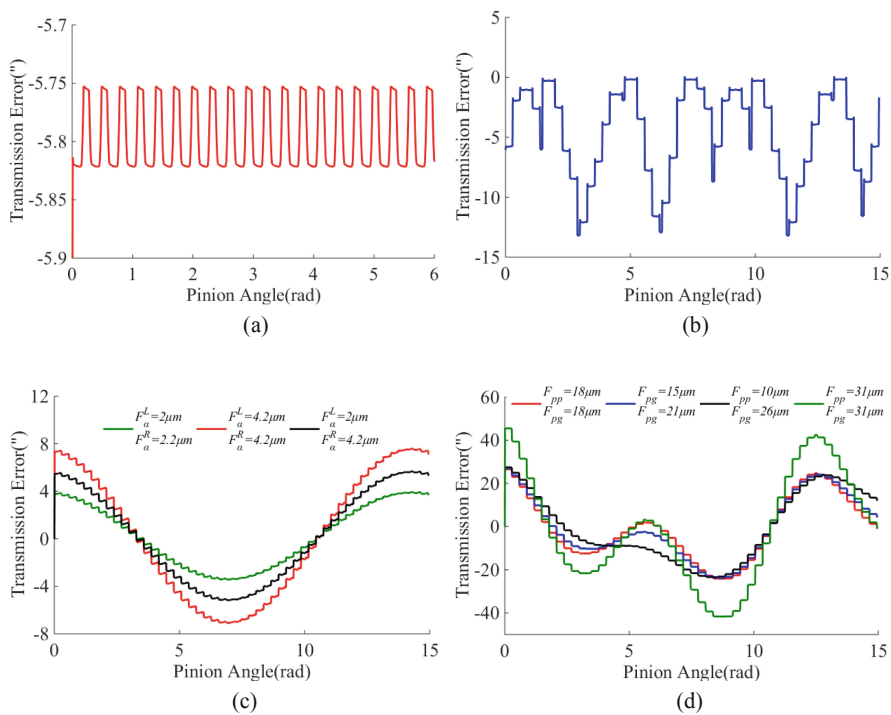


Fig. 6. Simulation results of herringbone gear transmission error: **a** asymmetric error $\Delta x = 6.95 \mu\text{m}$; **b** asymmetric error range is 0–15 μm ; **c** tooth profile error; **d** tooth cumulative pitch error.

5 Conclusions

This paper presents a quasi-static model for TE analysis of a single-pair of herringbone gear drive with 12-DOF, considering the asymmetric error of the double helical line, tooth profile error and circular pitch accumulated error. Using the model, the influences of each error on the TE are analyzed. The results show that the circular pitch accumulated error and tooth profile error cause a cyclical TE with small fluctuations; while the impact of the circular pitch accumulated error is bigger than that of tooth profile error; the asymmetric error of the double helical line yields some step variation TE, and the larger the asymmetric error, the larger the TE. The analysis indicates that the proposed model and method are feasible.

Acknowledgments. This work was supported by the National Key R&D Program of China (No. 2018YFB2001504) and National Natural Science Foundation of China (No. 51375065, U1808213).

References

1. Radu, M., Andrei, L., Andrei, G.: A perspective on gear meshing quality based on transmission error analysis. *IOP Conf. Ser. Mater. Sci. Eng.* **444**(5), 052011 (2018)

2. Park, G., Kim, K., Lee, B., Kim, W.: Correlation of transmission error prediction with vibration measurements for helical gears. In: *Proceedings of the 22nd International Congress on Sound and Vibration: Major Challenges in Acoustics, Noise and Vibration Research* (2015)
3. Li, Z., Mao, K.: The tooth profile modification in gear manufacture. *Appl. Mech. Mater.* **10–12**, 317–321 (2008)
4. Hu, Y., Ryali, L., Talbot, D., Kahraman, A.: A theoretical study of the overall transmission error in planetary gear sets. *Proc. Inst. Mech. Eng. Part C-J. Mech. Eng. Sci.* **233**(21–22), 7200–7211 (2019)
5. Leque, N., Kahraman, A.: A three-dimensional load sharing model of planetary gear sets having manufacturing errors. *J. Mech. Des.* **139**(3), 033302 (2017)
6. Bonori, G., Pellicano, F.: Non-smooth dynamics of spur gears with manufacturing errors. *J. Sound Vib.* **306**(1–2), 271–283 (2007)
7. Guo, F., Fang, Z.: Experimental and theoretical study of gear dynamical transmission characteristic considering measured manufacturing errors. *Shock Vib.* **2018**, 1–20 (2018)
8. Dong, H., Zhang, C., Bai, S., Wang, D.: Modeling, analysis and testing of load distribution for planetary gear trains with 3D carrier pinhole position errors. *Int. J. Precis. Eng. Manuf.* **20**(8), 1381–1394 (2019)
9. Liang, X., Zuo, M., Patel, T.: Evaluating the time-varying mesh stiffness of a planetary gear set using the potential energy method. *Arch. Proc. Inst. Mech. Eng. Part C J. Mech. Eng. Sci.* **288**, 535–547 (2014)
10. Velex, P., Maatar, M.: A mathematical model for analyzing the influence of shape deviations and mounting errors on gear dynamic behavior. *J. Sound Vib.* **191**(5), 629–660 (1996)



Meshing Limit Line of Conical Worm Pair

Yaping Zhao[✉] and Xiao Zhang

Northeastern University, Shenyang, China
zhyp_neu@163.com

Abstract. Based on the theory regarding algebraic equation of higher degree, a method to compute the meshing limit line for a conical worm drive is brought forward. No iteration is needed to perform this method so the corresponding computer program can be simpler. By employing this method, it is mathematically proved that the meshing limit line does not exist on the internal flank of a conical worm tooth and two meshing limit lines exist on the external flank of the tooth. The numerical results illustrate that the two meshing limit lines on the external flank generally are all outside of the practical tooth surface of the worm and the practical tooth surface is on the useful side of the meshing limit line. This signifies that the working length of a conical worm may fully cover its whole thread length at least theoretically. At the toe of a conical worm, the meshing limit line is nearest to the tooth surface of the worm, and the risk that the meshing limit line enters into the worm tooth surface is the most at that position.

Keywords: Conical worm pair · Meshing limit line · Algebraic equation with higher degree · Gear geometry · Mechanical transmission

1 Introduction

The conical worm drive was originally invented by Oliver E. Saari of Illinois Tool Works in 1954 [1]. Afterwards, the company registered a trademark for such a mechanical transmission product by using “Spiroid Gears” [2]. In a Spiroid gearing, the reference surface of the worm is conical and the mating member is a face-type gear, which looks like a hypoid gear. The helicoidal surface of the worm is finish-turned by a lathe tool with straight blade. The teeth of the mating gear may be machined by a conical hobber, whose generating surface is completely identical to the helicoid of the mating worm, on a common hobbing machine.

Until now, the knowledge about the meshing principle of such a mechanical drive is considerably limited in the English references so far as the author has known. In the near past, the representative works [3–5] are listed in References of this paper.

In the 1980s, Dong [6] studied the meshing limit line of a conical worm drive. According to the meshing theory for gearings, the meshing limit line is the envelope to the family of the instantaneous contact lines on the generating surface [7]. That is to say, the meshing limit line constitutes the natural boundary of the conjugate zone on the tooth surface of the driving member so that it will affect the working length of a worm.

Thus the influence will spread to the contact ratio and the load carrying capacity of a worm drive. For a cylindrical worm pair, the meshing limit line always appears on the practical tooth surface of the worm [8, 9]. How about the circumstance of the conical worm pair? The clear and convincing answer will be given in this work.

2 Theoretical Foundation for Determining Meshing Limit Line

A rotating coordinate system $\sigma_1 \left\{ O_1; \vec{i}_1, \vec{j}_1, \vec{k}_1 \right\}$ shown in Fig. 1 is associated with the worm and its unit vector \vec{k}_1 lies along the axial line of the worm and points to the heel. The point O_1 is the middle point of the worm thread length. The vector equation of the worm helicoid can be represented in σ_1 as

$$(\vec{r}_1)_1 = u \cos v_s \cos \theta \vec{i}_1 + u \cos v_s \sin \theta \vec{j}_1 + (u \sin v_s + p_s \theta) \vec{k}_1 \tag{1}$$

where (u, θ) are the two curvilinear coordinates of the surface, v is the inclination angle of the tooth profile in the worm axial section, and p is the worm helix parameter. For the internal tooth surface of the worm which faces to the toe of the worm, i.e. the so-called i flank, $s = 1$. For the external tooth surface of the worm which faces to the heel of the worm, i.e. the so-called e flank, $s = 2$. As recommended by Ref. [6], $v_1 = 10^\circ$ on the i flank and $v_2 = -30^\circ$ on the e flank.

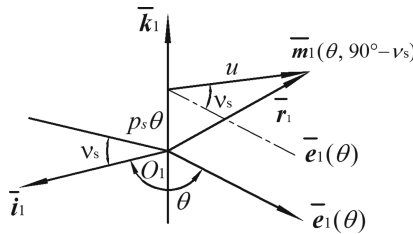


Fig. 1. Schematic diagram to indicate formation principle of worm helicoid

By means of the methodology addressed in differential geometry, the unit normal vector of the worm helicoid can be worked out by employing the characteristics of the circular and sphere vector functions [7] from Eq. (1) as

$$(\vec{n}_1)_1 = \frac{\frac{\partial(\vec{r}_1)_1}{\partial u} \times \frac{\partial(\vec{r}_1)_1}{\partial \theta}}{\left| \frac{\partial(\vec{r}_1)_1}{\partial u} \times \frac{\partial(\vec{r}_1)_1}{\partial \theta} \right|} = \frac{u \vec{m}_1(\theta, -v_s) - p_s \vec{g}_1(\theta)}{\sqrt{u^2 + p_s^2}} \tag{2}$$

During the mesh of the worm pair, two static coordinate systems $\sigma_{o1} \left\{ O_1; \vec{i}_{o1}, \vec{j}_{o1}, \vec{k}_{o1} \right\}$ and $\sigma_{o2} \left\{ O_2; \vec{i}_{o2}, \vec{j}_{o2}, \vec{k}_{o2} \right\}$ are used to denote the original position of them, respectively, as shown in Fig. 2. The unit vectors \vec{k}_{o1} and \vec{k}_{o2} are along the axial lines of the pinion and gear, respectively, and perpendicular to each

other. The unit vector \vec{k}_{o1} coincides with the unit vector \vec{k}_1 of the rotating coordinate system σ_1 while \vec{k}_{o2} points to the heel of the gear. The unit vectors \vec{i}_{o1} and \vec{i}_{o2} are collinear, and all along the common perpendicular of the axial lines of the pinion and gear, i.e. the unit vectors \vec{k}_{o1} and \vec{k}_{o2} . The point O_2 is the foot point of the common perpendicular at the axial line of the worm gear.

Via coordinate system transformation, the radius vector \vec{r}_1 and the unit normal vector \vec{n}_1 in Eqs. (1) and (2) can be represented in the static coordinate system σ_{o1} as

$$(\vec{r}_1)_{o1} = u\vec{m}_{o1}(\theta + \varphi_1, -\nu_s) + p_s\theta\vec{k}_{o1}, \tag{3}$$

$$(\vec{n}_1)_{o1} = \frac{u\vec{m}_{o1}(\theta + \varphi_1, -\nu_s) - p_s\vec{g}_{o1}(\theta + \varphi_1)}{\sqrt{u^2 + p_s^2}}. \tag{4}$$

where φ_1 is the rotating angle of the worm during the meshing process.

In the process of the mesh of the worm and its mating worm gear, the worm revolves around its axis \vec{k}_{o1} while the worm gear revolves around its axis \vec{k}_{o2} . Without loss of generality, it is assumed that the angular velocity of the worm is 1 rad/s so that the angular velocity vectors of the worm and worm gear can be represented in σ_{o1} as

$$(\vec{\omega}_1)_{o1} = \vec{k}_{o1}, (\vec{\omega}_2)_{o1} = -\frac{1}{i_{12}}(-\vec{j}_{o1}) = \frac{1}{i_{12}}\vec{j}_{o1} \tag{5}$$

where i_{12} is the transmitting ratio of the worm drive.

Form Eq. (5) and by definition, the relative velocity vector of the worm drive can be achieved in the static coordinate system σ_{o1} as

$$(\vec{V}_{12})_{o1} = [(\vec{\omega}_1)_{o1} - (\vec{\omega}_2)_{o1}] \times (\vec{r}_1)_{o1} - (\vec{\omega}_2)_{o1} \times (\vec{O}_2\vec{O}_1)_{o1} \tag{6}$$

where $(\vec{O}_2\vec{O}_1)_{o1} = a\vec{i}_{o1} + z_0\vec{k}_{o1}$ as illustrated in Fig. 2. Here a is the center distance of the worm drive, and $z_0 = L_w/2 + z_A = L_w/2 + k_A a$ as demonstrated in Fig. 2. Meanwhile L_w is the axial length of the worm thread and k_A is the installation parameter of the worm. Their values are recommended to take as $L_w \approx 0.73a$ and $k_A \in [0.4, 0.8]$ on the basis of the meshing analysis for the worm gearing.

From Eqs. (4) and (6) and by the definition in the meshing theory for gearings [7], the meshing function of the worm pair can be ciphered out as

$$\Phi(u, \theta, \varphi_1) = (\vec{n}_1)_{o1} \cdot (\vec{V}_{12})_{o1} = \frac{-p_s}{i_{12}\sqrt{u^2 + p_s^2}} [A \sin(\theta + \varphi_1) + B \cos(\theta + \varphi_1) + C] \tag{7}$$

where $A = u \sin \nu_s + p_s \theta + z_0$, $B = -u \cos \nu_s (u \cos \nu_s + A \tan \nu_s) / p_s$, and $C = -r_{\nu_s} u \cos \nu_s / p_s$, in which r_{ν_s} is the pitch radius of the related equivalent cylindrical worm, and $r_{\nu_s} = a - i_{12} p_s$.

According to the theory well established in Ref. [10], a meshing limit point can be determined after solving the following three nonlinear equations with unknowns u , θ and φ_1 as

$$\Phi(u, \theta, \varphi_1) = 0, \frac{\partial \Phi}{\partial \varphi_1} = 0, u \sin \nu_s + p_s \theta - L_z = 0 \tag{8}$$

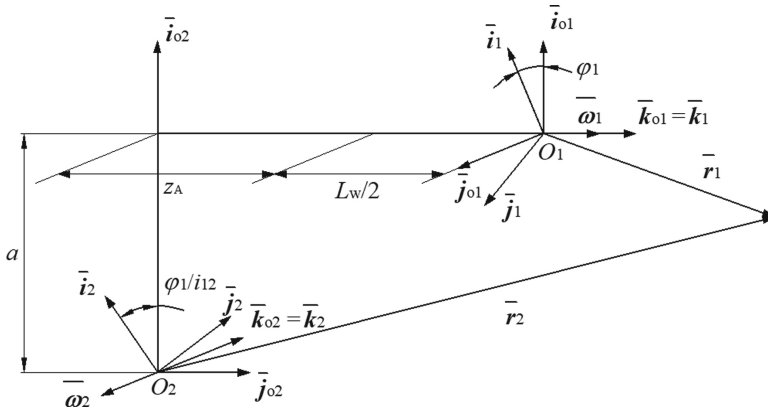


Fig. 2. Coordinate systems for studying mesh of worm drive

The third expression in Eq. (8) is the position equation established in accordance with the axial position of the meshing limit point along the worm axial line. L_z is the axial coordinate of a meshing limit point to be determined, $L_z \in [-L_w/2, L_w/2]$, and its value needs to be given in advance. When L_z fetches different values, different meshing limit points can be obtained from Eq. (8). Based on this, the meshing limit line can then be attained by virtue of interpolation method.

Eliminating $\sin(\theta + \varphi_1)$ and $\cos(\theta + \varphi_1)$ from the first two expressions in Eq. (8) yields $A^2 + B^2 - C^2 = 0$. Submitting the expressions of $A, B,$ and C attached to Eq. (7) into this formula leads up to

$$X^4 + 2A \tan \nu_s X^3 + (A^2 \tan^2 \nu_s - r_{vs}^2) X^2 + p_s^2 A^2 = 0 \tag{9}$$

where $X = u \cos \nu_s$, and in terms of the third expression in Eq. (8) and the expression of the coefficient A affiliated to Eq. (7), $A = L_z + z_0 = \text{const}$. Equation (9) is a quartic equation with respect to the only one unknown X .

After solving the quartic algebraic Eq. (9), the value of u can be acquired. Next the value of θ can be figured out from the third expression in Eq. (8) as $\theta = (L_z - u \sin \nu_s) / p_s$. Finally, a meshing limit point can be ascertained.

The root situation of the unary quartic Eq. (9) may be roughly expounded as below: two couples of conjugate imaginary root, which conveys that the meshing limit line does not exist on the worm helicoidal surface; two different real roots and a couple of conjugate imaginary root, which stands for that there are two meshing limit lines on the worm helicoidal surface; four different real roots, which denotes that four meshing limit lines exist on the worm helicoidal surface. Of course, the existence of the meshing limit line on the worm helicoidal surface does not signify that the limit line can come into the practical tooth surface of the worm.

Thus it can be seen, the meshing limit line can be obtained from Eq. (9). Not only that, the existence of the meshing limit line completely depends on the existence of the real root of the quartic Eq. (9). Hence Eq. (9) may be called the control equation of the meshing limit line.

3 Solving Control Equation and Analyzing Existence of Its Real Root

In this study, the Ferrari technique [11] is adopted to seek the radical solution for the unary quartic Eq. (9) in order to detect the existence of the meshing limit line.

The resolvent equation of the unary quartic Eq. (9) can be achieved as

$$2Y^3 + \left(r_{vs}^2 - A^2 \tan^2 v_s\right) Y^2 - 2Y p_s^2 A^2 - r_{vs}^2 p_s^2 A^2 = 0 \quad (10)$$

Equation (10) is a unary cubic algebraic equation with respect to Y . So as to obtain the radical solution of Eq. (10), it is necessary to eliminate the quadratic term regarding Y in Eq. (10). For this reason, letting $Y = w + \Delta w$ in Eq. (10) leads to

$$w^3 - \frac{1}{12} p_w w - \frac{1}{108} q_w = 0 \quad (11)$$

where $p_w = (A^2 \tan^2 v_s - r_{vs}^2)^2 + 12 p_s^2 A^2 > 0$, $q_w = p_w (A^2 \tan^2 v_s - r_{vs}^2) + 6 p_s^2 A^2 \times (A^2 \tan^2 v_s + 8 r_{vs}^2)$. In addition, $\Delta w = (A^2 \tan^2 v_s - r_{vs}^2) / 6$.

Hereinafter it is mathematically proved that $A^2 \tan^2 v_s - r_{vs}^2 > 0$ to explain $q_w > 0$ and $\Delta w > 0$.

The worm helix parameter can be computed as

$$p_s = \frac{a \cos(v_s \mp \Delta_1)}{i_{12} \cos v_s}. \quad (12)$$

where Δ_1 is the half apex angle of the reference cone of the worm, which usually has a standard value, and $\Delta_1 = 5^\circ$. For the double-sign term, the upper sign is taken on i flank ($s = 1$) while the lower sign is taken on the e flank ($s = 2$).

Based on Eq. (12), the reference radius of the related equivalent cylindrical worm can approximately be figured out as

$$r_{vs}^2 = a^2 \tan^2 v_s \sin^2 \Delta_1. \quad (13)$$

By means of the expression of the coefficient A attached to Eq. (9) and Eq. (13), it is possible to have

$$A^2 \tan^2 v_s - r_{vs}^2 = \tan^2 v_s \left[\left(L_z + \frac{L_w}{2} + k_A a \right)^2 - a^2 \sin^2 \Delta_1 \right]. \quad (14)$$

Due to $-0.5L_w \leq L_z \leq 0.5L_w$, $0 \leq L_z + 0.5L_w \leq L_w$, and then

$$k_A a \leq L_z + \frac{L_w}{2} + k_A a \leq L_w + k_A a.$$

Considering the range of L_w and k_A yields

$$[0.4, 0.8]a \leq L_z + \frac{L_w}{2} + k_A a \leq L_w + k_A a = [1.13, 1.53]a.$$

As a result,

$$[0.16, 0.64]a^2 \leq \left(L_z + \frac{L_w}{2} + k_A a \right)^2 \leq [1.2769, 2.3409]a^2. \tag{15}$$

On account of $\sin^2 \Delta_1 = \sin^2 5^\circ = 0.007596$ and in line with Eqs. (14) and (15), it may have

$$A^2 \tan^2 \nu_s - r_{vs}^2 > 0 \tag{16}$$

In the light of Eq. (16), $\Delta w > 0$. Also due to $p_w > 0, q_w > 0$.

According to the theory on algebraic equation with higher degree [11], the discriminant of Eq. (11) can be worked out as

$$\Delta_w^{(s)} = \frac{q_w^2}{4 \times 108^2} - \frac{p_w^3}{27 \times 12^3} = \frac{-p_s^2 A^2}{27 \times 12^2} (p_w - p_{w1})(p_w - p_{w2}) \tag{17}$$

where
$$p_{w1,2} = \frac{1}{8} (A^2 \tan^2 \nu_s + 8r_{vs}^2) (5A^2 \tan^2 \nu_s + 4r_{vs}^2 \pm 3A \tan \nu_s \sqrt{A^2 \tan^2 \nu_s + 8r_{vs}^2}).$$

As already stated, $s = 1$ and $\nu_1 = 10^\circ$ on the i flank. After omitting the higher order small quantity, $r_{v1} = a \tan 10^\circ \sin 5^\circ$ and $p_1 = a \cos 5^\circ / i_{12}$. On the basis of these and from Eq. (17), it is possible to prove that $\Delta_w^{(1)} < 0$.

This indicates that the unary cubic Eq. (11) is irreducible and has three different real roots at this time. After one real root of Eq. (11) is reaped, a related real root of Eq. (10) can be computed as

$$Y_i = \Delta w + w_i = \Delta w + \frac{1}{3} \cos\left(\frac{1}{3}\mu\right) \sqrt{(A^2 \tan^2 \nu_1 - r_{v1}^2)^2 + 12p_1^2 A^2} > 0 \tag{18}$$

where $\mu = \arccos[q_w / (p_w \sqrt{p_w})], \mu \in (0, 90^\circ)$.

On the e flank, $s = 2$ and $\nu_2 = -30^\circ$. After omitting the higher order small quantity, $r_{v2} = -a \sin 5^\circ / \sqrt{3} < 0$ and $p_2 = p_1$. From Eq. (18), it is hence possible to prove that $\Delta_w^{(2)} > 0$ on the e flank because $i_{12} > 6\sqrt{2} \cot 5^\circ / \sqrt{5} = 43$ for the frequently-used transmission ratio range and $k_A > \sqrt{10} \sin 5^\circ$ in general.

In view of this, the unary cubic Eq. (11) has one real root and a couple of conjugate imaginary root. The real root of Eq. (11) can be computed by right of the Cardano's Formula [11] and then the relevant real root of Eq. (10) can be ciphered out as

$$Y_e = w_1 + w_2 + \Delta w > 0 \tag{19}$$

where $w_1 = \sqrt[3]{\frac{q_w}{216} + \sqrt{\Delta_w^{(2)}}} > 0, w_2 = \sqrt[3]{\frac{q_w}{216} - \sqrt{\Delta_w^{(2)}}} > 0$.

Equations (18) and (19) reveal $Y_i > 0$ and $Y_e > 0$. On account of this, it can be discovered that $\xi = p_s A / Y \in (0, 1)$ is true for both $Y = Y_i$ and $Y = Y_e$ in terms of Eq. (10).

From the expression of Δw , it is possible to have $\Delta w > r_{vs}^2$ due to $k_A > \sqrt{7} \sin 5^\circ$ in the light of the value range of k_A . As a result, $Y > r_{vs}^2$ is true for both Y_i and Y_e on the grounds of Eqs. (18) and (19). Furthermore, $2Y > r_{vs}^2$ certainly.

After determining Y from Eq. (18) or (19), two unary quadratic equations with respect to X can be deduced from the control Eq. (9) as

$$f_1^{(s)}(X) = X^2 + A \tan \nu_s \left(1 + \frac{(-1)^s Y}{\sqrt{Y^2 - p_s^2 A^2}} \right) X + Y + (-1)^s \sqrt{Y^2 - p_s^2 A^2} = 0 \quad (20)$$

$$f_2^{(s)}(X) = X^2 + A \tan \nu_s \left(1 - \frac{(-1)^s Y}{\sqrt{Y^2 - p_s^2 A^2}} \right) X + Y - (-1)^s \sqrt{Y^2 - p_s^2 A^2} = 0 \quad (21)$$

where on the i flank, $s = 1$ and $Y = Y_i$ while on the e flank, $s = 2$ and $Y = Y_e$.

The discriminants of the unary quadratic Eqs. (20) and (21) can be worked out as

$$\Delta_1^{(s)} = \left(Y + (-1)^s \sqrt{Y^2 - p_s^2 A^2} \right) \left[2((-1)^s - 1) + \frac{r_{vs}^2}{Y} (1 + (-1)^s) - (-1)^s \xi^2 \right] \quad (22)$$

$$\Delta_2^{(s)} = - \left(Y - (-1)^s \sqrt{Y^2 - p_s^2 A^2} \right) \left[2(1 + (-1)^s) - \frac{r_{vs}^2}{Y} (1 - (-1)^s) - (-1)^s \xi^2 \right] \quad (23)$$

On the i flank, $\Delta_1^{(1)} < 0$ in Eq. (22) due to $\xi \in (0, 1)$ as already pointed out. On the other hand, it may be proved that $\Delta_2^{(1)} < 0$ in Eq. (23) in line with $w_i \leq 2\sqrt{3}aA \cos 5^\circ / 3i_{12}$ obtained from Eq. (18).

Because of $\Delta_1^{(1)} < 0$ and $\Delta_2^{(1)} < 0$, the two unary quadratic equations $f_1^{(1)}(X) = 0$ and $f_2^{(1)}(X) = 0$ in Eqs. (20) and (21) do not have real root. That is to say, neither does the control Eq. (9). This displays that the meshing limit line does not exist on the i flank of a tooth of the worm.

On the e flank, $s = 2$ and it is possible to prove that $\Delta_1^{(2)} > 0$ in Eq. (22) due to $i_{12} > 3\sqrt{3} / (\sqrt{2} \tan 5^\circ) = 42$ within the range of the frequently-used velocity ratio. This means that the unary quadratic equation $f_1^{(2)}(X) = 0$ in Eq. (20) has two different real roots.

It may be proved that $\Delta_2^{(2)} < 0$ from Eq. (23) in terms of $\xi \in (0, 1)$. This implies the unary quadratic equation $f_2^{(2)}(X) = 0$ in Eq. (21) has no real root.

Thus it can be seen, when $s = 2$, the control Eq. (9) has two different real roots and a couple of conjugate imaginary root, which means that there are two meshing limit lines on the e flank of a tooth of the worm. Certainly, it should rely on further numerical computation to detect whether the existing limit line enters into the practical worm tooth surface or not.

The two real roots of the control Eq. (9) can easily be worked out by solving the quadratic equation $f_1^{(2)}(X) = 0$ in Eq. (20).

4 Numerical Investigations

In fact, the meshing limit line on the worm helicoid is a helical line. In order to illustrate its relative position to the worm tooth surface, the meshing limit line is projected to the axial section of the worm and then drawn in Fig. 3. In Fig. 3, the coordinates are (L_z, X) .

In Fig. 3, the main parameters of the worm drive are $a = 100$ mm, $i_{12} = 51$ and the number of the worm threads $Z_1 = 1$.

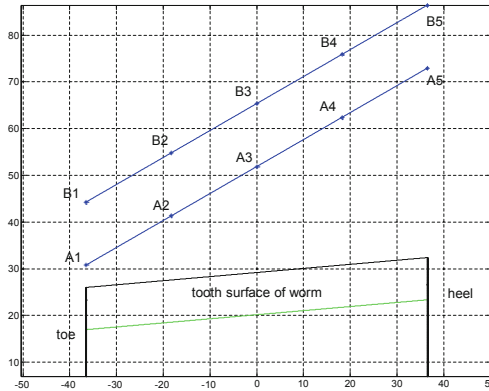


Fig. 3. Meshing limit line in worm axial section

Here computing the meshing limit point at the toe of the worm is taken as an example to explain the corresponding numerical result.

At this place on the *i* flank, $L_z = -L_w/2$ and from Eq. (17), it is possible to discover $\Delta_w^{(1)} = -1.6972 \times 10^{11} \text{ mm}^{12} < 0$. Then it can be figured out that $\Delta_1^{(1)} = -205.8651 \text{ mm}^2 < 0$ and $\Delta_2^{(1)} = -161.2683 \text{ mm}^2 < 0$ from Eqs. (22) and (23). In consequence, the control Eq. (9) has no real root on the *i* flank and the meshing limit line is of inexistence on the *i* flank of a tooth of the worm.

Also at this place but on the *e* flank, i.e. the points A_1 and B_1 in Fig. 3, it can be ciphered out $\Delta_w^{(2)} = 4.1546 \times 10^{12} \text{ mm}^{12} > 0$ from Eq. (17). This gives rise to $Y_e = 2.8063 \times 10^7 \text{ mm}^2$ from Eq. (19). This causes that $\Delta_1^{(2)} = 181.9484 \text{ mm}^2 > 0$ and $\Delta_2^{(2)} = -0.0013 \text{ mm}^2 < 0$ from Eqs. (22) and (23). Accordingly, $X_1 = 44.2722$ mm and $X_2 = 30.7834$ mm can be attained from Eq. (20). This implies that there are two meshing limit lines on the *e* flank of a tooth of the worm. Nevertheless, such two limit lines do not enter into the worm tooth surface as illustrated in Fig. 3, and the tooth surface locates at the useful side of the meshing limit line.

5 Conclusions

The computation of the meshing limit line for a conical worm drive can be boiled down to solve the real root for a unary quartic equation. On the basis of the theory regarding

algebraic equation of higher degree, a method to compute the meshing limit line for a conical worm gear set is put forward. No iteration is needed to carry out this method so the corresponding computer program can be simpler.

By employing this method, it is mathematically proved that no meshing limit line is on the i flank of a worm tooth and two meshing limit lines are on the e flank of the tooth.

The numerical results illustrate that the two meshing limit lines on the e flank are all outside of the practical tooth surface of the worm and the practical tooth surface is on the useful side of the meshing limit line. This means that, unlike cylindrical worms, the whole thread length of a conical worm may be utilized at least theoretically.

At the toe of a conical worm, the meshing limit line is nearest to the tooth surface of the worm. As a consequence, the risk that the meshing limit line enters into the worm tooth surface is the most at that position.

Acknowledgments. This study was funded by the Open Fund of the Key Laboratory for Metallurgical Equipment and Control of Ministry of Education in Wuhan University of Science and Technology (2018B05) and the National Natural Science Foundation of China (51475083).

References

1. Sarri, O.E.: Speed-reduction gearing. Patent No. 2696125. United States Patent Office (1954)
2. Dudley, D.W. (ed.): Gear Handbook. McGraw-Hill Book Company Inc, New York (1962)
3. Litvin, F.L., Donno, M.D.: Computerized design and generation of modified spiroid worm-gear drive with low transmission errors and stabilized bearing contact. *Comput. Methods Appl. Mech. Eng.* **162**, 187–201 (1998)
4. Kirov, V.: Design of spiroid hobs. *J. Mater. Process Technol.* **88**, 208–215 (1999)
5. Zhang, Y., Xu, H.: Pitch cone design and avoidance of contact envelope and tooth undercutting for conical worm gear drives. *ASME J. Mech. Des.* **125**, 169–177 (2003)
6. Dong, X., et al.: Design of Worm Drives (蜗杆传动设计), vol. 2. China Machine Press, Beijing (1987). (in Chinese)
7. Dong, X.: Meshing Theory Foundation for Gearings (齿轮啮合理论基础). China Machine Press, Beijing (1989). (in Chinese)
8. Zhao, Y.: On meshing limit line of ZC1 worm pair. In: Proceedings of European Conference on Mechanism Science, Aachen, Germany (2018)
9. Zhao, Y.: Meshing limit line of involute worm drive. In: Advances in Mechanism and Machine Science (Proceedings of IFToMM World Congress 2019), Krakow, Poland. Mechanisms and Machine Science, vol. 73 (2019)
10. Meng, Q., Zhao, Y.: Meshing limit line of the conical surface enveloping conical worm pair. *Proc. Inst. Mech. Eng. Part C J. Mech. Eng. Sci.* **234**(2), 693–703 (2019)
11. Okunev, L.Y.: Translated into Chinese by Yang, C.: Advanced Algebra (高等代数). Commercial Press, Shanghai (1956). (in Chinese)



Acoustic Emission Monitoring of Teeth Surface Damage Process in a Planetary Gearbox

Enrique Caso, Alfonso Fernandez-del-Rincon, Pablo Garcia,
Alberto Diez-Ibarbia, and Javier Sanchez-Espiga^(✉)

Department of Structural and Mechanical Engineering,
ETSIT University of Cantabria, Santander, Spain
javier.sanchezespiga@unican.es

Abstract. Each different sensor technology has advantages and disadvantages in pursuit of detection and diagnostic before a catastrophic failure in condition monitoring. Acoustic emission (AE) records the high frequency waves generated by diverse physical sources, employing a piezoelectric sensor. These AE perturbations are produced in the interaction of the gears and other components such as bearings. The asperity contact between surfaces is a fundamental source of AE waves. The good sensitivity of such sensor to any behavior variation of the contacts leads AE to its application in the monitoring of surface damage. This paper investigates the surface damage progression in one gear of a planetary transmission by AE monitoring. One pinion is subjected to a natural but accelerated wearing, thanks to the lack of teeth surface treatment. The evolution of this gear and its influence in the acquired AE signals, centered on the AE event width, are used to analyze the response and potential benefits of this technique in the condition monitoring of planetary gearboxes.

Keywords: Acoustic emission · Planetary gearbox · Condition monitoring · Gear degradation

1 Introduction

The asperities interaction of the involved teeth is the main thesis of the AE generation explanation in gear meshing [9]. The asperities present in the profile topography because of the inherent roughness provoke rupture and deformation when they contact with opposite surface asperities. It generates acoustic waves. It also provokes modifications in the asperity distribution over the surface, introducing randomness.

A defect on the tooth surface supposes a modification of the good conditions topography. The defect detection is conditioned by the sensitivity to this different contact. Surface defects can produce protuberances over the mean profile.

Whenever the exceeding material under deformation is removed, defect information in the AE signal could disappear [9], depending on the references consulted. But AE sensors were proved to be sensitive to pitting detection and pit size progression, being the AE r.m.s. levels directly related to the removed material [3]. There is no definitive evidence that surface asperities should be the main or the only source [7]. Some authors have evidenced contradictory results and lack of proving experiments, taking into account other possible source mechanisms in the contact behavior as lubricant pressure perturbation, changing sliding/rolling condition, backlash, tooth deformation and tooth impact [1].

Different contact behavior has effect in the acquired AE signals. Therefore, AE seems to be an optimal technology for monitoring surface damage due to its sensitivity to the contact interaction. The surface degradation has been evidenced with AE monitoring by using condition indicator analysis as tendencies in the signal r.m.s. value [10]. In comparison with vibrations analysis, AE present the disadvantage of the acoustic waves overlap and intensity attenuation. That could shadow the targeted monitoring. On the other hand, acceleration seems to be not directly affected by soft changes over the teeth surfaces. A successful study of surface degradation using AE has been carried out, employing a parallel shaft transmission with spur gears [6].

Some experimental works have been carried out for the application of AE to planetary gearbox monitoring. These experiments were conducted introducing components with artificial defects as partially or totally removed tooth [11], or cuts in bearing elements [5] and also the localization of seeded faults through the AE waves time of arrival [12]. The authors have drawn attention to the particularities that complicate the AE monitoring in this transmissions. Adaptive noise reduction filters have been applied to the AE signals for the defect detection when the sensor is placed in the external casing [5]. Direct transmission path or wireless sensor inside the gearbox have provided a better noise to signal ratio of the internal components AE activity [4]. Vibrations and AE have been compared in some of these works. AE signals have been more effective at the early detection of faults in planetary gearboxes [5]. Different size defects have been distinguished through AE. The studies of AE in planetary gearbox have been centered on the application of fault diagnosis processing algorithms. Through signal processing and neural network classification, severe defects in sun, planet and ring have been detected [11]. Common analysis methods for AE include the downgrading of the AE at rates of vibrations, involving demodulation or envelope analysis of the AE signal [1].

This present work provides an experimental approach to the surface degradation of a planetary transmission gear using AE. A simple algorithm to detect the surface behavior based in AE event width is proposed for a possible implementation in condition monitoring. The aim of this method is to avoid the limitations of data storage and computational handling of these high sampling frequency signals when commonly employed indicators (r.m.s., kurtosis, etc.) [2] do not show sensitivity.

2 Experimental Procedure

The test stage consists of a planetary gearbox with three planets, equally spaced and sequentially phased. The sun is the most critical component in this configuration because its relative dimensions. For the tests, the original sun of this stage is replaced by another gear without surface treatment, in order to accelerate the surface degradation under load. The wearing is monitored by successive AE and auxiliary measurements. In addition, visual inspections of the components and the control of the sun weight are performed. These additional controls are used to correlate the AE signals with the surface behavior, to control the backlash increasing and the lubrication quality due to the removed material.

The complete experiment is performed through the repetition of the following procedure. The transmission is operated during one hour, starting the first tests under light speed and load conditions. The load and speed are increased to maintain the degradation progression rate. AE signals are acquired during the test at periodic intervals to register small modifications in the degradation process. Once the work time has elapsed, the sun is dismantled and cleaned maintaining the other components without change. The sun is weighed and photographed to evaluate the surface behavior. After finishing the inspection, the cleaned sun is mounted again in its previous position inside the transmission, ready to the next test. Each test parameters are shown in Table 1.

Table 1. Test parameters description, gear weight and oil debris presence.

Test number	Speed (rpm)	Load (masses)	Final weight (g)	Weight variation (g)	Metallic debris in the oil (concentration/size/shape)
1	270	3	400.36	-0.55	High/big/elongated and dust
2	270/570	3	399.76	-0.60	High/medium/elongated and dust
3	270/570	3	399.73	-0.03	Low/small/principally dust
4	270/570	3	399.73	-	Low/small/principally dust
5	270/570	6	399.68	-0.05	Minor/small/dust
6	270/570	6	399.68	-	Minor/small/dust
7	270/570	6	399.65	-0.03	Minor/small/dust
8	570	6	399.64	-0.01	Minor/small/dust
9	570	6	399.61	-0.03	Minor/small/dust

* The initial weight of the test gear was 400.91 g.

In this work, the focus is placed on the sun gear surface damage. Moving components generate AE waves during the gearbox operation, spreading acoustic waves in all directions. These signals are attenuated because of the distance and its passing through interfaces. A direct transmission path for the acoustic waves from the target gear to the sensor allows to acquire signals where the sun degradation is predominant. A device has been used in order to hold the sensor at the edge of the sun shaft allowing the safe operation. The signals are acquired using a slip ring incorporated in the sensor holding device.

3 Results and Discussion

The nine tests performed are described in Table 1. These tests started with undamaged gear until the pitting spread along teeth surfaces (Figs. 4, 5, 6 and 7). The AE signals employed to monitor the sun gear are acquired through the on-board sensor placed in the sun shaft (Fig. 1).

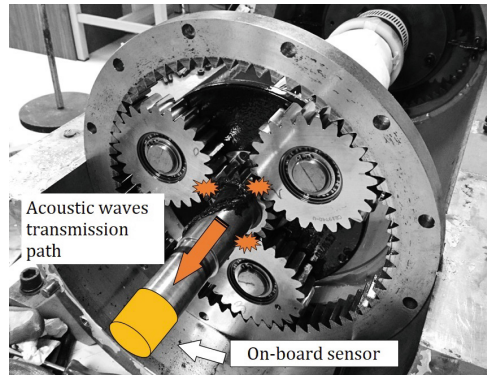


Fig. 1. Sensor positions in the partially dismantled planetary gearbox.

3.1 Gear Damage and AE Signals Description

The process of gear surfaces degradation can be divided into different stages. In the first place, during the initial wearing process, the sun teeth profiles have been modified until they fit with the planets. Secondly, the applied load acting upon the sun planet contacts has changed the surface finish by its polishing. Finally, the pitting has appeared spreading along the teeth flank.

During the first 2 work hours (test 1 and 2), the planets teeth have acted as carving tools, removing the exceeding profile material that disturbs the fluid movement of the system. Material removal has continued until the gears fit better. Metallic particles can be observed immersed in the oil bath when the planetary gearbox is opened for inspection. The most important reduction in gear weight has happened in these two first tests (Table 1). A time domain evaluation of the AE signal does not show the apparition of extreme amplitude peaks. Instead, the AE energy generation spread itself across time as wide continuous bursts. AE intensity is generated during a time interval, not being concentrated in one sudden defined peak event (Fig. 2).

The material removal is identified in the AE signals as the merge of the successive AE bursts or as the rise of the continuous noise level between them. These events exceed the time duration of the sudden energy liberation observed when appropriate healthy gears are used. The decrease of severe degradation has induced a reduction of events width.

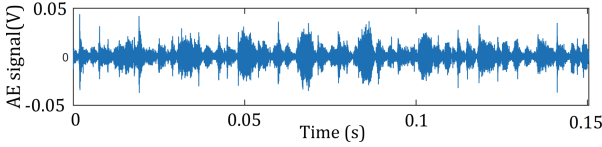


Fig. 2. Signal showing the gear mesh AE burst generated in test 1

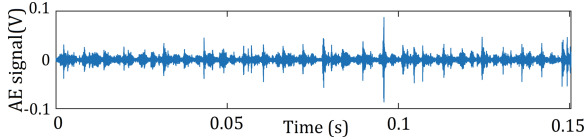


Fig. 3. Signal showing the gear mesh AE burst generated in test 3.

During test 3, the AE pattern shows through the thinner bursts that the material removal has been attenuated (Fig. 3). A new meshing behavior is manifested in a stabilization in the gear weight variation. The presence of smaller particles in the lubrication oil has also indicated the new condition. With the AE signals acquired at the end of test 3, it can be concluded that the initial severe degradation process has finished (see Table 1). The gear teeth have been deformed, presenting a polished surface and also some scratches along the sliding direction (Fig. 4). The polished surface is provoked by the sun-planet load transference, appearing like the footprint of planet teeth. This polishing could generate a superficial hardening of the non treated gear. During the following two test, surfaces and gear weight have remained stable.

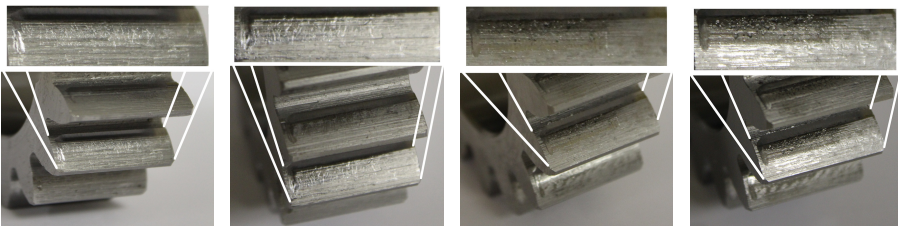


Fig. 4. Gear at the end of test 3. **Fig. 5.** Gear at the end of test 5. **Fig. 6.** Gear at the end of test 7. **Fig. 7.** Gear at the end of test 9.

Between tests 5 and 8, the surfaces have turned more polished and the pitting craters appearing still continues. The polishing has progressed along the teeth surfaces. The pitting has evolved slowly with shallow and small size craters. The most clear AE burst events of all tests are displayed in the signals acquired during this time. The AE events generated during the meshing have adopted a more similar shape than healthy gears, showing sudden AE energy releases (Fig. 8).

Pitting severity has increased in the last two tests. It has progressed along the tooth surface by the multiplication of craters presence. The depth and diameter of previous craters have been augmented. The polished area made by the planets teeth footprint has become completely affected by the pitting. AE bursts pattern becomes wider in these tests. The width of these bursts is not extreme as in the initial material removal, but it is significantly bigger than the ones in test 7 (Fig. 8). The tests have been stopped at this time because the aim is the monitoring of an incipient damage.

3.2 Burst Width as Condition Indicator

In the previous signals description, it has been observed that AE events width coincide with the damage process. These time domain signal patterns are related with an incorrect contact between the gears. In good condition of the gear geometry and teeth surfaces, the meshing is shown through the AE signals as a marked burst. These bursts exhibit a high peak value followed by a sudden attenuation in the acoustic wave amplitude fluctuations. Regarding this behavior, the AE event width could be a useful condition indicator in gear surface damage monitoring. An algorithm is developed to calculate a width parameter of the AE signals avoiding the application of complex processing (as pattern recognition) to obtain an obvious interpretation. It is based in a previous work [8] where a method for data reduction in AE signals consisting of a triangular signal is defined.

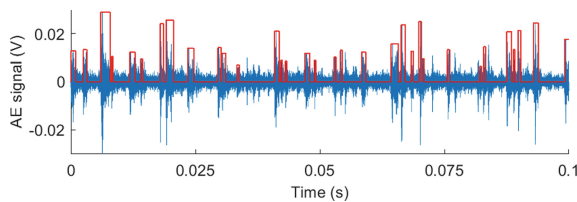


Fig. 8. Burst signal from test 7 AE signal.

An adequate fixed threshold for all acquisitions is selected to distinguish between the burst related with the gear mesh and the continuous noise level (Fig. 8). The threshold is also surpassed by random sudden peaks, whose very thin width could disturb the appropriate average width calculation. To avoid the influence of these peaks in order to describe the signal peak width, the events under the mean value of peak width are not taken into account. After this process, the averaged width of the signal events is computed as a condition indicator of the surface contact behavior.

The condition indicators as signal amplitude, r.m.s., kurtosis or crest factor do not exhibit an identification of the different degradation stages. The AE condition indicator values fluctuate along the tests without distinction between the

work under the initial extreme material removal and the more correct operation in the rest of the tests (Figs. 9 and 10). The frequency domain analysis of the AE signals through the envelope spectrum can only make distinction between the initial stage and the rest because of the noisy spectrum due to the peak merging.

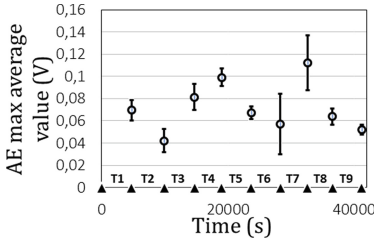


Fig. 9. Average AE max peak progression.

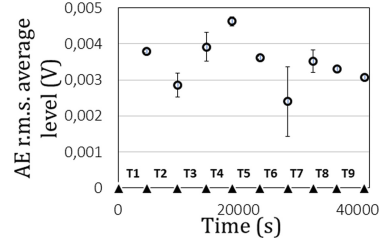


Fig. 10. Average AE r.m.s. progression.

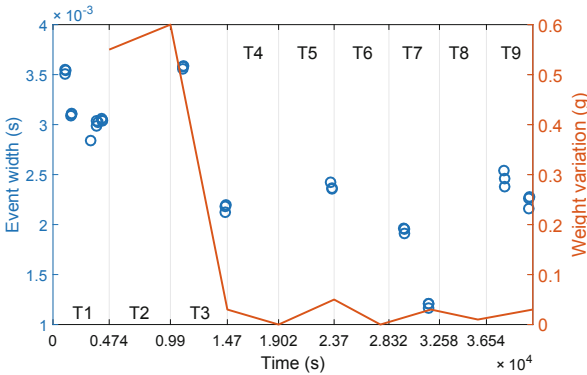


Fig. 11. Event width indicator and gear weight variation progression.

The progression of the averaged AE event width indicator is shown in Fig. 11. The obtained results from each test signal present a behavior description that fits better with the damage evolution over the teeth surfaces. Therefore, the initial stage of material removal generates wider acoustic emission events, translated into higher values of the width indicator. The AE event width continues in reducing its value, coinciding with the stabilization of surface degradation at the end of test 3. After a slight width increase at test 5, the indicator value performs a decrease in test 7. This decreasing coincides with the polishing surface stage, which is mentioned in the previous description of the damage evolution. The more defined bursts in form of sudden peaks provide a lower indicator value. After this stage, the pitting hardness is increased during tests 8 and 9, resulting

in rising event width in test 9. This algorithm shows a more similar performance than the condition indicators as r.m.s. or kurtosis describing the surface damage progression. This simple approach could be greatly enhanced in future works taking into account more parameters in the resultant signal processing.

4 Conclusions

The extreme material removal produced in the first stages of the tests implies a hard drag and surface roughness deformation. This is not translated into a higher amplitude of AE events but in longer AE activity time interval during each teeth meshing. Beyond the lubrication regime, metal-metal contact between teeth surfaces during material removal is proved. The presence of metallic particles in the oil and meshing area could affect the mechanisms involved in the flattening and rounding of asperities. Unexpected AE burst patterns are generated because this extreme asperity contact of rough damaged surfaces.

A clear definition of AE event pattern with high amplitude peaks is showed after the polishing of contact areas when the surface degradation progress becomes stable. AE energy release is concentrated around one point of the meshing angle because of the modification of surface finish. The friction forces between the polished surfaces end with pitting progression. The backlash between the sun gear and planet gears has been increased, favoring a fluid operation and also impact contact. On the other hand, the backlash increase provides a better lubrication film free of debris.

The AE averaged peak width seems to be a good indicator of the surface damage according to the experimental results. The AE activity interval is registered with this indicator. Surface damage can be monitored by applying a simple algorithm which calculates a value of the AE event width. Further investigations on burst event width could offer a better understanding of AE sources in gear mesh. A more complex algorithm based in this parameter could achieve more accurate gear surface diagnosis.

Acknowledgements. This work has been supported by project DPI2017-85390-P funded by the Spanish Ministry of Science, Innovation and Universities (MICINN) and RM16-XX012 PredictEA project funded by SODERCAN.

References

1. Barrueto Novoa, A., Molina Vicuña, C.: New aspects concerning the generation of acoustic emissions in spur gears, the influence of operating conditions and gear defects in planetary gearboxes. *Insight - NDT CM* **58**, 18–27(10) (2016)
2. Caso, E., Fernandez-del-Rincon, A., Garcia, P., Iglesias, M., Viadero, F.: Monitoring of misalignment in low speed geared shafts with acoustic emission sensors. *Appl. Acoust.* **159** (2019). 107092. ISSN 0003-682X
3. Eftekharijad, B., Mba, D.: Seeded fault detection on helical gears with acoustic emission. *Appl. Acoust.* **70**(4), 547–555 (2009). ISSN: 0003682X

4. Elasha, F., Greaves, M., Mba, D., Addali, A.: Application of acoustic emission in diagnostic of bearing faults within a helicopter gearbox. *Procedia CIRP* **38**, 30–36 (2015)
5. Elasha, F., Greaves, M., Mba, D., Fang, D.: A comparative study of the effectiveness of vibration and acoustic emission in diagnosing a defective bearing in a planetary gearbox. *Appl. Acoust.* **115**, 181–195 (2017)
6. Feng, P., Borghesani, P., Chang, H., Smith, W.A., Randall, R.B., Peng, Z.: Monitoring gear surface degradation using cyclostationarity of acoustic emission. *MSSP* **131**, 199–221 (2019)
7. Molina Vicuña, C.: Effects of operating conditions on the Acoustic Emissions (AE) from planetary gearboxes. *Appl. Acoust.* **77**, 150–158 (2014)
8. Molina Vicuña, C., Höweler, C.: A method for reduction of Acoustic Emission (AE) data with application in machine failure detection and diagnosis. *MSSP* **97**, 44–58 (2017). ISSN 10961216
9. Tan, C.K., Mba, D.: Identification of the acoustic emission source during a comparative study on diagnosis of a spur gearbox. *Tribol. Int.* **38**(5), 469–480 (2005)
10. Toutountzakis, T., Mba, D.: Observations of acoustic emission activity during gear defect diagnosis. *NDT E Int.* **36**(7), 471–477 (2003)
11. Yoon, J., He, D.: Planetary gearbox fault diagnostic method using acoustic emission sensors. *IET Sci. Meas. Technol.* **9**(8), 936–944 (2015)
12. Zhang, Y., Lu, W., Chu, F.: Planet gear fault localization for wind turbine gearbox using acoustic emission signals. *Renew. Energy* **109**, 449–460 (2017)



Impact of Position and Tooth Thickness Errors on Planetary Transmission Under Different Meshing Phase

Javier Sanchez-Espiga^(✉), Alfonso Fernandez-del-Rincon, Miguel Iglesias, Ana de-Juan, and Fernando Viadero

Structural and Mechanical Engineering Department, ETSIIT University of Cantabria, Santander, Spain
sanchezespij@unican.es

Abstract. This work focuses on the impact of different kind of errors into planetary transmissions performance. These errors involve position errors, both tangential and radial, and tooth thickness errors. From a quasi-static point of view, the incidence of those errors is analysed and how they affect the load sharing of the transmission. At the same time, the load sharing is affected by the geometrical configuration of the transmission, so a study of the influence of the mentioned errors given those geometrical differences is performed. Besides, the interaction between errors is analysed for planetary transmissions given the torque and the rotating sense for every geometrical configuration considered.

Keywords: Mesh phasing · Planetary transmissions · Position error · Tooth thickness error

1 Introduction

Planetary transmissions are a good solution to transmit high torques in a limited space. Its compactness and sturdiness makes them a better solution for such an application than simple gear transmissions.

On the other hand, planetary transmissions are more exposed to the possibility of errors either manufacturing or mounting errors among others. Besides, the complexity of the planetary transmissions and the bigger amount of moving elements makes impossible avoiding errors. Hence, whenever planetary transmissions are modelled [1, 4, 6, 9, 10] the existence of errors must be considered.

The study of the influence of different kinds of errors in gear transmissions and especially in planetary transmissions has been focus of several research works [3, 5, 7, 12, 13, 16]. Likewise, the influence of the transmission geometry in terms of mesh phasing has been studied both from quasi-static and dynamic approaches [2, 4, 8, 15]. However, the effect of those errors in transmissions with different mesh phasing has not been studied.

Given the mentioned previous works, it is necessary and it is presented in this work, the study of the influence of errors in planetary transmissions under different mesh phasing conditions. Therefore, the scope of this study includes position and tooth thickness errors in in-phase (IP) and sequentially phased (SP) transmissions. For this study, the load sharing is considered the most representative magnitude in the results to show the impact of the errors, given the quasi-static approach.

2 Method

For this work, a 2D three-planet planetary gear transmission model is used [2]. The model uses a semi-analytical approach to solve the contact problem between the surfaces of teeth pairs. Both, finite element models (FEM) and the Weber-Banashek approach are employed to obtain the stresses in the contact. Apart from the contact solution, a torque balance in the planets is searched. Therefore, the balance in the system is obtained and the load distributed in each branch. The errors considered will be as mentioned before, position and tooth thickness errors, as well as, IP and SP transmissions [8, 14].

2.1 Transmissions Considered

The teeth number in the wheels for each transmission lead to an IP, where $Z_s = 36$, $Z_p = 17$, and $Z_r = 72$ and a SP, where $Z_s = 37$, $Z_p = 17$, and $Z_r = 71$, transmission [8, 14]. In both cases, planets are equally spaced, at a distance of $2\pi/3$ between consecutive planets in the carrier. In three-planet planetary transmissions, flexibility in the wheel supports helps on balancing the load sharing [11]. Hence, in order to study, in depth, the influence of the errors and geometry of the transmission, the wheel supports are considered infinitely rigid.

The coordinate frames employed for the errors are set in each wheel centre and the radial error decreases the mounting distance between sun and planet (Fig. 1). Focusing on the pinhole position errors, they are defined in the two directions of a polar coordinate system. Therefore, there are radial and tangential errors, where radial refers to errors on the line that connects sun and pinhole centres and tangential are tangent to the carrier circumference.

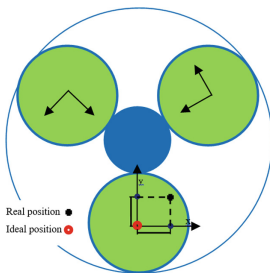


Fig. 1. Transmission and position error geometry

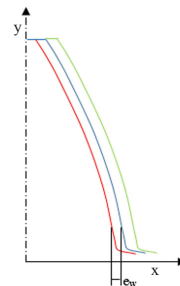


Fig. 2. Tooth thickness error, excess (green) and default (red)

When considering the tooth thickness error, it is important to know the ideal length between teeth flanks [17], referring to the length of a straight line tangent to the base circle. The amount of teeth considered depends on the size of the wheel. This tooth thickness error (Fig. 2) will refer to half, for each flank, the difference between the ideal and the real value for the previous mentioned measurement.

In terms of errors, Table 1 shows the values considered for each. These values for the errors are considered appropriate given the size of the wheels and the transmission. At the same time, in [7] the influence of the radial error is proved to be smaller than the tangential one, but not negligible. Therefore, bigger radial errors are included. The errors will be introduced just in the planet 1 and its pinhole. For all the simulations the input torque is 900 Nm in positive and negative sense, where positive is counter-clockwise and negative is clockwise sense.

Table 1. Errors included in each case of study

Case	e_t (μm)	e_r (μm)	e_w (μm)
1	5	0	0
2	0	20	0
3	5	20	0
4	5	0	-5

3 Results

In order to appreciate the distribution of load between planets, the Load Sharing Ratio (LSR) [7] is considered the most appropriate parameter. It shows the relative amount of load in each planet, in relation to the total load in the system.

$$LSR_i = \frac{T_{pi-s}}{T_{ext}}; i = 1, 2, 3; \quad (1)$$

Where T_{pi-s} refers to the torque between the i th-planet and the sun and T_{ext} refers to the applied torque into the sun which in this case is the inlet to the transmission.

3.1 Negative Torque

For IP transmissions without errors the load sharing corresponds to 33% of the load in each planet. For a SP transmission a reference in its behaviour in terms of LSR appears in [15]. In SP transmissions the average load level in each planet will correspond to the same as in the IP transmissions for an errorless set.

The results for case 1 are shown and then a comparison of the load level in planet 1, which includes the errors, for each case. A tangential pinhole position error moves the position of the planet and therefore, modifies the point in the meshing line for the planet with error and the geometry of the contact. Thus, the planet with error will increase or decrease its load level depending on the torque sense.

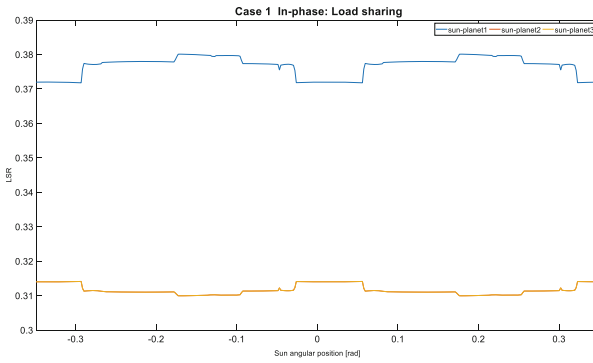


Fig. 3. LSR in case 1 in IP transmission.

These simulations (Fig. 3 and 4) show the effect of the tangential error for IP and SP transmissions, and given the torque sense and the definition of the pinhole position errors, a positive tangential error augments the load level in the planet that includes it (Fig. 5).

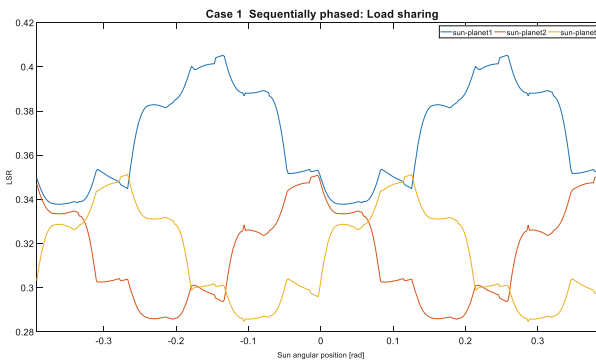


Fig. 4. LSR in case 1 in SP transmission.

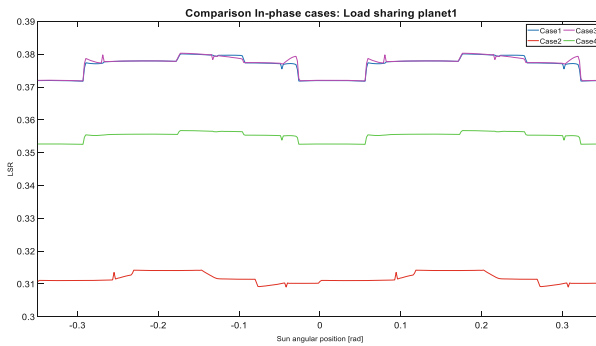


Fig. 5. Comparison of LSR in planet 1 in IP transmission.

In the comparisons, the effect of the different errors is visible, mainly in the SP set Fig. 6. The incidence of the radial error (Case 2) is smaller than the tangential (Case 1) due to the geometrical impact of each error. A tangential movement of the planet modifies more the meshing between a pair of teeth than the radial one, but whenever this errors act together the effect is bigger and in the case of the radial error even opposite to the effect of this error alone. This is more visible in the comparison for IP transmissions between Case 2 and Case 3. The radial error alone decreases the load level in planet 1 but in Case 3 compared to Case 1 the radial error slightly augments the load.

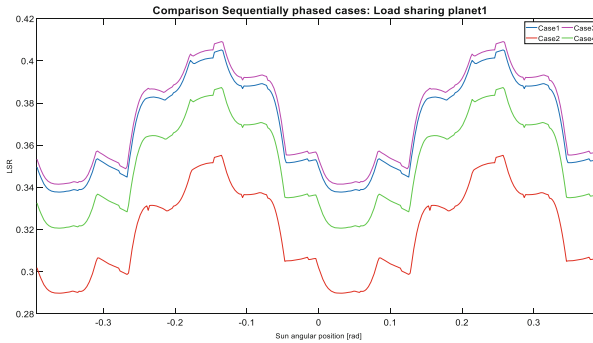


Fig. 6. Comparison of LSR in planet 1 in SP transmission.

3.2 Positive Torque

For these simulations the torque sense is changed and therefore the effect of the errors.

The change in the torque sense influences the incidence of the position errors. Therefore, in Case 1 the influence of the tangential error is the opposite as when the torque was negative. Hence, the planet 1 is the least loaded and the other two are overloaded comparing with its ideal load level. The difference in load between planets correspond with the same as in Fig. 3 and Fig. 4.

However, given the symmetry of the tooth thickness errors in both flanks this is not expected for every case of study as it can be seen in Fig. 7 and Fig. 8. The influence of the tooth thickness error does not depend on the torque sense.

As it appears in the figures above, the behavior of the IP transmission for the Cases 2 and 4 is almost identical. Thus, there is an analogy between both cases even though the considered errors and its values are completely different. At the same time, it is visible the effect of the change in the torque sense and its influence in the effect of tangential errors. Also comparing with the previous analysis and due to the change in the torque sense the tooth thickness and tangential error do not add their effects up, in this case they act oppositely. Due to it the mentioned parallelism between Case 2 and Case 4. Whereas in the SP transmission the difference between those cases is obviously bigger. This difference is due to sequential mesh phasing and the fact that each meshing is in a different point along the meshing line. At the same time, the difference between cases 1 and 3 are bigger for the SP transmission. Therefore, the effect of the sequential mesh phasing influences considerably the LSR for the same errors as in an IP transmission.

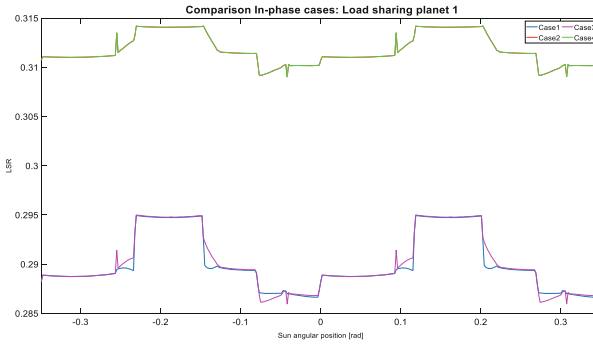


Fig. 7. Load sharing in planet 1 in IP transmission.

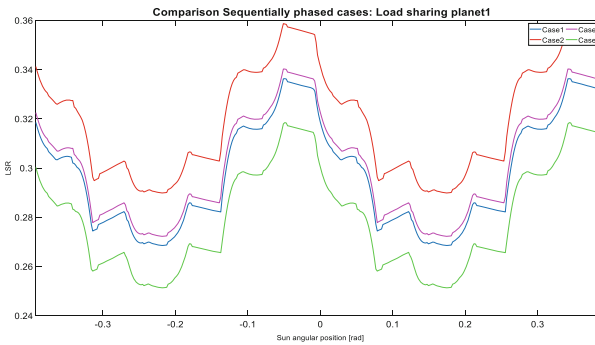


Fig. 8. Comparison of LSR in planet 1 in SP transmissions.

4 Conclusions

Hereinafter, the conclusions obtained from the results to the simulations performed are presented.

Firstly, taking into account the errors considered the torque sense play a crucial role. Given that, this work proves that errors could combine their effect or neutralize each other depending on the torque sense. Therefore, a planet repositioning considering the tooth thickness error in its teeth and the pinhole position errors could lead to a more balanced behavior.

Including different mesh phasing configurations leads to observe that the incidence of radial pinhole position error is higher in SP than in IP configurations. This error cannot be considered negligible as it was mentioned in other works, even less in SP transmissions. The differences in the tensional state in the contacts for a sequentially phased transmission make the impact of the radial error more notable in sequentially phased transmissions. On the contrary, in-phase transmissions have every contact at the same point of the line of action and the effect of the errors is distributed between the N planets equally.

Acknowledgments. The authors would like to acknowledge Project DPI2017-85390-P funded by the Spanish Ministry of Economy, Industry, and Competitiveness for supporting this research. Besides, the authors acknowledge SIEMENS-GAMESA for its collaboration in this work.

References

1. Abousleiman, V., Velex, P.: A hybrid 3D finite element/lumped parameter model for quasi-static and dynamic analyses of planetary/epicyclic gear sets. *Mech. Mach. Theory* **41**(6), 725–748 (2006)
2. Ambarisha, V.K., Parker, R.G.: Suppression of planet mode response in planetary gear dynamics through mesh phasing. *J. Vib. Acoust.* **128**(2), 133 (2006)
3. Bodas, A., Kahraman, A.: Influence of carrier and gear manufacturing errors on the static load sharing behavior of planetary gear sets. *JSME Int J., Ser. C* **47**(3), 908–915 (2004)
4. Gill-Jeong, C.: Numerical study on reducing the vibration of spur gear pairs with phasing. *J. Sound Vib.* **329**(19), 3915–3927 (2010)
5. Gu, X., Velex, P.: A dynamic model to study the influence of planet position errors in planetary gears. *J. Sound Vib.* **331**(20), 4554–4574 (2012)
6. Iglesias, M., Fernandez del Rincon, A., de-Juan, A., Diez-Ibarbia, A., Garcia, P., Viadero, F.: Advanced model for the calculation of meshing forces in spur gear planetary transmissions. *Meccanica* **50**(7), 1869–1894 (2015)
7. Iglesias, M., Fernandez-del-Rincon, A., de-Juan, A., Garcia, P., Diez-Ibarbia, A., Viadero, F.: Planetary transmission load sharing: manufacturing errors and system configuration study. *Mech. Mach. Theory.* **111**, 21–38 (2017)
8. Inalpolat, M., Kahraman, A.: A dynamic model to predict modulation sidebands of a planetary gear set having manufacturing errors. *J. Sound Vib.* **329**(4), 371–393 (2010)
9. Kahraman, A.: Load sharing characteristics of planetary transmissions. *Mech. Mach. Theory* **29**(8), 1151–1165 (1994)
10. Kahraman, A.: Static load sharing characteristics of transmission planetary gear sets : model and experiment. In: *Transmission and Driveline Systems Symposium*, vol. 1, pp. 1–10 (1999)
11. Ligata, H., Kahraman, A., Singh, A.: A closed-form planet load sharing formulation for planetary gear sets using a translational analogy. *J. Mech. Des.* **131**(2), 021007 (2009)
12. Ligata, H., Kahraman, A., Singh, A.: An Experimental study of the influence of manufacturing errors on the planetary gear stresses and planet load sharing. *J. Mech. Des.* **130**(4), 041701 (2008)
13. Ma, P., Botman, M.: Load sharing in a planetary gear stage in the presence of gear errors and misalignment. *J. Mech. Des. Trans. ASME* **107**(1), 4–10 (1985)
14. Peng, D., Smith, W.A., Randall, R.B., Peng, Z.: Use of mesh phasing to locate faulty planet gears. *Mech. Syst. Signal Process.* **116**, 12–24 (2019)
15. Sanchez-Espiga, J., Fernandez-del-Rincon, A., Iglesias, M., Viadero, F.: Influence of the phase in planetary gears load sharing and transmission error, vol. 73 (2019)
16. Velex, P., Maatar, M.: A mathematical model for analyzing the influence of shape deviations and mounting errors on gear dynamic behaviour. *J. Sound Vib.* **191**(5), 629–660 (1996)
17. Wildhaber, W.: Measuring tooth thickness of involute gears, p. 1923 (1923)



Profile Shifting Coefficients of Spur Gears with Balanced Specific Sliding Coefficients at the Points Where the Meshing Stars and Ends

Tiberiu Alexandru Antal^(✉)

Technical University from Cluj-Napoca, Cluj-Napoca, Romania

Tiberiu.Alexandru.Antal@mep.utcluj.ro

Abstract. The paper gives a new method for obtaining the specific sliding coefficients for involute spur gears. While sliding coefficients are determined in the technical literature using differential geometry, this paper is using a kinematical method to achieve the same result. Based on the equalization conditions of the specific sliding coefficients at the points where the meshing begins (A) and ends (E) the profile shifting coefficients can be computed in order to design gears with their geometrical dimensions optimised for a longer lifetime.

Keyword: Addendum modification · Balancing · Kinematical method · Profile shifting coefficients · Spur gears · Specific sliding coefficients

1 Introduction

Gear trains are used to transmit mechanical power. Profile shift, also known as ‘addendum modification’ or ‘correction’ is used to obtain well defined distances between the axes as well as to improve some aspects of gear operation in order to ensure the correct meshing of teeth flanks over a longer time [1–3].

In the general case, the geometrical dimensions of the helical and the involute spur gears are taking into account the x_1 and x_2 profile shifting coefficients. These values can be determined based on different criteria, some of them are discussed in [4–11]. This paper presents a method of establishing the profile shifting coefficients using the equalization, also known as balancing, of the specific sliding coefficients, at the A and E points, where the meshing begins and ends. The technical literature gives the determination of specific sliding coefficients using differential geometry. The following work is based on a new kinematical method that was developed based on the recommendation from [12] and [13] in the general case of spatial gears [14] and it is customized for planar gears. The magnitude of sliding coefficients allows us to predict the wear and heating of the wheels in the gear. We are interested to keep these values limited and balanced in order to obtain in the design phase wheels with better lifetime. One of the areas that lends itself to the use of this design method is that of the medical robots where the gears must maintain their operating accuracy although they are subject to wear [15–17].

© The Editor(s) (if applicable) and The Author(s), under exclusive license to Springer Nature Switzerland AG 2020

D. Pisla et al. (Eds.): EuCoMeS 2020, MMS 89, pp. 272–278, 2020.

https://doi.org/10.1007/978-3-030-55061-5_31

2 Sliding Between Two Surfaces in the General Case

Specific sliding coefficients are used in this paper to appreciate the wear and lubrication of the teeth flanks during gear operation. In order to analyse the sliding process we consider two surfaces (see Fig. 1) that are in contact after a line or a point that represent the teeth flanks of a parallel axis gear. Between the two surfaces in contact, during the transmission of the motion, in the general case, there is a relative velocity \vec{V}_{12} (surface 1 velocity relative to the surface 2 at point P). During the Δt time, the point P describes on the surface 1 the curve arc ΔS_1 and on the surface 2 the curve arc ΔS_2 . If there is only rolling between the two surfaces we have $\Delta S_1 = \Delta S_2$. In the case of rolling with sliding $\Delta S_1 \neq \Delta S_2$. The difference in length between the two arcs is the sliding and it is written as $\Delta S_{12} = \Delta S_1 - \Delta S_2$.

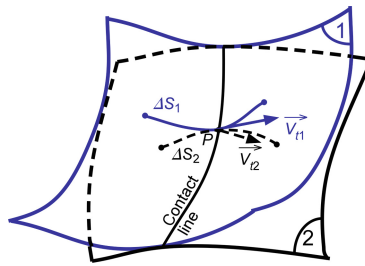


Fig. 1. Surfaces in contact.

The specific sliding of the surface 1, relative to the surface 2, can be expressed in the relationship:

$$\zeta_{12} = \lim_{\Delta S_1 \rightarrow 0} \frac{\Delta S_1 - \Delta S_2}{\Delta S_1} = \lim_{\Delta S_1 \rightarrow 0} \frac{\Delta S_{12}}{\Delta S_1} = \lim_{\Delta t \rightarrow 0} \frac{\frac{\Delta S_{12}}{\Delta t}}{\frac{\Delta S_1}{\Delta t}} \tag{1}$$

Noting that $\Delta S_{12}/\Delta t = V_{12}$ and $\Delta S_1/\Delta t = V_{t1}$ where V_{12} is the surface 1 relative speed with respect to the surface 2 of the contact point P and V_{t1} the moving speed of the contact point P on the surface 1, the specific sliding of the surface 1 with respect to the surface 2 can be determined with the expression:

$$\zeta_{12} = \frac{V_{12}}{V_{t1}} \tag{2}$$

Form (2), based on [13] and [14], it can shown that:

$$\zeta_{12} = \frac{\vec{V}_{12} \bullet \vec{V}_{12}}{\vec{V}_1 \bullet \vec{V}_{12}} \tag{3}$$

where \vec{V}_1 is the velocity of the surface 1 at point P. The specific sliding of the surface 2 with respect to the surface 1 is expressed with the relationship:

$$\zeta_{21} = \lim_{\Delta S_2 \rightarrow 0} \frac{\Delta S_2 - \Delta S_1}{\Delta S_2} = \lim_{\Delta S_1 \rightarrow 0} \frac{\Delta S_{21}}{\Delta S_2} = \lim_{\Delta t \rightarrow 0} \frac{\frac{\Delta S_{21}}{\Delta t}}{\frac{\Delta S_2}{\Delta t}} \tag{4}$$

Noting that $\Delta S_{21}/\Delta t = V_{21}$ and $\Delta S_2/\Delta t = V_{t2}$ where V_{21} is the surface 2 relative speed with respect to the surface 1 of the contact point P point and V_{t2} the speed of the contact point P on the surface 2 the specific sliding of the surface 2 with respect to the surface 1 can be determined with the expression:

$$\zeta_{21} = \frac{V_{21}}{V_{t2}} \tag{5}$$

From (5), based on [13] and [14], it can shown that:

$$\zeta_{21} = \frac{\vec{V}_{21} \bullet \vec{V}_{21}}{\vec{V}_2 \bullet \vec{V}_{21}} \tag{6}$$

where \vec{V}_2 is the velocity of the surface 2 at point P.

As shown in [1] the relationships (3) and (6) have general validity and can be used to determine and analyze the sliding phenomena, both in planar gears as in spatial gears. Also, with the help of the above relations, the teeth sliding can be studied, both in the case of involute tooth profile gears as in the case the teeth are made after a certain profile.

3 Sliding Between the Flanks in the Case of the Cylindrical Spur Gears

The general formulae from (3) and (6) will be customized in the case of an external cylindrical gear having an involute tooth profile (external spur gears). The peripheral speed of the point P in relation to O_1 is:

$$\vec{V}_1 = \vec{\omega}_1 \times \vec{r}_1 = \begin{vmatrix} \vec{i} & \vec{j} & \vec{k} \\ 0 & 0 & -\omega_1 \\ x & y - r_{w1} & z \end{vmatrix} \tag{7}$$

The peripheral speed of the point P in relation to O_2 is:

$$\vec{V}_2 = \vec{\omega}_2 \times \vec{r}_2 = \begin{vmatrix} \vec{i} & \vec{j} & \vec{k} \\ 0 & 0 & \omega_2 \\ x & y + r_{w2} & z \end{vmatrix} \tag{8}$$

The relative speed of the tooth flank 1, relative to tooth 2, at point P becomes:

$$\vec{V}_{12} = \vec{V}_1 - \vec{V}_2 = \begin{vmatrix} \vec{i} & \vec{j} & \vec{k} \\ 0 & 0 & -\omega_1 \\ x(1 + u_{21}) & y(1 + u_{21}) & 0 \end{vmatrix} \tag{9}$$

where $u_{21} = \omega_2/\omega_1$ is the ratio of the angular velocities. From (3), (7) and (9) the specific sliding ζ_{12} will be expressed as follows:

$$\zeta_{12} = (1 + u_{21}) \frac{x^2 + y^2}{x^2 + y(y - r_{w1})} \tag{10}$$

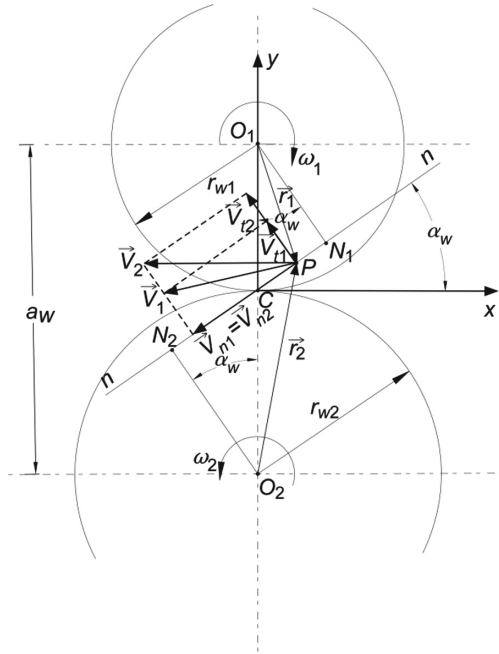


Fig. 2. Kinematics of the external spur gears.

From Fig. 2 we have $y = x \tan(\alpha_w)$ and (18) can be written as:

$$\zeta_{12} = (1 + u_{21}) \frac{x}{x - r_{w1} \sin(\alpha_w) \cos(\alpha_w)} \tag{11}$$

For the N_1 point $x = r_{w1} \sin(\alpha_w) \cos(\alpha_w)$ and $\zeta_{12} \rightarrow \infty$, for the N_2 point $x = -r_{w2} \sin(\alpha_w) \cos(\alpha_w)$ and $\zeta_{12} = 1$. The relative speed of the tooth flank 2, relative to tooth 1, at point P becomes:

$$\vec{V}_{21} = \vec{V}_2 - \vec{V}_1 = \begin{vmatrix} \vec{i} & \vec{j} & \vec{k} \\ 0 & 0 & \omega_2 \\ x(1 + u_{12}) & y(1 + u_{12}) & 0 \end{vmatrix} \tag{12}$$

where $u_{12} = \omega_1/\omega_2$ is the ratio of the angular velocities. From (6), (9) and (12) the specific sliding ζ_{21} will be expressed as follows:

$$\zeta_{21} = (1 + u_{12}) \frac{x^2 + y^2}{x^2 + y(y + r_{w2})} \tag{13}$$

Substituting y in (13) we have :

$$\zeta_{21} = (1 + u_{12}) \frac{x}{x + r_{w2} \sin(\alpha_w) \cos(\alpha_w)} \tag{14}$$

For the N_2 point $x = -r_{w2} \sin(\alpha_w) \cos(\alpha_w)$ and $\zeta_{21} \rightarrow \infty$, for the N_1 point $x = r_{w1} \sin(\alpha_w) \cos(\alpha_w)$ and $\zeta_{21} = 1$.

With the help of the relationships (11) and (14), the specific sliding can be determined at any point on the line of action, in the case of the external involute gears.

4 Specific Sliding Coefficients at the Points Where the Meshing Starts (a) and Ends (E)

Using (11) and (14), the specific sliding coefficients at points A and E (Fig. 3), where the meshing starts and ends, can be determined, in the case of the external spur gears. For the point A, where the teeth meshing begin (Fig. 3), (11) becomes:

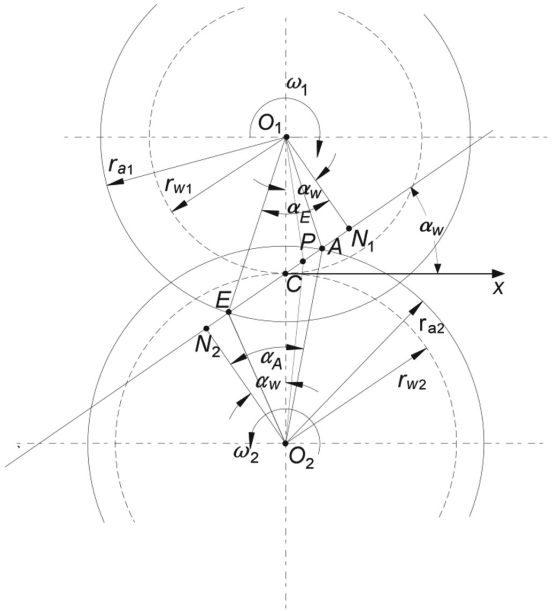


Fig. 3. The beginning (A) and ending (E) of meshing of external spur gears

$$\zeta_{12A} = (1 + u_{21}) \frac{x_A}{x_A - r_{w1} \sin(\alpha_w) \cos(\alpha_w)} = (1 + u_{12}) \frac{1 - \Psi_A}{1 + u_{12}(1 - \Psi_A)} \tag{15}$$

where $\Psi_A = \frac{\tan(\alpha_A)}{\tan(\alpha_w)}$ and $u_{12}u_{21} = 1$.

For point E, where teeth meshing ends (Fig. 3), (11) becomes:

$$\zeta_{12E} = (1 + u_{21}) \frac{-\frac{x_E}{\cos(\alpha_w)}}{-\frac{x_E}{\cos(\alpha_w)} - r_{w1} \sin(\alpha_w)} = (1 + u_{12}) \frac{\Psi_E - 1}{u_{12}\Psi_E} \tag{16}$$

where $\Psi_E = \frac{\tan(\alpha_E)}{\tan(\alpha_w)}$.

For point A, where teeth meshing starts (Fig. 3), (14) becomes:

$$\zeta_{21A} = (1 + u_{12}) \frac{\frac{x_A}{\cos(\alpha_w)}}{\frac{x_A}{\cos(\alpha_w)} + r_{w2} \sin(\alpha_w)} = (1 + u_{12}) \frac{\Psi_A - 1}{\Psi_A} \tag{17}$$

For point E, where the teeth meshing ends (Fig. 3), (14) becomes:

$$\zeta_{21E} = (1 + u_{12}) \frac{-\frac{x_E}{\cos(\alpha_w)}}{-\frac{x_E}{\cos(\alpha_w)} + r_{w2} \sin(\alpha_w)} = (1 + u_{12}) \frac{\Psi_E - 1}{\Psi_E - (1 + u_{12})} \tag{18}$$

To balance the specific sliding at the base of the tooth we put the condition:

$$\zeta_{12A} = \zeta_{21E} \tag{19}$$

From (15) and (18) we can write:

$$(1 + u_{12}) \frac{1 - \Psi_A}{1 + u_{12}(1 - \Psi_A)} = (1 + u_{12}) \frac{\Psi_E - 1}{\Psi_E - (1 + u_{12})} \tag{20}$$

or

$$\Psi_A = \frac{u_{12} \Psi_E}{1 + \Psi_E(u_{12} - 1)} \tag{21}$$

The same result must be reached if the condition is:

$$\zeta_{12E} = \zeta_{21A} \tag{22}$$

From (16) and (19) we can write

$$(1 + u_{12}) \frac{\Psi_E - 1}{u_{12} \Psi_E} = (1 + u_{12}) \frac{\Psi_A - 1}{\Psi_A} \tag{23}$$

or

$$\Psi_A = \frac{u_{12} \Psi_E}{1 + \Psi_E(u_{12} - 1)} \tag{24}$$

5 Conclusions

In [4–6], the general formulae from (3) and (6) were used to determine and analyze the sliding phenomena in the case of helical gears. The following research shows that (3) and (6) can also be used in the case of gears with parallel axis, specifically in the case of external spur gears. The theoretical research also proves that, based on (21) and (24), the equalization of the specific sliding at the base of the tooth leads to the equalization of the specific sliding at the tip of the tooth. The final expression of the balancing condition of the specific sliding coefficients in (21) or (24) allow the determination of the x_1 and x_2 profile shifting coefficients, for specific (z_1, z_2) number of teeth pairs based on the general balancing algorithm used in [9] and [11].


References

1. Erney, G.: Gears, p. 460. Technical Publishing House, Budapest (1983)
2. Niemann, G., Winter, H.: Machine Elements -, vol. II. Springer Verlag, Berlin (1983)
3. Linke, H.: Cylindrical Gears: Calculation - Materials - Manufacturing. Carl Hanser Verlag, Munich – Berlin (1996)
4. Antal, T.A., Antal, A.: Helical gear dimensions in the case of the minimal equalized specific sliding. In: SYROM 2009 - Proceedings of the 10th IFToMM International Symposium on Science of Mechanisms and Machines, pp. 85–93 (2009)
5. Antal, T.A.: A new algorithm for helical gear design with addendum modification. *Mechanika* **77**(3), 53–57 (2009)
6. Antal, T.A., Antal, A.: A design method of crossed axes helical gears with increase uptime and efficiency. *Mech. Mach. Sci.* **5**, 641–648 (2010)
7. Antal, T.A., Antal, A.: The use of genetic algorithms for the design of mechatronic transmissions with improved operating conditions. In: 3rd International Conference on Human System Interaction, HSI'2010 - Conference Proceedings, pp. 63–66 (2010)
8. Baglioni, S., Cianetti, F., Landi, L.: Influence of the addendum modification on spur gear efficiency. *Mech. Mach. Theory* **49**, 216–233 (2012). <https://doi.org/10.1016/j.mechmach.2011.10.007>
9. Antal, T.A.: Addendum modification of spur gears with equalized efficiency at the points where the meshing stars and ends. *Mechanika* **21**(6), 480–485 (2015)
10. Antal, T.A.: The power lost by friction, between the teeth flanks, for cylindrical spur gears, at the points where the meshing stars and ends. *Acta Technica Napocensis, Ser. Appl. Math. Mech.* **57**(1), 7–10 (2014)
11. Antal, T.A.: Addendum modification of cylindrical spur gears with equalized powers lost by friction between the teeth flanks at the points where the meshing stars and ends. *Acta Technica Napocensis, Ser. Appl. Math. Mech.* **57**(3), 329–334 (2014)
12. Szekely, I.: Mechanism, Multiplication Workshop of the Polytechnic Institute of Cluj-Napoca, pp. 273 (1974, in Romanian)
13. Sauer, L., Horovitz, B., Vasu, T., Miloiu, G.: Gears Materials, Design, Technology, Control, vol. 1–2, pp. 670. Technical Publishing House (1970, in Romanian)
14. Antal, A.; Potra, T.: Sliding in gears with cross axles. *Construcția de mașini* 45(10-11-12), 45–47 (1993, in Romanian)
15. Pislă, D., Plitea, N., Vaida, C.: Kinematic modeling and workspace generation for a new parallel robot used in minimally invasive surgery. In: Lenarcic, J., Wenger, P. (eds.) *Advances in Robot Kinematics: Analysis and Design*, pp. 459–468. Springer, Dordrecht (2008)
16. Pislă, D., Gherman, B., Vaida, C., Plitea, N.: Kinematic modelling of a 5-DOF hybrid parallel robot for laparoscopic surgery. *Robotica* **30**(7), 1095–1107 (2012)
17. Pislă, D., Gherman, B., Plitea, N., Gyurka, B., Vaida, C., Vlad, L., Graur, F., Radu, C., Suciuc, M., Szilaghi, A., Stoica, A.: PARASURG hybrid parallel robot for minimally invasive surgery. *Chirurgia (Bucharest)* **106**(5), 619–625 (2011)

Dynamics of Multi-body Systems



Simplified Method to Predict Clearance Evolution Effects Due to Wear Through MBD Simulation

Manuel Ordiz¹ (✉) , Javier Cuadrado², Mario Cabello¹, Daniel Dopico², Iban Retolaza¹, and Aitor Cenitagoya¹

¹ Ikerlan Technology Research Centre, Basque Research and Technology Alliance (BRTA), Mondragón, Spain

{mordiz, mjcabello, iretolaza, acenitagoya}@ikerlan.es

² Universidade da Coruña, Ferrol, Spain

{javier.cuadrado, daniel.dopico}@udc.es

Abstract. This paper studies the effect of wear that occurs in the contact between pin and bushing in revolute joints with clearances due to manufacturing tolerances, and the evolution of the size and shape of the free spaces with the work cycles. The objective is to propose an efficient method to estimate, during the design procedures of a machine or mechanism, the variation of the clearance and its shape. Ease of analysis and efficiency is prioritized over accuracy, which anyway must be kept within admissible levels. In order to streamline the application of the method to any multibody system, SolidWorks has been used for design and multibody simulations, and Excel for calculation of the wear suffered by the joints.

Keywords: Clearance · Wear · Shape · Multibody dynamics

1 Introduction

Machines and mechanisms are formed by components which are connected by several types of joints or kinematic pairs. Joint dynamics is a complex problem that has been studied in the last decades and that is not solved yet [1]. Contact between bodies at joints is subject to load, relative motion or, generally, a combination of both. Moreover, other phenomena as wear and clearances make the problem even more difficult.

When designing real mechanisms, the influence of the clearances in the kinematic pairs must be taken into account. While they streamline the assembly of the parts composing the joint, they also add additional dynamics that, in limit cases, may cause the structural failure of the full machine or of any of its parts. Furthermore, clearances change machine kinematics and, hence, they affect its functional precision.

The effect of clearances has been studied in the literature [2]. As said in [3], clearances cause vibration, impacts and, consequently, wear in the joints. Wear makes the clearance increase in size along time, which leads to higher vibration and impacts and, hence, to

wear increase. This process repeats until the machine cannot provide service anymore due to lack of precision, excessive vibration or even a structural failure in the mechanism.

In this work, a simplified method for the prediction of the evolution of clearances in revolute joints due to wear is proposed. It is based on the use of multibody-dynamics simulation, and can be applied in the design of real machines. Three versions of the method will be compared in terms of accuracy and computational efficiency.

2 Wear Approximation

Several methods can be found in the literature to estimate wear [4]. Generally, they derive from Reye's method [5], the first proposed method to predict the wear occurring between two surfaces with relative motion. For example, Holm's method considered that atoms of the surface asperities move and collide with each other. Archard's method claimed that several aspects should be taken into account: the wear itself, the patch contact area and pressure, the sliding distance and the material properties. Nowadays, this method is the most frequently used and most modern methods are based on it [6].

In this work, Archard's method has been used due to its simplicity and accuracy, but not the original one but the modified version proposed by [7]. The fundamental equation is:

$$\frac{hA}{s} = F_N k_w \quad (1)$$

where h is the depth of wear (magnitude to be obtained), A is the patch contact area, s is the sliding length, F_N is the normal contact force, and k_w is a parameter that depends on the materials. For the sake of simplicity, the sliding length will be estimated by assuming that there is permanent contact between pin and bushing. As for k_w , it will be taken from the experimental data provided in [7].

From the previous equation, the depth of wear is worked out as:

$$h = k_w \frac{F_N}{A} s \quad (2)$$

The patch contact area, A , is obtained, from Hertz theory, for a contact between two cylinders:

$$A = 2bL \quad (3)$$

where L represents the contact length and b is defined as:

$$b = \left(\frac{4F_N \rho^*}{\pi L E^*} \right)^{0.5} \quad (4)$$

with,

$$\rho^* = \frac{R_j R_i}{R_j - R_i} \quad (5)$$

$$E^* = \frac{E_j E_i}{E_j(1 - \nu_i^2) + E_i(1 - \nu_j^2)} \quad (6)$$

where R_i is the pin radius and R_j is the bushing radius, E represents the Young's modulus and ν the Poisson's modulus.

The contact force is modeled as a nonlinear spring-damper element:

$$F_N = k\delta^n + c\dot{\delta} \quad (7)$$

where k is the contact stiffness, δ is the penetration between bodies, n is the penetration exponent, c represents the damping coefficient and $\dot{\delta}$ is the penetration speed.

As said in the Introduction, three versions of the method will be applied to estimate wear. In all the three it is assumed that wear is suffered by the bushing only. In the two first, it is supposed that wear leads to an increase in the radius of the bushing so that, in the simulation of the mechanism following a wear update, the bushing radius will be:

$$R_j = R_j + h \quad (8)$$

However, the third version of the method divides the bushing into several sectors, setting a reference point as representative of each sector. Wear is calculated at the reference point and applied to the whole sector. In this way, the shape of the bushing will lose its circular shape as wear evolves, as it will be different at each sector.

3 Implementation

In this Section, an example is presented to show the implementation of the proposed method: the slider-crank mechanism illustrated in Fig. 1. An ideal motor makes the crank rotate at 150 rpm and the mechanism performs 42,000 cycles of the crank.

First, the mechanism is built in SolidWorks according to the data in Table 1, and a clearance of 0.1 mm is introduced in the revolute pair connecting the crank and the coupler. The crank is made of aluminium while the coupler is made of steel, so that it is assumed that wear is suffered by the crank only, the body containing the bushing. The remaining joints are considered ideal, with exception of the slider, for which dry friction is included. A virtual sensor is defined that monitors the normal contact forces at the joint with backlash.

The total number of cycles is divided into a number of blocks. For each block, the normal contact forces are considered constant. These forces are obtained in a multibody-dynamics simulation of the mechanism, with the updated value of the clearance size. Each simulation spans two turns of the crank but, to avoid the transient that takes place during the first turn, only the forces calculated during the second turn are recorded. To determine the normal contact force, an algorithm is created that implements the modified Archard's method described in the previous Section. Data for the contact problem are gathered in Table 2.

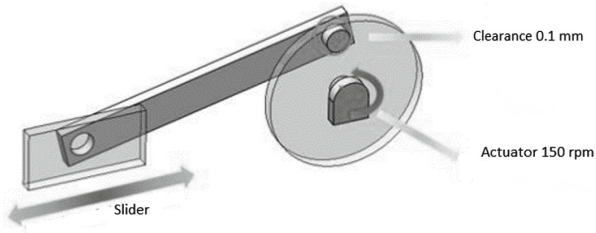


Fig. 1. Slider-crank mechanism with clearance in the revolution joint between the crank and the coupler

Table 1. Data for the slider-crank mechanism

Body	Length (mm)	Mass (kg)	Inertia (kg·mm ²)
Crank	50	3.0	7360
Coupler	220	0.19	880
Slider	–	0.70	360

Table 2. Data for the contact problem

Parameters	Value
Pin radius	10.0 mm
Bushing radius	10.1 mm
Contact length	6.0 mm
Initial clearance	0.1 mm
Pin Young module (steel)	207 GPa
Bushing Young module (aluminum)	71.7 GPa
Pin Poisson coefficient	0.29
Bushing Poisson coefficient	0.33
Restitution coefficient	0.9
Friction coefficient	0.1
Threshold velocity	1 mm/s
Contact stiffness	$7.95 \times 10^{10} \text{ N/m}^{1.5}$
Wear coefficient	150 rpm

For each simulation, once the normal contact forces have been obtained, the three versions of the method anticipated in Sect. 2 are applied. In the first version, the RMS

value of the normal contact forces obtained during the full turn of the crank is considered to calculate the depth of wear. In the second version, the RMS value is substituted by the maximum value. The third version is different, since the bushing is divided into sectors and a reference point is selected as representative of each sector. The normal contact force calculated at each reference point is considered to derive the depth of wear in the corresponding sector, thus allowing non-uniform wear of the bushing. Figure 2 shows the eight points used in the example.

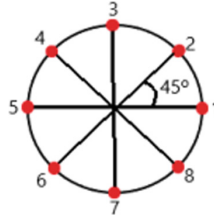


Fig. 2. Distribution of reference points on the bushing surface

4 Results and Comparison

The first version of the method yields a wear that increases almost linearly with respect to the cycles (turns of the crank), as shown in Fig. 3. The evolution of the clearance is depicted in Fig. 4.

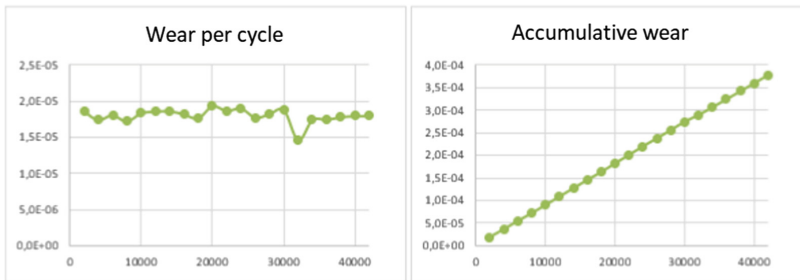


Fig. 3. Wear evolution for the first version of the method

The second version of the method also yields a wear that increases almost linearly with respect to the cycles (turns of the crank), as shown in Fig. 5. The evolution of the clearance is depicted in Fig. 6.

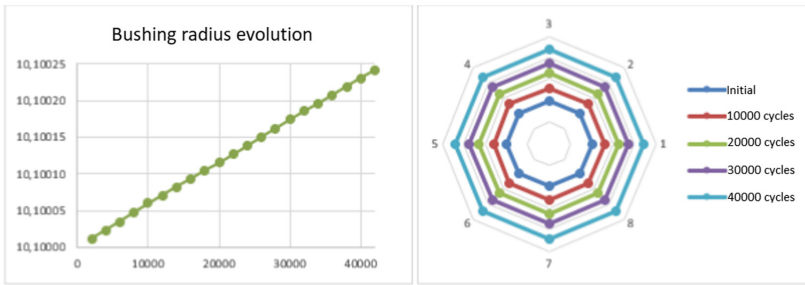


Fig. 4. Clearance evolution for the first version of the method

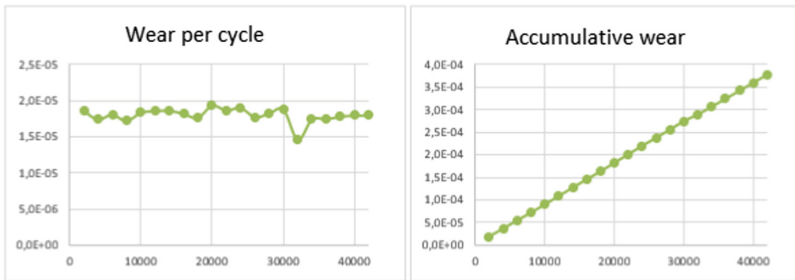


Fig. 5. Wear evolution for the second version of the method

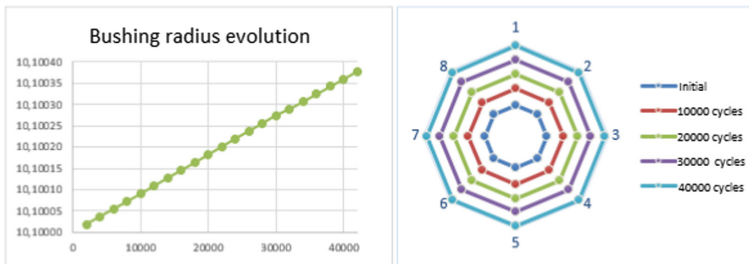


Fig. 6. Clearance evolution for the second version of the method

The third version of the method yields a non-uniform increase of the clearance in all its directions. Figure 7 shows the shape of the bushing after each simulation corresponding to each block of cycles. As it can be seen, wear is maximum in the horizontal direction (points 1 and 5), the direction of the slider motion, and minimum in the vertical direction (points 3 and 7).

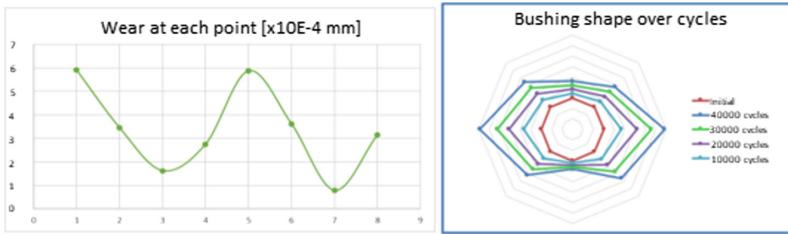


Fig. 7. a) Total wear at each reference point; b) Shape evolution for the bushing

Figure 8 shows a comparison of the bushing shapes obtained, once all the cycles have been completed, by the three versions of the method. While wear at points 1 and 5 is similar for all the three versions of the method, wear at points 3 and 7 seems to be overestimated by the two first versions of the method.

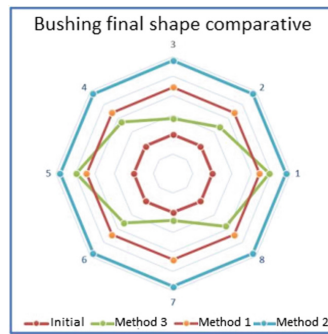


Fig. 8. Final shape of the bushing for the three versions of the method

5 Conclusions

In this work, a method based on a modified Archard's theory has been proposed, with three different versions. A slider-crank mechanism was taken as example and the wear suffered by the revolute joint connecting the crank and the coupler was analyzed. It was supposed that the pin, belonging to the coupler, was made of a hard material, while the bushing, belonging to the crank, was made of a soft material, so that wear affected the latter only. The working conditions of the mechanism were established and an initial value was given to the clearance at the revolute joint of interest. Then, the wear undergone by the bushing was estimated through the three versions of the method.

The third version of the method, which discretizes the bushing surface into a number of sectors, provides a prediction of the bushing shape evolution. Looking at the obtained results, it seems that assuming a uniform wear in the bushing surface is not possible, as made by the two first versions of the method. Therefore, although the computational effort required by the simulations is as many times lower for the two first versions of the

method as discretization sectors have been taken for the third one, results indicate that wear is certainly non uniform and, hence, discretization is needed to obtain a reasonable estimate of clearance evolution.

References

1. Tian, Q., Liu, C., Machado, M., Flores, P.: A new model for dry and lubricated cylindrical joints with clearance in spatial flexible multibody systems a new model for dry and lubricated cylindrical joints with clearance in spatial flexible multibody systems, April 2011. <https://doi.org/10.1007/s11071-010-9843-y>
2. Gummer, A., Sauer, B.: Modeling planar slider-crank mechanisms with clearance joints in RecurDyn. *Multibody Sys. Dyn.* **31**(2), 127–145 (2012). <https://doi.org/10.1007/s11044-012-9339-2>
3. Bai, Z.F., Zhao, Y., Chen, J.: Dynamics analysis of planar mechanical system considering revolute clearance joint wear. *Tribol. Int.* **64**, 85–95 (2013). <https://doi.org/10.1016/j.triboint.2013.03.007>
4. Ma, J., Qian, L.: Modeling and simulation of planar multibody systems considering multiple revolute clearance joints. *Nonlinear Dyn.* **90**(3), 1907–1940 (2017). <https://doi.org/10.1007/s11071-017-3771-z>
5. Alexander, F., Bustamante, S., Manuel, J., Restrepo, V.: Estudio Del Modelo De Desgaste Propuesto Por Archard Study of the model of wearing proposed by Archard. *Dyna* **72**, 27–43 (2005). <http://www.scielo.org.co/pdf/dyna/v72n146/a03v72n146.pdf>
6. Flores, P., Ambrósio, J.: Revolute joints with clearance in multibody systems. *Comput. Struct.* **82**(17–19), 1359–1369 (2004). <https://doi.org/10.1016/j.compstruc.2004.03.031>
7. Xu, L.X., Han, Y.C., Dong, Q.B., Jia, H.L.: An approach for modelling a clearance revolute joint with a constantly updating wear profile in a multibody system: simulation and experiment. *Multibody Sys. Dyn.* **45**(4), 457–478 (2018). <https://doi.org/10.1007/s11044-018-09655-z>



A Modular Geometric Approach to Dynamics Modeling of Fully-Parallel PKM by Example of a Planar 3RPR Mechanism

Andreas Müller^(✉)

Johannes Kepler University, Linz, Austria
a.mueller@jku.at

Abstract. The modeling of parallel kinematic machines (PKM) has been a topic of ongoing research since PKM started to gain popularity more than twenty years ago. Due to the modular setup of most PKM, research has been conducted towards modular modeling paradigms. This applies in particular to so-called fully parallel PKM. Recently, a general modeling approach was introduced for such PKM, which rests on a Lie group formulation of the kinematics and dynamics. Therein, the PKM kinematics is described by means of screw coordinates, which makes this a user-friendly approach free from restrictive modeling conventions. In this paper, application of the method is demonstrated for a simple planar 3RPR PKM.

Keywords: Parallel kinematics machines · Modeling · Kinematics · Dynamics · Modularity · Lie groups · Screws · Product of exponentials · Parallel computing

1 Introduction

Parallel kinematic manipulators (PKM) offer significant advantages over classical serial manipulators, in particular regarding their dynamic capabilities [4, 9]. In order to exploit and optimize these advantages, systematic approaches for modeling the kinematic and dynamics have been important topics since beginning of research that started almost three decades ago. The kinematics modeling using screws, and increasingly Lie group theory, has become an established approach, but no general approach to the dynamics modeling of PKM has found a wider acceptance. While any formulation for modeling general multibody systems can be applied, the robotics community needs tailored modeling approaches, in particular such that take into account the modularity inherent to the majority of PKM. There are basically two formulations reported in the literature that respond to this demand; one is the formulation by Angeles [1] and the other that by Briot and Khalil [2]. Both yield equations of motion (EOM) in terms of

joint coordinates. Recently, another modeling approach for fully parallel PKM was reported in [7]. The latter makes explicit use of the modularity of PKM, and supports a modular modeling. For details, and for a short discussion of the methods in [1, 2], the reader is referred to [7].

The aim of this paper is to demonstrate the method [7] by means of a simple 3RPR example. Figure 1 shows a model of the 3RPR PKM in its reference configuration. It consists of $L = 3$ structurally identical limbs, which can be regarded as modules, that are connected to the platform, each comprising two revolute joints and an (actuated) prismatic joint. The idea of the modular modeling approach is to derive a model for a *prototypical limb*, which is then inserted ('mounted') between ground and platform. The modeling method [7] involves the following steps:

1. Kinematics modeling of a prototypical limb
2. Dynamics modeling of a prototypical limb
3. Definition of the mount geometry at the ground
4. Definition of the mount geometry at the platform
5. Inverse velocity kinematics of individual limbs, and thus of the mechanism
6. Assembly of the overall model

In the following, these steps are discussed in some detail for the 3RPR, as far the space limit allows. The method makes use of the matrix formalism of the Lie group $SE(3)$. The reader not familiar with this is referred to the text books [3, 8, 10]. A condensed overview can also be found in the papers [5, 6].

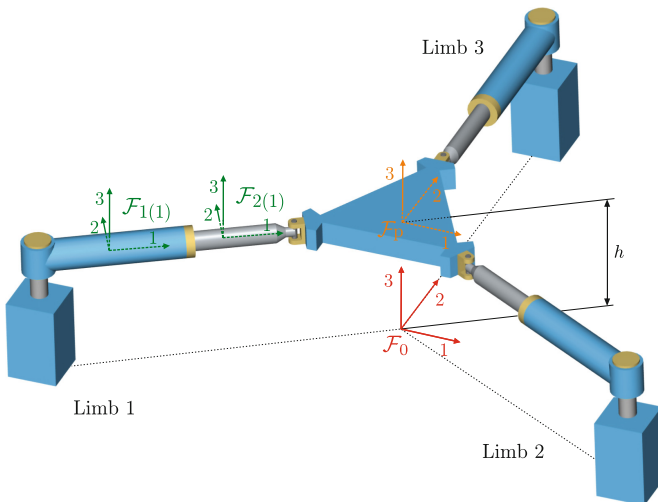


Fig. 1. Model of a planar 3RPR parallel manipulator.

2 Kinematics of the Limb Prototype

2.1 Configurations of the Bodies in the Limb Prototype

In the final PKM model an inertial frame (IFR) \mathcal{F}_0 is attached at the ground, and a frame \mathcal{F}_p is attached at the platform (usually representing the end-effector), Fig. 1. The prototypical limb, on the other hand, is modeled separately w.r.t. to a construction frame \mathcal{F}'_0 located (w.l.o.g.) at the axis of the first revolute joint (Fig. 2).

Denote with $\bar{\vartheta}' = (\vartheta'_1, \vartheta'_2)$ the joint variables of the prototypical limb when disconnected from the platform (ϑ'_1 -angle of revolute joint, ϑ'_2 -translation of prismatic joint), and with $\vartheta' = (\vartheta'_1, \vartheta'_2, \vartheta'_3)$ the vector of all joint variables (ϑ'_3 -angle of last revolute joint) when connected to the platform.

The joint screw coordinates w.r.t. construction frame \mathcal{F}'_0 in the reference configuration $\vartheta' = \mathbf{0}$ are ($a := L_1 + L_2 - \vartheta'_{20}$, ϑ'_{20} -initial displacement of prismatic joint)

$$\mathbf{Y}'_1 = (0, 0, 1, 0, 0, 0)^T, \mathbf{Y}'_2 = \frac{1}{2}(0, 0, 0, \sqrt{3}, 1, 0)^T, \mathbf{Y}'_3 = \frac{1}{2}(0, 0, 1, a, -\sqrt{3}a, 0)^T. \quad (1)$$

A reference frame \mathcal{F}'_i , $i = 1, 2$ is attached at each of the two bodies (see Fig. 1, omitted in Fig. 2). The configuration of body 1 and 2, i.e. the configuration of \mathcal{F}'_i w.r.t. \mathcal{F}'_0 , is determined by the product of exponentials as ($c_i := \cos \vartheta'_i$, $s_i := \sin \vartheta'_i$)

$$\begin{aligned} \mathbf{C}'_1(\bar{\vartheta}') &= \exp(\mathbf{Y}'_1 \vartheta'_1) \mathbf{A}'_1 = \begin{pmatrix} \frac{1}{2}(\sqrt{3}c_1 - s_1) & \frac{1}{2}(-c_1 - \sqrt{3}s_1) & 0 & \frac{1}{4}L_1(\sqrt{3}c_1 - s_1) \\ \frac{1}{2}(c_1 + s_1\sqrt{3}) & \frac{1}{2}(\sqrt{3}c_1 - s_1) & 0 & \frac{1}{4}L_1(c_1 + s_1\sqrt{3}) \\ 0 & 0 & 1 & z_{10} \\ 0 & 0 & 0 & 1 \end{pmatrix} \\ \mathbf{C}'_2(\bar{\vartheta}') &= \exp(\mathbf{Y}'_1 \vartheta'_1) \exp(\mathbf{Y}'_2 \vartheta'_2) \mathbf{A}'_2 \\ &= \begin{pmatrix} \frac{1}{2}(\sqrt{3}c_1 - s_1) & \frac{-1}{2}(c_1 + \sqrt{3}s_1) & 0 & \frac{1}{4}(2L_1 + L_2 + 2(\vartheta_2 - \vartheta_{20}))(\sqrt{3}c_1 - s_1) \\ \frac{1}{2}(c_1 + s_1\sqrt{3}) & \frac{1}{2}(\sqrt{3}c_1 - s_1) & 0 & \frac{1}{4}(2L_1 + L_2 + 2(\vartheta_2 - \vartheta_{20}))(c_1 + s_1\sqrt{3}) \\ 0 & 0 & 1 & z_{20} \\ 0 & 0 & 0 & 1 \end{pmatrix} \end{aligned} \quad (2)$$

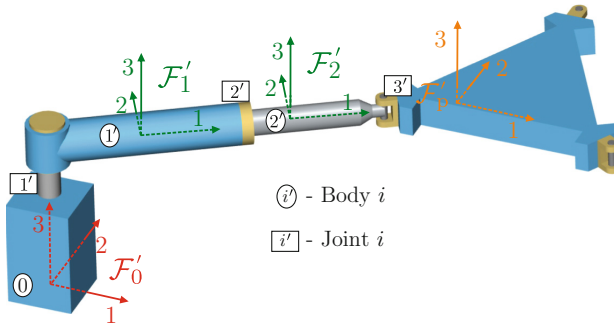


Fig. 2. Prototypical Limb with platform. Construction frame \mathcal{F}'_0 located at the axis of first joint.

with reference configurations $\mathbf{A}'_i = \mathbf{C}'_i(\mathbf{0}) \in SE(3)$ of the bodies (ref. Fig. 3)

$$\mathbf{A}'_1 = \begin{pmatrix} \frac{\sqrt{3}}{2} & -\frac{1}{2} & 0 & \frac{\sqrt{3}L_1}{4} \\ \frac{1}{2} & \frac{\sqrt{3}}{2} & 0 & \frac{L_1}{4} \\ 0 & 0 & 1 & z_{10} \\ 0 & 0 & 0 & 1 \end{pmatrix}, \quad \mathbf{A}'_2 = \begin{pmatrix} \frac{\sqrt{3}}{2} & -\frac{1}{2} & 0 & \frac{1}{2}\sqrt{3}(L_1 + \frac{L_2}{2} - \vartheta_{20}) \\ \frac{1}{2} & \frac{\sqrt{3}}{2} & 0 & \frac{1}{2}(L_1 + \frac{L_2}{2} - \vartheta_{20}) \\ 0 & 0 & 1 & z_{20} \\ 0 & 0 & 0 & 1 \end{pmatrix}. \quad (3)$$

The platform configuration is give by $\mathbf{C}'_p(\vartheta') = \exp(\mathbf{Y}'_1\vartheta_1)\exp(\mathbf{Y}'_2\vartheta_2)\exp(\mathbf{Y}'_3\vartheta_3)\mathbf{A}'_p$

$$\mathbf{C}'_p(\vartheta') = \begin{pmatrix} c_{1+3} & -s_{1+3} & 0 & \frac{1}{4}(2(a + \vartheta_2)(\sqrt{3}c_1 - s_1) - (L_2 - \rho)(\sqrt{3}c_{1+3} - s_{1+3})) \\ s_{1+3} & c_{1+3} & 0 & \frac{1}{4}(2(a + \vartheta_2)(c_1 + s_1\sqrt{3}) - (L_2 - \rho)(c_{1+3} + s_{1+3}\sqrt{3})) \\ 0 & 0 & 1 & z_{p0} \\ 0 & 0 & 0 & 1 \end{pmatrix} \quad (4)$$

($c_{1+3} := \cos(\vartheta'_1 + \vartheta'_3)$, $s_{1+3} := \sin(\vartheta'_1 + \vartheta'_3)$). It is assumed that $z_{10} = z_{20} = z_{p0} = h$.

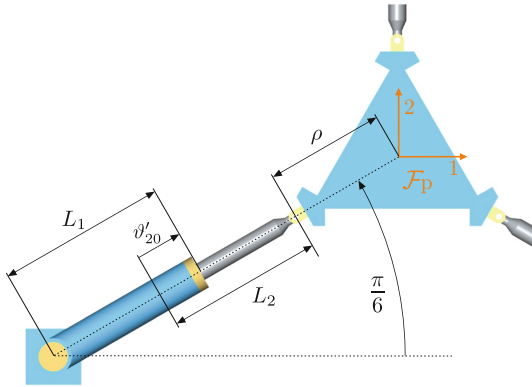


Fig. 3. Top view of 3RPR parallel manipulator.

2.2 Twists of the Bodies in the Limb Prototype

The body-fixed twist of body $i = 1, 2$ is determined as $\mathbf{V}^{b'i} = \mathbf{J}'_i \dot{\vartheta}'^i$ with

$$\mathbf{J}'_1 = \begin{pmatrix} 0 & 0 & 1 & 0 & 0 & 0 \\ 0 & 0 & 0 & 0 & \frac{L_1}{2} & 0 \end{pmatrix}^T, \quad \mathbf{J}'_2 = \begin{pmatrix} 0 & 0 & 1 & 0 & a + \vartheta_2 - \frac{1}{2}L_2 & 0 \\ 0 & 0 & 0 & \frac{1}{2}\sqrt{3} & \frac{1}{2} & 0 \end{pmatrix}^T \quad (5)$$

the body-fixed Jacobians, whose j th column is determined by $\mathbf{J}'_{i,j} := \mathbf{Ad}_{\mathbf{C}'_{i,j}} \mathbf{Ad}_{\mathbf{A}'_j}^{-1} \mathbf{Y}'_j$. Here \mathbf{Ad} is the screw transformation matrix [10] and $\mathbf{C}'_{i,j} = \mathbf{C}'_i^{-1} \mathbf{C}'_j$. The platform twist (twist of \mathcal{F}'_p) is given by $\mathbf{V}^{b'p} = \mathbf{J}'_p \dot{\vartheta}'^p$ with the platform Jacobian

$$\mathbf{J}'_{\mathbf{p}} = \begin{pmatrix} 0 & 0 & 1 & \frac{1}{4}(L_2 - \rho) - \frac{1}{2}(c_3 - \sqrt{3}s_3)(a + 2\vartheta) & \frac{1}{2}(a + \vartheta_2) & (s_3 + \sqrt{3}c_3) - \frac{1}{4}\sqrt{3}(L_2 - \rho) & 0 \\ 0 & 0 & 0 & \frac{1}{2}s_3 + \frac{1}{2}\sqrt{3}c_3 & & \frac{1}{2}c_3 - \frac{1}{2}\sqrt{3}s_3 & 0 \\ 0 & 0 & 1 & \frac{1}{2}a & & -\frac{1}{2}\sqrt{3}a & 0 \end{pmatrix}^T \quad (6)$$

with columns determined by $\mathbf{J}'_{\mathbf{p},j} := \mathbf{Ad}_{\mathbf{C}'_{\mathbf{p},j}} \mathbf{Ad}_{\mathbf{A}'_j}^{-1} \mathbf{Y}'_j$, where $\mathbf{C}'_{\mathbf{p},j} = \mathbf{C}'_{\mathbf{p}}^{-1} \mathbf{C}'_j$.

3 Kinematics of a General Limb

The individual limbs are modeled by inserting copies of the limb prototype. These copies are mounted at the ground and the platform at dedicated mount frames. In order to build limb $l = 1, 2, 3$ the mount frame $\mathcal{F}'_{\mathbf{p}}$ at the platform of the prototype is identified with the mount frame $\mathcal{F}_{\mathbf{p}(l)}$ at the platform of the PKM (Fig. 4), and the construction frame \mathcal{F}'_0 of the prototype is identified with the mount frame $\mathcal{F}_{0(l)}$ (Fig. 5). That is, a copy of the limb prototype is inserted between $\mathcal{F}_{0(l)}$ and $\mathcal{F}_{\mathbf{p}(l)}$.

The configuration of the mount frames $\mathcal{F}_{0(l)}$ relative to the IFR \mathcal{F}_0 of the PKM is denoted with $\mathbf{S}_{0(l)} \in SE(3)$, and that of $\mathcal{F}_{\mathbf{p}(l)}$ relative to $\mathcal{F}_{\mathbf{p}}$ with $\mathbf{S}_{\mathbf{p}(l)} \in SE(3)$. For demonstration purpose, the frames $\mathcal{F}_{\mathbf{p}(l)}$ are located at a distance of $\rho/2$ from the platform frame $\mathcal{F}_{\mathbf{p}}$ (Fig. 4). With the given geometry in Fig. 3, 4, and 5

$$\mathbf{S}_{\mathbf{p}(1)} = \begin{pmatrix} 1 & 0 & 0 & -\frac{\sqrt{3}}{4}\rho \\ 0 & 1 & 0 & -\frac{1}{4}\rho \\ 0 & 0 & 1 & 0 \\ 0 & 0 & 0 & 1 \end{pmatrix}, \quad \mathbf{S}_{\mathbf{p}(2)} = \begin{pmatrix} -\frac{1}{2} & -\frac{\sqrt{3}}{2} & 0 & \frac{\sqrt{3}}{4}\rho \\ \frac{\sqrt{3}}{2} & -\frac{1}{2} & 0 & -\frac{1}{4}\rho \\ 0 & 0 & 1 & 0 \\ 0 & 0 & 0 & 1 \end{pmatrix}, \quad \mathbf{S}_{\mathbf{p}(3)} = \begin{pmatrix} -\frac{1}{2} & \frac{\sqrt{3}}{2} & 0 & 0 \\ -\frac{\sqrt{3}}{2} & -\frac{1}{2} & 0 & \frac{1}{2}\rho \\ 0 & 0 & 1 & 0 \\ 0 & 0 & 0 & 1 \end{pmatrix}$$

$$\mathbf{S}_{0(1)} = \begin{pmatrix} 1 & 0 & 0 & -\frac{\sqrt{3}}{2}R \\ 0 & 1 & 0 & -\frac{1}{2}R \\ 0 & 0 & 1 & 0 \\ 0 & 0 & 0 & 1 \end{pmatrix}, \quad \mathbf{S}_{0(2)} = \begin{pmatrix} -\frac{1}{2} & -\frac{\sqrt{3}}{2} & 0 & \frac{\sqrt{3}}{2}R \\ \frac{\sqrt{3}}{2} & -\frac{1}{2} & 0 & -\frac{1}{2}R \\ 0 & 0 & 1 & 0 \\ 0 & 0 & 0 & 1 \end{pmatrix}, \quad \mathbf{S}_{0(3)} = \begin{pmatrix} -\frac{1}{2} & \frac{\sqrt{3}}{2} & 0 & 0 \\ -\frac{\sqrt{3}}{2} & -\frac{1}{2} & 0 & R \\ 0 & 0 & 1 & 0 \\ 0 & 0 & 0 & 1 \end{pmatrix}.$$

The body-fixed frame of body $i = 1, 2$ of limb $l = 1, 2, 3$ is denoted with $\mathcal{F}_{i(l)}$ (Fig. 1). The configuration of body i in limb l is obtained by a frame transformation from the mount frame $\mathcal{F}_{0(l)}$ to the actual IFR \mathcal{F}_0 : $\mathbf{C}_{i(l)}(\bar{\boldsymbol{\vartheta}}(l)) = \mathbf{S}_{0(l)} \mathbf{C}'_{i(l)}(\bar{\boldsymbol{\vartheta}}(l))$. The platform configuration is obtained by further transforming from the mount frame $\mathcal{F}_{\mathbf{p}(l)}$ at the platform to the platform frame: $\mathbf{C}_{\mathbf{p}}(\boldsymbol{\vartheta}(l)) = \mathbf{S}_{0(l)} \mathbf{C}'_{\mathbf{p}}(\boldsymbol{\vartheta}(l)) \mathbf{S}_{\mathbf{p}(l)}^{-1}$. The Jacobian of the platform when connected to limb l is accordingly $\mathbf{J}_{\mathbf{p}(l)}(\boldsymbol{\vartheta}(l)) = \mathbf{Ad}_{\mathbf{S}_{\mathbf{p}(l)}} \mathbf{J}'_{\mathbf{p}}(\boldsymbol{\vartheta}(l))$. Therein, $\bar{\boldsymbol{\vartheta}}(l)$ and $\boldsymbol{\vartheta}(l)$ are the respective vectors of joint variables of limb l .

The end-effector of the planar 3-DOF 3RPR PKM performs planar motions. The task space velocities, summarized in $\mathbf{V}_{\mathbf{t}} = (\omega_3, v_1, v_2)^T \in \mathbb{R}^3$, are the corresponding three components of the platform twist $\mathbf{V}_{\mathbf{p}}$. This is formalized as $\mathbf{V}_{\mathbf{t}} = \mathbf{P}_{\mathbf{p}} \mathbf{V}_{\mathbf{p}}$ with

$$\mathbf{P}_{\mathbf{p}} = \begin{pmatrix} 0 & 0 & 1 & 0 & 0 & 0 \\ 0 & 0 & 0 & 1 & 0 & 0 \\ 0 & 0 & 0 & 0 & 1 & 0 \end{pmatrix}. \quad (7)$$

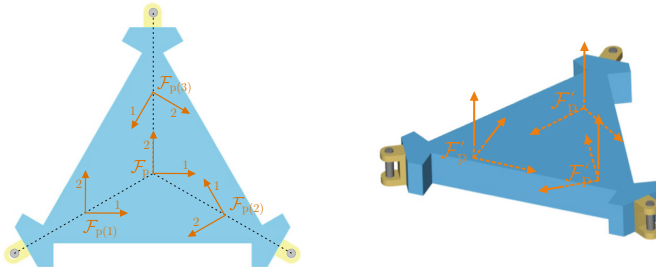


Fig. 4. Mount frames $\mathcal{F}_{p(l)}$ at the platform.

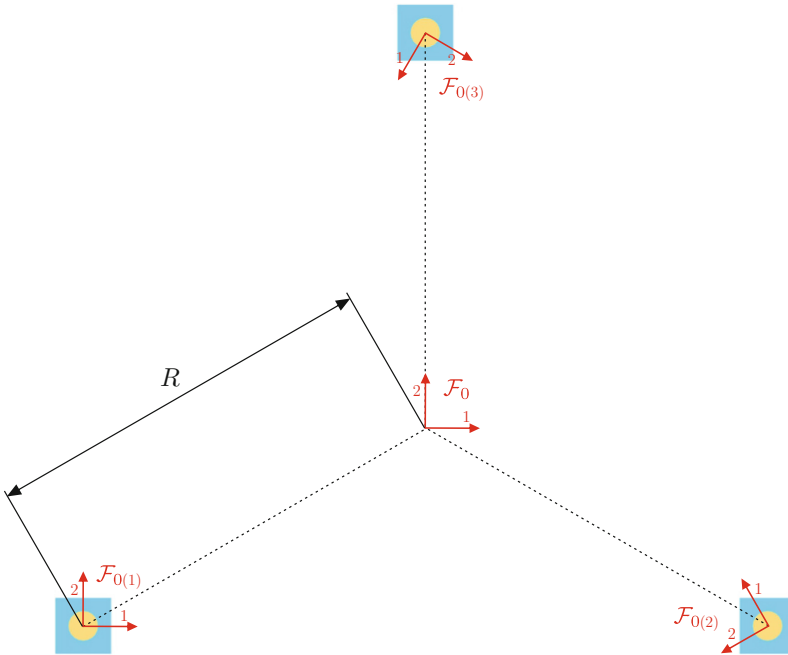


Fig. 5. Mount frames $\mathcal{F}_{0(l)}$ at the ground.

The *task space Jacobian of limb l* is the corresponding 3×3 submatrix $\mathbf{J}_{t(l)}$ of \mathbf{J}_p . In any admissible configuration, $\mathbf{V}_t = \mathbf{J}_{t(l)} \dot{\boldsymbol{\vartheta}}_{(l)}$ holds for all limbs $l = 1, 2, 3$.

4 Inverse Kinematics of the Mechanism

The *inverse kinematics of limb l* , which determines the velocities of all joints in terms of the task space velocity, is solved with $\dot{\boldsymbol{\vartheta}}_{(l)} = \mathbf{J}_{t(l)}^{-1} \mathbf{V}_t$. Summarizing these relations for all limbs yields the inverse kinematics solution for the mechanism,

i.e. the velocities of all joints in terms of the platform velocity, as

$$\dot{\boldsymbol{\vartheta}} = \mathbf{F}\mathbf{V}_t, \quad \text{with} \quad \mathbf{F} = \begin{pmatrix} \mathbf{J}_{t(1)}^{-1} \\ \mathbf{J}_{t(2)}^{-1} \\ \mathbf{J}_{t(3)}^{-1} \end{pmatrix}. \quad (8)$$

Removing the velocities $\dot{\boldsymbol{\vartheta}}_{3(l)}$ of the three joints connecting the limbs $l = 1, 2, 3$ to the platform yields the joint velocities of limb l when disconnected from the platform as $\dot{\boldsymbol{\vartheta}}_{(l)} = \bar{\mathbf{F}}_{(l)}\mathbf{V}_t$, with $\bar{\mathbf{F}}_{(l)} = \bar{\mathbf{P}}_{(l)}\mathbf{J}_{t(l)}^{-1}$ where $\bar{\mathbf{P}}_{(l)} = (\mathbf{I}_{2,3}, \mathbf{0}_{2,1})$ simply removes the $\dot{\boldsymbol{\vartheta}}_{3(l)}$ so that $\dot{\boldsymbol{\vartheta}}_{(l)} = \bar{\mathbf{P}}_{(l)}\dot{\boldsymbol{\vartheta}}_{(l)}$. These relations are also summarized as

$$\dot{\boldsymbol{\vartheta}}_{(l)} = \bar{\mathbf{F}}\mathbf{V}_t, \quad \text{with} \quad \bar{\mathbf{F}} = \begin{pmatrix} \bar{\mathbf{F}}_{(1)} \\ \bar{\mathbf{F}}_{(2)} \\ \bar{\mathbf{F}}_{(3)} \end{pmatrix}. \quad (9)$$

5 Motion Equations

The inverse kinematics solution (9) allows constructing the EOM of the PKM from the EOM of the individual limbs. The EOM of limb l attain the form

$$\bar{\mathbf{M}}_{(l)}\ddot{\boldsymbol{\vartheta}}_{(l)} + \bar{\mathbf{C}}_{(l)}\dot{\boldsymbol{\vartheta}}_{(l)} = \bar{\mathbf{Q}}_{(l)} + \bar{\mathbf{Q}}_{(l)}^{\text{act}}. \quad (10)$$

The EOM (10) are given in closed form in terms of the joint screws and the geometric Jacobian [3, 5, 7]. Gravity forces have been omitted since the planar 3RPR PKM is assumed to move only horizontally. The EOM of the limbs are thus independent from the choice of IFR (left-invariant w.r.t. $SE(3)$ -actions). They can hence be constructed for the limb prototype and reused for all limbs. The EOM of the platform (single rigid body) can be written as

$$\mathbf{M}_p\dot{\mathbf{V}}_p - \mathbf{ad}_{\mathbf{V}_p}^T \mathbf{M}_p \mathbf{V}_p = \mathbf{W}_p. \quad (11)$$

These are the Newton-Euler equations in the general form using arbitrary reference frame [1, 5], where \mathbf{M}_p is the constant inertia matrix, \mathbf{ad} is the screw product matrix (also called the spatial cross product matrix), and \mathbf{W}_p is the applied wrench. With the kinematic relation (9), Jourdain's principle yields

$$\begin{pmatrix} \mathbf{P}_p \\ \mathbf{F} \end{pmatrix}^T \begin{pmatrix} \mathbf{M}_p \dot{\mathbf{V}}_p - \mathbf{ad}_{\mathbf{V}_p}^T \mathbf{M}_p \mathbf{V}_p \\ \bar{\mathbf{M}}_{(1)}\ddot{\boldsymbol{\vartheta}}_{(1)} + \bar{\mathbf{C}}_{(1)}\dot{\boldsymbol{\vartheta}}_{(1)} \\ \bar{\mathbf{M}}_{(2)}\ddot{\boldsymbol{\vartheta}}_{(2)} + \bar{\mathbf{C}}_{(2)}\dot{\boldsymbol{\vartheta}}_{(2)} \\ \bar{\mathbf{M}}_{(3)}\ddot{\boldsymbol{\vartheta}}_{(3)} + \bar{\mathbf{C}}_{(3)}\dot{\boldsymbol{\vartheta}}_{(3)} \end{pmatrix} = \begin{pmatrix} \mathbf{P}_p \\ \mathbf{F} \end{pmatrix}^T \begin{pmatrix} \mathbf{W}_p + \mathbf{W}_p^{\text{grav}} \\ \bar{\mathbf{Q}}_{(1)} + \bar{\mathbf{Q}}_{(1)}^{\text{act}} \\ \bar{\mathbf{Q}}_{(2)} + \bar{\mathbf{Q}}_{(2)}^{\text{act}} \\ \bar{\mathbf{Q}}_{(3)} + \bar{\mathbf{Q}}_{(3)}^{\text{act}} \end{pmatrix}. \quad (12)$$

Inserting the relation (9) and its time derivative yields the *task space formulation* of the EOM of the 3RPR PKM in the form

$$\mathbf{M}_t \dot{\mathbf{V}}_t + \mathbf{C}_t \mathbf{V}_t = \mathbf{W}_t + \mathbf{W}_t^{\text{act}}. \quad (13)$$

The explicit expressions for $\mathbf{M}_t(\bar{\boldsymbol{\vartheta}})$, $\mathbf{C}_t(\bar{\boldsymbol{\vartheta}}, \dot{\bar{\boldsymbol{\vartheta}}})$, and \mathbf{W}_t can be found in [7].

6 Conclusion and Further Aspects

The modeling method introduced in [7] has been applied to a simple 3-DOF PKM. It was demonstrated how the kinematics and dynamics of the three limbs can be modeled by reusing the models of a prototype limb, and how these give rise to the overall EOM for the PKM. It should be clear how the proposed method can be applied to more complex PKM. It is worth to consider the computational effort. For the presented 3-DOF example it is computationally most efficient to use the obtained EOM in closed form. From a general perspective, however, it should be emphasized that the modularity translates directly into parallelizability. This applies to the kinematics as well as to the EOM. All computation for the kinematics of the individual limbs and the inverse kinematics solutions $\dot{\mathbf{v}}_{(l)} = \bar{\mathbf{F}}_{(l)} \mathbf{V}_t$ in (9) can be performed independently in parallel. The same is true for the EOM (10). In a final step these are assembled to the overall EOM. Another aspect of the modular approach is that any formulation of the EOM (10) of the limbs can be used in (12). The geometric Lie group formulation [3, 5, 7] is an approach that is easy to use and to implement. But if the models of the limbs as submodules are already available, these can be used alternatively.

Acknowledgements. This work has been supported by the LCM K2 Center for Symbiotic Mechatronics within the framework of the Austrian COMET-K2 program.

References

1. Angeles, J.: Fundamentals of Robotic Mechanical Systems, 3rd edn. Springer, Cham (2007)
2. Briot, S., Khalil, W.: Dynamics of Parallel Robots. Springer, Cham (2015)
3. Lynch, K.M., Park, F.C.: Modern Robotics. Cambridge (2017)
4. Merlet, J.: Parallel Robots. Springer, Dordrecht (2006)
5. Müller, A.: Screw and lie group theory in multibody dynamics -recursive algorithms and equations of motion of tree-topology systems. *Multibody Syst. Dyn.* **42**(2), 219–248 (2018)
6. Müller, A.: Screw and lie group theory in multibody dynamics -motion representation and recursive kinematics of tree-topology systems. *Multibody Syst. Dyn.* **43**(1), 1–34 (2018)
7. Müller, A.: Dynamics modeling of topologically simple parallel manipulators: a geometric approach. *Appl. Mech. Rev.* **72**, 26 (2020)
8. Murray, R., Li, Z., Sastry, S.: A Mathematical Introduction to Robotic Manipulation. CRC Press (1994)
9. Sartori Natal, G., Chemori, A., Pierrot, F.: Dual-space control of extremely fast parallel manipulators: payload changes and the 100 g experiment. *IEEE Trans. Control Syst. Technol.* **23**(4), 1520–1535 (2015)
10. Selig, J.: Geometric Fundamentals of Robotics. Springer, New York (2005)



Chaos Illustrations in Dynamics of Mechanisms

Stelian Alaci¹ (✉), Catalin Alexandru², Florina-Carmen Ciornei¹, Ioan Doroftei³,
and Luminita Irimescu¹

¹ Stefan cel Mare, University of Suceava, Suceava, Romania
stelian.alaci@usm.ro, {florina,lumi}@fim.usv.ro

² Transilvania University, Brasov, Romania
calex@unitbv.ro

³ Gheorghe Asachi Technical University of Iasi, Iasi, Romania
idorofte@tuiasi.ro

Abstract. The paper illustrates the occurrence of chaos phenomenon when dynamic modelling of a mechanical system is performed. The equations of motion of a 2DOF physical planar pendulum are obtained and subsequently they are numerically integrated. The same system is also modelled using dedicated software. The numerical results and the ones given by the software coincide only for a short duration after launching. The paper highlights the strong dependence of the evolution of the system upon the initial conditions, confirming the existence of the chaos phenomenon. It is also revealed the connection between the accuracy of the initial conditions and the dimension of the corresponding interval.

Keywords: 2DOF physical planar pendulum · System dynamics · Chaos

1 Introduction

Differential equations are an essential instrument when describing the behaviour of a technical system. In order to integrate these equations, the initial values of the parameters and their derivatives should be stipulated. Both the theory of nonlinear differential equations [1] and the engineering applications [2–5] confront the situation when a small variation of initial values leads to a significant variation of the solution, aspect that is known as the *chaos phenomenon* [6].

One of the simplest dynamical models where the chaos phenomenon displays is the double planar mathematical pendulum [7] which is an idealized planar physical pendulum consisting in two jointed rigid bodies, one of which is also jointed to the ground.

This 2DOF physical pendulum is also the simplest kinematical chain from the structure of a mechanism or a robot.

2 The Equations of Motion

The 2DOF planar physical pendulum, presented in Fig. 1, consists of two jointed rods, 1 and 2, where the first rod, 1 is hinged to the ground. The angles θ_1 and θ_2 formed by the

rods with the vertical direction are used for defining the position of the pendulum. The inertial characteristics of the two rods are: the mass, $M_{1,2}$, the distance between the joint axis and the centre of mass (CM), $\xi_{1,2}$, and the principal central moment of inertia, $J_{G_{1,2}}$. Assuming ideal joints, the single applied forces acting upon the system are the weights of the rods, $M_{1,2}\mathbf{g}$. Due to the fact that the friction forces from joints were neglected, the problem can be solved via the Lagrange's equations:

$$\frac{d}{dt} \frac{\partial E}{\partial \dot{q}_k} - \frac{\partial E}{\partial q_k} = \sum \mathbf{F}_k \frac{\partial \mathbf{r}_k}{\partial q_k} \tag{1}$$

where q_k are generalized coordinates of the system used here, θ_1 and θ_2 , E is the kinetic energy of the system and \mathbf{F}_k are the external forces. The kinetic energy of the system is:

$$E = \sum \left(J_{G_k} \dot{\theta}_k^2 / 2 + M_k \mathbf{v}_{G_k}^2 / 2 \right) \tag{2}$$

After the calculus, the next system of differential equations is obtained:

$$\begin{cases} (J_{O_1} + M_2 L_1^2) \ddot{\theta}_1 + \cos(\theta_2 - \theta_1) L_1 M_2 \xi_2 \ddot{\theta}_2 - \sin(\theta_2 - \theta_1) M_2 L_1 \xi_2 \dot{\theta}_2^2 + \\ (M_1 \xi_1 + M_2 L_2) g \sin \theta_1 = 0 \\ M_2 L_1 \xi_2 \cos(\theta_2 - \theta_1) \ddot{\theta}_1 + J_{O_2} \ddot{\theta}_2 + \sin(\theta_2 - \theta_1) M_2 L_1 \xi_2 \dot{\theta}_1^2 + M_2 \xi_2 g \sin \theta_2 = 0 \end{cases} \tag{3}$$

For the particular case $\xi_{1,2} = L_{1,2}$ and $J_{G_{1,2}} = 0$, the system of Eqs. (3) becomes the known system of the 2DOF planar mathematical pendulum, given in [7]. The system can be solved using a numerical method and the one chosen for this case is the Runge–Kutta IV method [8]. This method requires that the system is solvable with respect to the highest order derivatives of the unknowns. The system (3) is linear with respect to $\ddot{\theta}_1$ and $\ddot{\theta}_2$ and thus it satisfies the above condition. The motion was also analysed via dedicated software, as presented in Fig. 2. Denoting by:

$$\Delta = \begin{vmatrix} J_{O_1} + M_2 L_1^2 & M_2 L_1 \xi_2 \cos(\theta_2 - \theta_1) \\ M_2 L_1 \xi_2 \cos(\theta_2 - \theta_1) & J_{O_2} \end{vmatrix} \tag{4}$$

The solution of the system of Eqs. (3) is:

$$\begin{cases} \ddot{\theta}_1 = - \frac{\begin{vmatrix} M_2 L_1 \xi_2 \sin(\theta_2 - \theta_2) \dot{\theta}_2^2 - (M_1 \xi_1 + M_2 L_1) g \sin \theta_1 & M_2 L_1 \xi_2 \cos(\theta_2 - \theta_1) \\ M_2 L_2 \xi_2 \sin(\theta_2 - \theta_1) \dot{\theta}_2^2 + M_2 \xi_2 g \sin \theta_2 & J_{O_2} \end{vmatrix}}{\Delta} \\ \ddot{\theta}_2 = - \frac{\begin{vmatrix} J_{O_1} + M_2 L_1^2 & M_2 L_1 \xi_2 \sin(\theta_2 - \theta_2) \dot{\theta}_2^2 - (M_1 \xi_1 + M_2 L_1) g \sin \theta \\ M_2 L_1 \xi_2 \cos(\theta_2 - \theta_1) & M_2 L_2 \xi_2 \sin(\theta_2 - \theta_1) \dot{\theta}_2^2 + M_2 \xi_2 g \sin \theta_2 \end{vmatrix}}{\Delta} \end{cases} \tag{5}$$

The equations of motion were integrated using MATHCAD software and for different values of the initial parameters the behaviour of the system proved to be completely changed. The trajectories of the ends and of the centre of mass of the rod 2 are presented in Fig. 3 for two sets of the launching angles (small angles and larger angles). For small launching angles, the curves show a smooth, quasi-periodic motion but for larger angles the motion is tumultuous, agitated, unpredictable and then, chaotic etc (Fig. 4).

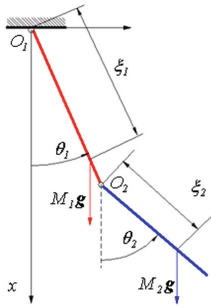


Fig. 1. The 2DOF planar pendulum

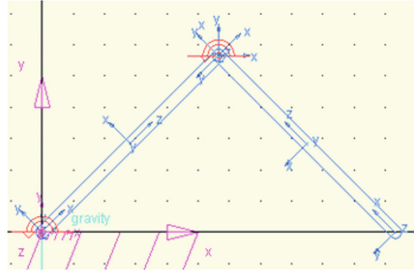


Fig. 2. Modelled double pendulum for $\theta_1 = 3\pi/4$, $\theta_2 = \pi/4$, $\omega_1 = \omega_2 = 0$

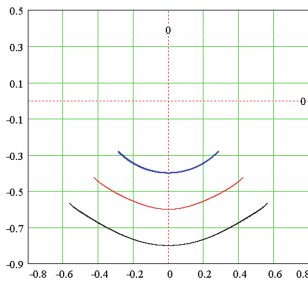


Fig. 3. Trajectories for $\theta_1 = \pi/4$, $\theta_2 = \pi/4$, $\omega_1 = \dot{\theta}_1 = 0$, $\omega_2 = \dot{\theta}_2 = 0$

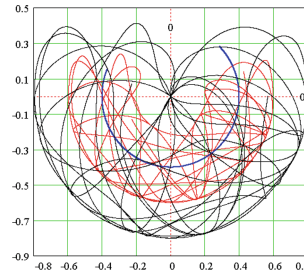


Fig. 4. Trajectories for $\theta_1 = 3\pi/4$, $\theta_2 = \pi/4$, $\omega_1 = \dot{\theta}_1 = 0$; $\omega_2 = \dot{\theta}_2 = 0$

3 The Comparison Between the Software Simulation and Numerical Solutions

In order to corroborate the solution obtained by numerical integration and the one given by the software MATHCAD, a double pendulum consisting of two identical rods, $L_1 = L_2 = 0.4\text{ m}$, was considered, as shown in Fig. 1. The dynamics of the pendulum was simulated by numerical integration of the system of Eqs. (3) and by applying the multibody dynamics method via the dedicated software MSC.ADAMS, for the following initial conditions:

$$\theta_1 = 3\pi/4, \theta_2 = \pi/4, \omega_1 = \dot{\theta}_1 = 0, \omega_2 = \dot{\theta}_2 = 0 \tag{6}$$

Figure 5 and Fig. 6 present the variation of angular velocity of the two rods, obtained by numerical integration (Fig. 5a, Fig. 6a) and by numerical software modelling (Fig. 5b, Fig. 6b). It can be noticed that the results are identical only for time duration of a few seconds (the region marked with yellow) after the launching.

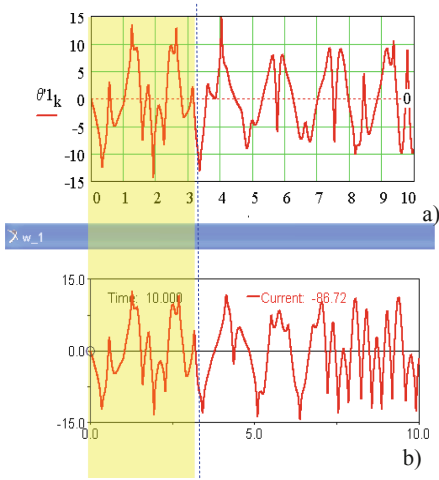


Fig. 5. The angular velocity for the rod 1

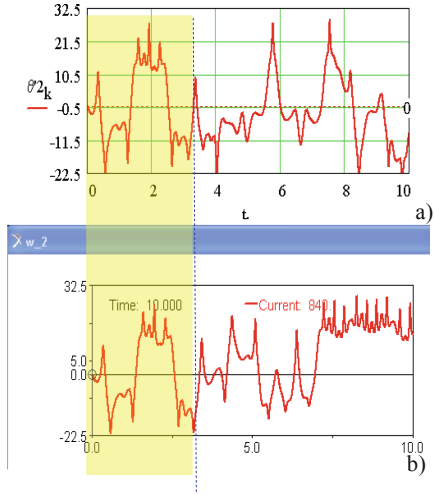


Fig. 6. The angular velocity for the rod 2

4 The Chaos Effect in Software Dynamical Modelling

Firstly, two identical mechanisms with the same initially conditions have been considered, aiming to test the software. It was established that, regardless of the duration of the period of analysis, all the parameters of the two pendulums presented identical variation.

Next, two identical mechanisms have been considered, placed symmetrically with respect to a vertical plane, as shown in Fig. 7. The chosen parameter for testing was the ordinate of the centre of mass of the rod 2, for each mechanism. The necessary condition for the identical motions is that the two ordinates should be equal. For the initial configurations, shown in Fig. 7, with the pendulums initially at rest, it was observed that for a short period the motions are the same and afterwards they become to differ.

In Fig. 8 there are plotted the time variations of the ordinates of the CM of the rods 2 obtained using the software. It can be observed that the two graphs are identical only for a limited time period after the start of the motion and then, the plots diverge. In Fig. 9 is presented a more suggestive plot, the dependency of one ordinate (right pendulum) with respect to the ordinate of the other (left pendulum). In the case when the two ordinates coincide, the plot overlaps to the bisector of the first quadrant angle (dashed line). When the two motions begin to be dissimilar, the plot has an irregular shape, with no developing rule and suggesting the idea of chaos. A first incipient conclusion is that the simulation obtained using the software is valid only for a short period of time, just after launching, referred as *corresponding interval*.

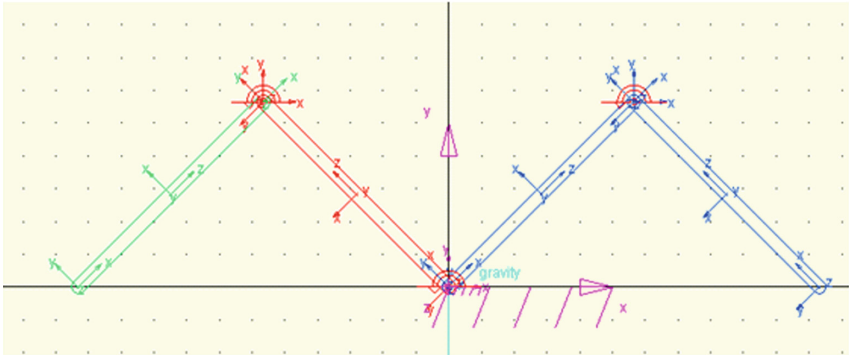


Fig. 7. Mirrored planar pendulums

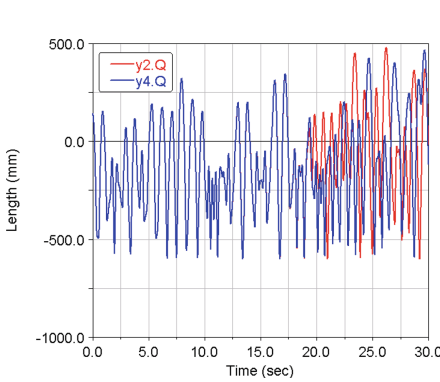


Fig. 8. Ordinates of CM of rods 2 vs time

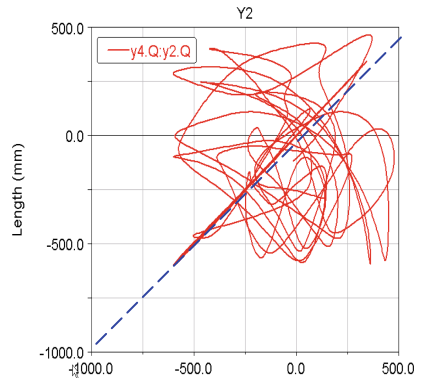


Fig. 9. Ordinate of CM2-left versus ordinate of CM2-right

5 The Estimation of the Effects of Inaccuracy of Initial Conditions in Numerical Integrating Modelling

Next it was assumed that one of the parameters characterizing the initial conditions θ_1 is slightly modified. More exactly, it was considered that θ_1 is 0.99999 of the exact value. This hypothesis is plausible since the error for a complete circle is:

$$\Delta\theta_1 = (360/10^5) \text{ deg} \approx 13'' \tag{7}$$

That is, a value significantly smaller than the precision of ordinary instruments, showing that the variation of the θ_1 parameter falls into the measuring accuracy. Figure 10 presents the comparison between the solutions obtained with the exact initial value (red) and the ones with imprecise initial values (blue). In Fig. 10a, the initial modified value is $\theta_{1\text{approx}} = 0.99999\theta_1$ and in Fig. 10b, $\theta_{1\text{approx}} = 0.999999\theta_1$ (that is, the error is one order of magnitude smaller). As expected, at the beginning of the motion, the “approximate” solution coincides to the “exact” solution. To be remarked that the

corresponding interval for the numerical integration is smaller than the interval for the multibody method solution. Another mention emerging from Fig. 10 is that the effect of increased precision of initial parameter stipulation (with one order of magnitude) is not reflected proportionally to the dimension of the corresponding interval. Specifically, though the accuracy of the initial parameter increased 10 times, the length of the corresponding interval grew with only a few percentages. From here it results the idea that increasing the measuring accuracy over a certain value is an unproductive action. To illustrate this concept, a set of altered values for the initial parameter are considered, given by:

$$\theta_{1approx} = (1 - 10^{-q})\theta_{exact} \tag{8}$$

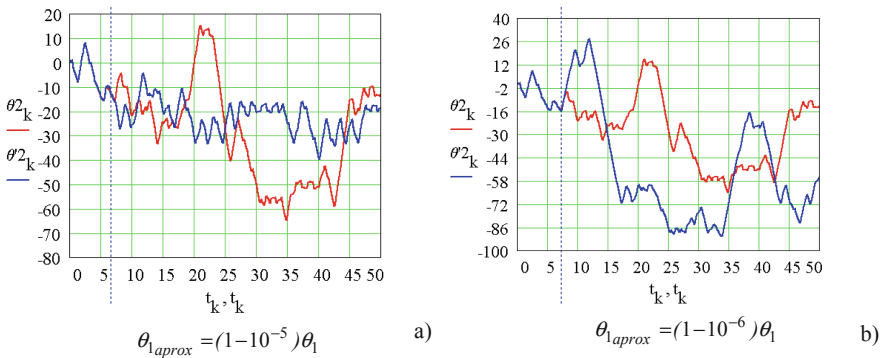


Fig. 10. Comparison between approximate and exact solutions for two different values of modified initial parameter

For a set of values of the accuracy for the initial conditions there were found the values of the corresponding interval, considering a certain parameter (θ_2) as objective. There were found the times for which the next condition is fulfilled:

$$|\theta'2 - \theta_2| \leq 0.01 \tag{9}$$

The notation B_s is used in Fig. 11 for the order number of the subinterval up to which the condition (9) is satisfied; obviously, the corresponding interval is proportional to B_s . The values of B_s have been found for the range $q = 1 \div 14$ and in Fig. 12 it is presented the dependency of the corresponding interval on the accuracy of the initial data, using semilogarithmic plot.

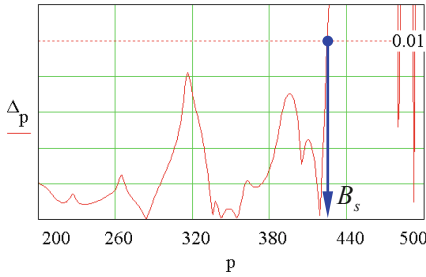


Fig. 11. The solution of Eq. (9)

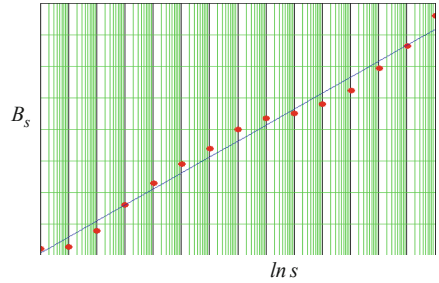


Fig. 12. The semilogarithmic plot of the correspondence interval versus the accuracy of initial parameter

From Fig. 12 it is suggested a quasi-linear variation in semilogarithmic plot and the possibility of approximating the points from the graph with a straight line. To be recalled that the graph from Fig. 12 was traced for a dynamical system with well specified structure, properties and initial conditions. From the plot, a first important conclusion emerges: *while the corresponding time presents a linear variation, the accuracy for the stipulation of initial parameters increases exponentially.* A second conclusion developing from the plot in Fig. 12 consists in the fact that *with known accuracy of the initial experimental data measurements, the dimension of the corresponding interval can be found. Reciprocate, when the dimension of the corresponding interval is known the required accuracy for evaluating the initial data can be found, fact that represents valuable information both technically and economically.*

6 Conclusions

The paper aims to draw attention to the results that can be provided by the numerical modelling methods used in system dynamics. The main concern of the work is to identify a dynamic system for which an analytical model exists. Regardless of the methods of modelling the dynamics of the system, it is expected that in the end, the same results are obtained. However, there are situations when the initial configuration of the system has such a strong influence on the description of the dynamic evolution of the system that, with any precision the initial kinematical state of the system is given, the results of the various applied methods begin to differ after a short interval from the beginning of the movement.

The motion of the 2DOF planar physical pendulum is analyzed, using two manners: a) the system of differential equations of motion is obtained by applying the Lagrange's equations of second kind and these are integrated via the Runge-Kutta IV algorithm; b) employing a specialised software for dynamical simulation and analysis. When the pendulum is launched from rest, for large angles as initial conditions, the results of numerical integration evidence the unpredictable character of the motion and the possibility of chaos occurrence. The results obtained by the two methods coincide only for short time duration, just after launching. Additionally, for two identical mirrored pendulums, the results of the computer simulation differ after a short time after launching.

It was accepted that the initial conditions are stipulated with a controlled accuracy and it was remarked that after a short time post-launching, the behaviours are completely dissimilar attesting the presence of chaos phenomenon. For a certain initial parameter, a set of errors are imposed in geometrical progression and the corresponding interval between exact and approximate signals increases exponentially.

References

1. Verhulst, F.: *Nonlinear Differential Equation and Dynamical Systems*, p. 306. Springer, Berlin (1996)
2. Lovasz, E.C., et al.: Path generating belt mechanisms as kinematic chains for mechatronic applications. In: Flores, P., Viadero, F. (eds.) *New Trends in Mechanism and Machine Science. Mechanisms and Machine Science*, vol. 24, pp. 111-119. Springer, Cham (2015)
3. Alaci, S., Ciornei, F.-C., Siretean, S.-T., Ciornei, M.-C., Țibu, G.-A.: Dynamical analysis of a 2-degrees of freedom spatial pendulum. In: *MATEC Web Conferences*, vol. 184, p. 01003 (2018). <https://doi.org/10.1051/mateconf/201818401003>
4. Bălută, G., Graur, A., Pentiuc, R., Diaconescu, C., Popa, C.: FEM analysis of brushless DC servomotor with fractional number per pole of slots. *Adv. Electr. Comput. Eng.* **14**(1), 103–108 (2014). <https://doi.org/10.4316/aecce.2010.03004>
5. Korka, Z.-I., Micloșină, C.-O., Cojocaru V.: Some aspects regarding the mathematical modeling and dynamic simulation of a single stage helical gearbox. In: *Applied Mechanics and Materials*. vol. 658, pp. 89–94 (2014). *Advanced Concepts in Mechanical Engineering I*
6. Ott, E.: *Chaos in Dynamical Systems*. Cambridge University Press, Cambridge (2002)
7. Gonzales, G.: *Single and Double Plane Pendulum*. <http://www.phys.lsu.edu/faculty/gonzalez/Teaching/Phys7221/DoublePendulum.pdf>
8. Hamming, R.: *Numerical Methods for Scientists and Engineers*. Dover Publications, New York (1962)



Cartesian Elastodynamics Model of a Full-Mobility PKM with Flexible Links

Qi Sun¹(✉), Jorge Angeles¹, and James Richard Forbes²

¹ Department of Mechanical Engineering and Centre for Intelligent Machines,
McGill University, Montreal, Canada

{sunqi, angeles}@cim.mcgill.ca

² Department of Mechanical Engineering, McGill University, Montreal, Canada
jforbes@cim.mcgill.ca

Abstract. The subject of this paper is the elastodynamics of a novel three-limb, full-mobility parallel-kinematics machine (PKM) with flexible links, intended for high-frequency, small-amplitude operations. By modeling the light-weight limb-rods as identical linearly elastic beams, the flexibility of the in-house developed SDelta robot is taken into account. The PKM is modeled as a six-dof *Cartesian* mass-spring undamped system. The Cartesian stiffness and mass matrices are derived based on the virtual-joint model. The elastodynamics performance of the SDelta prototype at the desktop scale is numerically evaluated. The calculation results shows that the prototype has the ability to operate at a frequency below 30 Hz with a 5-kg payload.

Keywords: Parallel-Kinematic Machine (PKM) · Flexible · Elastodynamics · Virtual joint

1 Introduction

The object of study in this paper is a class of three-limb, six-dof symmetric parallel-kinematic machines (PKMs), dubbed SDelta [1]. This class is a simpler alternative to the well-known Stewart-Gough platform [2–4], as it contains fewer components, while keeping its motors on the base. The SDelta architecture simplifies the modeling, analysis and control of the PKM and reduces the inertial load on the system, making it a good candidate for high-frequency, small-amplitude (HFSA) applications. The SDelta robot consists of one moving platform (MP) and one base platform (BP), connected via three limbs. Each limb is a CPS¹ serial chain, as shown in Fig. 1. As well, each actuated C joint is driven by a two-dof actuator, the C-drive [5], capable of driving the T-shaped element in Fig. 1, henceforth referred to as the *tube*, with a cylindrical motion: rotation

¹ C, P and S stand for cylindrical, prismatic and spherical joints, respectively, the actuated joint being underlined.

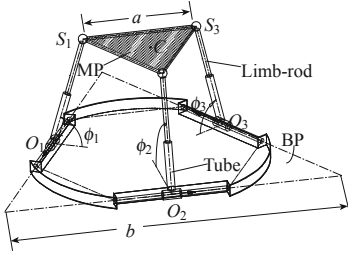


Fig. 1. Architecture of the SDelta robot

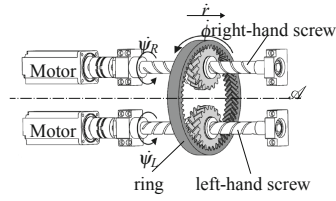


Fig. 2. A schematic of the planetary-gear C-drive

by angle ϕ around an axis, \mathcal{A} , and translation r in a direction parallel to the same axis. The C-drive works based on the synchronized rotation of two nuts, run by two parallel screws, one right-, one left-hand, with the same pitch, as depicted in Fig. 2. Synchronization is achieved by means of the planetary gear train, which transmits the rotation and translation of the planet gears to the ring. The output angular velocity can be adjusted based on the pitch radii of the planets and the ring gear.

Generally, for dynamics analyses, parallel robots are modeled as multi-rigid-body systems. However, for HFSA applications, where high accelerations occur, the inherent flexibility of the light-weight limbs should be taken into account in the design and control of the robot. Thus, the SDelta robot is modeled as a multi-body system with rigid and flexible links [6]. In this vein, the elastodynamics, which studies the dynamic response of flexible multi-body systems to external and inertial loads, should be taken into consideration in the design and control. In elastodynamics, the natural frequencies of the PKM, calculated from the elastodynamics model, determine a poor region of operation frequencies, where unwanted resonant vibrations are likely to occur. For HFSA applications, the lowest natural frequency of parallel robots should be placed above the expected spectrum of operation frequencies.

This paper focuses on the elastodynamics of the SDelta robot. In Sect. 2, assumptions and simplifications are made. The virtual-joint model of the PKM is established. In Sect. 3, the robot is modeled as a *Cartesian* mass-spring undamped system. The Cartesian stiffness matrix and its counterpart mass matrix are calculated. In Sect. 4, the numerical natural frequencies of the SDelta prototype are calculated to determine its elastodynamic performance.

2 Virtual-Joint Model of the PKM

The hypothesis underlying the elastodynamics model of the SDelta, illustrated in Fig. 1, is summarized as: all friction forces are neglected; all links are modeled as rigid bodies, except for the limb-rods. The latter, connecting the C-drive tubes to the MP, are light and slender, thereby being significantly more flexible than the other links. The PKM is modeled as a multi-body system with rigid and flexible links.

In the elastodynamics analysis, all the motors are assumed to be locked. When an external wrench is applied on the MP, each limb-rod is subjected to a force, perpendicular to its axis at its upper end, as transmitted from the S joint. Moreover, friction between piston and tube is neglected, the rod thus not being subjected to any axial force. In this case, bending occurs in the light, slender rod, which deforms in a direction perpendicular to its axis. Therefore, the three limb-rods connecting the BP with the MP, are modeled as three identical clamped-free beams of uniform circular cross-section. The elastic behavior of j th limb-rod is governed by

$$F_j = k_r w_j, \quad w_j = \sqrt{w_{c_j}^2 + w_{n_j}^2}, \quad k_r = \frac{3E\pi d_r^4}{16l_r^3} \tag{1}$$

where E , d_r and l_r are the Young modulus, the diameter and the length of the limb-rod; besides, k_r the stiffness of the same rod. Moreover, w_j is the maximum deflection of the j th limb-rod due to the normal fore F_j acting on its upper end. The deflection w_j is decomposed into two components, w_{c_j} and w_{n_j} ; one is along the j th C-drive axis, while the other is normal to the plane spanned by the j th C-drive axis and the j th limb-rod axis.

Inspired by the virtual-joint method [7, 8], for elastodynamics modeling, each flexible limb-rod is replaced with a rigid rod carrying a virtual P joint located on its upper end. The direction of this joint is parallel to the deflection of the limb-rod, the joint variable being the deflection of the rod at the upper end. Then, the virtual-joint model of the whole PKM is illustrated in Fig. 3, using the notation in Table 1.

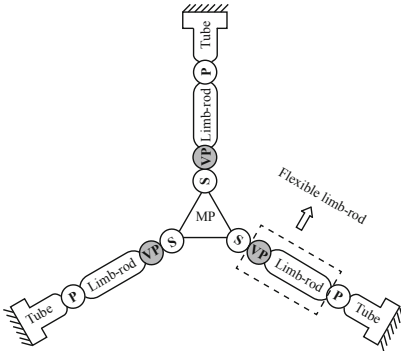


Fig. 3. Virtual-joint model of the PKM

Table 1. Geometrical representations of the components in the virtual-joint model

Component	Representation
P, S joints	
Virtual P joint	
Rigid link	
Rigid MP	
Base	

In the virtual-joint model, the virtual P joints are regarded as actuated joints, while the rest P and S joints as passive joints. The maximum deflections of the the limb-rods are selected as the generalized coordinates to define the perturbed

posture of the PKM under the applied wrench. The generalized coordinates are stored in a six-dimensional array, namely,

$$\mathbf{q} = [w_{c1} \ w_{n1} \ w_{c2} \ w_{n2} \ w_{c3} \ w_{n3}]^T \tag{2}$$

Then, each limb becomes a PPS chain. For the j th limb, the twist of the MP is described as

$$\mathbf{t} = \mathbf{J}_j \dot{\boldsymbol{\vartheta}}_j \tag{3a}$$

with

$$\mathbf{J}_j = \begin{bmatrix} \mathbf{0} & \mathbf{0} & \mathbf{0} & \mathbf{e}_j & \mathbf{f}_j & \mathbf{g}_j \\ \mathbf{f}_j & \mathbf{e}_j & \mathbf{g}_j & \mathbf{e}_j \times \mathbf{p}_j & \mathbf{f}_j \times \mathbf{p}_j & \mathbf{g}_j \times \mathbf{p}_j \end{bmatrix} \tag{3b}$$

$$\mathbf{t} = [\boldsymbol{\omega}^T \ \dot{\mathbf{c}}^T]^T, \quad \dot{\boldsymbol{\vartheta}}_j = [\dot{b}_j \ \dot{w}_{cj} \ \dot{w}_{nj} \ \dot{\theta}_{j1} \ \dot{\theta}_{j2} \ \dot{\theta}_{j3}]^T \tag{3c}$$

where \mathbf{t} is the MP twist, consisting of the MP angular velocity $\boldsymbol{\omega}$ and the velocity $\dot{\mathbf{c}}$ of the MP center of mass (c.o.m.); $\dot{\boldsymbol{\vartheta}}_j$ the joint-rate array of j th limb; besides, \mathbf{J}_j is the Jacobian matrix of the j th limb. Moreover, $\mathbf{0}$ is the three-dimensional zero vector; \mathbf{p}_j the vector stemming at the center of the j th S joint and ending at the MP c.o.m.; \mathbf{e}_j the unit vector parallel to the C-drive axis; \mathbf{f}_j the unit vector parallel to the limb axis; and $\mathbf{g}_j \equiv \mathbf{e}_j \times \mathbf{f}_j$. Furthermore, \dot{b}_j denotes the rate of the P joint in the j th limb, while $\dot{\theta}_{j1}$, $\dot{\theta}_{j2}$ and $\dot{\theta}_{j3}$ denote the rates of the S joint in the j th limb.

Eliminating the passive joint rates, the kinematic relation of the virtual-joint model is described as

$$\mathbf{N}\mathbf{t} = \dot{\mathbf{q}}, \quad \mathbf{N} = \begin{bmatrix} (\mathbf{e}_1 \times \mathbf{p}_1)^T & \mathbf{e}_1^T \\ (\mathbf{g}_1 \times \mathbf{p}_1)^T & \mathbf{g}_1^T \\ (\mathbf{e}_2 \times \mathbf{p}_2)^T & \mathbf{e}_2^T \\ (\mathbf{g}_2 \times \mathbf{p}_2)^T & \mathbf{g}_2^T \\ (\mathbf{e}_3 \times \mathbf{p}_3)^T & \mathbf{e}_3^T \\ (\mathbf{g}_3 \times \mathbf{p}_3)^T & \mathbf{g}_3^T \end{bmatrix} \tag{4}$$

3 Elastostatics

In the elastodynamics analysis, the PKM is assumed to be locked at a particular posture. When an external wrench is applied on the MP, due to the deflections of the flexible limb-rods, the MP undergoes a *small-amplitude displacement* (SAD) screw w.r.t. the MP. The PKM is modeled as a six-dof *Cartesian* mass-spring undamped system. Its linearized dynamics, in terms of the SAD screw of the MP takes the form

$$\mathbf{M}\ddot{\mathbf{x}} + \mathbf{K}\mathbf{x} = \mathbf{0}, \quad \mathbf{x} = \begin{bmatrix} \boldsymbol{\theta} \\ \mathbf{u} \end{bmatrix} \tag{5}$$

where \mathbf{M} and \mathbf{K} are the 6×6 Cartesian symmetric positive-definite mass matrix and stiffness matrix of the system, while \mathbf{x} is the SAD screw of the MP. Moreover, $\boldsymbol{\theta}$ is the (three-dimensional) small-amplitude rotation vector of the MP and \mathbf{u} the (three-dimensional) small-amplitude translation vector of the MP c.o.m.

Moreover, based on Eq. (4), the expression for the generalized coordinates in terms of the SAD screw of the MP is²

$$\mathbf{q} = \mathbf{N}\mathbf{x} \quad (6)$$

3.1 Cartesian Stiffness Matrix

The Cartesian stiffness matrix of the PKM is calculated as the Hessian matrix of the total potential energy w.r.t. the MP SAD screw. The elastic potential energy is stored in the three flexible limb-rods. Therefore,

$$V = \sum_{j=1}^3 V_j = \sum_{j=1}^3 \frac{1}{2} k_r (w_{cj}^2 + w_{nj}^2) = \frac{1}{2} \mathbf{q}^T \mathbf{K}_q \mathbf{q} = \frac{1}{2} \mathbf{x}^T (\mathbf{N}^T \mathbf{K}_q \mathbf{N}) \mathbf{x} \quad (7a)$$

with

$$\mathbf{K}_q = k_r \mathbf{1}_6 \in \mathbb{R}^{6 \times 6} \quad (7b)$$

where \mathbf{K}_q is the generalized stiffness matrix and $\mathbf{1}_6$ the 6×6 identity matrix. The relation between \mathbf{q} and \mathbf{x} was derived based on the virtual-joint model in Sect. 2. Then, the Cartesian stiffness matrix is a *congruent transformation* of the generalized stiffness matrix, i.e.,

$$\mathbf{K} = \mathbf{N}^T \mathbf{K}_q \mathbf{N} \quad (8)$$

3.2 Cartesian Mass Matrix

The Cartesian mass matrix of the PKM is calculated as the Hessian of the total kinetic energy w.r.t. the MP SAD screw. There are four moving bodies in the PKM, namely, the three limb-rods and the MP.

Based on the virtual-joint model, under the external wrench, the limb-rods will slide along the tubes. Therefore, their kinetic energy is calculated as

$$T_r = \sum_{j=1}^3 T_{rj} = \sum_{j=1}^3 \frac{1}{2} m_r \dot{b}_j^2 = \frac{1}{2} \dot{\mathbf{b}}^T \mathbf{M}_r \dot{\mathbf{b}} \quad (9a)$$

with \dot{b}_j denoting the sliding rate of the j th P joint, while \mathbf{M}_r and $\dot{\mathbf{b}}$ denote the mass matrix and the joint-rate array of the three limb-rods:

$$\mathbf{M}_r = \text{diag}(m_r, m_r, m_r), \quad \dot{\mathbf{b}} = [\dot{b}_1 \ \dot{b}_2 \ \dot{b}_3]^T \quad (9b)$$

where m_r denotes the mass of the limb-rod.

² Under *small-amplitude rotation*, the angular velocity can be regarded as the time derivative of the rotation vector. Therefore, $\mathbf{x} = \mathbf{t}\Delta t$ and $\mathbf{q} = \dot{\mathbf{q}}\Delta t$, with Δt denoting a small time-increment.

Let \mathbf{h}_j denote the Plücker array of the line passing through the center of the j th S joint and parallel to \mathbf{f}_j , namely,

$$\mathbf{h}_j = [\mathbf{f}_j^T (\mathbf{f}_j \times \mathbf{p}_j)^T]^T, \quad j = 1, 2, 3 \quad (10)$$

The unit screw \mathbf{h}_j is reciprocal³ to all the columns of the Jacobian \mathbf{J}_j in Eq. (3b), except for the one associated with the rate \dot{b}_j . Thus,

$$\mathbf{h}_j \mathbf{\Gamma} \mathbf{t} = [(\mathbf{f}_j \times \mathbf{p}_j)^T \mathbf{f}_j^T]^T \begin{bmatrix} \mathbf{0} \\ \mathbf{f}_j \end{bmatrix} \dot{b}_j = \dot{b}_j, \quad \mathbf{\Gamma} = \begin{bmatrix} \mathbf{O} & \mathbf{1}_3 \\ \mathbf{1}_3 & \mathbf{O} \end{bmatrix} \quad (11)$$

where \mathbf{O} is the 3×3 zero matrix, while $\mathbf{\Gamma}$ is a swapping matrix⁴.

Then, the relation between $\dot{\mathbf{b}}$ and \mathbf{t} is expressed as

$$\mathbf{H} \mathbf{t} = \dot{\mathbf{b}}, \quad \mathbf{H} = \begin{bmatrix} \mathbf{h}_1 \mathbf{\Gamma} \\ \mathbf{h}_2 \mathbf{\Gamma} \\ \mathbf{h}_3 \mathbf{\Gamma} \end{bmatrix} = \begin{bmatrix} (\mathbf{f}_1 \times \mathbf{p}_1)^T \mathbf{f}_1^T \\ (\mathbf{f}_2 \times \mathbf{p}_2)^T \mathbf{f}_2^T \\ (\mathbf{f}_3 \times \mathbf{p}_3)^T \mathbf{f}_3^T \end{bmatrix} \quad (12)$$

Moreover, the kinetic energy of the MP is calculated as

$$T_m = \frac{1}{2} m_m \dot{\mathbf{c}}^2 + \frac{1}{2} \boldsymbol{\omega}^T \mathbf{I}_m \boldsymbol{\omega} = \frac{1}{2} \mathbf{t}^T \mathbf{M}_m \mathbf{t}, \quad \mathbf{M}_m = \begin{bmatrix} \mathbf{I}_m & \mathbf{O} \\ \mathbf{O} & m_m \mathbf{1}_3 \end{bmatrix} \quad (13)$$

where \mathbf{M}_m is the 6×6 inertia dyad of the MP, with the MP mass m_m and the MP inertia tensor \mathbf{I}_m defined at the MP c.o.m.

Based on the Eqs. (9), (12) and (13), the Cartesian mass matrix of the PKM is

$$\mathbf{M} = \frac{\partial^2 (T_r + T_m)}{\partial \mathbf{t}^2} = \mathbf{H}^T \mathbf{M}_r \mathbf{H} + \mathbf{M}_m \quad (14)$$

3.3 Natural Frequencies and Natural Modes

The natural frequencies and natural modes of the system are then calculated by solving the eigenproblem of the elastodynamics model of the PKM, namely,

$$(\lambda_i^2 \mathbf{M} - \mathbf{K}) \mathbf{f}_i = \mathbf{0}, \quad i = 1, 2, \dots, 6 \quad (15)$$

with λ_i denoting the i th natural frequency of the system, \mathbf{f}_i the i th natural mode of the system. The eigenvector \mathbf{f}_i is not dimensionally-homogenous. It has a screw structure, its upper three-dimensional part bearing units of rad, its lower part bearing units of m. Therefore, the natural modes \mathbf{f}_i are also termed the eigenscrews of the system.

³ The screws \mathbf{s}_1 and \mathbf{s}_2 are said to be reciprocal, if $\mathbf{s}_1^T \mathbf{\Gamma} \mathbf{s}_2 = 0$.

⁴ The matrix $\mathbf{\Gamma}$ swaps the two three-dimensional vectors in a screw, a twist or a wrench, hence the moniker.

4 Numerical Results

A desktop-scale SDelta robot has the dimensions:

$$r = 150 \text{ mm}, \quad R = 450 \text{ mm}, \quad a = \sqrt{3}r, \quad b = \sqrt{3}R, \quad h = 150 \text{ mm} \quad (16)$$

where r denotes the circumradius of the base triangle in the the MP plane and R its counterpart in the BP plane. The thickness of the MP plate is $d_{MP} = 12.5 \text{ mm}$. The MP plate has uniform density, its centroid thus being the same as its c.o.m. Moreover, 3003 Aluminium Alloy is selected as the material of the MP and Titanium as the material of the limb-rods. The length l_r , the diameter d_r and the Young modulus of each limb-rod are

$$l_r = 115 \text{ mm}, \quad d_r = 11.5 \text{ mm}, \quad E = 105 \text{ GPa} \quad (17)$$

Moreover, we assume that a solid cube payload is attached to the MP. The mass m_l and the side length a_l of the payload are assumed to be

$$m_l = 5 \text{ kg}, \quad a_l = 85 \text{ mm} \quad (18)$$

Furthermore, the mass of the payload is uniformly distributed.

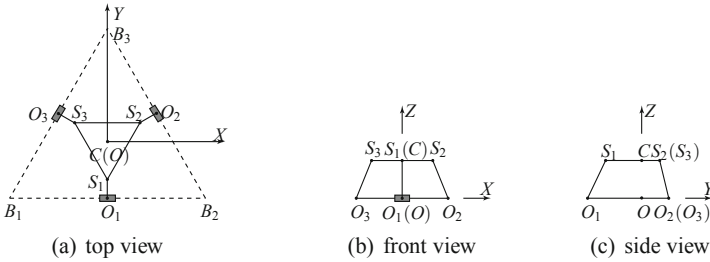


Fig. 4. Three view drawing of the symmetric posture

The Cartesian stiffness and mass matrices are posture-dependent. Next, the elastodynamics of the PKM will be evaluated at the “symmetric posture”, as shown in Fig. 4. The plane of the MP triangle is parallel to that of its BP counterpart. The centroid C of the MP is right above the centroid O of the BP. The “symmetric” posture is chosen, because at this posture, the SDelta robot is most likely to attain the maximum dexterity (minimum condition number of the forward Jacobian matrix).

First of all, the Cartesian stiffness and mass matrices are calculated according to Eqs. (8) and (14). Then, the natural frequencies and eigenscrews are derived by solving the eigenproblem associated with the *dynamic matrix* $\mathbf{D} \equiv \mathbf{M}^{-1}\mathbf{K}$

[9]. At the symmetric posture, the numerical natural frequencies of the system are arrayed in vector \mathbf{w}_f ⁵, namely,

$$\mathbf{w}_f = [31.80, 31.80, 42.04, 137.87, 137.87, 324.21]^T \text{ (Hz)} \quad (19)$$

According to the above numerical results, the lowest natural frequency of the system is 31.80 Hz. Therefore, in order to avoid resonance, the operation frequency of the SDelta with 5-kg payload should be lower than 30 Hz, which allows for a broad band of operation.

5 Conclusions

The elastodynamics analysis of a three-limb, full-mobility parallel robot, dubbed the SDelta, was reported. By modeling the light-weight limb-rods as identical linearly elastic beams, the flexibility of the SDelta robot is taken into account. The PKM is modeled as a 6-dof mass-spring undamped system. The posture-dependent Cartesian stiffness and mass matrices were derived. Then, the natural frequencies and natural modes of the system were calculated. Numerical results of the elastodynamics analysis of the SDelta were derived at a specific posture, for a prototype at the desktop scale. According to the results, the prototype can operate within a frequency spectrum of 30 Hz, under a 5-kg payload, which allows for a broad band of operation.

Acknowledgments. The first author would like to acknowledge the McGill Engineering Doctoral Award (MEDA) and the Chinese Scholarship Council (CSC) for their financial support. The second and third authors acknowledge the support received from Canada's Natural Sciences and Engineering Research Council (NSERC) through Grants No. RGPIN-2015-03864 and RGPIN-2016-04692, respectively.

References

1. Li, W., Angeles, J.: A novel three-loop parallel robot with full mobility: kinematics, singularity, workspace, and dexterity analysis. *ASME J. Mech. Robot.* **9**, 051003 (2017)
2. Podhorodeski, R.P.: A class of parallel manipulators based on kinematically simple branches. *ASME J. Mech. Des.* **116**, 908–914 (1994)
3. Merlet, J.P.: Parallel robots. In: *Solid Mechanics and Its Applications*. Springer (2006)
4. Briot, S., Khalil, W.: *Dynamics of Parallel Robots*. Springer, Heidelberg (2015)
5. Karim Eskandary, P., Angeles, J.: The translating II-joint: design and applications. *Mech. Mach. Theory* **122**, 361–370 (2018)
6. Sun, Q., Angeles, J., Forbes, J.R.: Elastostatics of a full-mobility PKM with flexible links. In: *ROMANSY 22-Robot Design, Dynamics and Control*, Rennes, France, pp. 34–41 (2018)

⁵ Notice that, as a result of the symmetric design of the PKM and the chosen posture, the mass and stiffness matrices are both isotropic in the X - Y plane, which leads two pairs of identical natural frequencies.

7. Salisbury, J.K., Craig, J.J.: Articulated hands: force control and kinematic issues. *Int. J. Robot. Res.* **1**(1), 4–17 (1982)
8. Gosselin, C.: Stiffness mapping for parallel manipulators. *IEEE Trans. Robot. Autom.* **6**(3), 377–382 (1990)
9. Wittbrodt, E., Adamiec-Wójcik, I., Wojciech, S.: *Dynamics of Flexible Multibody Systems: Rigid Finite Element Method*. Springer, Heidelberg (2007)



Synthesis of Function Generator Four-Bar Linkages: Minimization of the Joint-Forces Constraining Structural-Related Quantities

Claudio Villegas^{1,2}(✉), Mathias Hüsing¹, and Burkhard Corves¹

¹ RWTH Aachen University, Aachen, Germany
villegas@igmr.rwth-aachen.de

² Universidad del Bio-Bio, Concepción, Chile

Abstract. In the design process of a mechanism, the dynamic behavior plays an important role. It could be the cause of unexpected high dynamic forces in later stages when it is not considered in the early stage of the design process. High forces could produce high stresses and high vibration levels. Several studies have been carried out in this area; however, only a few consider structural criteria and the eigenfrequencies in the early stage of the process. Low forces and an adequate structure should lead to good dynamic behavior. In this work, we present a method to synthesize function generator four-bar linkages that takes into account structural criteria in a joint-forces minimization-maximization problem. Its objective function is the reaction force on the mechanism joints. The problem's constraints are the maximum stress on the links, the first eigenfrequency of the mechanism and the deflection of the crank and the rocker. With this method, the links' lengths and cross-sectional areas of the mechanism are obtained for a given task. As condition, we assumed that the crank rotates with constant angular speed and its shaft works as a torsional spring. Moreover, the rocker moves a body with constant inertia. The resultant mechanisms are compared with those obtained with a traditional crank-rocker synthesis method, according to VDI 2130. To compare both methods, the maximum force, maximum stress, deviation of the rocker angle at its dead-center positions and RMS vibration of the crank and rocker of each mechanism are calculated using MSC ADAMS™. The results show that the mechanisms obtained with our method have better stress and vibratory levels than those obtained with a traditional approach.

Keywords: Min-max problem · Eigenfrequency · Stress · Kinetostatic analysis · Dynamic behavior

1 Introduction

High-speed mechanisms require to be designed with focus on their dynamic behavior [4]. Not considering this behavior in the first stage of the design process may lead to several unwanted loops in the process. Therefore, several studies have been carried out to optimize the mechanisms' dynamic performance. Some of them have concentrated on

© The Editor(s) (if applicable) and The Author(s), under exclusive license to Springer Nature Switzerland AG 2020

D. Pisla et al. (Eds.): EuCoMeS 2020, MMS 89, pp. 314–321, 2020.

https://doi.org/10.1007/978-3-030-55061-5_36

the minimization of the shaking force and the shaking moment using genetic algorithms [3]. In [1] is presented a dynamic balancing of four-bar linkages with a subsequent step of shape optimization to reduce even more the shaking force and shaking moment. Others have focused on reducing the velocity and acceleration of mechanisms [4], minimizing the joint forces on path generator four-bar linkages [5] or on function generator four-bar linkages (FGFBLs) [12]. The mentioned studies improve the dynamic behavior of mechanisms. However, in those and other studies [2], the objective functions and the constraints are contained in the area of mechanisms, leaving outside the structural analysis. Moreover, with exception of [12], it was not considered the inertial effect of the body the mechanism moves. Furthermore, the stiffness of the shaft that drives the mechanism was not included in the optimizations.

The authors of [2] proposed a multidisciplinary design of mechanism, which contemplates two levels of optimization. One of them is the mechanism level, *i.e.* accuracy of the task. The other is the structural level, *i.e.* the mechanism mass and stress magnitude. Other multistage design method was developed in [8] considering kinematic synthesis and dynamic optimization. Moreover, velocity profiling was also considered in [9]. These studies address the structural and dynamic behavior of the mechanisms, yet none of the publications we analyzed integrates the eigenfrequency of the mechanism as an indicator of good dynamic behavior.

In this work, a method to calculate the dimensions of FGFBLs is presented. This method minimizes the maximum force in the mechanism joints while constraining structural-related variables. These variables are the links' maximum von Mises stresses, first minimum eigenfrequency and deflection of the crank and the rocker of the mechanism. The effects of the body that the rocker moves is integrated in the model as a constant inertia. The stiffness of the driving shaft is also included. Fulfilling these conditions would lead to FGFBLs with good dynamic behavior and a reduction in the number of design loops in comparison to a traditional design process.

2 Methods

The FGFBL used in this work is presented in the Fig. 1(a). A_0 and B_0 represent the fixed joints, A and B denote the moving joints in the stretched or outer dead-center position (subindex S) and the folded or inner dead-center position (subindex F). The lengths l_i are denoted with $i = 1, 2, 3$ and 4 for the frame, the crank, the coupler and the rocker, respectively. The angles φ , ψ and μ are the crank, rocker and transmission angle, correspondingly. This mechanism is synthesized to fulfill a task. The task is defined by the angle ψ_H the rocker swings between its dead-center positions and the angle φ_H the crank describes while it rotates in the same direction than the rocker [11]. The angular speed Ω and the external inertia the rocker moves I_e are constant.

Let X be the vector of independent variables (Eq. 1)

$$X = [\varphi_S \ c_{s2} \ c_{s3} \ c_{s4} \ k_t], \quad (1)$$

where the crank angle in the stretched position φ_S defines the length of the moving links. c_{s2} , c_{s3} , c_{s4} are the links' cross-section areas and the stiffness of the drive shaft is k_t . To have one optimization variable for each cross-section, rectangular cross-sectional areas

with wide-depth ratio 4:1 are assigned to the crank and the rocker. Moreover, the coupler is calculated as a square cross-section. Those dimensions allow calculating forces and other magnitudes given the Elasticity E and the density ρ of the mechanism's material, under the assumption of uniform mass distribution on each link.

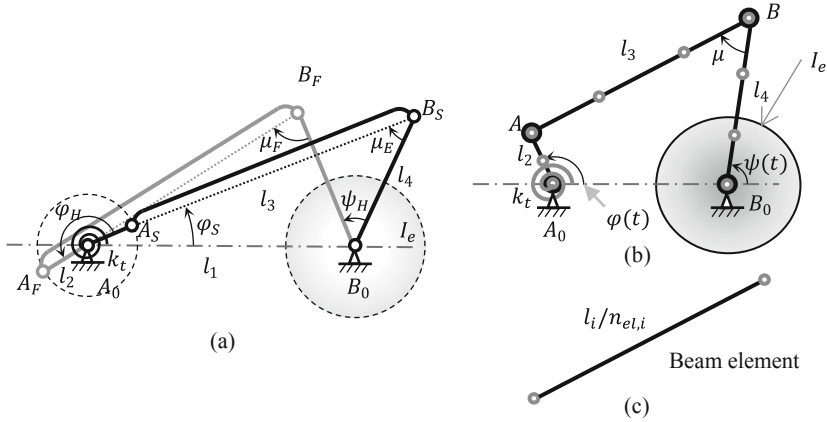


Fig. 1. Scheme of the FGFBL synthesized in this work. (a) Dead-center construction [11]. In black for the stretched position. In gray for the folded position. (b) FEM used in this study with three elements per link. (c) A beam element.

To obtain the dimensions of a FGFBL with minimized force and acceptable dynamic behavior, a minimization – maximization problem is set (Eqs. 2.a–2.d)

$$\min_X F_M \tag{2.a}$$

subject to :

$$\sigma_{M,i} - S_f < 0, i = 2, 3, 4 \tag{2.b}$$

$$\delta_{M,j} - l_j/D_j < 0, j = 2, 4 \tag{2.c}$$

$$f_{n1,m} - r_f \Omega < 0 \tag{2.d}$$

where F is the force on the joints of the FGFBL. The subindex M indicates the maximization of a variable and the subindex m indicates minimization. $\sigma_{M,i}$ is the maximum von Mises stress on each link. On the coupler is also included the effect of buckling. S_f is the equivalent fatigue strength of the material. $\delta_{M,j}$ is the maximum deflection of the crank or the rocker, l_j is the length of the crank or the rocker and D_j is the maximum admissible ratio between l_j and $\delta_{M,j}$. This ratio is obtained with the calibration of the method. $f_{n1,m}$ is the minimum first eigenfrequency of the system. r_f is the minimum admissible ratio between $f_{n1,m}$ and Ω . It is calculated as (Eq. 3)

$$r_f = n_H r_H + 0.5 \tag{3}$$

where n_H is the first spectral harmonic of the rocker angular acceleration, which amplitude is lower than 10% of that of its fundamental component. r_f is obtained only with the initial mechanism. r_H is an amplification value to be calibrated.

The minimization of F_M is called the outer problem and every variable with a subindex m or M is an inner problem. The calculation of F is based on the kinematics and kinetostatics of the mechanism. With the applied and the inertial forces, the internal forces in every link are determined, and then, the stresses and deflections. Furthermore, for the calculation of $f_{n1,m}$, a simple finite element model (FEM) of the mechanism is assembled. Every link is simulated as an Euler beam, and their mass and stiffness matrices are set as in [10]. In this model, the influence of I_e and k_s is included in the nodes where they act (Fig. 1(b) and (c)).

In every step of the outer problem, a FGFBL is synthesized to solve the inner problems globally. The inner problems are mapped together with 181 points distributed in the 360° of the crank rotation domain. Then, the best approximations are chosen as start values. They initiate a Simplex Search method [7] to find the solution of every inner problem for the current step. The outer problem is solved with the use of the Sequential Quadratic Program (SQP) method in MATLAB, command FMINCON [6]. The objective function OF of the outer problem is modified with a Quadratic Penalty method [7]. It includes the constraints in OF (Eq. 4)

$$\begin{aligned}
 OF = F_M + \frac{1}{2\nu_{QB}} & \left(\sum_{i=2}^4 \max \left[0, (\sigma_{i,M} - S_F)^2 \right] \right. \\
 & + \sum_{i=1}^2 \max \left[0, \left(\delta_{2i,M} - \frac{l_i}{D_i} \right)^2 \kappa_{delta} \right] \\
 & \left. + \max \left[0, (r_f \Omega - f_{n2,m})^2 \kappa_f \right] \right), \tag{4}
 \end{aligned}$$

where $\nu_{QB} > 0$ decreases with every step of the outer problem’s resolution. κ_δ and κ_f (Eqs. 5 and 6) are constants that keep the constraints comparable. Every time the outer program converges to an optimum that does not fulfill the constraints, the vector X is modified to fulfill them, and the optimization continues.

$$\kappa_\delta = (3E/l_1)^2 \tag{5}$$

$$\kappa_f = (S_F/r_f \Omega)^2. \tag{6}$$

The calibration of the variables D_2 , D_4 and r_H is realized for an arbitrary task. The variables D_2 and D_4 are parametrized for the values [100, 120, 140, 160, 180]. To calibrate r_H , an initial FGFBL is synthesized. With this linkage, the harmonic n_H is found. Using the selected harmonic n_H , r_f is obtained with the parametrization of r_H for [3, 3.5, 4]. The results of the parametrizations are tested in MSC ADAMS™ until a solution fulfills the given task with an error ψ_{dev} lower than 0.1%. This error is the maximum percent deviation of the rocker angle at its dead-center positions.

Table 1. Tasks chosen. $S_f = 170$ MPa.

Task	Design variable				
	ψ_H deg	φ_H deg	Ω rpm	I_e kg-mm ²	l_1 mm
I	90	165	120	50000	500
II	70	150	300	10000	250
III	110	180	600	500	200
IV	70	210	1200	100	200

Four task are proposed (Table 1) to calculate FGFBLs with our methodology. To compare the results of this method, FGFBLs in accordance to [11] are synthesized for every task. Thus, their links' lengths are obtained for a condition of maximized minimum μ . The cross-sections of the links are calculated with a min-max optimization for the joint force with the constraints (2.b) and (2.c). Each of the comparison mechanism are simulated with two different drive shaft diameters. One of the diameters is calculated to resist the maximum drive torque T . The other has the same stiffness than the FGFBL obtained with our method. The drive shafts have an arbitrary length of 45 mm. The main method is named Min-Max-Force (mMF), and the other Max-Min Transmission Angle one and two (MmTA-1 and MmTA-2). MmTA-2 is a second iteration of MmTA-1. They are simulated in MSC ADAMSTM as a flexible multibody simulation and its joint forces, Root Mean Square (RMS) vibration of the crank and the rocker, maximum stresses on the links and maximum rocker angle deviation ψ_{dev} are used to compare the FGFBLs to each other.

3 Results and Discussion

This section describes the results of the calibration and the behavior of the optimized mechanisms for each task. A comparison is presented to verify the effectivity of the method.

3.1 Calibration

The calibration was carried out for the task $\psi_H = 70^\circ$, $\varphi_H = 195^\circ$. The mechanism's external inertia used is $I_e = 1 \times 10^5$ kg – mm², crank rotational speed $\Omega = 300$ rpm and frame length $l_1 = 500$ mm. The material elasticity used is $E = 200$ GPa, density $\rho = 7800$ kg/m³, and fatigue strength $S_F = 170$ MPa.

The calibration process started with $D_2 = 100$, $D_4 = 100$ and $r_H = 4$. If the synthesized mechanism did not fulfill the calibration condition then D_4 was increased. In case D_4 reached 180 and the calibration condition was still not fulfilled, then D_2 was increased and D_4 reseted to 100. If the condition was fulfilled, r_H was decreased. The calibrated values are $D_2 = 100$, $D_4 = 180$ and $r_H = 3.5$ (Table 2).

Table 2. Results of the calibration for $D_2 = 100$ using the rocker maximum angular deviation at its dead-center positions ψ_{dev} as a percent value of ψ_H . NC means not calculated.

r_H	D_4				
	100	120	140	160	180
3	NC	NC	NC	NC	0.10
3.5	NC	NC	NC	0.11	0.09
4	0.18	0.14	0.13	0.11	0.10

3.2 Results of the Method

After the calibration, the four task shown in Table 1 are used to compare the results of this study, as described in the Methods chapter. For each task, the resulting maximum force, the percent deviation of the rocker at its dead-center positions (Table 3), RMS vibration of the crank and the rocker (Table 4) and maximum von Mises stresses (Table 5) are analyzed.

From Table 3, it is evident that changing the shaft diameter obtained in MmTA-1 to the one used in MmTA-2 improves significantly the behavior of the mechanism for every task analyzed. Therefore, only the methods mMF and MmTA-2 are compared.

Table 3. Maximum force F_M in N and ψ_{dev} as a percent value of ψ_H

Method	Task							
	I		II		III		IV	
	F_M	ψ_{dev}	F_M	ψ_{dev}	F_M	ψ_{dev}	F_M	ψ_{dev}
mMF	133.5	0.08	578.0	0.05	114.9	0.09	2178	0.03
MmTA-1	1466	2.06	2071	1.25	953.4	0.90	5223	0.03
MmTA-2	141.9	0.10	611.9	0.08	118.7	0.11	2155	0.04

Table 4. RMS value of the velocity vibration of the crank (2) and the rocker (4) in their transverse direction in mm/s

Method	Task							
	I		II		III		IV	
	2	4	2	4	2	4	2	4
mMF	1.98	6.24	0.64	7.15	3.61	5.17	10.4	5.35
MmTA-2	7.92	6.80	14.1	16.7	6.93	6.58	18.6	5.73

The maximum forces obtained with mMF and MmTA-2 are similar for every task (Table 3). For the first three task, the mMF method synthesizes mechanisms with lower

maximum force. For the last task, the maximum force of the mechanism synthesized with the mMF method is only 1.07% higher than that of the mechanism synthesized with the MmTA-2 method. For the mMF and MmTA-2 method, the rocker angular deviations are similar, but always lower for the mMF method. Table 4 shows that the RMS vibration values of the crank and the rocker are lower in a mechanism synthesized with the mMF method than in those synthesized with the MmTA-2 method. Table 5 shows that the stresses associated to the mMF method are lower than the others are. The only exception found is in Task III, where the rocker calculated with the MmTA-2 method resists a lower maximum stress than its homologous calculated with mMF. The stresses on the coupler obtained with MmTA-2 method exceed the stress limit in the tasks I and II. This does not happen with the mMF method in this study.

Table 5. Maximum von Mises stress on the crank (2), coupler (3) and rocker (4) in MPa

		Task			
Link	Method	I	II	III	IV
2	mMF	28.17	16.32	68.58	118.6
	MmTA-2	67.01	121.1	77.51	168.1
3	mMF	16.67	22.38	25.19	83.29
	MmTA-2	221.7	215.2	105.3	132.8
4	mMF	33.67	40.65	57.63	32.09
	MmTA-2	37.87	54.55	52.79	34.71

4 Conclusions

The results show that the proposed method can synthesize FGFBLs with maximum forces on the joints and angular output deviations similar to a traditional approach. However, the dynamic behavior of the designed mechanisms is always superior in RMS vibration value and most of the times in stress value. The reason for this could be the eigenfrequency constraint. On one hand, the traditional method applied MmTA-1 required a second iteration to make its results comparable to those of mMF method. Even in the second iteration, MmTA-2 gave coupler dimensions that resisted maximum stresses higher than the given limit of 170 MPa. This means that a third iteration is necessary to find a coupler that satisfies the material strength condition. On the other hand, after calibration, the mMF method calculated the dimensions of FGFBLs with an acceptable dynamic behavior solving the outer optimization problem once. As future work is proposed to extend this method to other linkages as six-bars mechanisms and to add precision points to the output angle.

References

1. Chaudhary, K., Chaudhary, H.: Optimal dynamic balancing and shape synthesis of links in planar mechanisms. *Mech. Mach. Theory* **93**, 127–146 (2015). <https://doi.org/10.1016/j.mechmachtheory.2015.07.006>
2. Chen, T.-Y., Yang, C.-M.: Multidisciplinary design optimization of mechanisms. *Adv. Eng. Softw.* **36**(5), 301–311 (2005). <https://doi.org/10.1016/j.advengsoft.2004.10.013>
3. Erkaya, S.: Investigation of balancing problem for a planar mechanism using genetic algorithm. *J. Mech. Sci. Technol.* **27**(7), 2153–2160 (2013). <https://doi.org/10.1007/s12206-013-0530-z>
4. Guj, G., Dong, Z.Y., Di Giacinto, M.: Dimensional synthesis of four bar linkage for function generation with velocity and acceleration constraints. *Meccanica* **16**(4), 210–219 (1981). <https://doi.org/10.1007/BF02128323>
5. Krašna, S., Ciglaric, I., Prebil, I.: Four-bar linkage design using global optimization approach. In: Marjanovi, D. (ed.) Proceedings of the 7th international design conference. Design 2002, pp. 1199–1204. Faculty of Mechanical Engineering and Naval Architecture, Zagreb (2002)
6. MATWORKS: FMINCON. Find minimum of constrained nonlinear multivariable function. <https://www.mathworks.com/help/optim/ug/fmincon.html>. Accessed 25 Jan 2020
7. Nocedal, J., Wright, S.J. (eds.): Numerical Optimization. Springer Series in Operations Research, 2nd edn. Springer, New York (2006)
8. Rayner, R., Sahinkaya, M.N., Hicks, B.: Combining inverse dynamics with traditional mechanism synthesis to improve the performance of high speed machinery. In: Proceedings of the ASME dynamic systems and control conference 2008. ASME 2008 Dynamic Systems and Control Conference, Ann Arbor, Michigan, USA, 20–22 October 2008, pp. 599–606. American Society of Mechanical Engineers, New York (2009). <https://doi.org/10.1115/dsc.c2008-2186>
9. Rayner, R.M.C., Sahinkaya, M.N., Hicks, B.: Improving the design of high speed mechanisms through multi-level kinematic synthesis, dynamic optimization and velocity profiling. *Mech. Mach. Theory* **118**, 100–114 (2017). <https://doi.org/10.1016/j.mechmachtheory.2017.07.022>
10. Vaidya, A.M., Padole, P.M.: A performance evaluation of four bar mechanism considering flexibility of links and joints stiffness. *TOMEJ* **4**(1), 16–28 (2010). <https://doi.org/10.2174/1874155X010040100016>
11. VDI 2130: Ebene Kurbelgetriebe; Konstruktion von Kurbelschwingen zur Umwandlung einer umlaufenden Bewegung in eine Schwingbewegung. VDI-Gesellschaft Produkt- und Prozessgestaltung (2130)
12. Villegas, C., Hüsing, M., Corves, B.: Dynamic synthesis of a crank-rocker mechanism minimizing its joint-forces. In: Uhl, T. (ed.) Advances in Mechanism and Machine Science. Proceedings of the 15th IFToMM World Congress on Mechanism and Machine Science. Mechanisms and Machine Science, vol. 73, pp. 3167–3176. Springer, Cham (2019)



Parametrization of a Real-Time Vehicle Model from Driving Tests for HiL Testing of Hydraulic Steering Systems

Ingomar Schröder¹(✉), Thomas Schmidt², Jørgen Krusborg²,
and Christoph Woernle¹

¹ Chair of Technical Mechanics / Dynamics, University of Rostock, Rostock, Germany

{[ingomar.schroeder](mailto:ingomar.schroeder@uni-rostock.de),[woernle](mailto:woernle@uni-rostock.de)}@uni-rostock.de

² Danfoss Power Solutions ApS, Nordborg, Denmark

{[t.schmidt](mailto:t.schmidt@danfoss.com),[jkrusborg](mailto:jkrusborg@danfoss.com)}@danfoss.com

Abstract. Hydraulic steering systems are used in construction and agricultural vehicles with high steering loads. Integration of advanced functionalities like driver-assistance systems and increased safety regulations requires the development of new steering system concepts like steer-by-wire systems. Hardware-in-the-loop (HiL) testing of physical steering systems in bidirectional interaction with a numerical vehicle model enables reproducible, safe and cost-efficient experimental analyses under various nominal and failure operating conditions in a laboratory environment. The present contribution describes the parametrization of a multibody vehicle model of an agricultural tractor based on measurements from driving tests and its integration into a HiL test bench for hydraulic steering systems. First results show the functionality of the HiL concept.

Keywords: Vehicle dynamics testing · Parameter optimization · Real-time simulation · Hardware-in-the-loop · Hydraulic steering

1 Introduction

Hydraulic steering systems are used in construction and agricultural vehicles with high steering loads. A steering unit driven by the steering wheel is connected by hydraulic pipes and hoses with one or more steering cylinders that actuate the steered vehicle wheels. A steering cylinder is supplied by a hydraulic power unit augmenting the steering wheel torque [7]. If the hydraulic power supply fails, the driver still has the option of manual emergency steering, whereby very high steering wheel torques are needed. Advanced steer-by-wire hydraulic steering systems only have an electrical coupling between the steering column and the steering cylinder. If the hydraulic power supply fails, the driver has no possibility to steer the vehicle. Very strict safety requirements are therefore imposed on vehicles with such steering systems, especially if they are to be certified for use on public roads.

Hardware-in-the-loop (HiL) simulation is a powerful development tool for complex vehicle systems that enables highly reproducible, cost-effective and safe tests in a laboratory environment independent from the availability of vehicles and test tracks. For testing hydraulic steering systems a HiL environment is being developed similar to [4]. The steering system is physically built up on the test bench and is bidirectionally coupled with a numerical vehicle model that simulates the reaction of the vehicle to the actuator forces generated by the steering cylinder. In the HiL test bench concept under consideration the numerically calculated reaction of the model is physically applied on the steering system by a hydraulic test bench actuator that is realized by an electrically driven hydraulic pump. The physical setup and control concept of the HiL test bench is described in [2]. In this contribution the development of a vehicle model for this HiL test bench, its parametrization by driving tests and first results of HiL simulations are presented.

2 Vehicle Model

The HiL test bench is intended to be used for testing hydraulic steering systems of various utility vehicles. As only few parameters of these vehicles are available, relatively simple vehicle models are built up that are to be parametrized by driving tests with the actual vehicles. A reduced model depth also corresponds to the objective of real-time capability needed for HiL testing.

The vehicle considered within the present study is a 12 t agricultural tractor with an unsprung rigid rear axle and a double wishbone front axle with hydro-pneumatic suspension. Thus the vertical and roll stiffness of the rear axle is only provided by the tyres. As driving manoeuvres on a flat road are only considered, the overall stiffness of the series-connected suspension and tire springs at the front axle has been comprised in an equivalent tire stiffness of a simplified rigid-axle model thus neglecting the independent suspension movements. The steering kinematics at the front axle has been reduced to a planar mechanism in the horizontal plane. The topology of the model, built up in the multibody simulation (MBS) environment Simscape Multibody [3], is shown in Fig. 1. The position of the steering axis of the front wheel carrier was known from CAD data enabling to take the steering axis offsets into account that define the effective lever arms of the tyre contact forces with respect to the steering axis. The model has 11 degrees of freedom (dof) comprising 6 dof of the spatial motion of the vehicle body, 4 dof of the wheels and 1 dof of the steering mechanism.

For a given steering cylinder force $F_{Cyl}(t)$ the model calculates the reaction of the vehicle including the cylinder position $s_{Cyl}(t)$ and its time derivative $\dot{s}_{Cyl}(t)$. Vice versa, for a given cylinder position $s_{Cyl}(t)$, the steering cylinder force $F_{Cyl}(t)$ can be calculated.

The tyre forces are calculated with a simplified Pacejka model [5]. The vertical forces $F_{z,ij}$ are calculated from the position and velocity of the wheel hub along the vertical axis. The longitudinal forces $F_{x,ij}$ and the lateral forces $F_{y,ij}$ are calculated using the magic formula [6] in dependence of the longitudinal slip and

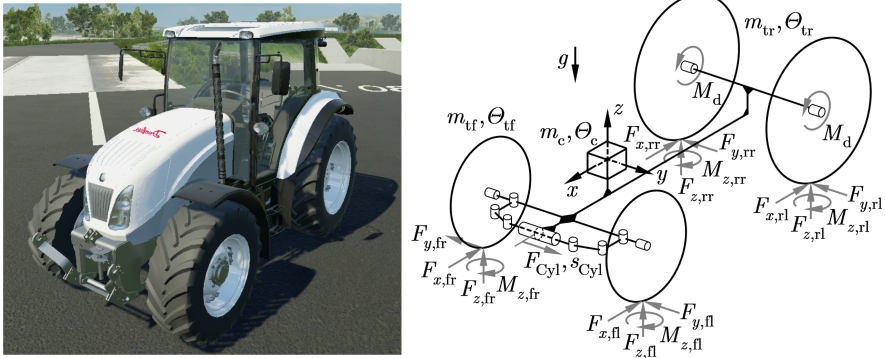


Fig. 1. Schematic overview of the vehicle model with the externally applied forces and torques

the lateral slip that are kinematically calculated from the actual state variables of the vehicle. Contributions resulting from wheel camber are neglected. The torques $M_{z,ij}$ along the vertical axis arise from the lateral forces $F_{y,ij}$ and the corresponding pneumatic trail which is described by a lookup table.

Within the present study driving manoeuvres with constant vehicle speed v are considered. The vehicle speed is achieved by a speed controller that generates a drive torque M_d on the rear wheels.

3 Driving Tests

Since very few parameters of the vehicle were known, especially those of the tyres, driving tests were carried out to parametrize and validate the vehicle model. All driving tests were performed on a dry solid flat road surface. The applied sensors and the corresponding measured quantities are listed in Table 1.

Table 1. Sensors utilised in the driving tests and the respective measured quantities

Sensors	Measured quantities
Correxit (Two axis optical sensor)	Longitudinal vehicle velocity Lateral vehicle velocity
Inertial Measurement Unit (IMU)	Vehicle accelerations (vehicle-fixed) Vehicle angular velocities (vehicle-fixed)
Two pressure sensors	Pressure steering cylinder chamber (left) Pressure steering cylinder chamber (right)
Draw-wire position sensor	Steering cylinder position
Steering robot	Steering wheel angle Steering wheel torque

The side slip angle and the steering cylinder force can be directly calculated from these measured quantities together with geometric parameters.

Sensor offsets were eliminated by driving straight ahead with different vehicle accelerations. The sensor data of the Correvit optical sensor and the IMU were then transformed in such a way that there were no more components in the lateral direction. The measured position value of the draw-wire sensor was set to zero.

In order to parametrize the vehicle model with the driving tests, it was necessary to carry out driving tests over the entire dynamic range of the vehicle. Both stationary and non-stationary driving conditions had to be captured. Previous driving tests have shown that a steep steering angle ramp is ideal for achieving this. The stationary driving condition is reached by keeping the steering wheel angle constant for a few seconds after the steering angle ramp is completed. Table 2 shows the combinations of vehicle speeds and stationary steering angles that were applied. The limit of subjective driving safety was reached at a lateral acceleration of about 4 m/s^2 to $4,5 \text{ m/s}^2$. The steering angle ramp was performed for steering angular speeds $5^\circ/\text{s}$, $10^\circ/\text{s}$ and $15^\circ/\text{s}$. Additional driving manoeuvres were carried out for validation purposes. These manoeuvres include sinusoidal steering inputs, double lane changes and a slowly increasing steering angle (spiral). All driving tests, with the exception of tracking a figure eight marked on the road surface, were performed using a steering robot mounted on the steering wheel. The desired vehicle speed was realized by the internal speed controller of the tractor.

Table 2. Combinations of vehicle speed and stationary steering angles that were used for the steep steering angle ramp manoeuvres

		Vehicle speed [km/h]					
		10	15	20	25	30	35
Steering angle [°]	5	•	•	•	•	•	•
	10	•	•	•	•	•	
	15	•	•	•	•		
	20	•	•	•			
	25	•	•	•			
	30	•	•				
	35						

4 Parameter Identification

As there were no force/torque measuring rims available for the driving tests to directly determine the tyre forces, the tyre model parameters were identified from the driving test measurements described in the previous section by an optimization. The flow chart of the optimization procedure is shown in Fig. 2.

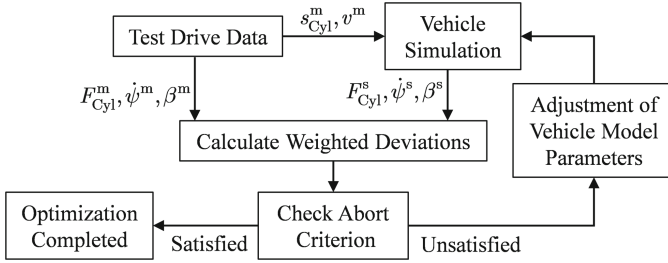


Fig. 2. Flow chart for the identification of the vehicle parameters based on the driving tests

The measured steering cylinder position s_{Cyl}^m and the vehicle speed v^m from the driving manoeuvres were used as input for the vehicle simulation. The steering cylinder force F_{Cyl}^s , the yaw rate $\dot{\psi}^s$ and the side slip angle β^s from the vehicle simulation are to be fitted to the corresponding measurements from the driving tests F_{Cyl}^m , $\dot{\psi}^m$ and β^m by adjusting the vehicle model parameters. The optimization criterion is the weighted sum of squared differences between F_{Cyl}^m , $\dot{\psi}^m$, β^m and F_{Cyl}^s , $\dot{\psi}^s$, β^s . For the optimization a generalized pattern search algorithm [1] is utilised.

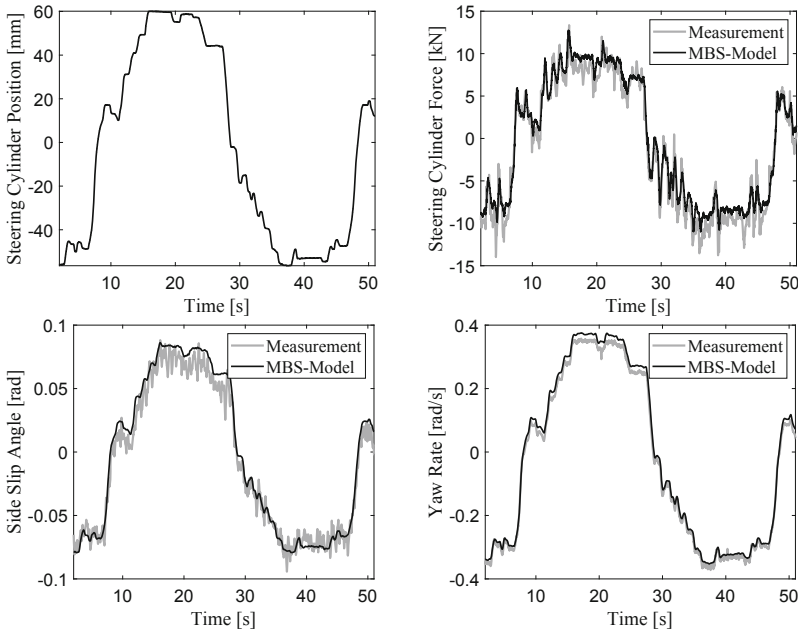


Fig. 3. Comparison of test drive data with the vehicle multibody simulation (MBS) model for a figure eight manoeuvre at a constant vehicle speed of 15 km/h

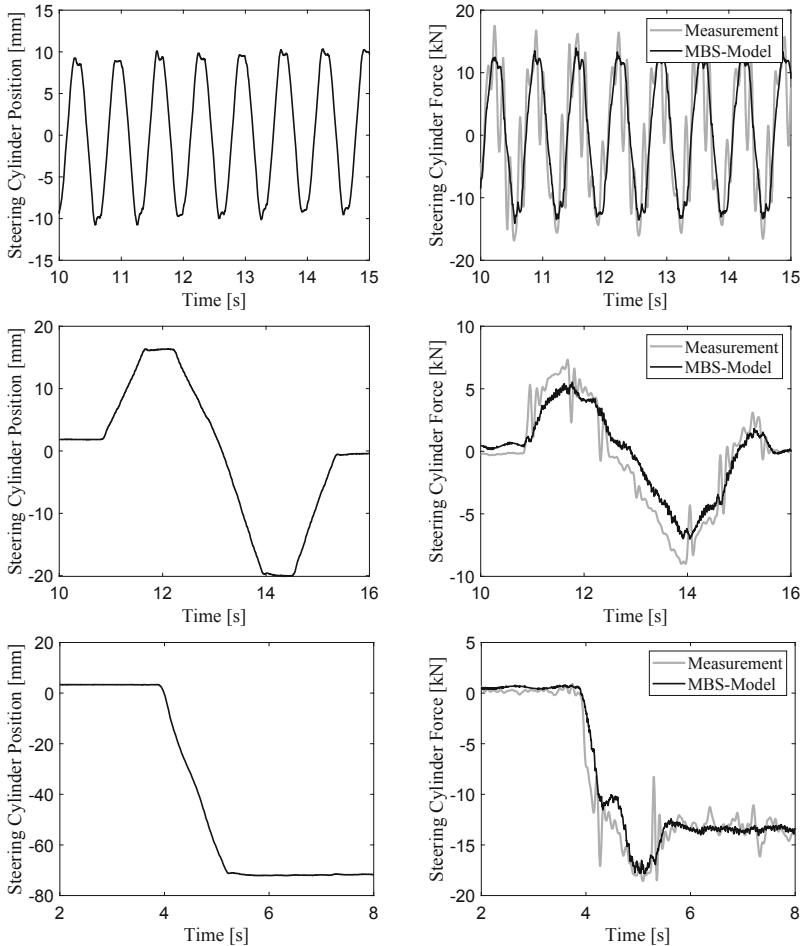


Fig. 4. Comparison of driving tests at a constant vehicle speed v with the vehicle multi-body simulation (MBS) **Top:** Sinusoidal steering movement at $v = 10$ km/h. **Middle:** double lane change at $v = 25$ km/h. **Bottom:** steep steering angle ramp at $v = 20$ km/h

Figures 3 and 4 exemplarily show outcomes of simulations with the optimized vehicle model for different driving manoeuvres. A steering cylinder position of 20 mm is equivalent to approximately 5° steering angle. It can be observed that the results from the vehicle model are well matched with the data of the driving tests. In Fig. 3a deviation between the left and the right curve can be seen. This most likely results from a slight overall slope of the road surface. Figure 4 shows an additional oscillation of the measured steering cylinder force. The exact source has not been clarified at present. It is assumed that it is caused from the steering hydraulics itself and not by the tyre forces.

5 HiL Test Bench

For HiL testing of hydraulic steering systems the vehicle model bidirectionally interacts with the physical steering system built up on the test bench. The physical setup and control concept of the test bench is described in [2]. The topology of the test bench is shown in Fig. 5. For the basic function tests of the test bench described here a purely passive emergency steering mode is considered, where the steering cylinder is hydraulically actuated by manually rotating the steering wheel without hydraulic power augmentation.

When the steering wheel is rotated, a differential pressure Δp is created in the output lines of the steering unit. The differential pressure Δp is used as the input for the vehicle model, where it is converted into an equivalent steering cylinder force F_{Cyl} by means of the effective piston area A . The steering cylinder position s_{CylRef} and its time derivative \dot{s}_{CylRef} are calculated by numerical integration of the equations of motion of the vehicle model and fed back to the test bench controller. The controller makes the position of the physical steering cylinder $s_{Cyl}(t)$ track the calculated trajectories of $s_{CylRef}(t)$ by adjusting the electrical current I_{Mot} corresponding to the torque of the servo motor actuating the hydraulic pump. The vehicle model is executed on a real-time target computer with an Intel Core i7-4790K (4.00 GHz) processor, 8 GB RAM and a Simulink Real-Time operating system. The HiL simulation runs with a fixed step size of 750 μ s. The data exchange between the simulation and the test bench controller is realized via Ethernet UDP.

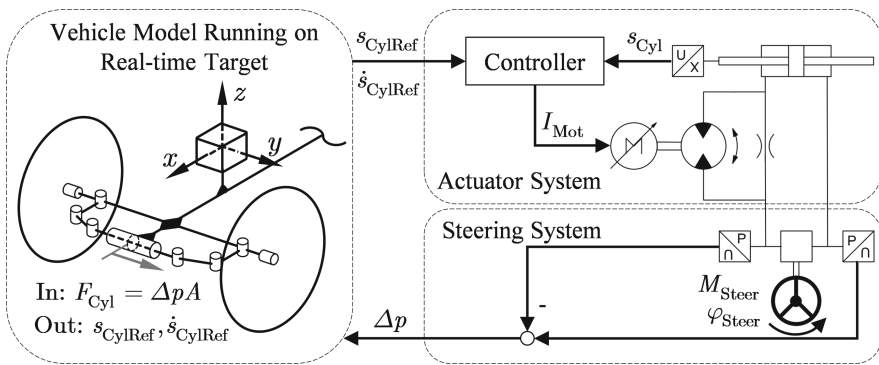


Fig. 5. Schematic overview of the test bench setup and communication with the vehicle model

Figure 6 shows the comparison between a measurement on the HiL test bench and a measurement from the driving tests for a steering wheel angle ramp. As a steering robot is not yet available for the test bench, the steering wheel angle was manually applied in such a way that the steering cylinder position equals the steering cylinder position of the driving test. The resulting steering cylinder

force is well matched to that obtained in the driving test. A slight deviation in the slopes of the steering cylinder forces can be traced back to different slopes of the steering cylinder position.

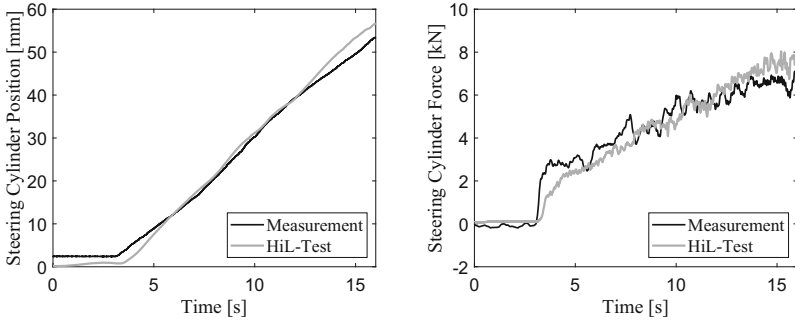


Fig. 6. Comparison of a driving test with measurements from the HiL test bench for a slowly increasing steering angle with a constant vehicle speed of 5 km/h

Implementations of a hydraulically actuated steering system and of a steering robot on the HiL test bench are currently under preparation. This will enable comparisons between the HiL test bench and driving tests with much higher dynamics.

6 Conclusion

A real-time capable vehicle model for HiL testing of hydraulic steering systems was built-up and parametrized from standardized driving tests. The validity of the vehicle model and its integration into the overall HiL test bench was described. First experiments with the HiL test bench demonstrate the basic functionality of the HiL concept. In a next step, HiL simulations with higher dynamics are to be carried out, requiring the test bench hardware to be enhanced. Furthermore, methods for compensating the actuator delay of the HiL test bench will be analysed and implemented.

Acknowledgements. This research and development project was supported by the European Regional Development Fund (EFRE). Support was also provided by the lead partner Technologie-Beratungsinstitut (TBI) according to the directive for support, development and innovation of the Ministry of Economics, Construction and Tourism of Mecklenburg-Vorpommern.

References

1. Audet, C., Dennis Jr., J.E.: Analysis of generalized pattern searches. *SIAM J. Optim.* **13**(3), 889–903 (2002)
2. Bruns, M., Schütz, L., Ennemark, P., Schmidt, T., Krusborg, J., Falkenstein, J.: HiL test bench as a development environment for hydraulic steering systems. In: *EuCoMeS 2020 – Proceedings of the 8th European Conference on Mechanism Science*. Springer, Heidelberg (2020)
3. The Mathworks, Inc., Natick, Massachusetts: MATLAB Version: 9.7 (R2019b)
4. Nippold, C., Küçükay, F., Henze, R.: Analysis and application of steering systems on a steering test bench. *Autom. Eng. Technol.* **1**(1–4), 3–13 (2016)
5. Pacejka, H.: *Tire and Vehicle Dynamics*. Elsevier, Amsterdam (2012)
6. Pacejka, H.B., Bakker, E.: The magic formula tyre model. *Veh. Syst. Dyn.* **21**(S1), 1–18 (1992)
7. Zardin, B., Borghi, M., Gherardini, F., Zanasi, N.: Modelling and simulation of a hydrostatic steering system for agricultural tractors. *Energies* **11**(1), 230 (2018)



Graphic Analysis of the Linear and Angular Momentum of a Dynamically Balanced 1-DoF Pantographic Linkage

Volkert van der Wijk^(✉)

Delft University of Technology, Delft, The Netherlands
v.vanderwijk@tudelft.nl

Abstract. This article presents a graphical analysis method for the verification of the gravity force balance and shaking force and shaking moment balance of a 1-DoF pantographic linkage. First the joint velocities of the linkage are graphically found of which the procedure is well known. To obtain the linear and angular momentum graphically, the mass and inertia of each element are modeled with two equivalent masses about the center of mass of the element, resulting in a mass and inertia equivalent model with solely point masses. The velocities of these point masses are obtained and each velocity vector is multiplied with the respective mass value to obtain vectors that represent the linear momentum. For force balance it is shown that the sum of all linear momentum vectors form a polygon. Subsequently the linear momentum vectors with their moment arms are transferred into an angular momentum diagram which for moment balance shows to sum up to zero.

Keywords: Graphic analysis · Linear and angular momentum · Gravity force balance · Shaking force and shaking moment balance · Pantograph.

1 Introduction

When mechanisms are shaking force and shaking moment balanced, they do not exert any dynamic reaction forces and moments to their base during (high-speed) motions [3, 5]. This reduces base vibrations significantly and when placed on floating platforms such as drones and cable robot end-effectors, balanced mechanisms do not disturb the position, orientation, and motion of the floating platform [2, 7]. For shaking force balance the linear momentum of all moving elements together must be constant (zero) while for shaking moment balance the angular momentum of all moving elements together must be constant (zero). A shaking force balanced mechanism is also gravity force balanced and therefore all methods for shaking force balancing are also applicable for gravity force balancing.

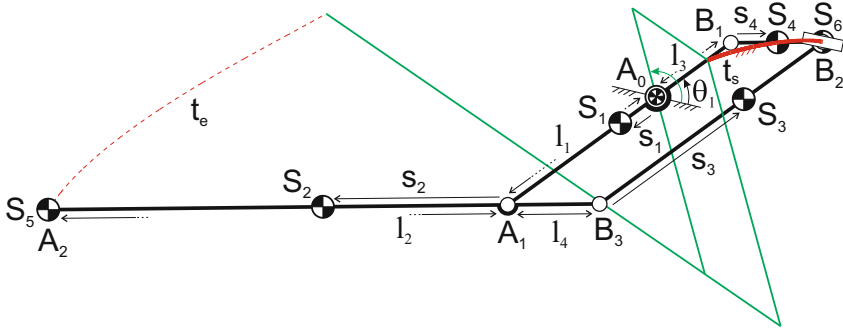


Fig. 1. 1-DoF dynamically balanced pantographic linkage in two poses with fixed joint A_0 and a slider in B_2 with slider trajectory t_s in red. The common CoM of all elements is stationary in A_0 .

While there are various methods for force balancing of a linkage, using counter-masses [1] or inherently balanced linkage architectures [6], for moment balancing of a linkage the methods are extremely limited [4]. Obtaining moment balance without additional elements is in most cases not possible [9].

In order to obtain a better understanding of moment balancing, the goal of this paper is to present a graphical method for the analysis of the linear and angular momentum of a linkage and to apply it to a 1-DoF dynamically balanced pantographic linkage to graphically show that the sums of linear and angular momenta are indeed zero. This will also give insight in the contribution of each linkage element to the total linear and angular momentum, i.e. in their contributions to the dynamic balance.

First the linkage is presented and the joint velocities are found graphically. Then the mass and inertia of each element are modeled with two equivalent masses to obtain a mass and inertia equivalent model with solely point masses. Subsequently the velocities and the linear momenta of the point masses are obtained graphically and are evaluated for force balance. As a final step, an angular momentum diagram is presented for evaluation of the moment balance.

2 Graphic Analysis of the Linear and Angular Momentum

Figure 1 shows a pantographic linkage consisting of the 4 links B_1A_1 , B_3A_2 , B_3B_2 , and B_1B_2 , which are connected with revolute pairs in A_1 , B_1 , B_2 , and B_3 , forming a parallelogram. In A_0 of link B_1A_1 the linkage has a revolute pair with the base, i.e. A_0 is the fixed joint. In joint B_2 there is a slider with fixed slider trajectory t_s which constrains the linkage to one degree-of-freedom (1-DoF) motion, indicated by angle θ_1 of the absolute rotation of link B_1A_1 . When in motion, the endpoint A_2 traces the trajectory t_e . The linkage is shown for two poses, the extended pose at the beginning of the slider trajectory with a relative

Table 1. Parameter values for dynamic balance of the pantographic linkage in Fig. 1.

[mm]	[mm]	[g]	[gmm ²]
$l_1 = 100$	$s_1 = 24.36$	$m_1 = 118.56$	$I_1 = 312454$
$l_2 = 250$	$s_2 = 100.57$	$m_2 = 302.95$	$I_2 = 2482640$
$l_3 = 50$	$s_3 = 97.05$	$m_3 = 150.19$	$I_3 = 503989$
$l_4 = 50$	$s_4 = 25.48$	$m_4 = 24.22$	$I_4 = 7275$
		$m_5 = 67.16$	$I_5 = 4581$
		$m_6 = 782.63$	$I_6 = n/a$

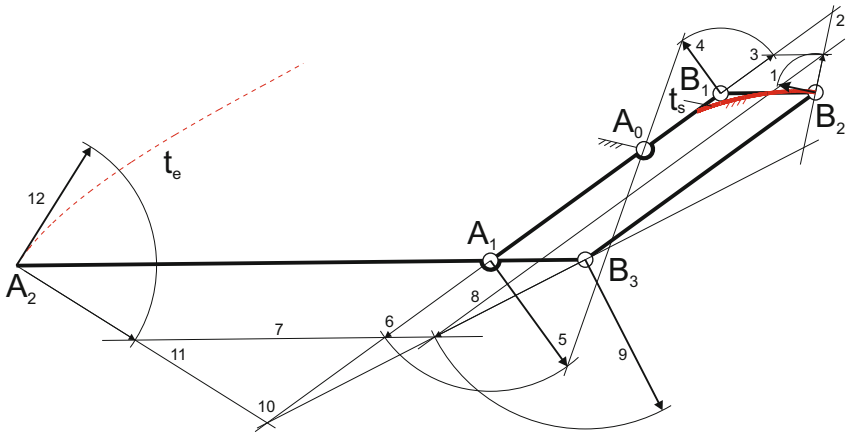


Fig. 2. Graphic analysis of the joint velocities with the velocity in B_2 known.

angle between links B_1A_1 and B_3A_2 of 35.4° and, in green, the retracted pose at the end of the slider trajectory.

The links have lengths l_i as illustrated in Fig. 1 and each of the 4 links has a mass m_i and an inertia I_i about the link center-of-mass (CoM) S_i , which is at a distance s_i from a joint as depicted. In addition, in A_2 there is the CoM S_5 of the end-effector with mass m_5 and inertia I_5 , rigidly mounted on link B_3A_2 , and in B_2 there is the CoM S_6 with mass m_6 , which is the mass of the slider parts and a counterweight together. The inertia of these last parts is not considered since they are solely in translational motion (the slider consists of a pin-in-slot of which the pin is fixed with and included in link B_3B_2 and the piston component that actuates the pin-in-slot motion is moving rectilinearly; the counterweight is a circular disc on the slider pin with negligible friction in between for which it does not rotate). With the values in Table 1 the linkage is completely force balanced and moment balanced, which was verified by a dynamic simulation showing that during motion the common CoM of all elements remains stationary in A_0 and that the sum of the angular momenta of all elements remains zero.

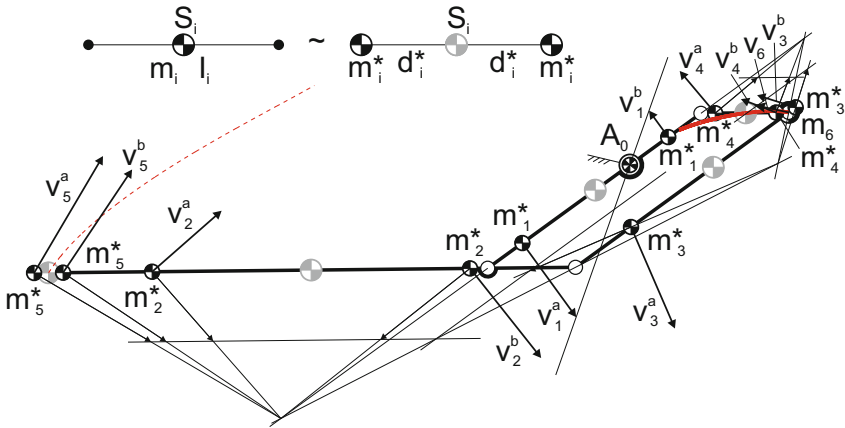


Fig. 3. Velocity analysis of the point masses of a dynamically equivalent model where the mass and inertia of each element are modeled with two equivalent masses.

The first step is the graphic analysis of the joint velocities, which is shown in Fig. 2 following the commonly known approach [8]. The velocity in B_2 is known as starting point and has a direction tangent to the slider trajectory t_s . By rotating it 90° , the intersection (2) with the line through A_1B_1 is found and subsequently intersection (3) and the velocity of B_1 (4) are derived. With the line through A_0 then the velocity of A_1 is obtained (5) which, after 90° rotation (6), determines line (7) which is parallel to line A_1A_2 . The intersection of line (7) with line (8), which is parallel to line B_2B_3 , determines the velocity of B_3 (9). Finally intersection (10) is obtained with which line (11) to A_2 is determined and the velocity in A_2 is found (12). As expected, the velocity vector in A_2 is indeed tangent to the traced end-effector trajectory t_e .

To be able to graphically analyze the angular momentum of the linkage, the mass and inertia of each element are modeled with two equivalent masses. This is the simplest possibility for dynamic equivalent modeling of planar motions for which also more than two equivalent masses can be used [10]. Figure 3 shows the dynamically equivalent model where each mass m_i , except m_6 for which no inertia is involved, has been divided in two equal equivalent masses $m_i^* = m_i/2$ both located at a distance d_i^* from the element CoM S_i , one on each side along the line through the link joints such that S_i is their common CoM. The distances d_i^* are determined by the inertia of the element and are derived from $I_i = 2(m_i^*d_i^{*2})$ as $d_i^* = \sqrt{I_i/m_i}$ with which the model is both mass and inertia equivalent with solely point masses. It is also possible to divide m_i in two different equivalent masses with two different lengths d_i^* or to place the equivalent masses off the line through the link joints which, however, would make the analysis more complicated than needed.

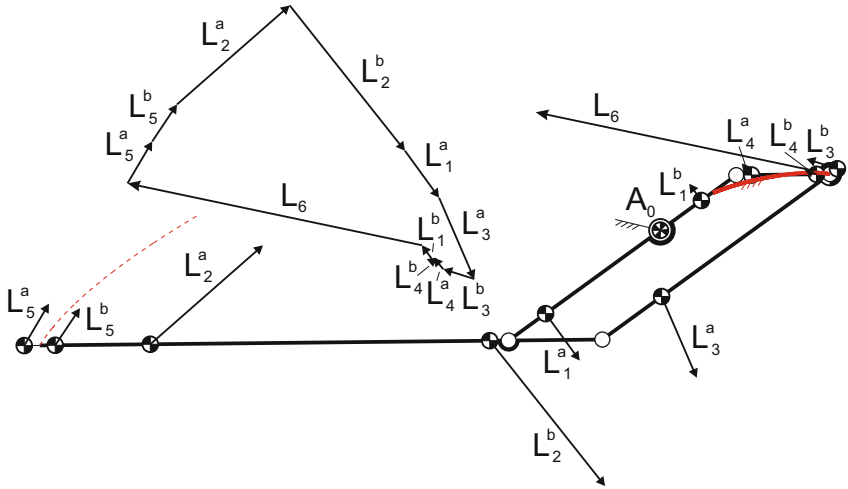


Fig. 4. Linear momentum vectors obtained by multiplying the velocity vectors with the respective mass values. The sum of the linear momentum vectors forms a polygon for force balance.

The velocity analysis of the 11 point masses is also shown in Fig. 3. Continuing with the graphical solution of the joint velocities in Fig. 2, with the instantaneous link centers of rotation the velocities of all point masses are readily obtained. This might contrast with the readability of the illustration of Fig. 3, for which the author apologizes.

The linear momentum of each point mass is obtained when each velocity vector in Fig. 3 is multiplied by its mass value. The resulting linear momentum vectors are shown in Fig. 4 which were obtained by multiplying the length of each velocity vector by its respective value $m_i/100$ with the mass values in Table 1, scaling the vectors to fit within the drawing.

The force balance can now be verified by adding all the linear momentum vectors together, which must form a polygon (i.e. a closed chain) since this means that the sum of the linear momenta of the linkage equals zero. The linear momentum polygon is also shown in Fig. 4.

The angular momentum of the linkage consists of the sum of the moments of the linear momentum vectors about the common CoM in A_0 . The moments of the linear momentum vectors are illustrated in Fig. 5 where each linear momentum vector has been shifted along its line of action to the endpoint of its moment arm. The angular momentum diagram in Fig. 6 is obtained from Fig. 5 when all the linear momentum vectors are rotated such that their moment arms are aligned with the same line u . Then all the linear momentum vectors are oriented vertically, either upwards or downwards.

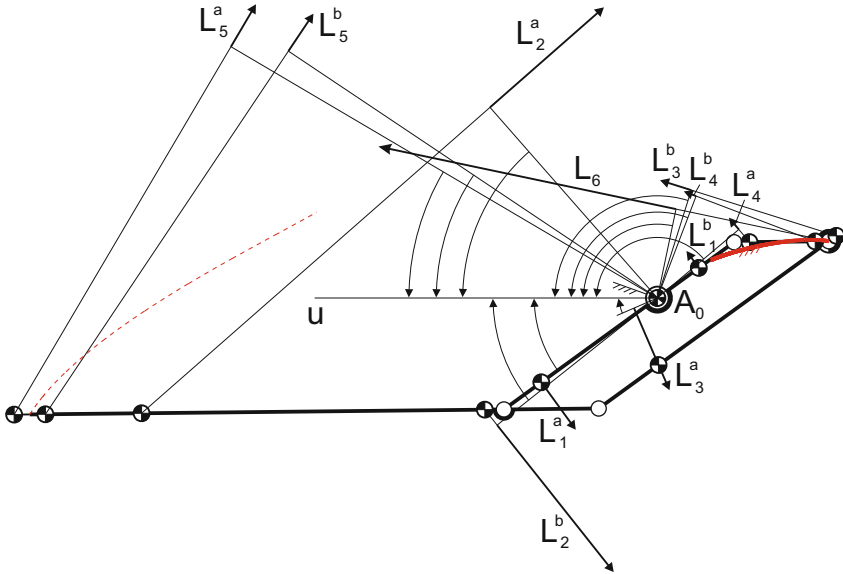


Fig. 5. Representation of the angular momenta of the linkage with the linear momentum vectors and their respective moment arms about the common CoM in A_0 .

The angular momentum of each linear momentum vector can be found by the graphical multiplication of lines for which the shown triangle of reference is used with a height of L_6 and a reference width equal to the moment arm of L_5^a . This results for each linear momentum vector into a diagonal line, which starts at 0 at the location of the vector (i.e. at the end of the moment arm) and crosses the vertical line H through A_0 - the angular momentum axis - at the value of its angular momentum.

For example, when L_2^a is placed in the reference triangle at the location of L_6 , which is shown in green, then the diagonal line of L_2^a is found as the line from the endpoint of L_2^a to the endpoint of the triangle. Subsequently this diagonal line is placed in the diagram at L_2^a on line u and crosses the H -axis in point h , which is the value of the angular momentum of L_2^a .

To sum the resulting angular momentum values, the diagonal lines have been vertically shifted such that each diagonal line starts at the height of the endpoint of the previous diagonal line. Of the upward directed linear momentum vectors the summed angular momentum is shown below A_0 and of the downward directed linear momentum vectors the summed angular momentum is shown above A_0 . For the total sum of the angular momenta to be zero, the part above A_0 must be equal to the part below A_0 , which is verified by the circular arc about A_0 .

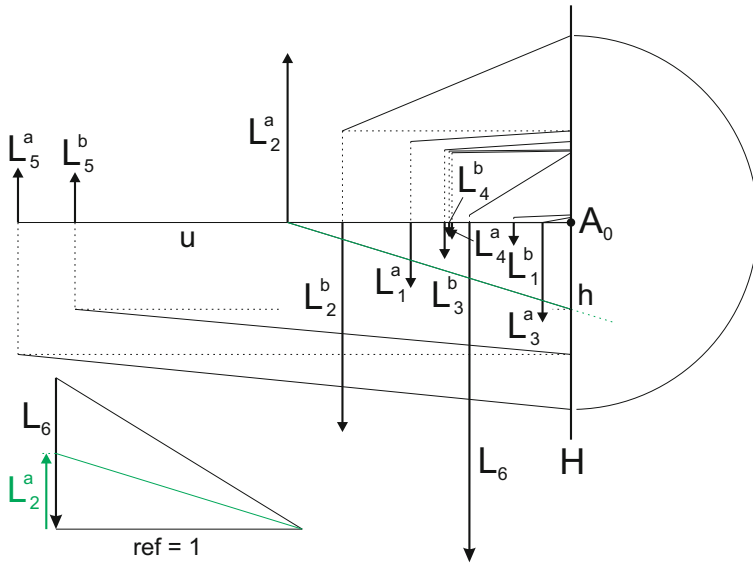


Fig. 6. Angular momentum diagram obtained by rotating all the linear momentum vectors such that their moment arms are aligned with the same line u . The angular momentum of each vector is found by the multiplication of lines with the help of a triangle of reference, gaining diagonal lines that intersect with the vertical angular momentum axis H through A_0 at the angular momentum values. The values of all intersections sum up to zero for moment balance.

3 Conclusions

In this paper it was shown how the linear momentum and the angular momentum of a linkage can be found graphically. As an example this was applied to verify the shaking force balance and the shaking moment balance of a 1-DoF pantographic linkage. The mass and inertia of each linkage element were modeled with two equivalent masses to obtain a dynamically equivalent model with solely point masses. The velocities of the point masses were derived graphically and the linear momenta of the point masses were found by multiplying the velocity vectors with their respective mass values. For force balance it was shown that the sum of the linear momentum vectors form a linear momentum polygon. The angular momentum was presented in an angular momentum diagram and showed to sum up to zero for moment balance. The presented graphical method may be of help to better understand the characteristics of force balance and, in specific, the characteristics of moment balance for the development of a synthesis method for moment balanced mechanisms. Extending the method to linkages with multiple degrees of freedom and to spatial linkages is an interesting next step.

Acknowledgements. This publication was financially supported by the Netherlands Organisation for Scientific Research (NWO, 15146). The author likes to thank Clément Gosselin for the fruitful discussions during the summer and fall of 2018 at Laval University in Quebec City, Canada.

References

1. Arakelian, V.G., Smith, M.R.: Shaking force and shaking moment balancing of mechanisms: a historical review with new examples. *Mech. Des.* **127**, 334–339 (2005)
2. Foucault, S., Gosselin, C.M.: On the development of a planar 3-DoF reactionless parallel mechanism. In: *Proceedings of DETC 2002, ASME* (2002)
3. Lowen, G.G., Berkof, R.S.: Survey of investigations into the balancing of linkages. *Mechanisms* **3**, 221–231 (1968)
4. Van der Wijk, V.: Shaking-moment balancing of mechanisms with principal vectors and momentum. *J. Front. Mech. Eng.* **8**(1), 10–16 (2013)
5. Van der Wijk, V.: Methodology for analysis and synthesis of inherently force and moment-balanced mechanisms - theory and applications (dissertation). University of Twente (2014). <https://doi.org/10.3990/1.9789036536301>
6. Van der Wijk, V.: The grand 4R four-bar based inherently balanced linkage architecture for synthesis of shaking force balanced and gravity force balanced mechanisms. *Mech. Mach. Theory* **150**, 103815 (2020)
7. Van der Wijk, V., Krut, S., Pierrot, F., Herder, J.L.: Design and experimental evaluation of a dynamically balanced redundant planar 4-RRR parallel manipulator. *Int. J. Rob. Res.* **32**(6), 744–759 (2013)
8. Wittenbauer, F.: *Graphische Dynamik*. Julius. Springer, Heidelberg (1923)
9. Wu, Y., Gosselin, C.M.: Design of reactionless 3-DOF and 6-DOF parallel manipulators using parallelepiped mechanisms. *IEEE Trans. Rob.* **21**(5), 821–833 (2005)
10. Wu, Y., Gosselin, C.M.: On the dynamic balancing of multi-dof parallel mechanisms with multiple legs. *Mech. Des.* **129**, 234–238 (2007)



Inverse Dynamics and Simulation of a Parallel Robot Used in Shoulder Rehabilitation

Paul Tucan¹, Nicolae Plitea¹, Calin Vaida¹, Bogdan Gherman¹, Giuseppe Carbone^{1,2},
Iosif Luchian^{1,3}, and Doina Pisla¹ (✉)

¹ CESTER, Technical University of Cluj-Napoca, 400114 Cluj-Napoca, Romania
{paul.tucan,nicolae.plitea,calin.vaida,bogdan.gherman,
iosif.luchian,doina.pisla}@mep.utcluj.ro

² DIMEG, University of Calabria, 97036 Cosenza, Italy
Carbone@unical.it

³ RobotVision S.R.L., Cluj-Napoca, Romania

Abstract. The paper presents the inverse dynamics of a medical parallel robot used for shoulder rehabilitation, namely ASPIRE robot. Using the robot inverse kinematics, the inverse dynamic model of ASPIRE is obtained in a closed form using the principle of virtual work associated with the equivalent dynamic lump masses of the experimental model. In addition, Siemens NX is used to perform the kinematic and dynamic simulation for the parallel robot. The simulation results are compared to those derived from the theoretic inverse dynamic model and the comparison shows the validity of the mathematical model.

Keywords: Parallel robot · Rehabilitation robotics · Inverse dynamics · Virtual work · Simulation

1 Introduction

Stroke is stated to be one of the leading causes of death and most common cause of disability around the world with more than 13 million new cases annually [1]. Worldwide, the average lifetime risk of stroke increased from 22.8% in 1990 up to 24.9% in 2016 [2]. These numbers are preconized to go even higher due to aging of the population and it is stated that in 2030 the European medical system will become unable to provide the medical personnel to help in the rehabilitation of the stroke survivors [3]. The rehabilitation of a stroke survivor is usually performed by a kinetotherapist that helps the patient in regaining the control of the impaired limb by performing repetitive rehabilitations motion of the limb. Due to repetitive nature of the procedure, robotic assisted rehabilitation devices have been largely discussed and implemented in the rehabilitation domain [4–12].

NESM [13] is an exoskeleton used for shoulder and elbow rehabilitation using a mobile platform. The robotic system consists of four active joints and it performs motion of adduction, abduction, flexion, extension, internal rotation and external rotation of the

shoulder and flexion/extension of the elbow. ETS-MARSE [14] is a 7-DOF robotic system for the rehabilitation of the upper limb. The robot uses 3 active revolute joints to perform the shoulder rehabilitation, one active revolute joint for the elbow flexion and extension, and another 3 active revolute joints for the pronation/supination of the forearm, radial/ulnar deviation and flexion/extension of the wrist. ParReEx [15] is a parallel robotic system for elbow and wrist rehabilitation. The robot consists of two modules: one 2-DOF module for elbow rehabilitation able to perform the flexion/extension of the elbow and pronation/supination of the forearm, and another 2-DOF module for flexion, extension, adduction and abduction of the wrist.

All the above rehabilitation systems have the similarity that during the rehabilitation motion the patient is directly attached to the mechanical structure of the system. This aspect implies that an extra attention should be paid to the safety of the patient during the procedure. A safe behavior of a robotic structure may be achieved through a complete understanding of the robotic structure from geometric, kinematic and dynamic point of view. For an efficient and robust control of the robot during the rehabilitation procedure the inverse dynamic model is necessary to be implemented in the control system of the robot. Jezernik et al. [16] uses inverse dynamics representation via minimization of the interaction forces to study the dynamic behavior of a rehabilitation robot during the procedure. Abdellatif and Heiman [17] use the Lagrangian formalism applied to a 6 DOF parallel manipulator in order to derive the dynamics of close-loop chains of the manipulators. Plitea [18] uses the virtual work principle to compute the inverse dynamics of a 5-DOF modular parallel medical robot. The virtual work principle used in the determination of the inverse dynamics has a high efficiency because it can eliminate forces and internal joints in order to straight forward determine the forces or torques of the robot.

This paper presents the inverse dynamic model of a parallel robot used in shoulder rehabilitation using the virtual work method. The inverse dynamic model is computed in order to validate the safe behavior of the robotic structure during the rehabilitation procedure. The inverse dynamic model is validated by comparing results of the numerical simulation of the analytical model in MATLAB compared with the results of the kinematic and dynamics simulation of the experimental model using Siemens NX. The second section of the paper presents the innovative parallel robot for shoulder rehabilitation, followed by 3rd section which describes the inverse dynamic model of the structure followed in Sect. 4 by the validation of the inverse dynamic model. The conclusions of the work are presented in the 5th section.

2 Innovative Parallel Robot for Shoulder Rehabilitation

ASPIRE is a parallel robotic structure for shoulder rehabilitation, with modular construction and is presented in Fig. 1 [8, 19]. First module of ASPIRE is a 3DOF relatively simple spherical mechanism that complies with the rehabilitation task by performing the flexion, extension, adduction, abduction, pronation and supination of the shoulder. The second module is a serial mechanism that allows the vertical repositioning of the entire robot in order to fit various anthropomorphic characteristics of patients. The mechanism is actuated by translational active joint q_4 and it is used before the medical procedure

in the set-up phase of the robot. The coordinate system of the robotic structure OXYZ is placed in the center of the spherical defined motion having the Z axis aligned vertically (parallel with the longitudinal plane of the patient) and the Y axis parallel with the coronal plane of the patient. The spherical mechanism is composed of two circular guides (G_1 and G_2) that constrain the motion of the final link to a motion on the surface of a sphere of radius R . The mechanism is actuated by two revolute active joints (q_1 and q_2). Joint q_1 moves the circular guide G_1 that slides along circular guide G_2 in order to obtain the flexion and extension motion of the shoulder, in the same time q_2 moves the circular guide G_2 that slides along G_1 to obtain the adduction and abduction motion of the shoulder. The passive revolute joint r_f is necessary to allow motion of both slides in the same time. The 3rd DOF is q_3 axis, a revolute active joint that allows the pronation and supination of the forearm mechanism, it is an independent axis that does not affect the kinematics of the spherical mechanism.

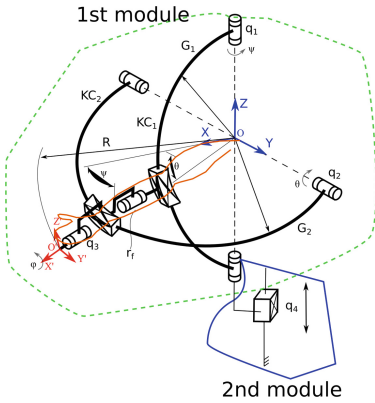


Fig. 1. Kinematic scheme of ASPIRE

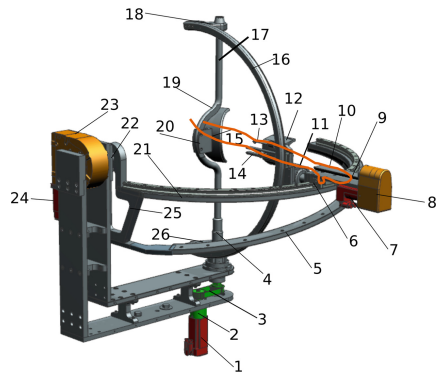


Fig. 2. ASPIRE experimental model

According to the Fig. 1 the inverse kinematics of the ASPIRE robotic structure was analyzed [19]. The motion of the robot can be described using two rotations: one rotation around OZ axis, namely R_1 with the angle ψ and the other one around OY namely R_2 with the angle θ . The center of the sphere is defined as $O(0,0,0)$ and the initial position of the human arm is as $U_0 = [R \ 0 \ 0]$. The final correspondence between θ , ψ and the ASPIRE active joints is:

$$\begin{cases} q_1 = \text{atan2}(\sin(\psi), \cos(\psi)) \\ q_2 = \text{atan2}(\sin(\theta), \cos(\theta)) \end{cases} \quad (1)$$

3 The Inverse Dynamic Model of ASPIRE

The definition of virtual work principle states that a mechanism is under dynamic equilibrium only if the total virtual work developed by all external, internal and inertia forces vanish during any virtual displacement [8]. The inputs of the inverse dynamic algorithm

are the motion laws of the last link of the robot, the inverse kinematic model of the robot and the masses of the robot elements while the outputs are the forces/torques at the level of actuators. In order to determine the inverse dynamic model, the following moving elements of the robot have been considered (Fig. 2): (1) is the motor of q_1 axis of mass M_1 , (2) is the gear box of (1) having the mass M_2 , (3) and (8) are the timing-belts of q_1 and q_3 with the mass M_3 , (4) is the first part of the vertical shaft with mass M_4 , (5) is lower part of G_2 circular guide with the mass M_5 , (6) is the element sliding along (21) with mass M_6 , (7) is the motor of q_3 with the mass of M_7 , (9) is the support for the q_3 motor with mass M_9 , (10) is the patient palm support with mass M_{10} , (11) is the revolute joint between the circular guides with mass M_{11} , (12) is the forearm rest with the mass M_{12} , (13) is the sliding rod for the forearm rest with mass M_{13} , (14) is the adjustment mechanism for the forearm rest with mass M_{14} , (15) is the shoulder rest with mass M_{15} , (16) is the G_1 circular guide with mass M_{16} , (17) is the upper part of the vertical shaft with mass M_{17} , (18) and (26) are the connecting elements of the vertical shaft with mass M_{18} , (19) is the circular part of the vertical shaft with mass M_{19} , (20) is the connector of the shoulder rest with mass M_{20} , (21) is the upper part of the slide G_2 with mass M_{21} , (22) is the shaft of gearbox (23) of motor (24) with mass M_{22} , M_{23} respectively M_{24} and (25) is the support of the circular guide G_2 with mass M_{25} . In order to develop the inverse dynamic model, two simplifying hypotheses were used: use of lumped masses and neglectation of friction forces. For using the masses of the moving components, a simple way is to concentrate them into one or several points of the component (e.g. a bar of length l and mass M has the dynamic equivalent of three points, two of equal mass, placed at the ends of the bar computed $m_A = m_B = 1/6 \cdot M$, and the point in the middle is computed using $m_C = 2 \cdot M/3$). For the components of ASPIRE structure, 41 equivalent masses resulted (Fig. 3).

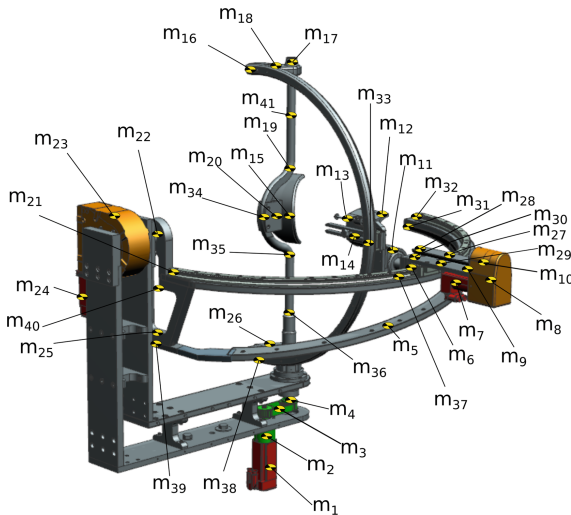


Fig. 3. Concentrated masses of ASPIRE elements

$$\begin{aligned}
 m_1 &= M_1; \quad m_2 = M_2; \quad m_3 = M_3; \quad m_4 = m_{35} = M_4/6; \quad m_5 = 2 \cdot M_5/3; \quad m_6 = M_6; \quad m_7 = M_7; \\
 m_8 &= M_3; \quad m_9 = m_{30} = M_9/6; \quad m_{10} = m_{28} = M_{10}/6; \quad m_{11} = M_{11}; \quad m_{12} = M_{12}; \quad m_{13} = M_{13}; \\
 m_{14} &= M_{14}; \quad m_{15} = M_{15}; \quad m_{16} = m_{38} = M_{16}/6; \quad m_{17} = m_{19} = M_{17}/6; \quad m_{18} = m_{26} = M_{18}; \\
 m_{20} &= M_{20}; \quad m_{21} = m_{32} = M_{21}/6; \quad m_{22} = M_{22} + M_{25}/6; \quad m_{23} = M_{23}; \quad m_{24} = M_{24}; \\
 m_{25} &= M_{25}/6; \quad m_{27} = 2 \cdot M_{10}/3; \quad m_{29} = 2 \cdot M_9/3; \quad m_{31} = m_{39} = M_5/6; \quad m_{33} = 2 \cdot M_{16}/3; \\
 m_{36} &= 2 \cdot M_4/3; \quad m_{40} = 2 \cdot M_{25}/3; \quad m_{41} = 2 \cdot M_{17}/3
 \end{aligned}
 \tag{2}$$

The coordinates of the concentrated mass points are given in Eq. 3 (Fig. 4).

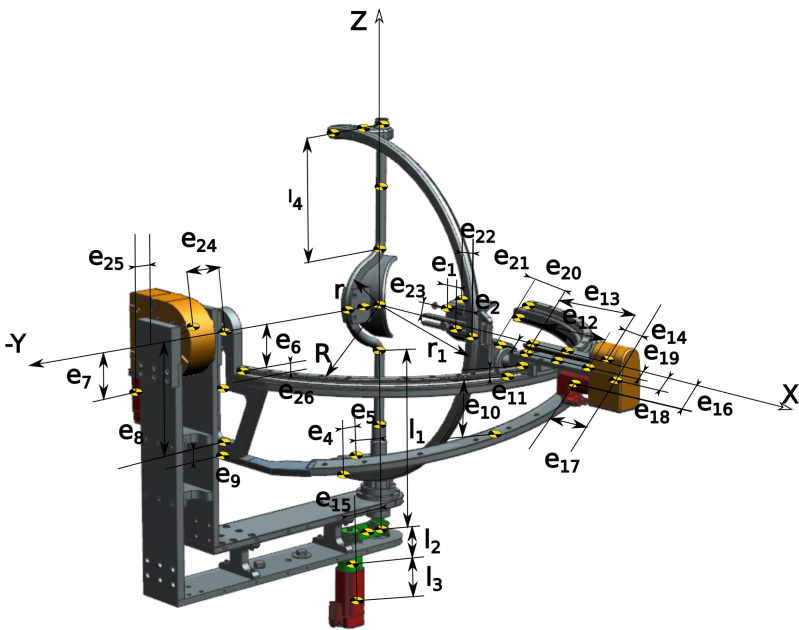


Fig. 4. Geometric parameters of ASPIRE

$$\begin{cases} X_1=0 \\ Y_1=e_{15} \\ Z_1=-(r+1+1_2+1_3) \end{cases} \begin{cases} X_2=0 \\ Y_2=e_{15} \\ Z_2=-(r+1+1_2) \end{cases} \begin{cases} X_3=0 \\ Y_3=e_{15}/2 \\ Z_3=-(r+1) \end{cases} \begin{cases} X_4=0 \\ Y_4=0 \\ Z_4=(-r+1) \end{cases} \begin{cases} X_5=\cos(q_2) \cdot R \cdot e_{10} \\ Y_5=0 \\ Z_5=\sin(q_2) \cdot R \cdot e_{10} \end{cases} \\
 \begin{cases} X_6=R \cdot \sin(q_1) \\ Y_6=\sqrt{R^2-X_6^2} \\ Z_6=\sin(q_2) \cdot R \cdot (e_6+e_{11}) \end{cases} \begin{cases} X_7=(R+e_{13}+e_{14}-e_{17}) \cdot \sin(q_1) \\ Y_7=\sqrt{(R+e_{13}+e_{14}-e_{17})^2-X_7^2} \\ Z_7=(R+e_{13}+e_{14}-e_{17}) \cdot \sin(q_2) \cdot e_{16} \end{cases} \begin{cases} X_8=(R+e_{13}+e_{14}) \cdot \sin(q_1) \\ Y_8=\sqrt{(R+e_{13}+e_{14})^2-X_8^2} \\ Z_8=(R+e_{13}+e_{14}) \cdot \sin(q_2) \cdot e_{19} \end{cases} \\
 \begin{cases} X_9=(R+e_{12}) \cdot \sin(q_1) \\ Y_9=\sqrt{(R+e_{12})^2-X_9^2} \\ Z_9=(R+e_{12}) \cdot \sin(q_2) \cdot e_{19} \end{cases} \begin{cases} X_{10}=(R+e_{13}) \cdot \sin(q_1) \\ Y_{10}=\sqrt{(R+e_{13})^2-X_{10}^2} \\ Z_{10}=(R+e_{13}) \cdot \sin(q_2) \end{cases} \begin{cases} X_{11}=(R-e_{20}) \cdot \sin(q_1) \\ Y_{11}=\sqrt{(R-e_{12})^2-X_{11}^2} \\ Z_{11}=(R+e_{12}) \cdot \sin(q_2) \cdot e_{21} \end{cases} \\
 \begin{cases} X_{12}=(r_1-e_{22}) \cdot \sin(q_1) \\ Y_{12}=\sqrt{(r_1-e_{22})^2-X_{12}^2} \\ Z_{12}=(r_1+e_{22}) \cdot \sin(q_2) \end{cases} \begin{cases} X_{13}=(r_1-(e_2+e_1)) \cdot \sin(q_1) \\ Y_{13}=\sqrt{(r_1-(e_2+e_1))^2-X_{13}^2} \\ Z_{13}=(r_1-(e_2+e_1)) \cdot \sin(q_2) \end{cases} \begin{cases} X_{14}=(r_1-e_{22}) \cdot \sin(q_1) \\ Y_{14}=\sqrt{r_1^2-X_{14}^2} \\ Z_{14}=(r_1-e_{22}) \cdot \sin(q_2) \end{cases} \begin{cases} X_{15}=0 \\ Y_{15}=0 \\ Z_{15}=0 \end{cases} \\
 \begin{cases} X_{16}=(e_5+e_4) \cdot \cos(q_1+\pi/2) \\ Y_{16}=(e_5+e_4) \cdot \sin(q_1+\pi/2) \\ Z_{16}=r+1_4 \end{cases} \begin{cases} X_{17}=0 \\ Y_{17}=0 \\ Z_{17}=r+1_4 \end{cases} \begin{cases} X_{18}=(e_5) \cdot \cos(q_1+\pi/2) \\ Y_{18}=(e_5) \cdot \sin(q_1+\pi/2) \\ Z_{18}=r_1 \end{cases} \begin{cases} X_{19}=0 \\ Y_{19}=0 \\ Z_{19}=r \end{cases} \\
 \begin{cases} X_{20}=(r/2) \cdot \cos(q_1+\pi/2) \\ Y_{20}=(r/2) \cdot \sin(q_1+\pi/2) \\ Z_{20}=0 \end{cases} \begin{cases} X_{21}=e_6 \cdot \sin(\pi/2-q_2) \\ Y_{21}=R \\ Z_{21}=e_6 \cdot \cos(\pi/2-q_2) \end{cases} \begin{cases} X_{22}=0 \\ Y_{22}=R \\ Z_{22}=0 \end{cases} \begin{cases} X_{23}=0 \\ Y_{23}=R+e_{24} \\ Z_{23}=0 \end{cases} \\
 \begin{cases} X_{24}=-e_{25} \\ Y_{24}=R+e_{24} \\ Z_{24}=-e_7 \end{cases} \begin{cases} X_{25}=e_8 \cdot \sin(\pi/2-q_2) \\ Y_{25}=R \\ Z_{25}=e_8 \cdot \cos(\pi/2-q_2) \end{cases} \begin{cases} X_{26}=(e_5) \cdot \cos(q_1+\pi/2) \\ Y_{26}=(e_5) \cdot \sin(q_1+\pi/2) \\ Z_{26}=r_1 \end{cases} \begin{cases} X_{27}=(R+e_{13}/2) \cdot \sin(q_1) \\ Y_{27}=\sqrt{(R+e_{13}/2)^2-X_{27}^2} \\ Z_{27}=(R+e_{13}/2) \cdot \sin(q_2) \end{cases} \\
 \begin{cases} X_{28}=R \cdot \sin(q_1) \\ Y_{28}=\sqrt{R^2-X_{28}^2} \\ Z_{28}=R \cdot \sin(q_2) \end{cases} \begin{cases} X_{29}=(R+e_{12}/2) \cdot \sin(q_1) \\ Y_{29}=\sqrt{(R+e_{12}/2)^2-X_{29}^2} \\ Z_{29}=(R+e_{12}/2) \cdot \sin(q_2) \cdot e_{19} \end{cases} \begin{cases} X_{30}=R \cdot \sin(q_1) \\ Y_{30}=\sqrt{R^2-X_{30}^2} \\ Z_{30}=R \cdot \sin(q_2) \cdot e_{19} \end{cases} \\
 \begin{cases} X_{31}=(e_6+e_{26}) \cdot \sin(\pi/2-q_2) \\ Y_{31}=-R \\ Z_{31}=(e_6+e_{26}) \cdot \cos(\pi/2-q_2) \end{cases} \begin{cases} X_{32}=(e_6) \cdot \sin(\pi/2-q_2) \\ Y_{32}=-R \\ Z_{32}=(e_6) \cdot \cos(\pi/2-q_2) \end{cases} \begin{cases} X_{33}=r_1 \\ Y_{33}=0 \\ Z_{33}=0 \end{cases} \begin{cases} X_{34}=r \cdot \cos(q_1+\pi/2) \\ Y_{34}=r \cdot \sin(q_1+\pi/2) \\ Z_{34}=0 \end{cases} \\
 \begin{cases} X_{35}=0 \\ Y_{35}=0 \\ Z_{35}=r \end{cases} \begin{cases} X_{36}=0 \\ Y_{36}=0 \\ Z_{36}=(-r+1)/2 \end{cases} \begin{cases} X_{37}=\cos(q_2) \cdot R \\ Y_{37}=0 \\ Z_{37}=\sin(q_2) \cdot R \end{cases} \begin{cases} X_{38}=(e_4) \cdot \cos(q_1+\pi/2) \\ Y_{38}=(e_4) \cdot \sin(q_1+\pi/2) \\ Z_{38}=r_1 \end{cases} \\
 \begin{cases} X_{39}=(e_8+e_9) \cdot \sin(\pi/2-q_2) \\ Y_{39}=R \\ Z_{39}=(e_8+e_9) \cdot \cos(\pi/2-q_2) \end{cases} \begin{cases} X_{40}=(e_8+e_9)/2 \cdot \sin(\pi/2-q_2) \\ Y_{40}=R \\ Z_{40}=(e_8+e_9)/2 \cdot \cos(\pi/2-q_2) \end{cases} \begin{cases} X_{41}=0 \\ Y_{41}=0 \\ Z_{41}=(r+1_4)/2 \end{cases}
 \end{cases} \tag{3}$$

Following the principle of the virtual displacements, the virtual work is defined using $\delta W = \delta q^T \cdot \tau + \sum_{i=1}^{41} \delta X_{Mi}^T \cdot (T_i^{Tr} + T_i^g) = 0$, $i = 1 \div 41$. Where $\delta q^T \cdot \tau$ is the virtual work of all actuating forces and torques ($\tau = [\tau_1, \tau_2]$) and $\sum_{i=1}^{41} \delta X_i^T \cdot (T_i^{Tr} + T_i^g)$ represents the sum of the virtual work computed from the inertial and gravitational forces of the equivalent system divided into 41 lumped masses. The matrices of the inertial and gravitational forces are:

$$T_i^{Tr} = - \begin{bmatrix} m_i^* & 0 & 0 \\ 0m_i^* & 0 & \\ 0 & 0 & m_i^* \end{bmatrix} \begin{bmatrix} \ddot{X}_i \\ \ddot{Y}_i \\ \ddot{Z}_i \end{bmatrix}; T_i^{Tr} = \begin{bmatrix} -m_i^* \ddot{X}_i \\ -m_i^* \ddot{Y}_i \\ -m_i^* \ddot{Z}_i \end{bmatrix}; T_i^g = \begin{bmatrix} 0 \\ 0 \\ -m_i^* g_i \end{bmatrix}, i = 1 \div 41 \quad (4)$$

The velocity vector of the 41 lumped masses is computed using equation $\dot{X}_{PE} = J_E \cdot \dot{q}$, $\dot{X}_{mi} = J_i \cdot \dot{q}$, $i = 1 \div 41$. The acceleration vector: $\ddot{X}_{PE} = J_E \cdot \ddot{q} + \dot{J}_E \cdot \dot{q}$, $\ddot{X}_{mi} = J_i \cdot \ddot{q} + \dot{J}_i \cdot \dot{q}$, $i = 1 \div 41$, and the virtual displacement is defined for the 41 lumped masses using: $\delta X_{mi} = J_i \cdot \delta q$, $i = 1 \div 41$ and its transpose $\delta X_{mi}^T = \delta q^T \cdot J_i^T$, $i = 1 \div 41$. By substituting the above equations in the expression of the virtual work it yields to $\delta W = \delta q^T \cdot \tau - \sum_{i=1}^{41} \delta q^T \cdot J_i^T \cdot M_i \cdot (\ddot{X}_{mi} + v_g) = 0$ and by simplifying, the actuator torque vector is obtained: $\tau = J \cdot M \cdot \ddot{q} (X + v)$.

4 Simulation Results and the Inverse Dynamic Model Validation Using Siemens NX

In order to validate the theoretic inverse dynamic model of ASPIRE, a flexion/extension and an adduction/abduction rehabilitation motion were selected and given as inputs of the numerical simulation using MATLAB [21] and in the same time of the graphical simulation using the experimental model of ASPIRE developed in Siemens NX disabling the friction forces and enabling the gravitation during the simulation. For the simulation of the flexion/extension motion the motion was $[-50^\circ, 50^\circ]$, while for the adduction abduction the motion $[-42^\circ, 68^\circ]$ was used.

Using isolated rehabilitation motions (flexion/extension and adduction/abduction) only axis q_1 and q_2 were moved one at a time while the axis q_3 remained still recording zero motion and was excluded from the graphical representation. The obtained results from both simulations were overlapped in a graphical representation (Fig. 5) showing good correlation between the curves of the torques obtained in NX and the ones obtained in MATLAB and in the same time the maximum error between from the two approaches was 8.17% for the first trajectory and 6.78% for the second trajectory, validating the mathematical dynamic model of the ASPIRE parallel robot. The experimental model of ASPIRE is presented in Fig. 6.

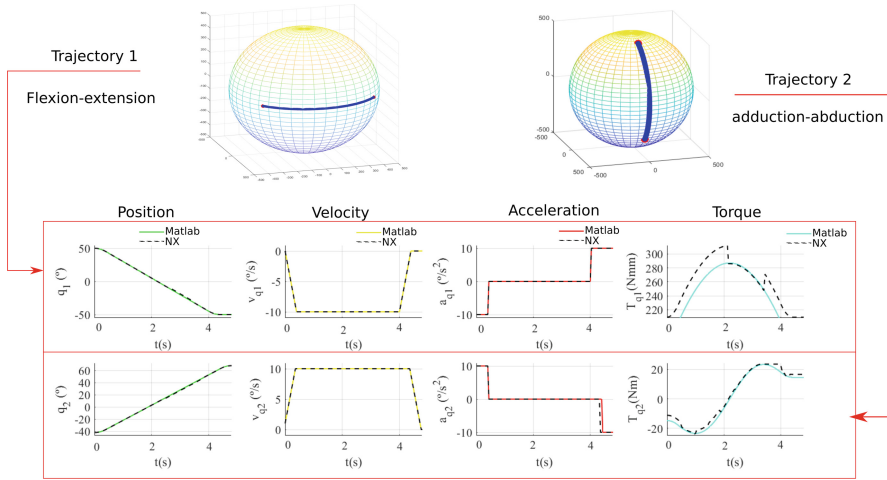


Fig. 5. Simulation results of the rehabilitation motion (trajectory 1 and trajectory 2)



Fig. 6. The experimental model of ASPIRE

5 Conclusions

The paper presents the inverse dynamics of a parallel robot for shoulder rehabilitation. The inverse dynamic model of the robot was determined using the virtual work principle with equivalent mass of the components. The inverse dynamic model was validated by simulating real rehabilitation motions (flexion/extension, adduction/abduction) in two virtual environments and by comparing the results obtained from both simulations. An analytical solution of the invers dynamic model was finally obtained in a fast computing

algorithm enabling its easy implementation in the control system of the robot. The developed dynamic model will be used in the control of ASPIRE for the implementation of assistive and passive-assistive strategies.

Acknowledgments. The paper presents results from the research activities of the project POCU/380/6/13/123927 – ANTREDOC, “Entrepreneurial competencies and excellence research in doctoral and postdoctoral studies programs”, project co-funded from the European Social Fund through the Human Capital Operational Program 2014–2020 and the project ID 37_215, MySMIS code 103415 “Innovative approaches regarding the rehabilitation and assistive robotics for healthy ageing” cofinanced by the European Regional Development Fund through the Competitiveness Operational Program 014–2020, Priority Axis 1, Action 1.1.4, through the financing contract 20/01.09.2016, between the Technical University of Cluj-Napoca and ANCSI as Intermediary Organism in the name and for the Ministry of European Funds.

References

1. Lindsay, M.P., et al.: World stroke organization (WSO): global stroke fact sheet 2019. *Int. J. Stroke* **14**(8), 806–817 (2019)
2. Virani, S.S., et al.: Heart disease and stroke statistics-2020 update: a report from the American heart association. *Circulation* **141**, e1–e458 (2020)
3. Multi-Annual Roadmap for Robotics in Europe, Robotics (2016)
4. Vaida, C., Birlescu, I., Pisla, A., Ulinici, I.M., Tarnita, D., Carbone, G., Pisla, D.: Systematic design of a parallel robotic system for lower limb rehabilitation. *IEEE Access* **8**, 34522–34537 (2020)
5. Carbone, G., Gherman, B., Ulinici, I., Vaida, C., Pisla, D.: Design issues for an inherently safe robotic rehabilitation device. In: Ferraresi, C., Quaglia, G., (eds.) *Advances in Service and Industrial Robotics. (RAAD 2017). Mechanisms and Machine Science*, vol. 49, pp. 1025–1032. Springer, Basel, Switzerland (2017)
6. Franceschini, M., et al.: Upper limb robot-assisted rehabilitation versus physical therapy on subacute stroke patients: a follow-up study. *J. Bodyw. Mov. Ther.* **24**(1), 194–198 (2019)
7. Major, K.A., Major, Z.Z., Carbone, G., Pisla, A., Vaida, C., Gherman, B., Pisla, D.: Ranges of motion as basis for robot-assisted post-stroke rehabilitation. *Hum. Vet. Med.* **8**, 192–196 (2016)
8. Plitea, N., Vaida, C., Carbone, G., Pisla, A., Ulinici, I., Pisla, D.: On the kinematics of an innovative spherical parallel robot for the shoulder rehabilitation. In: Carvalho, J., Martins, D., Simoni, R., Simas, H., (eds.) *Multibody Mechatronic Systems. (MuSMe 2017). Mechanisms and Machine Science*, vol. 54, pp. 464–473. Springer, Basel, Switzerland (2017)
9. Tucan, P., Vaida, C., Plitea, N., Pisla, A., Carbone, G., Pisla, D.: Risk- based assessment engineering of a parallel robot used in post-stroke upper limb rehabilitation. *Sustainability* **11**(10), 1–28 (2019)
10. Tarnita, D., et al.: Static and dynamic analysis of osteoarthritic and orthotic human knee. *J. Bionic Eng.* **16**, 514–525 (2019)
11. Gherman, B., et al.: On the singularity-free workspace of a parallel robot for lower limb rehabilitation. *Proc. Rom. Acad.* **20**(4), 383–391 (2019)
12. Berceanu, C., Tarnita, D.: Aspects regarding the fabrication process of a new fully sensorized artificial hand. In: *Proceedings of the International Conference ModTech, (MODTECH 2010). New face of TMCR*, pp. 123–126 (2010)

13. Trigili, E., et al.: Design and characterization of a shoulder-elbow exoskeleton with compliant joints for post-stroke rehabilitation. *IEEE ASME Trans. Mechatron.* **24**, 1485–1496 (2017)
14. Brahmi, B., Saad, M., Rahman, M.H., Ochoa-Luna, C.: Cartesian trajectory tracking of a 7-DOF exoskeleton robot based on human inverse kinematics. *IEEE Trans. Syst. Man Cybern. Syst.* **49**, 600–611 (2019)
15. Birlescu, I., Pisla, D., Gherman, B., Pisla, A., Vaida, C., Carbone, C., Plitea, N.L.: On the singularities of a parallel robotic system used for elbow and wrist rehabilitation. In: Lenarcic, J., Parenti-Castelli, V., (eds.) *Advances in Robot Kinematics. (ARK 2018)*. Proceedings of the International Symposium on Advances in Robot Kinematics, 1–5 July 2018, Bologna, Italy, vol. 8, pp. 203–211. Springer, Cham, Switzerland (2018)
16. Jezernik, S., Colombo, G., Morari, M.: Automatic gait-pattern adaptation algorithms for rehabilitation with a 4-DOF robotic orthosis. *IEEE Trans. Robot. Autom.* **20**(3), 574–582 (2004)
17. Abdellatif, H., Heiman, B.: Computational efficient inverse dynamics of a 6-DOF fully parallel manipulator by using the Lagrangian formalism. *Mech. Mach. Theory* **44**(1), 192–207 (2009)
18. Plitea, N., Szilaghyi, A., Cocorean, D., Vaida, C., Pisla, D.: Inverse dynamics and simulation of a 5-DOF modular parallel robot used in brachytherapy. *Proc. Rom. Acad. Ser. A* **17**(10), 67–75 (2016)
19. Vaida, C., Plitea, N., Pisla, D., Carbone, G., Gherman, B., Ulinici, I.: Spherical Robot For Medical Recovery Of Upper Limb Proximal Area, patent no. RO132233-A0
20. Lanczos, C.: *The Variational Principles of Mechanics*. Dover Publication INC, New York (1986)
21. MATLAB Homepage. <https://www.mathworks.com/>. Accessed 25 Jan 2020



Periodic Walking Motion of a Humanoid Robot Based on Human Data

Anne Kalouguine^{1,2}, Christine Chevallereau¹, Sébastien Dalibard²,
and Yannick Aoustin¹(✉)

¹ Ecole Centrale de Nantes, Université de Nantes, CNRS, LS2N,
44000 Nantes, France

{anne.kalouguine, christine.chevallereau, Yannick.Aoustin}@ls2n.fr

² SoftBank Robotics, 43, Rue du Colonel Pierre Avia, 75015 Paris, France
{anne.kalouguine, sebastien.dalibard}@softbankrobotics.com

Abstract. Human walking has been intensely studied, but it is difficult to reproduce on humanoid robots that maintain awkward movements. Three main difficulties exist. (i) Different joint kinematics and size between humans and robots. (ii) A rolling motion of the foot which is often impossible to execute with humanoid robots that walk with their feet flat. (iii) A difference in the dynamic model of a robot compared to a human that makes a copy of a human movement lead to unstable walking. In order to take into account the first two difficulties, the specifications for reproducing human movements are adjusted. To ensure stability, a previously developed dynamic model called *Essential Model* is used. The zero moment point (ZMP) is imposed, and the horizontal evolution of the centre of mass (CoM) is computed to satisfy the ZMP.

Keywords: Humanoid robot · Human-like walking · Center of mass · Zero moment point · Essential model

1 Introduction

Humanoid robots are complex mechatronic machines due to their numerous degrees of freedom, physical characteristics such as their weight, the limitations of their actuators, the unilateral constraints with the ground etc. To design walking motions is a complex challenge [1]. To overcome these difficulties, many researchers define the walking motions by using the linear inverted pendulum (LIP) model [2]. This model is efficient to obtain walking motions, but the resulting gait is not very human-like and the dynamic influence of the different bodies of the humanoid robot is not taken into account. Several approaches to imitate the human motion have been developed. For example a walking gait based on human-like virtual constraints has been investigated in [3] for the robot Nao. Sakka, who carried out a work about the imitation of human motion with Nao, also performed this type of study [4]. However, their approach does not consider the constraints on the ZMP trajectory, which are essential for stability.

The purpose of this work is to design a periodic walking motion with single support (SS) and double support (DS) phases, which is based on the *Essential model* [5] for Romeo - a humanoid robot with $n = 31$ generalized coordinates. The trajectory of the ZMP is imposed, the horizontal position of the CoM is free to adapt to the ZMP evolution. The CoM is thus computed from this ZMP evolution. The original contribution is that the remaining $n - 2$ generalized coordinates are prescribed by using trajectories inspired from human walking data. The recorded human motions are approximated by sinusoidal functions of time.

The paper is outlined as follows. The main characteristics of human walking are presented in Sect. 2. A reference walking motion based on human data is presented in Sect. 3. This section highlights the necessity of the *Essential model*, which is then detailed in Sect. 4. The cyclic walking motion is stated in Sect. 5. Numerical results are analyzed in Sect. 6. Section 8 offers our conclusions and perspectives.

2 Study of Human Walking

Duration of Different Phases: Human walking can be decomposed according to important events that occur during the walking. A gait cycle consists of two steps. The duration of different phases is measured as a percentage of a cycle duration. The percentage of DS phase varies from 9 to 17% depending on the age and velocity of the human [6] (Fig. 1).

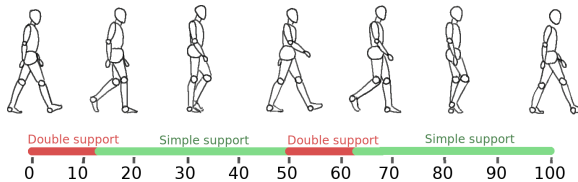


Fig. 1. SS and DS phases duration, measured as percentage of complete cycle.

Step Placement: The step length and width vary widely depending on morphology and age. For a young healthy adult the step length varies widely (from 0.40 to 0.80 m for larger velocities), same as the step width (from 0.125 to 0.22 m, with width decreasing for larger velocities) [6, 7].

CoM Trajectory: Human CoM trajectory is close to a sinus in longitudinal, transverse and vertical directions [6]. The magnitude and period of oscillations in transverse direction vary with speed [8]. In vertical direction the magnitude of the oscillations increases with velocity and is equal to about 2% of body height.

ZMP Trajectory: The ZMP (Zero Moment Point) goes from the heel to the tip of each foot [9], which corresponds to the rolling motion of the feet and the

mobility of the human sole. The trajectory of the ZMP changes depending on the footwear of the human [10].

Swing Foot Motion: The motion of the swing foot can be separated in two components, the trajectory of the swing foot as a whole and the orientation of the sole. We observe nearly vertical landing and takeoff trajectories, with most of the horizontal movement performed in the middle of SS.

Trunk Motion: The trunk, which represents 60% of the weight, has significant angular oscillations [11]: in the saggital plane, the amplitude is of about 2° around the equilibrium position (which varies with the walking velocity but is typically between 5 and 13° , leaning forward). In the frontal plane, the oscillations amplitude varies from 3 to 6° depending on the velocity.

Hip Motion: The oscillations of the hip and the basin allow to make bigger steps, to smoothen the trajectory of the CoM. The amplitude of the oscillations around the vertical axis is of about 10° [6].

Arm Swing: The arm swing in human locomotion is speculated to be useful to reduce the contact wrench on the support foot, as well as the global cost of walking [12, 13].

3 Human Trajectory and Humanoid Robot

Once the human trajectories are found, they can be applied to a humanoid robot. However, that does not give a viable walking motion. Romeo is a prototype platform issued by company Softbank Robotics, see Fig. 3 a). It is 1m 47 tall, weighs 36kg and features 31 degrees of freedom groups into the configuration vector q . The duration of the DS phase is chosen to be close to 12% of the cycle duration $2 \cdot T$, where $T = T_{DS} + T_{SS}$, $T_{DS} = 0.15$ s and $T_{SS} = 0.60$ s are the durations of the DS phase and SS phases. It is impossible to achieve a step size of 0.75 m as what is observed for humans, because the pelvic rotation and rolling motion of the stance foot is necessary for these larger steps, see [14]. It is necessary to adapt the parameters of trajectories for Romeo. The step width is chosen to be 0.20 m to satisfy a safe clearance between Romeo's ankles. The step length is chosen in the range 0.15 to 0.20 m, which corresponds to a 0.30–0.40 m displacement of the swing foot and a velocity of 0.83 to 1.1 km/h. A summary of the other adaptations is shown in the following Table 1. We approximate most periodic functions by a sinus to have a simple model that is infinitely differentiable.

Once we have adapted the human walking motion to the $n = 31$ variables of Romeo, we tried to run it on the robot model. Due to differences in dynamics, the ZMP position resulting from these trajectories will not satisfy the equilibrium condition. We checked that the ZMP trajectory is outside the support polygon, as is visible in Fig. 2

To solve this problem, we need to impose the ZMP trajectory instead of the CoM by using the *Essential model* first introduced in [5].

Table 1. Main parameters of the trajectories for Romeo

Variable	Period	Mean value	Magnitude	Phase
Motion along Z of the CoM	T	1.12 (leg length)	About 2% of height	Minimum in middle of DS
Motion along X of the CoM	Linear progression	—	—	—
Motion along Y of the CoM	T	0	About 2% of height	Zero around 80% of DS
Trunk roll	T	0	5°	Minimum in middle of DS
Trunk pitch	T	6°	2°	Maximum at beginning and end of DS
Swing foot height	Cycloid 2T	—		
Swing foot pitch	Cycloid 2T	—	-20° to 81°	Minimum right after impact

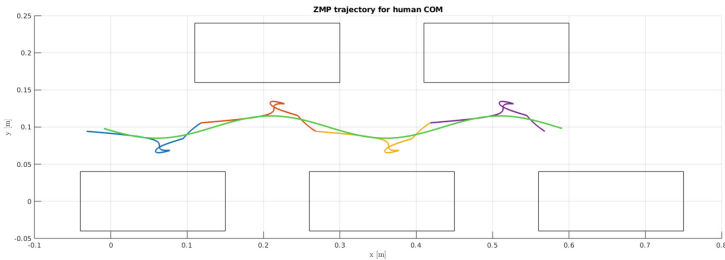


Fig. 2. ZMP (multicolored) obtained if the human COM motion (in green) is applied to the robot Romeo.

4 Essential Model

Instead of imposing as many trajectories as there are degrees of freedom (DoFs), we will leave two DoFs to allow for a better placement of the ZMP. Since the relation between ZMP and CoM is considered as a determining feature of human gait [2, 15], and the positions of CoM and ZMP are strongly linked, we choose

to “set free” the horizontal coordinates $r_f = (x, y)$ of CoM in order to adapt to the imposed trajectory of the ZMP.

To take inspiration from the human motion, let us introduce $r \in \mathbb{R}^{31 \times 1}$:

$$r = (r_f, r_c)^\top = (x, y, z(t), x_f(t), y_f(t), z_f(t), \psi_f(t), \theta_f(t), \phi_f(t), \psi_{tr}(t), \theta_{tr}(t), \phi_{tr}(t), q_{13}(t), \dots, q_{31}(t))^\top. \quad (1)$$

We define r_c as the vector of the 29 variables of r for which the trajectories are imposed. $z(t)$ defines the desired altitude of the CoM. $x_f(t), y_f(t), z_f(t)$ and $\psi_f(t), \theta_f(t), \phi_f(t)$ describe the desired position and desired orientation of the free foot, and $(\psi_{tr}, \theta_{tr}, \phi_{tr})$ give the desired orientation of the torso link. The upper-body variable joints are defined by q_{13} to q_{31} . The desired motion for $r_c(t)$ is defined based on human motion as summarized in Table 1.

The robot configuration can be defined by the vector q or r and a geometric model can be built. Let $q = g(r_f, r_c)$, \dot{q} and \ddot{q} are deduced thanks to the kinematic models as follows:

$$\dot{q} = J_f \dot{r}_f + J_c \dot{r}_c, \quad \ddot{q} = J_f \ddot{r}_f + \dot{J}_f \dot{r}_f^2 + J_c \ddot{r}_c + \dot{J}_c \dot{r}_c^2. \quad (2)$$

Here $J_f \in \mathbb{R}^{31 \times 2}$ and $J_c \in \mathbb{R}^{31 \times 29}$. In the current study the evolution of r_c is chosen as a function of time, thus the joint evolution can be expressed as function of $r_f, \dot{r}_f, \ddot{r}_f$ and t only:

$$q = g_t(r_f, t), \quad \dot{q} = J_f \dot{r}_f + v(t, r_f), \quad \ddot{q} = J_f \ddot{r}_f + \dot{J}_f \dot{r}_f^2 + a(t, r_f, \dot{r}_f). \quad (3)$$

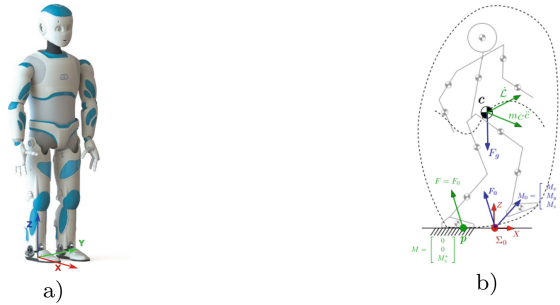


Fig. 3. a) Photography of Romeo. b) Illustration of the global equilibrium.

To evaluate the feasibility of a walking trajectory, it is necessary to calculate the effects of external forces acting on the humanoid robots. The origins of these external forces are the gravity force F_g and the ground reaction forces acting applied on each foot Fig. 3 b). The resulting effect of the ground reaction is

defined by the wrench $\in \mathbb{R}^{6 \times 1} (\mathbf{F}_0, \mathbf{M}_0)^\top = (F_x, F_y, F_z, M_x, M_y, M_z)^\top$ in a reference frame Σ_0 . The global equilibrium of the robot can be written as:

$$\begin{pmatrix} \mathbf{F}_0 \\ \mathbf{M}_0 \end{pmatrix} = \begin{pmatrix} A_F \\ A_M \end{pmatrix} \ddot{q} + \begin{pmatrix} d_F(q, \dot{q}) \\ d_M(q, \dot{q}) \end{pmatrix} \quad (4)$$

where $q \in \mathbb{R}^{31 \times 1}$ is the joint vector of the robot.

Using Eq. (3), the global equilibrium (4) can be rewritten:

$$\begin{pmatrix} \mathbf{F}_0 \\ \mathbf{M}_0 \end{pmatrix} = \begin{pmatrix} A_{Fr}(t, r_f) \\ A_{Mr}(t, r_f) \end{pmatrix} \ddot{r}_f + \begin{pmatrix} d_{Fr}(t, r_f, \dot{r}_f) \\ d_{Mr}(t, r_f, \dot{r}_f) \end{pmatrix} \quad (5)$$

Let $\mathbf{p} = (p_x, p_y, 0)^\top$ be the global zero moment point (ZMP). Its coordinates p_x and p_y satisfy:

$$F_z p_x + M_y = 0, F_z p_y - M_x = 0. \quad (6)$$

(p_x, p_y) must be inside the convex hull of support for all times in order to satisfy the dynamic equilibrium condition [16]. To be sure to find a periodic motion that satisfies the equilibrium condition, we choose a desired evolution $(p_x(t), p_y(t))$ of the ZMP. During the SS phase the desired motion of the ZMP is a function of time to define a migration of the ZMP from the heel to the toe of the stance foot. In DS phase the desired motion of the ZMP is defined by a linear evolution from the final position of the ZMP at the end of the SS phase on the stance foot, until the initial position of the ZMP at the beginning of the SS on the next stance foot. Using Eq. (6), and using the 3th, 4th and 5th lines of (5), we obtain:

$$\begin{aligned} (A_{Frz}(t, r_f) \ddot{r}_f + d_{Frz}(t, r_f, \dot{r}_f)) p_x(t) + A_{Mry}(t, r_f) \ddot{r}_f + d_{Mry}(t, r_f, \dot{r}_f) &= 0 \\ (A_{Frz}(t, r_f) \ddot{r}_f + d_{Frz}(t, r_f, \dot{r}_f)) p_x(t) - A_{Mrx}(t, r_f) \ddot{r}_f - d_{Mrx}(t, r_f, \dot{r}_f) &= 0 \end{aligned} \quad (7)$$

that isolates the essential characteristic of the walking that is the relationship between the ZMP and the CoM. Solving of Eq. (7) gives the *Essential model* describing the acceleration of the horizontal positions x and y of the CoM, that are defined to achieve to an imposed evolution of the ZMP:

$$\ddot{r}_f = f(r_f, \dot{r}_f, t, p_x(t), p_y(t)). \quad (8)$$

By integration of (8) from initial conditions we can calculate the current values of \dot{r}_f , i.e \dot{x} , \dot{y} , and r_f , i.e x , and y . To sum up, the evolution of x and y is not imposed in order to allow them to adapt to the imposed evolution of the ZMP. With this strategy to define a reference trajectory of walking, which is based on the *Essential model* (8) and $r_c(t)$, no approximations are made to the dynamic model when designing the humanoid walking. The method ensures the feasibility of a walking trajectory from the point of view of the condition on the ZMP. The choice of $z(t)$ of the CoM allows to satisfy the positivity of the vertical component of the resultant ground reaction force during the walking. The condition of no slipping can be checked based on the knowledge of \ddot{r}_f and \ddot{z} .

Then the torques required to produce the motion have to be calculated. During the SS phase, considering the stance foot motionless on the ground, we can define the dynamic behavior of the robot:

$$\tau = A_r(t, r_f)\ddot{r}_f + d_r(t, r_f, \dot{r}_f) \quad (9)$$

In DS phase effort $\begin{pmatrix} F_{ext} \\ M_{ext} \end{pmatrix}$ are applied on the second leg, (9) becomes

$$\tau = A_r(t, r_f)\ddot{r}_f + d_r(t, r_f, \dot{r}_f) + J_{ext}^\top \begin{pmatrix} F_{ext} \\ M_{ext} \end{pmatrix}. \quad (10)$$

The global equation gives the global reaction force \mathbf{F}_0 , \mathbf{M}_0 , but the distribution on both legs is free and will modify the actuation torque. During double support, the global ZMP is the barycentre of the two local ZMPs on each foot, this implies that the global ZMP and the local ZMPs are aligned. The evolution of the global ZMP is chosen in order that during all the DS, the two local ZMPs keep a constant pose corresponding to the final pose of the ZMP in SS : p_5 , and the initial pose of the ZMP for the next SS : p_2 . We can calculate the vertical reaction force on leg 1 and 2 F_{1z} and F_{2z} by solving this system:

$$\begin{aligned} \frac{p_{1x}F_{1z} + p_{2x}F_{2z}}{F_{1z} + F_{2z}} &= p_x \\ \frac{p_{1y}F_{1z} + p_{2y}F_{2z}}{F_{1z} + F_{2z}} &= p_y \end{aligned} \quad (11)$$

To avoid slipping, the ratio between tangential and normal force for the global equilibrium is conserved for each leg. The components F_{1x} , F_{1y} , F_{2x} , and F_{2y} are calculated to satisfy:

$$\begin{aligned} \frac{F_{1x}}{F_{1z}} &= \frac{F_{2x}}{F_{2z}} = \frac{F_{1x} + F_{2x}}{F_{1z} + F_{2z}} \\ \frac{F_{1y}}{F_{1z}} &= \frac{F_{2y}}{F_{2z}} = \frac{F_{1y} + F_{2y}}{F_{1z} + F_{2z}} \end{aligned} \quad (12)$$

By using (11) and (12) we find $M_z = M_{1z} + M_{2z}$. The moment around the z axis is also share between the two legs using a similarly distribution to the force components (12) as follows:

$$\frac{M_{1z}}{F_{1z}} = \frac{M_{2z}}{F_{2z}} = \frac{M_{1z} + M_{2z}}{F_{1z} + F_{2z}} \quad (13)$$

5 Periodic Walking

The target walking motion is periodic, with a step that is composed of SS phase and a DS phase. There is no impact at the end of the SS phase. To find the

walking motion a boundary problem is solved as follows. The algorithm starts from an initial guess of CoM position and velocity $(x(t_0), y(t_0), \dot{x}(t_0), \dot{y}(t_0))$ at the start of DS phase. The condition for periodicity is

$$(x(t_0), y(t_0), \dot{x}(t_0), \dot{y}(t_0)) = (x(t_0 + T), y(t_0 + T), \dot{x}(t_0 + T), \dot{y}(t_0 + T)) \quad (14)$$

tacking into account the change of the reference frame when the two legs switch their role just after the end of the current step. So $\dot{x}(t_0 + T), \dot{y}(t_0 + T)$ are the initial velocities of the CoM in DS of the next step. The boundary value problem is, what are $x(t_0), y(t_0), \dot{x}(t_0)$ and $\dot{y}(t_0)$ such that after integration of (8) over the time interval $[t_0, t_0 + T]$ the cyclic condition (14) is satisfied.

6 Numerical Results

We obtained a cyclic trajectory for a step size of 0.15 m, all other parameters being the same as described in Table 1. A stick-diagram over one cycle of this cyclic walking motion is presented Fig. 4 and Fig. 5.

We observe on Fig. 4 that the COM trajectory is oscillating in the Y direction a lot more than what is typical for human walking. This difference can be explained by the slightly larger step width (necessary because of geometric constraints on Romeo) and the overall slower walking velocity. Indeed, the slower the walking gait, the closer it gets to semi static, and the larger the COM oscillations in Y direction [7].

This result can be compared to the “raw” ZMP trajectory based on a human-like COM trajectory without constraints on the ZMP, as presented on Fig. 2. It is obvious that this trajectory would not be viable, as the ZMP trajectory is outside of the convex hull of the foot during single support phase. This proves the relevance of the approach used with the Essential Model, imposing constraints on the ZMP position rather than COM allows to achieve a dynamically stable walking motion.

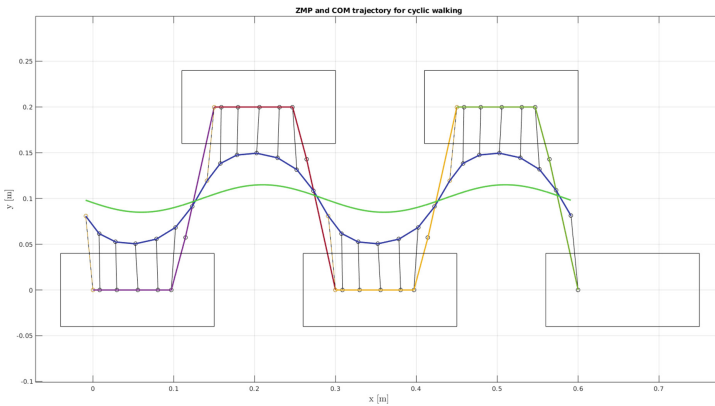


Fig. 4. Obtained COM trajectory (in blue) for the imposed human-like ZMP trajectory (multicolored), compared to a typical human COM trajectory (in green).

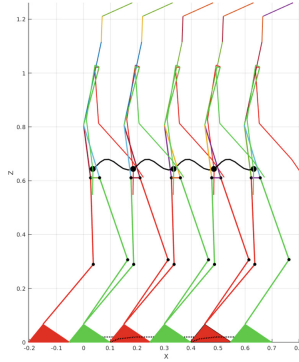


Fig. 5. Stick-diagram of a walking.

7 Effect of ZMP Evolution on Torques

The results presented above correspond to an evolution of the ZMP going from the heel to the tip of each foot (see Fig. 4). The torque at the ankle is directly affected by the pose of the ZMP. It can be seen in Fig. 6 (2nd image), that the propulsive torque is low at the beginning of the step. As a consequence, a high propulsive torque is required at the knee joint (Fig. 6 (3th image)). In fact this high torque exceeds the limits of the actuator (shown in dotted line) of the robot Romeo. We explored the effect of the influence of ZMP evolution. The results show that a modification of the ZMP trajectory influences the torques in the support knee and in the support ankle. A ZMP that has a constant position in

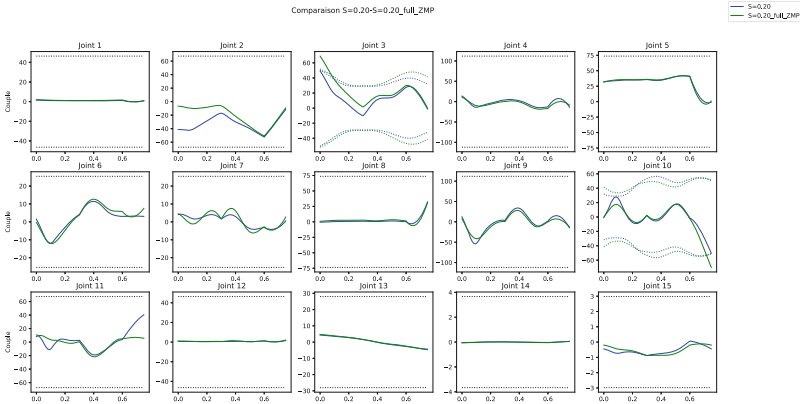


Fig. 6. Joint torques (N.m) versus time (s): comparison of the torque in the lower part of the robot for two cyclic trajectories with a step size of 0.20 m and a period of 0.75 s. The trajectory in green is with a human like ZMP evolution in DS, and the trajectory in blue has a ZMP constrained to the front of the foot.

front of the foot allows a higher propulsive force at the beginning of the SS, and thus allows to decrease the propulsive force at knee, and then produce a knee torque compatible with the actuator of Romeo.

8 Conclusions

We developed a 3D cyclic walking motion for a humanoid robot, Romeo. Each step is composed of a SS phase and a DS phase. The design is based on the use of the *Essential model* that ensures the feasibility of the motion by satisfying the ZMP condition, which is the hardest constraint to meet. The other generalized variables of the robot are defined as smooth periodic functions of time taking inspiration from human walking motions. A dynamic model and the global equilibrium of the robot prove that the obtained walking motions are valid. The perspectives are to complete the cyclic walking motions with a starting phase and a stopping phase and to test a set of walking motions with an experimental platform.

References

1. Tlalolini, D., Aoustin, Y., Chevallereau, C.: Design of a walking cyclic gait with single support phases and impacts for the locomotor system of a thirteen-link 3D biped using the parametric optimization. *Multibody Sys.Dyn.* **23**(1), 33–56 (2010)
2. Kajita, S., Hirukawa, H., Harada, K., Yokoi, K.: *Introduction to Humanoid Robotics*, vol. 101. Springer (2014)
3. Ames, A.D., Cousineau, E.A., Powell, M.J.: Dynamically stable bipedal robotic walking with NAO via human-inspired hybrid zero dynamics. In: *Proceedings of the 15th ACM International Conference on Hybrid Systems: Computation and Control*, pp. 135–144. ACM (2012)
4. Sakka, S.: *Imitation des mouvements humains par un robot humanoïde sous contrainte d'équilibre*. HDR, Université Pierre et Marie Curie (UPMC) (2017)
5. De-León-Gómez, V., Luo, Q., Kalouguine, A., Pámanes, J.A., Aoustin, Y., Chevallereau, C.: An essential model for generating walking motions for humanoid robots. *Robot. Auton. Syst.* **112**, 229–243 (2019)
6. Rose, J., Gamble, J.G.: *Human Walking*, 3rd edn. Williams & Wilkins (2006)
7. Orendurff, M.S., Segal, A.D., Klute, G.K., Berge, J.S., Rohr, E.S., Kadel, N.J.: The effect of walking speed on center of mass displacement. *J. Rehabil. Res. Develop.* **41**(6) (2004)
8. Jurcevic Lulic, T., Muftic, O.: Trajectory of the human body mass centre during walking at different speed. In: *DS 30: Proceedings of DESIGN 2002, the 7th International Design Conference, Dubrovnik* (2002)
9. Grundy, M., Tosh, P., McLeish, R., Smidt, L.: An investigation of the centres of pressure under the foot while walking. *J. Bone Joint Surg. Br.* Vol **57**(1), 98–103 (1975)
10. Sardain, P., Bessonnet, G.: Zero moment point-measurements from a human walker wearing robot feet as shoes. *IEEE Trans. Syst. Man Cybern. Part A Syst. Hum* **34**(5), 638–648 (2004)

11. Thorstensson, A., Nilsson, J., Carlson, H., Zomlefer, M.R.: Trunk movements in human locomotion. *Acta Physiologica Scandinavica* **121**(1), 9–22 (1984)
12. Meyns, P., Bruijn, S.M., Duysens, J.: The how and why of arm swing during human walking. *Gait Posture* **38**(4), 555–562 (2013)
13. Aoustin, Y., Formalskii, A.M.: 3D walking biped: optimal swing of the arms. *Multi-body Syst. Dyn.* **32**(1), 55–66 (2014). <https://doi.org/10.1007/s11044-013-9378-3>
14. Kinugasa, T., Chevallereau, C., Aoustin, Y.: Effect of circular arc feet on a control law for a biped. *Robotica* **27**(4), 621–632 (2008)
15. Koolen, T., de Boer, T., Rebula, J., Goswami, A., Pratt, J.: Capturability-based analysis and control of legged locomotion, part 1: theory and application to three simple Gait models. *Int. J. Robot. Res.* **31**(09), 1094–1113 (2012)
16. Vukobratovic, M., Borovac, B.: Zero-moment point—thirty five years of its life. *Int. J. Humanoid Rob.* **1**(1), 157–173 (2004)

Industrial Applications



Sailing/Coasting Enabled by Mechatronic Starting Devices

Madhusudan Raghavan^(✉)

General Motors R&D, Warren, MI, USA
madhu.raghavan@gm.com

Abstract. Engine start quality and seamless engine start/stop are key elements of drive quality and customer acceptance in today's electrified propulsion architectures. Two novel mechatronic devices have been created for premium engine start/stop. One concept uses a motor/generator in place of the traditional alternator, coupled to a mechatronic switching device for selectable geared or belted operation of the motor/generator. The second starter concept uses a two-speed gear scheme inserted between the starter motor and crankshaft flywheel for smooth engine starts. In the present work, the use of these starter devices in vehicles with sailing/coasting mode as well as in mild hybrid propulsion systems is described. Sailing/coasting mode of operation is enabled by the quick engine re-start capability of these starters allowing seamless switching between fuelled and unfuelled engine operation. This could reduce fuel consumption by about 3–6% on the NEDC driving cycle, without regenerative braking. One may further hybridize the propulsion system by adding a battery for storing regenerative braking energy. Using such an architecture, a 6–8% fuel economy improvement on the WLTP certification driving cycle may be achieved, depending on voltage and power levels implemented, as well as energy storage systems included.

Keywords: Starter · Start/stop · Mild hybrid · Sailing · Coasting

1 Introduction

Transportation is the source of approximately 25% of greenhouse gas (GHG) emissions worldwide [1]. Light or mild electrification (under 50 V) of the propulsion system is one approach to reducing GHG. It appears to have mass-market potential because of the favorable value proposition it offers. Smooth, fast engine starts are critical elements of such mild hybrid systems.

A start/stop system switches off the engine when the vehicle comes to a stop, thereby eliminating the consumption of fuel and the release of emissions during engine idling. However, this creates the need for fast engine restart systems to achieve satisfactory tip-in response when the driver depresses the accelerator to drive away. Prior work in start/stop systems are as follows. Wellmann et al. [2] perform an assessment of various start/stop systems and investigate the delay in tip-in response and launch performance

when the driver depresses the accelerator when the engine is off. Storey et al. [3] describe experiments to study the difference in particulate mass emissions for GDI engines with and without start/stop systems. Xu et al. [4] present a coupled magnetic-thermal model to study the reason for the damage of the starter motor of a start/stop system of a city bus. Wishart et al. [5] describe the testing of idle-stop systems to see whether real-world fuel savings of such systems are in line with those predicted by the EPA fuel economy certification cycles. Inglis et al. [6] describe a novel start/stop system that injects compressed air into appropriate cylinders in the engine to get the engine spinning before it is fueled and sparked. Henein et al. [7] study the operation of engine starts and stops in electrified propulsion systems with a focus on the effects of engine temperature on engine cranking torques and start-up emissions. Costlow [8] describes advancements in lead-acid battery technology, in particular, enhanced flooded batteries and absorbent glass mat batteries, driven primarily by the projected growth in start/stop system market volumes.

Fonseca et al. [9] quantify the CO₂ potential of start/stop systems by comparing two diesel-powered vehicles in urban driving conditions. Tamai et al. [10] describe a 36 V belted alternator starter system with a 7 kW MGU installed on a 1.9L four-cylinder engine, delivering 12–14% fuel economy improvement on the FTP city cycle and about 1% improvement on the FTP highway cycle. Canova et al. [11] describe the creation of a nonlinear control algorithm to execute smooth stops and restarts on a diesel engine, wherein the cranking torques are much higher than for a gasoline engine due to the higher compression ratio. Raghavan and Balhoff [12] describe a 12 V belted alternator starter system that can execute engine start/stop functions as well as improve engine responsiveness by means of torque addition to the driveline during transient maneuvers. Raghavan [13] investigates various light electrification architectures ranging from 12 V start/stop systems to 48 V electrified transmissions, to assess their optimality when applied to a range of vehicle types and motor/generator locations. Raghavan et al. [14, 15], investigate engine start quality, NVH, and cranking speed, and present experimental data showing that faster cranking is better.

The present work describes how two new starter concepts that yield fast, smooth engine starts, may be integrated into propulsion architectures to yield fuel economy improvements via sailing/coasting and mild hybridization.

2 Mechatronic Starters for Fast, Smooth Engine Starts

This section begins with a brief description of these two novel starters created for quick engine starts. They are described in considerable detail in Raghavan [15]. In the present, the key points regarding these starters are summarized to provide the reader with context for the following section on Sailing/Coasting. The first of the two proposed starter concepts is shown in Fig. 1 and is comprised of a motor/generator mounted on the engine, which can be selectively connected to either the gears on its left side (dashed rectangle) or to the accessory belt sprocket (with clutch) on its right side. Thus, the motor/generator can be either geared or belted to the crankshaft with very different ratios, allowing for either geared starter cranking or belted driveline hybrid operation (regenerative braking, torque boosting, etc.) This device provides better starts than a

traditional starter because the motor/generator can be designed to be five to ten times more powerful than a starter motor.

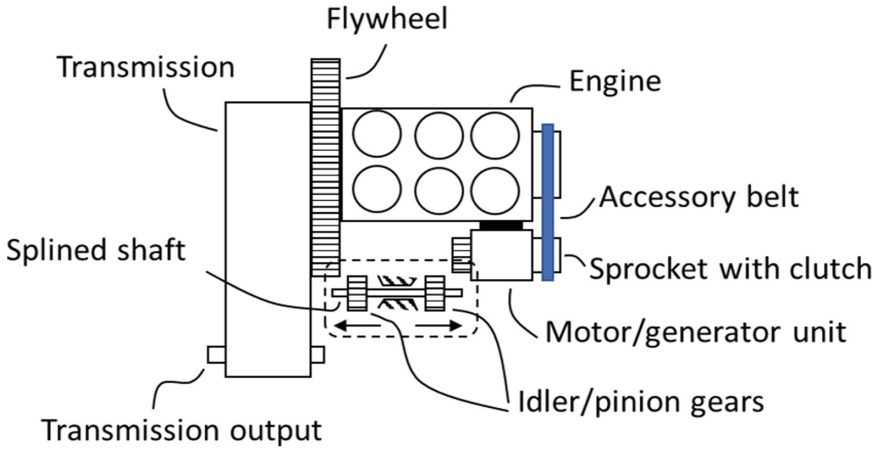


Fig. 1. Engine with a geared/belted mechatronic starter

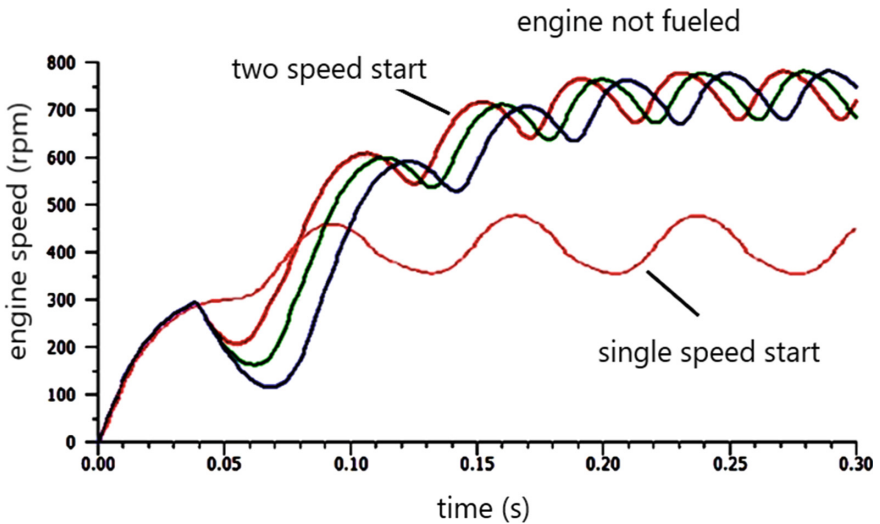


Fig. 2. Engine rpm for conventional vs. two-speed starter

The second starter of interest is comprised of a two-speed geartrain inserted between the starter motor and the crankshaft flywheel. By starting the cranking process with a high gear ratio and then switching to a lower ratio once the engine is rotating, the starter motor is able to crank the engine to a higher than normal rpm prior to ignition. This results in quieter starts. The details of operation of this starter are presented in Raghavan [15], and the resulting output crankshaft speed is shown in Fig. 2.

The following section describes how this fast start capability may be harnessed to achieve eco modes such as sailing/coasting which result in improved fuel economy with minimum additional cost to the driveline.

3 Application to Sailing/Coasting and Mild Hybridization

Of the two proposed starter systems, the first one enables a considerably faster start, but with the added cost of the alternator being replaced by a motor/generator unit. Additionally, a bi-directional tensioner must be added to the front-end accessory drive belt, in order to allow driveline torque boosting operation as well as belted engine starts. In contrast, the second proposed starter enables smooth starts by cranking the engine to a higher rpm prior to ignition. In this case, the added cost is that of the two-speed gearset in place of the single ratio gearset of the conventional starter.

The terms “sailing” and “coasting” are used interchangeably and refer to the mode of operation when the engine is shut off and disconnected to minimize engine drag losses during decelerations. This is popular in Europe and China with the high penetration of manual transmissions. When the engine is decoupled from the driveline during coasting, one possible operating strategy is to keep the engine running at idle for quick re-engagement to the driveline when the driver demands acceleration. This idle operation of the engine during coasting continues to use fuel. The proposed concepts in this paper get around this problem, as they enable ultra-fast re-starts and thus potentially allow one to maximize the true “engine off” time periods during coasting, thus maximizing fuel economy. Coasting may be thought of as a vehicle transient state between cruising and braking. The various sailing/coasting modes of operation are shown in Fig. 3.

A typical driving maneuver is divided into 6 sections or modes. In mode 1, the vehicle is initially stopped (perhaps at a traffic light) with the engine in Auto Stop mode. In mode 2, the driver releases the brake pedal and depresses the accelerator pedal. The engine

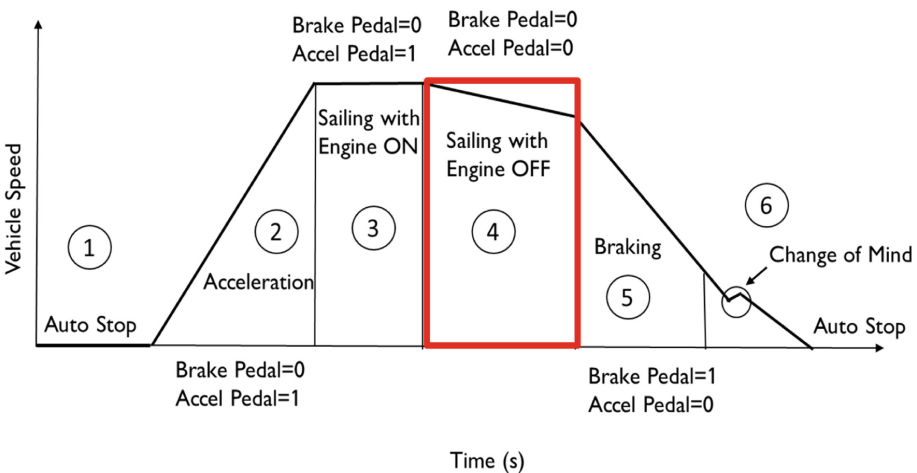


Fig. 3. Sailing/coasting

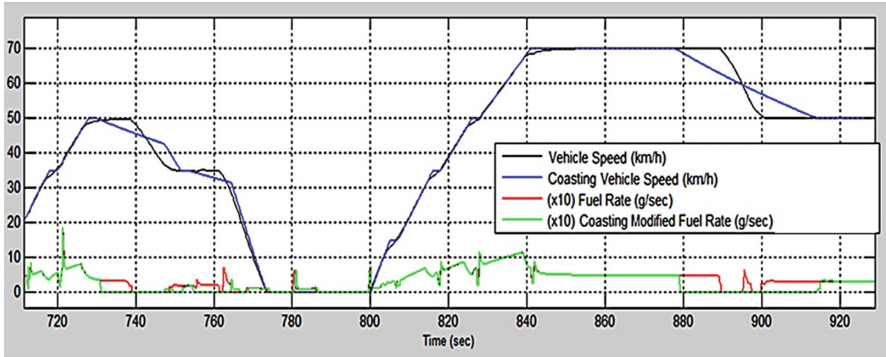


Fig. 4. Fuel consumption with sailing/coasting on a certification driving cycle

starts and provides torque to accelerate the vehicle as indicated by the linearly increasing speed. Once the vehicle reaches the desired cruising speed the driver reduces pressure on the accelerator allowing the vehicle to sail/coast in mode 3. The engine remains on but is disconnected from the driveline. In mode 4, the sailing/coasting operation is continued, but with the engine disconnected and shut off. In mode 5, the driver depresses the brake pedal to slow the vehicle down as needed. In mode 6, the vehicle continues to slow down, but with the starter ready to make a quick engine re-start in case of a “change of mind” situation, wherein the driver decides to increase speed instead of slowing down (as when a traffic signal turns green). If this change of mind situation does not occur the vehicle comes to a complete stop at the end of mode 6.

Figure 4 shows how the sailing/coasting mode may be used to save fuel on the modified NEDC certification driving cycle. The so-called modification refers to the permissible deviations from the NEDC cycle as required by the sailing/coasting maneuvers. The black line indicates stipulated vehicle speed on the original NEDC driving cycle. The blue line indicates how the sailing/coasting mode may be used to approximate the sharp decelerations on the stipulated driving cycle with more gradual coasting maneuvers. This allows one to save fuel as indicated by the differences between the red curve (fuel rate for stipulated vehicle speed) and the green curve (fuel rate for the sailing/coasting approximation). Note that the green fuel rate drops to zero during the sailing/coasting portions while the red curve remains non-zero on these portions. Conservative estimates suggest that this type of sailing/coasting on the NEDC driving cycle could save about 3–6% of the fuel consumed. This does not require a large additional battery, as regenerative braking energy is not stored for this mode of operation.

Prior mention was made of the ability of the motor/generator-based starter concept in belted mode to execute super-fast restarts and thus maximize fuel savings while ensuring adequate acceleration response. Experimental data backing up this claim are shown in Fig. 5, where one may see engine rpm plots for a fired engine start using the motor/generator (blue) and the conventional starter (red) on a port fuel-injection equipped engine. The engine rpm ramp rate achieved with the motor/generator unit far exceeds that of the conventional starter, resulting in a 400 ms faster spin up to 550 rpm.

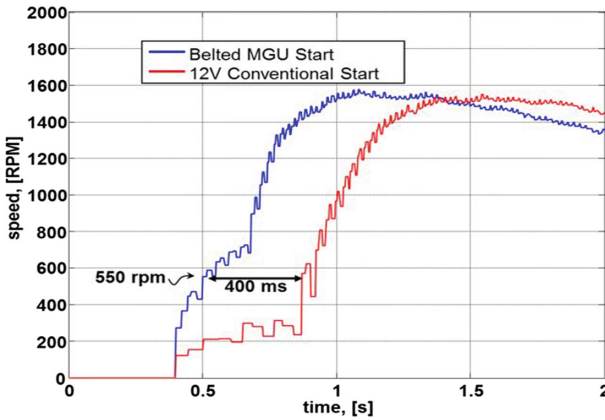


Fig. 5. Motor/generator vs. a conventional starter

Moving on from sailing/coasting, one may go a step further in mild hybridization by making the additional investment in a battery for storing regenerative braking energy. This leads to additional fuel economy gains. When the motor/generator unit of the starter is coupled to a 120 Wh Li-ion battery, such a system, with optimal (energy loss minimization) supervisory powertrain control, can yield 6–8% of fuel economy improvement on the WLTP driving cycle [12]. Figure 6 shows simulation plots of cumulative battery regeneration energy (i.e., a summation of energy flow into the battery) during the WLTP driving cycle, for a 1350 kg. passenger vehicle equipped with this system. The red curve shows the results of a 12 V implementation of such a system and the blue curve shows a 48 V implementation. The black curve is the vehicle speed trace during the WLTP cycle. Overall, approximately 1000 to 1200 kJ of regenerative braking energy is captured in the battery during the driving cycle, using a blended braking system comprised of electrical and friction braking. This energy, when utilized in the propulsion system to offset 12 V electrical loads as well as for driveline torque boosting (i.e., exerting electrical torque on the crankshaft via the motor, in place of mechanical torque from the engine), results in the above-mentioned fuel savings. This has been confirmed experimentally on instrumented test vehicles.

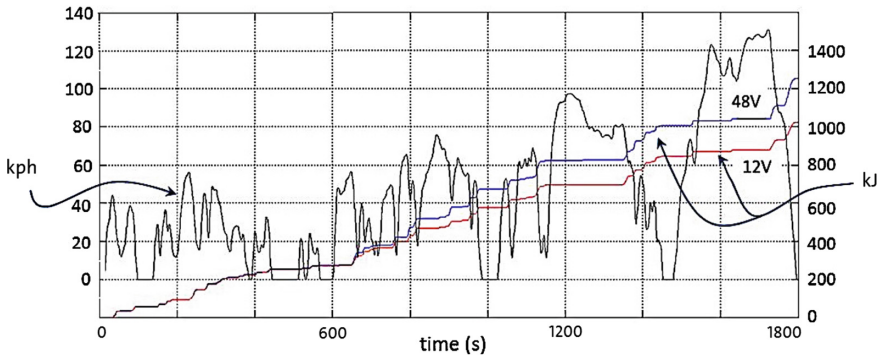


Fig. 6. Cumulative regenerative braking energy into the battery for WLTP

4 Conclusion and Future Work

The present study has investigated the use of two novel fast mechatronic starters for sailing/coasting operation wherein the engine is disconnected and shut off during vehicle deceleration. The fast starters allow quick engine re-start and re-connection to the drive-line in response to driver power demand. The use of this sailing/coasting mode of operation could save about 3–6% fuel on the NEDC driving cycle. Beyond sailing/coasting, one may further increase the level of mild hybridization by adding a battery for regenerative braking energy storage. In such an architecture, the motor/generator-based starter, in belted mode, enables hybrid functions such as torque boosting and regenerative braking to achieve a 6–8% improvement in fuel economy on the WLTP driving cycle. Furthermore, it is likely that a quicker engine start executed in the belted MGU mode, requires less injected fuel and consequently produces less emissions. However, this aspect has not yet been investigated in the present study and could be the subject of future research.

References

1. Greene, D., Plotkin, S.: Reducing greenhouse gas emissions from U.S. transportation. Pew Center on Global Climate Change, pp. 1–80, May 2003
2. Wellmann, T., Govindswamy, K., Tomazic, D.: Integration of engine start/stop systems with emphasis on NVH and launch behavior. SAE Technical Paper 2013-01-1899
3. Storey, J., Moses-DeBusk, M., Huff, S., Thomas, J., Eibl, M., Li, F.: Characterization of GDI PM during vehicle start-stop operation. SAE Technical Paper 2019-01-0050
4. Xu, Z., Tao, N., Du, M., Liang, T., Xia, X.: Damage prediction for the starter motor of the idling start-stop system based on the thermal field. SAE Int. J. Commer. Veh. **10**(2), 443–452 (2017). <https://doi.org/10.4271/2017-01-9181>
5. Wishart, J., Shirk, M., Gray, T., Fengler, N.: Quantifying the effects of idle-stop systems on fuel economy in light-duty passenger vehicles. SAE Technical Paper 2012-01-0719
6. Inglis, A., Timewell, R., Maskerine, S.: A novel compressed air starting system. SAE Technical Paper 2003-01-2279
7. Henein, N., Taraza, D., Chalhoub, N., Lai, M., Bryzik, W.: Exploration of the contribution of the start/stop transients in HEV operation and emissions. SAE Technical Paper 2000-01-3086
8. Costlow, T.: Powering up the new stop-start systems. Automotive Engineering, June 2016
9. Fonseca, N., Casanova, J., Valdes, M.: Influence of the stop/start system on CO₂ emissions of a diesel vehicle in urban traffic. Transp. Res. Part D Transp. Environ. **16**(2), 194–200 (2011)
10. Tamai, G., Hoang, T., Taylor, J., Skaggs, C., Downs, B.: Saturn engine stop-start system with an automatic transmission. SAE Trans. **110**, 270–280 (2001)
11. Canova, M., Guezennec, Y., Yurkovich, S.: On the control of engine start/stop dynamics in a hybrid electric vehicle. ASME J. Dyn. Syst. Meas. Control **131**(6), 1–12 (2009)
12. Raghavan, M., Balhoff, A.: Electrical torque addition mechanism for engines with high levels of EGR. In: EuCoMeS 2018: Proceedings of the 7th European Conference on Mechanism Science, pp. 165–172 (2018)
13. Raghavan, M.: Mild electrification across a spectrum of vehicle types. FISITA Technical Paper No. F2018-EHV-009 (2018)
14. Raghavan, M., Bucknor, N., Donikian, V.: The kinematics and dynamics of engine start systems. In: IFToMM Asian MMS Conference, Bangalore (2018)
15. Raghavan, M.: Novel mechanisms to improve the start quality of automotive engines. In: IFToMM World Congress, Krakow (2018)



Embedded Installation of Robot Operating System on Elbrus-Based Control Platform—High-Reliable Industrial Application

Alexander Tachkov^{1(✉)} and Andrei Vukolov²

¹ Science and Educational Center “Robotics”,
Bauman Moscow State Technical University, Moscow, Russia
tachkov@bmstu.ru

² ELETTRA Sincrotrone Trieste S.C.p.A.,
Area Science Park Basovizza, Trieste, Italy
andrey.vukolov@elettra.eu

Abstract. Robot Operating System (ROS) is widespread framework allowing researchers to create functional control environments for robotic systems. But one of the main problems connected with ROS installation is its distribution actually snapped almost explicitly to Debian/Ubuntu Linux and their package bases for x86 and ARM architectures. If the embedded proprietary platform is required to be used for creation of the robot (e.a. to work with non-standard hardware interfaces), ROS installation becomes non-trivial task. In this case it requires to build all ROS modules from sources and to integrate the obtained binaries into control system manually. This paper discusses the case of ROS installed and integrated into high-reliable general purpose industrial control platform based on proprietary hardware equipped with Elbrus VLIW (*VLIW (Very Long Instruction Word)*)—CPU architecture that allows to embed set of operations into single machine instruction for assembly-level parallelization) CPU. The advantages of embedded ROS installation, peculiarities of its integration into a robot and licensing issues are also described.

Keywords: Robot Operating System · Elbrus CPU · Embedded systems · Control systems for robotics · Industrial robotics · Software

1 Introduction

For the embedded systems the main peculiarity of software installation is high level of integrity. Often the system is oriented to super-automatic mode to operate without human control most times it is turned on. This requires both high reliability of the software itself and specialized system elements dedicated to hardware intercommunication. Mainstream robotic middleware such as ROS [11]

allows software to be built in terms of reusable and individually tested components that can be deployed in separate execution environments, including industrial applications [10].

ROS provides the specialized environment for information exchange between autonomous programs (*nodes*) run under control of host machine's operating system [9]. Each node encapsulates control functions dedicated to single element of the system minimizing functional overlapping. The nodes are connected into graph using named asynchronous channels called *topics*. The data serialized into binary formatted *messages* are transferred through the topics using selective broadcasting model from the sender (*publisher*) to one or many *subscribers* which define callback functions to operate on the messages synchronously once they would be received. The master program *rosmaster* marshals message distribution between the set of nodes run to implement the current control system. ROS also provides its own CMake-based build system *catkin* which generates programmatic bindings to treat serialized data and to create callback functions using several languages including C++, CommonLISP, Python and Java. The ROS nodes can be encapsulated within named *packages* which allows researchers to distribute their solutions as open source programs. The described conditions turn ROS into a graph-based loosely-coupled control solution. This kind of solutions increases reliability of the whole control system because it allows to operate when one or more nodes malfunction within the graph. Due to open source distribution, ROS also supports many devices using drivers developed by community.

One of the main problems connected with ROS deployment is following. ROS actually snapped almost explicitly to Debian/Ubuntu Linux distributions and their package bases for x86 and ARM architectures. This paper presents a generic approach to deployment and integration of ROS into high-reliable general purpose industrial control platform based on proprietary hardware equipped with Elbrus VLIW CPU [8].

2 Background and Related Work

There have been several attempts to adopt ROS for non ROS-compliant client processes and environments. These works exploit several approaches. The first example, *rosbridge* [4] is a middleware abstraction layer which provides a simple, socket-based programmable access to robot's interfaces and algorithms provided by ROS. Koubaa et al. [7] developed *roslink*, a new protocol to integrate ROS with IoT devices. It defines a lightweight asynchronous communication layer between the robot and the end-user environment through the cloud.

Although some existing methods [21, 22] offer the adaptation for environments provided on embedded systems for ROS deployment, but for almost all of them it is not possible to port the open source ROS packages directly on because of many native techniques and consents which the embedded systems don't implement.

As one of the most successful projects of ROS adoption *mROS* should be mentioned [15]. It is a lightweight runtime environment running ROS nodes. It

has been designed to be run on an embedded device having a mid-range CPU. It consists of a real-time operating system (RTOS) kernel image and embedded TCP/IP protocol stack. In order to allow the program executed on the embedded device to behave as ROS node, Takase et al. provided support two ROS-compliant communication protocols to exchange data with external system working under control of native ROS installation.

As it was described above, integration of ROS into the environment deployed on embedded platform is constrained, at first, by absence of official support of continuous deployment system called *ROS Build Farm* [2] on most embedded platforms. The ROS Build Farm is cluster-based distributed deployment system. It could be deployed only on the system supporting *servlet* technology, Apache Tomcat, for example. The macro processor used to build ROS packages is *Jenkins* [12] which requires Java Runtime Environment to run. Most embedded systems do not have such infrastructure, so they are unsupported by ROS Build Farm. The official ROS community throw away the support for such systems preferring x86 and ARM. To avoid the described restrictions the authors decided to develop the build process for ROS by themselves for *Elbrus* platform to create complete port with possibility to mirror and rebuild also most of open source software packages using repositories [16, 19].

2.1 Elbrus Embedded Platform

The key peculiarity of Elbrus embedded platform used to deploy ROS as it is described here is assembly-level parallelization. In such architecture compiler distributes VLIW commands between hardware arithmetic solvers programmatically. The CPU core contains several (6 for Elbrus-8C architecture) *fused-multiply-add* (FMA) solvers allowing to perform up to 2 operations on 64-bit floating point numbers per core tick [8]. This peculiarity may accelerate some operations but it requires special optimization algorithms implemented in compiler and operating environment. The systems developed with Elbrus CPUs are controlled by “Elbrus” operating system. It inherits POSIX and Debian Linux storage and program build rules [20] which eases deployment of Linux-based applications. In case presented here it allowed authors to avoid cross-compilation with no necessity to rebuild basic concepts and programmatic models on which ROS based on. It should be noted that ROS community does not recommend to build ROS entirely on the local machine and it suggests to use `.deb` packages provided by the build farm instead.

2.1.1 Licensing

Especially for embedded installations on proprietary hardware licensing is an issue [16]. Because Elbrus computer is the full proprietary solution being installed on demand, it is needed to avoid as much proprietary drivers, adapters etc. as we can. ROS is distributed under conditions of BSD license [1]. This license allows user to distribute the created source code and binaries using both free and commercial models. Integration of proprietary software into the developed solution

is also allowed. Thus it allows to integrate both free and proprietary software into the same solution. To avoid any licensing issues, all software deployed onto Elbrus platform described in this paper developed under BSD 3-Clause license. Internal Elbrus drivers and system software are developed under internal license of MCST¹ company the manufacturer of Elbrus computers.

3 Embedding ROS into Elbrus Operating Environment

3.1 Target Setting

ROS is the most widespread free robotic framework so it is natural for initiating researchers to use it creating new control systems. But ROS officially supports only Debian/Ubuntu Linux and Windows 10 x64 (from 2019) installed on most common AMD64, x86 and ARM CPUs. Thus the target for this paper is set to build and test Elbrus embedded computer system as the specialized industrial-grade controller for robotics, compatible with x86 PC on interface level. Tests should be performed on real robotic system equipped with mechanics for ready-to drive state.

The task of embedding ROS into Elbrus operating environment for any purpose is completely new. There were some undocumented attempts to build functional ROS on Elbrus-equipped machine without significant results. The main reason of unsuccessful builds revealed during the investigation was ambiguous names of libraries, namespaces and functions between Debian Linux and Elbrus OS [14] in case that Elbrus OS is developed without strict implementation of X Desktop Group (XDG) naming standards. To avoid this problem the team of BMSTU center “Robotics” decided to isolate new ROS installation into new XDG-compliant system tree to install it as whole entity. As a side effect this also made it available to avoid versioning problem for packages because of “freezing” of versions of the system software installed into the created tree.

As the “frozen” versions of the system libraries required by ROS have eliminated the problem of package versioning as deployment of ROS became completely independent of the Elbrus OS packaging system based on `apt`. Because the Center uses Gitlab as complex continuous versioning and deployment solution [19] the decision was made to create a Git-based distributable project called *ROS Deployment System* which could automate the deployment process completely. It should be versioned according to Elbrus OS and CPU architecture evolution. This project consists of the following components:

- Storage facility for environmental variables. After deployment the new `bash` shell should be set up using data stored here;
- The script providing authentication credentials for Gitlab to access the repositories keeping modified ROS sources;
- User interaction provider to ensure the credentials are provided by authorized Gitlab user;

¹ <http://mcst.ru/>.

- Path injection tool for Elbrus OS embedding the XDG tree being deployed onto the system;
- Debian package deployment provider. It automatically deploys the special patched versions of system libraries. These libraries are built manually and they are distributed using `apt` and Debian-compatible packaging system.

The path injection tool does all work to make isolated XDG tree containing ROS. The part of the path injection script is presented in Listing 1.

Listing 1. Path injection script

```

1  if [[ ! -d "${EXT_ROOT}" ]]
2  then
3      mkdir "${EXT_ROOT}"
4  fi
5  if [[ ! -d "${MCST_REPO}" ]]
6  then
7      mkdir "${MCST_REPO}"
8  fi
9  mkdir "${EXT_LIB}" &&
10 mkdir "${EXT_INCLUDE}" &&
11 cp -v /etc/profile /etc/profile.old && mkdir "${EXT_PKGS}"
12 cp -v /root/.bashrc /root/.bashrc.old
13 cat "${RUN_ROOT}/path-injection.head" > /etc/profile
14 cat "${RUN_ROOT}/path-injection.head" > /root/.bashrc
15 cat /etc/profile.old >> /etc/profile && cat /root/.bashrc.old >> /root/.bashrc
16 cat "${RUN_ROOT}/path-injection.tail" >> /etc/profile
17 cat "${RUN_ROOT}/path-injection.tail" >> /root/.bashrc
18 cp -v /etc/ld.so.conf /etc/ld.so.conf.old
19 sed -i "i\
20 ${EXT_LIB}\
21 ${ROS_ROOT}/lib\
22 " /etc/ld.so.conf && ldconfig

```

The developed set of scripts builds whole ROS distribution for near 6h on most common used Elbrus-4C CPU equipped with 4 cores and 866 MHz of base frequency per core. The graphical user interface is not built because Elbrus in embedded installation does not provide any graphical output.

4 Testing

To ensure deployed ROS distribution's ability to work the series of tests was performed. The testing facility (Fig. 1) was established using Elbrus computation unit and Intel Core-i3 master workstation connected via gigabit network. On Fig. 1 the data sources are indicated in the bottom left. There are two LiDAR sensors: Velodyne HDL-32E producing 3D point clouds and Hokuyo UXM-30LX-EW producing regular 2D laser scans. The ROS `.bag` archive files were recorded from the LiDAR sensors installed on the all-terrain remote controlled vehicle on which ROS was installed as control framework. Thus the full imitation of real robot's workflow was obtained similar to approach described in [13]. The `.bag` files contained synchronized data and control commands were also included with LiDAR output. This setup with the structure of the testing facility allowed to test many aspects of ROS workflow including building of computation graphs, interprocess communication, network-based data publishing, realtime coordinate transformations, overall performance.

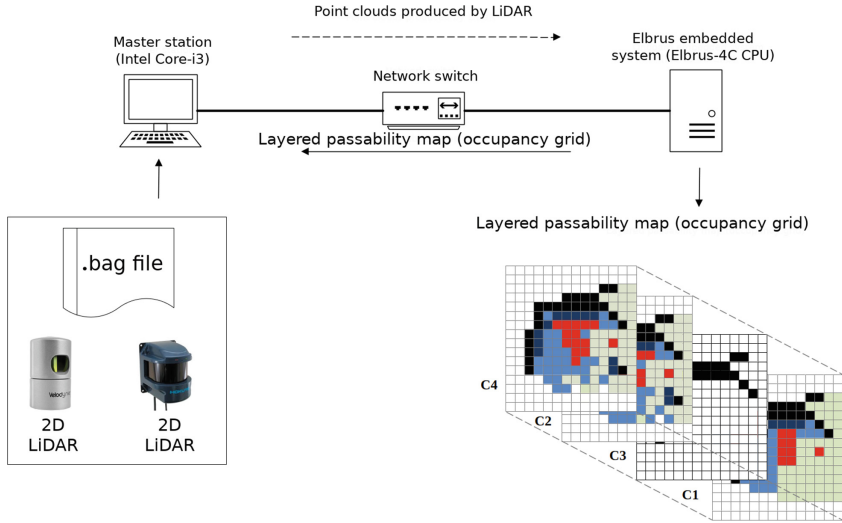


Fig. 1. Testing facility

Thus the described facility tested Elbrus with embedded ROS installation as the central high-reliable controller. The main task that were run on it was production on a layered map consisting of 4 layers (Fig. 1). The $C1-C3$ layers contain the data from obstacle classifiers developed in center “Robotics”. The $C1$ classifier is obstacle classifier with 3D point cloud input [18] detecting the obstacles that the vehicle can not pass. The second one also receives 3D point cloud as the input producing profile passability estimation [17]. The third classifier is the analogue of $C3$ with 2D laser scans as input. Each classifier produces 8-bit 800×800 occupancy grid updated as the iteration of an algorithm ends. The $C4$ layer contains Bayesian output of all other layers [5]. The $C4$ layer is become updated any time when any of the $C1-C3$ layers are updated, consequently cell per cell, to indicate obstacles with different grade of passability for the vehicle. These tasks should be considered as high loads because the frequency of map updates needed to be maximal for the current installation of controller.

During the test sessions the master workstation (Fig. 1) ran `rosmaster` node with `.bag` file playback, so it produced raw data at almost the same flow rate as an actual vehicle. The obstacle classifiers and map configuration server were run in slave mode on Elbrus machine connected to local area network through gigabit switch. All machines involved in the tests were equipped with identical ROS distribution Melodic Morenia. The testing facility set up as it is described here allows to determine possible sources of errors within the embedded installation of ROS on high data flow rate. Six Elbrus machines equipped with the same hardware configuration were tested and they shown high stability and reliability running the tasks for at least 30 min. For each machine the installation algorithm of ROS was the same, as it is provided by *ROS deployment system*

described above. For the time of experiment no system errors were produced so the reliability of the embedded ROS installation on Elbrus machines was considered sufficient.

5 Performance Comparison

In order to have a performance estimation of the embedded machines equipped with completely new CPUs the performance comparison between four machines was performed on the same task described above. The machines were embedded machines equipped with 4-core (4C) and 8-core (8C) Elbrus CPUs (both with only physical cores), and the others were Intel Core-i3 3223 and Intel Core-i7 7600HQ dual- and quadro-core respectively. It should be indicated that Intel machines were used both have dual hyper-threaded virtual cores. The software deployed on the machines during the performance comparison was actually identical to the software deployed on them during reliability tests but it had profiling instruction set integrated to measure the average execution times for functional objects. The results and description of the comparison are presented in Table 1. The measured periods of time include duration of treatment for the whole 800×800 layered map accompanied with visualization.

As it could be seen from Table 1 the average time of point cloud treatment run on 4-core Elbrus CPUs is about 10 times slower than on Intel CPUs. This result could be considered as correlation between frequency ratios of the processors (about 3000 MHz vs. 680 MHz). Also Elbrus OS does not contain high performance mathematical library like Eigen. Instead of it the vendor provides his own library called em1 which is not compatible with ROS. The proportional performance reduction could be also observable for updating of layers $C1$ and $C2$. For the $C3$ layer performance for all machines revealed practically the same. This issue appears due to lacking performance of ROS internal tf library performing conversions between coordinate systems. For Bayesian convolution the performance of 4-core Elbrus CPU is about 9.5 times lower than the Intel machines have so the correlation persists as it is shown above. For 8-core Elbrus CPU the results of the tests should be considered roughly comparable so the internal parallelisation of the Elbrus CPU could be considered effective for at least 8-core machine. The results of performance comparison can be considered repeatable: the work of another authors [3, 6] shows similar results.

Table 1. Performance comparison (layers as they are indicated on Fig. 1)

CPU	$t_{average}$, s	Standard deviation	t_{max} , s	t_{min} , s
Obstacle classifier - point cloud treatment				
Elbrus-4C	0.276	0.043	0.520	0.195
Elbrus-8C	0.143	0.012	0.206	0.114
Intel Core-i3	0.032	0.006	0.189	0.020
Intel Core-i7	0.035	0.011	0.063	0.020
Passability classifier				
Elbrus-4C	0.147	0.021	0.268	0.116
Elbrus-8C	0.064	0.007	0.106	0.054
Intel Core-i3	0.016	0.003	0.025	0.010
Intel Core-i7	0.015	0.007	0.038	0.008
Map updater (layer $C1$)				
Elbrus-4C	0.065	0.019	0.364	0.036
Elbrus-8C	0.030	0.026	0.152	0.002
Intel Core-i3	0.012	0.005	0.086	0.009
Intel Core-i7	0.009	0.011	0.044	0.001
Map updater (layer $C2$)				
Elbrus-4C	0.025	0.010	0.291	0.011
Elbrus-8C	0.012	0.024	0.137	0.002
Intel Core-i3	0.003	0.005	0.038	0.001
Intel Core-i7	0.003	0.007	0.049	<0.0001
Map updater (layer $C3$)				
Elbrus-4C	0.048	0.016	0.350	0.006
Elbrus-8C	0.043	0.029	0.198	0.002
Intel Core-i3	0.038	0.015	0.123	0.001
Intel Core-i7	0.039	0.016	0.115	0.001
Bayesian convolution (layer $C4$)				
Elbrus-4C	1.465	0.093	1.781	1.325
Elbrus-8C	0.729	0.030	0.903	0.680
Intel Core-i3	0.155	0.012	0.272	0.134
Intel Core-i7	0.153	0.012	0.188	0.124

6 Conclusions

The installation of ROS framework onto industrial-grade controller equipped with Elbrus CPU could be considered successful for both 4-core and 8-core machine. The developed deployment system produces ready-to-drive vehicle controller environment. ROS installed on the Elbrus OS should be also considered

fully functional. The reliability of obtained system was verified during the tests. Thus the main target of this paper to deploy and test ROS on Elbrus-based controller is reached. The automated deployment framework was also developed using the scripts. The whole ROS environment now should be considered ready to be deployed on Elbrus-based systems as distribution with fixed version.

Also the performance comparison were performed to suggest Elbrus 8-core CPU to be considered as a concurrent solution for Intel Core CPUs equipped with operating system following POSIX (in Debian edition) and XDG standards, such as most Debian-based Linux distributions. The comparison between performance parameters of x86-based and Elbrus-based platforms should be considered incorrect because of VLIW architecture peculiarities besides the native code for x86 CPU could be adopted and run on Elbrus CPU. However, adopted native x86 machine code does not provide parallelism which is accessible for code natively compiled on Elbrus CPU.

There are the possibilities to improve performance of ROS on Elbrus platform using, features of platform-specific multithreaded libraries like `eml` and ports of existing tools. The described peculiarities of Elbrus platform and operating system allows to present Elbrus as completely new computational platform ready for *Big Data* tasks and supercomputing solutions.

Acknowledgements. Authors want to acknowledge **Alexey Kozov** the engineer of Science and Educational Center “Robotics” for his efforts to organize and supervise the testing process.

References

1. The 3-Clause BSD License. OpenSource.org Public Domain Website. <https://opensource.org/licenses/BSD-3-Clause>
2. ROS build farm online documentation. ROS Wiki pages website. <http://wiki.ros.org/buildfarm>. Accessed 08 Jan 2020
3. Bocharov, N.A., Paramonov, N.B., Timofeev, G.S., Panova, O.Y.: Performance of computer systems with Elbrus-8C processor for robotic systems’ tasks. *Nanoindustry* (82), 79–84 (2018). (in Russian)
4. Crick, C., Jay, G., Osentoski, S., Pitzer, B., Jenkins, O.C.: Rosbridge: ROS for non-ROS users. In: Christensen, H., Khatib, O. (eds.) *Robotics Research*, pp. 493–504. Springer, Cham (2017)
5. Fankhauser, P., Hutter, M.: A universal grid map library: implementation and use case for rough terrain navigation, pp. 99–120. Springer, Cham (2016). https://doi.org/10.1007/978-3-319-26054-9_5
6. Gorobets, A.V., Nejman-zade, M.I., Okunev, S.K., Kalyakin, A.A., Sukov, S.A.: Performance processor Elbrus-8C in supercomputer applications of computational gas dynamics (2018). (in Russian). Preprints of IPM im. M.V. Keldysha, N152
7. Koubaa, A., Alajlan, M., Qureshi, B.: ROSlink: bridging ROS with the internet-of-things for cloud robotics. In: Koubaa, A. (ed.) *Robot Operating System (ROS)*, pp. 265–283. Springer, Cham (2017)

8. Kozhin, A., Polyakov, N., Alfonso, D., Demenko, R., Klishin, P., Kozhin, E., Slesarev, M., Smirnova, E., Smirnov, D., Smolyanov, P., Kostenko, V., Gruzdov, F., Tikhorskiy, V., Sakhin, Y.: The 5th generation 28nm 8-core VLIW Elbrus-8c processor architecture. In: Proceedings of 2016 International Conference on Engineering and Telecommunication (EnT), pp. 86–90 (2016). <https://doi.org/10.1109/EnT.2016.027>. <https://www.researchgate.net/publication/312487200-The-5th-Generation-28nm-8-Core-VLIW-Elbrus-8C-Processor-Architecture>
9. Mahtani, A., Sánchez, L., Fernández, E., Martínez, A.: Effective Robotics Programming with ROS. Packt Publishing Ltd., Birmingham (2016)
10. Ong, S.K., Yew, A.W.W., Thanigaivel, N.K., Nee, A.Y.C.: Augmented reality-assisted robot programming system for industrial applications. *Robot. Comput. Integr. Manuf.* **61**, 101,820 (2020)
11. Quigley, M., Conley, K., Gerkey, B., Faust, J., Foote, T., Leibs, J., Wheeler, R., Ng, A.Y.: ROS: an open-source robot operating system. In: ICRA Workshop on Open Source Software, vol. 3, p. 5. Kobe University, Japan (2009)
12. Seth, N., Khare, R.: ACI (automated continuous integration) using Jenkins: key for successful embedded software development. In: 2015 2nd International Conference on Recent Advances in Engineering & Computational Sciences (RAECS), pp. 1–6. IEEE (2015)
13. Suyatinov, S.I.: Conceptual approach to building a digital twin of the production system, pp. 279–290. Springer, Cham (2020). https://doi.org/10.1007/978-3-030-32579-4_22
14. Tachkov, A., Kozov, A., Vukolov, A.: Peculiarities of porting of the Robotic Operating System framework onto Elbrus platform. *Softw. Syst. Int. Res. Pract. J.* **32**(4), 655–664 (2019). (in Russian). <https://doi.org/10.15827/0236-235X.128.655-664>
15. Takase, H., Mori, T., Takagi, K., Takagi, N.: mROS: a lightweight runtime environment of ROS 1 nodes for embedded devices. *J. Inf. Process.* **28**, 150–160 (2020)
16. Titov, A., Vukolov, A.: Free and open source software for technical texts editing, its advantages and experience of usage on TMM training in Bauman University. *Mech. Mach. Sci.* **64**, 208–215 (2019). https://doi.org/10.1007/978-3-030-00108-7_23
17. Volosatova, T.M., Kozov, A.V., Ryzhova, T.P.: Analysis of methods for detecting obstacles in the navigation system of a mobile robot. In: Evgrafov, A.N., Popovich, A.A. (eds.) Proceedings of Modern Mechanical Engineering: Science and Education (MMESE 2018) the 7th International Scientific and Practical Conference, pp. 420–429. Polytechnical University Publishing House, St. Petersburg (2018). (in Russian)
18. Volosatova, T.M., Kozov, A.V., Vukolov, A.Y.: Structural obstacle recognition method and its application in elevated terrain objects search. In: Proceedings of 2018 International Russian Automation Conference (RusAutoCon), pp. 1–5. IEEE Proceedings (2018)
19. Vukolov, A., Titov, A., Lapteva, M.: Application of modern free collaborative software development instruments for training process. In: Evgrafov, A.N., Popovich, A.A. (eds.) Proceedings of Modern Mechanical Engineering: Science and Education (MMESE 2019) the 8th International Scientific and Practical Conference, pp. 15–30. Politech-Press, St. Petersburg (2019). (in Russian). <https://doi.org/10.1872/MMF-2019-2>
20. Ward, B.: How Linux Works: What Every Superuser Should Know, 2nd edn. Piter Publishing, St. Petersburg (2014). (Russian ed. by M. Raytman)

21. Wei, H., Huang, Z., Yu, Q., Liu, M., Guan, Y., Tan, J.: RGMP-ROS: a real-time ROS architecture of hybrid RTOS and GPOS on multi-core processor. In: 2014 IEEE International Conference on Robotics and Automation (ICRA), pp. 2482–2487. IEEE (2014)
22. Wei, H., Shao, Z., Huang, Z., Chen, R., Guan, Y., Tan, J., Shao, Z.: RT-ROS: a real-time ROS architecture on multi-core processors. *Future Gener. Comput. Syst.* **56**, 171–178 (2016)



Calibration Study of a Continuously Variable Transmission System Designed for pHRI

Emir Mobedi¹ and Mehmet İsmet Can Dede²(✉)

¹ Italian Institute of Technology, Genoa, Italy
emir.mobedi@iit.it

² Izmir Institute of Technology, Urla, Turkey
candede@iyte.edu.tr

Abstract. Variable stiffness actuators (VSAs) have been used in many applications of physical human-robot interfaces (pHRI). A commonly employed design is the spring-based VSA allowing the user to regulate the output force mechanically. The main design criteria of these actuation systems are the adjustment of output force independent from the output motion, and shock absorbing. In our recent work, we implemented certain modifications on the two-cone friction drive continuously variable transmission system (CVT) so that the CVT can be employed in pHRI systems. Subsequently, the optimized prototype is developed. In this study, we introduce the prototype of this new CVT systems, and its force calibration tests. The results indicate that the manufactured CVT is capable of displaying the desired output force throughout its transmission ratio range within a tolerance.

Keywords: Continuously Variable Transmission (CVT) · Variable Stiffness Actuation (VSA) · Physical human-robot interface

1 Introduction

In early industrial robot applications, robots were operating in a working cell isolated from the working area of the human co-workers due to the safety reasons. Following the establishment of ISO 10218-1 standards, collaborative robots emerged in the industrial settings [1]. These robots are capable of regulating their physical interaction by the employment of compliant control methods [2] and/or with the help of specific mechanical solutions [3]. The latter one, which is most commonly developed and termed as VSAs, requires certain design requirements such as independent torque and motion variation [4]. In our recent work, we proposed a new CVT design by considering the aforementioned criteria [5]. The main motivation was to have a variable transmission ratio (in other words, the stiffness of the actuation system) to satisfy the variation of the torque amplification independent of the motion. The design is based on two-cone friction-drive CVT system with a transmission wheel in between the two cones to transmit the torque from the input cone to the output cone. In the design phase, the fundamental modification is carried out by changing the transmission wheel with a sphere allowing the transmission

© The Editor(s) (if applicable) and The Author(s), under exclusive license to Springer Nature Switzerland AG 2020

D. Pisla et al. (Eds.): EuCoMeS 2020, MMS 89, pp. 381–388, 2020.

https://doi.org/10.1007/978-3-030-55061-5_43

variation independent from output motion via holonomic motion capability of the sphere on the cones. However, as a result of this solution, new problems arise related to the bidirectional motion requirements of the pHRI application domain. In the clock-wise (CW) direction, the transmission can be achieved without any slip within the nominal torque transmission limits since the tangential friction forces (P_1 and P_2) pull the sphere into the cones (Fig. 1b). However, in the counter-clock-wise (CCW) direction, tangential friction forces (P_3 and P_4) push the sphere out of the cones, and this leads to slippage at the contact points even though the nominal transmission torque is not violated (cone-sphere, Fig. 1a). To overcome this problem, a second sphere, which is drawn with a red dashed circle in Fig. 1a, is added to the system. Additionally, springs with pretension are used for pushing the spheres to the cones to form an equal amount of normal force at the friction surfaces (F_1 and F_2 in Fig. 1a).

In this paper, the work carried out for the force calibration of this new CVT is presented. The next section presents the test setup for the calibration procedure.

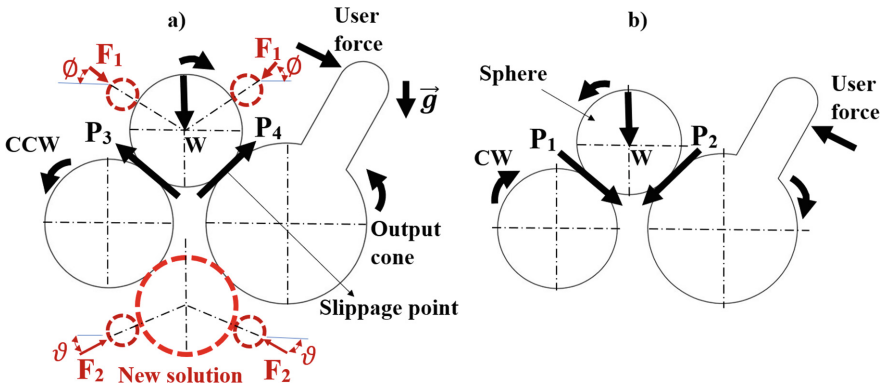


Fig. 1. The illustration of the new CVT: (a) the double-sphere CVT, (b) the working principle of the single-sphere CVT

2 The Test Setup of the New CVT System

In this section, test setup for the calibration procedure of the new CVT is introduced, which is presented in Fig. 2. The CVT system is composed of the two cones, a carriage with two spheres, an input torque motor (Motor-1), and a linear motion system coupled to a motor (Motor-2) that changes the location of the transmission elements (the spheres) which is shown in Fig. 2b.

In the test setup, the following components are used; (1) a force sensor (Kistler, type 9017B) that is fixed to the handle to measure the output force, (2) a capstan drive to transmit the output cone’s torque to the handle, (3) three absolute encoders (MagAlpha, TBMA702-Q-RD-00A) to observe whether there are slippages between the cones and the spheres, and the capstan drive. The encoder that appears on the right side of Fig. 2.a

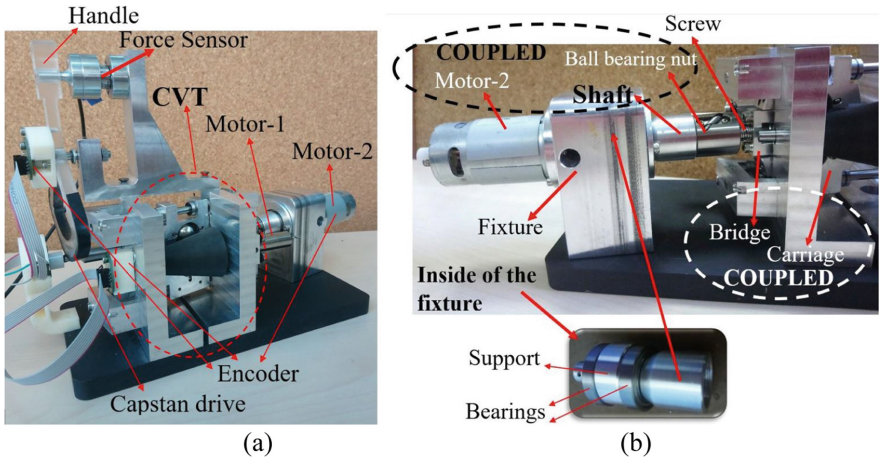


Fig. 2. Illustrations of the new CVT: (a) the CVT prototype (b) the design of the linear motion mechanism

is coupled to Motor-2 so that a closed-loop position control is employed to move the carriage mechanism that is changing the location of the spheres (Z distance).

The friction material covering the cones is chosen as EPDM rubber with 70 shore hardness. The neoprene material used in HAPKIT [6] is the basis for this selection, which has also the same shore value. After the cones are covered with the friction material, cones' angle (θ), length (L), and the minimum cone radii (r_1) are measured by a profile projector machine (Mitutoyo) (a contactless measurement method). The measurement results are presented in Table 1.

Table 1. Comparison between the desired and measured dimensions of the CVT

# of the cone	r_1 (mm)	θ (rad)	L (mm)
1	9.4635	12.2883°	49.57
2	9.4525	12.3122°	50.08
Selected values	9.455	12.295°	49.825
Desired values	9	12.5°	50.76

The difference the measured and designed parameters is the manufacturing errors due to the manufacturing process with grinding, CNC milling, and turning machines. Therefore, the tests are conducted by using the average of the measured dimensions of the cones, which are stated as the selected values in Table 1.

3 The Output Force Calibration of the CVT

The aim of this experiment is to observe if the desired maximum output force can be reached, which is selected as 6 N by considering the HAPKIT limitations [6]. The handle’s dimensions are illustrated in Fig. 3.

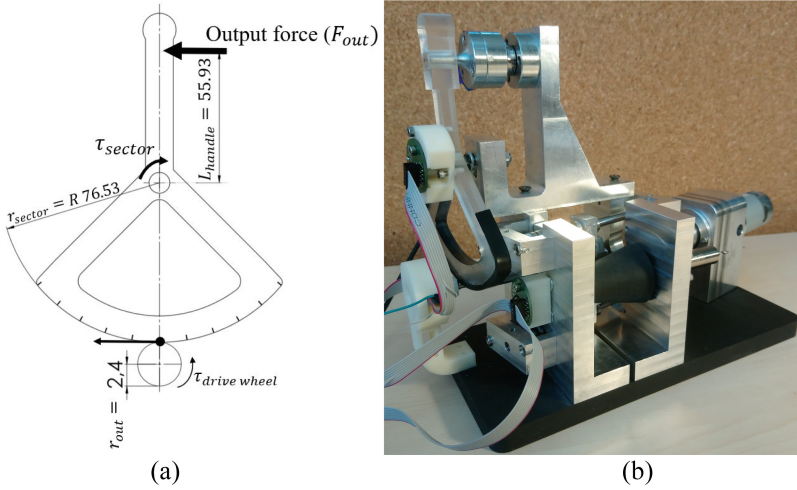


Fig. 3. (a) The illustration of the dimensions of the HAPKIT v2.0 (b) picture of the manufactured CVT with its handle

Accordingly, output torque of the CVT system, $\tau_{drivewheel}$, is calculated with respect to the presented dimensions in the following equations.

$$\tau_{sector} = F_{out}L_{handle} = (6) (55.93) = 335.58 \text{ mNm} \tag{1}$$

$$\tau_{drivewheel} = \tau_{sector} \frac{r_{out}}{r_{sector}} = (335.58) \frac{(2.40)}{(76.53)} = 10.523 \text{ mNm} \tag{2}$$

Finally, the input torque to be supplied to the input cone is calculated (τ_{in}) is presented in Eq. (3).

$$\tau_{in} = \frac{\tau_{drivewheel}r_2}{r_3\delta} \tag{3}$$

In Eq. (3), r_2 and r_3 represents the effective input and output cone radii, respectively. The derivation of these parameters is carried out in [5]. δ is varying between 0.97 and 0.99, which is a function of the spheres’ location (Z). This δ parameter is obtained as a result of force analyses, which is not presented in this paper due to space considerations. To calculate the necessary current, the torque constant of the Motor-1 (7.3 mNmA^{-1}) is considered.

At the beginning of the experiment, the tests are conducted by taking into account the calculated input torque values (theoretical torques) according to Eq. 3. First, the

carriage mechanism is located at the initial position where the transmission ratio is at the minimum level ($Z = 46.5461$ mm).

When lower input torques are applied to the input cone, the output force is not changed, hence, the transmission is not achieved between the cones. The reason for this problem is the manufacturing errors and the viscoelastic behavior of the friction material. During the bias torque experiments, observation of a minimum of 0.05 N force change at the handle is required to set the torque value as the bias torque.

In Fig. 4, the data set, including measured force, applied current, and the positions of the handle, output cone, and input cone is presented for the location of the spheres at $Z = 36.54$ mm. According to this Figure, the measured output force reaches the peak point at 0.6 s, and then slightly decreases. The issue stems from the viscoelastic behavior of the friction material, which is commonly known as the relaxation of the rubber. Therefore, the measured force values are recorded after the relaxation period. For instance, in Fig. 5, the recorded force values are between 1–1.2 s. On the other hand, the angular position of the input cone changes during this interval since the spheres are pressed inside the cones when the input torque is supplied to the system. In the course of this period, the angular positions of the cones are changed, and after the torque transmission is stopped, they are move back with a slight error with respect to their original positions. Nevertheless, this situation prevents both the actuator and the user from unexpected impacts, which is defined in the literature as shock absorbing phenomenon for VSAs [3].

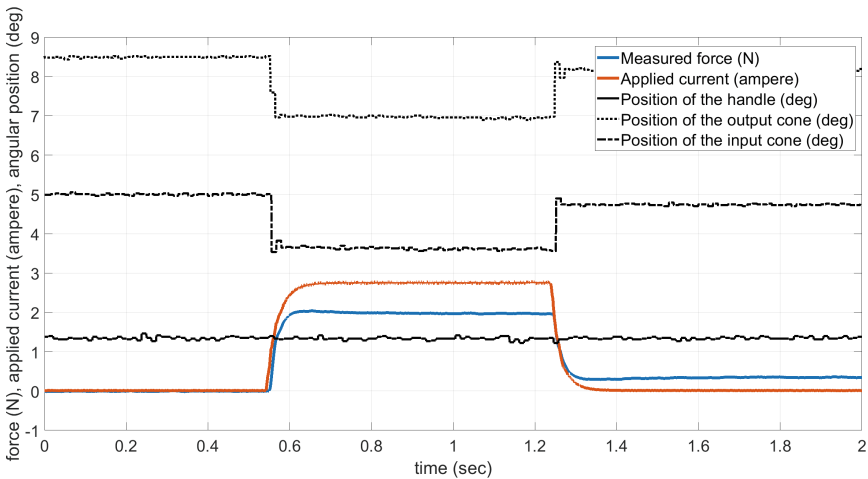


Fig. 4. The data set illustration for $Z = 36.54$ mm

During the force calibration experiments, maximum 5° slippage between the cones is taken as an acceptable position error.

The results of the non-calibrated experiment are presented in Fig. 5. The red dashed lines at ± 6 N presents the desired output forces at each direction. At each test point, the experiment is conducted for three times to check whether the repeatable data is acquired.

Moreover, it is clear that, as the carriage mechanism with the spheres approaches to the point where the output cone diameter is at its maximum value, the measured output force reaches the minimum level. In other words, even if it is expected to obtain the same output force value (6 N) in all the test points, the efficiency of the CVT reduces as the ratio between the input and output cone contact radii decreases. This situation is defined in the literature as the spin effect leading to extra rotation on the sphere [7].

Another phenomenon that is experienced in the tests is when the torque is applied to the input cone, the viscoelastic material covered on the cones is compressed by the sphere. It is as if a spring is compressed. After a test, if a second experiment is conducted, the measured force is decreased since the spheres submerged into the cones. Hence, after each experiment, an inverse torque is applied to the CVT so that there is no energy accumulation within the friction material. The value of the release term is selected as 0.5 A.

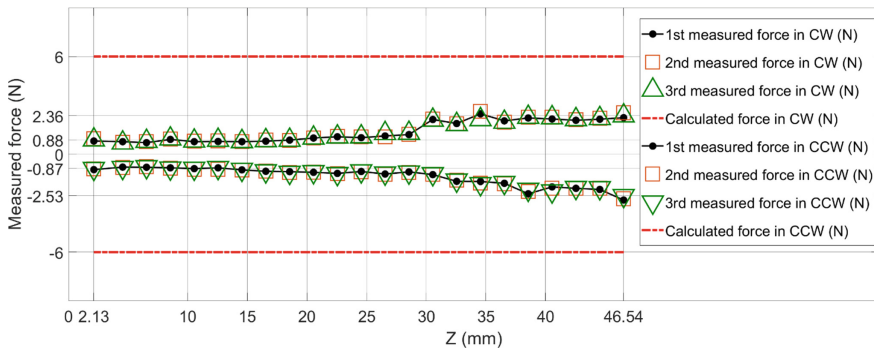


Fig. 5. The results of the non-calibrated desired continuous output force experiment

In the calibration experiment set, the current of the motor-1 is regulated manually to result in the desired output force, which is 6 N, at the handle. Moreover, the release term is set precisely for each test point to acquire repeatable force data.

In Fig. 6, the calibration results are illustrated. Consequently, it is observed that the CVT system is capable of displaying the desired force with repeatable data. The tolerance is chosen as 6 ± 0.3 N. In the same fashion of the non-calibrated experiment, at each test point, the experiment is conducted three times in each direction.

Also, considering the applied current, there is a similar trend for both CW and CCW directions. This means that the pretension of the spring forces is close to each other for the upper and lower sphere, and the covering of the cones with the friction material is achieved with minimal errors. The reason why the applied currents for CW direction is greater than CCW is that the normal force of the upper sphere cannot be adjusted precisely because of the gravitational load. On the other hand, the normal force of the lower sphere can be regulated as the pretension springs compensate both its gravity and the normal force from the lower part.

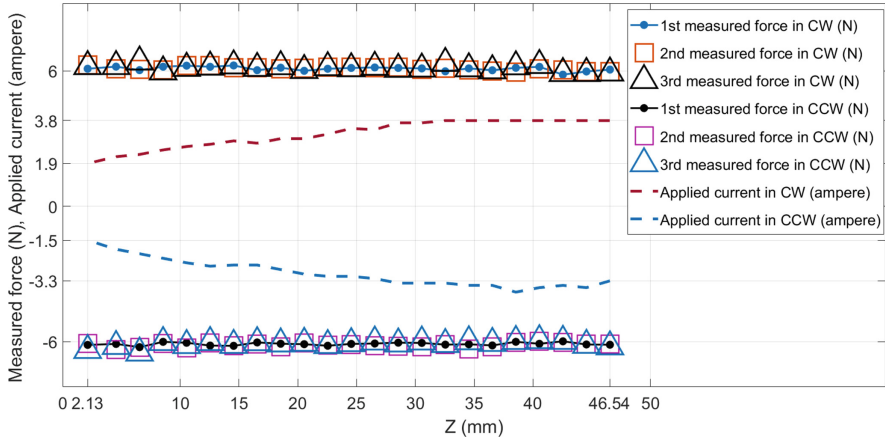


Fig. 6. The results of the calibrated desired continuous output force experiment

4 Discussions and Conclusions

In our previous studies, we introduced a CVT mechanism that is designed specifically to be used in pHRI applications. In this study, the force calibration of this CVT mechanism is presented. Results show that the proposed CVT has the capability to display 6 N output force which was assigned by considering the HAPKIT output force capabilities [6]. In Fig. 6, it is observed that the required amount current is increased when the distance along the Z-direction is varied from one end to the other end (in other words increased). This is due to change in the transmission ratio and also transmission efficiency which changes along the Z-direction. As a future study, we will introduce the optimization methodology of this new CVT based on its static force and variation of the transmission efficiency analyses.

Acknowledgments. This work is supported in part by The Scientific and Technological Research Council of Turkey via grant number 117M405.

References

1. Peternel, L., Tsagarakis, N., Ajoudani, A.: A human-robot co-manipulation approach based on human sensorimotor information. *IEEE Trans. Neural Syst. Rehabil. Eng.* **25**, 811–822 (2017)
2. Salisbury, J.K.: Active stiffness control of a manipulator in cartesian coordinates. In: *IEEE Conference on Decision and Control including the Symposium on Adaptive Processes*, pp. 95–100 (1980)
3. Wolf, S., Hirzinger, G.: A new variable stiffness design: matching requirements of the next robot generation. In: *IEEE International Conference on Robotics and Automation*, pp. 1741–1746 (2008)
4. Tonietti, G., Schiavi, R., Bicchi, A.: Design and control of a variable stiffness actuator for safe and physical human-robot interaction. In: *IEEE International Conference on Robotics and Automation*, pp. 526–31 (2005)

5. Mobedi, E., Dede, M.İ.C.: Geometrical analysis of a continuously variable transmission system designed for human-robot interfaces. *Mech. Mach. Theory* **140**, 567–585 (2019)
6. Martinez, M.O., Morimoto, T.K., Taylor, A.T., Barron, A.C., Pultorak, J.D.A., Wang, J., Kaiser, A.G., Davis, R.L., Blikstein, P., Okamura, A.M.: 3-D printed haptic devices for educational applications. In: *Proceedings of the IEEE Haptics Symposium*, pp. 126–133 (2016)
7. De Novellis, L., Carbone, G., Mangialardi, L.: Traction and efficiency performance of the double roller full-toroidal variator: a comparison with half- and full-toroidal drives. *J. Mech. Des.* **134**(7), 1–14 (2012)



Maneuvers Possibility for the Spacecraft Equipped with Liquid-Fuelled Engines Operating with Different Kinds of Fuel

Alexander Titov¹(✉), Andrei Vukolov², Margarita Lapteva¹,
and Gleb Prokurat³

¹ Aerospace Faculty, Bauman Moscow State Technical University, Moscow, Russia
aservqq@gmail.com, margosha-lapteva.1997@yandex.ru

² ELETTRA Sincrotrone Trieste S.C.p.A.,
Area Science Park Basovizza, Trieste, Italy
andrey.vukolov@elettra.eu

³ Design Faculty, Moscow State University of Communication and Informatics,
Moscow, Russia
evolvingc@yandex.ru

Abstract. This paper compares possibility for the spacecraft equipped with liquid-fuelled rocket engine to change orbital plane for purposes of space debris collection. The simple method of orbital plane rotation angle calculation is described. Also recommendations for fuel components selection made using possible orbital plane rotation angle as the main factor.

Keywords: Space debris · Debris collector · Space flight · Orbital maneuvers · Rocket engineering · Orbital plane

1 Introduction

Since the beginning of space exploration, many spacecrafts have been launched that have a limited service life. After a certain period of use, the device is put into *orbit of the burial site*, where it would be placed in uncontrollable state.

There are two main orbits for space debris disposal: low and geostationary. For purposes of disposal the space debris should be classified by size and weight as set of uncontrollable objects. At orbital speeds of about 8 km/s the fragments of debris of 1–10 cm diameter could damage almost any operating spacecraft. Thus such fragments should be completely removed to open the burial site for further debris collection.

The most commonly considered task is elimination of garbage apparatus descending from the parking orbit into the atmosphere. This way could be considered ineffective because of material dissipation. The materials from which the spacecrafts are made, are often expensive and e.a. toxic, so they should be accessible for harvesting.

2 Target Setting

A garbage collector considered here (Fig. 1) is a hypothetical spacecraft with key parameters indicated in Table 1. In fact, it should be considered as universal space tug (possible object of standardization) with interchangeable payload. The payload is considered as the device with cube geometry with 2 m edge.

Table 1. Spacecraft key parameters

Parameter	Value	Unit
Mass of the payload (spacecraft without fuel)	1500	kg
Mass of the fuel charge	3000	kg

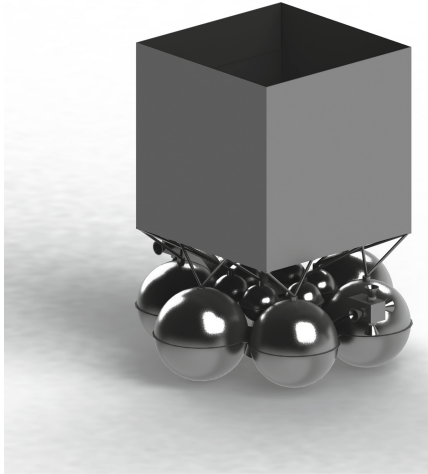


Fig. 1. Concept drawing of the space debris collector

For debris collector spacecraft the main control problem is orbit changing. The main aspect of this problem is changing the circular orbit to the one located in another plane and returning back to collect and reload the debris to the main module. The target is set in this paper to the task of only changing the orbit of the spacecraft to another plane without affection for height. The debris collector considered as liquid-fuelled with rocket engines with constant specific impulse. The fuel density, self ignition etc. and other characteristics are not taken into consideration. Also, stabilization of the device (suppression of external moments) is considered already implemented, and fuel is not consumed additionally, except for the designed maneuver.

For example: movement of the spacecraft from orbital plane with inclination of 52° to the one with 62,8° requires the specific impulse calculated for the round-trip flight. With the same method the maximum allowable angle between orbital planes for existing types of liquid fuel components are also calculated and calculations are described below.

3 Methodology

The calculation basics are partially based on [1, 10].

3.1 Velocity

The required increment of spacecraft’s speed should be calculated using Tsiolkovsky’s equation:

$$\Delta V = J_y \ln \left(\frac{M_H}{M_K} \right) \tag{1}$$

where J_y —is a specific impulse, M_H —mass of whole “rocket train” at $t = 0$, M_K —mass of the discharged “rocket train” at $t = t_0$ without detached sections. For a two-way flight, the characteristic speeds in both directions are assumed the same: $\Delta V_1 = \Delta V_2 \Rightarrow \Delta V_1 - \Delta V_2 = 0$.

Intermediate weight M^* equals the mass of the spacecraft with remaining fuel after the first maneuver¹:

$$\begin{aligned} \Delta V_1 &= J_y \ln \left(\frac{M_H}{M^*} \right) \\ \Delta V_2 &= J_y \ln \left(\frac{M^*}{M_K} \right) \end{aligned} \tag{2}$$

Then:

$$J_y \ln \left(\frac{M_H}{M^*} \right) - J_y \ln \left(\frac{M^*}{M_K} \right) = 0, \quad \ln \left(\frac{M_H}{M^*} \right) - \ln \left(\frac{M^*}{M_K} \right) = 0 \tag{3}$$

$$\ln \left(\frac{M_H/M^*}{M^*/M_K} \right) = 0 \Rightarrow \frac{M_H/M^*}{M^*/M_K} = 1 \Rightarrow \frac{M_H \cdot M_K}{(M^*)^2} = 1 \tag{4}$$

Now:

$$M^* = \sqrt{M_H M_K} \tag{5}$$

$$\Delta V_1 = \Delta V_2 = J_y \ln \left(\frac{M_H}{\sqrt{M_H M_K}} \right) = J_y \ln \left(\sqrt{\frac{M_H}{M_K}} \right) = \frac{1}{2} J_y \ln \left(\frac{M_H}{M_K} \right) = \Delta V \tag{6}$$

And on the final step we have:

$$\Delta V = \frac{1}{2} J_y \ln \left(\frac{M_H}{M_K} \right) = \frac{1}{2} J_y \ln \left(\frac{4500}{1500} \right) = J_y \cdot 0.5493 \tag{7}$$

In the last equation the two things should be taken into consideration: forced acceleration (impulse change) ΔV and specific impulse J_y [8].

¹ Here and below the aviatic evolution notation is used in formulas for angular values.

3.2 Spatial Trajectory

The schema of spatial maneuver is presented on Fig. 2.

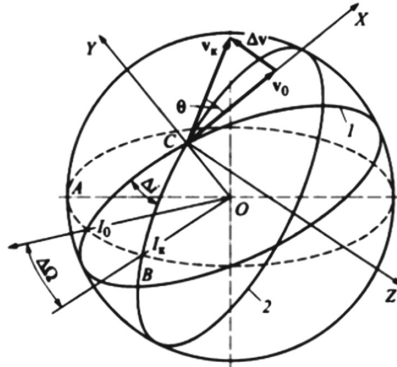


Fig. 2. Spatial maneuver

Impulse of speed ΔV can be found geometrically using cosine theorem:

$$\Delta V = \sqrt{V_1^2 + V_2^2 - 2V_1V_2 \cos \Delta i}$$

For circular orbits of the same height, we consider the characteristic velocity as a constant and the angles of rotation for orbital plane are considered particularly small so we can expand $\cos(\Delta i)$ into a row:

$$\cos(\Delta i) = 1 - \frac{\Delta i^2}{2} \tag{8}$$

Then $\Delta V = V\Delta i$, where Δi is angle of the orbit plane rotation. The final evolution is shown on Fig. 3.

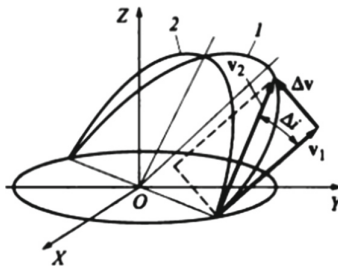


Fig. 3. Impulse for orbit plane changing evolution

Let the height 1000 km is considered. Then

$$V = \sqrt{G \frac{M}{R}} \quad (9)$$

Here gravitational constant is $G = 6,67 \cdot 10^{-11} \text{ m}^3 \cdot \text{kg}^{-1} \cdot \text{s}^{-2}$, Earth's mass $M = 5,972 \cdot 10^{24} \text{ kg}$, height from the Earth's center is $R = 7371 \text{ km}$. Now:

$$V = \sqrt{G \frac{M}{R}} = \frac{6,67 \cdot 10^{-11} \cdot 5,972 \cdot 10^{24}}{7,371 \cdot 10^6} = 7351,22 \text{ m/s} \quad (10)$$

Summarizing the calculations, we obtain:

$$\Delta i = \frac{\Delta V}{V} = \frac{\frac{1}{2} J_y \ln \left(\frac{M_H}{M_K} \right)}{\sqrt{G \frac{M}{R}}} = 7,472 \cdot 10^{-5} J_y \quad (11)$$

4 Fuel Component Pairs: Brief Description

4.1 Ethanol–Liquid Oxygen

This combination of fuel components [1, 7] was used at the dawn of aircraft and rocket science on short-range ballistic missiles such as the German *V-2* and the American *Redstone* [9]. Due to the small specific impulse (about 2450 m/s), this pair has been superseded by more effective combinations.

4.2 Kerosene–Liquid Oxygen

Often used in the first stages of launch vehicles. Examples of use: *P-7*, *Saturn-5* [5], *Titan* [4], *Falcon* [3]. Usage of kerosene reduces the cost of starting, because it is not cryogenic component. The specific impulse is about 2950 m/s, which is a good enough indicator to actively use these components as rocket fuel.

4.3 Asymmetric Dimethylhydrazine–Nitrogen Tetra-Oxide

These fuel components are used in *Proton* and *Fregat* tug modular spacecrafts. This pair has several advantages, including self-ignition, stable flame front, relatively high density in comparison with liquid gases. From the other side, there is no significant difference in specific impulse between this pair and kerosene–liquid oxygen pair (see Sect. 4.2). Also these components are chemically aggressive and extremely toxic [2, 6]. It eliminates them completely from manned flights.

4.4 Liquid Hydrogen–liquid Oxygen

These components produce almost the highest specific impulse among the chemical fuel component pairs [9]. From the other side, these cryogenic liquids are most problematic loads in the rocketry [4, 8]. The usage of this component pair is very limited all around the world despite advantages.

4.5 Specific Thrust Comparison

Table 2 represents most common cases of fuel pairs with their values of specific thrust [4, 8].

Table 2. Specific thrust comparison (s)

Component pair	Liquid oxygen	Nitrogen-tetra-oxide	Nitric acid	Liquid fluorine
Liquid hydrogen	453			412
Kerosene	335	309	313	
Ethanol	255			
Liquid methane	360			
Asymmetric dimethylhydrazine	344	318		
Hydrazine				370

5 Orbital Plane Movement Estimation

Using equations defined above, here the comparison is made between values of possible orbital plane rotation angles for different kinds of fuel (Fig. 4, b). Also the graph (Fig. 4, a) shows linear dependency between specific impulse and the described Δi angle.

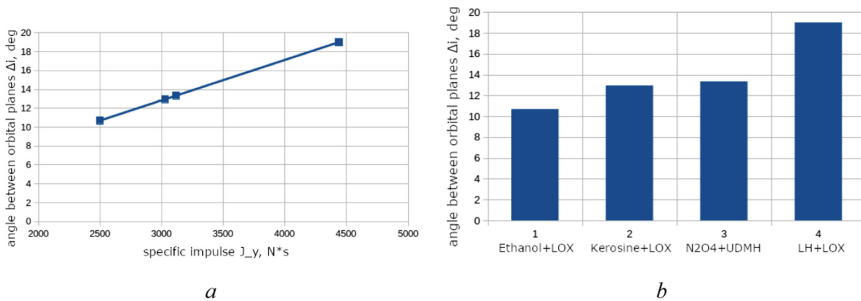


Fig. 4. Comparison of calculated possible orbital plane rotation angles

The final comparison is presented in Table 3.

Table 3. Results comparison for orbital plane rotation for different kinds of fuel

Component pair	P , s	J_y , m/s	Δi , deg
Ethanol—Liquid oxygen	255	2499	10.70
Kerosene—Nitrogen tetra-oxide	309	3028	12.96
Asymmetric dimethylhydrazine—Nitrogen tetra-oxide	318	3116	13.34
Liquid hydrogen—Liquid oxygen	453	4439	19.01

6 Conclusions

In the described example design the main assumption was made that mass of fuel accumulated on the spacecraft is the same in all cases. Thus the estimations made in this paper allows only to make recommendations for further research. As the space debris collector presumes as reusable orbital vehicle with possibility to be automatically refuelled, the recommendations should be made assuming the possibility to store large amounts of fuel components in space as obligatory feature. The task declared in this article can be solved with the components like *Asymmetric dimethylhydrazine—Nitrogen tetra-oxide* or *Kerosene—Nitrogen tetra-oxide*. Cryogenic fuel also solves this task but become less able to recommend because of evaporation and delivery problems. The comparison showed cryogenic pair *Liquid hydrogen—Liquid Oxygen* gives the most value of the specific impulse and it would be used for future researches which require maximal maneuver possibility (e.g. for the maximal angle between orbital planes).

References

1. Liquid-fueled rocket engines. MIT. MIT website. <http://www.im.lcs.mit.edu/rocket/>
2. Annual Report on Carcinogens: Summary. USA National Toxicology Program Public Information Office (1985)
3. Dinardi, A., Capozzoli, P., Shotwell, G.: Low-cost launch opportunities provided by the Falcon family of launch vehicles. In: Proceedings of the Fourth Asian Space Conference (2008)
4. Alemasov, V.E., Dregalin, A.F., Tishin, A.P.: Theory of Rocket Engines. Mashinostroenie, Moscow (1989). (in Russian)
5. Bilstein, R.E.: Stages to Saturn: A Technological History of the Apollo/Saturn Launch Vehicles. NASA SP-4206, Washington, D.C. (1980)
6. Carlsen, L., Kenessov, B.N., Batyrbekova, S.Y.: A QSAR/QSTR study on the environmental health impact by the rocket fuel 1,1-Dimethyl Hydrazine and its transformation products. *Environ. Health Insights* **1** (2008). <https://doi.org/10.4137/EHI.S889>
7. Clark, J.D.: Ignition!: An Informal History of Liquid Rocket Propellants. Rutgers University Press, New Brunswick (1972)
8. Dorofeev, A.A.: Basics on Theory of Heat Rocket Engines. Bauman Moscow State Technical University (1999). (in Russian)

9. Huzel, D.K., Huang, D.H.: Design of liquid propellant rocket engines. Scientific and Technical Information Office, National Aeronautics and Space Administration (NASA) (1971)
10. Zelentsov, V.V., Kazakovtsev, V.P.: Basics of Ballistic Design for Satellite Spacecrafts. Bauman Moscow State Technical University, Moscow (2012). (in Russian)



HiL Test Bench as a Development Environment for Hydraulic Steering Systems

Michael Bruns¹ (✉), Ludger Schütz¹, Poul Ennemark², Thomas Schmidt²,
Jørgen Krusborg², and Jens Falkenstein¹

¹ Chair of Transmission and Drive Technology, University of Rostock, Rostock, Germany
{michael.brun, ludger.schuetz, jens.falkenstein}@uni-rostock.de

² Danfoss Power Solutions ApS, Nordborg, Denmark
{PEnnemark, t.schmidt, jkrusborg}@danfoss.com

Abstract. Innovative steering systems require extensive testing procedures before they are ready for on-road use. Safety, durability and comfort aspects have to be proven before mass production even starts. These processes can take high amounts of test drives on specially equipped prototype vehicles, which is expensive, difficult to reproduce and sometimes even dangerous. To enhance all aspects of the testing process, a hardware-in-the-loop (HiL) test bench for hydraulic steering systems is developed at the University of Rostock, which will be used to emulate several vehicle parameters, driving maneuvers and system failures of the steering system.

As an answer to component modularity of steering systems, this HiL test bench is designed to keep up with fast test environment modification without any effort. Therefore, the interfaces between the steering system and the vehicle reactions are determined in the hydraulic system, instead of the steering mechanics. This makes it possible to reduce the amount of mechanical steering components, such as the respective steering axle, on the test bench and emulate their characteristics in the vehicle model, to start testing even in the development state.

Keywords: Hydraulic steering · Hardware-in-the-loop test bench · Four quadrant servo pump · Cylinder end stop

1 Introduction

Hydrostatic steering systems are used in various commercial and agricultural vehicles, such as tractors, combines, dumpers etc. Those vehicles require high steering forces, therefore conventional mechanical steering systems are typically not installed. The hydrostatic steering unit becomes the interface between the vehicle and the driver, but also between innovative support and safety systems, for example, GPS based field driving patterns and driving speed based steering limitations. Therefore, the effects of system failures are rising, because the steering system becomes an active part of the vehicle control. To get this systems on-road ready, extensive testing and failure analysis is required. Starting this procedure even in the development state and preventing dangerous situations for the test driver requires a test bench, which can emulate specified driving situations and procedure [3, 4].

© The Editor(s) (if applicable) and The Author(s), under exclusive license to Springer Nature Switzerland AG 2020

D. Pisla et al. (Eds.): EuCoMeS 2020, MMS 89, pp. 397–404, 2020.

https://doi.org/10.1007/978-3-030-55061-5_45

1.1 Innovative Steering Systems

Along with rising demands for automation and safety, user comfort receives higher and higher focus. Electro-hydraulic steering systems are developed to meet these requirements by giving the ability to perform specific functionalities on request. The combination of hydraulic power and computer precision makes the steering system one of the most connected control units of commercial and agricultural vehicles using the hydraulic system and the signal network for example CAN bus.

1.2 HiL Development Environment

HiL test benches represent a cost-effective and safe alternative to driving tests in a prototype vehicle. They ensure reproducible results and perform durability tests completely automated. They also give the ability to include high resolution measuring devices without interfering with vehicle components [2].

According to the demand of various realistic test situations, a model of the test vehicle is developed by the project partner [5]. The model allows adjustments or changes of the main steering characteristics and interacts with the tested steering system using the HiL test bench.

2 HiL Test Bench Concept

The hydrostatic steering unit in the vehicle is connected hydraulically to the steering cylinder, which drives the mechanics. Considered heavy vehicles require high steering forces and therefore high hydraulic pressures, which can easily be emulated by an electro-hydraulic actuator. To ensure realistic steering system tests during an early development state, the interfaces between the emulated physical system and the test object are determined as close to the test object as possible. In this case, the main test object is the hydrostatic steering unit, its interfaces to the vehicle model are determined to be the hydraulic connections to the steering cylinder. This allows to test the hydrostatic steering unit, even if the according steering mechanics, such as the steering cylinder or steering axle, are not available yet.

2.1 System Comparison

The real steering system consists of the hydrostatic steering unit, the steering cylinder and the steering mechanics (Fig. 1(a)). The hydrostatic steering unit acts as the steering input with the steering wheel angle φ_{Steer} and the steering wheel torque M_{Steer} , resulting in a pressure differential Δp across the steering cylinder. Multiplied by the piston area A_{Cyl} , the hydraulic force F_{Steer} is acting at the steering cylinder. Due to vehicle geometry (e.g. toe) and external forces affecting the wheels, steering reaction forces F_{React} also act on the steering cylinder and its stroke will be s_{Cyl} .

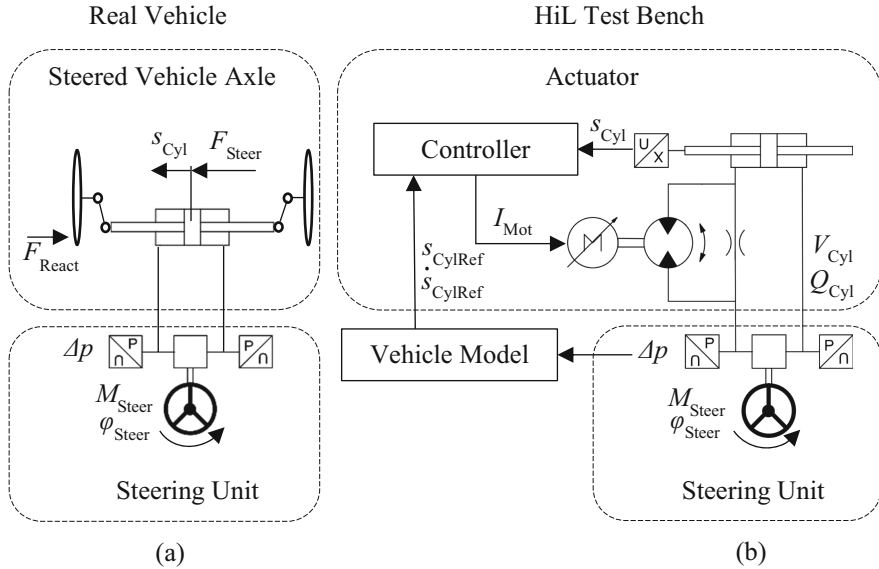


Fig. 1. Real vehicle and HiL test bench

However, the HiL test bench consists of the hydrostatic steering unit and the HiL actuator (Fig. 1(b)), with φ_{Steer} and M_{Steer} are resulting in a pressure differential Δp , too. This pressure differential Δp acts on the HiL actuator, which emulates the reaction forces, calculated by the vehicle model.

2.2 HiL Actuator

The actuator, as shown in Fig. 1(b), is a combination of a four quadrant servo pump, a bypass orifice and a measuring cylinder connected to a LVDT (linear variable differential transformer) displacement transducer for measuring the cylinder stroke s_{Cyl} . The actuator is designed to control the real cylinder stroke s_{Cyl} of the measuring cylinder according to the calculated vehicle model and therefore the flow rate Q_{Cyl} and volume V_{Cyl} passing through the hydrostatic steering unit. The bypass orifice is designed to ensure the required minimum speed of the servo pump depending on the hydraulic pressure differential. The servo pump is speed controlled and torque precontrolled.

2.3 HiL Structure

The vehicle model receives the measured pressure differential Δp and calculates the time varying reference values for the cylinder stroke s_{CylRef} and the cylinder speed \dot{s}_{CylRef} . These references represent the real steering cylinder values of the vehicle. The HiL actuator then controls s_{Cyl} and \dot{s}_{Cyl} on the test bench, multiplied by the piston area A_{Cyl} the values V_{Cyl} and Q_{Cyl} are defined, which closes the loop. The HiL structure with its reaction order is shown in Fig. 2.

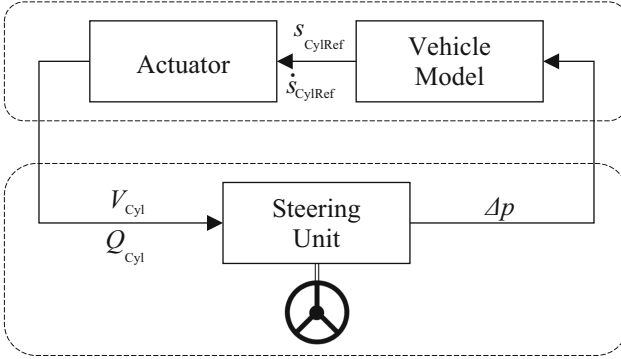


Fig. 2. Overall HiL control structure

3 Hydraulic Actuator Control

The reference values s_{CylRef} and \dot{s}_{CylRef} are the inputs of the actuator. The cylinder stroke reference s_{CylRef} is required for position control of the cylinder in later steps. The cylinder speed reference \dot{s}_{CylRef} gives the cylinder’s volumetric flow rate reference Q_{CylRef} :

$$Q_{CylRef} = \dot{s}_{CylRef} \cdot A_{Cyl} \tag{3.1}$$

Q_{CylRef} is being used for calculating the servo pumps volumetric flow rate reference Q_{PmpRef} , which consists of three parts described in the following.

During operation, the pressure differential Δp is measured and transmitted to the real-time control. To provide minimum speed of the servo pump, the bypass orifice is slightly opened. Its adjustment S_{Orf} , Δp and oil temperature T are inputs for calculating the model-based volumetric flow rate Q_{OrfRef} , which flows through the orifice. Furthermore, Δp , T , Q_{CylRef} and Q_{OrfRef} are used to calculate the leakage volumetric flow rate of the servo pump $Q_{LeakRef}$. These three mentioned volumetric flow rates are further processed. They are summed up to the servo pumps volumetric flow rate reference Q_{PmpRef} . With the hydraulic servo pumps displacement V_h , this value corresponds to the precontrolled angular velocity of the servo pump $\omega_{PmpPrectrl}$, see Eq. (3.2).

$$\omega_{PmpPrectrl} = (Q_{PmpRef}/V_h)2\pi \tag{3.2}$$

By time derivation and filtering of $\omega_{PmpPrectrl}$, provided by an DT1-element (first-order lag derivative term), results the precontrolled angular acceleration of the servo pump $\alpha_{PmpPrectrl}$. Furthermore, it is used for calculating the precontrolled acceleration torque. The described processes are shown in Fig. 3.

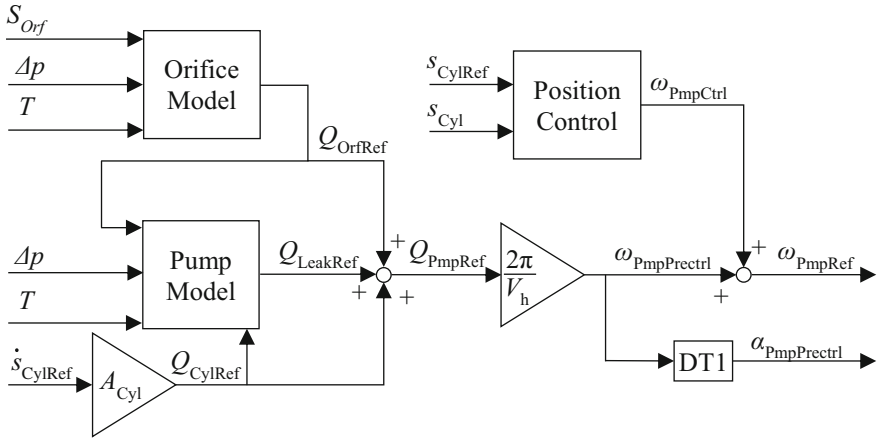


Fig. 3. Test bench actuator precontrol and position control

The cylinder stroke reference s_{CylRef} and the measured cylinder stroke s_{Cyl} are used by the position control to calculate the required angular velocity of the servo pump $\omega_{PmpCtrl}$. Summed up with $\omega_{PmpPreCtrl}$ results in the servo pump angular velocity reference ω_{PmpRef} , which is transmitted to the inverter of the servomotor. In addition to this value, the inverter gets a precontrolled torque $M_{PmpPreCtrl}$ which includes the precontrolled acceleration torque by using $\alpha_{PmpPreCtrl}$, displayed in Fig. 3. It is also calculated to compensate the pressure differential Δp and other physical effects e.g. friction of rotating parts.

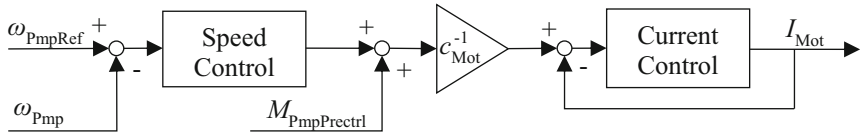


Fig. 4. Basic control structure of the servomotor inverter

The output of the speed control in addition to $M_{PmpPreCtrl}$ divided by the motor torque constant c_{Mot} results in the reference value for the current control of the inverter, which sets the servomotor current I_{Mot} , shown in Fig. 4. During controlled operation of the hydraulic actuator, V_{Cyl} and Q_{Cyl} are caused and affecting the hydrostatic steering unit, see Fig. 2.

4 Experimental Results

For the first measurements on the HiL test bench under development, the hydrostatic steering unit is in emergency steering mode, whereby its internal dosing pump operates as a hand pump building up pressure manually [1]. Figure 5 shows the test bench.

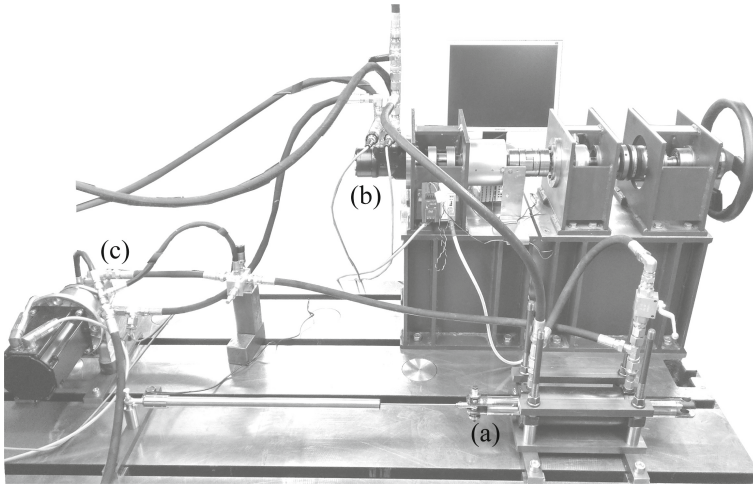


Fig. 5. HiL test bench. (a) measuring cylinder. (b) steering unit. (c) servo pump.

4.1 Cylinder End Stop HiL Model

To describe the test bench dynamics, a simplified HiL model of a hydraulic steering cylinder is used to emulate the end stop. The input value is Δp and the output values are s_{CylRef} and \dot{s}_{CylRef} , as shown in Fig. 2.

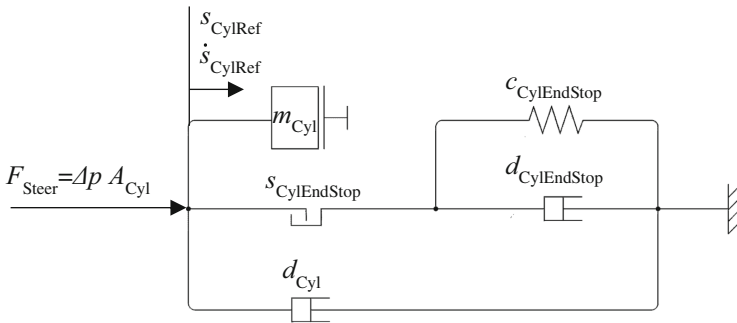


Fig. 6. Simplified hydraulic cylinder end stop model

This specific model of a hydraulic steering cylinder end stop is based on a contact stiffness and contact damping model as shown in Fig. 6, and should be seen as a benchmark for the test bench dynamics. The steering force F_{Steer} and the viscous damping force $d_{Cyl} \cdot \dot{s}_{Cyl}$ act against the inert mass m_{Cyl} of the steering cylinder. When the end stop is reached at $s_{CylRef} = s_{CylEndStop}$, the additional forces with the end stop stiffness $c_{CylEndStop}$ and the end stop damping $d_{CylEndStop}$ act against m_{Cyl} , too, according to the real cylinder characteristics [6]. The values $c_{CylEndStop}$ and $d_{CylEndStop}$ are determined like the real cylinder characteristic tested in Sect. 4.2, which is a common steering cylinder for commercial vehicles.

4.2 Compared Cylinder End Stop Results

The test procedure is to act with constant steering speed ω_{Steer} at the hydrostatic steering unit, until reaching the steering cylinder end stop. To compare the emulated results, the procedure first is performed with a real steering cylinder. The constant steering speed results in constant cylinder speed \dot{s}_{Cyl} and almost constant Δp until the mechanical end stop is reached. In Fig. 7 the cylinder stroke s_{Cyl} and Δp are shown. The end stop of this cylinder is reached at a stroke of $s_{\text{Cyl}} = 35$ mm and a raising of Δp is clearly visible, as shown in Fig. 7(a). This is the result of rotational inertia of the hydrostatic steering unit and its operator and one important aspect of judging the steering feeling. To test the emulated steering cylinder end stop, the model shown in Fig. 6 is used as a simple HiL model. The emulated end stop is implemented by dynamic operation of the servo pump, not by the mechanical cylinder end stop.

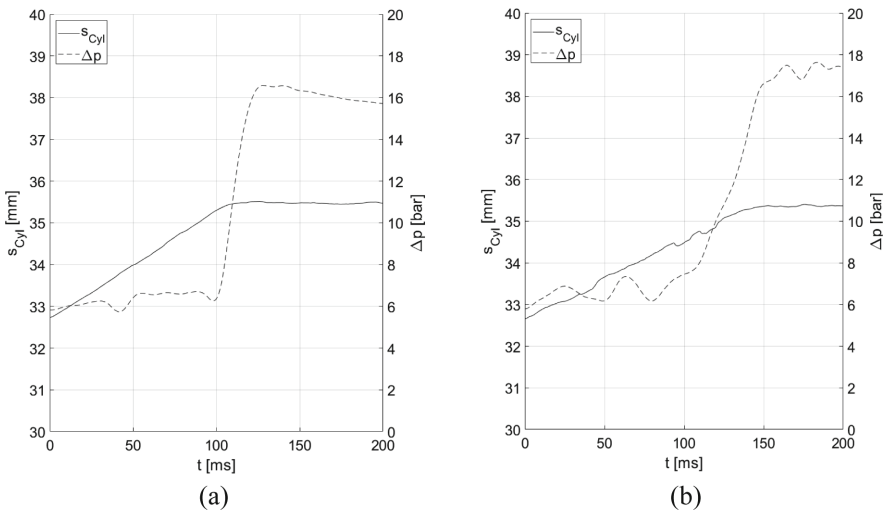


Fig. 7. Real (a) and emulated (b) steering cylinder end stop characteristics

As shown in Fig. 7(b) the main behavior of the emulated end stop is a plausible result in itself. The raising of Δp when reaching the end stop is 0.2 bar/ms so the significant raise of Δp , which characterizes the end stop is done after 40 ms. The still reduced dynamics is mainly determined by the currently available servomotor. An extension with a servomotor with higher dynamics is planned.

5 Conclusion

The objective of this research was to investigate the performance of a prototype HiL test bench as a development environment for steering systems. The main innovation compared to existing test benches is the reduction of mechanical steering components and the transfer of their properties into the virtual vehicle model.

The use of a servo pump, which operates in four quadrants, combined with a leakage free hydraulic measuring cylinder, provides a simple hydraulic actuator with high potential. The shown system reduction allowed effortless changes in test environments by just selecting the according vehicle model parameters.

Knowing the capabilities, further investigation of the actuator dynamics will increase the effectivity of this HiL test bench and help to perform more realistic test procedures in steering system development.

Acknowledgments. This research and development project was supported by the European Regional Development Fund (EFRE). Support was also provided by the lead partner Technologie-Beratungsinstitut (TBI) according to the directive for support, development and innovation of the Ministry of Economics, Construction and Tourism of Mecklenburg-Vorpommern.

References

1. Gebhardt, N.: Fluidtechnik in Kraftfahrzeugen. Springer, Heidelberg (2016)
2. Koch, A.: Entwicklung eines Hardware-In-The-Loop-Prüfstandes zur Untersuchung der Drehschwingungen und Bremssystemkoordination bei Einzelradantrieben von Elektrofahrzeugen. Dr. Hut, München (2017)
3. Nippold, C., Küçükay, F., Henze, R.: Analysis and application of steering system on a steering test bench. *Automot. Engine Technol.* **1**, 3–13 (2016)
4. Schmidt, D.: Entwurf eines fehlertoleranten Lenkventils für Steer-by-Wire Anwendungen bei Traktoren. *Karlsruher Schriftreihe Fahrzeugsystemtechnik*, KIT Karlsruhe (2014)
5. Schröder, I., Schmidt, T., Krusborg, J., Woernle, C.: Parametrization of a real-time vehicle model from driving tests for HiL testing of hydraulic steering systems. In: *EuCoMeS 2020 Proceedings of the 8th European Conference on Mechanism Science*. Springer (2020)
6. The MathWorks, Inc.: Double-Acting Hydraulic Cylinder. <https://www.mathworks.com/help/physmod/hydro/ref/doubleactinghydrauliccylinder.html>. Accessed 13 Feb 2020



Contact Detection Approach Between Wheel and Rail Surfaces

Filip Marques¹✉, Hugo Magalhães^{2,3}, Joao Pombo^{2,3,4}, Jorge Ambrósio³, and Paulo Flores¹

¹ CMEMS-UMinho, Universidade do Minho, Guimarães, Portugal
{fmarques, pflores}@dem.uminho.pt

² Institute of Railway Research, School of Computing and Engineering,
University of Huddersfield, Huddersfield, UK
{h.magalhaes, j.pombo}@hud.ac.uk

³ IDMEC, Instituto Superior Técnico, Universidade de Lisboa, Lisbon, Portugal
jorge.ambrosio@tecnico.ulisboa.pt

⁴ ISEL, IPL, Lisbon, Portugal

Abstract. This work presents a general formulation to identify the contact points for the interaction between wheels and rails in the context of railway dynamics simulations. This formulation treats the wheel and rail as parametric surfaces and searches the contact between each wheel strip and the rail independently to avoid the numerical difficulties due to the wheel concave zone. This methodology assumes the rail as locally straight and takes advantage that its potential contacting surface is always convex. For the evaluation of contact forces, two Hertzian-based models are employed for normal and creep forces. A trailer vehicle running on a curved track is used to demonstrate the effectiveness of this methodology.

Keywords: Wheel-rail contact · Contact detection · Multibody dynamics · Parametric surfaces

1 Introduction

The vehicle-track interaction has a significant impact on the dynamics of railway vehicles, therefore, the computational modeling of wheel-rail contact interaction has been investigated in terms of contact search [1], normal and creep forces evaluation [2], determination of contact patch shape [3], among others. In fact, the development of more accurate and efficient methodologies to evaluate wheel-rail contact improves the reliability and applicability of railway dynamics simulation.

A typical contact detection procedure between wheel and rail involves the geometric definition of both bodies and the identification of the contact location. There are two main methodologies to handle this problem, namely the constraint and the elastic approaches. The former considers the bodies fully rigid, a set of nonlinear kinematic constraints are defined, and the contact forces are determined during the resolution of the equations of motion [4], while the latter allows penetration between bodies, since they can locally

deform, and the normal forces are obtained with a spring-like behavior [5]. The elastic approach is employed here.

Wheel and rail elements are typically defined through parametric surfaces in which their profiles are described by continuous functions. In most cases, their interaction occurs between the rail head and wheel flange or wheel tread, which represent non-conformal configurations. However, in the wheel transition zone, conformal contact can occur, leading to the appearance of numerical problems [6]. Some authors neglect the concave transition zone between tread and flange to avoid these issues [2], however, the results' accuracy may become compromised.

The main objective of this work is to present a methodology for the contact detection between wheel and rail surfaces. The remainder of this paper is divided as follows. Section 2 explains the surfaces parametrization as well as the procedure to identify the contact points. In Sect. 3, the contact force models utilized here are described. A trailer vehicle running on a curved track is used as example of application in Sect. 4. Finally, some conclusions are provided in Sect. 5.

2 Wheel and Rail Parametrization

An accurate mathematical description of the wheel and rail contacting surfaces improves the accuracy on the contact detection. Therefore, the rail is obtained through the sweep of its cross-section along a given path, and the wheel is defined by the revolution of its cross-section. Here, both surfaces are parametrized, namely a point on the rail is given by the path's arclength (s_r) and its lateral coordinate (u_r), and a point on the wheel surface is defined through the angular parameter (s_w) and the lateral coordinate (u_w). This parametrization is schematically represented in Fig. 1. Moreover, both wheel and rail profiles are defined through analytical functions given in the respective standards and represented in Fig. 2.

Two arbitrary points, P and Q , located on rail and wheel surfaces can be given as function of the surface parameters. Regarding point P , the arclength of the rail $s_{r,P}^{side}$ allows to identify the position of a given rail cross-section, \mathbf{r}_r^{side} , and its orientation by a set of vectors \mathbf{t}_r^{side} , \mathbf{n}_r^{side} and \mathbf{b}_r^{side} , which represent the tangent, normal and binormal vectors, respectively, as depicted in Fig. 1. Thus, the rail transformation matrix can be defined as

$$\mathbf{A}_r^{side} = [\mathbf{t}_r^{side} \quad \mathbf{n}_r^{side} \quad \mathbf{b}_r^{side}] \tag{1}$$

Hence, the position of point P is calculated as

$$\mathbf{r}_P^{side} = \mathbf{r}_r^{side} + \mathbf{A}_r^{side} \left\{ 0 \quad u_{r,P}^{side} \quad f_{r,P}^{side} \right\}^T \tag{2}$$

where $u_{r,P}^{side}$ is the rail lateral parameter of point P , and $f_{r,P}^{side}$ denotes the ordinate of the rail profile for $u_{r,P}^{side}$, as shown in Fig. 2 (left). Moreover, the superscript *side* stands for "L" or "R", whether it refers to the left or right elements, respectively.

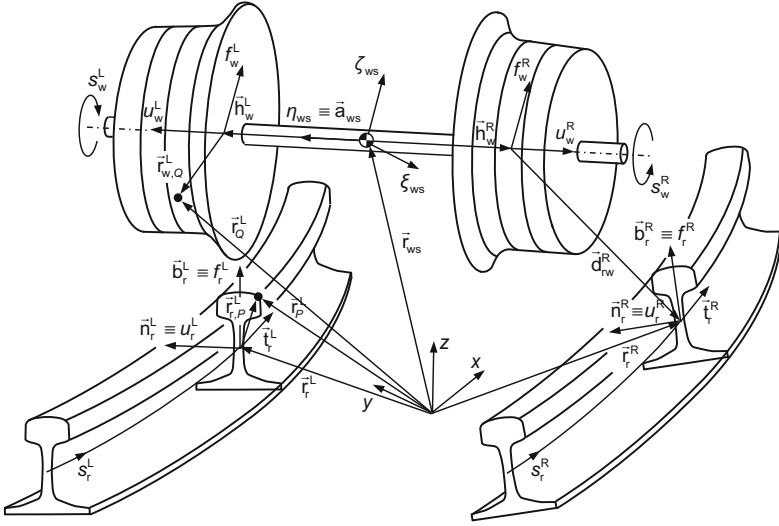


Fig. 1. Parametrization of wheel and rail surfaces

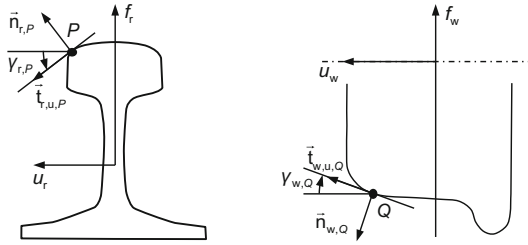


Fig. 2. Representation of both rail and wheel profiles and their local coordinate system.

In order to obtain the rail position and orientation to be used for the contact detection, it must be found the parameter s_r^{side} that minimizes the distance between the wheel and rail profiles represented by \mathbf{d}_{rw}^{side} , shown in Fig. 1, and calculated as

$$\mathbf{d}_{rw}^{side} = \mathbf{r}_r^{side} - (\mathbf{r}_{ws} + \mathbf{h}_w^{side}) \tag{3}$$

in which \mathbf{r}_{ws} defines the location of wheelset mass center and \mathbf{h}_w^{side} is the relative position between the wheelset mass center and the wheel profile origin given as

$$\mathbf{h}_w^L = H/2 \cdot \mathbf{a}_{ws} \quad \text{or} \quad \mathbf{h}_w^R = -H/2 \cdot \mathbf{a}_{ws} \tag{4}$$

where H denotes the distance between both wheel profiles and \mathbf{a}_{ws} is the wheelset axial unit vector. The minimum distance can be obtained by satisfying

$$\mathbf{d}_{rw}^{side} \cdot \mathbf{t}_r^{side} = 0 \tag{5}$$

Hence, s_r^{side} is obtained and utilized to determine the rail profile location, \mathbf{r}_r^{side} , and orientation, \mathbf{A}_r^{side} , for the remaining contact search. In what concerns to point Q on the

wheel surface, it is defined following the representation of Fig. 1 as

$$\mathbf{r}_Q^{side} = \mathbf{r}_{ws} + \mathbf{h}_w^{side} + \mathbf{A}_w^{side} \mathbf{A}_{w,s}^{side} \left\{ 0 \ u_{w,Q}^{side} \ f_{w,Q}^{side} \right\}^T \quad (6)$$

in which $u_{w,Q}^{side}$ is the lateral wheel surface parameter of point Q , $f_{w,Q}^{side}$ denotes the ordinate of the wheel profile function for the position $u_{w,Q}^{side}$, as represented in Fig. 2 (right), and \mathbf{A}_w^{side} is the wheel transformation matrix which allows to obtain a wheel coordinate system aligned with the rail frame, and it can be computed as

$$\mathbf{A}_w^{side} = \left[\mathbf{n}_w^{side} \ \mathbf{a}_w^{side} \ \mathbf{b}_w^{side} \right] \text{ in which } \begin{cases} \mathbf{a}_w^{side} = \mathbf{a}_{ws} \\ \mathbf{b}_w^{side} = \mathbf{t}_r^{side} \times \mathbf{a}_w^{side} / \left\| \mathbf{t}_r^{side} \times \mathbf{a}_w^{side} \right\| \\ \mathbf{n}_w^{side} = \mathbf{a}_w^{side} \times \mathbf{b}_w^{side} \end{cases} \quad (7)$$

The transformation matrix $\mathbf{A}_{w,s}^{side}$ specifies the rotation around the wheel axis, which depends on the angular surface parameter, $s_{w,Q}^{side}$, and is defined as

$$\mathbf{A}_{w,s}^L = \begin{bmatrix} \cos(s_{w,Q}^L) & 0 & \sin(s_{w,Q}^L) \\ 0 & 1 & 0 \\ -\sin(s_{w,Q}^L) & 0 & \cos(s_{w,Q}^L) \end{bmatrix} \text{ or } \mathbf{A}_{w,s}^R = \begin{bmatrix} -\cos(s_{w,Q}^R) & 0 & -\sin(s_{w,Q}^R) \\ 0 & -1 & 0 \\ -\sin(s_{w,Q}^R) & 0 & \cos(s_{w,Q}^R) \end{bmatrix} \quad (8)$$

Based on the relation between wheel and rail coordinate systems, the roll angle, φ , and yaw angle, α , are obtained through successive rotations of vector \mathbf{a}_w^{side} . In order to find the potential contact points, one constraint concerns the parallelism between both normal vectors. Considering the rail is locally straight, the normal vector to the wheel surface must be in the plane formed by \mathbf{n}_r^{side} and \mathbf{b}_r^{side} , which yields that the first element of the wheel normal vector in the rail coordinate system must be zero. This vector is obtained from the following consecutive rotations

$$\mathbf{n}_{w,Q,r}^{side} = \mathbf{R}_\varphi^{side} \mathbf{R}_\alpha^{side} \mathbf{A}_{w,s}^{side} \mathbf{n}_{w,Q,w}^{side} \quad (9)$$

in which $\mathbf{R}_\varphi^{side}$ and \mathbf{R}_α^{side} are the rotation matrices of roll and yaw angles, respectively, and the normal vector to the wheel surface in local coordinates is given as

$$\mathbf{n}_{w,Q,w}^{side} = \left[0 \ \sin(\gamma_{w,Q}^{side}) \ -\cos(\gamma_{w,Q}^{side}) \right]^T \quad (10)$$

where $\gamma_{w,Q}^{side}$ denotes the wheel contact angle on point Q , which is represented in Fig. 2, and can be calculated as function of the profile function as

$$\gamma_{w,Q}^{side} = \arctan(f'_{w,Q}{}^{side}) \quad (11)$$

It must be noted that the remaining vectors represented in Fig. 2 can be similarly obtained. Thus, imposing that the first element of the $\mathbf{n}_{w,Q,r}^{side}$ is zero, it yields

$$s_{w,Q}^{side} = \arcsin\left(-\tan(\alpha^{side}) f'_{w,Q}{}^{side}\right) \quad (12)$$

Moreover, the distance vector between wheel and rail potential contact points, \mathbf{d}^{side} , must also be parallel to both normal vectors. Thus, it is possible to calculate the increment of location of rail contact point so \mathbf{d}^{side} also falls in the plane formed by \mathbf{n}_r^{side} and \mathbf{b}_r^{side} , as depicted in Fig. 3. This increment is determined as

$$\Delta x^L = \left(\left| f_{w,Q}^L \right| f_{w,Q}^{\prime L} - u_{w,Q}^L \right) \sin(\alpha^L) \quad \text{or} \quad \Delta x^R = \left(u_{w,Q}^R - \left| f_{w,Q}^R \right| f_{w,Q}^{\prime R} \right) \sin(\alpha^R) \quad (13)$$

Accordingly, Eq. (2) must be replaced by

$$\mathbf{r}_P^{side} = \mathbf{r}_r^{side} + \mathbf{A}_r^{side} \left\{ \Delta x^{side} \quad u_{r,P}^{side} \quad f_{r,P}^{side} \right\}^T \quad (14)$$

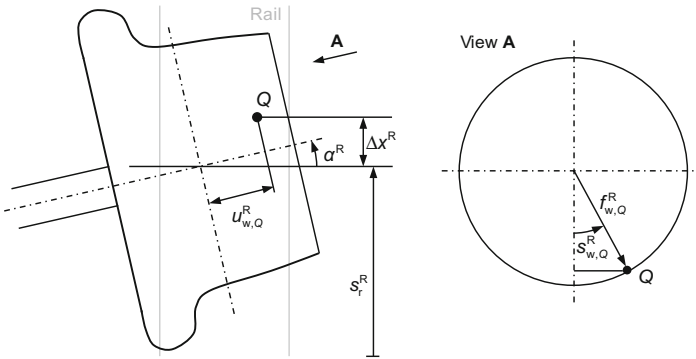


Fig. 3. Representation of the increment on longitudinal direction for the contact point in the rail.

The wheel angular coordinate and the longitudinal position along the rail can be analytically evaluated with Eq. (12) and (13), respectively. Thus, the contact points only depend on $u_{w,Q}^{side}$ and $u_{r,P}^{side}$. For each wheel strip, the rail lateral parameter which ensures that \mathbf{d}^{side} and $\mathbf{n}_{r,P}^{side}$ are parallel can be obtained by solving

$$\mathbf{d}^{side} \cdot \mathbf{t}_{r,u,P}^{side} = 0 \quad (15)$$

Therefore, to find the contact points, an optimization problem must be formulated to find the wheel strip with the largest penetration which is given as

$$\delta = \left\| \mathbf{d}^{side} \right\| \quad \text{if} \quad \mathbf{n}_{r,P}^{side} \cdot \mathbf{d}^{side} < 0 \quad (16)$$

3 Contact Forces Models

The contact forces play a key role on the dynamic behavior of the multibody systems, since they must consider the geometrical and physical properties of the contacting bodies and contribute for the stable resolution of the equations of motion.

Regarding the normal contact force evaluation, a Hertzian-based model is utilized here [7] which can be expressed as

$$f_n = \begin{cases} K\delta^n c_e & \dot{\delta} \leq -v_0 \\ K\delta^n [c_e + (1 - c_e)(3r^2 - 2r^3)] & -v_0 < \dot{\delta} < v_0 \\ K\delta^n & \dot{\delta} \geq v_0 \end{cases} \quad \text{where } r = \frac{\dot{\delta} + v_0}{2v_0} \quad (17)$$

where K is the contact stiffness that depends on the local geometric and material properties, δ denotes the penetration depth, $\dot{\delta}$ represents the penetration velocity, v_0 denotes the tolerance for the penetration velocity, c_e is the coefficient of restitution, and n is an exponent that defines the degree of nonlinearity.

In what concerns to the creep forces, Polach method is adopted in this work since it complies with Hertz theory by considering an elliptical contact patch [8]. The longitudinal and lateral creep forces and spin creep moment are evaluated as

$$f_x = f \frac{v_x}{v_C}, \quad f_y = f \frac{v_y}{v_C} + f_{yS} \frac{\phi}{v_C}, \quad m_z = 0 \quad (18)$$

where v_x , v_y and ϕ are the longitudinal, lateral and spin creepages, respectively, v and v_C denote the magnitude of translational creepage and the modified translational creepage, f is the tangential contact force caused by the longitudinal and spin creepages and f_{yS} expresses the lateral tangential force due to spin creepage.

Both forces act as external forces on the wheelsets and are included on the equations of motion which, for constrained multibody systems, can be given as [9]

$$\begin{bmatrix} \mathbf{M} & \Phi_{\mathbf{q}}^T \\ \Phi_{\mathbf{q}} & \mathbf{0} \end{bmatrix} \begin{Bmatrix} \ddot{\mathbf{q}} \\ \boldsymbol{\lambda} \end{Bmatrix} = \begin{Bmatrix} \mathbf{g} \\ \boldsymbol{\gamma} - 2\alpha \dot{\Phi} - \beta^2 \Phi \end{Bmatrix} \quad (19)$$

in which \mathbf{M} denotes the global mass matrix, $\Phi_{\mathbf{q}}$ expresses the Jacobian matrix of the constraints equations, $\ddot{\mathbf{q}}$ is the generalized accelerations, $\boldsymbol{\lambda}$ denotes the vector of Lagrange multipliers, which represent the reaction forces on ideal joints, \mathbf{g} is the vector of external generalized forces, $\boldsymbol{\gamma}$ is the right-hand side vector of acceleration constraint equations, Φ and $\dot{\Phi}$ denote the violation of constraints at position and velocity level, respectively, α and β are feedback control parameters of Baumgarte technique for constraints stabilization. Equation (19) must be solved in each time step to get the system's accelerations, which are then integrated over time.

4 Example of Application

A trailer vehicle negotiating a left curve with a radius of 300 m is used as application case. This multibody model includes 11 bodies, namely 4 wheelsets, 4 axleboxes, 2 bogie frames and the carbody. The vehicle starts with a forward velocity of 18.3 m/s, being the total simulation time 41 s. The initial configuration considers a lateral misalignment of 2 mm to promote the hunting motion of the system.

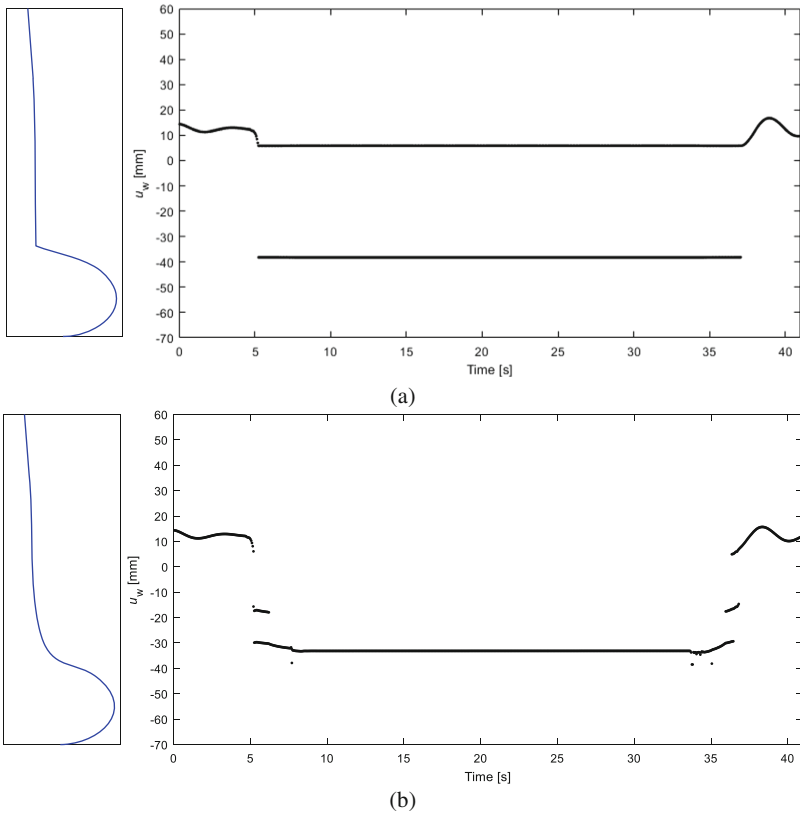


Fig. 4. Representation of the location of the main point of contact for each patch over time.

The contact in the right wheel of the leading wheelset of the front bogie is analyzed in detail, since it is the external wheel relatively to the curve where the flange contact occurs. Thus, Figs. 4(a) and (b) display the location of the several contact points in the wheel profile over time for the simplified profile and real profiles, respectively. For the beginning of motion, it is verified that both profiles perform a hunting motion due to the initial misalignment. This can be seen through the wave-like behavior in the contact location. During the curve negotiation, bigger differences are identified. With the simplified profiles, the contact is determined independently in the tread and flange, and it is observed that there is simultaneous contact in the tread and flange from 5.2 s until 37.1 s. On the other hand, for real profiles, during most of the curve, only one contact patch exists, which is in the wheel transition zone. However, in some periods, the wheel and rail may interact in more than one location which results in multiple contact patches.

5 Conclusions

A methodology for contact detection between wheel and rail considering realistic geometries is presented here. This method uses the assumption that the rail is locally straight

and searches the strip which corresponds to the maximum virtual penetration for each contact patch. The dynamic simulation of a trailer vehicle running on a curved track verifies the effectiveness of the proposed methodology. The results show that this approach allows the existence of multiple contact patches in each wheel-rail pair and that the simplification of the wheel profile in the transition zone does not allow an accurate identification of the contact points.

Acknowledgments. The first author is supported by the Portuguese Foundation for Science and Technology (FCT) under grant PD/BD/114154/2016. This work is also supported by FCT with the reference project UIDB/04436/2020. This work was supported by FCT, through IDMEC, under LAETA, project UIDB/50022/2020.

References

1. Marques, F., Magalhães, H., Pombo, J., Ambrósio, J., Flores, P.: A three-dimensional approach for contact detection between realistic wheel and rail surfaces for improved railway dynamic analysis. *Mech. Mach. Theory* **149**, 103825 (2020)
2. Magalhães, H., Marques, F., Liu, B., Antunes, P., Pombo, J., Flores, P., Ambrósio, J., Piotrowski, J., Bruni, S.: Implementation of a non-Hertzian contact model for railway dynamic application. *Multibody Syst. Dyn.* **48**(1), 41–78 (2019)
3. Sun, Y., Zhai, W., Guo, Y.: A robust non-Hertzian contact method for wheel–rail normal contact analysis. *Vehicle Syst. Dyn.* **56**(12), 1899–1921 (2018)
4. Shabana, A.A., Tobaa, M., Sugiyama, H., Zaazaa, K.E.: On the computer formulations of the wheel/rail contact problem. *Nonlinear Dyn.* **40**(2), 169–193 (2005)
5. Malvezzi, M., Meli, E., Falomi, S., Rindi, A.: Determination of wheel-rail contact points with semianalytic methods. *Multibody Syst. Dyn.* **20**, 327–358 (2008)
6. Marques, F., Magalhães, H., Ambrósio, J., Flores, P.: Approach for conformal contact detection for wheel-rail interaction. In: 7th European Conference on Mechanism Science - EuCoMeS 2018, Aachen, Germany. *Mechanisms and Machine Science*, vol. 59, pp. 71–78 (2019)
7. Machado, M., Moreira, P., Flores, P., Lankarani, H.M.: Compliant contact force models in multibody dynamics: evolution of the Hertz contact theory. *Mech. Mach. Theory* **53**, 99–121 (2012)
8. Polach, O.: A fast wheel-rail forces calculation computer code. *Vehicle Syst. Dyn.* **33**(Sup1), 728–739 (1999)
9. Nikravesh, P.E.: *Computer Aided Analysis of Mechanical Systems*. Prentice Hall, Englewood Cliffs (1988)



Counter-Rotating Savonius Wind Turbine

Marat Dosaev^(✉), Liubov Klimina, Anna Masterova, Vitaly Samsonov,
and Yury Selyutskiy

Institute of Mechanics of Lomonosov Moscow State University, Moscow, Russia
dosayev@imec.msu.ru

Abstract. The mathematical model of a small-scale counter-rotating Savonius wind turbine is constructed and studied. Rotors are located one above the other. Their shafts are coaxial. The shaft of one Savonius rotor carries the rotor of an electric generator, and the shaft of the other carries the stator of the same generator. Savonius rotors are supposed to rotate in opposite directions. Thus, the relative angular speed of the generator rotor with respect to the stator is increased. The generator is connected to the local electrical circuit. Operation modes corresponding to autorotations of Savonius rotors in the wind flow are discussed. The trapped power in such regimes is estimated. It is shown that the chosen design of the wind turbine is characterized by the same maximum power coefficient as a classical single Savonius rotor, but with double increase of the relative angular speed of the generator rotor with respect to the stator. Parameters of the system that provide maximum trapped power coefficient are found.

Keywords: Wind turbine · Savonius rotors · Dynamical system · Steady motion · Stability · Trapped power

1 Introduction

The general scheme of a counter-rotating vertical axis wind turbine was proposed rather recently [1]. This scheme supposes that the device consists of two counter-rotating vertical axis wind rotors located one above the other; one of them carries the rotor of an electric generator, while the other carries the stator. Thus, the interaction between two rotating parts of the turbine is represented by the electromechanical interaction between the rotor and the stator of the generator. In the same time, the aerodynamic interaction between two wind rotors can be neglected: each rotor doesn't have considerable influence upon the airflow about the other rotor. This is the crucial difference compared with a counter-rotating scheme, where two turbines are located at the same altitude close to each other like in [2]. In case of [2], the aerodynamic interaction between rotors can be used to increase the power efficiency of the system (for this purpose, rotors should be located in the optimal position with respect to each other).

The advantage of the design [1] with respect to the classical single vertical axis wind turbine results in the increase of the angular speed of the rotor of the electric generator with respect to the stator. The level of electrical load is adjusted in order to increase

the power efficiency of the turbine. For the case of a small-scale Darrieus type counter-rotating wind turbine, this effect was demonstrated in the context of the model [3]. In general, the counter-rotation scheme can be applied for a wide range of classical wind turbines [4] and even for novel types of vertical axis wind power systems such as those proposed in [5–7].

Here the model of a small-scale counter-rotating Savonius type wind turbine is constructed. The model contains a small number of parameters and is represented by a second order dynamical system. The steady operation modes of this device are studied that correspond to asymptotically stable fixed points of the dynamical system. The principal scheme of analysis of the system is rather similar to that applied in [3, 8].

The trapped power is estimated. The effect of increasing of the relative angular speed of the rotor of a generator with respect to the stator is described. In some cases such effect can ensure high enough angular speed; and additional gear mechanism isn't necessary. This is one of the advantages of the construction. If, a gear mechanism is still needed due to conditions of operation, then the solution discussed in [4] can be applied. Other advantages are decrease in the total angular momentum of the system, which results in reduction of gyroscopic loads.

2 Description of the Model

Mechanical system consists of two similar vertical axis Savonius type wind rotors coaxial to each other, located one above the other, and intended to rotate in opposite directions around the axis Oz (Fig. 1). The stator of an electric generator is fixed to the shaft of the 1st Savonius rotor, and the rotor of this generator is fixed to the shaft of the 2nd Savonius rotor. The generator is connected to the local electric circuit with the external resistance R .

The wind flow has constant velocity V . Angles φ_i ($i = 1, 2$) of rotation of two rotors are counted in opposite directions. Thus, the angular speed Ω_1 of the 1st rotor is positive if this rotor rotates clock-wise (looking from the tip of the Oz axis), and the angular speed Ω_2 of the 2nd rotor is positive if it rotates counter clock-wise.

Both rotors are supposed to have similar geometric and mass characteristics. Let r be the radius of each rotor and J be the moment of inertia of each rotor about the axis Oz . In order to describe the aerodynamic torque T_i acting upon the i^{th} rotor we use the quasi-steady approach [9]:

$$T_i = 0.5\rho SV^2 r C_m(\varphi_i, \lambda_i), \quad \lambda_i = r\Omega_i/V. \quad (1)$$

In expressions (1), ρ is the density of the air, S is the area of the cross-section of the rotor, λ_i is the so-called tip speed ratio of the rotor.

The function $C_m(\varphi_i, \lambda_i)$ is the dimensionless aerodynamic torque coefficient that can be approximated using experimental data. For the classical (S-shape) Savonius rotor, this function is π -periodic and can be represented in the form of Fourier series with respect to a variable 2φ [9]. Main harmonics are the most essential. Here the following approximation is used:

$$C_m(\varphi, \lambda) = C_T(\lambda) + (k_1\lambda + k_2) \sin(2\varphi) + (k_3\lambda + k_4) \cos(2\varphi). \quad (2)$$

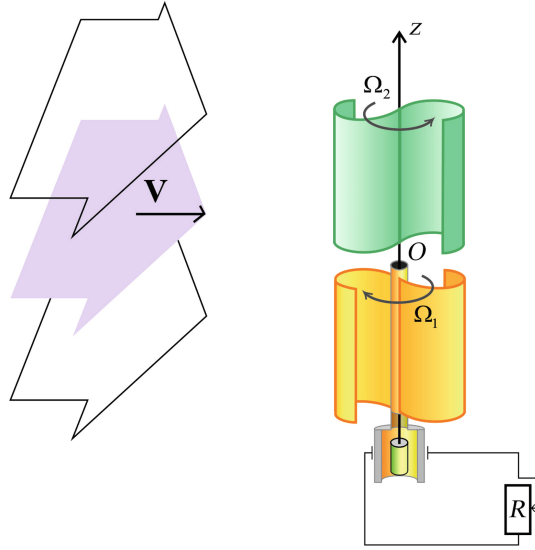


Fig. 1. The scheme of the counter-rotating Savonius wind turbine

In (2), the function $C_T(\lambda)$ is described using experimental data obtained in [10]. Here the following approximation of this function is used (Fig. 2):

$$C_T(\lambda) = -0.118\lambda^5 + 0.48\lambda^4 - 0.5\lambda^3 - 0.2\lambda^2 + 0.25\lambda + 0.26; \quad (3)$$

The interaction between the rotor and the stator of the generator is described by the electromechanical torque T_e (from the model [11]):

$$T_e = \frac{C}{(\sigma + R)}(\Omega_1 + \Omega_2). \quad (4)$$

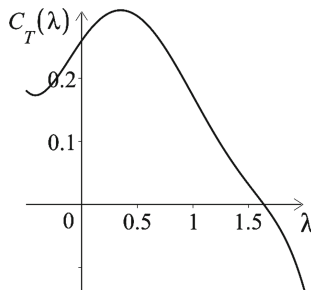


Fig. 2. Dimensionless coefficient (3) of the average aerodynamic torque acting on the Savonius rotor.

In relation (4), C is the constant coefficient of electromechanical interaction, and σ is the internal resistance of the generator.

For the further analysis, we introduce dimensionless time $\tau = r^{-1}Vt$ and use dimensionless variables λ_i .

3 Equations of Motion and Averaging Method

Equations of motion of the system in dimensionless variables have the following form (the dot denotes derivative with respect to the dimensionless time τ):

$$\begin{cases} \dot{\varphi}_i = \lambda_i, & i = 1, 2, & \varepsilon = \frac{\rho S r^3}{2J}, \\ \dot{\lambda}_1 = \varepsilon(C_m(\varphi_1, \lambda_1) - c(\lambda_1 + \lambda_2)), \\ \dot{\lambda}_2 = \varepsilon(C_m(\varphi_2, \lambda_2) - c(\lambda_1 + \lambda_2)), & c = \frac{2C}{V\rho S r^2(\sigma + R)}. \end{cases} \quad (5)$$

Here parameter ε is responsible for inertial properties, and c is the dimensionless external load coefficient. Suppose that ε is small parameter, and variables λ_i are bounded from zero. Perform the averaging of the system (5):

$$\begin{cases} \dot{\lambda}_1 = \varepsilon(C_T(\lambda_1) - c(\lambda_1 + \lambda_2)), \\ \dot{\lambda}_2 = \varepsilon(C_T(\lambda_2) - c(\lambda_1 + \lambda_2)). \end{cases} \quad (6)$$

Correlation between solutions of the system (5) and the averaged system (6) over a finite time interval is described by the theorem [12] (similar averaging was performed in the model of a double rotor Darrieus wind turbine in [3]).

In more complicated cases of averaging over angles, the behavior of the system near a resonance may not be described well by the averaged system: trapping into resonance may occur [13, 14]. But coupling terms in (5) do not depend on the angles, so the behavior near a resonance is described correctly by the same averaged system (6), at least, over finite time intervals (the corresponding averaging procedure is performed in [3] for the system with similar coupling terms).

In what follows, we suppose that an asymptotically stable fixed point $(\lambda_1^*, \lambda_2^*)$ of the system (6) corresponds to a steady operation mode of the wind turbine (when $\lambda_i^* \neq 0$). Similar approach is used in [15] for another problem of motion in media.

Values λ_i^* depend on c . In particular, the number of possible steady operation modes depends on c . Further, parametrical analysis of characteristics of steady modes is performed.

4 Steady Operation Modes

For the fixed point of the system (6), the following holds:

$$\begin{cases} C_T(\lambda_1^*) = C_T(\lambda_2^*), \\ \frac{C_T(\lambda_1^*)}{\lambda_1^* + \lambda_2^*} = c. \end{cases} \quad (7)$$

Notice, that the parameter c is positive due to its physical meaning.

Due to the qualitative features of the function $C_T(\lambda)$ (Fig. 2), the system (7) can have one or three solutions $(\lambda_1^*; \lambda_2^*)$ depending on the value of the parameter c (the case of two solutions is a singular situation). The qualitative features of the function $C_T(\lambda)$ are as follows: it has one local maximum that corresponds to some positive value of tip speed ratio λ ; it has also one local minimum that corresponds to a certain negative value of λ ; there is a certain non-zero value of $\lambda = \tilde{\lambda}$, for which the equality $C_T(\tilde{\lambda}) = C_T(-\tilde{\lambda})$ holds.

The geometrical locus of points $(\lambda_1^*; \lambda_2^*)$ obtained for different values of c is shown in the Fig. 3. Solid lines correspond to attracting fixed points, and dashed lines, to repelling ones. Point “A” in the figure corresponds to the case $c \rightarrow 0$ (no electrical load: $R \rightarrow \infty$). Points “B₁”, “B₂” (where $\lambda_i^* = \pm\tilde{\lambda}$) and point (0; 0) correspond to the case $c \rightarrow \infty$ (electrical load is extremely large for the device).

At the point “K”, the bifurcation occurs: with decreasing of the coefficient c , the saddle point of the system (6) bifurcates into three fixed points: one stable node (branch “KA”) and two saddles.

From the point “K” to each of points “M₁”, “M₂”, the coefficient c decreases from the value c_K to the value c_M (compare with Fig. 4). From points “M_i” to points “B_i”, the coefficient c increases.

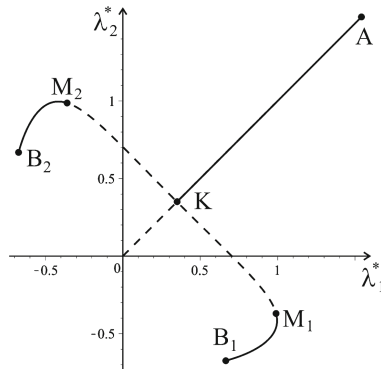


Fig. 3. Geometrical place of steady solutions of the dimensionless averaged system (6).

The trapped power coefficient c_p in steady operation modes depending on the external load coefficient c is represented in the Fig. 4. Solid lines correspond to attracting fixed points, and dashed lines, to repelling ones. Designations of bifurcation points are similar to those in the Fig. 3.

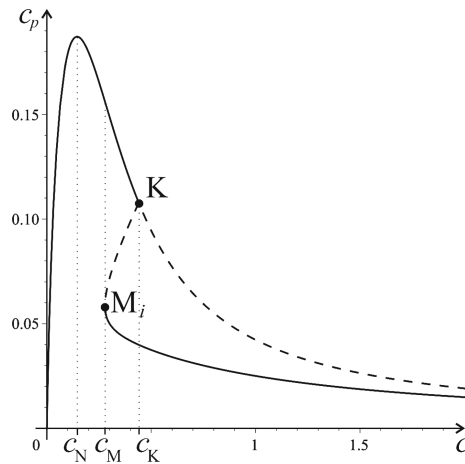


Fig. 4. Trapped power coefficient vs. the dimensionless external load coefficient c .

The maximum trapped power is achieved for $c = c_N$ in an attracting steady motion with modules of angular speeds equal to each other.

5 Discussion

Two types of steady solutions of the system (6) are identified: symmetrical (with $\lambda_1^* = \lambda_2^*$) and asymmetrical (with $\lambda_1^* \neq \lambda_2^*$). Solutions with $\lambda_1^* = \lambda_2^*$ are principally similar to the case of a single Savonius rotor. However, all steady modes of a single rotor are attracting [9], which is not the case for a double turbine.

The trapped power coefficient corresponding to symmetrical solutions is higher than that for asymmetrical case. Thus, operation modes with $\lambda_1^* = \lambda_2^*$ are preferable. Notice that, for a certain range the of external load coefficient $c \in (c_M, c_K)$, two types of attracting operation modes are possible (Fig. 4). In such case, the system can be attracted to the asymmetrical regime (with low power) even if the initial angular speed of one rotor is rather high. However, the most preferable regime (with maximum trapped power) is achieved for the value of load coefficient $c = c_N$, for which no other autorotation regimes are found (Fig. 4).

The trapped power coefficient corresponding to symmetrical steady solutions (with $\lambda_1^* = \lambda_2^*$) equals to that for a single Savonius rotor (with the tip speed ratio $\lambda = \lambda_1^* = \lambda_2^*$). But, for a counter-rotating turbine the average, the relative angular speed corresponding to steady solutions is twice higher than that for the single rotor (while the electromechanical torque is twice lower). Thus, using the double rotor construction is in a certain sense equivalent to using the increasing gear.

6 Conclusions

The mathematical model of a counter-rotating Savonius wind turbine is constructed. Steady modes of the system are analyzed depending on the external load coefficient. It

is shown that the number of such modes and their stability depend on this parameter. The trapped power in operation modes is estimated.

The comparison with a classical single rotor Savonius turbine shows that the double rotor system possesses additional type of operation modes. The main advantage of the double rotor system compared with the single rotor one consists in doubling of the average angular speed of the rotor of the generator with respect to the stator in operation modes.

The power coefficient diagram (Fig. 4) allows predicting the efficiency of the system depending on the external load coefficient c . This coefficient can be adjusted (e.g. by controlling the external resistance R) in such a way as to increase the trapped power.

In further research, it is reasonable to describe effects related with dependence of the aerodynamic torque upon angles of rotation of Savonius rotors. The analysis of the averaged system performed here can be used as an initial approximation for the study of periodic or quasi-periodic solutions of the entire system (5).

Acknowledgments. This work was partially supported by the Russian Foundation for Basic Research, projects NN 18-31-20029, 19-31-90073.

References

1. Flaherty, R.A., Burton, C.A.: Counter-rotating vertical axis wind turbine assembly. US Patent No. 20120148403 A1 (2011)
2. Dabiri, J.O.: Potential order-of-magnitude enhancement of wind farm power density via counter-rotating vertical-axis wind turbine arrays. *J. Renew. Sustain. Energy* **3**(4), 043104 (2011)
3. Klimina, L., Shalimova, E., Dosaev, M., Lokshin, B., Samsonov, V.: Two-frequency averaging in the problem of motion of a counter-rotating vertical axis wind turbine. In: Awrejcewicz, J. (ed.) *Dynamical Systems in Theoretical Perspective*, vol. 248, pp. 183–192. Springer, Cham (2018)
4. Saulescu, R., Jaliu, C., Munteanu, O., Climescu, O.: Planetary gear for counter-rotating wind turbines. *Appl. Mech. Mater.* **658**, 135–140 (2014)
5. Didane, D.H., Rosly, N., Zulkaffi, M.F., Shamsudin, S.S.: Performance evaluation of a novel vertical axis wind turbine with coaxial contra-rotating concept. *Renewable Energy* **115**, 353–361 (2018)
6. Dosaev, M., Klimina, L., Selyutskiy, Yu.: Wind turbine based on antiparallel link mechanism. In: Wenger, P., Flores, P. (eds.) *New Trends in Mechanism and Machine Science. Mechanisms and Machine Science*, vol. 43, pp. 543–550. Springer, Cham (2017)
7. Klimina, L.: Dynamics of a slider-crank wave-type wind turbine. In: *Proceedings of the 14th IFToMM World Congress, IFToMM, Taipei, Taiwan*, pp. 582–588 (2015)
8. Klimina, L., Shalimova, E., Dosaev, M., Garziera, R.: Closed dynamical model of a double propeller HAWT. *Procedia Eng.* **199**, 577–582 (2017)
9. Selyutskiy, Y.D., Klimina, L.A., Masterova, A.A., Hwang, S.S., Lin, C.H.: Savonius rotor as a part of complex systems. *J. Sound Vib.* **442**, 1–10 (2019)
10. Bach, G.: Untersuchungen über Savonius-Rotoren und verwandte Strömungsmaschinen. *Forschung auf dem Gebiet des Ingenieurwesens A* **2**(6), 218–231 (1931)
11. Dosaev, M.Z., Samsonov, V.A., Selyutskii, Y.D., Lu, W.-L., Lin, C.-H.: Bifurcation of operation modes of small wind power stations and optimization of their characteristics. *Mech. Solids* **44**(2), 214–221 (2009)

12. Volosov, V.M.: The method of averaging. Dokl. Akad. Nauk SSSR **137**(1), 21–24 (1961). (in Russian)
13. Sanders, J.A., Verhulst, F., Murdock, J.: Averaging Methods in Nonlinear Dynamical Systems. Springer, New York (2007)
14. Awrejcewicz, J., Starosta, R., Sypniewska-Kamińska, G.: Decomposition of governing equations in the analysis of resonant response of a nonlinear and non-ideal vibrating system. Nonlinear Dyn. **82**(1–2), 299–309 (2015)
15. Akulenko, L.D., Leshchenko, D.D., Chernousko, F.L.: Fast motion of a heavy rigid body about a fixed point in a resistive medium. Mech. Solids **17**(3), 1–8 (1982)

Cable Robots



An Inverse Kinematic Code for Cable-Driven Parallel Robots Considering Cable Sagging and Pulleys

Marc Fabritius¹(✉) and Andreas Pott²

¹ Fraunhofer Institute for Manufacturing Engineering and Automation, Stuttgart, Germany

`marc.fabritius@ipa.fraunhofer.de`

² University of Stuttgart, Stuttgart, Germany

`andreas.pott@isw.uni-stuttgart.de`

Abstract. A key advantage of cable-driven parallel robots, compared to other robot types, is their large workspace. Despite this fact, experiments in previous works have shown that cable-driven parallel robots often cannot fully realize their theoretically estimated workspace in practice.

To remedy this shortcoming, a new inverse kinematic code is developed which considers the previously neglected effects of both cable sagging and pulleys. For a realistic exemplary robot, the new kinematic code yields a 19.5% larger wrench-feasible workspace volume for the catenary-pulley model than previous codes. This result shows that the effects of cable sagging and pulleys should be considered in the kinematic codes, especially for large cable-driven parallel robots.

Keywords: Cable-driven parallel robots · Inverse kinematic code · Wrench-feasible workspace · Cable sagging · Pulley model

1 Introduction

Many works in the field of cable-driven parallel robots (CDPR) study their workspace as its large size distinguishes them from other types of robots [8, 11]. The kinematic codes used to control CDPR are commonly based on the standard geometric model [8, section 3.2], which assumes that their cables are straight lines and neglects the effects of their weight and pulleys. Research by Kraus [4, p. 91] and Riehl et al. [10] shows that in practice these simplifications decrease the workspace volume and positioning accuracy of CDPR. To improve these qualities, Kozak et al. [3] apply the catenary model to the cables of CDPR and Goutfarde et al. [1] analyze its combination with a pulley model. Merlet [5] presents an algorithm for finding all solutions of the inverse kinematic problem for the catenary model.

To apply these models on a CDPR in practice, this work introduces a new inverse kinematic code for redundantly constrained CDPR based on a combined

catenary-pulley model. This code computes feasible and continuous cable lengths that can be used by a future CDPR controller.

The structure of this work is as follows: Sect. 2 introduces the necessary definitions and assumptions. The catenary-pulley model is derived in Sect. 3.

Based on this model, Sect. 4 develops a new inverse kinematic code. Section 5 evaluates the new code for an exemplary CDPR and compares it to a state-of-the-art one. Finally, Sect. 6 provides the conclusion and outlook.

2 Definitions and Assumptions

A CDPR consists of $m \in \mathbb{N}$ cables which are used to manipulate the pose $(\mathbf{r}, \mathbf{R}) \in \text{SE}_3$ of its platform. Each cable $i \in \{1, \dots, m\}$ originates from a winch at a fixed point \mathbf{a}_i and is wound around a pulley of radius r , with a panning axis \mathbf{e}_i . The weight of the cable segment on the pulley is neglected. It is assumed that the pulley is statically balanced around its panning axis \mathbf{e}_i and that there is no friction in this axis or between the cable and the pulley. The other end of each cable i is connected to the platform at the distal endpoint \mathbf{b}_i in the platform coordinate frame \mathcal{K}_p . Its location $\mathbf{r} + \mathbf{R}\mathbf{b}_i$ in the world coordinate frame \mathcal{K}_0 depends on the platform's position $\mathbf{r} \in \mathbb{R}^3$ and orientation $\mathbf{R} \in \text{SO}_3$. The suspended cable between the pulley and the platform is modeled according to Irvine's catenary model [2] with the parameters: weight force density μg , Young's modulus E , and cross-section area A .

Figure 1 illustrates the catenary-pulley model for a cable of a CDPR. All symbols and force vectors associated with this model are highlighted in blue and, for better readability, the cable's index i is omitted from them.

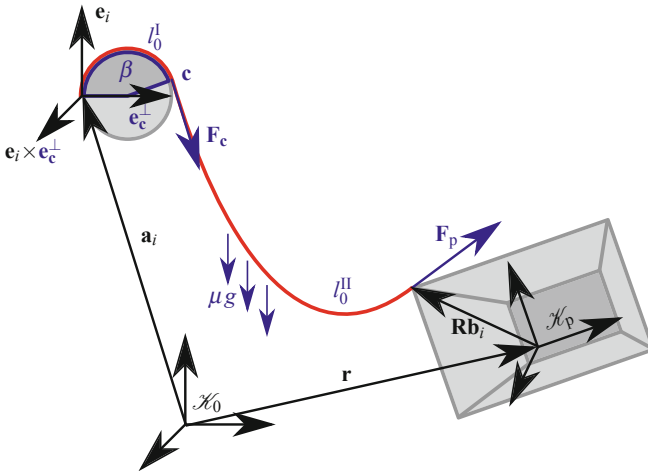


Fig. 1. Illustration of the catenary-pulley model for cable i

An unstretched cable length l_0 is considered feasible for a given platform pose (\mathbf{r}, \mathbf{R}) if the resulting cable force $\|\mathbf{F}_c\|$ in the first section of the cable, at the pulley, lies within the feasible interval $\|\mathbf{F}_c\| \in [f_{\min}, f_{\max}]$. This condition is imposed on the cable's force near the winch \mathbf{F}_c instead of at the platform \mathbf{F}_p , since in practice the maximal cable force f_{\max} of a CDPR is usually constrained by its winches or motors and not the cables themselves.

3 The Catenary-Pulley Model

The catenary-pulley model determines the location of the distal endpoint $\mathbf{d}_i(\mathbf{F}_c, l_0)$ of a cable i , which is attached to the platform, in \mathcal{X}_0 as a function of its force \mathbf{F}_c and unstretched cable length l_0 . Two sections of the cable are distinguished, which contain the unstretched cable lengths l_0^I and l_0^{II} with $l_0 = l_0^I + l_0^{II}$.

The first section is wound on the pulley between the points \mathbf{a}_i and \mathbf{c} , as shown in Fig. 1. The force vector \mathbf{F}_c defines the direction in which the cable tangentially leaves the pulley at the point \mathbf{c} and its norm $\|\mathbf{F}_c\|$ represents the force in the cable at this point. The plane in which the pulley lies is spanned by its panning axis \mathbf{e}_i and the orthogonalized direction $\mathbf{e}_c^\perp = \frac{\mathbf{F}_c - \langle \mathbf{F}_c, \mathbf{e}_i \rangle \mathbf{e}_i}{\|\mathbf{F}_c - \langle \mathbf{F}_c, \mathbf{e}_i \rangle \mathbf{e}_i\|}$ of the cable force \mathbf{F}_c .

Using these axes, the location of \mathbf{c} can be expressed in \mathcal{X}_0 as

$$\mathbf{c} = \mathbf{a}_i + r \mathbf{e}_c^\perp + \frac{r}{\|\mathbf{F}_c\|} (\langle \mathbf{F}_c, \mathbf{e}_c^\perp \rangle \mathbf{e}_i - \langle \mathbf{F}_c, \mathbf{e}_i \rangle \mathbf{e}_c^\perp). \quad (1)$$

The wrapping angle β of the cable around the pulley from \mathbf{a}_i to \mathbf{c} is given by

$$\beta = \text{atan2}(\langle \mathbf{F}_c, \mathbf{e}_c^\perp \rangle, \langle \mathbf{F}_c, \mathbf{e}_i \rangle). \quad (2)$$

Due to the assumption of no friction between the pulley and the cable, the force $\|\mathbf{F}_c\|$ in the cable on the pulley is constant. The unstretched cable lengths of the first l_0^I and second l_0^{II} cable sections are calculated as

$$l_0^I = \frac{\beta r}{1 + \frac{\|\mathbf{F}_c\|}{EA}} \quad \text{and} \quad l_0^{II} = l_0 - l_0^I. \quad (3)$$

The vertical component of the cable force vector at the platform $\mathbf{F}_p = \mathbf{F}_c + \mu g l_0^{II} \mathbf{e}_z$ accounts for the weight $\mu g l_0^{II}$ of the cable in the second section, i.e. the catenary.

The horizontal cable force components are denoted as $\mathbf{F}_{x,y} = [\langle \mathbf{F}_c, \mathbf{e}_x \rangle \langle \mathbf{F}_c, \mathbf{e}_y \rangle 0]^\top$. Hereby, \mathbf{e}_x , \mathbf{e}_y and \mathbf{e}_z denote the axes of \mathcal{X}_0 . Finally, the location of the distal endpoint $\mathbf{d}_i(\mathbf{F}_c, l_0)$ can be calculated in \mathcal{X}_0 , using Irvine's catenary model [2], as

$$\begin{aligned} \mathbf{d}_i(\mathbf{F}_c, l_0) = & \mathbf{c} + \frac{l_0^{II}}{2EA} (\mathbf{F}_p + \mathbf{F}_c) \\ & + \frac{1}{\mu g} \left(\log \left(\frac{\|\mathbf{F}_p\| + \langle \mathbf{F}_p, \mathbf{e}_z \rangle}{\|\mathbf{F}_c\| + \langle \mathbf{F}_c, \mathbf{e}_z \rangle} \right) \mathbf{F}_{x,y} + (\|\mathbf{F}_p\| - \|\mathbf{F}_c\|) \mathbf{e}_z \right). \end{aligned} \quad (4)$$

With this expression, the loop closure equation of the catenary-pulley model for cable i is formulated as

$$\mathbf{d}_i(\mathbf{F}_c, l_0) - (\mathbf{r} + \mathbf{R}\mathbf{b}_i) = \mathbf{0} \in \mathbb{R}^3. \tag{5}$$

The new inverse kinematic code, which is introduced in the next section, requires this equation system to be solved for a feasible unstretched cable length l_0 and direction (θ, φ) of the cable force \mathbf{F}_c , while its norm $\|\mathbf{F}_c\|$ is fixed. For this purpose, the cable force is expressed in spherical coordinates $\mathbf{F}_c = [\|\mathbf{F}_c\| \ \theta \ \varphi]^\top$.

Equation (5) can then be solved for (l_0, θ, φ) using numerical methods like Newton-Raphson. Once a solution is found, it is necessary to calculate how the cable forces at the pulley \mathbf{F}_c and the platform \mathbf{F}_p change when the unstretched cable length l_0 is modified by the winch. These relationships are captured by the partial derivatives $\frac{\partial \mathbf{F}_p}{\partial l_0}$ and $\frac{\partial \mathbf{F}_c}{\partial l_0}$. They are derived by taking the derivative $\frac{d}{dl_0}$ of the loop closure equation with the constrain that the platform pose (\mathbf{r}, \mathbf{R}) remains constant:

$$\mathbf{0} = \frac{d}{dl_0} (\mathbf{d}_i(\mathbf{F}_c, l_0) - (\mathbf{r} + \mathbf{R}\mathbf{b}_i)) = \frac{d}{dl_0} \mathbf{d}_i(\mathbf{F}_c, l_0). \tag{6}$$

This can be reformulated in terms of partial derivatives of $\mathbf{d}_i(\mathbf{F}_c, l_0)$

$$\mathbf{0} = \frac{d}{dl_0} \mathbf{d}_i(\mathbf{F}_c, l_0) = \frac{\partial \mathbf{d}_i(\mathbf{F}_c, l_0)}{\partial \mathbf{F}_c} \frac{\partial \mathbf{F}_c}{\partial l_0} + \frac{\partial \mathbf{d}_i(\mathbf{F}_c, l_0)}{\partial l_0^\text{II}} \frac{\partial l_0^\text{II}}{\partial l_0}. \tag{7}$$

With the relationship $\frac{\partial l_0^\text{II}}{\partial l_0} = 1$ obtained from Eq. (3), the partial derivatives of the cable forces can be expressed as

$$\frac{\partial \mathbf{F}_c}{\partial l_0} = - \left(\frac{\partial \mathbf{d}_i(\mathbf{F}_c, l_0)}{\partial \mathbf{F}_c} \right)^{-1} \frac{\partial \mathbf{d}_i(\mathbf{F}_c, l_0)}{\partial l_0^\text{II}} \quad \text{and} \quad \frac{\partial \mathbf{F}_p}{\partial l_0} = \frac{\partial \mathbf{F}_c}{\partial l_0} + \mu g \mathbf{e}_z. \tag{8}$$

In the following section, these expressions are used to linearize the catenary-pulley model.

4 An Inverse Kinematic Code for the Catenary-Pulley Model

Inverse kinematic codes for CDPR compute feasible cable lengths \mathbf{l}_0 for a given platform pose (\mathbf{r}, \mathbf{R}) and external wrench \mathbf{w}_ext . The inverse kinematic code developed in this section is based on the definition of feasible cable lengths from Sect. 2.

It is aimed at redundantly constrained CDPR and inspired by Pott’s force distribution method [7], which uses the least squares solution of the wrench equilibrium equation for the standard geometric model [8, Eq. 5.9 on p. 167] of CDPR as a starting point to calculate feasible cable forces. In contrast to the setting of the standard geometric model, the wrench equilibrium equation for the

catenary-pulley model is nonlinear in the cable forces. Therefore, this kinematic code linearizes the cable wrench \mathbf{w}_i of each cable i around the unstretched cable lengths l_0^i , that are obtained by solving the catenary-pulley model as described in Sect. 3 for the fixed cable force norm $\|\mathbf{F}_c\| = \frac{1}{2}(f_{\min} + f_{\max})$ in the middle of the feasible interval $[f_{\min}, f_{\max}]$. The resulting wrench equilibrium equation is linear in the additional cable length parameters Δl_0^i :

$$\mathbf{0} = \mathbf{w}_p + \mathbf{w}_{\text{ext}} + \sum_{i=1}^m \mathbf{w}_i + \sum_{i=1}^m \frac{\partial \mathbf{w}_i}{\partial l_0} \Delta l_0^i. \quad (9)$$

Hereby, \mathbf{w}_{ext} and \mathbf{w}_p denote the wrenches on the platform due to external influences and the platform mass m_p , respectively. The wrench of each cable i and its derivative are given by

$$\mathbf{w}_i = - \begin{bmatrix} \mathbf{F}_p \\ \mathbf{R}\mathbf{b}_i \times \mathbf{F}_p \end{bmatrix} \quad \text{and} \quad \frac{\partial \mathbf{w}_i}{\partial l_0} = - \begin{bmatrix} \frac{\partial \mathbf{F}_p}{\partial l_0} \\ \mathbf{R}\mathbf{b}_i \times \frac{\partial \mathbf{F}_p}{\partial l_0} \end{bmatrix}. \quad (10)$$

The vectors \mathbf{F}_p and $\frac{\partial \mathbf{F}_p}{\partial l_0}$ are calculated from the solution of the catenary-pulley model as described in Sect. 3. The parameters Δl_0^i are determined as the least squares solution of Eq. (9).

Similarly, as in [7], the cable lengths $l_0^i + \Delta l_0^i$ are further modified to comply with the force limits f_{\min} and f_{\max} . It is checked whether for all cables $i \in \{1, \dots, m\}$, the cable force at the pulley lies within the feasible interval

$$\left\| \mathbf{F}_c + \frac{\partial \mathbf{F}_c}{\partial l_0} \Delta l_0^i \right\| \in [f_{\min}, f_{\max}]. \quad (11)$$

If this is not true for all cables $i \in \{1, \dots, m\}$, the cable j whose force is the furthest outside of the feasible interval is selected. Its force is reset to the limit which it previously violated, e.g. f_{\max} , by recalculating Δl_0^j as a root of the quadratic equation

$$f_{\max}^2 = \left\| \mathbf{F}_c + \frac{\partial \mathbf{F}_c}{\partial l_0} \Delta l_0^j \right\|^2 = \left\| \frac{\partial \mathbf{F}_c}{\partial l_0} \right\|^2 (\Delta l_0^j)^2 + 2 \left\langle \mathbf{F}_c, \frac{\partial \mathbf{F}_c}{\partial l_0} \right\rangle \Delta l_0^j + \|\mathbf{F}_c\|^2. \quad (12)$$

Since the cable force previously violated the force limit, this quadratic equation must have two distinct, real roots. Regardless of which limit was violated, Δl_0^j is set to be the larger or smaller root of Eq. (12) depending on whether the sign of $\left\langle \mathbf{F}_c, \frac{\partial \mathbf{F}_c}{\partial l_0} \right\rangle$ is positive or negative. Based on this new value of Δl_0^j , the wrench \mathbf{w}_j in Eq. (9) is updated according to Eq. (10) with the new cable force at platform $\mathbf{F}_p + \frac{\partial \mathbf{F}_p}{\partial l_0} \Delta l_0^j$. The term containing Δl_0^j is subsequently removed from Eq. (9) as the length and force of cable j are now fixed. A new least squares solution for the remaining parameters Δl_0^i with $i \in \{1, \dots, m\} \setminus \{j\}$ is calculated.

This procedure of updating \mathbf{w}_j for the cable j that violates the condition from Eq. (11) the most, removing the corresponding term Δl_0^j from Eq. (9) and computing a new least squares solution of the wrench equilibrium for the remaining

cable parameters Δl_0^i , is repeated until either Eq. (11) is satisfied for all cables, or the solution for the remaining six parameters Δl_0^i is infeasible.

To reduce the error due to the linearization of the catenary-pulley model, the steps, which are described until here, are repeated a second time for the remaining parameters Δl_0^i . Hereby the catenary-pulley model of each such cable i is recalculated for the fixed cable force norm of either $\left\| \mathbf{F}_c + \frac{\partial \mathbf{F}_c}{\partial l_0} \Delta l_0^i \right\|$ or a limit of the feasible interval $[f_{\min}, f_{\max}]$ if it was violated.

If Eq. (11) is now satisfied for all cables, the inverse kinematic code has found feasible cable lengths $l_0^i + \Delta l_0^i$ for the pose (\mathbf{r}, \mathbf{R}) and external wrench \mathbf{w}_{ext} .

Otherwise, it failed and considers the given pose unfeasible.

5 Comparison to a State-of-the-Art Inverse Kinematic Code

In this section, the new inverse kinematic code is compared to a state-of-the-art code in terms of the resulting workspaces and cable forces for an exemplary CDPR.

The state-of-the-art inverse kinematic code is a combination of the force distribution method from [7] and the pulley kinematics from [6].

The workspace of the CDPR is calculated by composing the new or the state-of-the-art inverse kinematics with a forward kinematics of the catenary-pulley model.

A platform pose (\mathbf{r}, \mathbf{R}) is within the workspace if, for the given external wrench \mathbf{w}_{ext} , the resulting cable forces are feasible according to the definition from Sect. 2.

As part of this work, all kinematic codes and the following comparison are implemented in WireX [9], an open source analysis and design software for CDPR.

The exemplary CDPR consists of $m = 8$ cables described by the catenary-pulley model with parameters resembling steel cables: $\mu g = 6 \frac{\text{N}}{\text{m}}$, $EA = 7 \cdot 10^6 \text{ N}$, $r = 0.25 \text{ m}$. The geometry of the cable robot $\{\mathbf{a}_i, \mathbf{b}_i\}_{i=1}^m$ is given by all sign combinations of the vectors $\mathbf{a}_i = [\pm 5.0 \text{ m} \pm 6.0 \text{ m} \pm 2.5 \text{ m}]^T$ and $\mathbf{b}_i = [\pm 0.5 \text{ m} \pm 0.3 \text{ m} \mp 0.4 \text{ m}]^T$. The panning axes of the pulleys are $\mathbf{e}_i = [1 \ 0 \ 0]^T$ for $i \in \{1, 2, 5, 6\}$ and $\mathbf{e}_i = [-1 \ 0 \ 0]^T$ for $i \in \{3, 4, 7, 8\}$. The cable force limits are $f_{\min} = 1000 \text{ N}$ and $f_{\max} = 10000 \text{ N}$. The external wrench \mathbf{w}_{ext} is set to be zero. The wrench induced by the platform's weight force $m_p g = 8000 \text{ N}$ is $\mathbf{w}_p = [0 \ 0 \ -m_p g \ 0 \ 0 \ 0]^T$, since its center of mass is at the origin of \mathcal{H}_p .

The workspace of the new inverse kinematics code for this CDPR has a volume of 157.2 m^3 and fully contains the one of the state-of-the-art code, which has a volume of 131.6 m^3 . This 19.5% increase can be attributed to the consideration of the nonlinear effects of cable sagging and pulleys.

Figure 2 shows a slice of the workspaces of the new (yellow) and the state-of-the-art code (green) in the XY-plane.

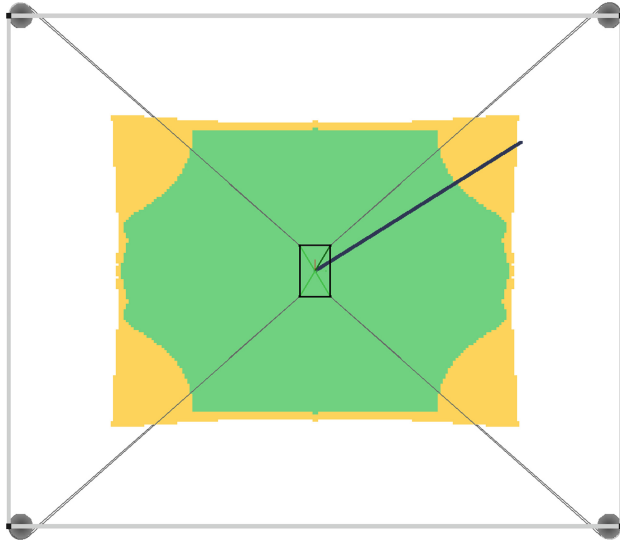


Fig. 2. Workspace comparison in the XY-plane

Along the black line, which starts at the center of the robot geometry and lies within the plane, the cable forces of the new and the state-of-the-art code are visualized in Fig. 3 in yellow and green, respectively.

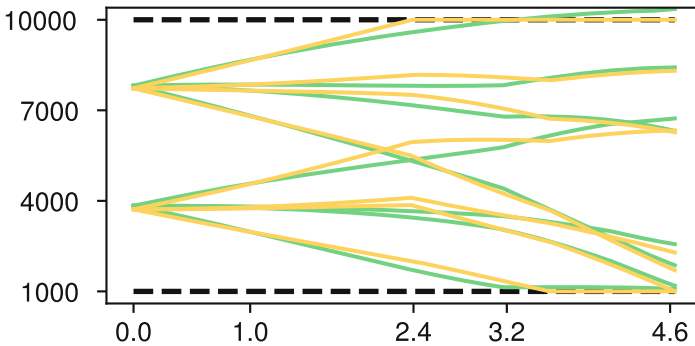


Fig. 3. Evolution of cable forces along a straight line

It can be observed that the new inverse kinematic code produces continuous cable lengths and forces. From the start until the 2.4m mark, its forces are similar to those of the state-of-the-art code. From that point on, one cable force of the new code is set to the force limit f_{max} . At 3.2m, the forces of the state-of-the-art code become unfeasible while the new code continues to find feasible cable lengths until a distance of 4.6m from the center.

The averaged computation time for one evaluation of the workspace criterion is $5.7 \cdot 10^{-3}$ s for the new code and $4.0 \cdot 10^{-3}$ s for the state-of-the-art code, as measured on a laptop with an Intel[®] Core[™] i5-7440HQ CPU running at 2.80 GHz.

The new code is slower because it requires solving the nonlinear catenary-pulley model for each cable as described in Sect. 3.

6 Conclusion and Outlook

This work presents a new inverse kinematic code for redundantly constrained CDPR that considers the effects of cable sagging and pulleys. For an exemplary CDPR, the new code yields continuous cable forces and a 19.5% larger workspace volume than a state-of-the-art code. This shows that considering the catenary-pulley model in the kinematic codes of CDPR can substantially increase the size of their workspace.

Future research could prove that the new code is indeed continuous as observed in this work. Furthermore, it should be implemented on a CDPR to evaluate its performance in practice.

Acknowledgements. This work was supported by the European Union's H2020 Program (H2020/2014–2020) under the grant agreement No. 732513 (HEPHAESTUS project).

References

1. Gouttefarde, M., Nguyen, D.Q., Baradat, C.: Kinetostatic analysis of cable-driven parallel robots with consideration of sagging and pulleys. In: *Advances in Robot Kinematics (ARK)*, pp. 213–221 (2014)
2. Irvine, H.: *Cable Structures*. MIT Press, Cambridge (1981)
3. Kozak, K., Zhou, Q., Wang, J.: Static analysis of cable-driven manipulators with non-negligible cable mass. *IEEE Trans. Rob.* **22**(3), 425–433 (2006)
4. Kraus, W.: *Force control of cable-driven parallel robots*. Ph.D. thesis, University of Stuttgart, Germany (2015)
5. Merlet, J.P.: On the inverse kinematics of cable-driven parallel robots with up to 6 sagging cables. In: *2015 IEEE/RSJ International Conference on Intelligent Robots and Systems (IROS)*, pp. 4356–4361. IEEE (2015)
6. Pott, A.: Influence of pulley kinematics on cable-driven parallel robots. In: *Advances in Robot Kinematics (ARK)*, pp. 197–204 (2012)
7. Pott, A.: An improved force distribution algorithm for over-constrained cable-driven parallel robots. In: *Computational Kinematics*, vol. 15, pp. 139–146. Springer (2014)
8. Pott, A.: *Cable-Driven Parallel Robots: Theory and Application*. Springer Tracts in Advanced Robotics, vol. 120. Springer (2018)
9. Pott, A.: *Wirex - an open source initiative scientific software for analysis and design of cable-driven parallel robots* (2019)

10. Riehl, N., Gouttefarde, M., Krut, S., Baradat, C., Pierrot, F.: Effects of non-negligible cable mass on the static behavior of large workspace cable-driven parallel mechanisms. In: 2009 IEEE International Conference on Robotics and Automation, pp. 2193–2198. IEEE (2009)
11. Verhoeven, R.: Analysis of the workspace of tendon based stewart platforms. Ph.D. thesis, University of Duisburg-Essen (2004)



Motion Generation for a Cable Based Rehabilitation Robot

Nicoleta Pop¹ (✉), Ionut Ulinici¹, Doina Pisla¹ (✉), and Giuseppe Carbone^{1,2}

¹ CESTER, Technical University of Cluj-Napoca, Cluj-Napoca, Romania
{nicoleta.pop, doina.pisla}@mep.utcluj.ro,
Ionut.Ulinici@omt.utcluj.ro

² DIMEG, University of Calabria, Calabria, Italy
giuseppe.carbone@unical.it

Abstract. Stroke is a high incidence disease which affects over 1 million people per year only in Europe. In the last years the post-stroke survival rate has increased a lot but still more than 70% of the survivors experience a certain level of motion impairment. This paper focuses on the necessity and advantages of introducing technologies in the field of post-stroke rehabilitation, and more specifically on introducing a cable-driven solution into the field, emphasizing their control system, design, motion particularities and experimental tests demonstrating the effect that cable structures have on maintaining a predefined trajectory despite deviations that may occur due to the patient's lack of control.

Keywords: Cable-driven robots · Upper limb · Control hardware · Trajectory

1 Introduction

An imminent personnel shortage in the field of post stroke physical therapy creates the need for alternate solutions. As a result, the most widely regarded mean of dealing with these developments in the automatization of the rehabilitation process. The introduction of rehabilitation robots in this environment would not only be to compensate the decreasing ratio of therapist/patient, but would also provide several advantages, such as the capacity of handling multiple patients simultaneously (under the supervision of a therapist), the capacity to provide real-time sensory feedback and psychological strain reduction (through audio/visual stimuli). Aside from these, aspects of robotic devices such as repeatability, precision and lack of a decrease in these, as a result of the non-existence of detrimental factors such as fatigue (as opposed to a human element), can make the rehabilitation procedure more efficient when dealing with a high volume of patients per day.

While there are several robotic rehabilitation devices available on the market for all limbs [9], few see themselves being implemented within clinical environments. The factors that contribute to this, are the complexity of the devices, the disbelief in the viability of these solutions and the high acquisition costs of such devices, here we shortly mention:

© The Editor(s) (if applicable) and The Author(s), under exclusive license to Springer Nature Switzerland AG 2020

D. Pisla et al. (Eds.): EuCoMeS 2020, MMS 89, pp. 432–439, 2020.

https://doi.org/10.1007/978-3-030-55061-5_49

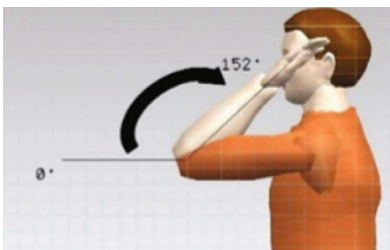
- A knee prototype proposed in [10] used for osteoarthritis rehabilitation has proven its efficiency through an static and a dynamic analysis presented in [11].
- RAISE [15] is a parallel rehabilitation robotic system that targets the hip, knee and ankle joints. RAISE has been designed for bed-confined patients, requiring the patient anthropometric data as input.
- RECOVER [16] is a parallel robotic system designed for lower limb rehabilitation, having two serialized modules (the hip-knee and the ankle module).
- ASPIRE [14] is a parallel rehabilitation device that targets the shoulder joint with an added forearm pronation/supination motion (to reach shoulder flexion/extension angular amplitudes over 90°), and executes trajectory based joint manipulation. The device requires angular amplitudes as input data, as the motion trajectories are predefined.
- ParReEx [5] is a parallel rehabilitation device that targets the elbow and wrist joints respectively. This device also uses predefined trajectories of the basic joint motions during rehabilitation and requires as input the angular values needed for each patient individually.

As a response we propose an end-effector based parallel wire-driven device, capable of upper limb rehabilitation that is presented in the following sections.

2 Requirements for Upper Limb Exercising

The upper limb motions are classified according to the joints involved in the movement process [8]. Hence, the main upper limb motions from the shoulder to the wrist are: shoulder flexion/extension, abduction/adduction, elbow flexion/extension, wrist flexion/extension, and abduction/adduction.

In this paper, the authors focus mostly at the elbow rehabilitation, more specifically at the flexion/extension (Fig. 1).



	Elbow flexion	
	Left	Right
Max	150°	152°
Mean	131.1°	137.7°
Min	56°	122°

Fig. 1. Elbow flexion [3]

The maximum, mean and minimum amplitude values of the elbow flexion are shown in Fig. 1, based on the measurements presented in [13] which were made on 21 patients. The results together with specific standards regarding the different anthropometric dimensions of the body segments represents the foundation of the development of an upper limb rehabilitation device. Furthermore, a set of technical characteristics

have to be taken into consideration to assure the safety and health of the patient and to minimize the risks that could occur during the rehabilitation exercises [8].

In order to define the rehabilitation process protocol for LAWEX, the proper arm motion range and parameters were identified, as it is reported in [1].

3 The LAWEX Cable Driven Robot

The LAWEX (LArm Wire driven EXercising device) is a cable-driven assistive device, whose first design was made that was designed and built at the Laboratory of Robotics and Mechatronics in Cassino [6, 8]. This mechanism's end-effector has a universal design that allows the rehabilitation of both the upper and lower human limb.

3.1 Mechanical Architecture

The actual design of LAWEX presents an open architecture of the system which is highly advantageous as it allows the patient to gain easy access within the device's workspace, during the rehabilitation procedure while also providing them with a less encumbering environment. The aluminum profiles used in the manufacturing of this robot ensure easy assembly and disassembly of the device and also an economical solution which makes it accessible [7].

The universal end effector is actuated through the use of four cables attached through two points. Each cable is actuated by one DC motor. The length of each cable can be modified by actuating the DC motors, which can extend or retract the cables [6, 8].

The cables are rolled on a system of pulleys assisted via a spring tensor that should be positioned as it is shown in Fig. 2 so the tensors guides the cables and stop them from slipping.



Fig. 2. The spring tensor position

The cables setup for each motor is presented in the Fig. 3. The installation of the cable in the pulley around the M1, M2, M4 (motor 1, 2 and 4) must be done clockwise and in order to rotate the motor clockwise, the values need to be increased, while for M3 (motor 3) cable installation and rolling must be done anti-clockwise. Similarly, to rotate the desired motor in the opposite direction, the values need to be decreased.

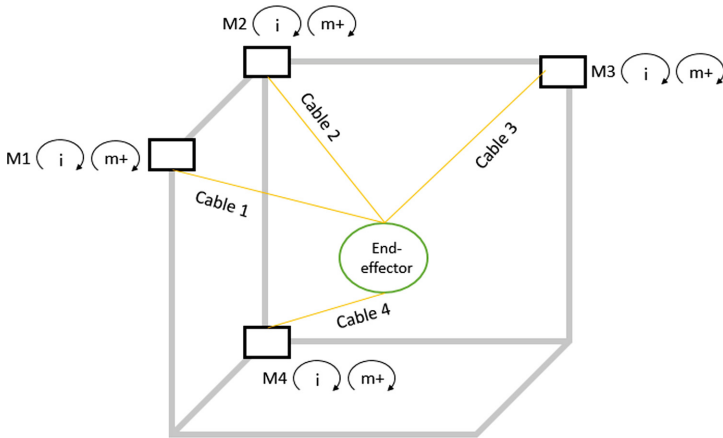


Fig. 3. LAWEX – cable setup

3.2 Control Hardware

The control box of the robotic system (Fig. 4), consists of an Arduino microcontroller, a PCA9685 controller, power supply and voltage regulators. The encoders are used to determine the current positions needed to obtain the speed input is generated which, together with the rotation direction is necessary. The motor drivers are interfaced with Arduino. For controlling the inputs given by the Arduino, the PWM technique is used [1, 2, 12].

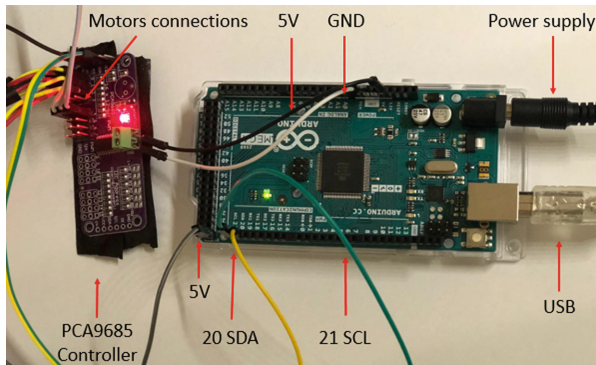


Fig. 4. PWM controller connected to Arduino.

Programming

The system can be programmed using the Arduino Integrated Development Environment (IDE) in two ways: by defining an arbitrary trajectory (Fig. 5) or by starting from the desired trajectory and applying the invers kinematic model to generate and to calculate the angular values for each motor (Fig. 6).

According to the first approach, the user need to introduce the proposed angular values of the motors until reaching the chosen home position for the desired trajectory. The main focus is to choose the angular values of the motors in such a way that all the cables are tensioned in that position. The values of the motors should be modified until you reach the desired tension in the cables. The cables must be tensioned for each position of the end-effector. After defining the first position, the programming point to point procedure is used to determine as many points as it is needed for defining a trajectory. In this step, a point to point discrete trajectory test using all the defined precision points can be done. Furthermore, the linear interpolation of these points is integrated using Matlab. Based on this interpolation, a continuous trajectory will be executed (Fig. 5).

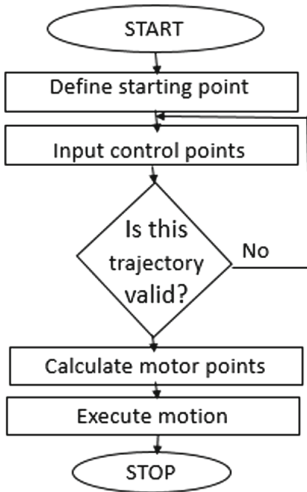


Fig. 5. Defining an arbitrary trajectory

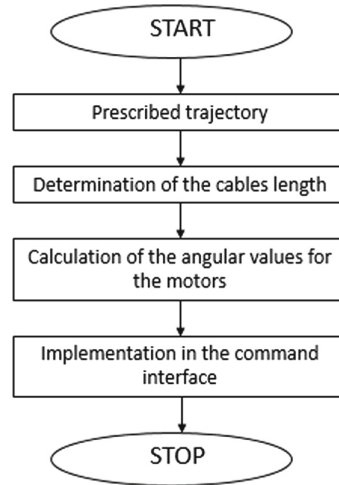


Fig. 6. Implementation of the kinematic model

The second method involves the implementation of the kinematic model of the robotic system (Fig. 6). First step consists of extracting the X, Y, Z coordinates from a prescribed trajectory. Further, the cables lengths are determined from the inverse kinematic model. Based on the kinematic equation Eq. (1), the obtained values are converted into angular values of the motors [1].

$$l_i = l_0 - \vartheta r_0 - \frac{\pi r_1}{2} - d_0 \tag{1}$$

Where l_0 represents the total length of the cable, r_0 is the driving pulley radius, r_1 is the radius of the second pulley and d_0 means the distance between the centers of the and ϑ is the angular displacement of the servomotors.

4 Experimental Tests

In this paper, the experimental tests focus on elbow flexion/extension, one of the most common used and efficient exercises for upper limb rehabilitation.

The experimental procedure consists of defining the (medical) protocol, performing the tests and interpreting the experimental results. Firstly the maximum angular amplitudes that the test subject is capable of reaching, must be noted, this can be done through the use of a simple goniometer. Furthermore, the patient's tendencies of deviating from a predefined trajectory must be observed, by first running several low speed repetitive motions, this is necessary to determine the most efficient trajectory that the end effector must take as well as the necessary cable tensions that need to be used to maintain a proper rehabilitative trajectory.

The running of a test is performed under the supervision of an operator and it is based on the mechanical interaction of the subject.

The tests have been carried out using the three cables configuration, respectively using the four cables, each connected to its corresponding actuator Fig. 7.

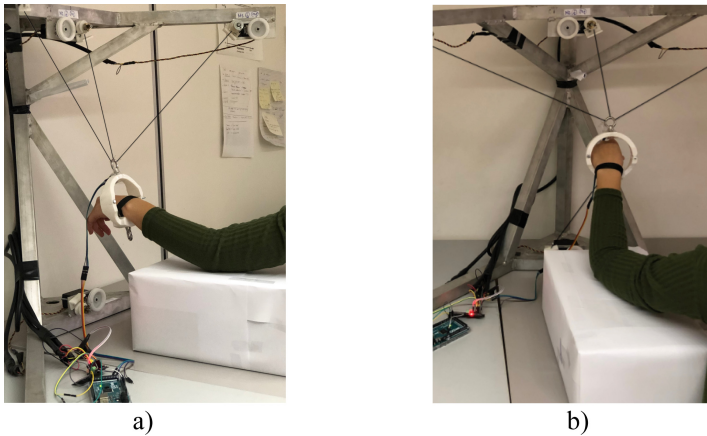


Fig. 7. Pictures taken during experimental tests: a) side view; b) front view.

In the three cable-based test (Fig. 8 a)), the cables are connected to the upper part of the platform to perform the elbow flexion/extension. The results show a more unconstrained movement of the arm, while the four cable test (Fig. 8 b)) reveals that by adding the fourth cable, positioned below the platform, the direction variations during motion execution are much smaller and frequent indicating a higher tendency towards greater stabilization as a result of a greater resistance from the end effector that prevents the patient from unintentionally forcing the end effector to deviate from the predefined trajectory, this can be observed in the plots in Fig. 8.

Consequently, there can be observe that during the end of 3 cable motion trajectory, close to the 15 mm x range and slightly above the -1350 mm z value, a sudden jog of the end effector is indicated, whereas with the 4 cable configuration the motion is visibly smoothed, the same elimination of sudden motion can be observed at the opposite end. This is highly important in reducing unwanted tensions in the beginning of the exercises and at the end, register the highest differences in values from the previous state that the system forces are at.

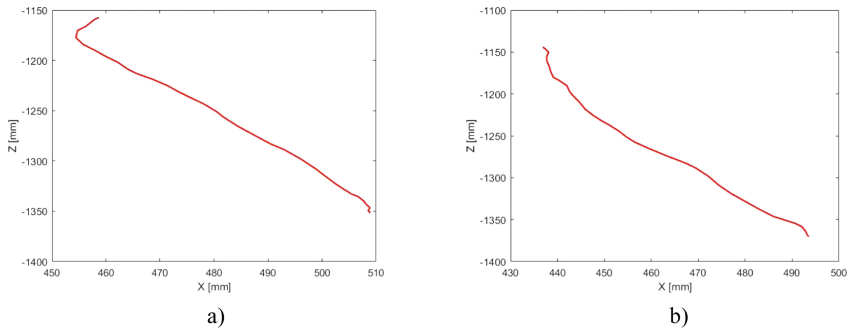


Fig. 8. Cable tests experimental results: a) three cables test; b) four cables test.

5 Conclusions

In this paper, a cable-driven robotic device LAWEX was presented. The device's capabilities, mechanical and structural characteristics are also highlighted, all of which are needed for reproducing the necessary motion for elbow rehabilitation. In order to validate the structure, experimental tests were described, mainly investigating the behavior of the end-effector in relation to the number of cables that are used in driving it, increasing or decreasing the precession with which the targeted limb follows on a predefined trajectory, and how the addition of extra cable can compensate for trajectory deviation and that could occur due to unintentional patient tremors. Future work involves further experimentation with the system to determine its viability in the post-stroke rehabilitation of both upper and lower limb motor afflictions.

Acknowledgements. The paper presents results from the research activities of the project ID 37_215, MySMIS code 103415 “Innovative approaches regarding the rehabilitation and assistive robotics for healthy ageing” co-financed by the European Regional Development Fund through the Competitiveness Operational Programme 2014-2020, Priority Axis 1, Action 1.1.4, through the financing contract 20/01.09.2016, between the Technical University of Cluj-Napoca and ANCSI as Intermediary Organism in the name and for the Ministry of European Funds.

References

1. Boschetti, G., Carbone, G., Passarini, C.: Cable failure operation strategy for a rehabilitation Cable-Driven Robot. *Robotics* **8**(1), 17 (2019)
2. Cafolla, D., Russo, M., Carbone, G.: CUBE, a cable-driven device for limb rehabilitation. *J. Bionic. Eng.* **16**, 492–502 (2019)
3. Carbone, G., Gherman, B., Ulinici, I., Vaida, C., Pisla, D.: Design issues for an inherently safe robotic rehabilitation device. *Mech. Mach. Sci.* **49** (2018)
4. Ellis, M.D., Sukal-Moulton, T.M., Dewald, J.P.: Impairment-based 3-D robotic intervention improves upper extremity work area in chronic stroke: targeting abnormal joint torque coupling with progressive shoulder abduction loading. *IEEE Trans. Robot* **25**, 549–555 (2009)
5. Gherman, B., Carbone, G., Plitea, N., Ceccarelli, M., Banica, A., Pisla, D.: Kinematic design of a parallel robot for elbow and wrist rehabilitation. *New Adv. Mech. Mach. Sci.* **57**, 147–157 (2018)

6. Laribi, M.A., Carbone, G., Zegloul, S.: On the optimal design of cable driven parallel robot with a prescribed workspace for upper limb rehabilitation tasks. *J. Bionic Eng.* **16**, 503–513 (2019)
7. Lazăr, V.A., Cafolla, D., Pisla, D., Carbone, G.: Design of a mechanical interface for a cable-driven rehabilitation device. In: Carbone, G., Ceccarelli, M., Pisla, D. (eds.) *New Trends in Medical and Service Robotics*, pp. 283–292. Springer, Singapore (2019)
8. Lazar, V.A., Pisla, D., Vaida, C., Cafolla, D., Ceccarelli, M., Carbone, G., León, J.F.R.: Experimental characterization of assisted human arm exercises. In: *Proceedings 2018 IEEE International Conference on Automation Quality and Testing, Robot AQTR 2018 – THETA 21st Edition*, pp. 1–6 (2018)
9. Oña, E.D., Cano-de la Cuerda, R., Sánchez-Herrera, P., Balaguer, C., Jardón, A.: A review of robotics in neurorehabilitation: towards an automated process for upper limb. *J. Healthc. Eng.* (2018).
10. Tarnita, D., Catana, N., Dumitru, N., Tarnita, D.: Design and simulation of an orthotic device for patients with osteoarthritis design and simulation of an orthotic device for patients with osteoarthritis. *Mech. Mach. Sci.* **38**, 61–77 (2016)
11. Tarnita, D., Pisla, D., Geonea, I., Vaida, C., Catana, M., Tarnita, D.N.: Static and dynamic analysis of osteoarthritic and orthotic human knee static and dynamic analysis of osteoarthritic and orthotic human knee. *J. Bionic Eng.* **16**, 514–525 (2019). <https://doi.org/10.1007/s42235-019-0042-3>
12. Thiago, A., Rogerio, G., Giuseppe, C., Marco, C.: Cable-driven robots in physical rehabilitation: from theory to practice. In: *Advanced Robotics and Intelligent Automation Manufacturing* (2020)
13. Vaida, C., Carbone, G., Major, K., Major, Z., Plitea, N., Pisla, D.: On Human robot interaction modalities in the upper limb rehabilitation after stroke. *Acta Tech. Napocensis Ser. Math. Mech. Eng.* **60**, 91–102 (2017)
14. Vaida, C., Plitea, N., Carbone, G., Birlescu, I., Ulinici, I., Pislă, A., Pislă, D.: Innovative development of a spherical parallel robot for upper limb rehabilitation. *Int. J. Mech. Robot Syst.* **4**, 256 (2018)
15. Vaida, C., Birlescu, I., Pislă, A., Ulinic, I., Tarnita, D., Carbone, G., Pislă, D.: Systematic design of a parallel robotic system for lower limb rehabilitation. *IEEE Access* **8**, 34522–34537 (2020)
16. Gherman, B., Birlescu, I., Plitea, N., Carbone, G., Tarnita, D., Pislă, D.: On the singularity-free workspace of a parallel robot for lower-limb rehabilitation. *Proc. Rom. Acad.* **20**(4), 383–391 (2019)



Failure Analysis of a Collaborative 4-1 Cable-Driven Parallel Robot

Stéphane Caro¹(✉) and Jean-Pierre Merlet²

¹ Centre National de la Recherche Scientifique (CNRS), LS2N, 44321 Nantes, France

`stephane.caro@ls2n.fr`

² Inria Sophia-Antipolis, 2004 Route des Lucioles, Valbonne, France

`Jean-Pierre.Merlet@inria.fr`

Abstract. Cable-Driven Parallel Robots (CDPRs) have been little used so far for collaborative tasks with humans. One reason is the lack of solutions to guarantee the safety of the operators in case of failure. Therefore, this paper aims to determine the possible failures of CDPRs when they are used for collaborative work with humans and to provide technical solutions to ensure the safety of the operators. A translational three degrees-of-freedom CDPR composed of four cables connected to a point-mass end-effector is considered as an illustrative example. The cables are supposed to be ideal, namely, they are not elastic and do not exhibit sagging.

Keywords: Cable-driven parallel robot · Cable sagging · Failure · Safety · Collaborative

1 Introduction

Cable-driven parallel robots (CDPR) are a special class of parallel robot where the rigid legs/links of a classical parallel robot (CPR) are substituted by cables that can be wound or unwound. This type of actuation offers a lower mechanical complexity (passive joints may not be used) compared to CPR and, more importantly, a wider range of leg lengths, thereby allowing for a larger workspace. In this paper we will consider a specific CDPR, the so-called $N-1$ CDPR, having N cables that are all attached to the same point B on the platform, whose center of mass is below this point. The cable lengths L_0 are changed by using rotary winches, whose rotations are measured by encoders. Provided that $N \geq 3$, such a CDPR is a 3-dof robot allowing only translational motion of the load, which is appropriate for many tasks [1, 3], e.g. for 3D printing [2] or metrology [13]. Basic control of the CDPR is based on a feedback loop on the L_0 that are estimated by using the measurement of the rotation angle of the winches. In the scope of this paper, the cables are supposed to be *ideal*, namely, they are not elastic and do not exhibit sagging. They are made up of synthetic material and, as a consequence, do not exhibit the dangerous whip effect of steel cables. As the winches

are assumed to be irreversible, there won't be any change in cable lengths if they are not actuated.

Furthermore, the winch dynamics is supposed to be not sufficient to correct the fast motion of the load during a failure. $\mathcal{F}_0(\mathbf{x}, \mathbf{y}, \mathbf{z})$ denotes the reference with \mathbf{z} the vertical axis.

This paper aims to determine the possible failures of CDPRs when they are used for collaborative work with humans, especially failures that may lead to a danger for the human operators. Failures of parallel robots have been addressed in [9, 11, 12] and for CDPR in [7, 8], but not with the purpose of ensuring the safety of co-workers.

2 Kineto-Static Analysis of a 4-1 CDPR

Being given the platform pose of a CDPR the lengths of the 4 cables are uniquely determined. On the other hand as soon as the lengths of 3 cables under tension are fixed, then the platform pose will be fully determined. As the cable lengths are never exactly measured we are not able to reach a platform pose, for which the four cables are in tension. While performing a trajectory the CDPR will usually have at most three cables in tension, possibly going temporarily through poses where all four cables are in tension, but we are not able to determine such a case. If A_i denotes the winch output point of cable i we will consider the convex hull \mathcal{H} of the A_i points in the plane $z = 0$ and A_{ip} will denote the projection of A_i in this plane and if M is a pose, then M_p will be its projection in the plane. It is easy to show that if M_p is strictly inside the triangle A_{ip}, A_{jp}, A_{kp} (denoted as (i, j, k) for short), then a static equilibrium will be obtained when cables i, j, k are in tension while cable $l \neq i, j, k$ is slack. However, there will be another cable configuration i, j, l with k slack that also leads to a mechanical equilibrium of the platform. Hence for a given platform pose two possible cable configurations, named the *main cables*, that share two cables (i, j) and only differ by the third cable, lead to a static equilibrium of the platform. In what remains, the Cartesian coordinates of points A_i expressed in meter are the following: $OA_1 (-8, 5, 5)$, $OA_2 (-8, -5, 5)$, $OA_3 (8, -5, 5)$, $OA_4 (8, 5, 5)$. The four points have the same height and lead to a rectangular workspace.

3 Possible Failures

The failures that are considered in this paper and may occur for a CDPR are the following:

1. the breaking of a cable;
2. failure of an encoder or of a motor or its control module: such failure may easily be detected as the integration of the voltage sent to the motor combined with a simple motor model will provide information of the expected motion of the encoder. If this information is not coherent with the measurement either because of a failure of the encoder or of the motor, we may stop the CDPR

and because of the usual high resolution of the encoder, the displacement of the platform will be minimal;

3. the *loop effect*: uncoiling an already slack cable may lead to a loop at the winch level that reverts the normal coiling process. Consequently, the cable length may decrease instead of increasing and therefore the altitude of the load will increase. This failure cannot be detected by using only the estimation of the L_0 based on the measurement of the winch rotation angles.
4. the winch may have a mechanical failure, e.g. break or losing the clutch that couples the drivetrain to the coiling unit.
5. depending on the velocity of the platform before an emergency stop, the robot may undergo significant sway motion, often putting two cables under tension and making the third cable loose.
6. cables can get stuck in the winch or on guiding pulleys. Cables leaving the pulleys may also slide about nearby elements.

Our objective is to ensure the safety of the operator. There are several means for this purpose:

- immobilize the robot
- move the robot at a low speed toward a safe pose
- move the load from its current pose along the vertical to a safe altitude to avoid any contact with the workers or environment
- put the load as quickly as possible on the ground to limit its motion

There are no general strategies that may be applied for each case and In this paper, it is assumed that this safety will be guaranteed if the unexpected motion of the CDPR is such that the load cannot reach an altitude that is lower than a given value z_l and higher than a threshold z_h because the cable tensions increase with the altitude of the platform and may lead to damages on the CDPR. Note that this assumption is not restrictive and the proposed methods can be extended to deal with other safety definition such as the avoidance of a given region.

3.1 Cable Breaking

With only the measurement of the L_0 the breaking of a cable cannot be detected. Hence the safety has to be ensured by the robot design and by restricting its workspace. As seen in Sect. 2, we have for a given pose in most cases three cables only in tension. The corresponding cable configurations are i, j, k or i, j, l . The breaking of k (l) will not affect the CDPR behaviour that much because the cable configuration will switch to i, j, l (k) with a little displacement of the platform. On the contrary, the robot behaviour will be highly affected if one of the main cables i, j breaks down.

Figure 1(a) shows the area where the platform can be in a static equilibrium for the CDPR at hand. Figure 1(b) illustrates the static workspace of the manipulator after one cable breakage.

Let us assume that \mathcal{H} is a rectangle whose corners are numbered 1, 2, 3, 4 and assume that at its current pose such that M_p is located both in the triangle

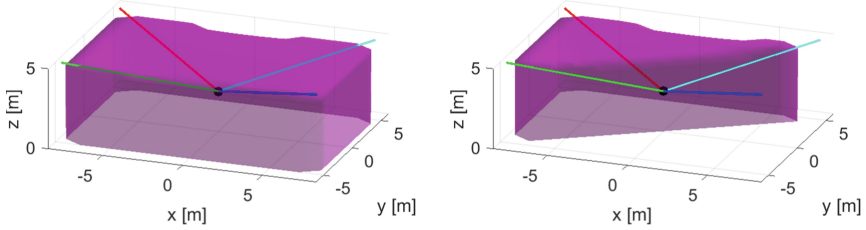


Fig. 1. On the left the static workspace of the CDPR. On the right the static workspace of the CDPR after cable 3 (blue cable) breakage.

123 and 124 leading to two possible cable configurations having 1,2 as main cables. If the CDPR is in the configuration 123 and cable 1 (2) breaks down, then the load will swing around the A_2A_4 (A_1A_3) line meaning that the load will move on a circle in a vertical plane that is perpendicular to A_2A_4 (A_1A_3) whose radius can be obtained as a function of the lengths of cables 2, 4 (1, 3). It is easy to show that if M lies in the cylinder with axis A_2A_4 (A_1A_3) and radius $z_a - z_l$, then the load will not go below z_l during the swinging motion after the breakage of cable 1 (2). However we have also to limit the load height to z_h in this cylinder. A *fully safe* zone is therefore obtained as the intersection of these two cylinders that lie below the altitude z_h . Figure 2 shows the full safe zone obtained for $z_l = 1$, $z_h = 4$. From Figs. 1(a) and 2, it is noteworthy that this safety consideration drastically shrink the CDPR workspace.

3.2 Adding Measurements

As seen previously the measurement of the L_0 is not sufficient to ensure the safety of CDPRs. Therefore it is necessary to consider other measurements with the objective to detect an abnormal behavior for the cables or for the whole CDPR, that may occur very quickly (e.g. during a cable breakdown). For this purpose we may measure at a high rate the cable tensions, the cables angles

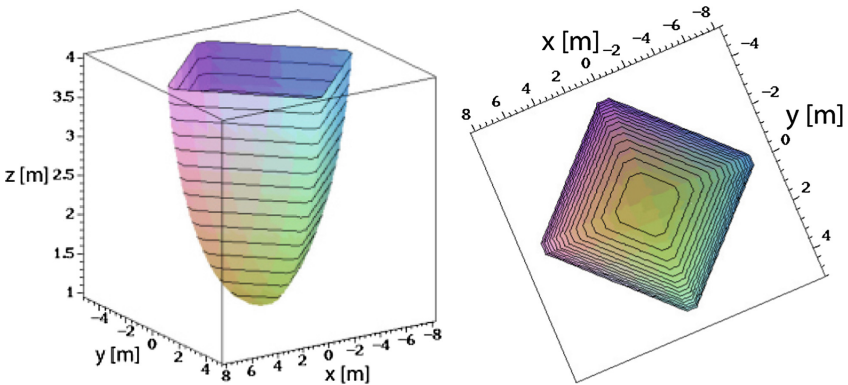


Fig. 2. 3D and top view of the safe zone when one cable breaks

with respect to the horizontal at A or B (with an optical sensor [6] or an IMU located close to B), or the load altitude (with a vertical distance sensor). Tension measurement is not satisfactory because it will be very difficult to distinguish between a normally slack cable or a broken cable. Measuring the z coordinate of the platform, which has an interest for control, is appropriate except in the case of a non-main cable breakage while measuring the angles covers all failure cases. In summary there are multiple sensor possibilities to detect a failure of such a CDPR.

3.3 Zones Covered by the Cables

In order to avoid any collision between the human operator and the cables, it is possible to prevent the human operator from getting into zones spanned by the cables with intangible barriers. For that matter, the zone spanned by each cable should be determined first. Some approaches are proposed in the literature are to determine the cable span of CDPRs [4, 5, 10].

For instance, Fig. 3(a) shows the area spanned by cable 1 (red cable) when the end-effector covers the rectangular parallelepiped of size $8\text{ m} \times 5\text{ m} \times 2.5\text{ m}$. Figure 3(b) the area spanned by the four cables when the end-effector covers the same regular shape. Accordingly, the white areas are free of collision with cables and can be travelled by the human operator while being sure that he/she will not get in contact with cables as long as there is no cable breakage. From Fig. 3, it is apparent that no human operator is allowed to approach the robot because most of the space is spanned by the cables. In this case, a typical safety measure is a fence or technical solutions must be adopted to allow interaction between human operators and the cables for low speed operations.

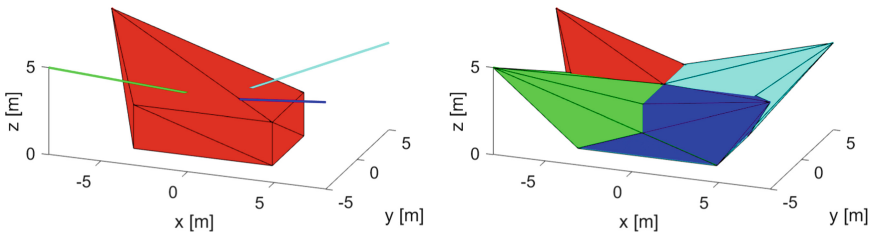


Fig. 3. On the left the area spanned by cable 1 (red cable) when the end-effector covers the rectangular parallelepiped of size $8\text{ m} \times 5\text{ m} \times 2.5\text{ m}$. On the right the area spanned by the four cables when the end-effector covers the same regular shape. Cables 1, 2, 3 and 4 are red, green, blue and cyan, resp. The white areas are free of collision with cables.

4 Ensuring Safety

A complete safety for the CDPR may be obtained by doubling each cable with a passive auxiliary cable as shown in Fig. 4. This cable goes from the load to an

output point close to A and has a counterweight at its free end. The cable goes through a pulleys circuit, which is designed in such way that when the main extend from its minimal to its maximal length, then the counterweight moves from the bottom to the top of the mast. On the last branch of the cable loop, a clamping mechanism allows one to stop the cable motion. The mass of the counterweight is just sufficient to overcome the friction in the pulleys and the tension in the auxiliary cables. Therefore, this mass does not modify the platform pose, although it will usually decrease the tensions in the four main cables. As an example we assume that at time 0 the CDPR is at pose $(-6, -3, 2)$ (which is outside of the safe zone) when cable 2 breaks down. At time 0.1 s the controller detects that cable 2 has broken down, stops the winches of all cables and clamps the auxiliary cable 2, whose stiffness is 10 000 N/m and has a damping factor of 200 Ns/m. Figure 4 shows the evolution of the z of the load as a function of time. It may be seen that the load quickly converges toward a safe position.

It may be noted that the auxiliary cables may be very close to the main cables, so that cable interference will not be an issue.

It may be thought that adding 4 cables, even passive ones, induces an increasing complexity. Hence we have investigated the use of a single auxiliary cable that will release a counterweight after a failure detection in order to raise the load at a safe height. However it has appeared that it is very difficult to determine the location of the output point of this cable and the mass of the counterweight so that the CDPR may be put in a safe position whatever the initial breakdown pose is. The dynamics of such a system is relatively simple but is very sensitive to the mass of the counterweight: if the mass is too low the system may fail to raise the load, while for a larger mass we obtain a very large upward motion of

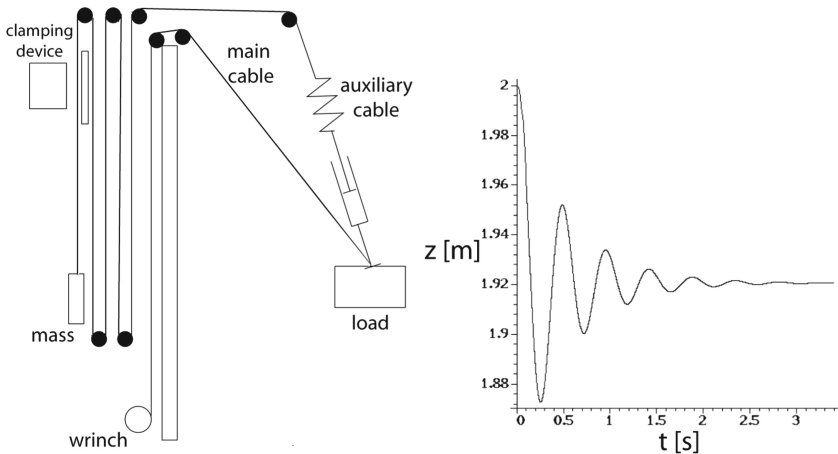


Fig. 4. On the left the principle of safety ensured by auxiliary cables. On the right the evolution with respect to time of the z -coordinate of the load after cable 2 breakdown.

the load before reaching the static equilibrium. Such a motion will put a large stress on the CDPР structure that will lead to additional safety issues.

5 Conclusion

This paper dealt with the possible failures of CDPРs when they are used for collaborative work with humans and provided some technical solutions to ensure the safety of the operators. There is no general strategy that can be applied in each case for ensuring this safety. We have considered a translational three degrees-of-freedom CDPР composed of four cables connected to a point-mass end-effector as an illustrative example. Failure possibilities have been identified, together with sensory means to detect the failure. The behaviour of the CDPР was studied in case of cable breakage and failure of an actuator and the loop effect was also investigated. Some technical solutions were proposed to ensure the safety of the human operator working in collaboration with the CDPР. For instance, a concept based on auxiliary cables and a clamping device was introduced to ensure safety in case of cable breakage.

Acknowledgements. This work was partly supported by the ANR CRAFT, grant ANR-18-CE10-0004.

References

1. Alikhani, A., et al.: Design of a large-scale cable-driven robot with translational motion. *Robot. Comput. Integr. Manuf.* **27**(2), 357–366 (2011)
2. Barnett, E., Gosselin, C.: Large-scale 3D printing with a cable-suspended robot. *Addit. Manuf.* **7**, 27–44 (2015)
3. Borgstrom, P., et al.: Discrete trajectory control algorithms for NIMS3D, an autonomous underconstrained three-dimensional cabled robot. In: *IEEE International Conference on Intelligent Robots and Systems (IROS)*, San Diego, pp. 253–260, 22–26 September 2007
4. Farzaneh Kaloorazi, H., Tale Masouleh, M., Caro, S.: Collision-free workspace of parallel mechanisms based on an interval-based approach. *Robotica* **35**(8), 1747–1760 (2017)
5. Lesellier, M., Gouttefarde, M.: A bounding volume of the cable span for fast collision avoidance verification. In: *Cable-Driven Parallel Robots (CableCon)*, Krakow, Poland, pp. 173–184. Springer (2019)
6. Merlet, J.P.: An experimental investigation of extra measurements for solving the direct kinematics of cable-driven parallel robots. In: *IEEE International Conference on Robotics and Automation*, Brisbane, 21–25 May 2018
7. Moradi, A.: Stiffness analysis of cable-driven parallel robot. Ph.D. thesis, Queen’s University, Kingston, April 2013
8. Notash, L.: Failure recovery for wrench capability of wire-actuated parallel manipulators. *Robotica* **30**(6), 941–950 (2012)
9. Notash, L., Huang, L.: On the design of fault tolerant parallel manipulators. *Mech. Mach. Theory* **38**(1), 85–101 (2003)

10. Pott, A.: Determination of the cable span and cable deflection of cable-driven parallel robots. In: *Cable-driven Parallel Robots (CableCon)*, Laval, Canada, pp. 106–116. Springer (2017)
11. Roberts, R., et al.: Characterizing optimally fault-tolerant manipulators based on relative manipulability indices. In: *IEEE International Conference on Intelligent Robots and Systems (IROS)*, San Diego, pp. 3925–3930, 22–26 September 2007
12. Ukidve, C., McInroy, J., Jafari, F.: Quantifying and optimizing failure tolerance of a class of parallel manipulators. In: *Parallel Manipulators, Towards New Applications*, pp. 45–68. ITECH, April 2008
13. Williams II, R., Albus, J., Bostelman, R.: 3D cable-based cartesian metrology system. *J. Robot. Syst.* **21**(5), 237–257 (2004)

Design Issues for Mechanisms and Robots



Software Optimization Problem Solver for Automated Linkage Design

Kirill Kuprianoff¹(✉), Christina Shutova¹, and Andrei Vukolov²

¹ Energetic Engineering Faculty, Bauman Moscow State Technical University,
Moscow, Russian Federation

`bdf-1@mail.ru`

² ELETTRA Sincrotrone Trieste S.C.p.A., AREA Science Park Basovizza, Trieste,
Italy

`andrei.vukolov@gmail.com`

Abstract. The selection and design of the kinematic diagram of the mechanism is the first stage in the creation of a technical device. In the design process, an optimization task inevitably arises, during the solution of which it is necessary to choose the best one from the proposed options according to certain criteria. This article proposes a software solution to automate this process. On the example of the synthesis of a planar mechanism by a given function of the output joint, the advantages of this automated approach are shown. When solving, the two methods are used: enumerating various geometric parameters for a given structural diagram of the mechanism and solving the forward kinematic problem, followed by finding the minimum of the target function, as well as solving the inverse kinematic problem for a given structural diagram of the mechanism.

Keywords: Optimization · Target function · Automation · Design · Planar mechanisms · Linkages

1 Introduction

At the moment, there are a number of specialized software products that allow the analysis of kinematic chains, but at the same time solving only the specific direct kinematics problem, without the possibility of solving the optimization problem and enumerating many solutions [1, 3, 13, 16]. Such packages and software systems include commercial software package ADAMS, which provides the ability to design and optimize kinematic chains. ADAMS is a powerful tool, but requires a high level of knowledge and experience with such programs. In addition, this program is proprietary [10, 11, 17, 18] and has strong licensing constraints. Also CATIA has the kinematic analysis tools which enable 3D modelling of compounds with any degree of freedom and the output of the motion curves of the mechanism parts, but they do not have the ability to optimize generated solutions [12]. There is a modern JavaScript library for modelling, visualization and

analysis of linkages called *mec2* [9]. It provides the main advantage—simplicity of code visualizing the linkage. But this solution has no possibility to multiply variants of calculation for given structural schema [9]. The another linkage design tool—WinMeCC [2, 5] is also proprietary. It provides user-friendly interface (Fig. 1¹) but very limited possibilities to build linkage libraries, open stocks and optimized collections.

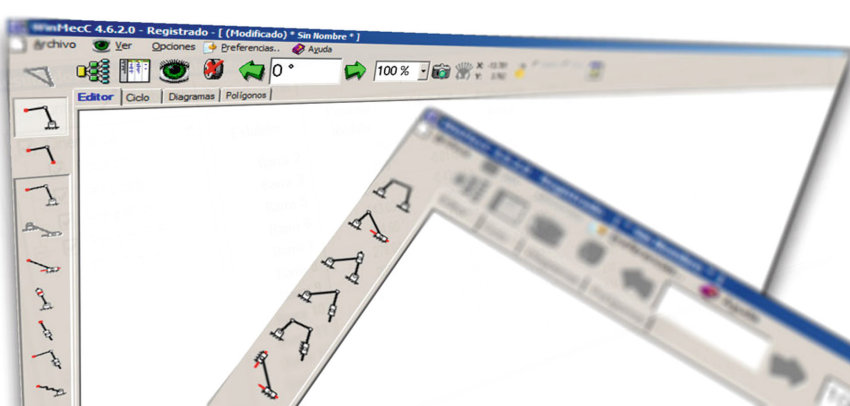


Fig. 1. WinMeCC—main window (advertisement from official website)

The program developed and implemented by the authors which is written in Python programming language is the open source solution aimed primarily to efficient enumeration of many variants of kinematic schemes, which allows, as the first approximation to obtain the semi-optimal or optimal solution. A library of mechanisms has also been created as a set of structural schemes with parametrically defined geometric parameters. Thus, this program gives user the freedom of choice both in the structure of the mechanism limited only by the size of the library, and in the selection of parameters with respect to which there will be a search for an optimal solution. The output of the program is a set of calculated parameters that provide minimized target function. This set of geometric snapshots can then be converted to several formats and visualized as motile mechanism using any of the above mentioned toolchains.

2 Advantages of Computer-Aided Design of Technological Systems

The main idea in the implementation of the program code was the principle of maximally free assignment of the base parameters and the whole model as it should be [6]. At the same time, it is obvious that excessive freedom of input of the initial data, meaning the creation of directly structural schemes from basic

¹ <http://en.winmecc.com/>.

elements, such as points and vectors, only leads to a complication of the initial data. The limitation in the form of a library of mechanisms makes it possible to speed up the process of formulating parameters for the program and at the same time avoids wasting time on the calculation of solutions in which it is impossible to obtain a satisfactory result. In addition, this approach reduces the number of errors that can be made when setting conditions in the program.

As a result, the user gets the opportunity to quickly and easily obtain an initial approximate solution for his task, with a minimum of effort spent directly on the formulation of the problem and the methods for solving it. This provides several advantages:

1. Significantly accelerate the process of obtaining a preliminary design, which can then be refined using more accurate software systems;
2. Elimination of deliberately unsatisfactory options, which also saves time spent on design and avoids further problems when working out a specific solution.

The resulting program has the ability to integrate with other programs. The output format of the program is simple to understand and easy to change, which allows the user to transfer geometric parameters to another program to visualize the solution, or to carry out further refinement calculations.

3 Synthesis of a Mechanism for a Given Function of the Output Joint: An Example of a Solution

Setting the initial data: Using the built-in library, the user chose several structural schemes for which the calculation will be done, and also sets the necessary output motion curve $\phi_{out} = f(\phi_1)$ for each scheme having one degree of freedom. The selected mechanisms with the names assigned to them are displayed in the left window. At the next stage, the parameters that will change during the calculation together with their range of variation, and the constants are set in the right window (Fig. 2).

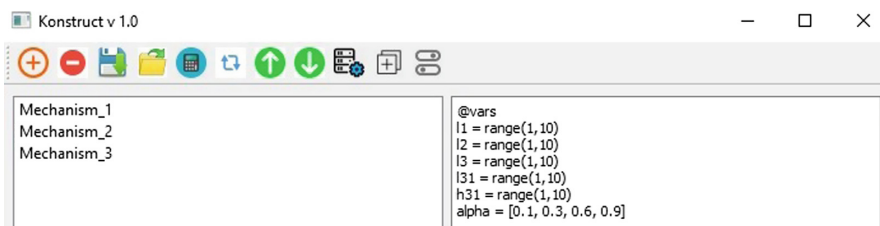


Fig. 2. Main window of the program

Examples of selection are shown in (Fig. 3).

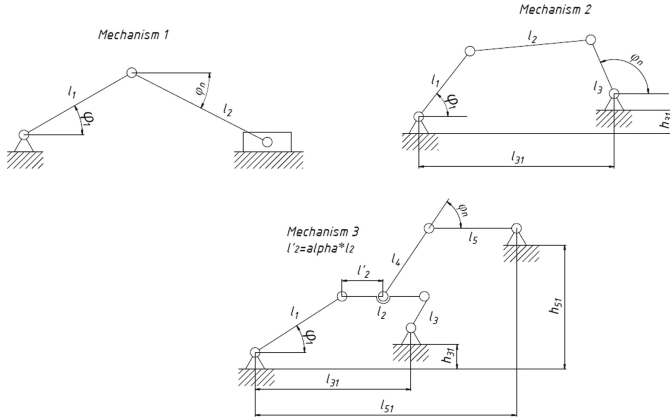


Fig. 3. Selection

3.1 Calculation of the Direct Kinematic Problem

The program performs optimization dimensional synthesis for each mechanism selected from the library, thus allowing to compare the results between different structural schemes to find the better solution. In the program code, equations for the selected mechanisms are automatically generated and solved, taking into account the selected variable parameters. The `result.txt` file is created at the output with all satisfactory parameters for which the task has a solution and the corresponding values of the target function. In our example, we need to find a mechanism for which the motion curve of the output joint is as close as possible to the required one and the target function is defined as

$$\Delta = \int_{\phi} (\phi_{out}^{calculated} - \phi_{out}^{given})^2$$

Figure 4 represents the obtained result.

The most optimal solution here is found by the minimum value of the target function and the motion curves are displayed for it (Fig. 6), where the red line is the user-defined output law for changing the angle, and the blue one is the obtained law by solving systems of equations.

During the calculation process, all internal parameters can be used to iteratively calculate not only the target function, but also any other functionality that the user sets manually, for example, the sum of the lengths of the links. The resulting functionalities are also added to the `result.txt` file. The architectural solution of the program implies the creation in the global memory area of all objects of the selected classes of mechanisms, as well as current variable parameters. Below is the part of the code that describes the function that starts the optimization calculation (Fig. 5).

```

l1: 4 l2: 8 l3: 5 l31: 6 h31: 9 ; Delta:928597.34
l1: 4 l2: 8 l3: 5 l31: 7 h31: 1 ; Delta:417189.43
l1: 4 l2: 8 l3: 5 l31: 7 h31: 2 ; Delta:1291859.53
l1: 4 l2: 8 l3: 5 l31: 7 h31: 3 ; Delta:869880.21
l1: 4 l2: 8 l3: 5 l31: 7 h31: 4 ; Delta:1538204.59
l1: 4 l2: 8 l3: 5 l31: 7 h31: 5 ; Delta:1294309.70
l1: 4 l2: 8 l3: 5 l31: 7 h31: 6 ; Delta:1202785.13
l1: 4 l2: 8 l3: 5 l31: 7 h31: 7 ; Delta:1211973.13
l1: 4 l2: 8 l3: 5 l31: 7 h31: 8 ; Delta:1294276.20
l1: 4 l2: 8 l3: 5 l31: 7 h31: 9 ; Delta:1437601.24
l1: 4 l2: 8 l3: 5 l31: 8 h31: 1 ; Delta:1065312.52
l1: 4 l2: 8 l3: 5 l31: 8 h31: 2 ; Delta:1802396.81
l1: 4 l2: 8 l3: 5 l31: 8 h31: 3 ; Delta:1695311.18
l1: 4 l2: 8 l3: 5 l31: 8 h31: 4 ; Delta:2480455.42
l1: 4 l2: 8 l3: 5 l31: 8 h31: 5 ; Delta:2137663.10
l1: 4 l2: 8 l3: 5 l31: 8 h31: 6 ; Delta:1957415.55
l1: 4 l2: 8 l3: 5 l31: 8 h31: 7 ; Delta:1897919.13
l1: 4 l2: 8 l3: 5 l31: 8 h31: 8 ; Delta:1931839.98

```

Fig. 4. Resulting dataset

```

1  def calcModel(self):
2      const_text, var_text = Calc.texthandler(self.code.toPlainText()) #
           Parsing code in right           window
3      Objects = deepcopy(self.Objects) # creating the copy of objects in left
           window
4      Variable_data = Calc.data_init(Objects, const_text) # Initialization of
           variables
5      Elements = Calc.elem_builder(Objects) # Building elements based on
           variables
6      Calc.elements_reInit(Elements) # Building elements based on variables
7      calc_text = Calc.var_texthandler(var_text)
8      exec(calc_text) # Run calculation for the generated task

```

Fig. 5. CalcModel function

The equations to be solved are compiled with respect to the variable parameters. The use of the global memory region allows sequential calculations, that is, to use the results obtained in one object, as source data for subsequent objects.

3.2 Visualization

To visualize the optimized kinematic scheme, a written script is used that converts the format of the program results to the JSON format which allows further work with the obtained linkage. For example constructing of the motion law of any joint. Choosing a specific kinematic scheme and link sizes from the result file, the user can convert this data and transfer it to the program for visualization. Converted input file obtained using the script, the constructed and visualized linkage are shown in (Fig. 7).

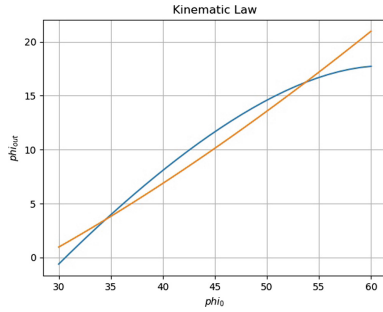


Fig. 6. Comparison of kinematic functions

```

model = {
  id: '4bar',
  gravity: false,
  nodes: [
    { id:"A0",x: 0+dx,y:0+dy,base:true },
    { id:"A", x:-57+dx,y:23+dy },
    { id:"B", x:-40+dx,y:80+dy },
    { id:"B0",x:10+dx,y:90+dy,base:true }
  ],
  constraints: [
    { id:"a",p1:"A0",p2:"A",len:{ type:"const" } },
    { id:"b",p1:"A", p2:"B",len:{ type:"const" } },
    { id:"c",p1:"B0",p2:"B",len:{ type:"const" } }
  ]
};

```

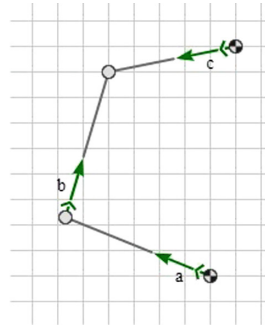


Fig. 7. Converted input file and graphic representation of the mechanism (screenshot of mec2 web canvas)

4 Development Prospects: Training

In addition to the direct use of the written program for designing linkages, when used, it becomes possible to process and analyse the obtained array of results, which allows to trace the influence of individual geometric parameters on the kinematics of the system. In addition, the use of structure libraries over time will develop the user’s intuitive thinking when choosing a kinematic scheme and variable parameters. Thus, the program will increase understanding of design issues among inexperienced designers, and for professionals it will become an additional tool for quick verification and analysis of their own ideas. Developing the idea of learning, the next step will be the implementation of full automation, in which the design experience is somehow saved in the form of a database and used in machine learning [14,15]. In this case, a trained ML system will be able to offer initial structural schemes itself, thereby leaving human user input only for the stage of formulating the problem. This approach can also stimulate development of special mechanics and assistance tools such as mechanisms with flexible parts and limited joint movement [4,7,19].

5 Conclusion

Optimization problems in the design of mechanisms were successfully solved in the implemented program code. On the example of solving the optimization problem of the synthesis of a planar mechanism according to the known motion curve of the output joint, it was shown:

- The ability to automate the design process, increasing the speed of development and the quality of the result;
- The ability to process a dataset for AI training based on the analysis of an existing array of solutions obtained using the program.

Thus, the written program is the first step to fully automate the design process [8]. The development of such programs is a promising direction, allowing us to take the class of optimization tasks to a new level. The next step for development of this program is to make it open source to increase possibilities for other developers to improve the code and to develop their own tools based on the free software model [17].

References

1. CATIA version 5-6 release 2015. Documentation in HTML format
2. WinMeCC - manual de usuario. Online User Manual. <http://winmecc.uma.es/guia-usuario-WinMecC.pdf>. Accessed 20 Jan 2020
3. ADAMS MSC team et al.: ADAMS User's Manual. MacNeal-Schwendler, Inc., Oakdale (2001)
4. Baryshnikova, O.: The creation of clean robots on the basis of a flexible elastic thin-walled elements. *Int. J. Mech. Eng. Robot. Res.* **8**(5), 759–763 (2019). <https://doi.org/10.18178/ijmerr.8.5.759-763>. <https://www.scopus.com/inward/record.uri?eid=2-s2.0-85071775978&doi=10.18178%2fijmerr.8.5.759-763&partnerID=40&md5=5b3c791bb6c0aae1e8bda9d4957e6559>
5. Bataller, A., Ortiz, A., Cabrera, J.A., Nadal, F.: WinMecC: software for the analysis and synthesis of planar mechanisms. In: Wenger, P., Flores, P. (eds.) *New Trends in Mechanism and Machine Science*, pp. 233–242. Springer, Cham (2017)
6. Belonozhko, P.P.: Assembly and service robotic space module. Mathematical model of the reduced system, pp. 337–347. Springer, Cham (2020). https://doi.org/10.1007/978-3-030-32579-4_27
7. Chernaya, L., Safonoff, I., Vukolov, A.: Design of cam mechanisms with swinging roller follower: the modern algorithm-based approach. In: Castejón, C., García-Prada, J.C., et al. (eds.) *Proceedings of ISEMMS 2017 the 2nd International Symposium on the Education in Mechanism and Machine Science*. Universidad Carlos III de Madrid, Springer, Madrid (2018). Preprint edn
8. Ghernik, A., Smirnov, N.: Development of the software for the automatization of kinematic calculation for closed kinematic scheme mechanisms, vol. 14 (2010). (in Russian)
9. Gössner, S.: Fundamentals for web-based analysis and simulation of planar mechanisms. In: *Proceedings of the 7th European Conference on Mechanism Science*, pp. 215–222 (2019). https://doi.org/10.1007/978-3-319-98020-1_25

10. Klein Breteler, A.: Kinematic optimization of mechanisms: a finite element approach (1987). <http://resolver.tudelft.nl/uuid:eca45c68-9353-4a64-8882-ab0b935eedc8>
11. Kovalenko, V.A.: State of deployment analysis of free software in institutions of the educational system in Russia (in Russian). *Pedagogical Educ. Russia* **6**, 188–192 (2013)
12. Krokmal, N.N., Krokmal, O.: General method of optimization kinematic synthesis of planar lever mechanisms based on its structural properties by example of the eight-link mechanism. In: *Proceedings of the 15th National Conference on Machines and Mechanisms (iNaCoMM 2011)* (2011). https://www.researchgate.net/publication/320023939-General_method_of_optimization_kinematic_synthesis_of_planar_lever_mechanisms_based_on_its_structural_properties_by_example_of_the_eight-link_mechanism
13. Pucheta, M., Cardona, A., Cugnon, F.: Kinematic optimization of planar linkages using Samcef BOSS-Quattro software. In: *5th Asian Conference on Multibody Dynamics 2010, ACMD 2010*, vol. 2, pp. 800–807 (2014)
14. Sarkar, D., Bali, R., Sharma, T.: *The Python Machine Learning Ecosystem*, pp. 67–118. Apress, Berkeley (2018). https://doi.org/10.1007/978-1-4842-3207-1_2
15. Semeraro, G., Esposito, F., Malerba, D., Fanizzi, N., Ferilli, S.: Machine learning + on-line libraries = IDL. In: Peters, C., Thanos, C. (eds.) *Research and Advanced Technology for Digital Libraries*, pp. 195–214. Springer, Heidelberg (1997)
16. Suyatinov, S.I.: Conceptual Approach to Building a Digital Twin of the Production System, pp. 279–290. Springer, Cham (2020). https://doi.org/10.1007/978-3-030-32579-4_22
17. Titov, A., Vukolov, A.: Free and open source software for technical texts editing, its advantages and experience of usage on TMM training in Bauman University. In: Castejón, C., García-Prada, J.C., et al. (eds.) *Proceedings of ISEMMS 2017 the 2nd International Symposium on the Education in Mechanism and Machine Science*. Universidad Carlos III de Madrid, Springer, Madrid (2018). Preprint edn
18. Vukolov, A.: Free and open source software applications for education of TMM discipline in Bauman University. In: Wenger, P., Flores, P. (eds.) *New Trends in Mechanism and Machine Science: Theory and Industrial Applications*, pp. 253–260. Springer, Cham (2017). https://doi.org/10.1007/978-3-319-44156-6_26. http://dx.doi.org/10.1007/978-3-319-44156-6_26
19. Zudina, O.V.: Process-oriented approach into Rao X simulation modeling system. In: Uhl, T. (ed.) *Advances in Mechanism and Machine Science*, pp. 531–536. Springer, Cham (2019)



Static Analysis and Design Strategy of Two Antagonistically Actuated Joints

Vimalesh Muralidharan¹(✉), Philippe Wenger^{1,2}, and Matthieu Furet^{1,2}

¹ Ecole Centrale de Nantes, 44321 Nantes, France
m.vimalesh94@gmail.com

² Laboratoire des Sciences du Numérique de Nantes (LS2N), CNRS,
44321 Nantes, France
{Philippe.Wenger,Matthieu.Furet}@ls2n.fr

Abstract. This paper compares the static performances of two types of antagonistically actuated joints: a revolute (R) joint and an antiparallelogram (X) joint. Both joints are equipped with lateral springs and actuated with two opposite cables running through the springs. The comparative study is conducted on the basis of their wrench-feasible workspace and stiffness. A methodology is proposed for the optimal design of each joint. Eventually, an R-joint and an X-joint, optimized for the same prescribed wrench-feasible workspace, are compared on the basis of their maximal actuation forces.

Keywords: Revolute joint · Antiparallelogram joint · Tensegrity · Antagonistic forces · Static analysis · Stiffness · Optimal design

1 Introduction

Most robotic manipulators are articulated with revolute joints (R-joints), which are either directly actuated with motors mounted on the joints, or remotely actuated with timing belts or gears. Cables can also be used as a way to transmit motion from the motors mounted on the ground. In cable-driven parallel manipulators (which are not in the scope of this paper), cables are used in place of the legs of a parallel manipulator. In cable-driven serial manipulators, a serial kinematic chain made of rigid links and joints is actuated with a set of cables arranged in parallel [1]. They are interesting solutions when a light-weight design is required and/or physical interactions with the environment are involved. Applications can be found in artificial hands [2], exoskeletons [3] or medical assistance devices. Like in classical robotic manipulators, revolute joints are generally used in cable-driven serial manipulators [1,4]. In this paper, an antiparallelogram joint, referred to as X-joint, is considered as an alternative choice. The X-joint is less popular than the parallelogram joint and, as far as we know, it has never been used in industrial robots. It was used in knee [5] and bird neck models [6], and in gear trains [7]. The X-shape tensegrity model

originally proposed by Snelson [8] has often been used in planar tensegrity mechanisms [6, 9–13]. In this paper, two antagonistically actuated joints (R-joint and X-joint) are studied. Both joints are equipped with two lateral springs and are actuated with two opposite cables running through the springs. Their static models are derived and their static performances are analyzed. A design methodology is proposed, which determines the minimal actuation forces required to reach a prescribed wrench-feasible workspace (WFW). Finally, an R-joint and an X-joint, optimized for the same WFW, are compared on the basis of actuation forces and stiffness.

2 Static Analysis of the Joints

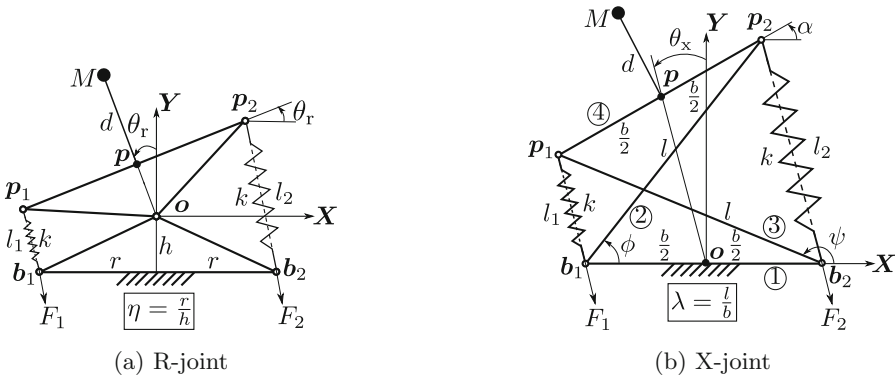


Fig. 1. Schematics of the joints under study: R-joint (left) and X-joint (right).

The schematic diagrams of the R-joint and the X-joint under study are shown in Figs. 1a and b, respectively. The R-joint is composed of two congruent isosceles triangles, one on top of the other, connected by a revolute joint at o . The triangles are defined by two geometric parameters: the semi-base length r , and height h . The configuration of this joint is described by the orientation angle (θ_r) of the upper triangle w.r.t. the vertical as shown in Fig. 1a. On the other hand, the X-joint is composed of three moving links 2, 3, 4 and a fixed link 1, each connected to its neighbours with a revolute joint. The links 1 and 4 are of length b , while the other two links are of length l . The configuration of the X-joint is defined by the orientation angle θ_x of the segment linking the midpoints of bars 1 and 4 w.r.t. the vertical as shown in Fig. 1b. Note that the assembly condition requires $l > b$.

Each joint is equipped with a pair of identical springs with spring constant k , to impart stiffness into the system. Also, the free-lengths of the springs are assumed to be zero in this study. For both the joints, a point mass M is attached to the segment $p_1 p_2$ at a distance d . The linear mass density (i.e., mass per unit

length) of the links is represented by ρ . Finally, the joints are actuated antagonistically by cables passing through the springs, imparting forces F_1 and F_2 , respectively, as shown in Fig. 1.

2.1 Static Equilibrium and Stiffness of the R-Joint

From Fig. 1a, l_1 and l_2 can be expressed in terms of θ_r as follows:

$$l_1 = 2 \left(h \cos \frac{\theta_r}{2} - r \sin \frac{\theta_r}{2} \right), \quad l_2 = 2 \left(h \cos \frac{\theta_r}{2} + r \sin \frac{\theta_r}{2} \right) \quad (1)$$

The rotation range of the R-joint is limited by singularities due to the actuating cables, in two different ways. Firstly, due to the occurrence of *force-closure singularity* (see [14]), when the points \mathbf{b}_i , \mathbf{o} , and \mathbf{p}_i ($i = 1$ or 2) become collinear. Secondly, due to the vanishing of l_1 or l_2 , where the direction of force applied by the respective cable becomes ill-defined. It can be shown that the limit of motion is due to force-closure singularity when $r < h$ and due to vanishing of l_i ($i = 1, 2$) when $r > h$. The rotation range depends on the link lengths and reaches its maximum amplitude $]-\frac{\pi}{2}, \frac{\pi}{2}[$ when $r = h$ (see [16] for more details).

Differentiation of the total potential energy of the joint w.r.t. θ_r yields the equation of static equilibrium, which is of the form: $G_r = \Gamma_r$, where,

$$G_r = C \sin \theta_r, \quad \text{with } C = \frac{1}{3} \left(6k \left(r^2 - h^2 \right) - 4\rho gh \left(r + \sqrt{r^2 + h^2} \right) - 3Mg \left(d + h \right) \right) \quad (2)$$

$$\Gamma_r = -F_1 \frac{dl_1}{d\theta_r} - F_2 \frac{dl_2}{d\theta_r} \quad (3)$$

The symbol G_r represents the wrench due to gravity and springs, while Γ_r represents the external wrench applied by the cables. The forces provided by the cables are limited physically, leading to: $F_1, F_2 \in [F_{\min}, F_{\max}]$. Since the coefficient of F_1 (resp. F_2) in Γ_r is always positive (resp. negative), the maximal (resp. minimal) boundary of the available wrench Γ_{\max} (resp. Γ_{\min}) is obtained when $F_1 = F_{\max}$ and $F_2 = F_{\min}$ (resp. $F_1 = F_{\min}$ and $F_2 = F_{\max}$) (see [16]). Considering these limits on Γ_r , it follows that the equation of static equilibrium can be satisfied only when: $G_r \in [\Gamma_{\min}, \Gamma_{\max}]$. The range of θ_r within which this condition is valid is the WFW of the joint.

The joint stiffness K_r is derived upon computing the second derivative of the total potential energy w.r.t. θ_r . We obtain:

$$K_r = C \cos \theta_r + \frac{1}{2} F_1 \left(-h \cos \frac{\theta_r}{2} + r \sin \frac{\theta_r}{2} \right) - \frac{1}{2} F_2 \left(h \cos \frac{\theta_r}{2} + r \sin \frac{\theta_r}{2} \right) \quad (4)$$

2.2 Static Equilibrium and Stiffness of the X-Joint

From Fig. 1b, l_1 and l_2 can be obtained in terms of θ_x as:

$$l_1 = -b \sin \theta_x + \sqrt{l^2 - b^2 \cos^2 \theta_x}, \quad l_2 = b \sin \theta_x + \sqrt{l^2 - b^2 \cos^2 \theta_x} \quad (5)$$

The singularities that limit the motion of the X-joint occur at $\theta_x = \pm \frac{\pi}{2}$, irrespective of the dimensions of the links.

The static equilibrium equation is obtained upon differentiation of the total potential energy of the joint w.r.t. θ_x as: $G_x = \Gamma_x$, where:

$$\begin{cases} G_x = C_1 \sin 2\theta_x + \frac{C_2 \sin \theta_x (2b^2 \cos^2 \theta_x - l^2)}{b\sqrt{l^2 - b^2 \cos^2 \theta_x}}, \\ \text{with } C_1 = 2(b^2 k - Mgd), C_2 = bg(M + \rho(b + l)) \end{cases} \quad (6)$$

$$\Gamma_x = -F_1 \frac{dl_1}{d\theta_x} - F_2 \frac{dl_2}{d\theta_x} \quad (7)$$

The symbols G_x and Γ_x possess the same physical meaning as G_r and Γ_r , respectively and the bounds of Γ_x are reached for the same force bounds as for the R-joint. The joint stiffness is obtained from the second derivative of the total potential function w.r.t. θ_x . Its expression is not reported here for lack of space, but can be found in [16].

3 Optimal Design of the Joints for a Specified WFW

In this study, the link lengths and the spring constant of the joints are considered to be the design variables, while the linear mass density and payload characteristics (ρ, M, d) are treated as parameters whose values are known *a priori*. The goal is to find optimal designs of the joints, such that the following conditions are met:

- The joint should possess the specified WFW of the general form: $[-\theta_{\max}, \theta_{\max}]$ with $\theta_{\max} < \frac{\pi}{2}$ to avoid singularities.
- The joint stiffness must be non-negative throughout the WFW for all admissible values of forces satisfying the equation of static equilibrium. Additionally, the stiffness must be equal to a prescribed value ($K_0 > 0$) when no actuation forces (F_1, F_2) are applied and equal to ($K_1 > 0$) at the boundary of the WFW.
- The force required to move the joint must be a minimum.

Due to symmetry of the joints about their respective zero orientations, ensuring $[0, \theta_{\max}] \in \text{WFW}$, ensures that $[-\theta_{\max}, 0] \in \text{WFW}$. Similar arguments can be made about the non-negativeness of the stiffness of the joints as well. This makes it sufficient to study just one half of the problem, i.e., $\theta_r > 0$ and $\theta_x > 0$. In the following, the positive boundary of WFW is denoted by θ_{rm} for the R-joint, and θ_{xm} for the X-joint. In order to satisfy the conditions listed above, a system of equations and inequalities have been formulated for the two joints as shown in Table 1 (assuming $F_{\min} = 0$). Physically, the first two conditions ensure that no singularities occur within the WFW and that the positive boundary of the WFW is formed by the intersection of the curves G_r (resp. G_x) and Γ_{\max} . The third and fifth conditions ensure that the stiffness of the joint is equal to K_0 in the absence of applied forces, and equal to K_1 at the boundary of the WFW. The remaining condition ensures that the joint possesses a non-negative stiffness at

the zero orientation when maximum forces are applied. The ratio of link lengths: $\eta(= \frac{r}{h})$ for the R-joint and $\lambda(= \frac{l}{b})$ for the X-joint have been introduced into the formulation, eliminating the variables h and l , respectively. This is because the ratio provides more insights into the problem and also simplifies the resulting expressions considerably. The conditions in Table 1 are then derived in terms of the joint parameters. Their expressions are not reported here for lack of space, but can be found in [16]. Using these expressions, design optimization problems for the R-joint and the X-joint are formulated and solved in the following.

Table 1. Formulation of the stipulated conditions for the R-joint and the X-joint.

R-joint	X-joint
$l_1(\theta_{rm}) > 0$ (8a)	No singularities when $(\theta_{xm} < \frac{\pi}{2})$ (9a)
$G_r(\theta_{rm}) + F_{\max} \frac{dl_1}{d\theta_r}(\theta_{rm}) = 0$ (8b)	$G_x(\theta_{xm}) + F_{\max} \frac{dl_1}{d\theta_x}(\theta_{xm}) = 0$ (9b)
$K_r(\theta_r = 0, F_1 = 0, F_2 = 0) = K_0$ (8c)	$K_x(\theta_x = 0, F_1 = 0, F_2 = 0) = K_0$ (9c)
$K_r(\theta_r = 0, F_1 = F_{\max}, F_2 = F_{\max}) \geq 0$ (8d)	$K_x(\theta_x = 0, F_1 = F_{\max}, F_2 = F_{\max}) \geq 0$ (9d)
$K_r(\theta_r = \theta_{rm}, F_1 = F_{\max}, F_2 = 0) = K_1$ (8e)	$K_x(\theta_x = \theta_{xm}, F_1 = F_{\max}, F_2 = 0) = K_1$ (9e)

3.1 Optimal Design of the R-Joint

It is noted that the set of design variables of the R-joint is formed by r , η , and k . Using Eq. (4) in Eq. (8c) results in the condition: $C = K_0$. From the expression of C provided in Eq. (2), it is possible to solve for k as:

$$k = \frac{\eta^2}{2r^2(\eta^2 - 1)} \left(K_0 + \frac{4r^2}{3\eta^2} \rho g \left(\eta + \sqrt{\eta^2 + 1} \right) + Mg \left(d + \frac{r}{\eta} \right) \right) \quad (10)$$

From the above equation, it is clear that the condition $\eta > 1$ is necessary to ensure that k remains positive. Also, from the inequality in Eq. (8a), the condition: $\eta < \cot \frac{\theta_{rm}}{2}$ is obtained. By substituting $C = K_0$ in Eq. (8b), the force required to reach the specified WFW is obtained as: $F_{\max} = \frac{K_0 \eta \sin \theta_{rm}}{r(\sin \frac{\theta_{rm}}{2} + \eta \cos \frac{\theta_{rm}}{2})}$. Using the above conditions, it can be shown that the inequality in Eq. (8d) is satisfied by default, when $\eta > 1$, for all values of $\theta_{rm} \in]0, \frac{\pi}{2}[$ (see [16] for details). Further, substituting $C = K_0$ and the above expression of F_{\max} in Eq. (8e), leads to:

$$\eta = \frac{K_0(1 - \cos \theta_{rm}) + 2K_1}{K_0(1 + \cos \theta_{rm}) - 2K_1} \tan \left(\frac{\theta_{rm}}{2} \right) \quad (11)$$

The above equation provides a simple relationship between the design specifications (θ_{rm}, K_0, K_1) and η . This is quite interesting because for a given set of specifications, the ratio of link dimensions remains fixed, irrespective of the payload (M, d) and the material of the links (ρ) . It is noted that the specifications K_0, K_1 , and θ_{rm} , must allow the bounds on: $\eta \in]1, \cot \frac{\theta_{rm}}{2}[$ to be satisfied, for the existence of feasible designs. Substituting for η from Eq. (11) into the

expression of F_{\max} and k (Eq. (10)), both of them can be obtained in terms of r , which is the only remaining variable. Thus, to minimize the force required to move the joint, the following optimization problem is posed:

$$\begin{aligned} \underset{r}{\text{Minimize}} \quad & F_{\max}(r) = \frac{(K_0(1 - \cos \theta_{\text{rm}}) + 2K_1)}{r} \sin\left(\frac{\theta_{\text{rm}}}{2}\right) \\ \text{subject to} \quad & r \in [0.025, 0.1], \\ & k \in [0, 2000], \end{aligned} \tag{12}$$

where r is the design variable of this problem. The constraint on η is not mentioned in the problem as it should be satisfied by the choice of K_0, K_1 , and θ_{rm} . Bounds on the variables r and k have been imposed in the problem due to practical considerations, such as, availability of corresponding components in the market and ease of fabrication/assembly. Using Eq. (10), equivalent algebraic conditions on r , corresponding to bounds on k can be obtained. These conditions would be used for defining the feasible design space of the R-joint. The first-order necessary condition for F_{\max} to achieve a local minima requires the vanishing of its derivative w.r.t. r . However, it is found that $\frac{dF_{\max}}{dr} = -\frac{(K_0(1 - \cos \theta_{\text{rm}}) + 2K_1)}{r^2} \sin\left(\frac{\theta_{\text{rm}}}{2}\right)$, is negative for all feasible values of the design variables and parameters. This implies that F_{\max} decreases with increase in r , and its minimum value would occur when r is as large as possible, while satisfying the constraints specified in Eq. (12). Further information on the minimum value of force and the corresponding design variables can be obtained by studying the behavior of F_{\max} inside the design space, as illustrated in Fig. 2a.

3.2 Optimal Design of the X-Joint

It is noted that the set of design variables of the X-joint is formed by: b, λ , and k . Using Eq. (9b) and Eq. (9e), it is possible to obtain the expression of F_{\max} reported in Eq. (15), and a relation between C_1 and C_2 of the form: $C_1 = \gamma_1 K_1 + \gamma_2 C_2$, where γ_1 and γ_2 are functions of λ and θ_{xm} , which are suppressed here due to lack of space (see [16] for details). Substituting this relation in Eq. (9c) leads to:

$$2\gamma_1 K_1 + \gamma_3 C_2 - K_0 = 0, \text{ where } \gamma_3 = 2\gamma_2 - \frac{\lambda^2 - 2}{\sqrt{\lambda^2 - 1}} \tag{13}$$

Substituting the expression of C_2 from Eq. (6) into Eq. (13), one obtains a quadratic equation in b as: $\rho g \gamma_3 (\lambda + 1) b^2 + M g \gamma_3 b + 2\gamma_1 K_1 - K_0 = 0$. Considering $b > 0$, this equation provides a unique solution to b in terms of λ as follows:

$$b = \frac{\sqrt{\gamma_3^2 g^2 M^2 - 4\gamma_3 g (\lambda + 1) \rho (2\gamma_1 K_1 - K_0)} - \gamma_3 g M}{2\gamma_3 g (\lambda + 1) \rho} \tag{14}$$

Using this expression of b , it is possible to obtain C_2 (from Eq. (6)), and then C_1 in terms of λ . Further, from the definition of C_1 (see Eq. (6)), the spring constant k can be found as: $k = \frac{C_1 + 2Mgd}{2b^2}$. Using Eq. (13), it can be shown that the inequality in Eq. (9d) reduces to: $K_0 + \frac{2bF_{\max}}{\sqrt{\lambda^2 - 1}} \geq 0$, which is satisfied by default, since all of its terms are positive. Thus, the optimization problem for the design of the X-joint is posed as follows:

$$\begin{aligned} \text{Minimize}_{\lambda} \quad & F_{\max}(\lambda) = \frac{C_2 \lambda^4 \sin \theta_{\text{xm}} \tan^2 \theta_{\text{xm}} + K_1 \tan \theta_{\text{xm}} (\lambda^2 - \cos^2 \theta_{\text{xm}})^{3/2}}{b \cos \theta_{\text{xm}} \left((\lambda^2 - \cos^2 \theta_{\text{xm}})^{3/2} - \sin^3 \theta_{\text{xm}} \right)} \\ \text{subject to} \quad & k \in [0, 2000], \\ & b \in [0.05, 0.2], \\ & \lambda \in [1, 5], \end{aligned} \tag{15}$$

where λ is the only design variable in this problem ($\lambda = \frac{l}{b}$). The bounds on k and b must be transferred to λ , to define the feasible design space for X-joint. However, due to the complicated functional relationship between variables, an equivalent set of algebraic conditions on λ could not be derived. Nevertheless, from a plot of b (resp. k) against λ , it is possible to identify the feasible regions visually, and then compute the corresponding limiting points numerically, to define the feasible design space (see Fig. 2b).

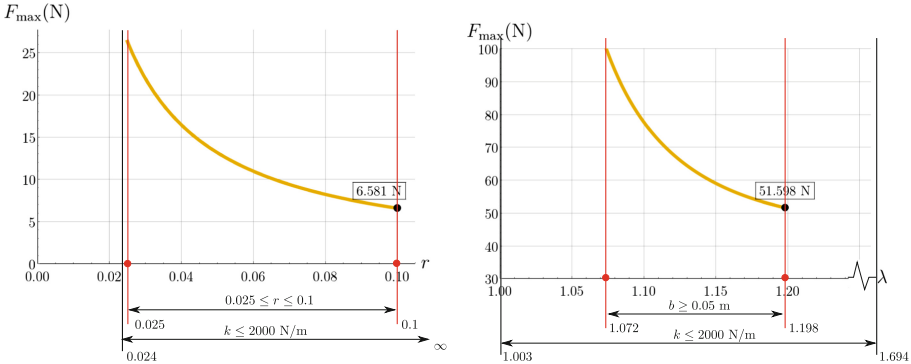
As in the previous case, the first-order necessary condition for F_{\max} to attain a minima is obtained from the condition: $\frac{dF_{\max}}{d\lambda} = 0$. The corresponding algebraic expression is too huge to be reported in this paper (see [16] for details). Solution to the said equation would provide the stationary points of F_{\max} . Firstly, it is essential to check if there are solution(s) that satisfy all the constraints specified in Eq. (15). Secondly, such solutions must be classified as a minimum or a maximum or an inflection point, through the second derivative test or by inspecting the plot of F_{\max} against λ , as illustrated in Fig. 2b. In case several minima exist within the feasible design space, then the one that corresponds to the least value of F_{\max} must be chosen. On the other hand, if no minima exists, then the solution to this problem must be at/near a boundary of the feasible design space, depending on whether the boundary point is included or not.

4 Numerical Examples and Inferences

All the links are considered to be 3D printed using ABS material with a circular cross section of diameter equal to 0.01 m, as in [15]. Consequently, the linear mass density (ρ) of the links is found to be 0.0825 kg/m. Point mass (M) and offset (d) values are considered to be: $M = 0.2$ kg and $d = 0.25$ m, respectively. Ideally, a suitable value for the prescribed stiffness (K_0, K_1) should be determined through experiments to estimate the amount of disturbance the joint must withstand. In this study, these values are chosen to be: $K_0 = 1$ Nm/rad and $K_1 = 0.6$ Nm/rad, for both the joints after verifying that the necessary conditions discussed in

Sects. 3.1 and 3.2 are satisfied. The WFW is stipulated to be $[-\frac{5\pi}{18}, \frac{5\pi}{18}]$ (i.e., $[-50^\circ, 50^\circ]$) for the two joints.

Using the above data, F_{\max} is plotted in the design space (r) of the R-joint as shown in Fig. 2a. It is observed that the feasible design space is formed by the constraint: $0.025 \leq r \leq 0.1$ (red). From the plot, F_{\max} attains its minimum value of 6.581 N when: $r = 0.1$ m, $\eta = 1.6399$ ($h = r/\eta = 0.061$), and $k = 129.2487$ N/m.



(a) R-joint: Plot of F_{\max} with r and boundary of constraints $0.025 \leq r \leq 0.1$ (red) and $k \leq 2000$ (black) (b) X-joint: Plot of F_{\max} with λ and boundary of constraints $b \geq 0.05$ (red) and $k \leq 2000$ (black)

Fig. 2. Variation of F_{\max} inside the feasible design space of the joints.

In Fig. 2b, F_{\max} is plotted against the design variable (λ) of the X-joint. It is observed that the feasible design space is reduced to $\lambda \in [1.072, 1.198]$, by the constraint $b \geq 0.05$ (red). It is found that the equation $\frac{dF_{\max}}{d\lambda} = 0$, results in $\lambda = 1.3$, which is outside the feasible domain. Thus, from the plot, the minimum value of $F_{\max} = 51.598$ N occurs when $\lambda = 1.1982$, $b = 0.05$ m ($l = \lambda b = 0.0599$), and $k = 287.2395$ N/m.

The optimal designs, corresponding forces, and bounds on stiffness of the joints are presented in Fig. 3. From the obtained results, the following inferences are made:

- From the link dimensions, it is observed that the width (resp. height) of the R-joint is 4 (resp. about 3.7) times more than that of the X-joint. The mass of the R-joint (without payload) is found to be 0.085 kg, which is about 4.5 times the mass of the X-joint, computed to be 0.018 kg.
- The stiffness upper bound of the R-joint (resp. X-joint) is reached when one of the applied forces is equal to F_{\min} (resp. F_{\max}). This shows that increasing the applied forces *decreases* the stiffness of the R-joint, while it *increases* the stiffness of the X-joint.

- The force required to move the R-joint is lower (about 1/8 times) when compared to the X-joint. This implies that the R-joint is more *sensitive* to small changes in the applied forces.
- The stiffness value of the X-joint is higher (about 9 times) when compared to the R-joint, around the zero orientation. Additionally, the distribution of stiffness is more uniform throughout the WFW for the R-joint, while relatively large differences in stiffness is observed for the X-joint inside its WFW, between the zero orientation and the boundary. Moreover, the difference between the minimal and maximal stiffness is greater for the X-joint, especially around the zero orientation. The X-joint is thus more suitable for variable stiffness.
- The value of spring constant (k) required is about two times greater for the X-joint than for the R-joint.

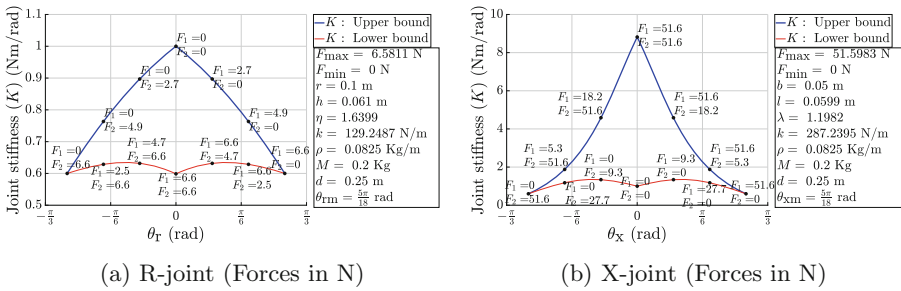


Fig. 3. Plots of stiffness bounds corresponding to the optimal design of the joints for a specified WFW of $[-\frac{5\pi}{18}, \frac{5\pi}{18}]$ with a payload: $M = 0.2$ kg, $d = 0.25$ m.

5 Conclusion

The static analysis of two antagonistically actuated joints with a point mass payload has been conducted in this study: the revolute (R) joint and the antiparallelogram (X) joint. An optimal design strategy has been proposed to minimize the actuation forces for a prescribed wrench-feasible workspace (WFW) with a prescribed stiffness at rest and at the WFW bounds. The joints have been compared in terms of their actuation forces and stiffness, when they are designed to possess the same WFW. It is found that the R-joint is heavier, requires lower forces, is more sensitive to applied forces, and possesses a more uniform stiffness distribution throughout its workspace. On the other hand, the X-joint reaches a higher stiffness near its zero orientation and exhibits relatively large variations in stiffness within its WFW. The stiffness of the X-joint can be easily increased by increasing the forces magnitude. For the R-joint, in contrast, the stiffness decreases when forces magnitude increases. In the future, the comparative study

and design strategy will take into account the dynamics and will be extended to manipulators with several R- and X-joints in series.

Acknowledgement. This work was conducted with the support of the French National Research Agency (AVINECK Project ANR-16-CE33-0025).

References

1. Ramadoss, V., Zlatanov, D., Zoppi, M.: Kinematic and workspace analysis of minimally routed cable driven open chains. In: Proceedings of the 15th World Congress in Mechanism and Machine Science, IFToMM 2019, Krakow, Poland (2019)
2. Baril, M., Laliberté, T., Guay, F., Gosselin, C.: Static analysis of single-input/multiple-output tendon-driven underactuated mechanisms for robotic hands. In: Proceedings of the ASME 2010 IDETC Conference, vol. 2, 34th Annual Mechanisms and Robotics Conference, Parts A and B, Montreal, QC, Canada, pp. 155–164 (2010)
3. Mao, Y., Agrawal, S.K.: Design of a Cable-Driven Arm Exoskeleton (CAREX) for neural rehabilitation. *IEEE Trans. Rob.* **28**(4), 922–931 (2012)
4. Chen, B., Cui, Z., Jiang, H.: Producing negative active stiffness in redundantly actuated planar rotational parallel mechanisms. *Mech. Mach. Theory* **128**, 336–348 (2018)
5. Hamon, A., Aoustin, Y., Caro, S.: Two walking gaits for a planar bipedal robot equipped with a four-bar mechanism for the knee joint. *Multibody Sys. Dyn.* **31**(3), 283–307 (2014)
6. Furet, M., Wenger, P.: Kinetostatic analysis and actuation strategy of a planar tensegrity 2-X manipulator. *ASME J. Mech. Robot.* **11**(6) (2019). <https://doi.org/10.1115/1.4044209>
7. Zhang, X., Deng, H., Wang, X., Pan, C., Xu, H.: Use of anti-parallelogram linkage mechanism and ordinary gear train for power transmission on a rotary engine. In: Proceedings of the Third International Conference on Mechanic Automation and Control Engineering, pp. 1041–1044 (2012)
8. Snelson, K.: Continuous tension, discontinuous compression structures. US Patent No. 3,169,611 (1965)
9. Arsenault, M., Gosselin, C.M.: Kinematic, static and dynamic analysis of a planar 2-DOF tensegrity mechanism. *Mech. Mach. Theory* **41**(9), 1072–1089 (2006)
10. Wenger, P., Chablat, D.: Kinetostatic analysis and solution classification of a class of planar tensegrity mechanisms. *Robotica* **37**(7), 1214–1224 (2019)
11. Boehler, Q., Charpentier, I., Vedrines, M.S., Renaud, P.: Definition and computation of tensegrity mechanism workspace. *ASME J. Mech. Robot.* **7**(4), 044502–044505 (2015)
12. Chen, S., Arsenault, M.: Analytical computation of the actuator and Cartesian workspace boundaries for a planar 2-degree-of-freedom translational tensegrity mechanism. *ASME J. Mech. Robot.* **4**(1), 011010 (2012)
13. Bakker, D.L., Matsuura, D., Takeda, Y., Herder, J.L.: Design of an environmentally interactive continuum manipulator. In: Proceedings of the 14th World Congress in Mechanism and Machine Science, IFToMM 2015, Taipei, Taiwan (2015)
14. Diao, X., Ma, O., Lu, Q.: Singularity analysis of planar cable-driven parallel robots. In: 2008 IEEE International Conference on Robotics, Automation and Mechatronics, pp. 272–277 (2008)

15. Furet, M., van Riesen, A., Chevallereau, C., Wenger, P.: Optimal design of tensegrity mechanisms used in a bird neck model. In: Corves, B., Wenger, P., Hüsing, M. (eds.) EuCoMeS 2018, vol. 59, pp. 365–375. Springer, Cham (2019)
16. Muralidharan, V.: Static analysis and design of revolute joint and antiparallelogram joint. Technical report, LS2N-CNRS, Ecole Centrale de Nantes (2020). <https://doi.org/10.13140/RG.2.2.17902.77120/1>



An Approach to Robotic End Effectors Based on Multistable Tensegrity Structures

V. Böhm^{1(✉)}, P. Schorr^{1,2}, T. Feldmeier¹, J.-H. Chavez-Vega^{1,2}, S. Henning²,
K. Zimmermann², and L. Zentner²

¹ OTH Regensburg, Regensburg, Germany

valter.boehm@oth-regensburg.de, thomas1.feldmeier@st.oth-regensburg.de

² TU Ilmenau, Ilmenau, Germany

{philipp.schorr,jhohan-harvey.chavez-vega,stefan.henning,
klaus.zimmermann,lena.zentner}@tu-ilmenau.de

Abstract. In this paper compliant multistable tensegrity structures with discrete variable stiffness are investigated. The different stiffness states result from the different prestress states of these structures corresponding to the equilibrium configurations. Three planar tensegrity mechanisms with two stable equilibrium configurations are considered exemplarily. The overall stiffness of these structures is characterized by investigations with regard to their geometric nonlinear static behavior. Dynamical analyses show the possibility of the change between the equilibrium configurations and enable the derivation of suitable actuation strategies.

Keywords: Compliant tensegrity structure · Multiple states of self-equilibrium · Variable stiffness

1 Introduction

The consideration of prestressed mechanically compliant structures as mechanisms is a promising recent research topic [1, 3, 5, 9, 11]. A specific class of these structures are compliant free standing tensegrity structures, consisting of a set of disconnected compressed members connected with a continuous net of compliant tensioned members. Known tensegrity mechanisms use conventional tensegrity structures with only one state of self-equilibrium. Tensegrity structures featuring multiple states of self-equilibrium, so-called multistable tensegrity structures, represent a specific type of tensegrity structure [2, 4, 7, 8, 10]. The consideration of compliant multistable tensegrity structures with members of pronounced elasticity and their use in mechanisms is promising due to the realization of structures with discrete variable stiffness. The main property of these structures is that their prestress states and therefore their overall stiffness differ in their equilibrium configurations. Applying these structures, e.g. end effectors with discrete variable stiffness can be realized (Fig. 1).

In the present article as a first step we focus on two-dimensional structures with simple topologies, consisting of only few members. In Sect. 2 modeling aspects and static behavior with regard to the overall stiffness of the structures is presented. Section is devoted to the actuation and the change between various equilibrium states. Finally, in Sect. 4 conclusions are given.

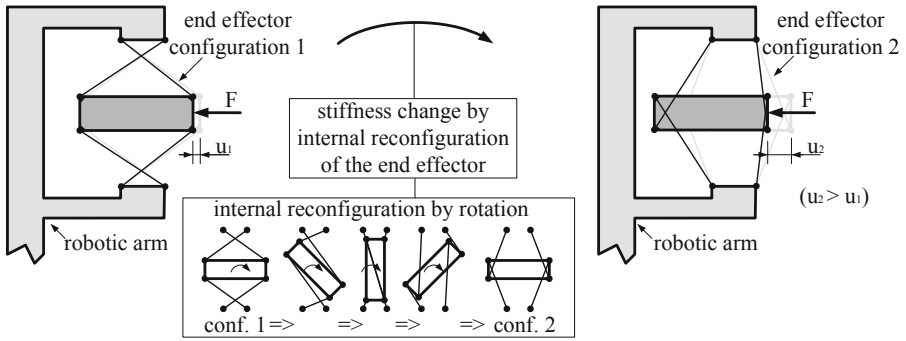


Fig. 1. Change of stiffness by reconfiguration of a multistable tensegrity structure.

2 Mechanical Modeling

For the following investigations the two-dimensional tensegrity structures depicted in Fig. 2 a), Fig. 3 a) and Fig. 6 a) are considered. The topology depicted in Fig. 2 a) consist of 10 members ($j = 1, 2, \dots, 10$) which are connected in 6 nodes ($i = 1, 2, \dots, 6$). According to the given load in the equilibrium state, the members $j = 1, 2, \dots, 6$ are classified as compressed members. The members $j = 7, 8, 9, 10$ are tensioned members. Corresponding to this approach the structure illustrated in Fig. 3 a) enables 10 compressed members and 4 tensioned members. The tensegrity shown in Fig. 6 a) features 8 compressed members and 4 tensioned members.

In order to describe the structural dynamics a mechanical modeling of the different members is necessary. The compressed members are usually realized by straight struts made of steel or aluminum. Those members j are described by the mass m_j and the moment of inertia $[I_j]$. Because of the two-dimensional consideration the specification of $\Theta_{zz,j}$ is sufficient. The resulting deformation due to the prestress of the structure is marginal. Thus, for the following investigations this issue is neglected and the compressed members are assumed to be rigid. The corresponding constant length of the member j is given by L_j . Thus, the parameter $\Theta_{zz,j}$ is given by $\Theta_{zz,j} = m_j L_j^2 / 12$. The tensioned members represent the flexible part of the compliant tensegrity structure. Those members are commonly realized by springs, or elastomers. In this work, these members are represented by springs with linear force-deformation characteristics. Therefore, the deformation behavior of the tensioned member j is formulated by the stiffness k_j and the initial length l_j . Occurring energy dissipation as a consequence

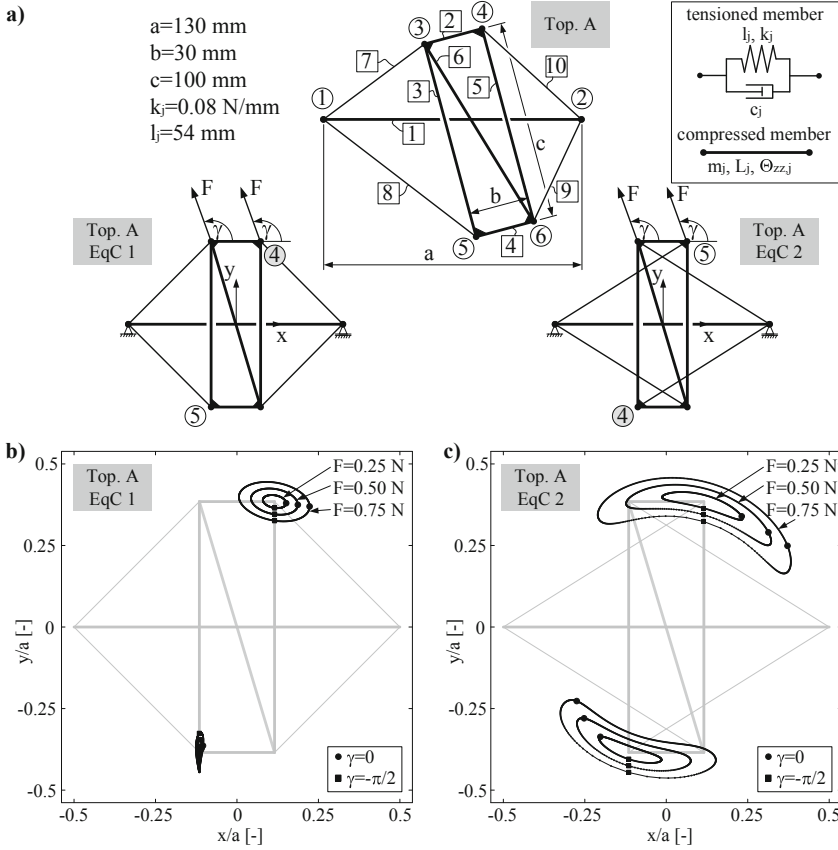


Fig. 2. Structure with topology A featuring two stable equilibrium configurations EqC 1 and EqC 2 (a); flexibility plots due to varying the magnitude and the orientation characterized by γ of the applied force on nodes 3 and 4 in EqC 1 (b) and on nodes 5 and 6 in EqC 2 (c).

of the deformation is taken into account by a damper with constant damping coefficient c_j . Finally, the mass of the tensioned members is marginal comparing to the compressed members. Therefore, these members are modeled as massless. The resulting mechanical models of the different members are depicted in Fig. 2 a) and Fig. 3 a). In the theoretical investigations collisions between the members are not considered. For future prototypes collisions can be prevented by applying constructive guidelines according to [2].

To describe the structural dynamics the LAGRANGE formalism is applied as shown in (1). The generalized coordinates of the system are summarized in the vector \mathbf{q} . The parameter T and Π represent the kinetic energy and the strain energy. Acting forces on the node i due to actuation and damping are given by \mathbf{F}_i .

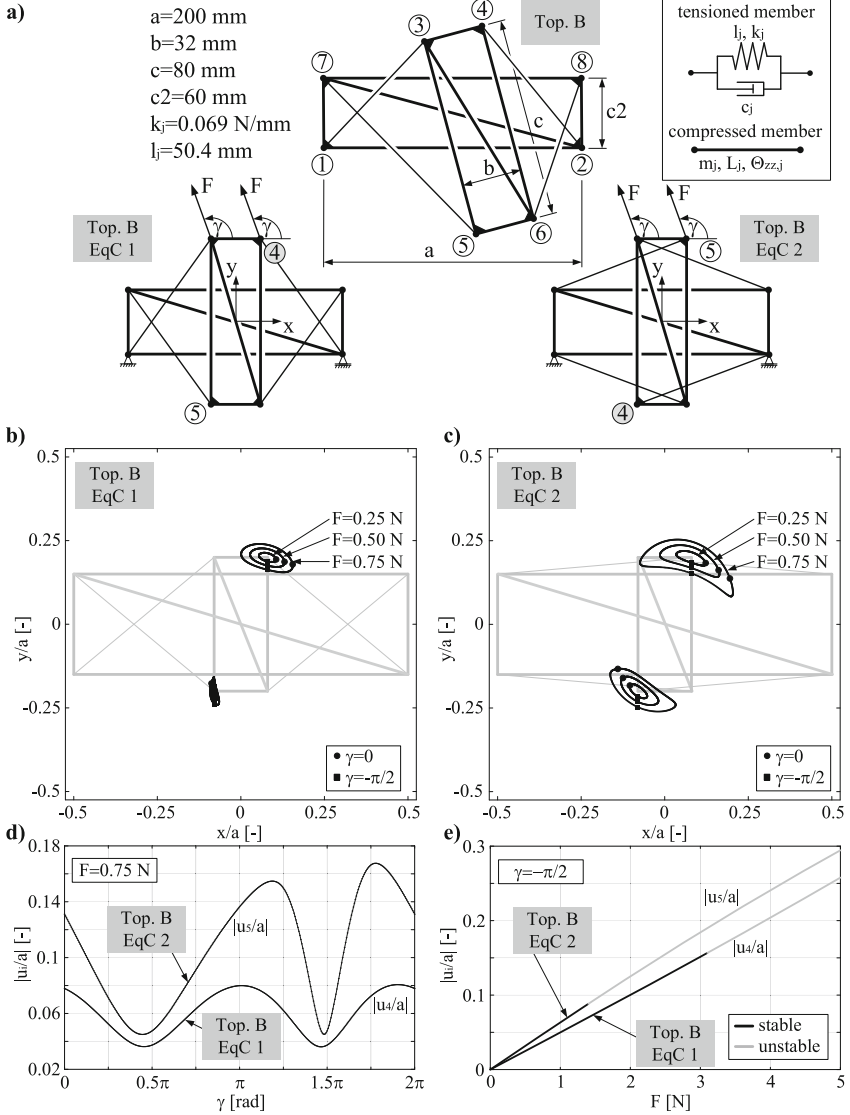


Fig. 3. Structure with topology B featuring two stable equilibrium configurations EqC 1 and EqC 2 (a); flexibility plots due to varying the magnitude and the orientation characterized by γ of the applied force on nodes 3 and 4 in EqC 1 (b) and on nodes 5 and 6 in EqC 2 (c). Nodal displacements depending on the orientation γ of the force (d) and the force magnitude F (e).

$$\frac{d}{dt} \frac{\partial T}{\partial \dot{q}_a} - \frac{\partial T}{\partial q_a} + \frac{\partial \Pi}{\partial q_a} = \mathbf{F}_i \cdot \frac{\partial \mathbf{r}_i}{\partial q_a} \quad (1)$$

This approach yields the nonlinear equations of motion. To predict the equilibrium states of these structures (1) is simplified by neglecting the dynamics terms (kinetic energy, damping) and the actuation. This yields the nonlinear system of equations formulated in (2) which is solved numerically in MATLAB.

$$\frac{\partial \Pi}{\partial q_a} = 0 \quad (2)$$

This equation has to be solved numerically. Moreover, to classify the detected equilibrium states as stable or unstable configurations the corresponding stability is evaluated using the Hessian of the strain energy.

For the presented tensegrity structures and the applied parameters the stable equilibrium configurations illustrated in Fig. 2 and Fig. 3 are detected. These results show, that both tensegrity structures enable two stable equilibrium configurations. Thus, these structures are classified as multistable tensegrity structures. Because of the symmetric topologies all detected equilibrium configurations are symmetric respective to the x - and y -axis. The stiffness of these structures is differing, due to the different prestress states (compare Fig. 2 b) - Fig. 2 c) and Fig. 3 b) - Fig. 3 c)). The corresponding flexibility plots relate the absolute node displacements to the applied load depending on the orientation of the load. These results confirm the different stiffness of the tensegrity structure due to different equilibrium configurations.

3 Changing the Equilibrium Configuration

In order to utilize the advantage given by the multistability of the tensegrity structures a reliable change between these stable states is necessary. Therefore, an actuation of the tensegrity has to be considered. The variation of the prestress state is given by the control of the initial length of two selected tensioned members for the structures shown in Fig. 2 and 3. The actuation of the tensegrity structure illustrated in Fig. 6 is given by external torques M_9 and M_{11} acting on the nodes 9 and 11.

The influence of the actuation parameters on the detected equilibria is investigated using bifurcation theory. Inspired by [6] existence ranges of the stable equilibrium configurations respective to the applied actuation parameters are derived. Leaving the existence range of the current equilibrium state yields a change into another stable state. In order to verify this approach numerical simulations considering (1) are evaluated in MATLAB using a common RUNGE-KUTTA method. In this work, the masses of the compressed members are estimated by $m_j = L_j \cdot 1 \text{ g/mm}$. According to existing prototypes the damping coefficient is chosen to $c_j = 0.0004 \text{ Ns/m}$. Following, the actuation strategy formulated in (3) and (4) is implemented. Here, \bar{a} represents the corresponding amplitude of the actuation strategy.

$$\Delta l = \begin{cases} \bar{a} t & \text{if } t \leq 1 \text{ s} \\ \bar{a} & \text{elseif } t \leq 2 \text{ s} \\ \bar{a} - \bar{a}(t - 1 \text{ s}) & \text{elseif } t \leq 3 \text{ s} \\ 0 & \text{else} \end{cases} \quad (3)$$

$$M = \begin{cases} \bar{a} t & \text{if } t \leq 1 \text{ s} \\ 0 & \text{else} \end{cases} \quad (4)$$

For various actuation strategies the change of the equilibrium configuration is evaluated. In Fig. 4 two exemplary actuation strategies are considered and the resulting displacement of the node 3 in the y -direction is evaluated for the structure with topology A. These results confirm that since the existence range of the current stable equilibrium is not left no change occurs. However, crossing the boundaries of the existence range yields a change into the second stable state.

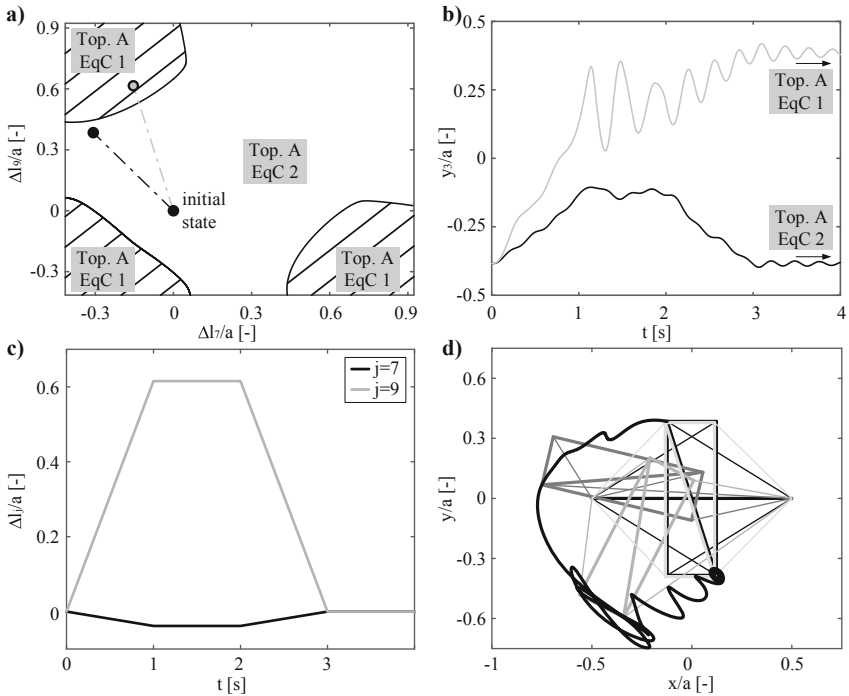


Fig. 4. Actuation of the structure with topology A by changing the free lengths of the tensioned members between nodes 1 and 3 ($j = 7$) and 2 and 6 ($j = 9$). a): existence ranges of the stable equilibrium configurations EqC 2; b): displacement of the node 3 in y -direction during and after actuation corresponding to two exemplary cases, depicted in a); c) actuation parameters for changing the equilibrium configuration; d): change of the equilibrium configuration - overall displacement of the structure during and after actuation.

In Fig. 5 selected results are depicted for the structure with topology B with respect to two exemplary actuation strategies. The results show, that the change between the equilibrium configurations of this structure is also possible by a proper actuation. The change between the equilibrium configurations is induced for both structures with topology A and B by the movement of the movable inner frame, built by members between the nodes 3...6. In Fig. 6 a) a further structure, based on the modified version of the structure with topology B, is depicted (topology B*). As the simulations corresponding to this structure show, the change between the equilibrium configurations EqC 1 and EqC 2 can be induced only by reconfiguration of the outer members (member between nodes 1 and 7 and member between nodes 2 and 8), without movement of the inner movable frame. Hence, the stiffness variation can be induced without an a priori movement of the inner movable frame.

The simulation results confirm the working principle of the tensegrity structure. The control of the nonlinear dynamics of the system is challenging. For example, an according force control law with position feedback can be applied. However, to derive a reliable actuation strategy a static consideration is sufficient.

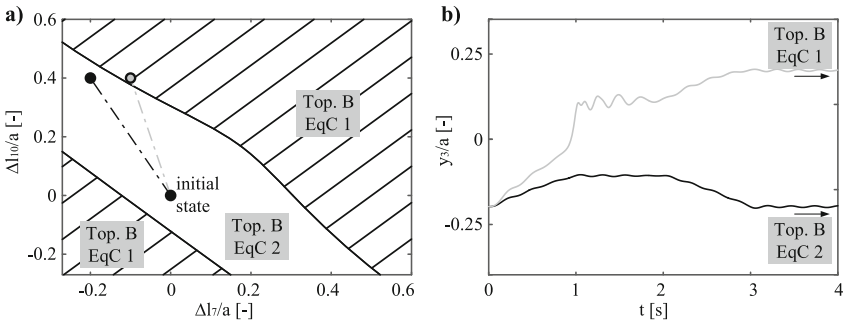


Fig. 5. Actuation of the structure with topology B by changing the free lengths of the tensioned members between nodes 1 and 3 (Δl_7) and 6 and 8 (Δl_{10}). a): existence ranges of the stable equilibrium configuration EqC 2; b): displacement of the node 3 in y -direction during/after actuation corresponding to two cases, depicted in a).

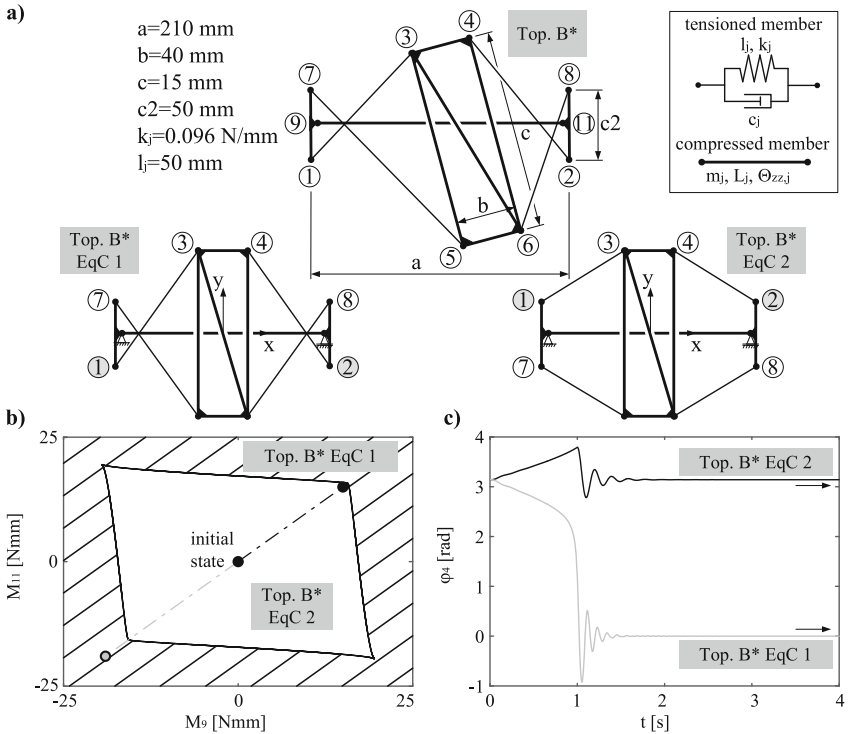


Fig. 6. Actuation of the structure with topology B* by applying external torques M_9 and M_{11} acting on the nodes 9 and 11. a) topology and member parameters; b): existence ranges of the stable equilibrium configuration EqC 2; c): rotation of the movable frame (with nodes 3...6) relative to the z -axis during/after actuation corresponding to two cases, depicted in b).

4 Conclusion

Compliant tensegrity structures with multiple states of self-equilibrium can be used as structures with discrete variable stiffness in technical applications. This work demonstrates that tensegrity structures, consisting of only few members, can have more than one stable equilibrium configuration and the overall stiffness of these structures differs in these configurations. This property results from different prestress states in the equilibrium configurations. The investigations show, that the discrete change of the overall stiffness can be induced by internal reconfiguration due to changing between the equilibrium configurations. Further research will focus on detailed consideration (workspace, overall mechanical compliance) of these mechanisms and on the development of demonstrators.

Acknowledgements. This work is supported by Deutsche Forschungsgemeinschaft (DFG) within the SPP 2100 - projects ZE714/14-1, BO4114/3-1. The authors acknowledge the valuable support of the students of the Tensegrity-Project-Group of the OTH Regensburg, Faculty of Mechanical Engineering during 2019.

References

1. Boehler, Q., et al.: Definition and computation of tensegrity mechanism workspace. *J. Mech. Robot.* **7**(4), 4 (2015). Paper No: JMR-14-1168
2. Böhm, V., et al.: Compliant multistable tensegrity structures. *Mech. Mach. Th.* **115**, 130–148 (2017)
3. Cretu, S.-M.: Innovative design in tensegrity field. *Procedia Eng.* **9**, 261–269 (2011)
4. Defosseuz, M.: Shape memory effect in tensegrity structures. *Mech. Res. Commun.* **30**(4), 311–316 (2003)
5. Santer, M., et al.: Compliant multistable structural elements. *Int. J. Solids Struct.* **45**, 6190–6204 (2008)
6. Schorr, P., et al.: Multi-mode motion system based on a multistable tensegrity structure. In: *IFTToMM World Congress on Mechanism and Machine Science*. Springer, Cham (2019)
7. Sumi, S., et al.: Compliant class I tensegrity structures for gripper applications. In: Corves, B., Hüsing, M., Wenger, P. (eds.) *EuCoMeS 2018*, pp. 392–399. Springer (2019)
8. Sumi, S., et al.: A multistable tensegrity structure with a gripper application. *Mech. Mach. Th.* **114**, 204–217 (2017)
9. Wenger, P., et al.: Kinetostatic analysis and solution classification of a class of planar tensegrity mechanisms. *Robotica* **37**(7), 1214–1224 (2019)
10. Xu, X., et al.: Multistable tensegrity structures. *J. Struct. Eng.* **137**(1), 117–123 (2011)
11. Zappetti, D., et al.: Phase changing materials-based variable-stiffness tensegrity structures. *Soft Robot.* (2019). <https://doi.org/10.1089/soro.2019.0091>



Experimental Analysis of an MBS System with Two Degrees of Freedom Used in an Eolian Water Pump

Eliza Chircan^(✉), Maria Luminita Scutaru, Ioan Calin Roșca, Sorin Vlase, and Marius Păun

Transilvania University, Brașov, Romania

{chircan.eliza, lscutaru, icrosca, svlase, m.paun}@unitbv.ro

Abstract. The paper analyzes the experimental analysis of a multibody system (MBS) having 2 DOF. The mechanism belongs to a water turbine pump, commonly used in small farms. The accelerations of different points of the mechanism are optically measured so that they can be used within the dynamic model with finite elements and, finally, the eigenpulsations of the system are determined. The obtained results are tested using an experimental bench.

Keywords: Eolian pump · Water pump · Wind · FEM · Eigenfrequency · MBS

1 Introduction

Regarding the exploitation of the wind energy potential, at present we can say that the technology has reached near maturity, the modern era of the exploitation and production of wind energy starting in the late 70s of the 20th century, in Denmark. There are many countries, especially in Europe, where wind turbines are widely used and this is favored by the specific geographical conditions. At present, there are thousands of functional wind turbines in the world, with a total installed capacity of 94,123 MW of which 60.70% are located in Europe. Although the modern era of wind energy exploitation has been opened by Denmark, at present the first place is occupied by Germany with an installed power of 22,247 MW, which represents 23.6% of the total electricity production resulting from the conversion of wind power. The following places are occupied by the US, Spain, India and China [8].

In the following, a mechanism of a wind power transmission to a water pump is presented. The paper proposes a study of this system, which can have a wide applicability in the field (Fig. 1).

The originality of this mechanism consists in the use of the inertia of a pendulum, in the continuous variation of the transmission ratio, as the input rotation (the force of wind) increases. This mechanism have 2 DOF, which could be chosen the angle of rotation at the input (lever AB), noted φ_1 , respectively the stroke of the pump, noted x_D .

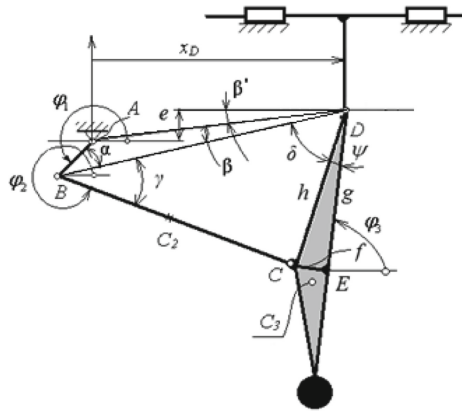


Fig. 1. The sketch of the mechanism closed by inertia [8]

Motion equations for this mechanism can be written in symbolic form:

$$[m]\{a\} = \{Q\} \tag{1}$$

The vector acceleration contains the angular acceleration of the crank and the acceleration of the piston. A large presentation of the procedures, free body diagrams and motion equations are presented in [8, 9]. If the acceleration vector is introduced into this equation, the following is obtained:

$$[m]([\{C_1\} \{C_2\}] \begin{Bmatrix} \varepsilon_1 \\ \ddot{x}_D \end{Bmatrix} + [\{C_3\} \{C_4\} \{C_5\}] \begin{Bmatrix} \omega_1^2 \\ \omega_1 \dot{x}_D \\ \dot{x}_D^2 \end{Bmatrix}) = \{Q\} \tag{2}$$

where $[m]$ is the inertias matrix of the two dimensional mechanism, ε_1 and ω_1 the angular acceleration respectively the angular speed of the crank, \ddot{x}_D and \dot{x}_D the acceleration respectively the velocity of the piston and $\{Q\}$ the vector of the generalized external and liaison forces.

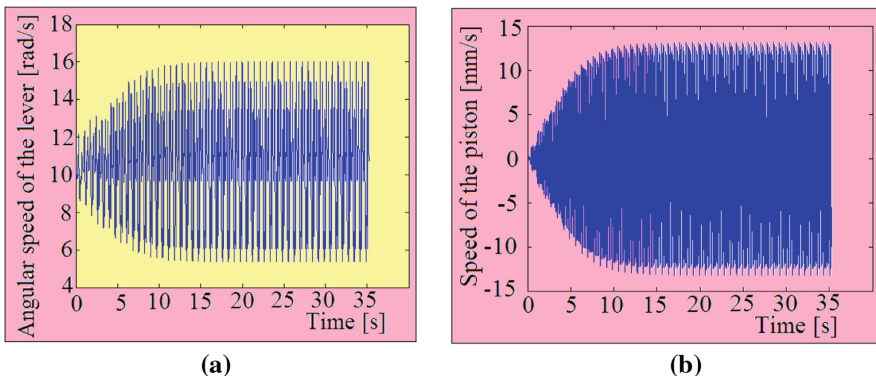


Fig. 2. a) Piston speed and b) Angular speed of the crank for an integration time of 30 s

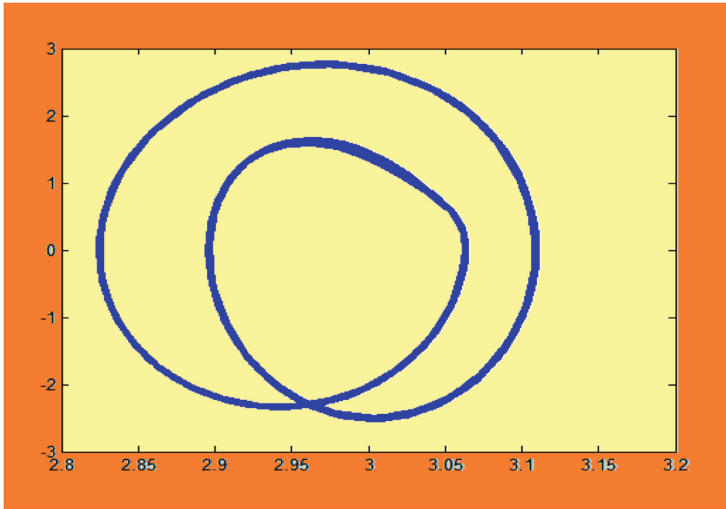


Fig. 3. Representation of the piston motion in the phase space

From the graphical representations above we can observe the existence of a stable integration process for long time intervals.

To eliminate the unknown reaction (liaison) forces, we multiply with the matrix $[\{C_1\} \{C_2\}]^T$ and we get [13]:

$$\begin{bmatrix} \{C_1\}^T \\ \{C_2\}^T \end{bmatrix} [m] (\{C_1\} \{C_2\}) \begin{Bmatrix} \varepsilon_1 \\ \ddot{x}_D \end{Bmatrix} + [\{C_3\} \{C_4\} \{C_5\}] \begin{Bmatrix} \omega_1^2 \\ \omega_1 \dot{x}_D \\ \dot{x}_D^2 \end{Bmatrix} = \begin{bmatrix} \{C_1\}^T \\ \{C_2\}^T \end{bmatrix} \{Q\} \quad (3)$$

By integrating the system of differential equations, theoretically, the solutions represented by the rotation angle and the displacement of the piston are obtained. In Fig. 2 are presented the velocity of the piston and the angular speed after integration and in Fig. 3 the motion of the piston in the phase space.

2 Finite Element Analysis of the Elastic Lever

In the literature there are presented several types of one-dimensional finite elements used in the MEF analysis of a beam system. In all cases it is considered that the deformation of an arbitrary point of the bar depends on the known deformations and their derivatives in the nodal points, which are usually chosen at the ends of the element. The interpolation functions chosen will determine the number of independent coordinates that will be needed to describe the deformation of the beam. This results in an inertial loading due to the mass of the bar element, the appearance of the Coriolis force and the change in stiffness due to the relative motion that changes the geometry of the element in a field of accelerations. It is assumed that the general rigid movement of the mechanism is known,

so the speeds and accelerations for all points of the continuous material are known. It is also assumed that the deformations of the various points on the bar are small enough and will not affect the rigid movement of the mechanism [1, 2]. This element is referred to a mobile $Oxyz$ coordinate frame that will move with the mechanical system. It is assumed that we know both the instantaneous position of the local reference mobile system, relative to a fixed global system $Ox_I y_I z_I$, as well as its movement referred to the global reference frame (velocity and acceleration of origin and angular velocity and angular acceleration) [3, 4, 7]. Depending on the coordinate vectors chosen $\{\delta_1\}$ and $\{\delta_2\}$, the displacement of a certain point M on the beam, noted $\{\delta\}$, can be written as follows:

$$\{\delta\} = \begin{Bmatrix} u \\ v \\ w \end{Bmatrix} = [N] \{\delta_e\} = [N] \begin{Bmatrix} \delta_1 \\ \delta_2 \end{Bmatrix} \quad \{\delta_e\} = \begin{Bmatrix} \delta_1 \\ \delta_2 \end{Bmatrix} \quad (8)$$

where the nodal displacements $\{\delta_1\}$ and $\{\delta_2\}$ compose the vector $\{\delta_e\}$ of independent coordinates corresponding to the finite element e and the matrix $[N]$ contains the interpolation functions. We have the equations of motion for a finite element written in simpler form, in the local reference system [12]:

$$\begin{aligned} & [m_e] \{\ddot{\delta}_e\} + 2[c_e(\omega)] \{\dot{\delta}_e\} + \left([k_{ei}] + [k_e(\varepsilon)] + [k_e(\omega^2)] \right) \delta_e = \\ & = \{q_e\} + \{q_e^*\} - \{q_e^i(\varepsilon)\} - \{q_e^i(\omega^2)\} - [m_{Ee}^i][I] \{\varepsilon_L\} - [m_{oe}^i][R]^T \{\ddot{r}_{oG}\} \end{aligned} \quad (11)$$

3 Tests and Results

In Fig. 5 is presented the test bench. Here a mechanism used for the transmission of the wind power to the water pump it is built in order to verify the methodology for the design and calculus of such system.

On this system two types of measurements will be made: the accelerations of the different points of the analyzed beam will be determined, they will be introduced into the equations of motion and the eigenfrequencies of the system will be calculated in this design solution, after which the eigenfrequencies of the beam will be determined experimentally and compared with the calculated eigenvalues. In this way the model used for the dynamic analysis of the system will be verified (Fig. 4).

The first measurements will be made to determine the accelerations of the different points of the beam. This will be done by optical methods, using a high speed camera. At present, the method based on motion analysis using a motion capture system is a very efficient and high perspective. Such a system of motion capture, consists of two major components:

- hardware component, represented by the video equipment and the elements necessary for mounting the system, particularly useful for the proper functioning;

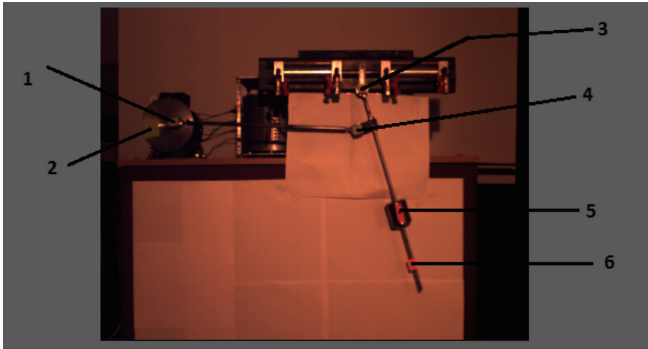


Fig. 4. Testing bench

- software component, represented by the applications with which the information existing in the video recorded by the camera is processed and brought in a form that allows the digitization of the data.

The camera will be mounted on a fixed support and perpendicular to the direction of movement of the pump, at a height to ensure that the entire mechanism is captured in the video material. Important to mention is that, with the decrease of the distance to the position of the camera, the efficiency of the system increases, being necessary to find the perfect balance between the duration of the operation of the mechanism, which will be sufficient, and a distance to the filmed mechanism sufficiently small to avoid it is lost from information [8].

In the first stage the film is obtained, taken from the camera. It is then loaded into the motion analysis application that is being worked on and the operator or the one performing the motion analysis sets the marker area. Establishing this area and how the application manages to track it over time are essentially the essential elements for efficient motion capture and analysis. Usually, the software will track an area of pixels, set by the operator, an area that ideally contains the area of interest as well as “different” pixels around the area of interest. By “different” pixels refers to pixels of a different color from the pixels of the area of interest, marked. In fact, the application follows this pixel composition along the movement but usually the coordinates of a single pixel in the middle of this area, belonging to the area of interest. These coordinates will then be obtained as the coordinates of the marker or area of interest.

Considering these considerations the Adobe After Effects application was used for following reasons:

- the efficiency in terms of the treatment of the motion, the method of re-cognizing the markers and the precision with which a trajectory of the marker is recognized;
- precision of tracking the trajectory according to several criteria;

- the extent to which the results can be subsequently processed in order to obtain the dimensions of the motion parameters that are analyzed.

The AOS X-PRI high speed camcorder, with a small size, has the possibility to make with sufficiently good accuracy, a sufficiently large number of recordings - frames/second - to capture the movement of the mechanism. Also the AOS X-PRI camcorder is equipped with a “trigger mechanism” type accessory, which can replace the command from the recording startup software.

The camera records images at a very high speed allowing the possibility to play them at a low speed through software (AOS Imaging Studio LIGHT). These selections can be made only when the camera is connected to the laptop and turned on, the recordings being started in the moment when all the LEDs on the camera control panel are green. On the other hand, the control panel of the Imaging Studio Light application is also found in the AOS camera.

In such way are determined the acceleration of the studied beam, acceleration that will be introduce further in the finite element analysis [5, 6]. It is possible to obtains theoretical these values but the results are not very good, the parameters describing the system being too numerous and too difficult to have good values for these. An experimental determination of the acceleration improves the finite element model.

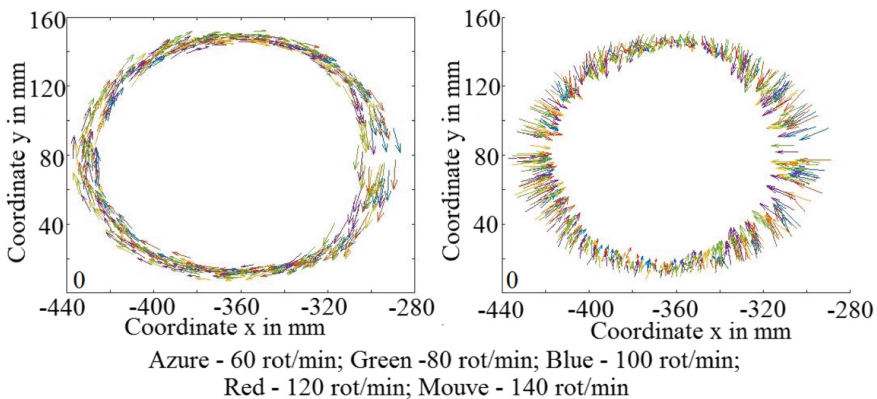


Fig. 5. The field of the a) velocities; b) the accelerations for the left end of the beam.

The field of accelerations and velocities, optically determined are presented in Fig. 5 and 6. These values were used to determine, by calculus, the eigenpulsations of the beam in the assembly of mechanism [10, 11, 14, 15]. The results are presented for two different speed of the crank in Fig. 7. Experimental measurements were made in order to determine the frequency spectrum of the beam.

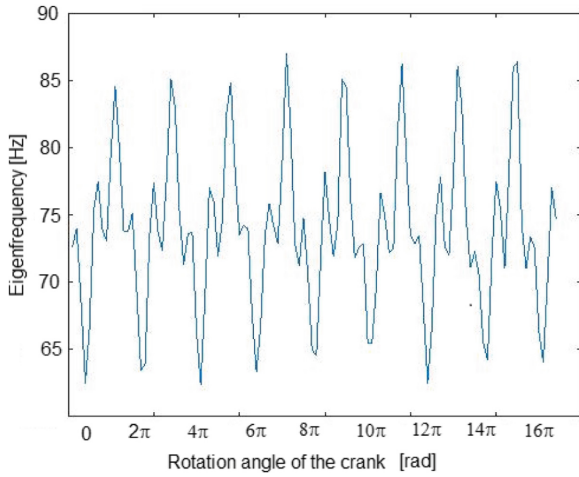


Fig. 6. Variation of the first eigenvalue during the rotation of the lever

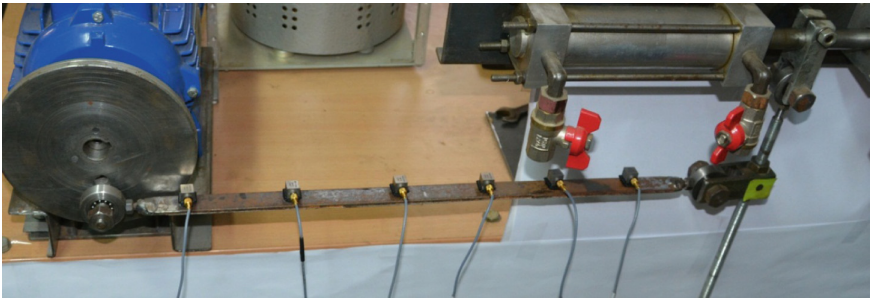


Fig. 7. Position of the five accelerometers

Frequency spectrum determinations were made using the five bar-mounted accelerometer. In the paper, one of these spectra is presented to be compared with the calculation results. It is found that the eigenfrequencies obtained by calculation fall within the range of values obtained experimentally (Fig. 8).

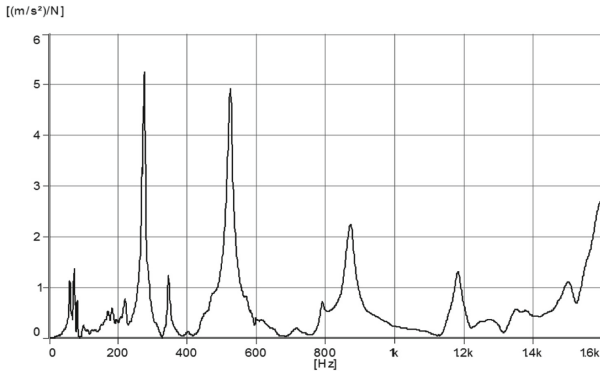


Fig. 8. Frequency spectrum

4 Conclusions

The last few decades are characterized by the use, in industry, of machines and tools, which operate at very high speeds and are subjected to very high forces, sometimes with shock. For all these systems, models have been developed, which take into account their deformability to avoid critical situations (loss of stability). Within the work, a model with finite elements of a wind mechanism for operating a water pump is developed. The mechanism has elastic elements in its composition. The model is improved by experimentally measuring the accelerations of the rigid movement of the mechanism, which are then introduced into the differential equations of the model used. The eigenfrequencies of the system are measured and the results obtained experimentally are to a satisfactory extent consistent with the results obtained in the case of theoretical calculation.

References

1. Cleghorn, W.L., Fenton, E.G., Tabarrok, K.B.: Finite element analysis of high-speed flexible mechanisms. *Mech. Mach. Theory* **16**, 407 (1981)
2. Erdman, A.G., Sandor, G.N., Oakberg, A.: A general method for kineto-elastodynamic analysis and synthesis of mechanism. *J. Eng. Ind. ASME Trans.* **94**(4), 1193 (1972)
3. Marin, M., Agarwal, R.P., Mahmoud, S.R.: Nonsimple material problems addressed by Lagrange's identity. *Boundary Value Problems* **2013**, 1–14 (2013)
4. Nath, P.K., Ghosh, A.: Steady-state response mechanism with elastic links by finite element methods. *Mech. Mach. Theory* **15**, 199 (1980)
5. Negrean, I., Crişan, A.-D.: Synthesis on the acceleration energies in the advanced mechanics of the multibody systems. *Symmetry* **11**(9), 1077 (2019)
6. Negrean, I., Crişan, A.-D., Vlase, S.: A new approach in analytical dynamics of mechanical systems. *Symmetry* **12**(1), 95 (2020)
7. Niculita, C., et al.: Optimal stacking in a multiply laminate used for the skin of adaptive wings. *Optoelectron. Adv. Mater. Rapid Commun.* **5**(11), 1233–1236 (2011)
8. Scutaru, M.L.: Habilitation Thesis, Transylvania of Braşov University (2014)
9. Scutaru, M.L., Mitrica, B.: Dynamical analysis of the mechanical system with two degrees of freedom applied to the transmission of the wind turbine. *Math. Prob. Eng.* **2016**, 9 (2016)

10. Teodorescu-Draghicescu, H., et al.: Finite element method analysis of some fiber-reinforced composite laminates. *Optoelectron. Adv. Mater. Rapid Commun.* **5**(7), 782–785 (2011)
11. Vlase, S., Danasel, C., Scutaru, M.L., et al.: Finite element analysis of a two-dimensional linear elastic systems with a plane “rigid motion”. *Rom. J. Phys.* **59**(5–6), 476–487 (2014)
12. Vlase, S.: Dynamical response of a multibody system with flexible elements with a general three-dimensional motion. *Rom. J. Phys.* **57**(3–4), 676–693 (2012)
13. Vlase, S.: Elimination of Lagrangian-Multipliers. *Mech. Res. Commun.* **14**(1), 17–22 (1987)
14. Vlase, S., Marin, M., Oechsner, A., et al.: Motion equation for a flexible one-dimensional element used in the dynamic analysis of a multibody system. *Continuum Mech. Thermodyn.* **31**(3), 715–724 (2019)
15. Zhang, X., Lu, J., Shen, Y.: Simultaneous optimal structure and control design of flexible linkage mechanism for noise attenuation. *J. Sound Vibr.* **299**(4–5), 1124–1133 (2007)



Design and Characterization of a 3D Printed Soft Pneumatic Actuator

Ditzia Susana Garcia Morales^(✉), Serhat Ibrahim, Benjamin-Hieu Cao,
and Annika Raatz

Institute of Assembly Technology, Leibniz University Hannover, Garbsen, Germany
{garcia,ibrahim,raatz}@match.uni-hannover.de, beni.hc@gmx.de

Abstract. In soft robotics, the successful development of soft robots involves careful designing that can benefit from current technologies. The use of Finite Element Method (FEM) software and additive manufacturing is essential to optimize the design before fabrication and to facilitate the process. Therefore, we present the design of a 3D printed low-pressure soft pneumatic actuator (SPA) with 3 DoF and a material characterization method to simulate the behaviour of the system. In attempt to define a suitable material modelling method and its reliability to simulate actuator behaviours, we introduce a characterization method and corroborate its efficiency through the evaluation of the performance using the FEM and preliminary tests of the actuator performance. The purpose of this article is to help future projects to effectively simulate the behaviour of 3D printed soft pneumatic actuators to improve the design before fabrication. Throughout the description of the process to effectively fabricate a functional SPA.

Keywords: Soft robotics · Soft actuators · Modelling · Material characterization

1 Introduction

Soft robotics is becoming increasingly important due to the paradigm shift from hard to soft materials which aims to improve the human-robot collaboration [1]. By changing the stiffness of the materials used to fabricate robots, more compliant bodies can be achieved. Recent research in the area shows promising results in locomotion, replicating biological organisms that exhibit soft and flexible structures with considerable force [2]. To design systems that can emulate organic mechanisms, the use of uncommon materials and the exploration of new technologies takes a substantial relevance in the research. Currently, soft actuators are mostly fabricated using two methods, casting process and additive manufacturing [3]. On the one hand, casting an actuator requires the use of moulds and multiple fabrication steps to achieve shapes basic geometries like cylinders [4,5]. Nevertheless, because of the use of moulds, this process has geometrical limitations (e.g. small cavities inside the actuators). Even so, casting permits

the use of a wide range of highly stretchable materials [6]. On the other hand, additive manufacturing offers a rapid single instance process achieving similar and even more complex and precise designs [3, 7]. Nonetheless, in contrast with the casting process additive manufacturing offers reduced material options [8]. Consequently, to explore the use of additive manufacturing optimized designs are required. Smart designs can be achieved through proper optimization. For this, the simulation of the system before fabrication is essential for the user to optimize the design to obtain the required performance. Thus, the correct simulation process has to be achieved through a proper material model suitable for a FEM simulation. For this, we describe the design of a soft pneumatic actuator (SPA) using a 3D printable material. We explain the process for the mathematical model of the material so that a FEM simulation can be set up for the pre-examination of the actuator. The model is validated and evaluated based on data experiments using a commercial angular sensor.

2 Design and Fabrication

The actuator described in this article has a general cylinder-like shape (Fig. 1). We used three linear channels separated 120° from each other. Each channel can displace in one direction. They are joined by internal support to provide stiffness to the SPA. Inside this support each channel is connected to a pipe to allow the air injection. For the design of the channels, we chose the concept of PneuNet which originally is formed by an array of chambers connected in series [5]. By using this concept, we guided the deformation areas of the chambers to optimize the pressure (Fig. 1(b)). We modified the geometry of the chambers to adopt a cylindrical shape (Fig. 1(a)). For the dimensions of this actuator, we followed a previous actuator developed by the Institute of Assembly Technologies [4]. The parameters specification of the channels were selected following the results from [9]. We set the chambers wall thickness, the separation between chambers, the internal geometry of the chambers as shown in Fig. 1(a). In this way, a relation of 1:2 between the deformed surface and undeformed surface is used and the chambers deformation focuses on the regions with a smaller wall thickness (Fig. 1(b)).

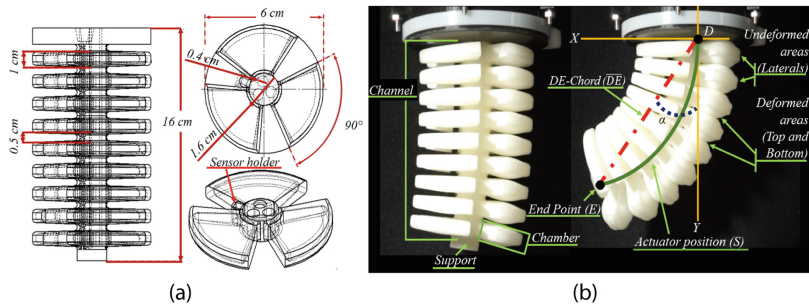


Fig. 1. 3D printed soft pneumatic actuator. (a) Sketch showing different views of the actuator and its dimensions. (b) SPA view of the actuator without (left) and with pressure (right).

It is important to mention that by changing the amount of chambers and the separation between chambers and channels length we can increase or decrease the angle of deflection [9]. The SPA uses pressure as the actuation method, in this way, the motion starts when the chambers are pressurized with air. During this time the chambers increase the volume and come into contact with each other. This event forces the actuator to bend in the opposite direction (Fig. 1(b)). By pressurizing single or multiple channels, the actuator can displace on different planes (XY and YZ). For the fabrication of the actuator, we use the 3D printer Keyence Agilista and the lowest stiffness silicone AR-G1L available for this printer.

3 Modelling

In soft robotics, the development of reliable models to predict their behaviour increases the potential of successful performance. Although, it is difficult to describe an analytical model of the system due to the non-linearities of the materials and the highly non-linear bending to pressure ratio created by the geometry of the chamber design. An accurate simulation of the behaviour leads to prior optimizations or adjustments of the design before fabrication, saving time and resources [10]. For this reason, we use FEM models (Abaqus CAE) to predict the performance of the system. We find the properties of the material describing a non-linear mechanical behaviour. Additionally, we included a linear elastic approach to help us to observe the differences of the actuator performance to support the use of a non-linear approach for this material.

3.1 Material Characterization

Initially, we performed a series of uniaxial tensile tests following the norm DIN ISO 527 to define the stress-strain relationship. For these tests, we printed specimen and performed 30 tests. The stress-strain relationship of the silicone AR-G1L is showed in Fig. 2. Here, the mean of the data can be observed together with the maximum and minimum values pointed out by the horizontal lines. The standard deviation of the stress is 0.1553 N/mm^2 , which is the deviation presented between the different tests. Next, following [13], where the current models for hyperelastic behaviours are mentioned, we chose Mooney Rivlin among other approaches (Ogden, Arruda-Boyce, etc.) as a feasible approach applicable to large strains (>60%) analysis. In order to fulfill a FEM model using this approach, we used the energy equation to describe how the deformation affects the energy state of the deformed body. In the FEM analysis software Abaqus the strain-energy ψ equation to appears as

$$\psi = C_1(I_1 - 3) + C_2(I_2 - 3) + \frac{1}{d_1}(J - 1)^2. \quad (1)$$

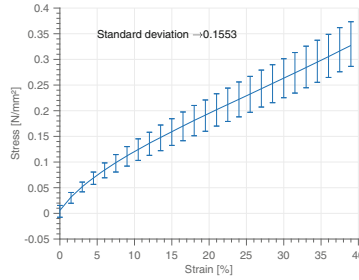


Fig. 2. Stress-strain relationship of the silicone AR-G1L, including the standard deviation of the tensile tests.

In this equation, the material constants for the general deformation are represented by C_1 and C_2 while the constant for volume change of the material is denoted by d_1 . These parameters define the behaviour of the material. Additionally, the equation includes the volume-dependent parameter J and the strains in their respective deformation states which are represented by the invariants I_1 and I_2 . The parameters I_1 and I_2 are calculated with the right Cauchy-Green tensor $\mathbf{C} \in \mathbb{R}^{3 \times 3}$ described in [14]. The right Cauchy-Green tensor results from the product of the deformation gradient tensor $\mathbf{F} \in \mathbb{R}^{3 \times 3}$ and its transposed. The deformation gradient \mathbf{F} represents the deformation of a material's point derived from the differential of the spatial directions of the possible displacements. The length variation $\Delta \mathbf{x}$ is the product of the strain ε and x which represents the uni-axial load element of the data for which the stress-strain relation is available with $\mathbf{x} \in \mathbb{R}^{3 \times 1}$ as the initial coordinate and $\tilde{\mathbf{x}} \in \mathbb{R}^{3 \times 1}$ as the deformed state of the material point. This function is formulated to analytically model the deformation of the tensile test based on an uniaxially loaded deformation rod. Δx results from the difference of \tilde{x} and x . From this we obtain

$$\frac{\tilde{x}}{x} = (1 + \varepsilon). \quad (2)$$

With Eq. (2) we assume that $\lambda = (1 + \varepsilon)$. The invariants I_1 , I_2 and the volume-dependent J are associated with the strain in deformation gradient \mathbf{F} , where in this case, only the first element of the tensor $\mathbf{F}_{11} = \lambda$ is defined by the uni-axial strain state. Assuming that the material is incompressible, the determinant of \mathbf{F} is equal to 1. The determinant of \mathbf{F} results from the multiplication of the diagonal entries, so the two remaining diagonal entries are equal to $\frac{1}{\sqrt{\lambda}}$. This results in the following matrix for the deformation gradient

$$\mathbf{F} = \begin{pmatrix} \lambda & 0 & 0 \\ 0 & \frac{1}{\sqrt{\lambda}} & 0 \\ 0 & 0 & \frac{1}{\sqrt{\lambda}} \end{pmatrix}. \quad (3)$$

Assuming an incompressible material, the parameter approaches the number 0. This leads to a very large number in Eq. (1), but this is compensated by

the parameter J . Since J is the determinant of the deformation gradient due to the incompressibility of the material. With $J=1$ the last part of the Eq. (1) becomes to 0. The missing parameters C_1 and C_2 in Eq. (1) are determined by an identification procedure. In this case, the model and experimental values of the true stress tensor $\sigma \in \mathbb{R}^{3 \times 3}$ are used. To obtain the true stress and the deformation from the Mooney-Rivlin model, we derived the strain-energy with respect to \mathbf{C} to define the second Piola-Kirchhoff stress, where $\tilde{\mathbf{T}}$ is a quantity that describes the stress in a body in an undeformed state [14]. Even though $\tilde{\mathbf{T}}$ does not exist physically, we can use it to calculate the true stress with

$$\tilde{\sigma} = \frac{1}{J} \mathbf{F} \tilde{\mathbf{T}} \mathbf{F}^T. \quad (4)$$

With the stress tensor $\tilde{\sigma}$ calculated from the analytical model, the first element $\tilde{\sigma}_{11}$ was used to calculate the two material parameters C_1 and C_2 using the least square method. This method is implemented in Matlab using the Matlab Optimization Toolbox with the Interior Point method [15] to fit the experimental data series to yield the material parameters. In the step of the calculation of $\tilde{\sigma}$, we use the program Mathematica modified with the package AceGen to generate a Matlab function that derives the stress output for a strain input according to the previously described approach. As a result of this process we obtained $C_1 = 0.1100$, $C_2 = 0.010$ and setted d_1 as 0. After this, we can use the material parameters in Abaqus to describe the behaviour of the material under deformation.

For the linear approach, we used the results from the tensile test (Fig. 2) and linearized the results to find an elastic modulus following the literature [11]. As a result, we find an elastic modulus of 3.1 MPa. Additionally, for a linear approach, a Poisson's Ratio is required. Because we assume our material to be incompressible we find in the same literature the value of 0.5 for incompressible rubber [12].

3.2 Setup Simulation

Concerning the configuration of the simulation parameters, we discretized the actuator model in a tetrahedron hybrid element mesh with ten nodes. As a boundary condition, the top end of the SPA is fixed. The load is applied in all inner surfaces of the chambers and tunnels, and is increased up over twelve timesteps from 0 kPa to 12 kPa with an additional gravity step. Additionally, to simulate the forces which appear after the outer chamber surfaces contact, the entire outer surface of the model has an interaction property of tangential behaviour assigned. As a result, we obtained a matrix with the coordinates that describe the displacements of the actuator, which are compared to the movements of the real SPA.

4 Preliminary Test

After the simulation, we experimentally corroborated the results of the FEM analysis. For this, we performed displacement tests applying pressure on one

chamber at the time. The actuator was displaced to different angular positions, shifting the values between 0° and 40° . During the experiments, we tracked the position using a two-axis bendable sensor. The sensor was positioned on the surface of the support opposite of the activated-channel between two channels (Fig. 1(a)). The test stand for testing the actuators was set up in preliminary work [16]. The acquired data was used to calculate the actuator position (S), which is defined as the central line of the internal support (green curve in Fig. 1(b)). In this way, the sensor angle (α) was used assuming a constant curvature of the actuator [17] to calculate the chord length of the actuator curvature ($\overline{DE} = \frac{S \sin(\alpha)}{\alpha}$), where S is equal to 13.5 cm. With this, we calculate the position of the point E for any angular value. It is also important to mention that we used only the information which describes a positive displacement meaning that we used the data when the actuator inflates and not when the actuator deflates, due to the inconsistency of the measurements. This is because the recovery time of the material will affect the sensor measurement. With the relevant data, we obtained the angle-pressure relationship of the SPA.

5 Performance Evaluation

From the simulation and the experiments, we obtained the position of the actuator in x and y coordinates at 12 kPa since this is the pressure value when the actuator achieves its maximum displacement. The results are presented in Fig. 3(a), here the position of the actuator using the angle sensor, a non-linear model and a linear approach are displayed. In the experiments, we measured an angle of 36.2° at 12 kPa with a constant curvature as the position of the actuator (green diamonds line). While in the simulation with the non-linear model of the actuator, we calculated an angle of 36.4° at 12 kPa with a different curvature (purple squares line) as in the experiments. Regarding the results of the simulation using a linear approach, we calculated an angle of 10° at

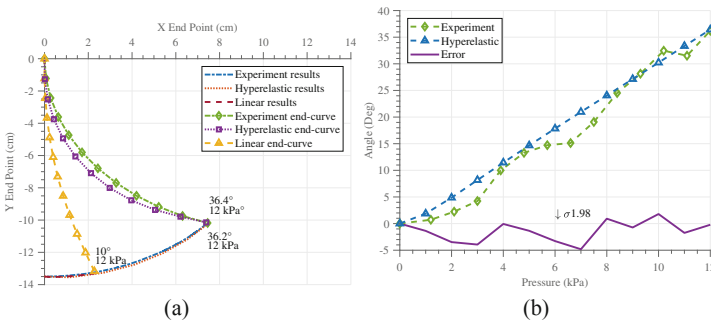


Fig. 3. Simulation and experiment results. (a) Actuator position S . (b) Angle-Pressure relations of the non-linear simulation and the experiment, and the standard deviation of the results.

12 kPa. Here the position of the actuator at this pressure (yellow triangular line) shows a major displacement from the half of the actuator (from - 6 cm in Y) till the end position of the actuator. From Fig. 3(a), we conclude that the linear approach poorly described the displacement of the actuator in contrast to the experiment results perceiving a difference around 26° . Indicating that the use of a linear approach in this material is not beneficial and does not give accurate information to be used as a reliable source for further simulations. In this way, we can continue with the following results, which are from the non-linear model of the actuator. For this, we decided to compare the relationship between angle and pressure. In Fig. 3(b), we can find the behaviour of the actuator in angular terms while pressure is applied. The simulation results (blue triangular line) showed a smooth displacement of the actuator from 0 to 36.4° , while in the experiments (green diamond line) we can observe abrupt increments at some pressure values. We notice that from the performance of the actuator, the position was affected by the design of the actuator. Because the motion of the actuator starts when the chambers are in contact (Sect. 2), shown in Fig. 1(b). This behaviour was not well appreciated in the simulation results. Thus, as a representative value of this in Fig. 3(b), we showed the error (purple line) between the experiment and the simulation to observe the difference in degrees and its standard deviation to evaluate how much is the difference of the simulation to the experiments.

6 Conclusions and Future Work

In this paper, we presented a 3D printed SPA with its corresponding material characterization and simulation. The SPA simulation was compared with the experiment demonstrating the feasibility of the proposed material characterization method. The presented design reduced the pressure used compared (12 kPa) to similar actuators like in [4] where the working pressure reached 30 kPa, [5] with 74 kPa approximately and [7] with an average working pressure of 60 kPa. This design does not present an increment in length or considerable axial expansion. The simulation approach is close enough to simulate the performance of SPA showing 0.2° at maximum working pressure (12 kPa), comparing the results with [5] where the simulation error was greater than 20° . The modelling process presented in this paper can be considered as a plausible approach for soft actuators. In future work, the simulation of the actuator will be extended so that possible fracture points can be predicted. The model developed in this paper will then be used to optimize the design of the 3D printed actuator. In this case, the parameters that are decisive for the deformation, such as chamber distance, number of chambers or wall thickness, will be adjusted using simulation and optimization algorithms to fabricate a more reliable soft actuator which can be used as a manipulator for handling applications.

Acknowledgements. This work was supported by the Deutsche Forschungsgemeinschaft (DFG, German Research Foundation) 405030609.

References

1. Polygerinos, P., Correll, N., Morin, S., Mosadegh, B., Onal, C., Petersen, K., Cianchetti, M., Tolley, M., Shepherd, R.: Soft robotics: review of fluid-driven intrinsically soft devices; manufacturing, sensing, control, and applications in human-robot interaction. *Adv. Eng. Mater.* **19**, 1438–1656 (2017)
2. Stephen, C., Carmel, M., Philip, L., Jimmy, H.: Bio-inspired soft robotics: material selection, actuation, and design. *Extreme Mech. Lett.* **22**, 51–59 (2018)
3. Schmitt, F., Piccin, O., Barbé, L., Bayle, B.: Soft robots manufacturing: a review. *Front. Robot. AI* **5**, 84 (2018)
4. Runge, G., Peters, J., Raatz, A.: Design optimization of soft pneumatic actuators using genetic algorithms. In: *IEEE International Conference on Robotics and Biomimetics*, Macau, pp. 393–400 (2017)
5. Mosadegh, B., Polygerinos, P., Keplinger, C., Wennstedt, S., Shepherd, R., Gupta, U., Shim, J., Bertoldi, K., Walsh, C., Whitesides, G.: Pneumatic networks for soft robotics that actuate rapidly. *Adv. Funct. Mater.* **24**, 2163–2170 (2014)
6. Huichan, Z., Yan, L., Ahmed, E., Robert, S.: Scalable manufacturing of high force wearable soft actuators. *Extreme Mech. Lett.* **3**, 89–104 (2015)
7. Kalisky, T., Wang, Y., Shih, B., Drotman, D., Jadhav, S., Aronoff-Spencer, E., Tolley, M.: Differential pressure control of 3D printed soft fluidic actuators. In: *IEEE/RSJ International Conference on Intelligent Robots and Systems*, Vancouver, pp. 6207–6213 (2017)
8. Zhu, M., Mori, Y., Xie, M., Wada, A., Kawamura, S.: A 3D printed two DoF soft robotic finger with variable stiffness. In: *12th France-Japan and 10th Europe-Asia Congress on Mechatronics*, pp. 387–391 (2018)
9. Hu, W., Mutlu, R., Li, W., Alici, G.: A structural optimisation method for a soft pneumatic actuator. *Robotics* **7**, 24 (2018)
10. Moseley, P., Florez, J.M., Sonar, H.A., Agarwal, G., Curtin, W., Paik, J.: Modeling, design, and development of soft pneumatic actuators with finite element method. *Adv. Eng. Mater.* **18** (2015)
11. Peel, L.: P97 investigation of high and negative Poisson's ratio laminates. In: *International SAMPE Symposium and Exhibition (Proceedings)*, vol. 50 (2005)
12. Mott, P.H., Roland, C.M.: Limits to Poisson's ratio in isotropic materials. *Naval Research Laboratory* (2009)
13. Kim, B., Lee, S.B., Lee, J., Cho, S., Park, H., Yeom, S., Han, P.S.: A comparison among Neo-Hookean model, Mooney-Rivlin model, and Ogden model for chloroprene rubber. *Int. J. Precis. Eng. Manuf.* **13**, 759–764 (2012)
14. Bonet, J., Wood, R.: *Nonlinear Continuum Mechanics for Finite Element Analysis*, pp. 99–160. Cambridge University Press, Cambridge (2008)
15. Ploskas, N., Samaras, N.: *Linear Programming Using MATLAB®*. Springer, Heidelberg (2017)
16. Ibrahim, S., Krause, J.C., Raatz, A.: Linear and nonlinear low level control of a soft pneumatic actuator. In: *RoboSoft 2019 IEEE-RAS International Conference* (2019)
17. Webster, R.J., Jones, B.A.: Design and kinematic modeling of constant curvature continuum robots: a review. *Int. J. Robot. Res.* **13**, 1661–1683 (2010)



Novel Planar Parallel Manipulator Using Geared Slider-Crank with Linear Actuation as Connection Kinematic Chain

Sanda Margareta Grigorescu^(✉), Antonio-Marius-Flavius Lupuți, Inocentiu Maniu, and Erwin-Christian Lovasz

Politehnica University of Timișoara, Timișoara, Romania
{sanda.grigorescu, inocentiu.maniu, erwin.lovasz}@upt.ro,
antonio.lupuți@student.upt.ro

Abstract. The paper deals with a second version of kinematic chain of the geared linkages with linear actuator using a slider crank base mechanism. This structure is recommended because geared linkage with linear actuation allows a large rotation angle with approximately linear transmission function in a large range and proper transmission angle. These characteristics and the direct actuation of the closest element to the mobile platform ensure the avoiding of the first order singularities.

Keywords: Parallel planar manipulator · Geared linkage with linear actuator · Kinematics · Singularity

1 Introduction

In recent times parallel manipulators have become an increasingly important branch due to the large scope requiring high accuracy, high ratio between the load of the platform and the weight of the manipulator, stiffness of the system and high speed. Due to these advantages, many researches are made on developing of new structures, kinematic [1–4] and dynamic analysis, singularity avoiding, optimizing the workspace [5] and synthesis of the planar parallel manipulators, opening new areas of applicability in medicine [6–10] industry [11], space [12] and other areas that require precision in positioning [13].

Today's parallel manipulators are enriched with novel cinematic structures according to their tasks. Structure and analysis are carried out in order to increase accuracy, optimize the workspace [1, 14] increase working space and speed [2, 5]. Merlet in [15] presents extensive and detailed summing up structures and architectures, singularities, calibration, direct and inverse kinematic. New generalizations and classifications [17] appear due to the large number of architectures, which inspires new research directions using different methods for different structures. In order to design a parallel robot, first of all the issue of singularity must be considered.

The geared inverted slider crank with linear actuation was exhaustive kinematic analyzed in [16] and [18] as connection chain for a planar parallel manipulator. The aim

of present and future works is to develop such a planar parallel manipulator and to use it in precision applications. The study is carried out on the positional inverse kinematic of the novel kinematic chain, focusing on the problem of singularities.

2 Geared Linkages with Linear Actuation

The geared linkages with linear actuation taken into account are focused only on mechanisms with parallel connected chains, which have a linear actuation and contain a gear pair. In [19, 20] is shown the type synthesis of the geared linkages, mentioned above, where two useful planetary geared linkage structures results: with inverted slider crank (As1) and slider crank as base linkages (As2) (Fig. 1).

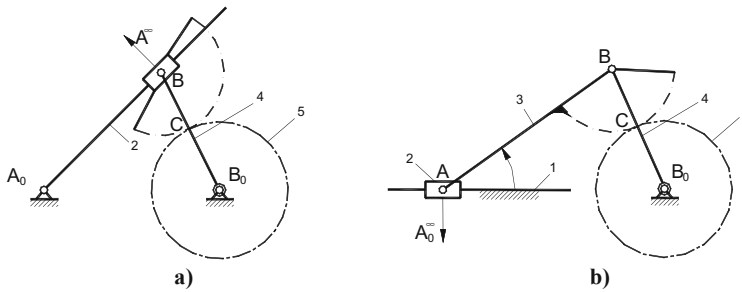


Fig. 1. Planetary geared linkage with linear actuation: (a) geared inverted slider crank with linear actuation, (b) geared slider crank with linear actuation

The present work focuses on the geared slider crank with linear actuation, so in the following will be developed the transmission function of the mechanism.

The geared slider crank with linear actuation (As3) contains a slider-crank as base linkage and a planetary gear pair, where the satellite gear is fixed with the coupler (Fig. 2). The general relationship for computing the transmission function of the geared linkages, according with [21], is obtained in the following form:

$$\chi(s) = (1 - \rho) \cdot \psi(s) + \rho \cdot \varphi(s), \tag{1}$$

where:

$\chi(s)$ - output angle,

$\rho = \pm r_3 / r_5$ - gears ratio,

$\varphi(s), \psi(s)$ - angles of the base linkage.

The angles $\varphi(s)$ and $\psi(s)$ of the base slider crank are computed considering the vector closed loop equation, in complex number, in the form:

$$(s_0 - s) + l_3 \cdot e^{i \cdot \varphi(s)} = l_4 \cdot e^{i \cdot \psi(s)}, \tag{2}$$

By multiplication the vector closed loop equation with his complex conjugate equation yield the relationship for computing the angle $\varphi(s)$:

$$\varphi(s) = \arccos\{[l_4^2 - l_3^2 - (s_0 - s)^2] / [2 \cdot l_3(s_0 - s)]\}, \tag{3}$$

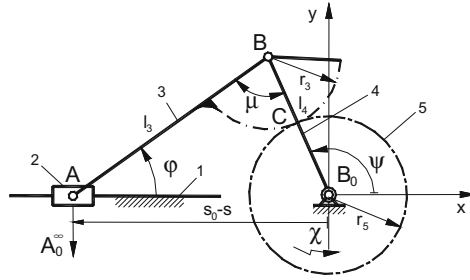


Fig. 2. Geared slider crank with linear actuation

Also, through isolation of the term which contains the angle $\varphi(s)$ in a side of the Eq. (2) and multiplication with his complex conjugate equation, yields the relationship for computing the angle $\psi(s)$:

$$\psi(s) = \arccos\{[l_4^2 - l_3^2 + (s_0 - s)^2]/[2 \cdot l_4(s_0 - s)]\}. \tag{4}$$

An important parameter of the base linkage is the transmission angle $\mu(s)$, in order to have a proper motion transmission that should be $\mu_{\min} \geq 30^\circ$ or $\mu_{\max} \leq 150^\circ$. The current transmission angle $\mu(s)$ is computed by the relationship:

$$\mu(s) = \psi(s) - \varphi(s). \tag{5}$$

By imposing the maximum and minimum transmission angles follows the initial stroke s_0 and the maximum stroke of the actuator (slider 2) s_{\max} :

$$s_0 = \sqrt{l_3^2 + l_4^2 - 2 \cdot l_3 l_4 \cdot \cos \mu_{\max}}, \tag{6}$$

$$s_{\max} = s_0 - \sqrt{l_3^2 + l_4^2 - 2 \cdot l_3 l_4 \cdot \cos \mu_{\min}}. \tag{7}$$

The first order transmission function of the geared linkage follows as:

$$\chi'(s) = (1 - \rho) \cdot \psi'(s) + \rho \cdot \varphi'(s), \tag{8}$$

where:

$$\varphi(s) = \frac{-(s_0 - s) - l_3 \cdot \cos \varphi(s)}{2 \cdot l_3 \cdot (s_0 - s) \sin \varphi(s)}, \quad \psi'(s) = \frac{(s_0 - s) + l_4 \cdot \cos \psi(s)}{2 \cdot l_4 \cdot (s_0 - s) \sin \psi(s)}. \tag{9}$$

3 Novel Planar Parallel Manipulator

The novel planar parallel manipulator should use geared slider crank links as connection chains, where the actuation is a linear one. Figure 3 shows the kinematic schema of the novel proposed planar parallel manipulator.

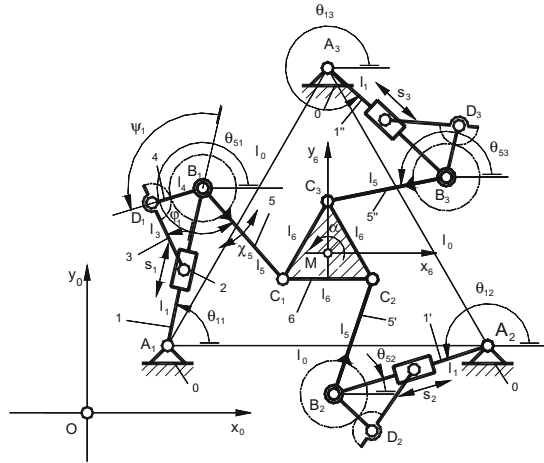


Fig. 3. Kinematic schema of the planar parallel manipulator 3-R(PRRGR)RR, using geared slider crank with linear actuation

The mentioned advantages of the geared inverted slider crank with linear actuation in [16], as well in [18] and [19] are maintained also for the geared slider crank with linear actuation. Some of them would be worth mentioning: large rotation angle of the output gear (5) with proper transmission angle and approximately linear transmission function $\chi(s)$, compact design of the novel chain and self-locking condition ensured by converting the movement with screw-nut. Also it is expected that this novel structure avoids also the first order singularities in a wider range.

The notation of this novel structure of parallel planar manipulator should be 3-R(PRRGR)RR, where R – revolute joint, P – prismatic joint and G - gear pair. In brackets () is indicated the parallel connected actuating kinematic chain and underlined (ex. P) the active joint [17]. The proposed structure of the parallel planar manipulator use 3 linear actuators $n_{act} = 3$, which actuate direct the output gears - elements 5, 5' and 5'' of the connection kinematic chains. Each connection kinematic chain contains 5 elements $n = 5, 5$ kinematic pairs with $f = 1 e_1 = 5$ and 1 kinematic pair with $f = 2 e_2 = 1$. By computing the degree of freedom DOF (mobility) of the whole manipulator structure with the relationship:

$$DOF = 3 \cdot (n - 1) - 2 \cdot e_1 - e_2 = 3 \cdot (17 - 1) - 2 \cdot 21 - 3 = 3. \quad (10)$$

Because the identity between the DOF and the number of the used actuators n_{act} the planar parallel manipulator follows a constrained motion and allows 3 DOF for the mobile platform (3): 2 translations along the Ox and Oy axis and one rotation around the Oz axis.

4 Singularities of the Novel Parallel with Linear Actuation Manipulator

A parallel planar manipulator has two types of singular configuration: when the mobile platform (triangle 6 in Fig. 3) does not move for non-zero actuated joints (B_1, B_2 and B_3)

velocities, named first order singularity and when the mobile platform moves (obtains extra degrees of freedom) even if the actuated joint velocities are zero, which is known as second order singularity.

The study of singularities starts with the known relation [15, 22]:

$$J_x \cdot \dot{X} + J_s \cdot \dot{S} = 0 \tag{11}$$

where J_s is a Jacobian matrix, its elements depend on the actuated joints strokes (s_1, s_2, s_3); J_x is also a Jacobian matrix with elements which are partial derivatives with respect to the mobile platform three DOF (or pose parameters: x_M, y_M, α), $\dot{X} = [\dot{x}_M \dot{y}_M \dot{\alpha}]^T$, $\dot{s} = [\dot{s}_1 \dot{s}_2 \dot{s}_3]^T$.

The study of singular poses of the planar parallel manipulator involves the inverse kinematics analysis, i.e. for given values of x_M, y_M, α , are calculated the corresponding values for driven joints values s_1, s_2, s_3 .

In account to the notations in Fig. 4, the vectors relation is:

$$\overrightarrow{OA_i} + \overrightarrow{A_iC_i} = \overrightarrow{OM} + \overrightarrow{MC_i} \quad i = 1, 2, 3 \tag{12}$$

The terms in Eq. (12) are:

$$\overrightarrow{OA_i} = \begin{bmatrix} x_{A_i} \\ y_{A_i} \end{bmatrix}, \overrightarrow{OM} = \begin{bmatrix} x_M \\ y_M \end{bmatrix}, \overrightarrow{MC_i} = \begin{bmatrix} x_{C_i} \\ y_{C_i} \end{bmatrix} = \begin{bmatrix} \cos \alpha & -\sin \alpha \\ \sin \alpha & \cos \alpha \end{bmatrix} \begin{bmatrix} x_{C_i}^{(6)} \\ y_{C_i}^{(6)} \end{bmatrix}, \tag{12'}$$

$$x_{C_1}^{(6)} = -\frac{l_6}{2}, y_{C_1}^{(6)} = -l_6 \cdot \frac{\sqrt{3}}{6}, x_{C_2}^{(6)} = \frac{l_6}{2}, y_{C_2}^{(6)} = -l_6 \cdot \frac{\sqrt{3}}{6}, x_{C_3}^{(6)} = 0, y_{C_3}^{(6)} = l_6 \cdot \frac{\sqrt{3}}{3},$$

$$x_{A_2} = x_{A_1} + l_0, y_{A_2} = y_{A_1}, x_{A_3} = x_{A_1} + \frac{l_0}{2}, y_{A_3} = y_{A_1} + \frac{l_0 \cdot \sqrt{3}}{2}$$

$$\overrightarrow{A_iC_i} = \begin{bmatrix} l_1 \cos \theta_{1i} + l_5 \cos \theta_{5i}(\chi_i(s_i)) \\ l_1 \sin \theta_{1i} + l_5 \sin \theta_{5i}(\chi_i(s_i)) \end{bmatrix}, i = 1, 2, 3$$

$$\theta_{5i}(\chi_i(s_i)) = \chi_i(s_i) + \Delta \chi_i, \quad i = 1, 2, 3$$

The terms $\Delta \chi_1, \Delta \chi_2, \Delta \chi_3$ are constant values, depending on designing conditions of the base mechanism (PRRGR) and on constrain conditions for maximizing the χ_i angles value. The relation (12') becomes:

$$\begin{bmatrix} x_M \\ y_M \end{bmatrix} = \begin{bmatrix} x_{A_i} \\ y_{A_i} \end{bmatrix} + \begin{bmatrix} l_1 \cos \theta_{1i} + l_5 \cos \theta_{5i}(\chi_i(s_i)) \\ l_1 \sin \theta_{1i} + l_5 \sin \theta_{5i}(\chi_i(s_i)) \end{bmatrix} - \begin{bmatrix} x_{C_i}^{(6)} \cos \alpha - y_{C_i}^{(6)} \sin \alpha \\ x_{C_i}^{(6)} \sin \alpha + y_{C_i}^{(6)} \cos \alpha \end{bmatrix} \tag{13}$$

The known parameters in Eq. (13) are: manipulators design parameters ($l_1, l_3, l_4, l_5, l_6, l_0$, and gear ratio ρ), fixed joints coordinates (x_{A_i}, y_{A_i}) with respect to the world coordinate system (x_0, y_0), TCP coordinates and orientation (x_M, y_M, α). The unknown parameters in Eq. (13) are the angles θ_{1i} and actuated angles θ_{5i} . Because the values θ_{5i} depend on transmission function $\chi(s)$ of the base mechanism, the strokes s_1, s_2, s_3 are interpolated from the approximately linear variation of the function $\chi = f(\chi(s))$.

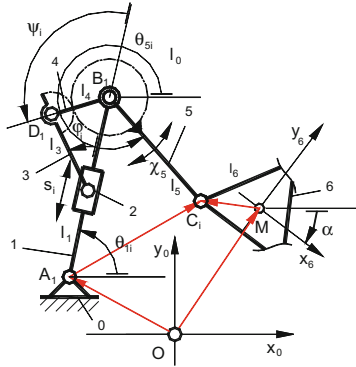


Fig. 4. A single chain kinematic schema R(PRRGR)RR of the novel planar parallel manipulator

Isolating the terms with unknown parameters, the Eq. (13) becomes:

$$\begin{bmatrix} l_1 \cos \theta_{1i} + l_5 \cos \theta_{5i}(\chi_i(s_i)) \\ l_1 \sin \theta_{1i} + l_5 \sin \theta_{5i}(\chi_i(s_i)) \end{bmatrix} = \begin{bmatrix} x_M \\ y_M \end{bmatrix} - \begin{bmatrix} x_{A_i} \\ y_{A_i} \end{bmatrix} + \begin{bmatrix} x_{C_i}^{(6)} \cos \alpha - y_{C_i}^{(6)} \sin \alpha \\ x_{C_i}^{(6)} \sin \alpha + y_{C_i}^{(6)} \cos \alpha \end{bmatrix} \quad i = 1, 2, 3 \quad (14)$$

The unknown angle values θ_{1i} might be eliminated by mathematical operations (square power and addition) and the resulted relation contains only the actuated angles θ_{5i} . The implicit function $F(X, S) = 0$ becomes, relying on the above equation:

$$\begin{aligned} F_i(X, S) &= F_i(x_M, y_M, \alpha, s_1, s_2, s_3) \\ &= \left(x_M + x_{C_i}^{(6)} \cos \alpha - y_{C_i}^{(6)} \sin \alpha - x_{A_i} - l_5 \cos \theta_{5i}(\chi_i(s_i)) \right)^2 + \quad i = 1, 2, 3 \quad (15) \\ &+ \left(y_M + x_{C_i}^{(6)} \sin \alpha + y_{C_i}^{(6)} \cos \alpha - y_{A_i} - l_5 \sin \theta_{5i}(\chi_i(s_i)) \right)^2 - l_1^2 = 0 \end{aligned}$$

where $X = [x_M, y_M, \alpha]$ and $S = [s_1, s_2, s_3]$.

The first singularity cases (the movement of driven element which cause the mobile platform stand-still) of the planar parallel manipulator are determined by the Jacobian matrix condition: $\det(J_s) = A_{3 \times 3} = 0$ and taking into account that $\partial F_i(X, S) / \partial s_j = 0, \quad i \neq j$ the Eq. (16) becomes:

$$\det(J_s) = \frac{\partial F_1(X, S)}{\partial s_1} \cdot \frac{\partial F_2(X, S)}{\partial s_2} \cdot \frac{\partial F_3(X, S)}{\partial s_3} = 0 \quad (16)$$

In conclusion, any term $\partial F_i(X, S) / \partial s_j = 0, \quad i = 1, 2, 3$ determines manipulator first singularity poses, which means:

$$\begin{aligned} \frac{\partial F_i(X, S)}{\partial s_i} = 0 &\Rightarrow \{ [x_M + x_{C_i}^{(6)} \cos \alpha - y_{C_i}^{(6)} \sin \alpha - x_{A_i} - l_5 \cos \theta_{5i}(\chi_i(s_i))] \sin \theta_{5i}(\chi_i(s_i)) - \\ &- [y_M + x_{C_i}^{(6)} \sin \alpha + y_{C_i}^{(6)} \cos \alpha - y_{A_i} - l_5 \sin \theta_{5i}(\chi_i(s_i))] \cos \theta_{5i}(\chi_i(s_i)) \} \cdot \chi_i'(s_i) = 0, \quad (17) \end{aligned}$$

Exploring the x - y - α space, giving corresponding values to the θ_{5i} from the inverse kinematics, the fulfilled condition (17) determines the first singularity poses of manipulator.

The second singularity manipulator configuration (the stand-still of driven element in special positions allow infinitesimal mobile platform movements) is determined by the condition $\det(J_x) = B_{3 \times 3} = 0$. In addition J_x depicts the manipulator workspace boundaries.

$$\frac{\partial F_i(X, S)}{\partial x_M} = 2 \cdot [x_M + x_{C_i}^{(6)} \cos \alpha - y_{C_i}^{(6)} \sin \alpha - x_{A_i} - l_5 \cos \theta_{5i}(\chi_i(s_i))], \quad i = 1, 2, 3 \tag{18}$$

$$\frac{\partial F_i(X, S)}{\partial y_M} = 2 \cdot [y_M + x_{C_i}^{(6)} \sin \alpha + y_{C_i}^{(6)} \cos \alpha - y_{A_i} - l_5 \sin \theta_{5i}(\chi_i(s_i))] \tag{19}$$

$$\begin{aligned} \frac{\partial F_i(X, S)}{\partial \alpha} = & 2 \{ [y_M + x_{C_i}^{(6)} \sin \alpha + y_{C_i}^{(6)} \cos \alpha - y_{A_i} - l_5 \sin \theta_{5i}(\chi_i(s_i))] (x_{C_i}^{(6)} \cos \alpha - y_{C_i}^{(6)} \sin \alpha) \\ & - [x_M + x_{C_i}^{(6)} \cos \alpha - y_{C_i}^{(6)} \sin \alpha - x_{A_i} - l_5 \cos \theta_{5i}(\chi_i(s_i))] (x_{C_i}^{(6)} \sin \alpha + y_{C_i}^{(6)} \cos \alpha) \} \end{aligned} \tag{20}$$

Because the explicit form of the equations expressing the singularities of first and second order is too complicated, it is not indicated in this paper.

5 Example Problem

The equations and relations presented above are applied for a set of numerical values of mechanism elements lengths of the parallel planar manipulation 3-R(PRRGR)RR. The geometrical parameters are presented in Table 1. The criteria of allocating links lengths of the parallel manipulator l_0, l_1, l_2 and l_6 are chosen in order to obtain lower sets of values fulfilling the condition $\det(J_x) = 0$ (singularities of second order). The optimal link lengths of the geared linkages were dimensioned on the criterion of maximizing the angle of driven elements $5, 5', 5''$ with proper values of the transmission angle ($\mu > 30^\circ$) by the slider-crank mechanism.

Table 1. Geometrical parameters of the R(PRRGR)RR manipulator and of the base mechanism

3-R(PRRGR)RR	Dimensions	Base mechanism	Dimensions
Frame platform length (0)	$l_0 = 240$ mm	Element 4 length	$l_4 = 120$ mm
Chain link length (1,1',1'',5,5',5'')	$l_1 = l_5 = 100$ mm	Gear ratio	$\rho = 2$
Mobile platform length (3)	$l_6 = 40$ mm	Initial stroke	$s_0 = 27.5$ mm
Element 3 length	$l_3 = 120$ mm	Maximum stroke	$s_{max} = 46,5$ mm

The absence of zero values for the partial derivatives of each parallel connected actuating kinematic chain (Fig. 5) confirm the supposition that the 3-R(PRRGR)R structure avoids the singularities of first order in the considered range.

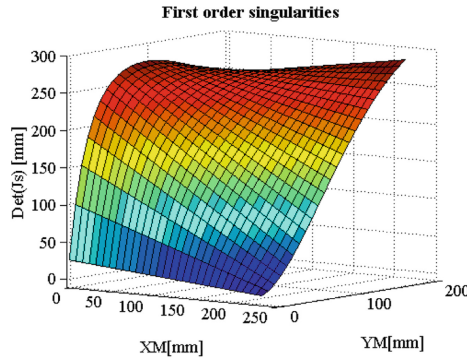


Fig. 5. First order singularities of the 3-R(PRRGR)R manipulator

Figure 6a shows the second order singularities of the 3-R(PRRGR)R manipulator in 3-D view, while the manipulator workspace is a 2D view of the same condition $\det(J_x) = 0$. The results are similar with other studies about planar 3-RRR manipulator.

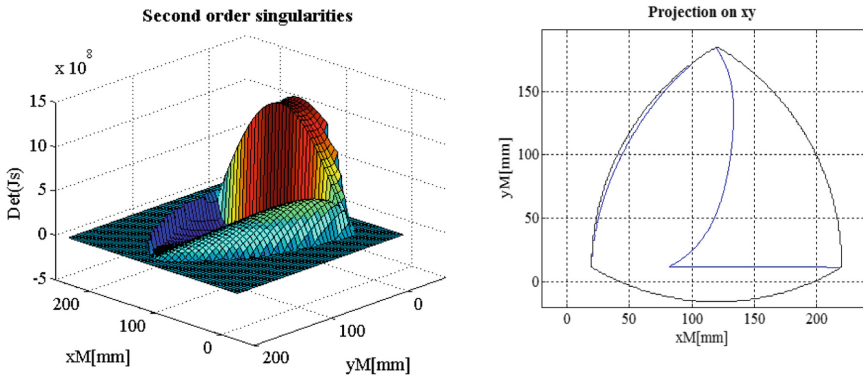


Fig. 6. Second order manipulator singularities in 3D (a) and 2D (b) representation

6 Conclusions

The authors propose a novel solution of a planar parallel manipulator 3-R(PRRGR)RR, which uses a geared slider crank with linear actuation.

The connections kinematic chains are actuated with electrical linear actuators. The oscillation angle forward and backward motion is controlled by means of a geared slider crank with linear actuator.

The analysis of the singularities of the manipulator using geared slider crank with linear actuation avoid the singularities of the first type, describe a large swing angle with optimal transmission angle of the base mechanism by choosing an optimal initial

and maximal stroke. More studies must be dedicated on base mechanism for synthesis problem and collision avoidance between elements sizes.

Further researches will focus on controlling the mobile platform linear and rotational motions, on manipulator dynamic aspects control and other order singularities. More features on motion control must be revealed for optimum pose precision versus application production cycle times.

References

1. Hamdoun, O., El Bakkali, L., Baghli, F.Z.: Analysis and optimum kinematic design of a parallel robot. *Procedia Eng.* **181**, 214–220 (2017)
2. Glazunov, V.A., Filippov, G.S., Rashoyan, G.V., Aleshin, A.K., Shalyukhin, K.A., Skvortsov, S.A., Antonov, A., Terekhova, A.N.: Velocity analysis of a spherical parallel robot. *IOP Conf. Series: J. Phys. Seria* **1260**, 112012 (2019)
3. Artemov, D., Masyuk, V., Orehov, S.Y., Pchelkina, I.V.: 3DoF parallel robot analysis. *IOP Conf. Ser. Mater. Sci. Eng. Seria* **489**, 012052 (2019)
4. Amine, S., Hanna, E.G.: Kinematic analysis of HALF parallel robot. *J. Eng. Sci. Technol. Rev.* **12**(5), 207–213 (2019)
5. Harada, T.: How to Expand the Workspace of Parallel Robots, *Kinematics*, Intech, pp. 95–111 (2017)
6. Gherman, B., Plitea, N., Vaida, C., Pisla, D.: Kinematic modelling of a new 5-DOF (Axis) parallel robot used in brachytherapy. *Appl. Mech. Mater.* **762**, 131–136 (2015)
7. Sajapin, S.N.: Smart parallel robots for massage. *IOP Conf. Series: Mater. Sci. Eng. Seria* **468**, 012028 (2018)
8. Tucan, P., Gherman, B., Major, K., Vaida, C., Major, Z., Plitea, N., Carbone, G., Pisla, D.: Fuzzy logic-based risk assessment of a parallel. *Int. J. Env. Res. Public Health* **17**, 654 (2020)
9. Chalongsongse, S., Chumnanvej, S., Suthakorn, J.: Analysis of Endonasal Endoscopic Transphenoidal (EET) surgery pathway and workspace for path guiding robot design. *Asian J. Surg.* **42**, 814–822 (2019)
10. Alvarez, J., Arceo, J.C., Armenta, C., Lauber, J., Bernal, M.: An extension of computed-torque control for parallel robots in ankle reeducation. *IFAC PapersOnLine* **52–11**, 1–6 (2019)
11. Staicu, S., Shao, Z., Zhang, Z., Tang, X., Wang, L.: Kinematic analysis of the X4 translational-rotational parallel robot. *Int. J. Adv. Robot. Syst.*, 1–12 (2018)
12. Song, X., Zhao, Y., Jin, L., Zhang, P., Chen, C.: Dynamic feed forward control in decoupling space for a four-degree-of-freedom parallel robot. *Int. J. Adv. Robot. Syst.*, 1–10 (2019)
13. Barz, T., Sommer, A., Wilms, T., Neubauer, P., Bournazou, M.N.C.: Adaptive optimal operation of a parallel robotic liquid handling station. *IFAC PapersOnLine* **51–2**, 765–770 (2018)
14. Popov, D., Klimchik, A.: Optimal planar 3RRR robot assembly mode and actuation scheme for machining applications. *IFAC PapersOnLine* **51–11**, 734–739 (2018)
15. Merlet, J.-P.: *Parallel Robots*, 2nd edn. Inria, Sophia-Antipolis, France, Springer (2006)
16. Lovasz, E.-C., Grigorescu, S.M., Mărgineanu, D.T., Gruescu, C.M., Pop, C., Ciupe, V., Maniu, I.: Geared linkages with linear actuation used as kinematic chains of a planar parallel manipulator. *Mech. Mach. Sci.* **31**, 21–31 (2015)
17. Hernandez, A., Ignacio Ibarreche, J.I., Petuya, V., Altuzarra, O.: Structural synthesis of 3-DoF spatial fully parallel manipulators. *Int. J. Adv. Robot. Syst.* **11**, 101, 1–8 (2014)
18. Lovasz, E.-C., Grigorescu, S.-M., Mărgineanu, D.-T., Pop, C., Gruescu, C.-M., Maniu, I.: Kinematics of the planar parallel Manipulator using Geared Linkages with linear Actuation as kinematic Chains 3-R(RPRGR)RR. In: *Proceedings of the 14th IFToMM World Congress*, Taipei, Taiwan (2015)

19. Modler, K.-H., Hollmann, C., Lovasz, E.-C., Perju, D.: Geared linkages with linear displacement actuator used as function generating mechanisms. In: Proceedings of the 11th IFToMM World Congress, Tian Jin, China, pp. 54–1259(2005)
20. Lovasz, E.-C., Modler, K.-H., Pop, C., Mărgineanu, D., Maniu, I.: Type synthesis and analysis of geared linkages with linear actuation. *Mechanika* **24**, 1 (2018)
21. Neumann, R.: Fünfgliedrige Räderkoppel-Schrittgetriebe Aufbau, Synthese, Eigenschaften. T.U. Dresden, German (1987)
22. Buium, F., Duca, C., Leonchi, D.: Problems regarding singularities analysis of a 0/3/3 parallel mechanism. *Appl. Mech. Mater.* **658**, 569–574 (2014)

Teaching and History of Mechanisms



Including the United Nations Sustainable Development Goals in Teaching in Engineering: A Practical Approach

Mikel Diez^(✉), Javier Corral, Asier Zubizarreta, and Charles Pinto

University of the Basque Country UPV/EHU, Leioa, Spain
{mikel.diez,j.corral,asier.zubizarreta,charles.pinto}@ehu.eus

Abstract. Changes carried out by the European Higher Education Area have allowed to design and develop new learning methodologies that focus on students as an active part of the education process. This allows to develop not only technical skills, but also the so-called soft skills. In addition, sustainability has become a key issue in recent years, being Education an important part of it. In this context, a novel educational project, Formula Student Bizkaia, has been proposed as an innovative way to address education in engineering that combines both student-centred learning and sustainability. In this work, the project structure, its motivation and foundations, and its alignment with the UN 2030 Sustainable Development agenda is detailed.

Keywords: Formula student · Sustainability · Project based learning · Teaching methodologies

1 Introduction

The European Higher Education Area (EHEA) [2], which nowadays includes 48 states, was born to fulfil several key goals: cooperation, mobility and opportunity. Since the Bologna declaration in 1999, EHEA members have worked in defining a common framework and tools for the higher education, updating the original goals to adapt them to a changing and demanding labour market.

To ensure competitiveness, European enterprises require workers with not only technical skills, but also the so-called soft skills. In fact, recent studies [11] have demonstrated a correlation between the development of soft skills and employability, as enterprises search for creative, innovative and autonomous workers able to work in changing environments.

However, current Higher Education study programmes do not usually include these skills. Hence, one of the new main goals of the EHEA, as stated in the 2015 Yerevan Ministerial Summit [1] is to promote Student-Centred Learning methodologies. This is, to make students an active part of the education process by providing tools and methodologies to develop technical and soft skills. Project

Based Learning (PBL), Problem Based Learning, Case Study Methods or Cooperative Learning are some of the methodologies proposed for this purpose.

In addition to the required methodology change, Higher Education also faces the need for educating on sustainability. The United Nations defined in 2015 the 2030 Agenda for Sustainable Development [9], where a set of 17 goals were defined to tackle the world's most critical issues, such as poverty, efficiency or climate change. Education was considered a key part of this strategy to develop a sustainable society [10].

In this context, the University of the Basque Country (UPV/EHU) has aligned with the 2030 UN Agenda for Sustainability. A new experimental teaching model named Cooperative and Dynamic Teaching (IKD) [6] was developed in 2010. The new model places the focus on the students as a leading element of their own training process. This also required to define retraining programmes for the teaching staff [13, 15] to help in the design, development and assessment of teaching strategies based on active methodologies such as PBL.

In addition, in 2019, the model was revised to include a third dimension, sustainability, and was named IKDi³ [6]. The new integrated teaching model combines a student-centred learning model aligned with the EHUagenda 2030 for Sustainable Development (2019–2025) [14]. In particular, the 4th Sustainable Development Goal (SDG), *Quality Education* was selected as the main goal for the IKDi³ teaching model, and a whole set of indicators were defined to evaluate its evolution. Moreover, the University of the Basque Country encouraged the creation of novel educational projects in this framework, to further develop the 4th SDG. Among these projects it is worth mentioning the Ocean i3 [8] project, the Law Clinic for Social Justice [7] or the Formula Student Bizkaia project [3].

This work is focused in the latter, the Formula Student Bizkaia project. The project starting point is a challenge to motivate the students: the design and construction of an electric Formula-type single-seater, to compete in inter-university Formula Student events. The challenge is addressed through the PBL methodology and considers not only the development of specific skills in the area of engineering, but also soft skills such as teamwork, leadership, resource management, communication, and sustainability among others.

The rest of the work is organised as follows: in Sect. 2, the context of the project will be detailed; in Sect. 3, the internal structure of the project and its educational model will be defined; Sect. 4 will detail how the UN 2030 Agenda for Sustainable Development has been considered within the project, and finally, the most important ideas will be summarised.

2 Formula Student

The context of Formula Student Bizkaia are the international Formula Student competitions. These define the challenge for the engineering students, which motivate them to improve their skills by means of a friendly competition with other universities.

The use of competitions as teaching tools [12] is not new, but in the engineering area the Formula Student competitions (Fig. 1), whose origin are the

American Formula SAE competitions, present an important differentiating factor: scale. Currently there are 16 official events around the world, eight in Europe, five in America, two in Asia and one in Australia, and more are appearing or aiming to become official each year. In each event, in the span of 5 to 6 days, more than 100 Universities and near 3000 students compete between each other, not only to prove who has designed the best car, but also who has managed to achieve the best engineering project overall.



Fig. 1. Participants in a formula student event

Each competition is divided in three different parts: Scrutineering, Static Events and Dynamic Events, which will be detailed next.

Scrutineering

At scrutineering, students must prove that they have followed the Formula Student ruleset [4,5] to build the car. Here, professional engineers take the role of scrutineers, and check every system of the car to ensure that the car is safe for its use in the track. Students must also show experimental results to justify the properties of the materials used to build the prototype.

Static Events

Static events are one of the most important ones, as they evaluate the engineering practices used to develop the vehicle. In these events, each team is evaluated by judges, which usually are professional engineers. Evaluation is carried out in three different areas: Business Plan, Cost and Sustainability, and Design. In the Business Plan event, students must think a way to make an economic profit of the car. They must design a viable business model, and they must convince the judges, acting as potential investors, that their business is the most profitable and secure one. To prepare it, students must consider every expenditure an actual company has, from labour cost, to marketing and distribution, as well as any income they may have to create a profitable business.

Cost and Sustainability event test students against their knowledge in manufacturing methodologies, design processes and the sustainability of the product

in its whole life cycle. In this event every part of the car is evaluated, and its mass-manufacturing cost justified. The objective of this event is not to create the cheapest vehicle of the competition, but to be able to justify the design choices from an economic and sustainable point of view. Students must learn that when they make design choices, they must consider the expenditures and the processes required for that design.

The final static event is the Design event. Here students defend the design choices they have made to build the car. Students must explain the followed design procedure, justifying the chosen solution against other alternatives. In this event the capacity of the team to justify the design and validate it in simulation and experimentally is also evaluated.

Dynamic Events

On the other hand, dynamic events take place only when the car has been completely certified in the Scrutineering. There are four dynamic events, each evaluating a dynamic capability of the designed vehicle: acceleration, skid-pad (cornering), autocross (fast lap) and endurance. The main event is the endurance, where the designed prototypes must complete 22 km in the least time possible, while consuming the least energy possible. In fact, this event is combined with an efficiency score, which gives extra points to the most efficient vehicles.

In summary, Formula Student competitions allow to evaluate both technical and soft skills. The competition encourages creativity, team working (even with other teams), partnership and networking, while opening to important engineering enterprises that attend to the event searching for future engineers. In addition, one interesting fact of these competitions is that each team is free to structure itself as they think best, with no constraints in the organisation, goals or methodologies to be applied. Therefore, there exist teams with a clear focus on motor-sport, while others focus on education. This variety of options has allowed Formula Student Bizkaia to define an innovative approach, different from other teams.

3 Formula Student Bizkaia: A Company Inside the University

Formula Student Bizkaia was founded in 2006, and after two hard-work years, in 2008, they participated in Formula Student UK 2008 for the first time. Since then, a vehicle has been designed, manufactured and tested each year, with a technological evolution from internal combustion engine vehicles to electric vehicles. Currently, Formula Student Bizkaia has become the largest educational project of the University of the Basque Country, with 4 advisors (teaching staff) and 50 students from different bachelor and master degrees participating each year.

The main goals of the project are:

1. To further enhance the education of students, offering an experience as close as possible to that of an engineering company and focusing on the development of soft skills.

2. To promote the talent of the participating students, their creativity and entrepreneurship.
3. To facilitate the employability of students, through complementary training and a close relationship with local engineering companies.

To achieve these goals, Formula Student Bizkaia project is structured as a real company, and tries to mimic the procedures existing in real engineering enterprises. This way, roles within the company are assigned to each student, standardised protocols and methodologies are used to manage resources, design processes are double-checked with appropriate supervision, and proper coordination and communication protocols are established. It is to be noted that this approach is different to other Formula Student projects.

3.1 Organisational Structure

The organisational structure of Formula Student Bizkaia is shown in Fig. 2. The Faculty Advisors are the lecturers supervising the project. Their role is to guide and provide advice to the team. Hence, they are part of the Management Board, in which strategic decisions are taken. In this board the Team Leader is the main responsible of the project for a given season. This student acts as a company CEO, accounting for both the success or failure of any task or event that is carried out during the season. To manage the team, the Team Leader has a group of assistants, which are also part of the Management Board: the Technical Managers, students in charge of the technical development and manufacture of the car; the Organisation Manager, who must coordinate all the students of the team for the different events and tasks not related to the technical part of the project; and finally the Financial Manager, treasurer of the team and the student who approves or denies any expenditure.

The rest of the team is structured in different working groups, each with a leader. The Group Leader is responsible for coordinating the group, managing its resources and fulfilling the requirements, dates and budget specified by the Management Board. Currently the project is divided in 6 different technical groups: Dynamics group, Chassis group, Aerodynamics group, Powertrain group, Electronics group and Simulation group. An additional Organisation group exist, whose leader is the Organisation Manager, and handles the marketing, event organisation, social media and multimedia areas of the project.

Team Members are the last set of students, which constitute each of the aforementioned groups. Team Members work in the tasks assigned by the Group Leader. In the technical groups, traditionally each member is responsible for a part or element of the vehicle.

3.2 Coordination

Coordination is a key element within the project. Although the organisation structure is pyramidal, communication is horizontal within the proposed structure, using cloud-based technologies and tools for this purpose.

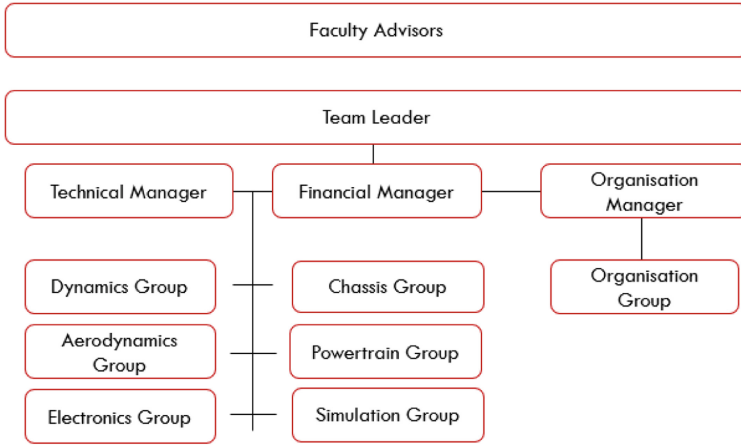


Fig. 2. Formula student Bizkaia team structure

Every week the team coordinates by three meetings at three different levels. The most high level meeting is for the Management Board, focusing on finances, human and material resources, events, and overall strategy.

A Technical meeting is carried out based on the information of the previous meeting, in which the technical development of the vehicle is overseen by the Management Board and all Group Leaders. Every technical decision in these meetings must be correctly justified to be executed. As any company, the team has established standardised protocols for performing purchases, event attending, contacting possible partners, and so on. Hence, if a protocol is not followed, that petition is denied, which can cause the delay of some materials, or the cancellation of an experimental test with the vehicle.

Finally, the technical and organisation decisions taken in the aforementioned two meetings are transmitted to each group in an internal Group Meeting, in which tasks are assigned, petitions are requested and group budget is distributed by the Group Leader.

Each meeting has its own public document with the decisions taken, so that information can flow horizontally. In addition, all team members are encouraged to participate in a meeting to present a proposal.

3.3 Educational Three Year Cycle

Apart from the workflow inside the team, the evolution from year to year is also similar to a company. Formula Student Bizkaia follows the “up or out” policy, in which students gain experience and escalate to roles with higher responsibility. The promotion of a team member to a responsibility role (leader or manager) is proposed by the rest of the team members. In this sense, responsibility, leadership

or team working skills are the typical skills the students choose for their future leaders.

The project is designed so students spend three years in it (see Fig. 3). The first year of a student inside the project is supposed to be a training one. During this period the student is part of a technical group and must learn how to work in the project, and familiarise himself with all the tools, the workflow and the schedule of the season. After the first year, the student must acquire a responsibility role, either as a technical group leader, or at least taking the design and fabrication of a part of the car under supervision. Finally, in the last year, it is supposed that the student has the required skills to assume a higher responsibility role. A third year student must assume either a role in the management team, or a leadership in a technical group.

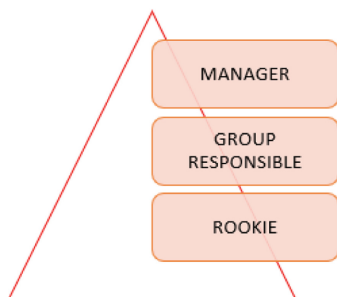


Fig. 3. Evolution of student during a three year stay in the project

This evolution, assuming different roles inside the team allows the student to acquire different skills. Each role provides a different perspective of the project, being more technical in the first years, and evolving to a project management perspective. This provides an important experience in the skills any company seeks for: leadership, handling team problems, budget constraints, technical issues, providers, ...

It is important to notice that the recruitment of the new team members is not carried out directly by the Faculty Advisors. Instead, the Team Leader, the Management Board and the Group Leaders define the specific needs for the current and future season, and handle the selection process of the candidates. This selection process involves a personal interview, in which the technical capabilities and his or her motivations are analysed. Thus, students assume the role of a Human Resources department.

4 Formula Student Bizkaia and Sustainable Development Goals

As stated in the introduction, education has an important role to play in sustainability. In this sense, in 2019, Formula Student Bizkaia was integrated into

the University of the Basque Country's IKDI³ program, with the aim to include this new dimension into the project.

This new focus will allow the students to have better perception and understanding of the finite resources of our planet and that values such as collaboration, equality, critical thinking and social commitment are essential to ensure a future for new generations.

The inclusion of the UN SDG into Formula Student Bizkaia project was carried out by analysing the compromises that the EHUagenda 2030 for Sustainable Development [14] already defined. In this sense, it was observed that due to the magnitude of the project, several training activities already carried out, were aligned with multiple SDG. Specifically, six of the SDGs are addressed through different tasks intrinsic to the project (Fig. 4):

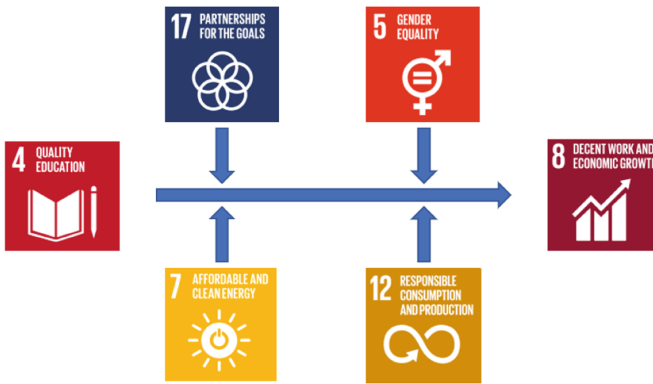


Fig. 4. Synergies between sustainable development goals and formula student Bizkaia

- SDG 4: Quality Education
- SDG 5: Gender Equality
- SDG 7: Affordable and Clean Energy
- SDG 8: Decent Work and Economic Growth
- SDG 12: Responsible Consumption and Production
- SDG 17: Partnerships

Following this consideration, the activities of the project related with the aforementioned SDG have been defined. Due to the academic nature of the project and the given main objective, this is, to facilitate employability of students, a horizontal axis of action has been defined. The project promotes a quality teaching-learning binomial (SDG 4) with a leading role of students, which gives them the skills to obtain a decent and qualified job that leads to economic growth (SDG 8).

As support for this proposal, they undertake vertically, from the base, two SDGs related to the technological and engineering proposal of the project (SDG 7

and SDG 12). Through the challenge of designing, manufacturing and competing with a complex engineering product such as an electric car, a conscience and commitment to the incorporation of the sustainability variable in the design and execution of the project is promoted in the students. This variable is incorporated in the decision making of early aspects such as design to other intermediates, such as manufacturing and, finally, to some of those involved in the final stage of competition (commitment between performance and consumption).

SDG 5 and SDG 17 are based over the aforementioned horizontal main axis. These two represent the character and commitment of the project with institutional and social values. All activities related to the project are carried out with equal opportunity perspective regardless of sex, race, religion or other characteristic. Additionally, the leading role of the participating women is defended and supported to create reference models for the participating students in future editions of the project. Finally, the FSB project can only be understood thanks to the large network of public-private collaborating agents that support it. This fact is a consequence of the proactive and tireless spirit in the materialisation of alliances and strategic collaborations that have ensured their survival since its gestation.

To measure the fulfilment of the SDG described above, 19 different indicators have been developed, measuring not only the different results of the project in the international competitions, but also the implication of the students in the different events that are carried out during the year. Another important proposed indicator group is the opinion of the students involved in the project about the SDG and their development during a season. Finally, social impact of the project is going to be measured by the number of partnerships, the social and diffusion events and the evaluation from the companies of the students that enter the labour market.

5 Conclusions

Innovation in education is sometimes a difficult task, specially in engineering schools, where the number of students makes it difficult to apply dynamic and interactive teaching methodologies. However, projects such as Formula Student allow teachers to develop new methodologies that can enhance the learning process of students. In this paper the Formula Student competitions are used as a challenge to motivate students to design build and test a Formula-type single-seater car. With that motivation, a company alike environment has been developed inside the University, so that students have a close experience to the labour market and the engineering practice. The project has also been aligned with the recent UN 2030 Agenda for Sustainable Development, which has been adopted by the University of the Basque Country in the EHUagenda 2030 (2019–2025) programme. In this context, the project has found that six of the sustainable development goals are addressed through different tasks already developed inside it. Finally, several indicators are presented to measure the project outcome in those SDG.

Acknowledgements. The authors wish to acknowledge the support received by The University of the Basque Country through the IKDi³ program, EUSKOIKER through project EV80025 and its main sponsors, the Diputación Foral de Bizkaia (DFB/BFA), Automotive Intelligence Center (AIC), Alunid, Batz, Bilbao city Council, Davines, Imedusa, Inarak, Ingemat, Sener Aerospace and Tecnalia Corporation, among others.

References

1. 2015 Yerevan Ministerial Conference. <http://ehea.info/cid101764/ministerial-conference-yerevan-2015.html>
2. European Higher Education Area. <http://www.ehea.info/>
3. Formula Student Bizkaia. <https://www.fsbizkaia.com>
4. Formula Student Germany rules. <https://www.formulastudent.de/fsg/rules/>
5. Formula Student IMechE Rules. <https://www.imeche.org/events/formula-student/team-information/rules>
6. IKD Aprendizaje Cooperativo y Dinámico. <https://www.ehu.es/es/web/sae-helaz/ikd>
7. Law Clinic for Social Justice. <https://www.ehu.es/es/web/zuzenbide/gzkj>
8. Ocean i3. <https://euskampus.eus/es/programas/campus-eurorregional/oceans-i3>
9. Transforming our world: the 2030 Agenda for Sustainable Development. <https://sustainabledevelopment.un.org/post2015/transformingourworld>
10. Annan-Diab, F., Molinari, C.: Interdisciplinarity: practical approach to advancing education for sustainability and for the sustainable development goals. *Int. J. Manag. Educ.* **15**(2), 73–83(2017). <https://doi.org/10.1016/j.ijme.2017.03.006>
11. Cinque, M.: “Lost in translation”. Soft skills development in European countries. *Tuning J. High. Educ.* **3**(2), 389 (2016). [https://doi.org/10.18543/tjhe-3\(2\)-2016pp389-427](https://doi.org/10.18543/tjhe-3(2)-2016pp389-427)
12. Gadola, M., Chindamo, D.: Experiential learning in engineering education: the role of student design competitions and a case study. *Int. J. Mech. Eng. Educ.* **47**(1), 3–22 (2019). <https://doi.org/10.1177/0306419017749580>
13. Guisasola, J., Garmendia, M.: El programa ERAGIN de formación en metodologías activas de la UPV/EHU. Aprendizaje basado en problemas, proyectos y casos: diseño e implementación de experiencias en la universidad (2014)
14. University of the Basque Country UPV/EHU: EHUagenda for sustainable development. <https://www.ehu.es/en/web/iraunkortasuna/ehuagenda-2030>
15. University of the Basque Country UPV/EHU: Bases para el desarrollo curricular de las titulaciones oficiales de la UPV/EHU (2010). www.ehu.es/es/web/sae-helaz/ikd-curriculum-garapena-oinarriak



Computer-Assisted Learning Used to Overconstrained Mechanism's Mobility

Simona Mariana Cretu and Ionut Daniel Geonea^(✉)

Faculty of Mechanics, University of Craiova, Craiova, Romania
simonamarianac@yahoo.com, igeonea@yahoo.com

Abstract. The aim of this study is to use within the teaching methodologies the ADAMS software for determining the mobility of the overconstrained mechanisms. Computer-assisted learning helps students to understand and calculate the parameters needed to apply the general structural formula for determining the mobility of overconstrained mechanisms. The paper presents a computerized procedure for determining mobility for mechanisms with one or more independent cycles, with the independent/dependent movements of the end-effector of the kinematic chain associated to a loop.

Keywords: ADAMS software · Overconstrained mechanisms · Mobility · Teaching methodology

1 Introduction

A permanent challenge for teachers is to find optimal methods so that students understand the complex engineering problems. Such complexity is raised by the calculation of the mobility of some overconstrained mechanisms or robots when the general structural formula from Eq. (1) is used; more precisely, for some mechanisms it is difficult to determine the parameter b_j .

$$M = \sum_{i=1}^p f_i - \sum_{j=1}^q b_j - \sum_{k=1}^p f_{passive\ k} \quad (1)$$

where: q is the number of independent kinematic chains, p is the number of joints of mechanism or robot, f_i is the connectivity of joint i , b_j is the mobility number for the loop j , $f_{passive\ k}$ is the number of passive degrees of freedom for the joint k .

Numerous theoretical studies regarding the mechanism mobility calculus have been made by scientists, such as [1–7]. Software packages (such as SolidWorks, Autodesk Inventor, MSC. Adams [8]) are an aid in teaching/learning both analysis and synthesis of mechanisms and robots. Different teaching/learning strategies that integrate computer-assisted design and programming in the analysis and design of mechanisms are presented in many studies, such as [9–17]. But we have not found works related to the computer-assisted teaching of the calculation of overconstrained mechanisms mobility by structural

formula. In [1, 2] a method for calculating the degree of mobility of the overconstrained mechanisms with the structural formula - which is based on the TRIZ inventive method – in detail it has been presented. On the same direction of study is [4], which refers to the computer assisted teaching of this subject; to illustrate the method, the parallel robot Tripteron (Fig. 1) was chosen. The Tripteron is a completely decoupled mechanism, in which the end-effector movements of the open chain associated to a loop are independent.

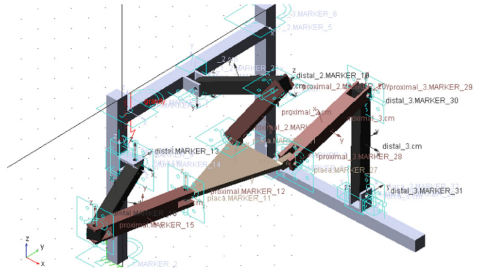


Fig. 1. Tripteron kinematic model with ADAMS/View software

The visual inspection of the movements of the end-effectors of open spatial kinematic chains, in conjunction with the interpretation of the kinematic diagrams offered by the ADAMS software [8], have been shown to facilitate the understanding by the students of the possible movements. The current paper comes to complete the authors' method [4] with the case when the end-effectors have movements dependent on each other. Two applications are treated here, one in which the movements of the end-effector from the open kinematic chain associated with a loop are independent (Sarrus linkage), and the other with movements dependent on each other (the parallelogram mechanism).

2 Problem Description

The strategy presented in works [1, 2] to calculate the mobility of mechanisms using the structural formula (Eq. 1) has the following steps: *a*) the number of independent kinematic chains is determined (q); *b*) the independent closed chains are transformed successively into open chains, by segmentation; *c*) for the final element of each open chain attached to the loops previously analyzed, the number of degrees of freedom is determined (b_j). Both the previous [4] and the present work refer to the computer-assisted teaching/learning to calculate the mobility of the mechanisms with the structural formula, following the written above steps. To solve step *b*), the mechanism is modeled in ADAMS. It is successively considered a closed chain, which is attached to the closed chains analyzed previously, and it is segmented. Since there may be dependent movements of the end-effector, an additional element (cross/double cross element for planar/spatial mechanisms) is inserted between the end-effector and the base. To solve step *c*) we define in ADAMS successively actuators between the end-effector of each open chain, attached to the closed chains analyzed previously and the base, with translational/rotational movements along/around the axes of the global reference system. We

check the possible independent movements by analyzing the kinematic diagrams posted by ADAMS.

The Calculus of Mobility for Sarrus Linkage

Sarrus linkage is an overconstrained mechanism that has six rotational joints. It has a single driving element and transforms a rotational movement into a translational one. The Sarrus linkage it was modelled in ADAMS View software, as is shown in Fig. 2. To calculate the mobility of the mechanism with Eq. (1), we utilize the concept based on the TRIZ method [1–3]. In this mechanism it is one independent kinematic loop ($q = 1$).

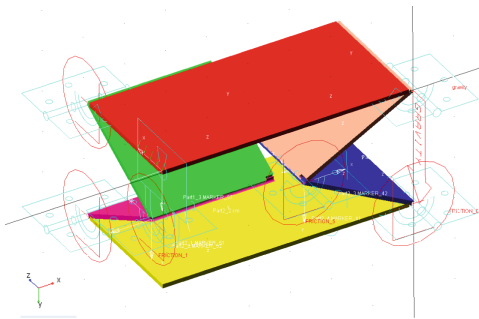


Fig. 2. Kinematic model of Sarrus linkage

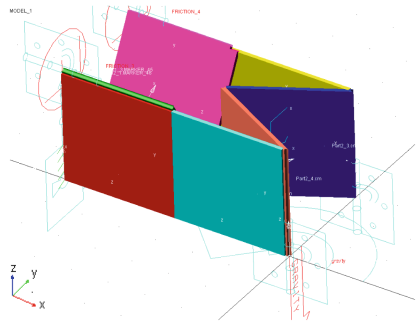


Fig. 3. Kinematic chain associated to Sarrus linkage

We split one element into two parts, and we are modeling in ADAMS the open kinematic chain. In Fig. 3, the open chain is repositioned, and the two parts have different colors (red and light blue), to see the segmentation. We obtain the number of the joints equal to the number of the kinematic elements, 6. Because each pair has one degrees of freedom, $f_i = 1, i = 1 \dots 6$, we write Eq. (2).

$$\sum_{i=1}^6 f_i = 6 \tag{2}$$

The end-effector (the light blue one) connectivity of the open kinematic chain associated to the single loop is 5 ($b_1 = 5$), because the last element has three translations and two rotations (T_x, T_y, T_z, R_x, R_z).

We define successively actuators between the end-effector and the base, with translational/rotational movements along/around the axes of the global reference system and check which independent movements are possible. For a clear view of the end-effector's movements, the friction coefficients in certain kinematic joints will be increased, reducing the movements of certain elements. Snapshots of the mentioned simulations are shown in Figs. 4, 5, 6, 7 and 8.

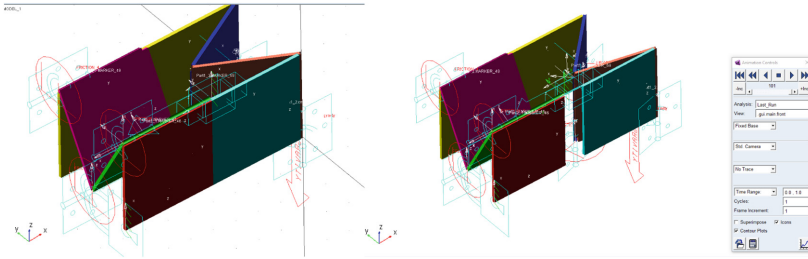


Fig. 4. Translation along X axis

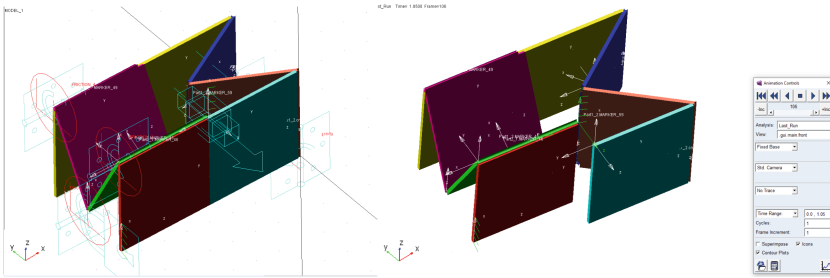


Fig. 5. Translation along Y axis

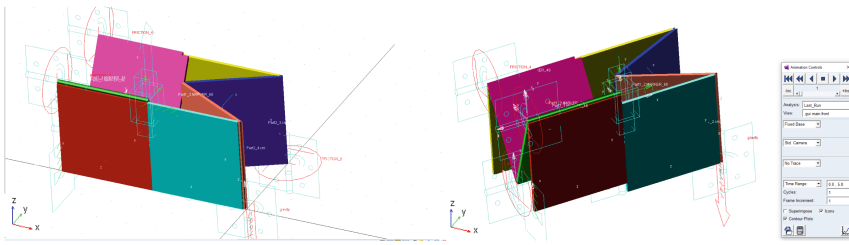


Fig. 6. Translation along Z axis

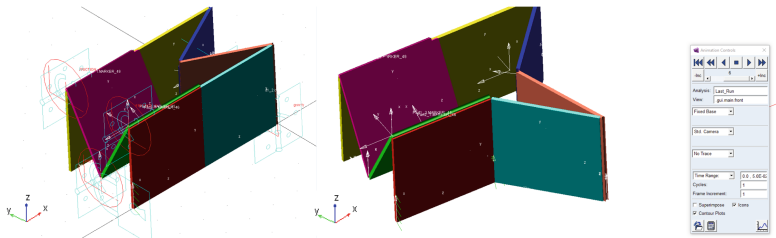


Fig. 7. Rotation around Z axis

Since there is no rotational joint in the kinematic chain with the axis parallel to the Y axis of the reference system, when we define actuator between ground and end-effector with rotation around Y axis, the simulation operation failed, that means this degree of freedom will be missing. In this case the conclusion is obvious, because the missing degree of freedom of the end-effector is a rotational one.

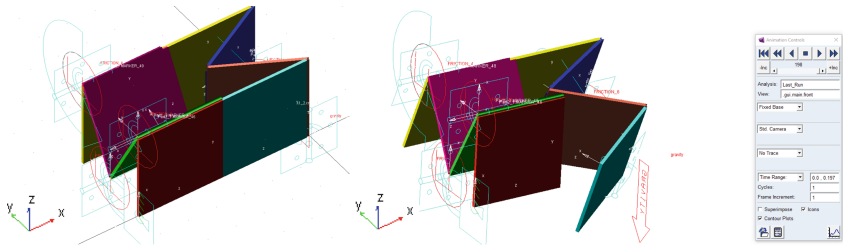


Fig. 8. Rotation around X axis

A more special situation arises if some independent translation movements are missing during simulation. In this case, the conclusion is not obvious, because it is possible that two or three movements are dependent, and they do not appear in the previous simulation. For this, the procedure is adapted as follows: an element is interposed between the end-effector and the base. It has the shape of a cross/double cross for the planar/spatial mechanisms, to allow the dependent effector's movements to be performed, if there are possible. An actuator is put into operation along one of the axes and will be observed visually and in the kinematic diagrams if dependent movements occur and after this the number of degrees of freedom is identified.

The Calculus of Mobility for Parallelogram Mechanism

For the mechanism modeled with ADAMS shown in Fig. 9, whose sides form parallelograms, the calculation of mobility by the segmentation method in detail is presented in works [1] and [3]. For the first independent cycle (Fig. 10) the mobility number is 3. The simulation of the three degrees of freedom of the end-effector in the first cycle is presented in Figs. 11, 12 and 13.

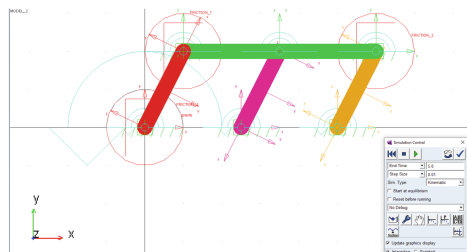


Fig. 9. Parallelogram mechanism modeled with ADAMS

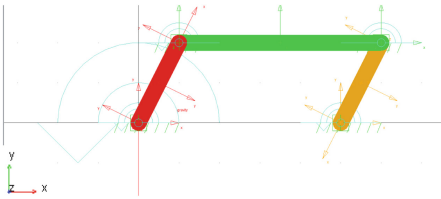


Fig. 10. The first independent cycle

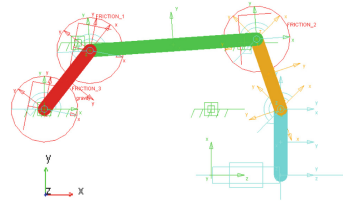


Fig. 11. Translation along X axis

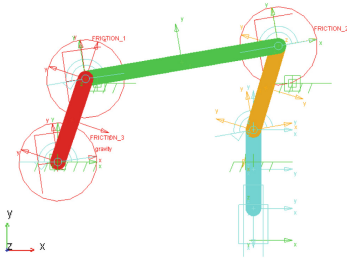


Fig. 12. Translation along Y axis

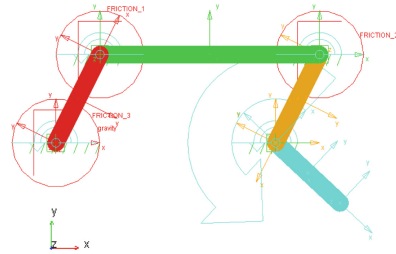


Fig. 13. Rotation around Z axis

For the second cycle (Fig. 14) the mobility number is 2. A rotation around the Z axis will be possible (Fig. 15) and the two independent translations, X (Fig. 16) and Y (Fig. 17), will appear as impossible (for example in Fig. 18).

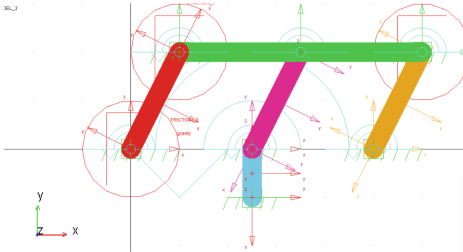


Fig. 14. The second cycle of the mechanism

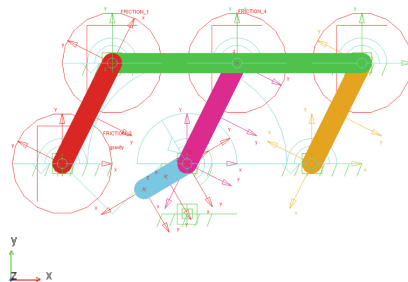


Fig. 15. Rotation around Z axis

To avoid these errors, the cross element was inserted between the end-effector and the base and an actuator was placed along the X axis, between the cross element and the base (Fig. 19). Following the simulation, it is observed visually (Fig. 20), but also in the superimposed kinematic diagrams (Fig. 21), the existence of a degree of freedom and the appearance of two dependent movements, translation along the X and Y axis.

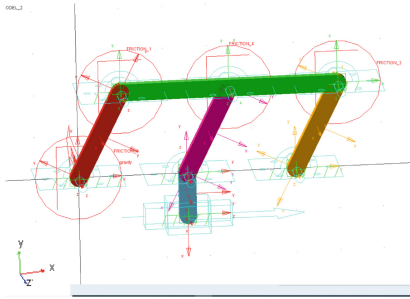


Fig. 16. Translational actuator upon X axis

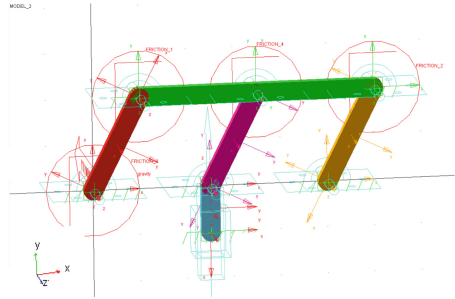


Fig. 17. Translational actuator upon Y axis



Fig. 18. Simulation failure detected by ADAMS

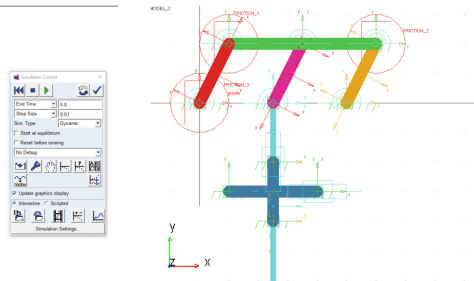


Fig. 19. Translational actuator on X axis

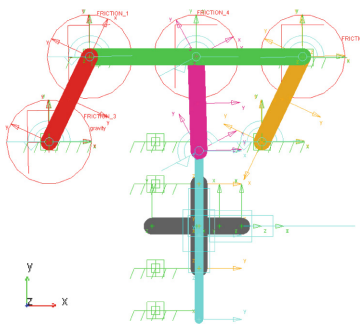


Fig. 20. Motion simulation with cross link

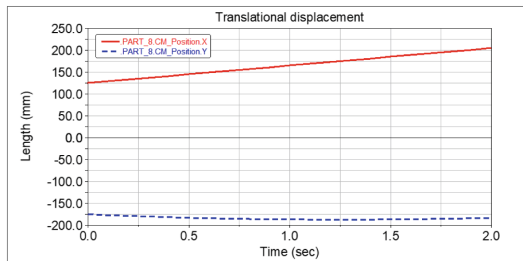


Fig. 21. Superimposed motion results of end-effector

3 Conclusions

The authors use computer-assisted learning/teaching based on the ADAMS software and develop a new teaching method for calculating the mobility of overconstrained mechanisms with a structural formula. The algorithm is based on the closed chain segmentation method, developed on the TRIZ inventive method. The closed chains are successively transformed into some open ones, and all 6 independent movements are imposed on the

end-effectors, setting joints between them and the base. In order to avoid errors due to the existence of dependent movements of the end-effectors, a cross/double cross element for planar/spatial mechanisms is introduced in each open chain. Thus, we determine the correct mobility number for each closed chain. The method is considered very useful in the teaching process, assuring an easy understanding by students of complex processes. This teaching strategy has been used at the Faculty of Mechanics of the University of Craiova since 2019 at the master courses for the optimization of the over-constrained mechanisms. Students have a better understanding of the theoretical principle of the method and can visualize each movement of the end-effector, both independent and dependent. For overconstrained mechanisms with complicated geometry, the method has proven its efficiency one hundred percent.






References

1. Cretu, S.M.: Applications of TRIZ to Mechanisms & Bionics. Academica Greifswald, Rostock (2007)
2. Cretu, S.M.: TRIZ method introduced to the calculation field. *Procedia Eng.* **9**, 500–511 (2011)
3. Cretu, S.M.: Global mobility of mechanisms. In: Wojnarowski, J., Adamiec-Wojcik, I. (eds.) *Theory of Machines and Mechanisms*, EdsBielsko-Biala, Poland, pp. 22–25 (2008)
4. Geonea, I., Cretu, S.M.: Computer graphics used to over constrained mechanisms' mobility. *J. Ind. Des. Eng. Graph.* **14**(1), 289–294 (2019)
5. Gogu, G.: Cebysev-Grubler-Kutzbach's criterion for mobility calculation of multi-loop mechanisms revised via theory of linear transformations. *Eur. J. Mech. A/Solids* **24**(3), 427–444 (2005)
6. Gogu, G.: Mobility of mechanisms: a critical review. *Mech. Mach. Theory* **40**(9), 1068–1097 (2005)
7. Chai, X., Li, Q.: Analytical mobility analysis of Bennett linkage using geometric algebra. *Adv. Appl. Clifford Algebras* **27**(3), 2083–2095 (2017)
8. ADAMS/View Software User Manual (2014)
9. Vereşiu, S., Rus, M., Mereuță E.: Using computer aided design in teaching mechanisms. In: *Mechanisms and Machine Science*, vol. 18. Springer, Cham (2014)
10. Campbell, M., Cheng, H.: Teaching computer-aided mechanism design and analysis using a high-level mechanism toolkit. *Comput. Appl. Eng. Educ.* **15**(4), 277–288 (2007)
11. Dumitru, N., Ploscaru, C., Oțăt, O.: *Mobile Mechanical Systems: Virtual Prototyping and Experimental Analysis*. Universitaria, Craiova, Romania (2018)
12. Tarnita, D., Grigorie, L., Malciu, R.: *Mechanisms. Laboratory Guidance Manual*. Universitaria Publishing House, Craiova (2017)
13. Kurtenbach, S., Prause, I., Weigel, C., Corves, B.: Comparison of geometry software for the analysis in mechanism theory. In: *New Trends in Educational Activity in the Field of Mechanism and Machine Theory*, vol. 19, pp. 193–201. Springer (2014)
14. Chang, K.H.: *Motion Simulation and Mechanism Design with SolidWorks Motion 2019*. SDC publications, Overland Park (2019)
15. Soylemez, E.: Using computer spreadsheets in teaching mechanisms. In: *Proceedings of EUCOMES 2008*, pp. 45–53. Springer (2008)

16. Corves, B.: Computer-aided lectures and exercises: graphical analysis and synthesis in mechanism theory. In: Proceedings of the 11th World Congress in Mechanism and Machine Science, China (2004)
17. Fanghella, P., Berselli, G., Bruzzone, L.: Analytical or computer-aided graphical methods for introductory teaching of mechanism kinematics? In: New Trends in Educational Activity in the Field of Mechanism and Machine Theory, vol. 64, pp. 149–156. Springer (2019)



Petrovaradin Fortress: Clock Tower Mechanism

Dijana Čavić , Maja Čavić , Marko Penčić  , and Milan Rackov 

Faculty of Technical Sciences, University of Novi Sad,
Trg Dositeja Obradovića 6, 21000 Novi Sad, Serbia
{dijana.cavic, scomaja, mpencic, racmil}@uns.ac.rs

Abstract. This paper presents an analysis of the mechanism found in the clock tower of the Petrovaradin Fortress in Novi Sad. The clock mechanism dates back to the beginning of the XVIII century and thus has great historical value. It consists of three interconnected mechanisms – the timing mechanism that keeps time and powers the clock hands, the quarter striking mechanism that sounds the quarter-hours and the full hour striking mechanism that sounds the full hours.

Keywords: History of mechanisms · Petrovaradin fortress · Clock tower mechanism · Timing mechanism · Quarter striking mechanism · Full hour striking mechanism

1 Introduction

The discovery, cataloguing and study of material remnants associated with industrial activities is known as industrial archeology. These remnants are referred to as industrial heritage, and can be buildings, machinery, artifacts, documents and other items used for the extraction, manufacture or transport of products. Industrial archaeology studies the remnants of technology in order to explain and describe the history of past industrial activities. It incorporates research methodology and technological tools from a wide range of disciplines such as history, archaeology, sociology, architecture, engineering, information technologies, etc. [6, 8].

Clock towers today are mostly admired for their aesthetics, but they once served an important purpose – they allowed people to tell time. Clocks were mounted on towers so that the chime could be heard over a long distance. Later, dials were put on the outside of the towers, and the towers themselves were placed near strategic points and were often the tallest structures there so the time could be easily read. Clock mechanisms are very intricate and they generally mark the hour (and sometimes segments of an hour) by striking bells but can also show various astronomical phenomena [10].

This paper presents the clock and its mechanism found in the Petrovaradin Fortress tower in the City of Novi Sad. The clock mechanism dates back to the beginning of the XVIII century, is completely authentic and fully functional, and has huge engineering and historical significance, which is why it attracted our attention. Our goal is to preserve and document the clock mechanism, in cooperation with the Institute for the Protection of Cultural Monuments of the City of Novi Sad.

2 History of Time Measurement

Timekeeping has been done in different ways throughout history. The oldest solar clock that makes use of rulers dates back to ancient Egypt [11]. Aside from this, Egyptian obelisks showed the time over four millennia ago in front of the temple of Heliopolis [2]. Water clocks or clepsydrae, were commonly used in ancient Greece and Rome [7]. In the Middle Ages, the length of the hour and the day was not absolute. From dawn to sunset the time always lasted for twelve hours, regardless of the time of the year. The first mechanical clock was made in the X century, but the timescale of today was not universally accepted until the XIV century [4]. The oldest known clock mechanism tailored to the equinox system was made in Milan in 1336 [12]. These clocks were all powered by weights and had only one clock hand. The first clock featuring a pendulum was created in the XVII century – Christiaan Huygens is usually credited as the inventor. Anchor escapement was designed in 1670 by William Clement. A second hand showing the minutes was introduced to clock design by Daniel Quare. In 1675, the spiral balance or the hairspring, which controls the oscillating speed of the balance wheel was invented and this allowed the miniaturization of the mechanism – accurate pocket watches [3].

3 Petrovaradin Fortress and Clock Tower

The Petrovaradin Fortress is located in Novi Sad, in Vojvodina, an autonomous province of the Republic of Serbia. It looms over the Danube river, on its right bank, overlooking the small town of Petrovaradin – Fig. 1(a). The Petrovaradin Fortress was built over a period of years, spanning from 1692 to 1780. The mind behind it was Sébastien Le Prestre de Vauban, a French military leader, architect and author that lived during the reign of Louis the IV. His idea was used as a template for an array of fortresses, including the Petrovaradin Fortress, which was named the “Gibraltar of the Danube” due to its strategic position and significance. Although it was an important military stronghold for most of its existence, today the Petrovaradin Fortress is considered a culturally and historically significant symbol of Vojvodina, as well as a major tourist attraction in this part of Europe [1].

Due to its unique position, shape and purpose, the clock tower – Fig. 1(b), is the most recognizable structure of the complex, and is frequently used as a trademark symbol for not only the Petrovaradin Fortress, but for the City of Novi Sad as well. The clock tower was raised on the northern rampart of the Upper Ludwig bastion, on the Upper Fortress. The original clock mechanism dates back to the beginning of the XVIII century, specifically the year 1702, as it is inscribed on the pendulum of the clock mechanism. However, also inscribed on the pendulum, but in a smaller font, are the years 1790, 1837, 1941 and 1952. Based on available historical sources, the clock mechanism originates from Alsace, and was a gift from Maria Theresa to the garrison stationed at the Petrovaradin Fortress. Circular clock-faces, which measure approximately 3 m in diameter, are placed on each of the four sides of the tower. What makes them unique is that the longer clock hand shows the hour and the shorter one shows the minute. It was created as such so that people working on the Danube river could see the time from a long distance – it is known as the “reversed clock”. Also, the guard shift change happened on the full hour,

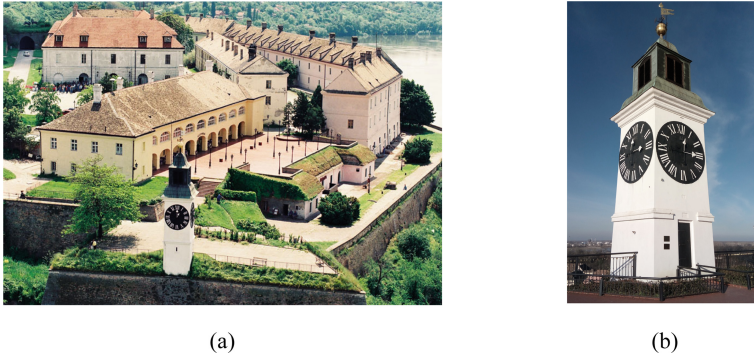


Fig. 1. Petrovaradin fortress in Novi Sad, AP Vojvodina, Serbia (a) and Clock tower (b)

so the minutes were not as significant. The clock hands have been kept as such to this day, since they were and still are considered a historical curiosity [5].

4 Clock Tower Mechanism

Available information about the Clock tower can be found in several publications [1, 5, 9]. However, almost no written data was found regarding the clock technology, operation or mechanical properties. Because of the lack of documentation, we performed a field survey to analyze the mechanism design and functional parameters, taking photographs, video material of the clock operation.

Figure 2 shows the clock tower mechanism, which consists of three interconnected mechanisms: the timing mechanism, tasked with timekeeping and control of the hour and minute hands – Fig. 2(a), the quarter striking mechanism, tasked with sounding on the quarter-hour – Fig. 2(b), and the full hour striking mechanism, tasked with sounding on every full hour – Fig. 2(c). The clock is placed in a birdcage – a side-by-side type of frame. The frame, and many of the mechanism parts were made from iron or bronze using blacksmithing tools, like rasps and files. All the bearings carrying the shafts were made from square-cross section tubes. The mechanisms were wound daily by hand up until 2016, when reconstruction efforts were undertaken and the winding process was made automatic through the use of electromotors.

4.1 Timing Mechanism

Figure 3 shows a simplified kinematic scheme of the timing mechanism. Gear G_1 and drum D_1 are fixed to shaft S_1 , and the drum can be set in motion by way of the potential energy of a weight W_1 . Gear G_1 meshes with gear G_2 . The gears G_2 , G_3 and G_4 are fixed to shaft S_2 . Gear G_3 meshes with gear G_5 , and gear G_4 with gear G_6 . Gear G_5 and a specially designed escapement wheel E are fixed to shaft S_3 . The escapement wheel E meshes with an anchor A . The anchor A and pendulum P , of which the length is adjustable, are fixed to shaft S_4 . Gears G_6 and G_7 are fixed to shaft S_5 , and they rotate with a rate of 1 rph (rotation per hour). Two identical gears G_8 and G_9 are fixed to

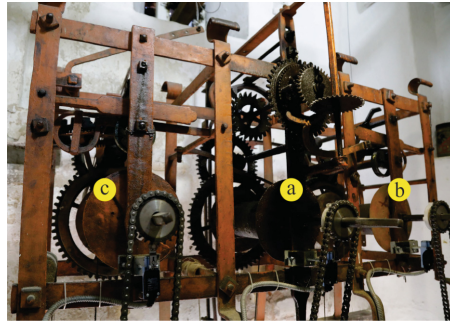


Fig. 2. Clock tower mechanism: (a) timing mechanism, (b) quarter striking mechanism and (c) full hour striking mechanism

shaft S_6 . Gear G_7 meshes with gear G_8 , with a transmission ratio equal to 1. Gear G_9 meshes with 4 identical gears G_{10} , with a transmission ratio also equal to 1. The identical gears G_{10} are fixed to four identical shafts S_7 , with each shaft individually powering a clock hand mechanism. The clock hand mechanism consists of two gear pairs G_{11}, G_{12} and G_{13}, G_{14} with a total transmission ratio equal to 12. Shaft S_7 powers the smaller minute clock hand, while gear G_{14} powers the larger hour clock hand. Gear G_6 houses four lifting pins LP_1 , which make contact with the lifting lever LL_1 every 15 min, on the quarter-hour; they slide along the lifting lever LL_1 and push it downwards, which activates the quarter striking mechanism.

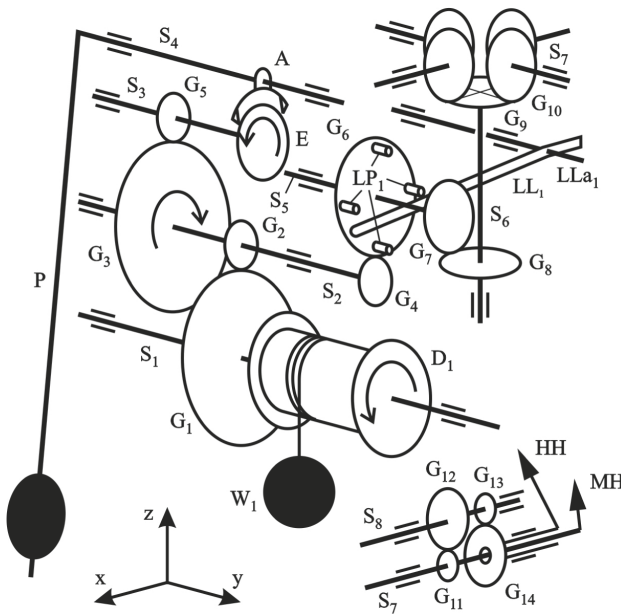


Fig. 3. Timing mechanism – simplified kinematic scheme

4.2 Quarter Striking Mechanism

Figure 4 shows a simplified kinematic scheme of the quarter striking mechanism. On the right end of the lifting lever LL_1 is a protrusion, called the lifting lever tooth LLT_1 – the point of contact with the cam lever CaL_1 . This cam lever has a tooth that enters a groove on the cam Ca_1 . The cam and counting levers (CaL_1 and CoL_1 , respectively) are fixed to each other and can rotate about a horizontal axis a_1 . The counting lever CoL_1 engages a notch on the counting wheel CW_1 , which has four equal notches and four ridges of unequal lengths. The ridge length ratio is 1:2:3:4. The counting wheel CW_1 is fixed to gear G_{15} by the striking pins SP_1 . Gear G_{15} , the counting wheel CW_1 and a drum D_2 are fixed to shaft S_9 , and the drum can be set in motion by way of the potential energy of a weight W_2 . The striking pins SP_1 periodically engage the striking lever SL_1 , which can rotate about a horizontal axis SLa_1 . An interaction between a striking pin SP_1 and the striking lever SL_1 causes this lever to rotate for a predetermined angle, which activates the hammer that then strikes the bell once, causing a single chime. Gears G_{16} and G_{17} are fixed to one end of shaft S_{10} , and cam Ca_1 is fixed on the other end. Gear G_{17} meshes with gear G_{18} . In addition, gear G_{18} , a fan F_1 and a warning wheel WW_1 , containing two warning pins WP_1 placed opposite one another, are fixed to shaft S_{11} .

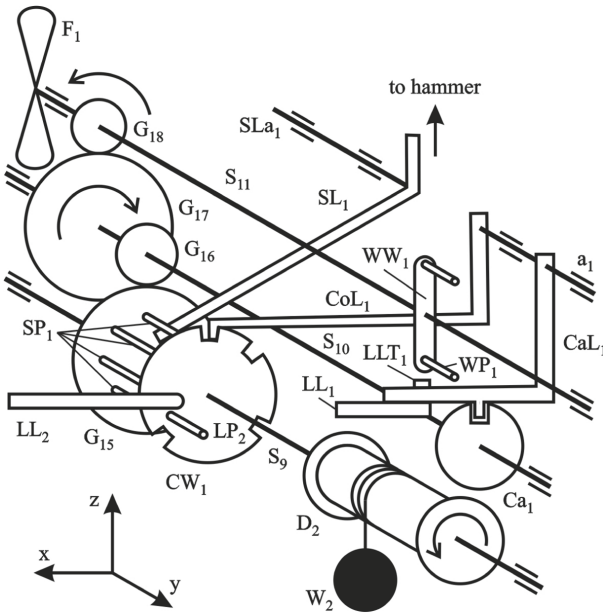


Fig. 4. Quarter striking mechanism – simplified kinematic scheme

When the mechanism approaches a quarter-hour, a lifting pin LP_1 engages the left end of the lifting lever LL_1 , pushing the lever downwards – see Fig. 3, which causes the opposite end of the lifting lever LL_1 to rise – see Fig. 4. Due to this, the lifting lever LL_1 lifts the cam lever CaL_1 and the counting lever CoL_1 . When the cam lever CaL_1 is

raised enough for the tooth to disengage from the notch on the cam Ca_1 , the mechanism is no longer locked in place, allowing the weight W_2 to start its descent and activate the rest of the mechanism. The fan F has two large blades that, when the fan spins, generate drag, thus controlling the speed of the quarter striking mechanism. The warning wheel WW_1 rotates as well, but it can only make a half-rotation before the warning pin WP_1 engages the lifting lever tooth LLT_1 , which stops the mechanism. The mechanism is now cocked and ready to start the bell striking process. It should be noted that the cam Ca_1 and the counting wheel CW_1 have been rotated as well.

On the full quarter-hour, the lifting pin LP_1 and lifting lever LL_1 disengage, causing the lifting lever LL_1 to descend, and with it the cam and counting levers (CaL_1 and CoL_1 , respectively) as well. Since the counting wheel CW_1 is now in a new position, the counting lever CoL_1 engages a ridge, instead of a notch, and slides along it. Due to this, the cam lever CaL_1 cannot descend enough for the tooth to engage the notch on the cam Ca_1 or the surface of the cam itself, so the cam Ca_1 rotates freely, allowing the mechanism to remain in motion. Every interaction between the striking lever SL_1 and a striking pin SP_1 causes a single strike to the bell. The mechanism stays in motion as long as the counting lever CoL_1 is sliding along the ridge on the counting wheel CW_1 . When the counting lever CoL_1 engages the next notch, both the counting and the cam levers (CoL_1 and CaL_1 , respectively) fully descend. This causes the tooth on the cam lever CaL_1 to engage the notch on the cam Ca_1 , thus stopping the mechanism and locking it in place. When the mechanism finishes sounding the final quarter-hour – a total of four strikes to the bell, lifting pin LP_2 engages a second lifting lever LL_2 , sliding along its surface and pushing the lifting lever LL_2 downwards, thus activating the full hour striking mechanism.

4.3 Full Hour Striking Mechanism

Figure 5 shows a simplified kinematic scheme of the full hour striking mechanism. A lifting lever LL_2 can rotate about a horizontal axis LLa_2 . On the left side of the lifting lever LL_2 is the lifting lever tooth LLT_2 , the point of contact with the cam lever CaL_2 . The cam lever CaL_2 has a tooth that engages a notch on a cam Ca_2 . The cam and counting levers (CaL_2 and CoL_2 , respectively) are fixed to each other and can rotate about a horizontal axis a_2 . The counting lever CoL_2 engages a notch on the counting wheel CW_2 , which has 12 equal notches and 12 ridges of unequal length. The ridge length ratio is 1:2:3:4:5:6:7:8:9:10:11:12. On the opposite face of the counting wheel CW_2 are gear teeth that form a worm gear WG . The counting wheel CW_2 is fixed to vertical shaft S_{15} . Gear G_{19} and a drum are fixed to shaft S_{12} , and the drum can be set in motion by way of the potential energy of a weight W_3 . Gear G_{19} meshes with gear G_{20} . In addition, gears G_{20} and G_{21} , a cam Ca_2 and a worm Wo are fixed to shaft S_{13} . The worm Wo meshes with the worm gear WG on the back of the counting wheel CW_2 . Striking pins SP_2 are fixed to the face of gear G_{19} , which periodically engage a striking lever SL_2 that can rotate about a horizontal axis SLa_2 . Each interaction between a striking pin SP_2 and the striking lever SL_2 , causes the striking lever to rotate and activate a hammer, which strikes the bell a single time. Gear G_{21} meshes with gear G_{22} . In addition, gear G_{22} , a fan F_2 and a warning wheel WW_2 containing two warning pins WP_2 placed opposite one another, are fixed to shaft S_{14} .

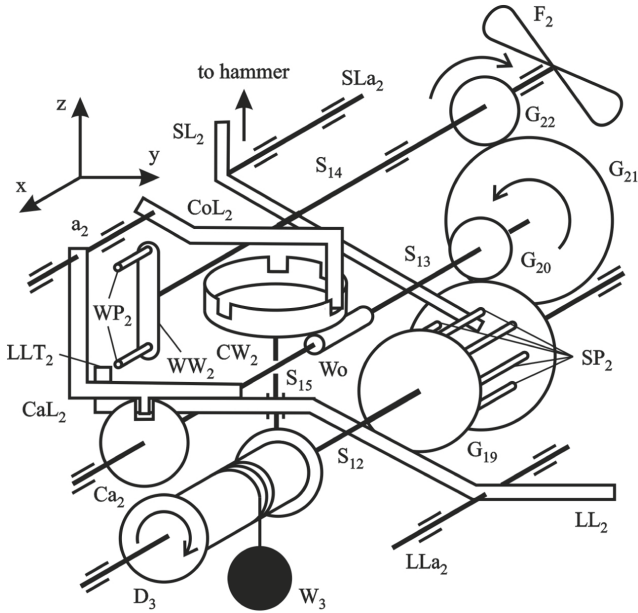


Fig. 5. Full hour striking mechanism – simplified kinematic scheme

When the mechanism finishes sounding the final quarter-hour – a total of four strikes to the bell, a lifting pin LP_2 – see Fig. 4, pushes the right end of the lifting lever LL_2 downwards – see Fig 5. This causes the left end of the lifting lever LL_2 to rise, raising the cam and counting levers (CaL_2 and CoL_2 , respectively). When the tooth of the cam lever CaL_2 disengages the notch in the cam Ca_2 , the mechanism is no longer locked in place and the weight can begin its descent. The fan F_2 has two large blades which, when it spins, generate drag thus controlling the speed of the full hour striking mechanism. The warning wheel WW_2 rotates as well, but it can only make a half-rotation before the warning pin WP_2 engages the lifting lever tooth LLT_2 , which stops the mechanism. The mechanism is now cocked and ready to start the bell striking process. It should be noted that the cam Ca_2 and the counting wheel CW_2 have been rotated as well.

When the lifting pin LP_2 and lifting lever LL_2 disengage, the lifting lever LL_2 descends, and with it the cam and counting levers (CaL_2 and CoL_2 , respectively) as well. Since the counting wheel CW_2 is now in a new position, the counting lever CoL_2 engages a ridge, instead of a notch, and slides along it. Due to this, the cam lever CaL_2 cannot descend enough for the tooth to engage the notch on the cam Ca_2 or the surface of the cam itself, so the cam Ca_2 rotates freely, allowing the mechanism to remain in motion. Every interaction between the striking lever SL_2 and a striking pin SP_2 causes a single strike to the bell. The mechanism stays in motion as long as the counting lever CoL_2 is sliding along the ridge on the counting wheel CW_2 . When the counting lever CoL_2 engages the next notch, both the counting and the cam levers (CoL_2 and CaL_2 , respectively) fully descend. This causes the tooth on the cam lever CaL_2 to engage the notch on the cam Ca_2 , thus stopping the mechanism and locking it in place.

5 Conclusion

The paper presents the clock tower mechanism of the Petrovaradin Fortress. The clock tower is the most recognizable structure of the fortress complex and is considered a symbol of both, the Petrovaradin Fortress and the City of Novi Sad. The clock mechanism was made in the beginning of the XVIII century and due to this has great historical value. The goal of this paper is to document, preserve and restore the clock tower mechanism. The first activity of this kind was done in 2013, when the tower building was restored and the mechanism serviced, and again in 2016, when efforts were undergone to update the electrical network and the hand winding mechanism was replaced with an automatic system powered by electromotors. Information regarding the construction and functional parameters of the mechanism was collected, as well as many photographs and videos that show how the mechanism works. In the future, a 3D model of the mechanism, as well as detailed technical documentation will be made, which will be the base of future research focusing on the kinematic and dynamic behavior of the clock mechanism.

Acknowledgements. This research project was made possible largely due to mister Lajoš Lukači, who has been the devoted caretaker of the clock tower mechanism for over 30 years. Also, the authors would like to extend their gratitude to Institute for the Protection of Cultural Monuments of the City of Novi Sad for providing accurate and plentiful information from their archives.

References

1. Palmer, M., Neaverson, P.: *Industrial Archaeology: Principles and Practice*. Routledge, New York (1998)
2. Hudson, K.: *Industrial Archaeology*. Thames, London (1964)
3. Rafael, L.G., Iván, D.R., Rubén, D.V.: The historical-technological study of monumental tower clocks: the town hall clock of Alcalá la Real, Jaén (Spain). In: Koetsier, T., Ceccarelli, M. (eds.) *Explorations in the History of Machines and Mechanisms: HMM 2012, HMMS*, vol. 15, pp. 293–307. Springer, Dordrecht (2012)
4. ScienceDaily.: One of world's oldest sun dial dug up in Kings' Valley, Upper Egypt. Universität Basel, Basel (2013). <https://www.sciencedaily.com/releases/2013/03/130314085052.htm>
5. Bruton, E.: *The History of Clocks and Watches*. Crescent, New York (1982)
6. Humphrey, J.W., Oleson, J.P., Sherwood, A.N.: *Greek and Roman Technology: A Sourcebook*. Routledge, New York (1998)
7. Dohrn-van Rossum, G., Dohrn, G.: *History of the Hour: Clocks and Modern Temporal Orders*. University of Chicago Press, Chicago (1996)
8. Vincent, C., Leopold, J.H., Sullivan, E.: *European Clocks and Watches: In the Metropolitan Museum of Art*. Metropolitan Museum of Art, New York (2016)
9. Davies, E.: *Inventions (Pockets)*. Dorling Kindersley Ltd., London (1995)
10. Babić, S.: *Petrovaradin Fortress Clock Tower*. The Institute for the Protection of Cultural Monuments of the City of Novi Sad, Novi Sad (2020). (in Serbian)
11. Gajić, R.: *Petrovaradin Fortress: Gibraltar on the Danube*. Krovovi, Sremski Karlovci (1993). (in Serbian)
12. Popov, D.: *Encyclopedia of Novi Sad*. Prometej, Novi Sad (1990–2010). (in Serbian)

Author Index

A

Al Hajjar, Nadim, 206
Alaci, Stelian, 297
Alexandru, Catalin, 297
Ambrósio, Jorge, 405
Angeles, Jorge, 305
Antal, Tiberiu Alexandru, 272
Aoustin, Yannick, 349

B

Banica, Alexandru, 155
Bîrle, Lorin, 123
Birlescu, Iosif, 155, 189
Böhm, V., 470
Bolboaca, Sorana D., 206
Bordure, Philippe, 181
Brişan, Cornel, 169
Bruns, Michael, 397
Burz, Alin, 189

C

Cabello, Mario, 281
Cao, Benjamin-Hieu, 488
Capalbo, Cristian Enrico, 115
Carbone, Giuseppe, 115, 131, 155, 339, 432
Caro, Stéphane, 440
Caroleo, Giammarco, 115
Caso, Enrique, 256
Čavić, Dijana, 528
Čavić, Maja, 528
Ceccarelli, Marco, 115
Cenitagoya, Aitor, 281
Chablat, Damien, 181
Chavez-Vega, J.-H., 470
Chevallereau, Christine, 349

Chircan, Eliza, 479
Chiroiu, Veturia, 169
Choudhury, Rutupurna, 103
Ciocan, Andra, 206
Ciornei, Florina-Carmen, 297
Condurache, Daniel, 48
Corral, Javier, 509
Corves, Burkhard, 314
Covaciu, Florin, 131
Cretu, Simona Mariana, 519
Cuadrado, Javier, 281

D

Dalibard, Sébastien, 349
Dede, Mehmet İsmet Can, 381
de-Juan, Ana, 265
Deng, Jiaming, 3
Diez, Mikel, 509
Diez-Ibarbia, Alberto, 256
Dong, Huimin, 239
Dopico, Daniel, 281
Doroftei, Ioan, 297
Dosaev, Marat, 198, 413
Dragne, Ciprian, 169
Dubrovin, Grigory, 138
Dumitru, Nicolae, 146

E

Elisei, Radu, 206
Ennemark, Poul, 397

F

Fabritius, Marc, 423
Falkenstein, Jens, 397
Feldmeier, T., 470

Fernandez-del-Rincon, Alfonso, 256, 265
 Flores, Paulo, 405
 Florian, Vlad, 219
 Flügge, Wilko, 86
 Forbes, James Richard, 305
 Froitzheim, Pascal, 86
 Fulea, Mircea, 78
 Furet, Matthieu, 459

G

Garcia Morales, Ditzia Susana, 488
 Garcia, Pablo, 256
 Geonea, Ionut Daniel, 519
 Georgescu, Marius, 146
 Gherman, Bogdan, 131, 189, 339
 Görgülü, İbrahimcan, 41
 Goryacheva, Irina, 198
 Gössner, Stefan, 28
 Graur, Florin, 206
 Grigorescu, Sanda Margareta, 496

H

Hajjar, Nadim Al, 219
 Handreg, Tobias, 86
 Hayes, M. John D., 19
 Henning, S., 470
 Hildebrandt, Erik, 86
 Hsiao, Cheng-Hao, 198
 Huang, Chih-Yuan, 198
 Hüsing, Mathias, 314

I

Ianoși-Andreeva-Dimitrova, Alexandru, 123
 Ibrahim, Serhat, 488
 Iglesias, Miguel, 265
 Ingalls, Colin, 19
 Ioan, Rodica, 169
 Irimescu, Luminita, 297

J

Jha, Ranjan, 181
 Ji, Hao, 3
 Ju, Ming-Shaung, 198

K

Kalouguine, Anne, 349
 Kapilavai, Aditya, 56
 Karel, Petr, 95
 Kiper, Gökhan, 41
 Klimina, Liubov, 413
 Koga, Tomoko, 11
 Koyanagi, Shunta, 11
 Krusborg, Jørgen, 322, 397

Küçükoğlu, Sefa Furkan, 41
 Kuprianoff, Kirill, 451

L

Lapteva, Margarita, 389
 Li, Ju, 35
 Lovasz, Erwin-Christian, 496
 Luchian, Iosif, 339
 Lupuți, Antonio-Marius-Flavius, 496

M

Magalhães, Hugo, 405
 Malyshev, Dmitry, 138
 Mândru, Dan Silviu, 123
 Maniu, Inocentiu, 496
 Marita, Tiberiu, 219
 Marques, Filip, 405
 Masterova, Anna, 413
 Merlet, Jean-Pierre, 440
 Michel, Guillaume, 181
 Mitrea, Delia, 219
 Mitrea, Paulina, 219
 Mobedi, Emir, 381
 Mocan, Bogdan, 78
 Mohan, Santhakumar, 103, 138
 Mois, Emil I., 206
 Morales-Cruz, Cuauhtémoc, 115
 Müller, Andreas, 289
 Munteanu, Ligia, 169
 Muralidharan, Vimallesh, 459
 Murar, Mircea, 78

N

Nawratil, Georg, 56
 Neamt, Gabriel Mihai, 219
 Nedevschi, Sergiu, 219
 Nozdracheva, Anna, 138

O

Ondrášek, Jiří, 95
 Ordiz, Manuel, 281

P

Patcas, Razvan, 78
 Păun, Marius, 479
 Pedrero, José I., 231
 Penčić, Marko, 528
 Pfüner, Martin, 19
 Pinto, Charles, 509
 Pisla, Adrian, 131, 155
 Pisla, Doina, 131, 155, 189, 339, 432
 Pleguezuelos, Miguel, 231
 Plitea, Nicolae, 339

Pombo, Joao, 405
 Pop, Nicoleta, 155, 432
 Pott, Andreas, 423
 Prokurat, Gleb, 389

R

Raatz, Annika, 488
 Rackov, Milan, 528
 Radu, Corina, 206, 219
 Raghavan, Madhusudan, 363
 Retolaza, Iban, 281
 Roșca, Ioan Calin, 479
 Rotzoll, Mirja, 19
 Rugină, Cristian, 169
 Rybak, Larisa, 103, 138

S

Samsonov, Vitaly, 413
 Sánchez, Miryam B., 231
 Sanchez-Espiga, Javier, 256, 265
 Sato, Taichi, 11
 Sayar, Erdi, 67
 Schmidt, Thomas, 322, 397
 Schorr, P., 470
 Schröder, Ingomar, 322
 Schütz, Ludger, 397
 Scutaru, Maria Luminita, 479
 Selyutskiy, Yury, 198, 413
 Shen, Huiping, 3, 35
 Shutova, Christina, 451
 Socaciu, Mihai, 219
 Stan, A. Florentin, 169
 Stănescu, Nicolae-Doru, 169
 Stefanescu, Horia, 219
 Steopan, Mihai, 78
 Sun, Qi, 305
 Sunilkumar, Parvathi, 103

T

Tachkov, Alexander, 370
 Tarnita, Daniela, 146

Tarnita, Danut-Nicolae, 146
 Timoftei, Sanda, 219
 Titov, Alexander, 389
 Tucan, Paul, 155, 189, 339

U

Ulinici, Ionut, 155, 189, 432

V

Vaida, Calin, 155, 206, 339
 van der Wijk, Volkert, 331
 Vancea, Flaviu, 219
 Venkateswaran, Swaminath, 181
 Viadero, Fernando, 265
 Villegas, Claudio, 314
 Vlase, Sorin, 479
 Vukolov, Andrei, 370, 389, 451

W

Wang, Delun, 239
 Wenger, Philippe, 459
 Woernle, Christoph, 86, 322
 Wu, Guanglei, 3, 35

X

Xu, Qing, 35

Y

Yakovenko, Anastasia, 198
 Yang, Ting-li, 35
 Yeh, Chien-Hsien, 198

Z

Zentner, L., 470
 Zhang, Chu, 239
 Zhang, Xiao, 247
 Zhao, Xuefei, 239
 Zhao, Yaping, 247
 Zimmermann, K., 470
 Zubizarreta, Asier, 509